

**PROCEEDINGS
OF THE**

**ARCTIC OCEANOGRAPHY
CONFERENCE & WORKSHOP**

JUNE 11 - 14, 1985



Sponsored
By

**Naval Ocean Research
And Development Activity,
And
Commander, Naval Oceanography
Command**

REQUESTS FOR RELEASE OF ARCTIC OCEANOGRAPHY CONFERENCE DOCUMENTS

To reduce the risk of undesired transfer of classified and technical data, certain papers that were presented at the Arctic Oceanography Workshop and Conference will be disseminated only when a "need-to-know" has been established. The following form letter provides the minimum information required by this command prior to release of a document. Each request will be handled on a case-by-case basis.

REFERENCE _____

DATE _____

From: _____

To : Naval Ocean Research and Development Activity, NSTL, Ms. 39529

SUBJ: REQUEST FOR RELEASE OF ARCTIC OCEANOGRAPHY CONFERENCE DOCUMENT

1. It is requested that this organization be provided with _____
Describe Documents in full
2. This request is based on the following "need-to-know" requirement _____
_____.
3. Facility clearance information: _____
(Clearance Level)
4. Facility point-of-contact: _____
(Name) (Telephone No.)

Signature

Title



DEPARTMENT OF THE NAVY
NAVAL OCEAN RESEARCH AND DEVELOPMENT ACTIVITY
NSTL, MISSISSIPPI 39529-5004

IN REPLY REFER TO
5050
Ser 332/662
20 Aug 85

From: J. P. Welsh, Chairman, Technical Committee

Subj: PROCEEDINGS OF THE ARCTIC OCEANOGRAPHY CONFERENCE AND WORKSHOP OF 11-14
JUNE 1985

The Arctic Oceanography conference and workshop hosted by the Naval Ocean Research and Development Activity (NORDA) and the Commander, Naval Oceanography Command (CNOG) provided an opportunity for a timely and important dialog between Navy fleet operational interests and the scientific/technical community. The theme of this conference was to articulate through contributed papers and exchange of ideas the capability and knowledge available to the Navy to meet the challenge of the Arctic environment to present and future Naval Operations.

To structure the conference, four general subject areas were stated: Operations, Buoys, Acoustics and Sea Ice. The call for papers requested abstracts on these four topics while stressing that other topics were of interest and welcome with the restriction that they relate to the effects of the Arctic environment on Navy Operations.

There are two categories of papers not contained in these proceedings. Classified papers received from the authors are held in the NORDA classified library and are available from NORDA on a need-to-know basis. A form is provided with this cover letter for request of a classified paper. The second category of papers are those not received by the printing deadline. These papers must be obtained from the individual authors. Annotations are provided in the table of contents of the proceedings to identify the two categories of papers not included. Responsibility for the classification and contents of the papers rest with the authors.

The conference was attended by over 300 individuals representing a broad spectrum of fleet interests and scientific/technical areas. Judging by the enthusiastic conversations and spirited discussions that occurred between participants, the forum was a success.

J. P. WELSH

PREFACE

The Arctic Oceanography conference and workshop hosted by the Naval Ocean Research and Development Activity (NORDA) and the Commander, Naval Oceanography Command (CNOG) provided an opportunity for a timely and important dialog between Navy fleet operational interests and the scientific/technical community. The theme of this conference was to articulate through contributed papers and exchange of ideas the capability and knowledge available to the Navy to meet the challenge of the Arctic environment to present and future Naval Operations.

To structure the conference, four general subject areas were stated: Operations, Buoys, Acoustics and Sea Ice. The call for papers requested abstracts on these four topics while stressing that other topics were of interest and welcome with the restriction that they relate to the effects of the Arctic environment on Navy Operations.

Two categories of papers are not contained in the proceedings. Classified papers received from the authors are held in the NORDA classified library and are available on a need-to-know basis. The second category of papers are those not received by the printing deadline. These papers must be obtained from the individual authors. Annotations are provided in the table of contents to identify the two categories of papers not included. Responsibility for the contents of the papers rest with the authors.

The conference was attended by over 300 individuals representing a broad spectrum of fleet interests and scientific/technical areas. Judging by the enthusiastic conversations and spirited discussions that occurred between participants, the forum was a success.

The preparation and conduct of a conference of this size required many people to make it work. The session chairman provided important input to direction and selection of the papers to be presented. Cooperation of the authors and the content of their presentations are the essence for the desired dialog between fleet and scientists. The excellent exchange between authors and participants made the conference a success. The details of logistics (the great shrimp boil), registration and the numerous other minutiae were coordinated by the Division of Continuing Education of the University of Southern Mississippi. Clearances and classified materials were handled by NORDA security. CNOG and NORDA staff directly involved in the planning, execution and wrap-up of the conference are recognized for a job well done.

To all of the above individuals be it known that the success of this endeavor could not have been without your contribution.



Dr. J. P. WELSH
Naval Ocean Research
and Development Activity



Mr. JERRY RESHEW
Naval Oceanography Command

ARCTIC OCEANOGRAPHY WORKSHOP

TABLE OF CONTENTS

Preface

i

ARCTIC OPERATIONS SESSION

Chairman, Mr. Jerry Carroll, U. S. Naval Oceanographic Office	PAGE
*"Arctic Submarine Operations", LCDR T. A. Tielking, USN, and LCDR D. G. Markham, USN, Naval Western Oceanography Center	
NS"Surface ASW Operations in the Marginal Ice Zone (MIZ)", Charles P. Pfarrer, Jr., Naval Oceanographic Office	
NS"Soviet Icebreaker Capabilities and Arctic Operations", CDR Lawson W. Brigham, United States Coast Guard	
"MIZEX Past Operations and Future Plans", Dean A. Horn, and G. L. Johnson Office of Naval Research	1
*"Mean- and Small-Scale Hydrodynamic Characterizations in the Arctic", Jeffrey H. Smart, Johns Hopkins University, Applied Physics Laboratory	
"International Ice Patrol Operations", CDR N. C. Edwards, Jr. and Dr. D. L. Murphy, United States Coast Guard	8
"Remote Sensing for Polar Icebreaker Navigation in Sea Ice", R. M. Hayes, United States Coast Guard	15
NS"High Latitude Submarine Terrain Warfare", LCDR John A. Jensen, USN, Naval War College	
*"Arctic Airborne Geophysical Survey", Otis E. Avery and Rudi G. Markl, Naval Oceanographic Office	
*"Arctic Bathymetric Survey Planning", William Hart, Naval Oceanographic Office	
"FNOC Arctic Operational Support", Ken Pollak and R.M. Clancy, Fleet Numerical Oceanography Center	25
"An Airborne Gravity Measurement System for use in the Arctic", John M. Brozena, Naval Research Laboratory	30
NS"ACV support for Arctic Operations", J. Offutt and J. V. Kordenbrock, David W. Taylor Naval Ship Research and Development Center	
*"Arctic Region Environmental Support Requirements", Louis J. Franc, Naval Oceanographic Office	

NS = NOT SUBMITTED

*CLASSIFIED, SEE Preface

ARCTIC BUOYS

PAGE

Chairman, Dr. Glenn D. Hamilton, National Data Buoy Center

*"Drifting Data Buoys in Support of Naval Operations in the Arctic", Ralph R. Miller, III, Computer Sciences Corporation

"Satellite Telemetry Buoys for Collection of Arctic Acoustic and Environmental Data", B. M. Buck and J. O. Anderson, Polar Research Laboratory 34

NS"Arctic Buoy Program--An Outlook", Roger Colony, Polar Science Center

"Arctic Temperature--Conductivity Buoys", James Morison, Polar Science Center/Applied Physics Laboratory 39

"Generation and Movement of Ice Islands Near the Canadian Arctic Archipelago", W. M. Sackinger and M. Yan, Geophysical Institute 44

"AIWEX Field Operations Planning and Execution", Andreas Heilberg, Polar Science Center/Applied Physics Laboratory 50

"Introduction to Service ARGOS and Drifting Buoy Logistics", R. M. Partridge, National Data Buoy Center 53

NS"Conceptual Design Approach for a Miniature Air-Sea Interaction Drifting (MASID) Buoy", Ronald P. Kozak, National Data Buoy Center

ARCTIC ACOUSTICS

Chairman, Dr. D. J. Ramsdale, Naval Ocean Research and Development Activity

*"High Frequency Underice Acoustic Scattering Measurements", R. Francois and G. Garrison, Univ. of Wash., Applied Physics Laboratory

"The Effect of the Physical Properties of Ice on the High Frequency Acoustic Backscatter from an Ice Keel Model", S. Chin-Bing, Naval Ocean Research and Development Activity 59

"A Simulation Model for High-Frequency Underice Acoustic Backscattering", G. C. Bishop, L. E. Mellberg, C. J. Albanese, S. E. Overdeep, NUSC, and W. T. Ellison, Marine Acoustics 71

"High Frequency Acoustic Reflection from Flat Sea Ice", J. W. Posey, G. H. Branch, S. A. Chin-Bing, Naval Ocean Research and Development Activity, and G. Tango, ODSI 80

*"An Under-ice High Frequency Mean Level Reverberation Model", C. J. Albanese, NUSC, and W. T. Ellison, Marine Acoustics

NS"Acoustic Scattering Measurements from the Underside of Laboratory Grown Sea Ice", T. Stanton, Univ. of Wisconsin and K. Jezek, CRREL

"Use of Penetrators to Estimate the Properties of Ice in the Arctic Regions", C. H. Yew, Univ. of Texas at Austin, Applied Research Laboratory	90
NS"An Arctic Acoustic Measurement System: Description and Performance", D. A. Milburn and T. A. Burke, Naval Ocean Research and Development Activity	
"Acoustic Bottom Interaction Considerations in the Arctic", W. Geddes, Planning Systems, Inc. and J. E. Matthews, Naval Ocean Research and Development Activity.	96
"Environmental Acoustic Data Base Development in the Arctic", G. Kerr, Naval Ocean Research and Development Activity.	107
"Under-ice Ambient Noise Variations as Related to Observable Ice Motion Parameters", J. K. Lewis and W. W. Denner, Science Applications International Corporation	111
NS"Nearfield Noise Measurements from an Arctic Pressure Ridge", B. M. Buck and J. H. Wilson, Polar Research Laboratory	
"Horizontal Directionality of Ice Edge Noise", C. Votaw, T. C. Yang, G. Giellis, and O. I. Diachok, Naval Research Laboratory	114
"Characteristics of Industrial Sounds in the Shallow Beaufort Sea", C. R. Greene, Greeneridge Sciences, Inc.	123
*"Arctic Ambient Noise Measurements", C. J. O'Neill, Naval Oceanographic Office, Acoustic Projects Division	
*"Arctic Sonobuoy Experiments", A. Horbach, Naval Air Development Center	
NS"MIZ Background Noise Measurements", J. B. Donald, Peter Stahl, John Sikorski, NUSC	
"Numerical Modeling of Acoustic Ice Interaction in the Arctic", Thomas N. Lawrence, Naval Ocean Research and Development Activity and G. Tango, ODSI.	138
NS"Modeling Low Frequency Underice Propagation Loss", R. Dicus, S. Wales, G. Giellis, S. Winnings and O. Diachok, Naval Research Laboratory	
"A Multi-Bounce, Single-Scatter, Ray Theoretic Model for Under-ice Predictions", A. Tolstoy, D. H. Berman, E. B. Wright and R. N. Baer, Naval Research Laboratory	149
NS"Buck/Wilson Arctic Transmission Loss Model", B. M. Buck and J. H. Wilson, Polar Research Laboratory	
*"Analysis of Underice Propagation in Baffin Bay and Davis Strait", D. F. Gordon, Naval Ocean Systems Center	

NS"Summary of Tristen Experimental Results", F. DiNapoli, R. Nielsen, M. Fecher, D. Potter, R. Mellen and P. Stocklin, NUSC

NS"Single Reflection Underice Acoustic Measurements in the Beaufort Sea", H. DeFerrari, N. Williams and H. Nguyen, Rosenstiel School of Marine and Atmospheric Science, Univ. of Miami

*"Mid-Frequency Underice Propagation Data in the Beaufort Sea", R. A. Fisher, D. J. Ramsdale, M. Z. Lawrence, A.J. Kramer, Naval Ocean Research and Development Activity

NS"Acoustic Measurements at Ice Camp RUBY", E. C. Gough, Planning Systems Inc.

NS"MIZ Propagation Loss Measurements", J. B. Donald, Peter Stahl, John Sikorski, NUSC

SEA ICE: ADDITIONAL PAPERS

Chairman, Dr. J. P. Welsh, Naval Ocean Research and Development Activity

"The Calculation of an Effective Thickness Term for Sea Ice Using Lagrangian Data", James K. Lewis and Warren W. Denner, Science Applications International Corporation 155

NS"Dense Brine Formation in Arctic Coastal Regions", Lon E. Hachmeister, Envirosphere Company

"Curious Plumes from Bennett Island", Pierre St. Amand, Naval Weapons Center, James Clark, U. S. Geological Survey and Michael Matson, NOAA 159

"Frequency-Domain Electromagnetic Ice-Sounding" I. J. Won and K. Smits, Naval Ocean Research and Development Activity 167

*"Electromagnetic Surveillance Sensors in the Arctic Region", J. F. Scarzello, R. E. Brown, D. S. Lenko and M. M. Kleiner, Naval Weapons Center,

SEA ICE: CHARACTERISTICS, BEHAVIOR, AND MEASUREMENTS

Chairman, Dr. W. F. Weeks, U. S. Army Cold Regions Research & Engineering Laboratory

NS"Digital Processing of Passive Ka-Band Microwave Images for Sea Ice", D. T. Eppler, L. D. Farmer and A. W. Lohanick, Naval Ocean Research and Development Activity

"Radiometric Imagery of Sea Ice", J. P. Hollinger and Mary Ruth Keller, Naval Research Laboratory and Bendix Field Engineering Corp. 173

"Remote Sensing of the Marginal Ice Zone During MIZEX 83 and 84", R. A. Shuchman, and B. A. Burns, Environmental Research Institute of Michigan 178

"Some Results of the MIZEX-West Ice Observation Program", R. D. Muench, Science Application, D. J. Cavalieri, NASA/GSFC, and G. R. Stegen, Science Applications International Corporation	190
"Variations in the Bering Sea Ice Coverage Related to Large-Scale Atmospheric Circulation Patterns", R. E. Englebretson, Science Applications International Corporation	198
"A Method for Determining Sea Ice Type and Inferred Ice Thickness Distributions from Aerial Photographs", L. D. Farmer and D. T. Eppler, Naval Ocean Research and Development Activity.	205
"Pressure Ridge Morphology and Physical Properties of Sea Ice in the Greenland Sea", W. B. Tucker, III, A. J. Gow and W. F. Weeks, USA, CRREL	214
"Coherence Estimates of Under-ice Profiles in the Beaufort Sea; An Indicator of Three Dimensional Structures", E. R. Levine, S. E. Overdeep, and D. N. Connors, NUSC	224
"The Number of Elastic Constants of Sea Ice", E. R. Floyd and B. L. Markham, Arctic Submarine Laboratory, NOSC	241
"Mechanical Properties of Multi-year Pressure Ridge Samples", J. A. Richter-Menge, USA, CRREL.	244
"Experience with a Biaxial Ice Stress Sensor", G. F. N. Cox, USA, CRREL	252
NS"A Numerical Model of Sea Ice Characteristics in the Arctic Basin for the Year 1983", R. H. Preller, Naval Ocean Research and Development Activity	
"The Numerical Simulation of Sea Ice Induced Gouges on the Shelves of the Polar Oceans", W. F. Weeks and W. B. Tucker, III, USA, CRREL.	259
"Cryospheric Data Management System for Special Sensor Microwave Imager DMSP Data: A Status Report", R. Weaver, National Snow and Ice Data Center, CIRES, Univ. of Colorado	266
"The Joint Ice Center Capabilities and Limitations in Sea Ice Analysis and Forecasting", LT H. S. Rosner, USN, NPOC, Joint Ice Center	271
Appendix	
Participants-listed alphabetically	281
Participants-listed by organization	294

MIZEX EAST, PAST OPERATIONS AND FUTURE PLANS

Dean A. Horn

and

G. Leonard Johnson

Executive Officer, MIZEX Program
Office of Naval Research

Program Manager Arctic Sciences
Office of Naval Research

ABSTRACT

The 1984 Marginal Ice Zone Experiment (MIZEX 84) seeking to understand the Arctic environment in the Fram Strait area was completed on 30 July. The largest Arctic marginal ice zone research program ever conducted, MIZEX 84 culminated years of science planning. This international Arctic program utilized the resources of eleven nations. Over sixty coordinated and complementary research projects were carried out by researchers from several scientific fields: oceanography, ice, meteorology, remote sensing, acoustics, biology and modeling. The MIZEX Science Group recently started planning a follow-on winter field research program. The main thrust of Winter MIZEX will be a closely coupled oceanographic and acoustics program to understand the oceanography of ice-ocean eddies and their impact on ambient noise and acoustic propagation including tomographic inversion. Other important Winter environmental interests will be ice edge phenomena, meteorology, ice kinematics/dynamics, and interaction of surface and internal waves with the ice-ocean eddies and with the ice cover.

INTRODUCTION

The marginal ice zones (MIZs) of the Arctic and Antarctic vary annually over an area of about 25 million km², or 7 percent of the world's ocean areas. Each year, the edge of the Arctic ice field migrates north and south up to 375 nautical miles. The processes and enormous energy interchange that control the location and behavior of the MIZ are of fundamental importance to meteorologists, biologists and oceanographers. Understanding the processes that determine the MIZ is also important to ocean transport, naval operations, environmental and living resource management. Sea-ice movement is a major factor in almost all aspects of Arctic offshore minerals development. The dynamic nature of pack-ice must be taken into account in the location of exploration rigs and production platforms, logistics, transportation and construction methods.

Scientifically the MIZ was basically unknown except for limited data bases which were usually concentrated in one discipline. The Office of Naval Research, realizing the importance of the area, took the initiative in organizing a concerted international environmental science program to

address MIZ processes. After a number of scientific meetings and workshops to determine the primary scientific questions and how should they best be addressed, the overall scientific issue was defined as follows: the air-sea-ice processes in the MIZ form a coupled mesoscale system, but there is no satisfactory understanding of the individual processes themselves or how they interrelate.

Equally important for MIZEX East, the scientific meetings and workshops also evolved an ad hoc, international organization of Arctic scientists, the MIZEX Science Group. This Group became the corporate body for planning, coordinating and managing MIZEX East. A MIZEX Science Plan¹ was prepared by the Group, reviewed by the appropriate science oversight authority of each participating nation (e.g., NAS for U.S.), and published to guide the interests and efforts of MIZEX participants.

Consequently, three large-scale field investigations were launched. The Bering Sea effort (MIZEX West) was conducted 5-27 February 1983 and two MIZEX East field programs (9 June - 8 May 1983 and 18 May - 30 July 1984) were carried out in the northern Greenland Sea. This paper will focus primarily on MIZEX East '84 and the planned Winter MIZEX East operations in March-April 1987 and 1988.

MIZEX EAST '84

The 1984 Marginal Ice Zone Experiment (MIZEX East 84), was conducted in the Fram Strait area between Greenland and Svalbard in midsummer during the period of greatest ice retreat (Fig. 1). The culmination of over four years of planning and a continuation of summer MIZEX 83, this 1984 international Arctic research program utilized the resources and expertise of eleven nations and was supported by several U.S. agencies. Core U.S. support for MIZEX came from the Office of Arctic Programs, ONR, with additional U.S. support provided by NASA, NOAA, NRL, NSF and NUSC. MIZEX 84 was the largest coordinated Arctic experiment yet conducted in the marginal ice zone and had the unique feature of an ad hoc organization established by the scientists themselves without any intergovernmental agreements, memoranda or treaties. This has proved to be an effective scheme for planning and conducting both the MIZEX 83 and 84 field operations.

The MIZEX 84 experiment utilized seven ships, eight remote sensing/meteorological aircraft and four helicopters, supporting a multidisciplinary team of 208 scientists and technicians plus ship and aircraft crews. Scientists, equipment and support, came from Canada, Denmark, Federal Republic of Germany, Finland, France, Ireland, Norway, Sweden, Switzerland, United Kingdom and United States. Figure 2 summarizes the participation for each platform.

The region of Fram Strait is environmentally active because the relatively warm Atlantic water enters the Arctic to the west of Svalbard and cold ice-choked Arctic water exits the Strait to the east of Greenland, resulting in a pronounced frontal and current system called the East Greenland Polar Front. The associated shear and frontal structures make this an extremely active area characterized by complex oceanographic and atmospheric structures (see Figure 1).

The detailed schedule of operations for carrying out the MIZEX 84 experiment was developed by the MIZEX Science Group over the preceding two years, 1982-84. Building on the MIZEX 83 experience, the operations plan with integrated schedule for all major programs was completed as planned with only minor field modifications necessary. Figure 3 summarizes the MIZEX 84 experiment.

Initial results from MIZEX 84 have been published as Volume 5 of the MIZEX Bulletin and are available from U.S. Army Cold Regions Research and Engineering Laboratory, Hanover N.H. 03755-1290 as CRREL Special Report 84-29. Some of the highlights are:

Oceanography

Lagrangian observations using freely drifting swallow floats were taken by J. C. Gascard of the Physical Oceanography Laboratory in Paris CNRS/MUSEUM. Ten acoustic Swallow floats, ballasted in order to be neutrally buoyant at preselected depths, were launched: 4 floats stabilized around 110 to 130 m depth and 6 around 200 to 260 m. Each float, equipped with a 1562 Hz transducer, sent a pulse every hour for tracking and was telemetering in situ temperature and pressure once every second day. Five listening stations received float signals, and float locations were computed by considering time of arrival and positions of the listening stations. Three stations were operational in real time from three different ships, POLARQUEEN, POLARSTERN AND KVITBJORN. Two additional autonomous listening stations, F1 and F2, were deployed at 700 m depth from ice floes which were tagged with Argos buoys and tracked by satellite. Later on (post-MIZEX cruises), two listening stations were mounted first on POLARSTERN (late July-early August) and later on LANCE (late August) extending the float tracking over a one month period in addition to the 50-day MIZEX period. Preliminary results have defined some features of Atlantic currents in the Fram Strait, below the ice, during this summer 84 season. Specifically, four features appeared related to the branching of the northward Atlantic

current towards the southward East Greenland current:

- northward Atlantic current flowing along the continental slope West of Yermak plateau and entering the Arctic basin.

- strong topographic features above Yermak plateau: (one float was trapped and entered the Arctic basin.)

- recirculation of Atlantic waters west of the Yermak plateau along the continental slope and in the deepest part of the Straits.

- southward flowing Atlantic current trapped in the East Greenland current.

Hundreds of CTD stations were obtained by the various ships, with the shallower ones concentrated on the mesoscale eddies. Tracking of 20-50 km scale eddies along the ice edge south of 79° N was carried out in coordination with R/V Kvitbjorn. Location of eddies by aircraft and satellite remote sensing in near real time enabled guidance of the ship toward the eddy features. One eddy was detected during the first synoptic CTD program with a center at approximately 79°50' N and 6°30' E. The diameter of this eddy was about 20-25 km. It was first tracked for 4 days with CTD sections taken in a "star" pattern through the eddy center and revealed almost no propagation. At the same time the ice edge, initially located just north of the eddy center, moved northward about 60 km. The second tracking period 7 days later gave no sign of the eddy, suggests a decay time of order 10 days. Second, the "stationary" Molloy Deep eddy with a scale of 60-100 km was documented by 3 sections all sampled to the bottom.

Besides the standard oceanographic equipment the following were utilized. An array of Cyclesondes was deployed from ice floes by Dr. J. Van Leer, U. Miami. The Cyclesondes recorded profiles of temperature, salinity, pressure, current speed, and direction, and one unit also recorded light transmissivity. Profiles were taken at preset intervals of 1/2 hour, 1 hour or two hours. Most data were sampled at 30 second intervals during each profile, giving about three meter vertical resolution.

The turbulence experiment for MIZEX 84 was designed to measure mean and fluctuating currents, temperature, and conductivity, at several levels in the upper ocean boundary layer beneath drifting ice. Special instrument clusters were built consisting of three small (4-cm diameter), partially ducted rotors mounted along three mutually orthogonal axes. These were used in conjunction with Sea Bird conductivity meters and oceanographic thermometers. Data from each cluster were transmitted to the surface, converted to digital frequencies by a deck unit, and recorded on floppy disk with a Hewlett-Packard microcomputer. The system is capable of handling 7 clusters (35 data channels) at a sampling rate of 6 per second.

A Flow Industries Inc. prototype Diode Laser-Doppler (DLVD) Velocimeter developed with Small Business Innovation Research funds from ONR was tested. This instrument sampled two components of flow by measuring Doppler shift of coherent light scattered from microscopic particles in a small (order 1 cm dimension) volume. The DLDV was mounted near one of the turbulence clusters for comparison. Initial indications are that there is excellent agreement between the two instruments.

CODAR (Coastal Oceanic Dynamics Application Radar), which measures the radial component of surface currents up to a distance of 50 km with a resolution of 1.2 km, was successfully used by VALDIVIA. Measurements of surface currents were carried out on 3 sections between Svalbard and the ice edge. At the ice edge approximately 20 CODAR stations were performed.

Sea Ice

In sea ice produced in the laboratory, the relative composition of salts in the brine entrained in the ice changes as a result of the selective precipitation of the salts from the brine when the ice is cooled. Calcium carbonate is the first to precipitate, beginning to do so just below the freezing point near -2°C , followed by sodium sulphate near -10°C . Almost no studies have been done to verify the laboratory results and their geophysical implications using sea ice produced under natural conditions. Several cores of first year and multi-year ice were collected throughout the MIZEX area. Not one showed anything like the degree of relative calcium enrichment expected on the basis of the laboratory results. Sulphate concentrations have not yet been determined, but based on the calcium data, little sulphate enrichment is expected. These results seem to show that the studies of ice produced under laboratory conditions cannot be used in any simple way to describe the composition of natural sea ice. Fram Strait sea ice has a much lower percent of frazil versus columnar ice than does the Antarctic sea ice (26% versus 60%).

Remote Sensing

Extensive ground truth to determine surface characterization was made in conjunction with the aircraft overflights. For example: Along each of the radiometer traverses, detailed studies were made of surface topography, spatial variations in snow depth, the occurrence of ice layers and lenses in the snow pack, and ponding of meltwater. These were compared with the corresponding radiometric records. At selected locations, surface characteristics were determined from core samples. For cold ice cases, these measurements included temperature, salinity, and density profiles in the snow and the top 30 cm of the ice together with the geometry and mean size of the snow grains. When the ice entered the transition to melting stage, free water content measurements in the snow and loose upper layers of the ice were included in the program. The crystal geometry and density of the loose granular layers were also obtained.

Active and passive microwave observations were able to distinguish ice types when the surface was dry, but when the snow was wet no clear discrimination between multi-year and first year was possible. The SAR demonstrated a potential for estimating total ice concentration, but more work is needed on the algorithm.

Meteorology

There was an extensive meteorological program and one dedicated meteorological research plane (DFVLR's Falcon 20). The aircraft is equipped with highly sensitive instruments to measure pressure, air flow angle, temperature and humidity, thus providing a high resolution representation of the turbulent state of the atmosphere. In addition, Eppley pyranometers and pyrgeometers were installed to measure upward and downward radiative fluxes. A downward looking PRT-6 radiometer and a radiotalimeter monitored the thermal properties and the roughness of the partly ice-covered ocean surface. The instrumentation has been further extended by the use of cloud physics probes (PMS-Knollenberg: FSSP and OAP-230X, KING-LWC-probe) and of an aerosol/cloud water sampling device which was developed and operated by the University of Stockholm. The on-board data registration provides a 10 Hz recording of all navigational (INS) and meteorological data and an additional 100 Hz recording of the highly variable temperature, pressure, humidity and flow angle sensors and radio-altimeter outputs. Additional meteorological data were acquired from the surface vessels. The following were observed to determine, among other things, the basic processes that lead to the formation and dissipation of arctic stratus clouds:

- turbulent fluxes of momentum, sensible and latent heat as function of height in the PBL as well as their mean values
- microphysical cloud properties such as drop size distribution and liquid water content
- radiative cloud properties (reflectivity, transmissivity and absorptivity)
- physico-chemical and optical properties of the atmospheric aerosol (P. Wendling).

Acoustics

The acoustics program consisted of multiple sound sources and both horizontal and vertical hydrophone arrays to determine the effect of the MIZ on signal propagation, coherence, reverberation and ambient noise. An autonomous, moored, acoustic source was installed to assess the stability of surface reflected acoustic paths for tomographic application. The source transmitted a 224 Hz carrier, phase modulated by a binary, maximal length, shift-register sequence, similar to the type of signal which has been used during several tomography experiments. Minor adjustments were made in signalling parameters to account for Doppler shifts due to the time-varying ocean surface. The signal was received by hydrophones

suspended through the ice by the MIT/WHOI scientific party aboard MV Kvitbjorn and by hydrophones deployed by MV HU Sverdrup.

It was determined that ambient noise levels in the 6000 Hz range can be attributed to thermal stress when ice drifts into warmer water, the lower frequency 5-100 Hz noise is primarily due to ice "quakes" as the ice breaks in response to wind and current stress.

WINTER MIZEX

Program Objectives

The planned winter MIZEX³ is a natural sequence to the earlier MIZ measurement programs. The winter season emphasizes or dramatically changes certain processes; to project the flavor of scientific challenges during winter some of the major objectives are summarized briefly here. It is planned to measure and understand:

- formation of Arctic atmospheric lows as influenced by the large temperature and water vapor contrast at the ice edge,
- growth, propagation, and decay of ocean eddies as affected by ice edge dynamical processes including strong winds,
- shape, size, configuration, and motion of the ice field created by strong forcing of intense incoming gravity waves,
- snow dryness and thickness characteristic of the winter MIZ as they affect EM reflectivity and emissivity,
- changes in acoustic refraction and coherence via winter-related changes in sound speed profiles, internal waves, and ocean eddies,
- intensification of ice cracking noise mechanisms as related to ocean eddies, gravity waves, and presence of recently frozen thin ice.

While the foregoing list is not complete, it should be clear that efforts during MIZEX 87 and 88 are to be centered on those attributes of the MIZ most characteristic of the winter season.

Beyond the focus on winter processes, we intend special emphasis on ocean eddy phenomena. Thus eddy genesis associated with atmospheric lows and winds become a central research element. Electromagnetic sensing via aircraft and satellites is to be employed in "real time" for identifying eddy fields, and in discerning limitations, if any, caused by advection of marker ice fields associated with strong winter winds or waves. Also central are acoustic interactions with eddies; the effects on acoustic propagation and ambient noise of the oceanographic mesoscale phenomena, principally ice-ocean eddies, and the forward modeling problem will be investigated. Inverse methods in which acoustics becomes the probe for quantifying the oceanography will be exercised and studied.

There will be five principal scientific interest areas studied in the Winter MIZ environment. They are acoustics, oceanography, meteorology, ice and wave studies, and remote sensing. All data will be utilized for model studies, development and refinement. However, as noted above, an especially large degree of interrelationship among the scientific disciplines during MIZEX 87 and 88 is planned and necessary. Indeed, the success of the program demands that this be achieved. EM remote sensing researchers require ground truth, acousticians must have water column sections and ice field dynamics, meteorologists need sea surface temperatures and surface roughnesses, and oceanographers must have atmospheric forcing functions. While such interdependence is not new, our needs are heightened by the especially strong role of acoustics in MIZEX 87 and 88, which is at the point of answering fundamental questions in ice noise generation and in the feasibility of MIZ ocean acoustic tomography.

Overall Experiment Strategy

The field experiments associated with the Winter MIZ program will involve three phases. The first phase pre-1987, will consist primarily of P3 overflights in the Fram Strait and Greenland Sea, prior to 1987 for observations of weather, sea, and ice conditions and synoptic ambient noise monitoring. Because there is very limited knowledge of the winter MIZ environment these flights will provide invaluable data for planning the later phases of the experimental program, with particular regard to spatial and temporal scales to be expected in contrast to the summer season, and with additional attention to flight and safety issues involved with ship, helo, and ice camp operations during the Winter season.

The second phase will center on a field experiment in the Fram Strait marginal ice zone in March and April of 1987. This experiment will include an icebreaker with a helicopter and fixed wing aircraft for meteorology and remote sensing as well as utilizing satellite remote sensing capabilities. Primarily this experiment will exercise the remote sensing capabilities for detection and tracking of ice-ocean eddies in the winter; provide the first comprehensive data set on the oceanography of the winter MIZ vital for acoustic modeling; provide the first data on important meteorological questions including cyclogenesis and surface atmospheric boundary conditions in the winter MIZ; provide data on ice and surface gravity wave interaction; and provide ambient noise data. This experiment will also provide valuable experience on ship and helo operations in the Winter MIZ environment.

The third phase will culminate in a field experiment in the Fram Strait marginal ice zone in March and April 1988. This experiment, much broader in scope than the 1987 experiment, will include an ice camp located approximately 100 km to 150 km from the ice edge in an area tentatively bounded by 78 N, 80 N, 0 E, and 3 E. The location of the ice camp relative to the ice edge will be determined based upon the ice/wave interaction studies of the 1987 experiment over the course of

the ice camp's 45 day lifetime. Acoustic receiving arrays and acoustic data acquisition systems as well as a meteorological station will be located at the ice camp. The tentative camp location was chosen so as to be west of the Yermak Plateau to provide deep water, in excess of 1000 m, to minimize effects of bottom interaction for acoustic propagation and tomography. Figure 4 presents an overview of the proposed Winter MIZEX 88 experiment.

A central idea behind the 1988 ice camp deployment is the distinct probability that much of the acoustics and ice dynamics at the camp, including ambient noise, acoustic scattering from the ice, spatial and temporal coherence of acoustic signals (from shots deployed north of the camp), will exhibit characteristics initially associated with deep Arctic conditions changing to conditions common to the marginal ice zone as the camp drifts from its initial location deep in the pack ice through the marginal ice zone to the ice edge.

Two helicopters will operate from the ice camp for remote acoustic and oceanographic data collection. An ice strengthened ship with helicopters and two open ocean ships are planned for this experiment. The ice ship and one open ocean ship will be primarily dedicated to oceanography, meteorology, and ice/wave programs while the other open ocean ship will tow an array and/or acoustic source(s). Fixed bottom moored acoustic sources and receivers will be deployed in the Greenland Sea and in the Fram Strait area. These sources and receivers will be part of both the Greenland Sea long term ocean acoustic tomography program as well as the MIZEX 87/88 program. These sources and receivers will be deployed in the Spring of 1987 and recovered in the Spring after MIZEX 1988.

With the experience gained from 1987, a major emphasis of the 1988 experiment will be to identify ice-ocean eddies, other mesoscale oceanographic phenomena, and internal waves in real time using remote sensing. Then scientists will conduct intensive oceanographic measurements, and simultaneously position the ship deployed acoustic sources and ship/helicopter deployed acoustic receivers to obtain the desired propagation and ambient noise geometry with respect to the eddy and ice fields.

DATA MANAGEMENT:

All MIZEX data, to be readily available and most useful to the scientific community as a whole, is being placed in the National Snow and Ice Data Center (NSIDC) in Boulder, CO (303-492-5171). NSIDC management of MIZEX data covers the following:

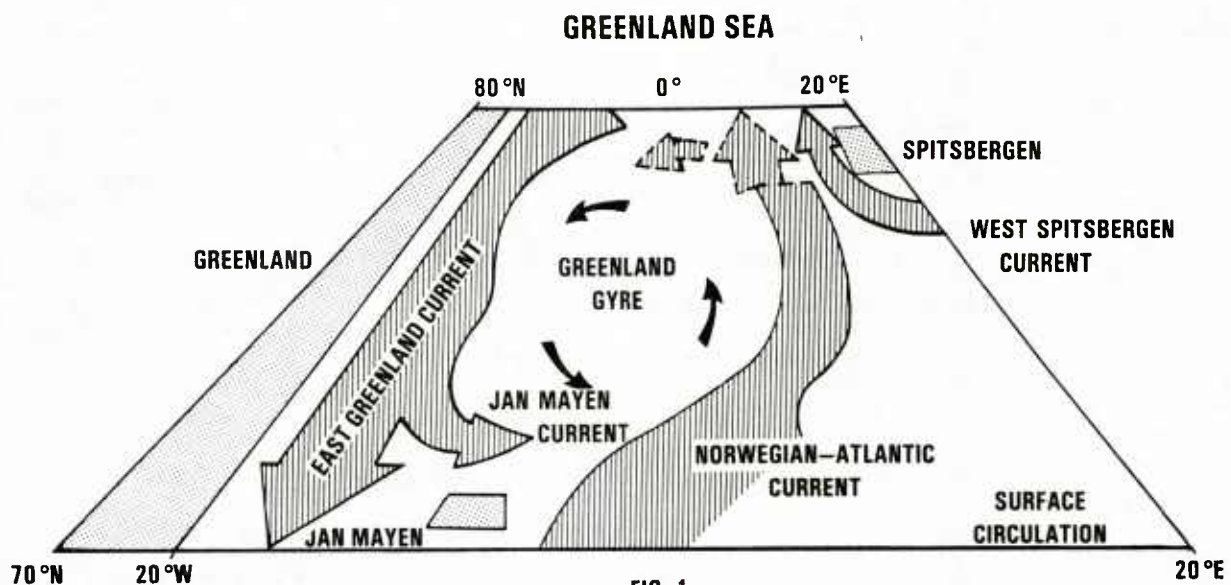
1. Establish and implement the data archival and accession program.
2. Establish and/or coordinate data interchange standards.

3. Coordinate data flow from principal investigators to the participating data centers and/or principal investigators.
4. Promote and facilitate interchange of data management information between principal investigators and other scientific data.

The data bank is operational with the majority of MIZEX West and MIZEX 83 data in the form of data reports and tapes readily accessible. MIZEX 84 data and reports are being added to the data bank as soon as they are received by NSIDC. An index (inventory) of the MIZEX holdings at NSIDC is available, on-line, on Telemail's MIZEX Bulletin Board.

REFERENCES

1. Johannessen, O. M., W. D. Hibler, III, P. Wadhams, W. J. Campbell, K. Hasselman, and I. Dyer (Editors), "MIZEX, a Program for Mesoscale Air-Ice-Ocean Interaction Experiments in the Arctic Marginal Ice Zone. II. A Plan for a Summer Marginal Ice Zone Experiment in the Fram Strait/Greenland Sea: 1984," U.S. Army Cold Regions Research and Engineering Laboratory, Hanover, N.H., (1983).
2. Johannessen, O. M. and D. A. Horn (Editors), "MIZEX 84 Summer Experiment PI Preliminary Reports," MIZEX Bulletin V, U.S. Army Cold Regions Research and Engineering Laboratory, Hanover, N.H., (1984).
3. Milhalevsky, P. (Editor) "Winter MIZEX 1987/1988, Preliminary Science Plan," unpublished draft MIZEX Planning Meeting, MIT, (1985).



MIZEX EAST RESEARCH AREA

MIZEX 84

FIELD OPERATIONS: MAY 18—JULY 30, 1984

SHIPS:

USNS LYNCH	(NRL)	MAY 18 — JUNE 28
HU SVERDRUP	(NDRE)	JUNE 1 — JUNE 25
MV POLARQUEEN*	(PSC)	MAY 29 — JULY 29
MV KVITBJORN	(PSC)	MAY 30 — JULY 30
MS HAKON MOSBY	(U. BERGEN)	JUNE 12 — JULY 15
FS POLARSTERN*	(A.W.I.)	JUNE 11 — JULY 18
FS VALDIVIA	(U. HAMB.)	JUNE 20 — July 18

*2 HELICOPTERS ON EACH SHIP

AIRCRAFT:

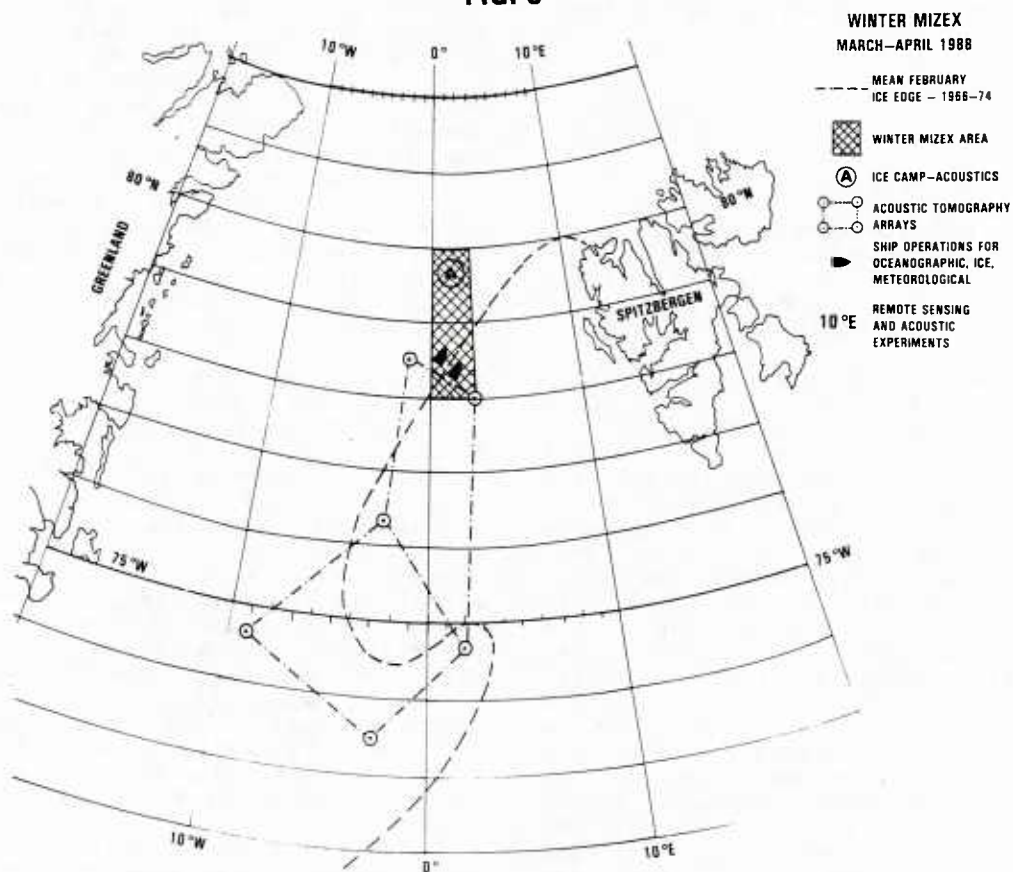
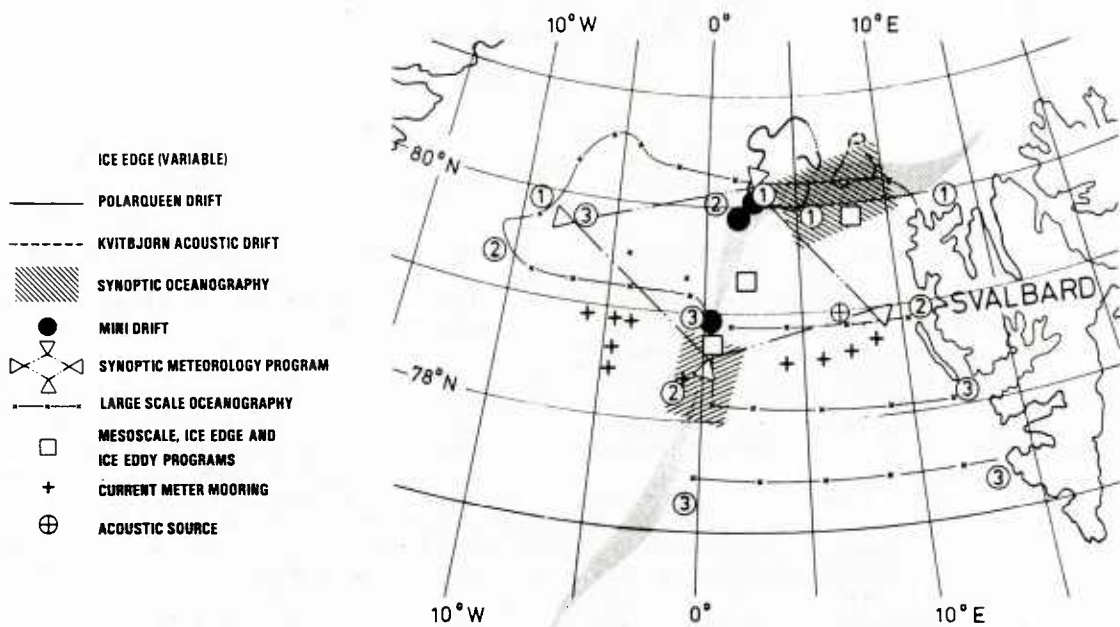
CCRS CV 580	(CANADA)	JUNE 26 — JULY 8 (8 FLTS)
CNES B-17	(FRANCE)	JUNE 30 — JULY 16 (6 FLTS)
NASA CV 990	(USA)	JUNE 8 — JUNE 30 (7 FLTS)
NOAA P-3	(USA)	JUNE 20 — JULY 7 (6 FLTS)
NRL P-3	(USA)	JUNE 24 — JULY 8 (7 FLTS)
GREENLAND ICE PATROL	(DENMARK)	MAY 29 — (1 FLT)
RNAF P-3	(NORWAY)	JUNE 11 — JULY 18 (6 FLTS)
DFVLR FALCON	(GERMANY)	JUNE 22 — JULY 14 (20 FLTS)

MIZEX PERSONNEL (FROM 10 NATIONS):

SHIPS	164
AIRCRAFT	36
SHORE SUPPORT	18
TOTAL	208

FIG. 2

MIZEX 84 PROGRAM OVERVIEW



INTERNATIONAL ICE PATROL OPERATIONS

CDR N. C. EDWARDS, JR.
and
D. L. MURPHY

Commander, International Ice Patrol
Avery Point,
Groton, CT 06340

ABSTRACT

Since 1914, the International Ice Patrol (IIP) has been conducted by the U. S. Coast Guard, to provide the North Atlantic Mariner with a warning of hazardous icebergs in the region of the Grand Banks of Newfoundland. During the iceberg season, March to August, IIP conducts iceberg reconnaissance flights using HC-130 aircraft equipped with the AN/APS-135 Side Looking Airborne Radar (SLAR) over those fog-covered, storm-tossed waters. Radio broadcasts and facsimile charts of the limits of all known hazardous ice are originated by Commander, International Ice Patrol (CIIP) from an operations center in Groton, Connecticut.

1. INTRODUCTION

Icebergs and sea ice have been hazards to navigation in northern waters for centuries, but the threat did not attract great international concern until the sinking of the RMS TITANIC in 1912.

Unlike sea ice which freezes in place, icebergs are of land origin. North Atlantic icebergs calve mostly from the glaciers on the west coast of Greenland and drift south through Baffin Bay and Davis Strait with the Labrador Current. Their visible size ranges from that of a grand piano (growler) to that of a large aircraft carrier (very large), but only represents one-eighth of the total mass which may be 10 million tons; the remaining seven-eighths is below the sea surface. As they drift into the North Atlantic shipping lanes near the Grand Banks of Newfoundland, icebergs present a major hazard to navigation. During the six month iceberg season, 135 million gross tons of merchant shipping crosses these ice infested waters. Even equipped with modern surface search radars, the ships cannot detect all icebergs, particularly growlers which may spend half of their time submerged. Poor detection

is due to the low reflective coefficient of ice (0.33), the iceberg's irregular shape and its surfaces sloping away from the radar beams.

The International Ice Patrol (IIP) was formed in 1914 to patrol the Grand Banks of Newfoundland (Figure 1), detect hazards to navigation and warn mariners of the threat. Under the 1960 Safety of Life at Sea (SOLAS) Convention, 20 member nations have agreed to share the 2.5 million dollar cost to conduct the patrol which the U. S. Coast Guard is tasked with.

2. HISTORY

The tragic sinking of the luxury liner RMS TITANIC on April 15, 1912 raised great international concern over the safety of navigation in the North Atlantic. The First Safety of Life at Sea (SOLAS) Convention, which met in 1913, inaugurated the International Ice Patrol and tasked the United States with managing the service. The original 13 member nations agreed to share the Ice Patrol expenses. A 1914 presidential order established the Ice Patrol and assigned it to the Revenue Cutter Service, which became the U. S. Coast Guard in 1917.

Early ice patrols were conducted by cutters that patrolled the southern, southeastern and southwestern limits of hazardous ice in the vicinity of the Grand Banks of Newfoundland. These cutters broadcasted the positions of the southernmost hazardous icebergs which drifted in those often fog-laden and storm-tossed waters. After World War II, aerial visual reconnaissance commenced and soon became the primary means of surveillance. Aerial reconnaissance permitted much wider coverage, but iceberg detection was still hampered by poor visibility and severe weather conditions. The limits of hazardous ice were broadcast to the mariner daily from land-based radio stations around the North Atlantic.

In 1983, the International Ice Patrol began using a side-looking airborne radar (SLAR) as the major detection tool, and for two years has successfully conducted

surveillance of the operations area, with only 5 vice 50 percent of the days lost due to poor weather.

3. PRESENT OPERATIONS

Today's Ice Patrol service is coordinated from an operations center in Groton, Connecticut from which Commander, International Ice Patrol deploys an Ice Reconnaissance Detachment (ICERECDET) for seven days every other week during the six-month ice season (March through August). Surface patrol vessels have been rarely used in the post-World War II era.

Flying from Gander, Newfoundland, a U. S. Coast Guard HC-130 (Hercules) aircraft equipped with Motorola AN/APS-135 SLAR patrol the operations area, which extends from 40°N to 52°N latitude and 39°W to 57°W longitude. A typical patrol can cover 35,000 nm² in 6 to 7 hours of surveillance from an altitude of 8,000 feet. In 1984, 476 SLAR flight hours were logged in 78 ice reconnaissance sorties.

The operations center maintains an iceberg plot showing the locations of icebergs detected by the ICERECDET, Canadian ice reconnaissance, offshore oil industry operations, and North Atlantic shipping. In 1984, a season record of 2,202 icebergs were estimated to have moved south of 48°N latitude, the traditional indicator of the severity of a season; the average amount is 386. The record number is possibly the result of colder than normal conditions during the year; but certainly the increased detection capability offered by SLAR has increased the number of sightings. In 1984, 49 percent of the sightings were made by the ICERECDET.

The SLAR is also very effective in detecting sea ice as illustrated in Figure 2. In addition to the International Ice Patrol, the SLAR (APS-94D) is presently being used operationally by Canadian ice reconnaissance aircraft to monitor sea ice coverage in support of Canadian shipping, oil industry and fishing interests. Once an iceberg has been sighted, its location, size, and shape are entered into a computer drift model¹ that is used to estimate the subsequent motion of the iceberg. The use of the model is necessary for two reasons; first, so that subsequent sightings of an iceberg are recognized as re-sights rather than as a new sighting and, second, that the position of an iceberg can be estimated if no resighting is made.

The drift model combines the effects of water drag, air drag, the Coriolis acceleration, and sea surface slope to determine the iceberg acceleration. The water drag is summed up over four current layers (dependent on the size of the

iceberg) by using a mean depth-independent geostrophic current plus a contribution due to the wind current. The wind-driven current is based on time-dependent Ekman dynamics.

Model input data are derived from several sources. The mean geostrophic current field is based on hydrographic surveys conducted by the Coast Guard since 1936. Because this mean current field has no recognition of temporal variability of the flow field, in 1983, Ice Patrol began air-deploying Tiros Oceanographic Drifters (TODs) and using their drifts to modify the historical field. Up to 12 buoys are deployed per season. Figure 3 shows tracks from buoys launched during the 1984 season. The wind input for the air-drag and wind-current computations are calculated from wind data provided every 12 hours from the Fleet Numerical Oceanography Center (FNOC) in Monterey, California.

A second numerical model is used to estimate the deterioration of an iceberg after its initial sighting. The model² uses water temperature, wave height, and wave period to calculate iceberg deterioration (approximately 85 percent of iceberg deterioration is due to wave effects). Water temperature and wave data are provided every 12 hours by FNOC.

4. RESEARCH

The International Ice Patrol research program addresses the three major technical areas of the operations: detection, drift and deterioration. The programs are briefly described below.

a. Detection.

The advent of SLAR as the primary iceberg detection device brought with it several problems. How effective is SLAR at detecting icebergs, and for what size range? How well can SLAR distinguish between icebergs and vessels?

To quantify the effectiveness of SLAR, IIP participated in the BergSearch '84 experiment sponsored by the Environmental Services Revolving Fund (ESRF) administered by the Canada Oil and Gas Lands Administration (COGLA). After flying 71 passes on ground-truthed icebergs, data analysis indicated that the SLAR will detect icebergs greater than 10m in length in moderate to calm seas with a repeatability of +/- 10 percent³.

IIP is continuing SLAR detection research in a cooperative experiment with the U. S. Coast Guard Research and Development Center scheduled for April - May 1985 as part of an IIP research cruise aboard USCGC EVERGREEN (WMEC 295).

b. Drift.

The major issue in the drift area is the temporal variability of the flow field. The IIP operations area contains two major current systems, the cold Labrador Current and the warm North Atlantic Current, with its associated eddies and meanders. A mean geostrophic flow field cannot describe this complex circulation well enough to predict iceberg motion adequately. The use of TOD's to provide near real-time current has shown some promise.

In 1984 an IIP oceanographic cruise aboard USCGC HORNBEAM compared the motion of TOD's drogued at 30m with the geostrophic flow field determined from a hydrographic survey. The buoy motions matched the calculated geostrophic flow well in the portion of the survey area in which there was a well-defined flow.

The IIP research program also includes iceberg drift studies during which a vessel follows an iceberg for up to 7 days, while at the same time, collecting meteorological data and monitoring the drift of several buoys in the vicinity of the iceberg. A 1985 research cruise aboard USCGC EVERGREEN will include two seven-day drift periods. These results will be used to test the drift predictions of the IIP iceberg drift model so that the prediction errors can be assessed.

Previous research has shown⁴ that ocean features can be detected by SLAR. Currently, IIP is investigating the usefulness of real-time detection of ocean fronts in the dynamic areas south and east of Grand Bank to assist in predicting iceberg drift. Figure 4 shows the sharp boundary between cold Labrador Current waters and warm Gulf Stream waters near the Tail of the Bank on 28 April 1985. This feature was supported by the National Oceanic and Atmospheric Administration Analysis of 22 April 1985 showing the sea surface temperature distribution.

c. Deterioration.

Two recent studies^{5,6} have shown that the algorithms that form the basis for the IIP iceberg deterioration model produce accurate predictions when on-scene input data are used. However, taken together, these two studies represent the deterioration of three icebergs, two of them grounded. In 1985, IIP is continuing iceberg deterioration research during a four-week cruise aboard USCGC EVERGREEN (WMEC 295). At most, this effort will add two more icebergs to the data set. Research into deterioration is time consuming and will likely continue for the next several years.

5. CONCLUSION

The International Ice Patrol is responsible for conducting the operational marine science program of the Coast Guard and has planned an active oceanographic program on the Grand Banks for the next four years. Through daily iceberg data exchanges with Canadian government and industry and the technological advances, i.e. SLAR, TOD, the IIP will keep the North Atlantic mariner informed of the hazardous ice which exists in and around the Grand Banks. Our goal is to maintain our record of no loss of life or property due to collision with an iceberg outside the advertised limits of all known ice while the service has been in operation.

6. REFERENCES

1. Mountain, D. G., 1980. On Predicting Iceberg Drift. Cold Regions Science and Technology, Vol 1: 273-282.
2. White, F. M., M. L. Spaulding, and L. Gominho, 1980. Theoretical Estimates of the Various Mechanisms Involved in Iceberg Deterioration in the Open Ocean Environment. U. S. Coast Guard, Office of Research and Development, Washington, DC 20593, 126 pp.
3. Rossiter, J. R., L. D. Arsenault, A. L. Gray, E. V. Guy, D. J. Lapp, R. O. Ramseier, and E. Wedler, 1984. Detection of Icebergs by Airborne Imaging Radars. Canadian Remote Sensing Conference, St. John's, Newfoundland, Aug. 1984.
4. LaViolette, P.E., 1983. The Grand Banks Experiment: A Satellite/Aircraft/Ship Experiment to Explore the Ability of Specialized Radars to Define Ocean Fronts. Report 49 Naval Ocean Research and Development Activity, NSTL Station, Mississippi 39529, 126 pp.
5. Anderson, I., 1984. Report of the Ice Patrol Service in the North Atlantic, Season of 1984 (In preparation).
6. Venkatesh, S., M. El-Tahan, and P. T. Mitten, 1985. An Arctic Iceberg Deterioration Field Study and Model Simulations. Annals of Glaciology, Vol 6. (In press).

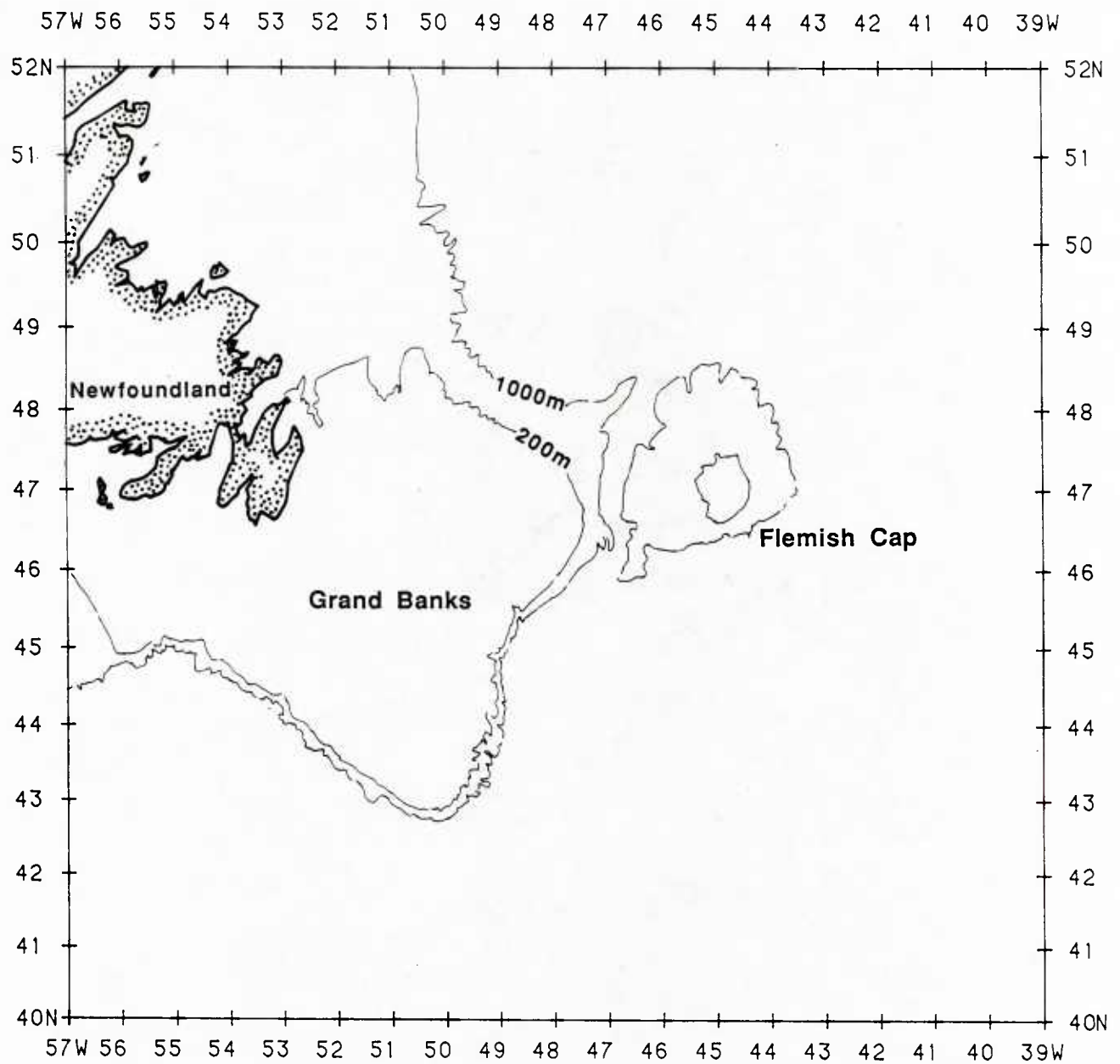


Figure 1. International Ice Patrol operations area.

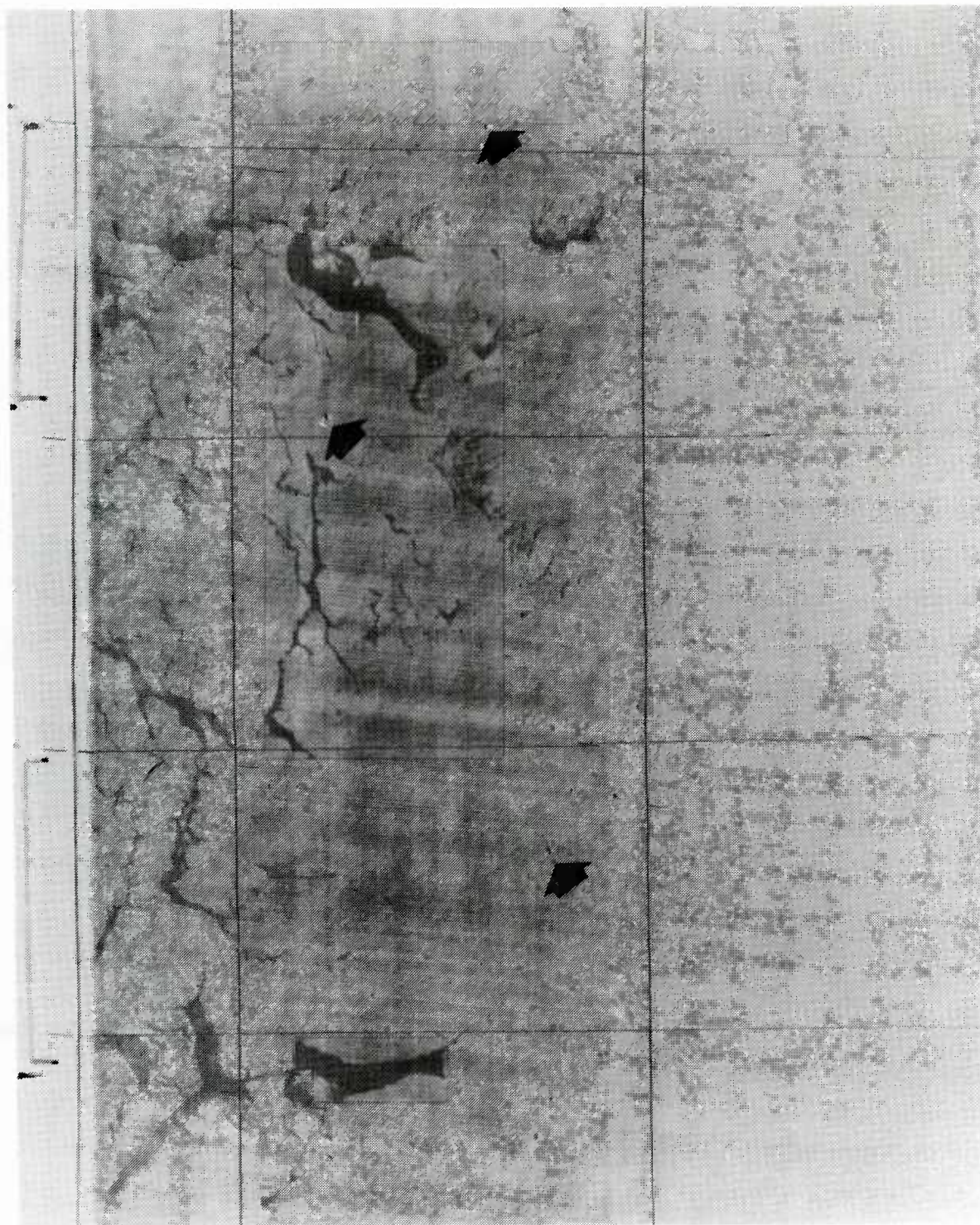


Figure 2. SLAR image taken from an altitude of 8000 feet shows icebergs (arrows) amidst patches of sea ice (dark patches).

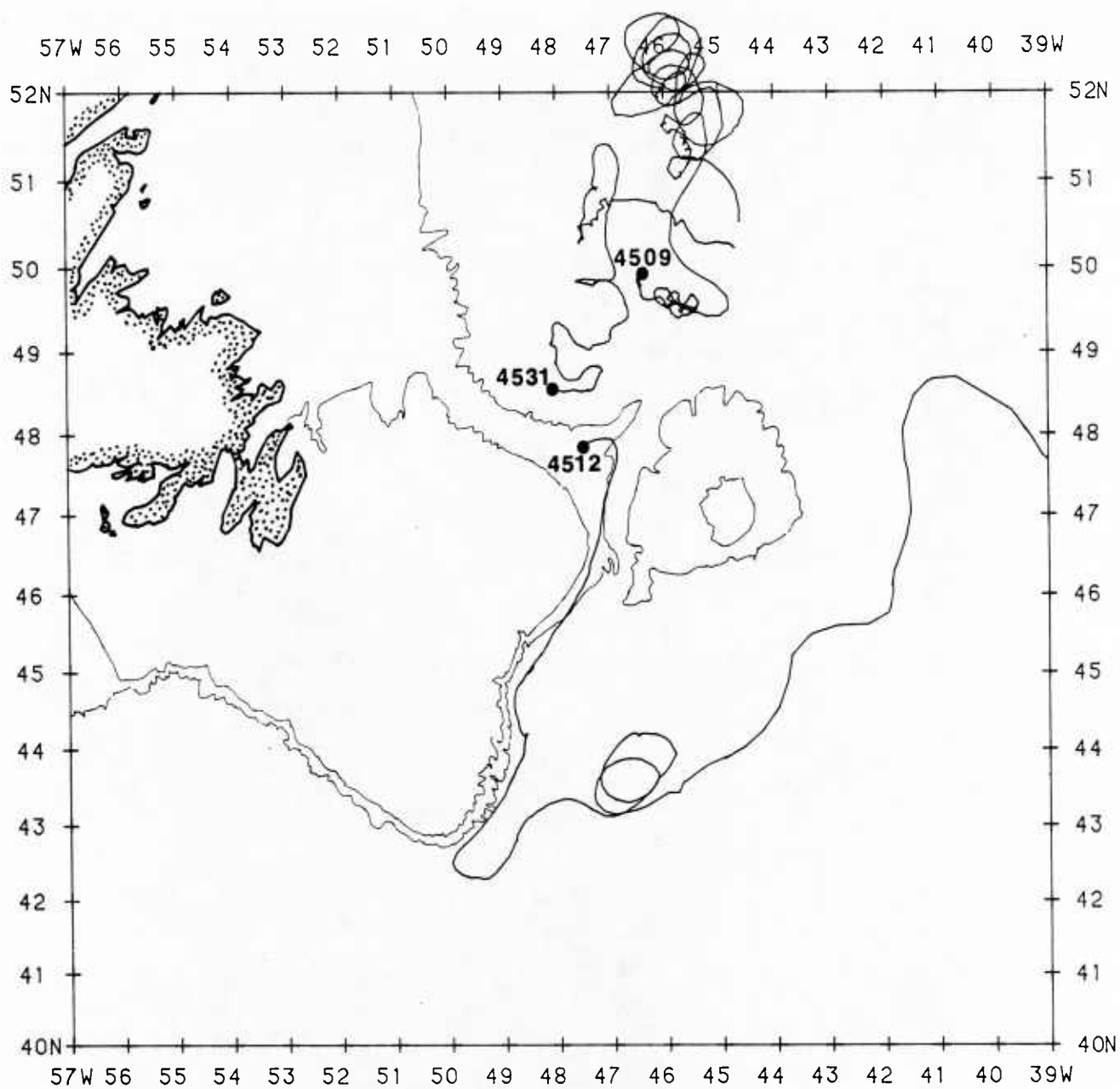


Figure 3. Tracks of three Tiros Oceanographic Drifters (4509, 4512, and 4531) deployed in the International Ice Patrol operations area during 1984.

REMOTE SENSING FOR POLAR ICEBREAKER NAVIGATION IN SEA ICE

RICHARD M. HAYES

ICE OPERATIONS DIVISION
U.S. COAST GUARD HEADQUARTERS
WASHINGTON, DC 20593

ABSTRACT

Icebreakers conduct expeditions to the polar regions during all seasons of the year. Knowledge of the sea ice conditions along an icebreaker's intended route comes either from recon by the vessel's embarked helicopters, or from the aloft conn on the mast. No current method has proved fully adequate for the routing of icebreakers in sea ice. This is especially true given the trend to extend operations into the fall and winter when sea ice conditions are the most severe and the prolonged darkness of the polar night precludes the use of conventional methods of recon. Consequently a certain degree of inefficiency must be accepted in terms of lost time, greater fuel consumption, increased wear and tear on the vessel and machinery, and a heightened chance of besetment. This paper discusses the need for remote sensing in support of icebreaker navigation in sea ice, the present capabilities and future possibilities.

1. INTRODUCTION

U.S. polar icebreakers routinely operate in the ice-covered waters of North America, Greenland and Antarctica. Their polar missions include the annual resupply of U.S. stations in the Arctic and Antarctic, logistical support, and scientific and engineering research. Historically, the Department of Defense and the National Science Foundation, together, have accounted for 75% of the total employment days for the polar icebreaker fleet [1]. DoD requirements encompass all of the above-mentioned activities in the arctic regions of Alaska and Greenland. The support is provided for both classified and unclassified projects.

Conventional icebreakers vary in their ability to break ice, principally, in accord with their displacement and propulsion power. The most powerful U.S. polar icebreakers can break 5 or more feet of undeformed, level sea ice at a continuous speed of 3 knots. In the backing and ramming mode this value can be exceeded by a factor of two to four.

Other polar icebreakers in the fleet are rated at 3-4 feet for level sea ice. Regardless of ice-breaking capability, all icebreakers can benefit from the intelligent use of sea ice reconnaissance to: 1) extend the range of polar operations, 2) avoid unnecessary wear and tear on the vessel and its machinery which add to maintenance costs and impair mission effectiveness, 3) conserve fuel to decrease costs and increase on-scene endurance time, and 4) decrease the likelihood of becoming beset with all of the concomitant danger and expense. Hence, the following discussion defines the role of remote sensing in polar icebreaker operations.

2. REQUIREMENT

The requirement for remote sensing originates with the twin goals of transiting ice-covered waters with maximum efficiency (i.e., in the swiftest manner with minimum fuel consumption) while at the same time avoiding hazards. The baseline measurements for supporting ice navigation have been determined from a poll of icebreaker commanding officers and others experienced in ice operations. This group constituted a subset of individuals in a 1983 Navy/NOAA Joint Ice Center survey of user requirements (Table 1). The information needed to support icebreaker routing and ice piloting may be summarized as follows:

- o Feature identification and location: ridges, rubble fields, leads, and polynyas
- o Extent and concentration by age/type
- o Ice thickness
- o Snow cover extent and thickness
- o Ice drift velocity
- o Internal stress

The ability to obtain timely, detailed and accurate information about sea ice conditions has both a strategic and tactical significance for icebreaker

TABLE 1. U.S. COAST GUARD SEA ICE RECONNAISSANCE REQUIREMENTS (PRELIMINARY)

PARAMETER	TYPE OF OBSERVATION	ACCURACY		OBSERVATIONAL REQUIREMENT				PRODUCT DELIVERY	
		DESIRED MIN		SPACE DESIRED	RESOLUTION MIN	FREQUENCY DESIRED	MIN	(TIME DELAY) DESIRED	MIN
Thickness	Area Average	0.2 m	1 m	50 m	1 km	daily	3 days	< 3h	< 1d
Boundary	Line Position	1 km	10 km	1 km	10 km	daily	3 days	< 3h	< 1d
Concentration	% of Area	5 %	10 %	1 km	10 km	daily	3 days	< 3h	< 1d
Motion	Point Displ.	100 m/d	2 km/d	5 km	20 km	0.25d	1 day	< 3h	< 0.25d
Ridging									
Density	Number/Area	10 %	25 %	100 m	1 km	daily	3 days	< 3h	< 1d
Orientation	Orientation	10 deg.	30 deg.	NA	NA	daily	3 days	< 3h	< 1d
Height	Ht.(Sail/Keel)	1 m	2 m	NA	NA	daily	3 days	< 3h	< 1d
Ice Type	Frac/Area by Type	5 %	10 %	1 km	10 km	daily	3 days	< 3h	< 1d
Leads									
Location	Line Position	20 m	100 m	100 m	1 km	0.5 d	1 day	< 3h	< 0.5d
Orientation	Orientation	10 deg.	30 deg.	NA	NA	0.5 d	1 day	< 3h	< 0.5d
Floe Position	Point Location	20 m	100 m	20 m	100 m	0.25d	1 day	< 3h	< 0.25d
Surface Melting	Frac/Area	5 %	10 %	50 m	1 km	daily	3 days	< 3h	< 1d
Snow Cover	Frac/Area	5%	10%	100 m	1 km	daily	3 days	< 3h	< 1d
	Thickness	0.2 m	0.5 m	50 m	1 km	daily	3 days	< 3h	< 1d

navigation. Wide area surveillance at less frequent intervals satisfies the strategic need for assessing the variability of the ice cover on a semi-basin or whole-sea basis for general route planning. Likewise data of these type are important for their contribution to the sea ice climatological record, a record which is used in designing new icebreakers and in delimiting the operating range of existing ones. The strategic requirements may be character-ized as being the less stringent ones in terms of spatial resolution and frequency of observation. For the most part, strategic requirements may be met by existing remote sensing systems.

Tactical support for icebreaker navigation implies a daily reconnaissance capability for an area equal to the maximum distance an icebreaker can travel in sea ice in one day (< 250 km). This requirement might be relaxed to an observational frequency of every other day with a coverage of 500 km in areas and at times where the sea ice is not highly dynamic. The key characteristics of a tactical ice reconnaissance system are:

- o All-weather, day/night capability (implies microwave sensors)

- o High spatial resolution and observational frequency
- o Near-real-time data processing and analysis (including time tag and geolocation for imagery)
- o Data telemetry to vessels in high latitudes

Tactical ice reconnaissance must be timely enough, in that the products have to arrive on-scene in time to incorporate the information they contain in the decision-making process for route planning, and be of sufficiently high enough resolution to discriminate features on a scale that is useful for ice piloting. The attributes for the measured parameters in Table 1 relate more to the tactical than the strategic requirements.

3. PRESENT CAPABILITY

U.S. Coast Guard icebreakers generally deploy with two embarked HH-52A 'Sea Guardian' helicopters (scheduled to be replaced by the HH-65A 'Dolphin' at the end of the decade). These helicopters are essential for general logistical support and add to the scientific research capability of the vessel, as well as being the primary reconnaissance vehicles for the icebreakers. While the advantages of

helicopter sea ice reconnaissance are evident -- extended range beyond vessel's height-of-eye, direct observation by human observer, etc. -- there are disadvantages from limitations associated with weather, visibility, darkness, range, and launch windows. Helicopter reconnaissance, being visual, cannot penetrate snow cover or peer through snow storms to identify ice conditions below. The only other alternative to helicopter reconnaissance is the shipboard radar and the vantage point offered to the observers in the aloft conn on the mast. These alternatives are, of course, extremely range-limited, and suffer from all of the weather and darkness restrictions of the helicopters except for the radar. Hence, one might say that icebreakers are very limited in their ability to supply, on their own, sea ice reconnaissance which can contribute to effective routing.

Recognizing these shortcomings, other nations have incorporated advances in remote sensing technology into their routine icebreaker operations where needed. The USSR operates the largest water-borne transportation system in ice-covered waters of the world along the Northern Sea Route. One report estimates that the annual cargo volume exceeded 15 million tons for the period of 1976-1980 through extension of the navigation season [2]. The Northern Sea Route, which supplies communities of the Soviet arctic from Murmansk to Provideniya, is supported by an aircraft- and satellite-based microwave ice reconnaissance system. Tactical reconnaissance is accomplished from fixed-wing aircraft equipped with side-looking airborne radar (SLAR) [3]. A real-aperture imaging radar aboard the COSMOS-1500 satellite provides both strategic and tactical sea ice surveillance. With direct satellite-to-ground links to processing centers at Novosibirsk and Khabarovsk, all-weather, day/night remote sensing is available to aid the icebreakers and cargo vessels along the Northern Sea Route. This system is credited with guiding the approximately 50 supply ships and icebreakers that had become trapped in the heavy arctic ice near Wrangel Island in the Chukchi Sea in the fall of 1983 [4].

In the western Arctic Canadian entrepreneurs are exploring the Beaufort and Labrador Seas for oil and gas, and the arctic islands for mineral resources. Private companies provide remotely-sensed reconnaissance so that industry might pursue their activities most economically and at reduced risk. Radar-equipped aircraft operate out of Inuvik, NWT in the Beaufort Sea to give the operators of arctic drill ships and man-made islands with rigs a detailed view of the

surrounding ice conditions, ice field motion, and the presence of any hazards to the rigs such as large multi-year floes and icebergs. This information is regularly relayed to the drill rigs and the commercial ice-breaking support vessels which tend them and are responsible for their safety. A similar operation is conducted from airfields in Newfoundland and Labrador to assess the ice conditions and to locate icebergs which are a threat to drilling operations off the east coast of Canada. In addition to assisting oil and gas exploration in this region, aircraft imaging radar is used to extend the navigation season of the ice-breaking ore carrier, M/V ARCTIC, between Little Cornwallis Island in the Canadian arctic archipelago and Europe [5].

Capabilities in the United States for supporting icebreaker navigation have been limited to the strategic. Regular sea ice analyses and forecasts for all polar regions are provided by the Navy/NOAA Joint Ice Center (JIC) in Suitland, Maryland. Radioteletype messages are transmitted weekly delineating the ice edge and ice concentrations within. Contoured ice charts are available in radio facsimile form in some select regions. These products are derived primarily from NOAA polar-orbiting satellite visible and infrared imagery (AVHRR), supplemented by some Nimbus passive microwave images and Navy aircraft reconnaissance [6]. At a recent briefing JIC noted the following limitations using currently available resources:

- o Limited all weather capability
- o Limited ability to determine ridging/keeling
- o Limited iceberg, polynya, and lead detection
- o Limited ability to determine age or ice thickness

In addition to receiving the Navy messages the two U.S. POLAR Class icebreakers (POLAR SEA and POLAR STAR) are equipped with modern APT (Automatic Picture Transmission) color interactive processing systems which allow them to receive low resolution (~ 4 km x 4 km) visible and infrared imagery from the polar-orbiting meteorological satellites.

While the above-mentioned services are adequate for strategic purposes they offer little or no capability for the tactical requirement. Describing the first use of the APT aboard the USCGC POLAR SEA in the Chukchi and Bering Seas during the winter 1983 cruise, the commanding officer said:

" Although the APT imagery showed much lighter ice conditions to the east of Nunivak and St. Lawrence Islands (Figure 1) the user group's project called for a transit to the west of these islands, an area shown by the APT to have fairly heavy ice concentrations. Our transit confirmed this and resulted in several days of backing and ramming operations, which was both time consuming and increased our fuel consumption considerably. It was agreed that, had it not been for the project requirements, our trip to the Chukchi Sea could have been accomplished quicker and on less fuel if we had gone up the east side of the islands, as had been suggested by the APT. Once past the Bering Straits, the APT was very influential in determining the ship's intended track and the direction in which the ice recon helo flights would be made. " [7]

One of the project scientists on that deployment stated in a trafficability study report that:

" In the Bering Strait, a route was specifically identified from APT products as containing thin ice and resulted in savings of both fuel and time (Figure 2). In summary, the shipboard APT system was employed as an operational aid to navigation. This satellite data proved to be extremely valuable in identifying the large scale features of the ice cover on the Bering and Chukchi Seas. " [8]

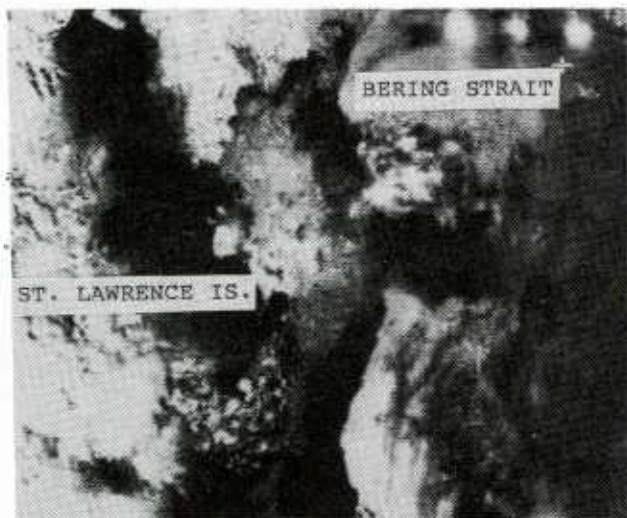
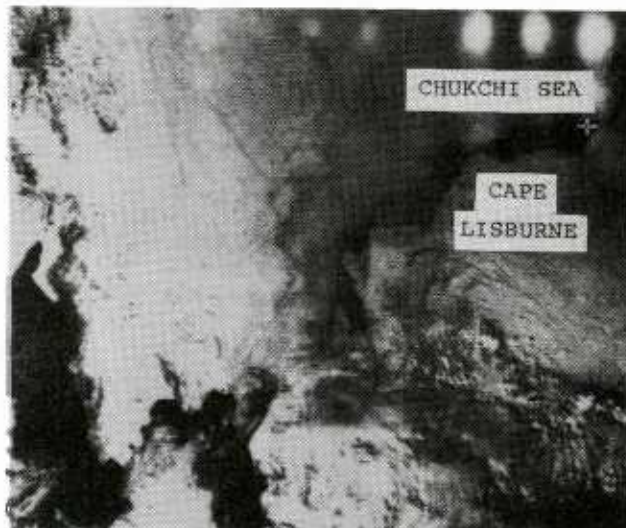


FIGURE 1. APT image (AVHRR-vis.) of the Bering Sea showing open water (or new ice) to the east of St. Lawrence Island and heavy ice concentrations to the west

FIGURE 2. APT image (AVHRR-vis.) of the northern Bering Sea and the Chukchi Sea showing a shore lead (or new ice) on the eastern side of Bering Strait continuing around into the Beaufort Sea



The commanding officer of POLAR SEA ends his evaluation of the APT with the following caveats:

" In conclusion it is felt that the APT system is quite an asset in weather and ice observation and in navigation planning. However its usefulness in navigation through ice is limited to its resolution and inability to 'see' through cloud cover. "

4. SEA ICE RECONNAISSANCE SENSORS

There are a number of sensor systems in existence, under development, or in the planning stages which show considerable promise for meeting many of the tactical requirements for supporting ice navigation. These systems, both airborne and spaceborne, consist mainly of microwave instruments which possess day/night and almost all-weather capability. Each of these sensors and their potential application for sea ice remote sensing will be discussed. (Table 2 provides a summary.)

SAR, SLAR -

Synthetic Aperture Radar and Side-looking Airborne Radar are terrain-mapping imaging radars. While both can and are flown in airplanes, only SAR can provide high-resolution images from spacecraft altitudes. Imaging radars have sufficient resolution (~ 20-30 m for spacecraft SAR) and an appropriate viewing geometry to

distinguish sea ice features of interest to navigation, as well as a limited capacity for ice classification.

Commercial aircraft SAR systems exist that have even higher resolution and real-time processing as well. There are plans to launch two satellites with SAR which could be utilized for sea ice reconnaissance -- ERS-1 (European Space Agency, 1989) and Radarsat (Canada, 1993) -- both operating at C-band (5.3 GHz) and having a nominal resolution of 25-30 m. Efforts to establish a U.S. ground station to receive and process these data at Fairbanks, Alaska are already underway. In addition to these "free-flyers" in near-polar orbits, several Shuttle Imaging Radar (SIR) experiments at X- and L-bands are planned for the latter half of this decade.

Advantages:

- feature identification (e.g., ridges, leads, floes, etc.)

- high resolution (SAR) (e.g., ≤ 10 m)
- limited classification (open water, 1st-yr, old)
- (dry) snow penetration
- ice motion vectors from repetitive coverage

Disadvantages:

- classification ambiguities: distinguishing open water in still air from new and young ice; 1st-yr from multi-yr during melt and freeze-up; wet snow cover
- very high data rates
- complex processing (SAR)

TABLE 2. PLANNED EARTH OBSERVATION SATELLITE SYSTEMS WITH RELEVANCE TO SEA ICE RECONNAISSANCE AND FORECASTING

MISSION ¹	NATION	YEAR	SENSORS ²		MEASURED OR INFERRED PARAMETERS	APPLICATION	
			TYPE	NAME		STRATEGIC	TACTICAL
DMSP	USA	1986	PM	SSM/I	ICE EXTENT/CONC.	GOOD	POOR
ERS-1	ESA ³	1989	SAR	AMI	ICE EXTENT/FEATURES TYPE	GOOD GOOD	GOOD FAIR
NROSS	USA	1989	PM	SSM/I	ICE EXTENT/CONC.	GOOD	POOR
JERS-1	JAPAN	1993	SAR	SAR	ICE EXTENT/FEATURES TYPE	GOOD GOOD	GOOD FAIR
RADARSAT	CANADA	1994-91	SAR	SAR	ICE EXTENT/FEATURES TYPE	GOOD GOOD	GOOD FAIR
NOAA J-M	USA	1986-?	DCLS	ARGOS	ICE DRIFT/WX/OCEANO	GOOD	FAIR
SPACE STATION	USA	199?	PM	AMR/HMMR	ICE EXTENT/CONC.	GOOD	GOOD
			SAR	SEASAR	ICE EXTENT/FEATURES TYPE	GOOD GOOD	GOOD FAIR
			SCAT	NSCAT	ROUGHNESS	GOOD	GOOD
			DCLS	DCLS	ICE DRIFT/WX/OCEANO	GOOD	FAIR

¹MISSION ACRONYMS: DMSP - Defense Meteorological Satellite Program; ERS-1 - ESA Remote Sensing Satellite; NROSS - Navy Remote Ocean Sensing System; JERS-1 - Japanese Earth Remote Sensing Satellite

²SENSOR ACRONYMS: PM - Passive Microwave Radiometer/Imager; SAR - Synthetic Aperture Radar; DCLS - Data Collection and Locating System; SCAT - Radar Scatterometer
 SENSOR NAMES: SSM/I - Special Sensor Microwave/Imager; AMI - Active Microwave Instrument; AMR/HMMR - Advanced Microwave Radiometer/High-Resolution Multifrequency Microwave Radiometer; NSCAT - NROSS Scatterometer

³ESA - European Space Agency

Passive Microwave Radiometers-

Passive microwave radiometers may also be flown at spacecraft as well as aircraft altitudes. They work at day and at night, can penetrate cloud cover, and are not affected by weather except for heavy precipitation. The resolution of spacecraft passive microwave sensors ranges from 30 km for the Nimbus 7 Scanning Multifrequency Microwave Radiometer (SMMR) [9] to 16 x 14 km for the Defense Meteorological Satellite's Special Sensor Microwave/Imager (SSM/I). SSM/I is scheduled for launch in 1986 [10]. Recent aircraft experiments at 90 and 140 GHz show considerable promise for discriminating among new, young, first-year, old ice, and open water [11]. Unlike SAR, however, the resolution of passive microwave imagers varies as a function of altitude. Hence, high resolution from spacecraft altitudes would require the use of extremely large antennas.

Advantages:

- sea ice edge location
- ice concentration by type
- wide-swath (1394 km for SSM/I)

Disadvantages:

- low resolution precludes all but very large feature identification from space and results in the spatial averaging of inhomogeneous ice types
- sensitivity to radio frequency interference [12]
- ice classification ambiguities introduced by ice that is wet or snow-covered

Impulse Radar-

One of the most useful parameters to be measured in support of ice navigation, yet one of the most difficult to accomplish, is ice thickness. A variety of techniques have been evaluated using electromagnetic and acoustic sensors to remotely estimate sea ice thickness [13]. Most of the results have been disappointing with a few notable exceptions. Impulse and FM/CW radars operating at low frequencies (10 - 300 MHz) have been shown to be capable of receiving and detecting signal returns from the ice/surface and ice/sea water interfaces under certain circumstances. Combining measurements, or in some cases estimates, of the relative dielectric constant of the ice with the time delays of

the radar signal from the two interfaces, allows an estimate of ice thickness of reasonable enough accuracy to be a contribution to ice navigation. It is in fact one such device, the 'Lyod' (or 'Ledostav'), that purportedly surveyed ice thickness along the route of the Soviet icebreaker LEONID BRESHNEV (formerly ARKTIKA) on her 1977 voyage to the North Pole [14].

Impulse radars have been investigated in the U.S. and Canada in an effort to document their capabilities and limitations [15]. Difficulties in the universal application of radars designed to measure ice thickness stem from the dielectric properties of sea ice and the effect they have on electromagnetic interaction. Young sea ice has a high saline content. As sea ice ages the inclusions of saline water form brine channels and drain toward the bottom layers; hence, the ice becomes less saline with time. Saline ice is said to be electromagnetically 'lossy', causing it to absorb and attenuate electrical radiation directed at it. Sea ice tends to contain brine and air pockets which scatter energy as well. Ice that has been deformed into ridges and hummocks are composed of blocks of ice enclosing voids filled with air and sea water which freezes and melts and re-freezes over time. Furthermore, studies have shown that when ice crystals are formed they tend to align themselves along a preferred c-axis, such that the electromagnetic energy is radiated differentially relative to a given azimuth angle with respect to the c-axis field.

The consequence of all of this is that: 1) the lossiness of the ice attenuates the signal to the extent that it is sometimes not possible to obtain a return from the ice/water interface; 2) low frequencies must be used to achieve penetration of the ice, thus reducing the vertical resolution of the measurement; 3) high gain systems are required to overcome the lossiness of the ice; 4) the inhomogeneity of the ice (e.g., brine and air in voids; melting/formation at the ice undersurface) leads to a lack of definition of the ice/water interface, hence, introducing errors in the thickness measurement; and 5) the c-axis orientation will affect the radar return relative to the orientation of the antenna and its polarization. Nevertheless some success has been achieved from sled and helicopter-mounted instruments making measurements near the ice surface [16,17]. Research to date indicates that impulse radar may be able to measure the thickness of level first year ice and possibly some multi-year ridges as well, but has not been shown to be successful on first-year ridges.

Advantages:

- limited capability for remote estimation of ice thickness

Disadvantages:

- must be conducted near the surface (≤ 30 m) from a slow-moving vehicle
- not capable of measuring thickness for all ice types and under all conditions
- the relative dielectric constant must be determined from samples or inferred from the ice type to calculate thickness (Note: This requirement may be eliminated through use of dual antennas)

Radar Altimeters and Scatterometers-

There are other kinds of active radars -- altimeters and scatterometers, for instance -- that can provide additional information about ice such as surface roughness. This is useful in modeling ice drift velocity and in characterizing ice type. However, either because of a narrow sensor swath and/or the nature of the parameter measured, these sensors will not be considered for inclusion in the baseline core of instruments of a reconnaissance system meeting the tactical requirements for ice navigation and piloting support. As mentioned above, non-microwave sensors have been eliminated from the outset as they cannot meet the all-weather, day/night criteria.

5. PILOT PROJECT

In November of 1984 an opportunity presented itself to demonstrate the feasibility of applying remotely-sensed data to aid icebreaker navigation under operational conditions. The USCGC POLAR SEA, on the 22nd of November during an Arctic Summer West '84 deployment to the Beaufort Sea, became temporarily beset in a ridge in a 'shear zone' area under considerable pressure approximately 110 km northwest of Prudhoe Bay, Alaska (Figure 3). Intera Radar Services Ltd. of Calgary, Alberta was asked and agreed to overfly POLAR SEA with their STAR-1 synthetic aperture radar operating out of Inuvik, NWT. The imagery taken on the 27th of November, when the POLAR SEA had managed to extract herself from a ridge 15-25 m deep, was processed on board the STAR-1 aircraft and air-dropped to the icebreaker at the completion of the reconnaissance flight.

In the image one can clearly see a series of ridges (bright linear features tending NW to SE) converging at a point where the icebreaker had become beset in the shear zone (Figure 4). Bright features in the

image are multi-year ice and dark areas are first-year or new ice. The trackline taken by the icebreaker the next day is shown on the imagery. Commenting on the use of the SAR imagery, POLAR SEA's commanding officer said,

" On that date [November 27], POLAR SEA had just backed free of a shear zone pressure area after being beset for five days. POLAR SEA was facing a transit through 10-30 miles of rubble fields and ridges created by shear zone activity on 22 November. The imagery provided excellent detail and clarity of the ice conditions; including the location of rubble fields and shear ridges. The imagery and ice reconnaissance using ship's helicopters allowed POLAR SEA to effectively choose a route through these areas of pressured ice . . . In my opinion, radar imagery has definite application to icebreaker operations in the Arctic. This is particularly true during the late and early periods of the ice season when darkness and weather often limit helicopter ice reconnaissance. " [18]

One might speculate with hindsight that had such imagery been routinely available to the icebreaker as part of an operational sea ice reconnaissance system, the ridge and rubble area of multi-year ice, and the focus of pressure developing there by the shearing motion, might have been recognized and avoided. It is noteworthy that this incident occurred at a time and place when daylight is limited to only a few hours of twilight each day.

6. THE FUTURE

Continued experimentation with aircraft remote sensing systems will lead to the further refinement of sensor parameters for sea ice reconnaissance (e.g., frequency, polarization, look angle, integration time, gain, etc.). In turn these developments will be translated into polar-orbiting satellite systems as evidenced by a couple of planned non-U.S. earth observation platforms [19] as well as those proposed for the U.S. Space Station during the next decade [20]. Spaceborne systems, both planned and proposed, with relevance to sea ice reconnaissance are summarized in Table 2.

It remains to be seen whether any of these systems will successfully evolve into a fully-operational sea ice monitoring program that could support tactical ice navigation. While progress is slowly made toward building and launching appropriate sensors there exists considerable concern over whether the data processing, analysis, and dissemination infrastructure will be developed and in place in time to exploit



FIGURE 3. Shipboard photograph of the shear ridge on which the USCGC POLAR SEA had become beset on 22 NOV 1984. Ridge was measured to be 15-25 meters deep. V-shaped indentation was made by the icebreaker's bow. (Photograph courtesy of Arctec Engineering, Inc.)

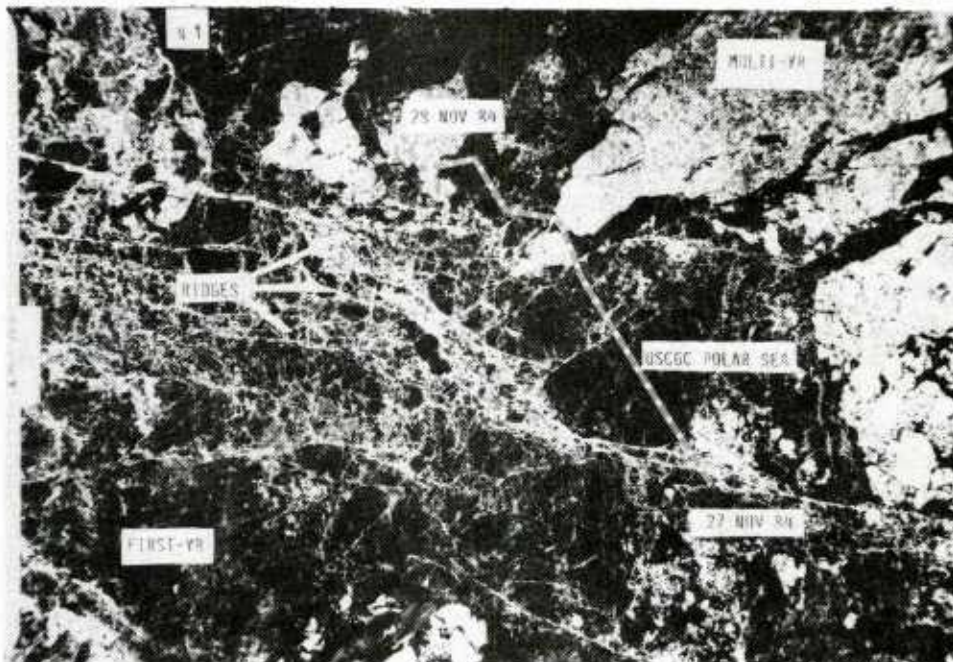


FIGURE 4. STAR 1 synthetic aperture radar image of the area surrounding USCGC POLAR SEA at approximately 71-36.8N, 148-35.2W on 27 NOV 1984. The imagery shows a series of ridges (bright linear features tending NW to SE) converging on at a point where POLAR SEA had become temporarily beset in a shear ridge. POLAR SEA's trackline the following day (29 NOV) is shown on the image. Scale is 1:250,000. (Imagery courtesy of Intera Technologies Ltd.)

these systems operationally. Nowhere has this problem been more succinctly addressed than in some of the planning documents for spaceborne ice reconnaissance systems such as ICEX [21] and Radarsat [22]. The key elements of such a system are:

- earth stations to receive, record, and process data from regions of interest
- data enhancement, analysis, forecasting and archival facility
- facility for dissemination of select products at low-to-moderate data rate to remote sites via DOMSAT links in near-real time

The required products are imagery with complementary analyses and forecasts. The imagery would be used for feature identification and location. Analyses could provide ice edge location, ice concentration by type, thickness estimates, and location of zones of convergence/divergence. Forecasts could predict ice drift and growth/melt.

Products would not be required in all regions at all times. An operations center could receive the reconnaissance requests and formulate a time/space coverage matrix that could be used for commanding spacecraft performance and scheduling of processing and analysis. This would presumably keep data rates and volume within manageable limits while still meeting the mission requirements. Nevertheless, this still implies the existence of near-real data processing capabilities for such high data rates and sensor complexities as found in SAR. Likewise it anticipates the development of algorithms for automatic image analysis such as might be possible for determining ice classification and ice pack drift vectors [23].

7. SUMMARY

In this paper sea ice reconnaissance has been treated from the point of view of a marine operator who is responsible for safely and efficiently navigating an ice-breaking vessel in ice-covered waters. Furthermore, emphasis has been on the tactical rather than the strategic needs for vessel navigation support. The requirements for operations are almost uniformly more stringent than for research. This is most particularly true for resolution, frequency of observation, and delay time for receipt of products. The key characteristics of an operational sea ice reconnaissance system are:

- day/night and all weather capability
- high resolution

- accurate geolocation
- reliable, scheduled access
- near-real-time processing and dissemination
- analysis aids and forecasts

The benefits to be derived on nearly all polar icebreaker deployments are found in the reduced fuel consumption, decreased wear and tear on the vessels and machinery, lowered incidence of damage, reduced chance of besetment, extended vessel range and endurance, and improved mission performance. When the mission requires operations at the limit of the vessels capabilities, or in the polar night, remote sensing support becomes critical to ensuring mission success.

Satellite systems, planned and proposed for the beginning of the next decade, building upon the success of the first oceanographic satellite, Seasat, in 1978 show the potential for meeting many of the sea ice reconnaissance requirements. Meanwhile, experimentation with aircraft sensors will refine instrument capabilities and provide the necessary data for developing the processing and analysis components of a fully-operational system.

8. ACKNOWLEDGEMENTS

I wish to express my appreciation to Mr. Marc Wride of Intera Technologies Ltd. for providing me with the STAR 1 imagery and to Mr. Richard Voelker of ARCTEC Engineering, Inc. for the photograph of the shear ridge.

9. REFERENCES

1. United States Polar Icebreaker Requirements Study, Interagency Report. U.S. Coast Guard, Washington, DC 20593, July 1984.
2. Tronin, V.A., V.A. Malinovsky, and Yu.A. Sandakov. Problems of river shipping in ice-bound conditions, Proceedings Intl. Assoc. Hydraulic Res., 7th Intl. Symposium on Ice, Hamburg, FRG, 27-31 August, 255-266, 1984.
3. Volkov, N.A. Ice Reconnaissance in the service of science and navigation, in Problems of the Arctic and the Antarctic, A.F. Treshnikov, ed., Vol 50, 9-18, Amerind Publishing Co., New Delhi for the Nat. Sci. Found., Washington, DC, 1982
4. Lenorovitz, J.M. "Soviets Form Cosmos Radar Data Network," Aviation Week and Space Technology, October 15, 23-24, McGraw Hill, NY, 1984

5. "Enhanced Marine Radar Being Used to Extend Arctic Shipping Season," Offshore Resources, vol. 3(1), 20, Spring 1985
6. Godin, R.H. The methodology and availability of Joint Ice Center services to commercial users, Conference Record: Oceans '84, 10-12 September, 944-949, Washington, DC, 1984
7. Little, B.S., (personal communication), Letter report on the use of APT aboard USCGC POLAR SEA, 1983
8. Voelker, R.P., F.A. Geisel, and K.E. Dane., Arctic Deployment of USCGC POLAR SEA - Winter 1983, ARCTEC Engineering, Inc., Columbia, MD, 1983
9. Swift, C.T., L.S. Fedor, and R.O. Ramseier, An algorithm to measure sea ice concentration with microwave radiometers, J. Geophys. Res., 90(C1), 1087-1099, 1985
10. Lo, R.C. and J.P. Hollinger, The Mission Sensor Microwave Imager, its applications and validation, Conference Record: Oceans '84, 13-12 September, 162-166, Washington, DC, 1984
11. Hollinger, J.P., B.E. Troy, Jr., R.O. Ramseier, K.W. Asmus, M.F. Hartman, and C.A. Luther, Microwave emission from high arctic sea ice during freeze-up, J. Geophys. Res., 89(C5), 8104-8122, 1984
12. Hollinger, J.P. and M.R. Keller, NRL RP-3A MIZEX 84 Experiment Report, in MIZEX Bulletin, V:MIZEX 84 Summer Experiment, PI Preliminary Reports, 114-121, U.S. Army Cold Regions Research and Engineering Laboratory, October 1984
13. Hickman, G.D., J.A. Edmonds, A review of technology for sensing ice characteristics, Rep. No. AST-R-200183, Applied Science Technology, Inc., Arlington, VA, January 1983
14. Kazanskiy, I., "'Lyod' sees through the ice floes, Teknika-Molodezhi, no.2, 48-49, 55, 1980
15. Rossiter, J.R., Review of impulse radar sounding of sea ice, Proceedings of the International Workshop on the Remote Estimation of Sea Ice Thickness, September 25-26, St. John's, Newfoundland, 77-108, 1979
16. Morey, R.M., Airborne sea ice thickness profiling using an impulse radar, Report No. CG-D-178-75, U.S. Coast Guard, Washington, DC, June 1975
17. Kovacs, A. and R.M. Morey, Anisotropic properties of sea ice in the 50- to 150 MHz Range, Geophys. Res., 84(C9), 5749-5759, 1979
18. Howell, J.T., (personal communication), Letter report from commanding officer of USCGC POLAR SEA evaluating Intera STAR-1 support during Arctic Summer West, January 1985
19. Earth Observing System, NASA Technical Memorandum 86129, Science and Mission Requirements Working Group Report, Goddard Space Flight Center, Greenbelt, MD, 1984
20. McElroy, J.H. and S.R. Schneider, The Space Station Polar Platform: Integrating Research and Operational Missions, NOAA Technical Report NESDIS 19, Washington, DC, January 1985
21. Ice and Climate Experiment (ICEX), Report of the Science and Applications Working Group, NASA, Goddard Space Flight Center, Greenbelt, MD, October 1979
22. RADARSAT Phase A Final Report, Vol. V, RADARSAT Project Office, Dept. of Energy, Mines and Resources, Ottawa, Ont, November 1982
23. Holt, B. and F.D. Carsey, Classification of sea ice types on Seasat imagery (abstract), EOS Trans. Am. Geophys. Union: 65(45), 932, November 3, 1984

FNOC ARCTIC OPERATIONAL SUPPORT

Kenneth D. Pollak and R. Michael Clancy

Data Integration Department
Fleet Numerical Oceanography Center
Monterey, CA 93943

ABSTRACT

Fleet Numerical Oceanography Center (FNOC) provides support for Arctic operations via products transmitted to the Naval Polar Oceanography Center (NPOC) and Navy ships. Weather and ice predictions, along with oceanographic analyses, climatologies and data bases of bottom depth, bottom sound loss and ambient noise, provide the basis for these products. In addition, new products derived from satellite data are planned for 1986-87.

1. INTRODUCTION

FNOC is a major production facility of the U.S. Naval Oceanography Command. It is the hub and master computer center of the Naval Oceanographic and Meteorological Support System, and provides real-time numerical products peculiar to the needs of the Department of Defense. Product distribution is achieved primarily via the Naval Environmental Data Network (NEDN), the Naval Oceanographic Data Distribution System (NODDS) and the Automatic Digital Network (AUTODIN) system. FNOC maintains a real-time global data base of environmental information and is linked via communications circuits to operational facilities of the U.S. Air Force and the National Oceanic and Atmospheric Administration.

Support for Arctic operations is provided primarily through NEDN products transmitted to NPOC. These products include charts of surface winds and pressures along with reported meteorological observations. Tabulated listings are also transmitted which give model forecasts of surface pressure, temperature, winds, precipitation, percent cloud cover and fog probability at specific locations. These

meteorological forecasts are produced by the Navy Operational Global Atmospheric Prediction System (NOGAPS, Rosmond¹). Higher resolution forecasts may soon be available using the Navy Operational Regional Atmospheric Prediction System (NORAPS, Hodur²) presently being tested for the Arctic.

FNOC also provides NPOC with estimates of ice drift and thickness obtained from empirical models. A more sophisticated model, which includes a detailed treatment of ice physics and predicts additional fields of interest, is presently being tested. These models will be discussed in Section 2.

To a lesser extent, hand tailored products for Navy ships are made and sent by mail. These are normally used for long range planning and are derived from bathymetry, bottom loss and ambient noise files, plus salinity and temperature climatologies.

2. ICE MODELS

A. Thorndike and Colony Ice Model

The Thorndike and Colony³ free drift ice model is run daily at FNOC to relate surface geostrophic winds and ocean currents to the movement of pack ice. This empirical model is based on drifting buoy data obtained during the First GARP Global Experiment and covers the arctic on a 380 km grid. The only inputs required are geostrophic winds computed from NOGAPS surface pressure forecasts.

Thorndike and Colony³ have shown that more than 70% of the variance of ice motion on time scales of a few days is explained by winds alone. Thus, the model optionally computes ice drift with or without currents. Two sources of currents are available: (1) those based on data from ice station and hydrographic station data (U.S. Navy Hydrographic

Office⁴), and (2) those obtained from the University of Washington based on three years of satellite positioned drifting buoy data. Model output sent to NPOC is a tabulated listing of ice drift at 207 locations in the Arctic.

B. Gerson Ice Model

A numerical ice forecasting system developed by Gerson⁵ and Gerson and Simpson⁶ was implemented at FNOC in 1977. Meteorological observations from fixed stations in the Arctic are received at FNOC four times per day and provide the necessary input to drive the model. Surface air temperatures are used to determine degree-days which are accumulated and used in ice thickness estimations. Ice thickness growth calculations are based on Zubov⁷, while thickness reduction uses the method of Bilello⁸. Estimates of ice drift, based on Shuleikin⁹, use surface winds collected every six hours and averaged for a 24 hour period. Listings of observed wind speed and air temperature, plus model estimates of ice thickness and drift at up to 100 stations, are transmitted to NPOC daily.

C. Hibler Ice Model

A dynamic thermodynamic sea ice model for the Arctic Ocean, which contains much more sophisticated physics than those described above, was recently implemented at FNOC. The model, developed by Hibler¹⁰, was programmed for operational use by the Naval Ocean Research and Development Activity and delivered to FNOC in 1984 (Preller¹¹). Daily model runs are made providing 24 hour forecasts of velocity, thickness, concentration, strength, growth and divergence/convergence of sea ice. The model grid size is 127 km with a domain covering the Central Arctic and most of the marginal seas.

Initialization of the model was from a three year spin up to steady state, using realistic forcing, installed on the FNOC computer system as a monthly model climatology. Subsequent model runs are restarted from the previous day's 24-hour forecast. Daily predictions of surface pressure, air temperature, solar radiation, vapor pressure, sensible plus evaporative heat flux and total heat flux required to drive the ice model are obtained from NOGAPS. Monthly climatologies of currents and oceanic heat fluxes, also required, are taken

from the Hibler and Bryan¹² study of a coupled ocean-circulation/sea-ice model.

Figure 1 shows the ice drift predicted by the model for 28 May 85. The cyclonic circulation of ice in the Barents Sea was produced by a 1007 mb low centered over the Yamal Peninsula, while the rapid westerly drift of ice along the east coast of Greenland was associated with a 980 mb low centered over Iceland. Figure 2 shows the ice thickness predicted by the model for the same time.

Comparisons were made of observed ice thickness from Garrett¹³ with the model's monthly climatological ice thickness averaged over one year. These results are shown in Figure 3. Although this comparison suggests that the model ice thickness is biased thin, the mean difference of 0.6 m is within the error estimate of the Garrett¹³ data. Note also from Figure 3 that the model climatology gives a good representation of the relative variation in observed ice thickness for the regions considered.

Using the terminology of Hurlburt¹⁴, ice kinematics and thermodynamics represent a Class 1 (strong, rapid and direct) response to atmospheric forcing, while ice thickness is a result of a Class 3 (slow but direct and integrated) response to this forcing. Useful predictions of these classes of oceanic phenomena require appropriate models driven by accurate atmospheric forcing, but not oceanographic (in this case sea ice) observations to provide initial conditions. The models convert the relatively well observed and well known atmospheric information into the desired but poorly observed and poorly known oceanographic information (see Hurlburt¹⁴). Thus, even without any link to observed ice conditions, the Hibler model is expected to be of value. Nevertheless, to further enhance the product, plans are to update the model predictions from the weekly NPOC hand analyses of ice concentration and ice edge. This information will be digitized at NPOC and transmitted to FNOC for incorporation into the model.

It will probably take a long time to build up operational experience with this model and discover all of its uses, as many of the fields it is capable of producing have never been available to the NPOC analysts before. For example, predictions of ice divergence and convergence may provide useful information for forecasting lead formation and closure. Predictions of ice thickness and strength may be a

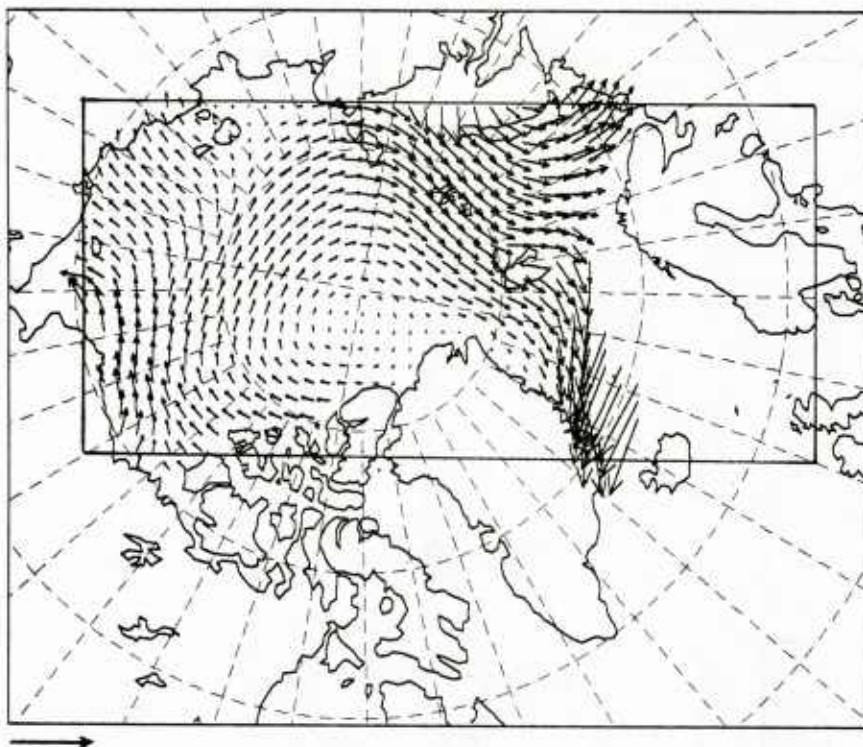


Figure 1. Model forecast of ice velocity for 28 May 1985. Arrow at lower left corner indicates 20 nautical miles per day. Inner rectangle shows model domain.

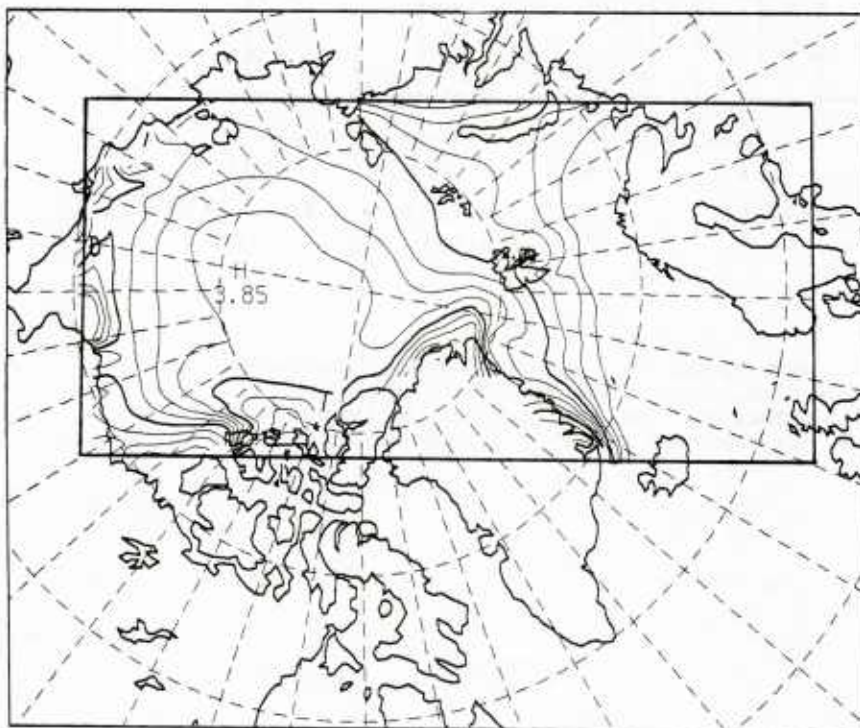


Figure 2. Same as Figure 1 but for ice thickness. Contour interval is 0.5 m.

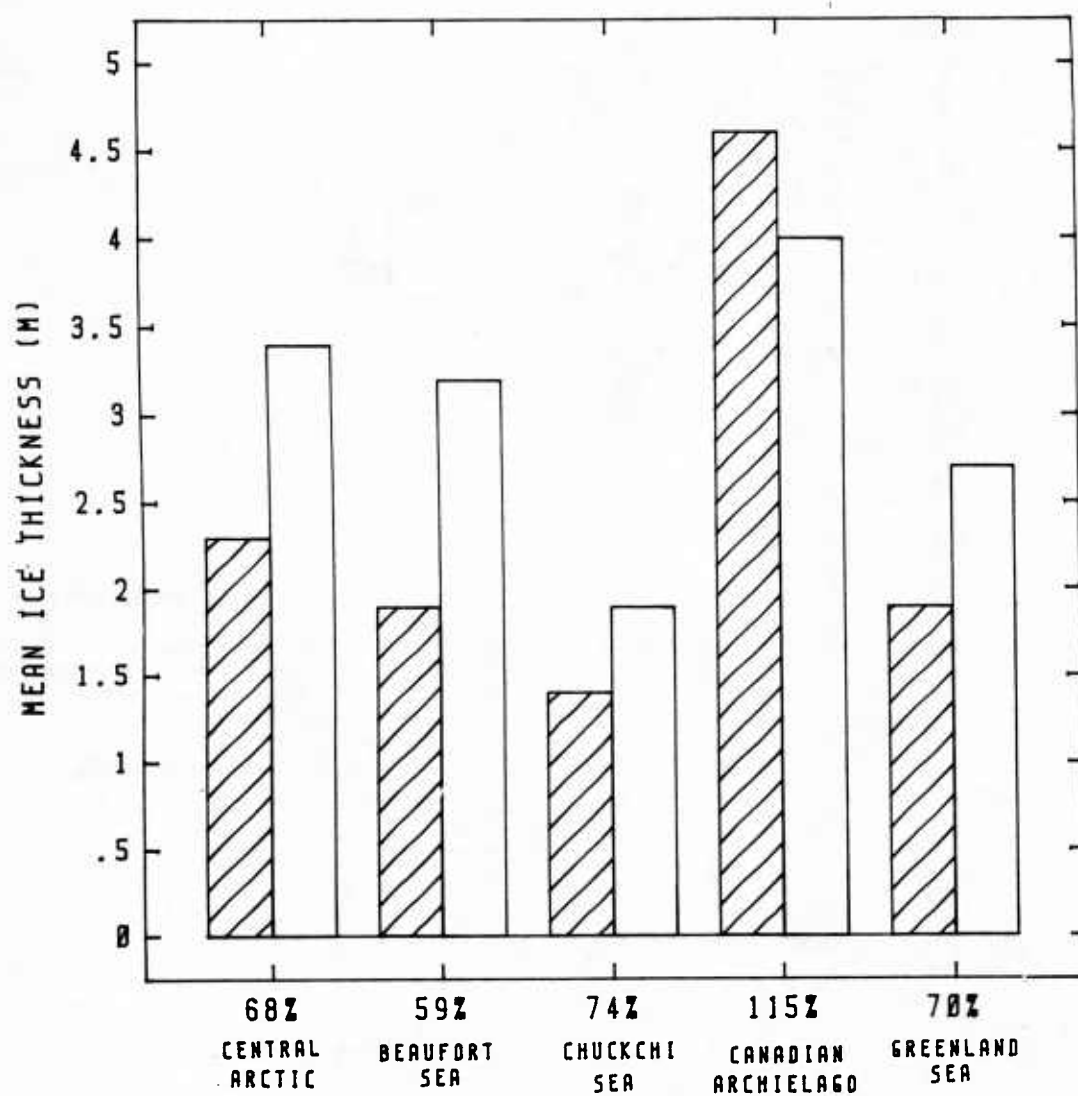


Figure 3. Mean annual ice thickness of model climatology (hatched bar) and observations (open bar) for different regions. Numbers below each bar indicate the ratio, expressed as percent, of modeled to observed thickness.

valuable tool in assessing submarine surfacing potential, while the model's ice kinematics may be useful for estimating ambient noise. Predicted changes in ice thickness and concentration may provide important guidance for subjective ice forecasts.

3. OUTLOOK

FNOC plans to steadily upgrade its support for arctic operations in the years ahead. An arctic NORAPS, providing higher spatial resolution forecasts and better treatment of orographic effects than NOGAPS, is currently being tested. Preliminary results suggest that NORAPS does a better job than the global model in predicting Skagerrak low development off the southern tip of Greenland. The arctic NORAPS will eventually be used to drive higher resolution regional versions of the Hibler ice model, planned for the Barents Sea, Greenland/Norwegian Sea, Sea of Okhotsk and Chukchi-Bering Sea.

New satellite products are expected in the next few years. Ice edge locations will be obtained from the GEOSAT altimeter, and synoptic scale views of ice concentration and type will be provided by the DMSP Special Sensor Microwave Imager. Raw data from these satellites will be processed at FNOC, with derived products transmitted to NPOC.

4. REFERENCES

1. T.E. Rosmond. NOGAPS: Navy Operational Global Atmospheric Prediction System. Preprint Volume, Fifth Conference on Numerical Weather Prediction, Monterey, Published by the American Meteorological Society, Boston, 1981, pp. 74-79.
2. R.M. Hodur. Description and Evaluation of NORAPS: The Navy Operational Regional Atmospheric Prediction System. Monthly Weather Review, 110, 1982, pp. 1591-1602.
3. A.S. Thorndike and R. Colony. Sea Ice Motion in Response to Geostrophic Winds. Journal of Geophysical Research, 87, 1982, pp. 5845-5892.
4. U.S. Navy Hydrographic Office. Oceanographic Atlas of the Polar Sea, Part II, Arctic. H.O. Publication 705, Washington, D.C.
5. D.J. Gerson. A Numerical Ice Forecasting System. Technical Report NOO RP 8, Naval Oceanographic Office, NSTL Station, MS, 1975, 138 pp.
6. D.J. Gerson and L.S. Simpson. Wind Drift of Sea Ice. Technical Report NOO RP 8-S, Naval Oceanographic Office, NSTL Station, MS, 1976, 21 pp.
7. N.N. Zubov. L'dy Arktiki (Arctic Ice). Northern Sea Route Directorate Press, Moscow, 1945, 491 pp., (translated by the U.S. Naval Oceanographic Office).
8. M.A. Bilello. Formation, Growth and Decay of Sea Ice in the Canadian Arctic Archipelago. Research Report 65, Snow Ice and Permafrost Research Establishment, Hanover NH, 1960.
9. V.V. Shuleikin. Drift of Ice Fields. Fizika Moria, Izdamie tret'e (Physics of the Sea, 3rd Edition). Press of the Academy of Sciences of the USSR, Moscow, 1953, pp. 113-129, translated by the U.S. Naval Oceanographic Office.)
10. W.D. Hibler III. A Dynamic Thermodynamic Sea Ice Model. Journal of Physical Oceanography, 9, 1979, pp. 815-846.
11. R. Preller. NORDA/FNOC Polar Ice Prediction System (PIPS)-Arctic: A Technical Description. NORDA Report 108, Naval Ocean Research and Development Activity, NSTL Station, MS, 1985, 50 pp.
12. W.D. Hibler III and K. Bryan. Ocean Circulation: Its Effects on Seasonal Sea-Ice Simulations. Science, 224, 1984, pp. 489-492.
13. R.P. Garrett. Temporal and Spatial Distributions of Arctic Sea Ice Thickness and Pressure Ridging Statistics. M.S. Thesis, Naval Postgraduate School, Monterey, CA, 1985, 167 pp.
14. H.E. Hurlburt. The Potential for Ocean Prediction and the Role of Altimeter Data. Marine Geodesy, 8, 1984, pp. 17-66.

AN AIRBORNE GRAVITY MEASUREMENT SYSTEM FOR USE IN THE ARCTIC

JOHN M. BROZENA

NAVAL RESEARCH LABORATORY

ABSTRACT

The Naval Research Laboratory has developed a prototype airborne gravity measurement system (AGMS). The system was initially designed for use over open water since the vertical accelerations of the aircraft are removed from the gravity signal by subtracting a double differentiated time series of altitudes. Altitudes were provided by an extremely accurate radar altimeter. Recently a pressure altitude sensor has been added to the AGMS which allows operation of the system without constant altimetric reference to the oceanic geoid. Only occasional absolute altitudes are necessary to constrain the variations in height of the isobaric surfaces. This modification to the AGMS makes operation possible in the ice covered regions of the Arctic. In this case the vertical accelerations can be calculated from the pressure altitudes which will be updated to absolute altitudes with laser or radar heights obtained whenever the aircraft passes over leads in the sea ice. The AGMS will make gravity surveying of the Arctic feasible for the first time.

INTRODUCTION

Naval applications for gravity data include corrections to inertial navigation, passive navigation, improvements to earth gravity models, and detection of hazards to navigation (seamount detection). Unfortunately the Arctic regions are inaccessible to surface ships or altimetric satellite measurements. Until now, submarines have provided the only practical gravity measurement platforms for large area Arctic surveys.

The Naval Research Laboratory recently completed a demonstration of a prototype airborne gravity measurement system over the eastern portion of North Carolina. The test was funded by the Defense Mapping Agency (DMA) and was designed to provide comparisons between the NRL fixed wing airborne data and the DMA ground truth. DMA performed the data comparisons. This demonstration was a continuation of NRL's airborne gravimetry program. For more background discussion on the program see Brozena (1984). This paper describes the experimental techniques of airborne data acquisition and analysis, and the application of this method of gravity measurement to the largely unsurveyed Arctic.

The AGMS consists of a LaCoste-Romberg air/sea gravity meter, Global Positioning System (GPS) navigation, radar and pressure altimeters, and data acquisition systems. The gravity meter provides total vertical acceleration (gravity plus accelerations due to aircraft motion). The GPS provides accurate positions and velocities for determination of Eotvos correction. Accelerations due to vertical motion of the aircraft are determined from the altimeter data. Data from all sources are buffered by onboard computer systems and stored on magnetic tape for post mission processing.

I. System Description

A. Gravimeter

The gravimeter utilized for the experiment was a LaCoste and Romberg air-sea meter, S-93, mounted on a three axis stabilized platform. The gravimeter outputs are recorded by a Hewlett-Packard mini computer system. Seventeen analog channels of data are scanned by a reed scanner and digitized by an A/D converter at a nominal two Hz rate. The channels of primary interest are the filtered beam position and the total cross coupling. Unfiltered beam position is prefiltered by a two Hz cutoff low pass filter and acquired at a 10 Hz rate. Spring tension is digitally encoded by the meter and sampled by the scanner. The digitized data are formatted, blocked and stored on disc and tape by the H-P 1000 minicomputer.

B. Altimeters

Two sources of altitude were used for this experiment, a pressure altimeter over land and a radar altimeter over water. The altitudes are required for the height correction and the platform vertical acceleration correction. The pressure system consists of a Rosemount 1201FG pressure transducer ported to a weathervaning static pressure probe. The probe is mounted on a 3.5m boom extending forward from the nose radome in order to remove the sensor from the turbulence and bow shock of the aircraft. The calibration of the pressure transducer is:

$$H = 145,441.86 [1 - (PA/PS) \cdot 1902623]$$

where H = altitude in feet

PA = sensor voltage at altitude

PS = sensor voltage at sea level

The voltage from the Rosemount is sampled and digitized at 10 Hz after anti-alias prefiltering. The radar altimeter is a high precision unit built at NRL. The return of a narrow (< two nsec) transmitted pulse is timed to an accuracy of approximately .2 nsecs. The radar is pulsed at a 10 kHz rate and 100 returns are averaged for each output altitude. This procedure produces a 100 Hz radar altitude time series with accuracies of a few centimeters depending on sea state. The short transmitted pulse length means that the illuminated area on the sea surface is pulse limited rather than antenna beam width limited. The area of interaction is only a few square meters of the sea surface closest to the radar antenna and within its 10 degree beamwidth. The altitudes are therefore unaffected by pitch and roll of five degrees or less. The spatial sampling rate at the nominal aircraft speed of 100 m/sec is one m which should be sufficient to avoid aliasing of the aircraft heights with sea waves. The averaging of the radar data is done in real time by a H-P 200 microcomputer which then transmits the averaged data to the H-P 1000 for blocking and storage.

C. Navigation

The nominal flight profiles for the experiment were; 1) five nautical mile track spacing in a grid pattern, 2) 200 knot aircraft speed and 3) 2000 foot altitude. Horizontal positioning and velocity data for Eotvos and latitude corrections were provided by the Texas Instruments HDUE Global Positioning System. The majority of the tracks were flown during periods of coverage by four satellites. For the location and dates of the flights the satellites were above the horizon between 2300 local and 0500 local. In general these hours provided a good environment for airborne gravity measurement with little turbulence and smooth isobaric surfaces. On one flight we did experience considerable turbulence from the passage of a cold front several hours prior to the flight. Except in cases of extremely bad geometry rms errors should be less than 15 m for position and 15 cm/sec for velocity. The GPS data were blocked and stored by the H-P 1000.

The equipment was installed aboard one of NRL's P-3A aircraft. This plane has a modified research interior and a belly radome which allows easy installation of the radar antennas. The nose radome was also modified to mount the pressure sensor boom.

II. Data Reduction and Analysis

A. Altimetry

The most difficult problem in the analysis of the experimental data proved to be combining the data from the pressure and radar altimeters into a

single continuous time series of altitudes. Several methods were attempted before adopting the current procedure described below:

1. Edit radar altimetry files into segments over water deleting data over land.
2. Build a file of radar heights for each track consisting of the start and end point of each over water segment and one data point per minute in between.
3. Determine the sea level pressure required to match the pressure altitude to the radar at each point in the abstracted radar data.
4. Fit a polynomial to the resulting spatial sea level pressure series to smooth the data. (See figure 1)
5. Recompute the pressure altitudes based on the smoothed sea level pressure estimates.
6. Build a combined altimetry time series using radar segments where possible and pressure data to fill in over land. (See figure 2)

This procedure emphasizes the use of radar altimetry where possible as it is probably more accurate. After the final altimetry series is constructed the data are filtered commensurately with the Lacoste filter and numerically differentiated twice to produce the vertical acceleration correction. The filtered heights are also used in the vertical gradient free air altitude correction. All final gravity values are reduced to sea level (no terrain correction).

POLYNOMIAL FIT TO SEA LEVEL PRESSURE WHICH FORCES PRESSURE-RADAR ALTIMETER MATCH

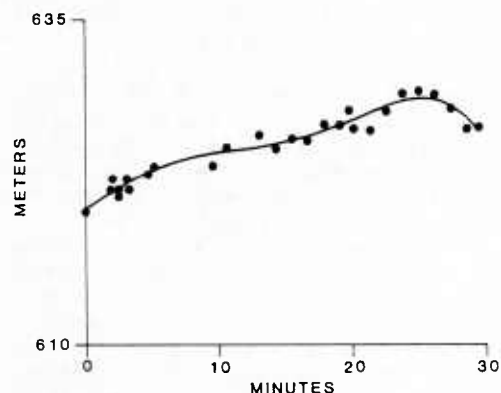


FIG. 1 The dots indicate radar altitude as a function of time. The line is a polynomial fit to these points. The fit is used to generate a sea level pressure which would result in the pressure altitude matching the line at each radar point.

B. Navigation

The GPS data require relatively little processing. The tapes are unblocked and the latitude, longitude and velocity data are stored on disc files. These files are edited for bad

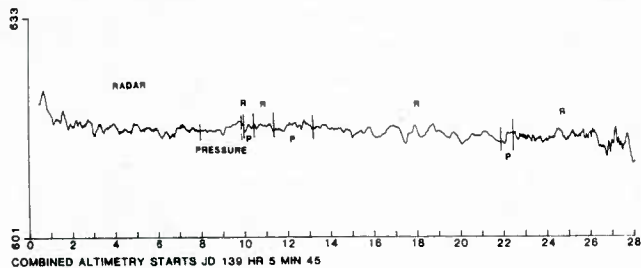


FIG. 2 Combined radar pressure altitude time series after adjustment to pressure data. Vertical axis in meters, horizontal in minutes.

positions and velocities which sometimes occur when switching to a new satellite or in cases of extremely bad geometry. The velocity data must also be filtered with the digital equivalent of the LaCoste hardware filter. Eotvos corrections are then calculated from the velocity data in the edited files and the standard gravity is obtained from the latitude.

C. Gravimetry

Spring tension, cross coupling and beam velocity are abstracted from the gravimetry tapes. These values are splined to equal time spacing and the proper scale factors for meter S-93 are applied. The spring tension is filtered to match the beam velocity and cross coupling and the resulting data are combined with the processed navigation and altimetry. The resulting raw gravity values are filtered backwards in time to remove phase lags caused by the forward filtering. At this point the gravity is in the form of profiles along the track. Plotting these profiles revealed that there were occasional large amplitude relatively short period (two-four minutes) deviations in the processed gravity in sections utilizing pressure altimetry for vertical acceleration corrections. These errors are probably produced by resonant vibration of the pressure sensor boom boom which occurred sporadically. The static pressure sensor receives ram air during these periods which then leaks out to restore ambient pressure. The resulting error looks like a decrease in altitude followed by an increase. A new digital FIR filter was designed to remove the shorter period excursions, but the longer deviations would have required such a long cutoff that significant features in the gravity field would also have been removed. These sections were removed manually and the resulting gaps filled by assuming that the free air gravity anomaly was equal to spring tension + meter offset + Eotvos correction + cross coupling - normal gravity, i.e. beam velocity - vertical acceleration = 0. The FIR filter was selected to have a cutoff wavelength of approximately 15 km (see figure 3). Profiles which extended outside the survey area received one or more passes of the filter which eliminated about one minute of data from the start and end of a profile.

The procedure described above resulted in

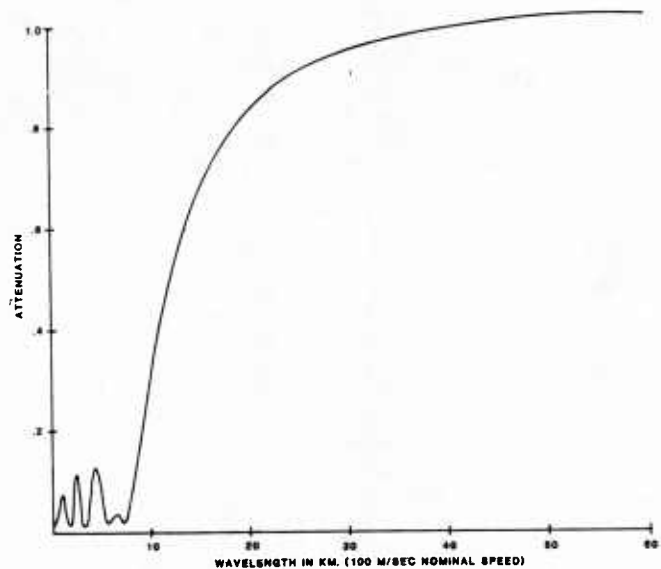


FIG. 3 Transfer function of one pass of the digital FIR filter applied to the profiles. In some cases multiple passes were used.

21 usable gravity profiles, 12 north-south and 9 east-west, with data gaps in two of the horizontal profiles. Because several of the profiles also began or ended inside the boundaries of the survey area there were 96 crossings where mis-ties could be examined. This examination revealed that several profiles were consistently low by several mGals. The most likely cause for low values is a slightly off level stable platform. A small constant determined by eye was added to each of the low profiles. After this rough adjustment the average mis-tie was -0.1 mGals and the rms difference was 3.8 mGals (fig. 4). A least squares adjustment to minimize mis-ties was then performed. This program

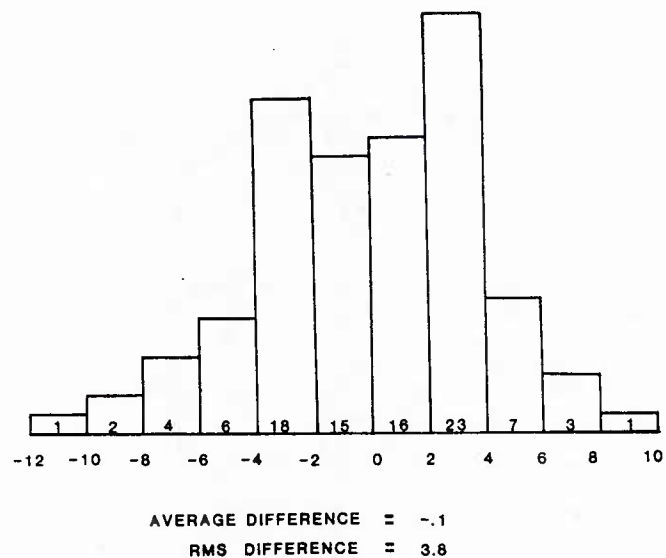


FIG. 4 Histogram plot of the mis-tie errors at 96 intersections prior to least squares adjustment.

ADJUSTED DIFFERENCES AT INTERSECTIONS

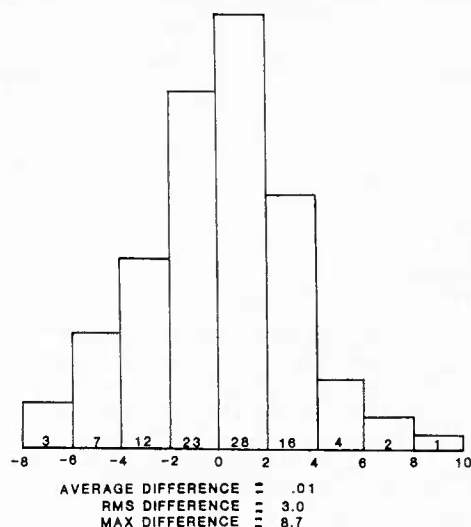


FIG. 5 Histogram plot of the mis-tie errors after least squares adjustment (linear error model, four tracks held fixed).

assumes a linear error model for each individual track and determines the constant and slope of a correction to be applied to each track. A correction of zero was specified for two vertical and two horizontal tracks to constrain the minimization. The tenth and twelfth vertical and the fifth and ninth profiles were chosen since the major portions of these tracks were over water. After the least squares corrections were applied the average mis-tie was .01 mGals and the rms difference was 3.0 mGals (figure 5). Since two pairs of vertical tracks (5-6 and 10-11) were almost coincident the data from each pair was averaged to yield single tracks. The final adjustment prior to contouring was to average the gravity values at cross overs and to interpolate these corrections along each track between cross overs. This final data set was then contoured at a two mGal interval (figure 6).

III. Conclusion

The final reduced data set was provided to DMA for error analysis. The preliminary report (Primrose, 1985) indicates an rms difference between the ground truth data and the NRL data of 2.5 mGals with a bias of 3.1 mGals. This is a comparison of both sets gridded to the same grid. There is some indication that a portion of this difference can be attributed to some gaps in the ground truth data. We have not determined the cause of the constant offset error, but it is probably due to a miscalibration of the radar altimeter. The results of the airborne gravity experiment indicate that the system is capable of producing detailed and self consistent surveys over the difficult land-sea interface, although the system was primarily designed for use over water.

The environment of the test region may be considered as highly analogous to the Arctic with leads in the ice replacing rivers through the swamps. I propose that the methods applied to the North Carolina demonstration would be applicable to gravity surveying in the Arctic. The pressure altimetry would provide the short period vertical accelerations of the aircraft. Isobaric slopes would be determined as in the test described here by radar or laser altitudes over any available open water. It may also be possible to determine long wavelength isobaric slopes from low pass filtered radar altitudes which would average out short period variations in the height of the ice surface above the geoid. Another alternative for constraining long period errors in the pressure altimetry is averaged GPS altitudes or Doppler carrier wave determined vertical velocities. Probably the ultimate source of three dimensional positioning will be provided by dynamic GPS interferometry. Although untried at aircraft velocities as yet, this technique should permit positioning to a few centimeters with short averaging periods (30-60 seconds) if baselines can be made short enough. In conclusion, the AGMS should still be considered a prototype needing development in both hardware and software, but I believe that the results presented here demonstrate the merit of developing and transiting this system to the surveying community. For the first time, detailed gravity surveying of the Arctic at close to shipboard accuracy is possible.

IV. References

- Brozena, J. M., 1984, A preliminary analysis of the NRL airborne gravimetry system: Geophysics, v. 49, p. 1060-1069.
- Primrose, W., 1985, Error analysis of the NRL airborne gravity test, DMA memo for record

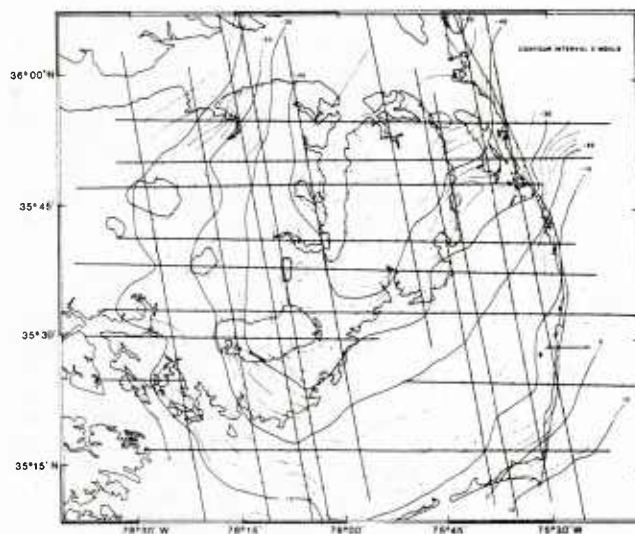


FIG. 6 Mercator contour plot of free-air gravity anomaly (reduced to sea level, no terrain correction).

SATELLITE TELEMETRY BUOYS FOR COLLECTION OF ARCTIC ACOUSTIC AND ENVIRONMENTAL DATA

B. M. Buck and J. O. Anderson

Polar Research Laboratory, Inc.
6309 Carpinteria Avenue
Carpinteria, CA 93013

ABSTRACT

Year around acoustic and related environmental data collection in the Arctic has always been difficult. For many years PRL experimented with data buoys using telemetry systems for data recovery and in 1975 began using satellite links, first NIMBUS/RAMS and later NOAA/ARGOS and others. Acoustic buoys include ambient noise buoys that measure averaged noise levels in 11 selectable 1/3 octave bands, propagation measurement buoys that measure received narrow band signal levels in 1/4 Hz bands, and a companion buoy that includes an acoustic projector that develops source levels in excess of one acoustic watt from 20 to 55 Hz. The latter two buoys also include ambient noise systems to measure noise levels at both the source and receiver. Underice environmental measurement systems include buoys that measure vertical temperature or temperature and conductivity profile and water currents at multiple depths. Meteorological parameters are also measured with manually installed or paradedropped systems.

INTRODUCTION

Data collection in the Arctic Ocean using manned stations is seasonally limited, costly, and sometimes dangerous. Automatic data stations (also referred to as "Arctic Data Buoys") are a means of getting around many of these problems and provide a very cost-efficient supplement, and, in some cases, even supplant manned ice operations. Design of these automatic stations is driven strongly by the Arctic's unique environmental parameters and their interplay. Also, the deployment methods and their limitations constrain the design.

PRL personnel have been working in the Arctic Ocean since 1961 - the early years while at General Motors Defense Research Laboratory. Much of the 1961 - 1971 work was performed using manned camps on pack ice in the high Arctic, but, men on the ice require aircraft, and aircraft are limited to the Arctic spring when there is a combination of refrozen leads for landing strips and sufficient daylight to enable landing. Because of the relatively short data time window and the high logistics cost for establishing and maintaining manned stations, there developed a strong interest

in the possibility of automatic telemetry stations for collecting data. (It should be mentioned that some of the impetus for developing automatic Arctic stations came from the successful uses the Russians made of their DARMS weather stations, primarily along their Northern Sea Route. They used medium frequency radio telemetry to relay met data and had the stations operating back in the early '50s.) Early stations used HF, VHF or micro wave telemetry. Line-of-sight, groundwave, skywave, troposcatter and even meteorburst propagation were tried with varying degrees of success - none spectacular. In the early '70s the prototype EARLS system of the NIMBUS 4 polar orbiting satellite, which was the precursor to the NIMBUS 6 RAMS and the later "operational" TIROS ARGOS system - was investigated by various laboratories including the Applied Physics Lab of the University of Washington and the Naval Research Laboratory. The former lab also built and field tested preliminary versions of the RAMS data buoys. EARLS had several limitations, but it marked a new era in Arctic data retrieval since it enabled the use of satellites at high latitudes, geostationary ones being "out of sight" and unusable.

The data retrieval picture improved dramatically in 1975 when the polar orbiting NIMBUS 6 satellite carrying a "RAMS" package was launched. This satellite allowed 32 bits of data to be telemetered in a burst transmission once a minute.

In anticipation of this satellite being launched, PRL developed an ice station that would measure in-water acoustic ambient noise in four 1/3 octave bands, barometric pressure and air temperature sampled at the three hour synoptic weather times of 0000Z, 0003Z, etc., hold these in memory for 24 hours and repeat their transmission to catch at least one NIMBUS 6 pass per day. Because of logistic exigencies, these stations were actually installed in the ice prior to the satellite launch. After an anxious wait, the systems performed beautifully and eight of them survived for more than a year, providing first-ever ambient noise data over all seasons as well as meteorological and ice drift data for the AIDJEX project (1).

The NIMBUS/RAMS system was superseded in 1978 by the ARGOS system carried on TIROS and NOAA satellites. This system, considered an

"operational" capability planned for many years use, is an improved version of the RAMS. Data capacity was boosted to 256 bits per transmission, enabling roughly up to around 3000 bits per satellite pass. Positional accuracy can be as good as 150 meters (50% circular probable error) per fix. Two satellites provide about 28 passes per day in the polar regions. PRL has developed a variety of Arctic as well as open ocean data collection systems using the ARGOS system.

Systems have also been developed using the LES-9 satellite which has a much higher data capability and also allows two way transmissions permitting functions of the buoy to be changed remotely by "command" signals. However, access to this satellite is somewhat limited and the telemetry equipment is more expensive than that used for ARGOS.

AMBIENT NOISE

For many years PRL made acoustic ambient noise and propagation measurements to provide background data for predicting performance of surveillance systems. The measurements made from "quiet" manned camps, were limited primarily to a few months in the spring when aircraft operating conditions permitted support of the camps. It was expected that significant seasonal variations would occur. This was verified initially by the unmanned ambient noise stations using RAM's telemetry briefly mentioned above. This capability was greatly expanded with the development of the SYNARGOS system (2). SYNARGOS is a micropower, automatic, ambient noise collection system. It measures ambient noise in eleven 1/3 octave bands whose center frequency can be selected depending on the application. Data in each band is averaged generally maintaining a constant bandwidth-time product. This was developed for obtaining synoptic environmental data in ice covered seas for periods exceeding one year. Synoptic data samples are stored in a 24-hour memory under microprocessor control and relayed by once per minute burst transmissions to the two NOAA series polar orbiting satellites. The satellites carry the ARGOS random access data collection system on board. Buoy positions are determined to within a circular probable error (50%) of less than 300 meters by doppler measurements made on the transmitted signal. Twenty-four SYNoptic ARGOS (SYNARGOS) ambient noise measurement buoys have been used successfully in the Arctic and MIZLANT; and four more modified units designed to rest on the bottom for a year before surfacing and transmitting their data have been deployed: two in the Bering Sea and two in the Eastern Arctic. The data is providing valuable long-term statistical sampling of the highly variant underice noise field of unstudied regions of the Arctic and Sub-Arctic. Development of the SYNARGOS System was sponsored by ONR (Code 425 Arctic).

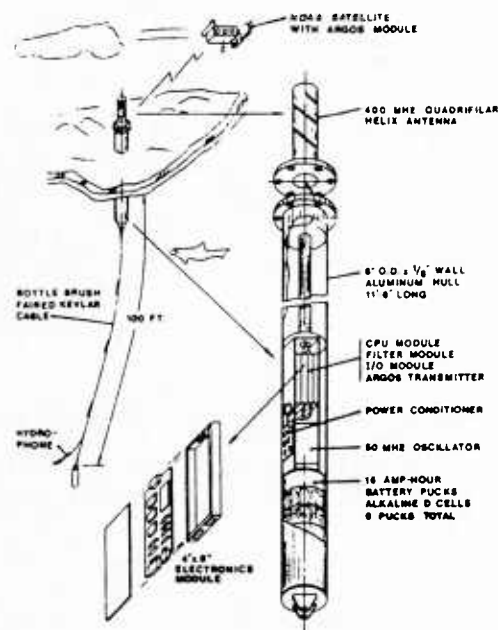


Figure 1. SYNARGOS Ambient Noise Buoy in Pack Ice

As a result of the SYNARGOS buoy programs, a vast amount of data has been archived at PRL. A start has been made in analysing this data in a program funded by the AEAS Program Office. The objective is to publish the data in atlas format to facilitate use of it by all interested parties. The approach used is to divide the Arctic into six areas:

- 1) North Barents Sea
- 2) Greenland Sea
- 3) East Central Arctic
- 4) West Central Arctic
- 5) Kara Sea
- 6) Chuckchi Sea

The data has been segregated by area and detailed analysis has begun. Information reported includes all buoy positions computed, number of data samples, average, standard deviation, maximum/minimum levels and percentile levels of ambient noise from the eleven 1/3 octave bands reported for each buoy by month. Summary percentile plots, buoy tracks, time series data and ice conditions forecast by the Navy/NOAA Joint Ice Center are also provided. Some work has been done on all areas, but the report for AREA 2 was the only one that could be completed on available funds (3).

THE NUMBER OF DATA SAMPLES IS 232

FREQUENCY	STATISTICS											N
HZ	AVG	STD DEV	MIN	5%	10%	25%	50%	75%	90%	95%	MAX	
5.0	73.7	6.9	58.9	64.8	66.3	69.2	72.3	75.2	79.4	85.4	100.2	230
10.0	74.7	6.7	63.2	67.3	68.2	72.3	75.6	80.3	84.4	87.1	99.5	230
12.0	76.2	5.9	61.1	67.7	68.6	71.8	76.0	79.3	83.9	84.9	93.3	230
15.0	73.3	5.1	61.1	66.3	67.2	70.1	72.3	76.2	80.1	82.2	92.9	230
20.0	75.0	4.4	64.8	68.3	69.2	72.1	74.3	77.5	80.4	82.1	90.2	230
25.0	73.6	4.3	64.4	67.8	67.8	70.6	73.3	75.8	79.3	82.6	87.6	230
30.0	72.6	4.6	59.0	65.8	67.1	69.3	72.5	75.3	79.3	81.4	87.4	230
40.0	71.9	4.8	58.0	63.5	64.5	67.4	70.3	73.5	76.5	80.3	84.5	230
50.0	68.3	4.8	56.3	61.5	63.0	64.8	67.4	70.3	73.9	76.9	81.9	230
100.0	61.1	5.9	50.7	52.7	53.5	56.7	60.3	65.5	69.8	71.6	79.0	230
320.0	53.3	3.1	44.5	50.2	51.2	50.2	52.7	54.1	59.0	60.7	65.5	230

Figure 2. Archived Ambient Noise Data Format

Use of SYNARGOS has since been expanded to the open ocean in the small, relatively low cost deep moored BREAM buoys built for NAVAIR/NAVOCEANO and drifting acoustic buoys designed for NAVELEX 612 (4)(5).

ACOUSTIC PROPAGATION

Most acoustic propagation measurements in the Arctic have been made using explosive charges as acoustic sources and all of the past Central Arctic measurements were made in the short spring season. Very limited work has been done with CW projectors, primarily small high frequency projectors or very large low frequency projectors. Over the past two years in an effort supported by NAVLEX 612 PRL has developed a relatively small nonresonant narrow band CW projector which covers the range between 20 Hz and 55 Hz in its current configuration. Output level is adjustable with a peak output of 1 acoustic watt (172 db re 1 yd) at the low end increasing to several acoustic watts at the higher frequencies, eg. 3.4 watts at 32 Hz.

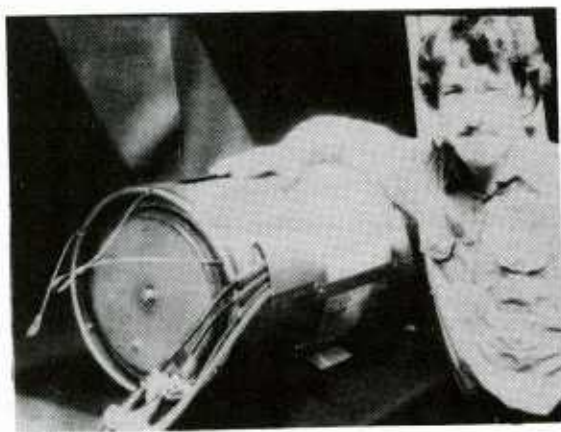


Figure 3. Non Resonant Acoustic Projector (NRAP)

The projector is based on a concept devised by H. A. Wilcox then at NOSC (6). It includes two pistons having an effective diameter of about 12 inches. The pistons are driven by an electric motor and flywheel through a linkage that effectively functions like a crank shaft with piston rods. Amplitude is adjusted by varying the location of a pivot point in the linkage using a second motor driving a ball screw. The system is relatively efficient since energy taken from the flywheel during the outward movement of the pistons is returned to the flywheel as the water pressure assists the inward motion of the pistons. Projector output is measured by measuring piston displacement with an LVDT pickup and also using monitor hydrophones mounted on the suspension/power cable. Piston seals are corrugated stainless steel bellows. The projector is pressure compensated to hold the pressure differential across the piston faces to about 8 psi. The package is about 14 inches in diameter and 30 inches long. The first projector was designed and built in a four month program and tested in the Arctic in the Spring of 1984. A second version of the unit incorporating refinements resulting from lessons learned in the earlier tests is attached to an in-ice buoy by a suspension/power cable which places the projector 300 feet below the surface. The buoy includes a power pack and controls for the projector and an ARGOS system which relays source level data from both the piston displacement sensor and the monitor hydrophone as well as other engineering data. The system controls operate the projector for eight minutes a day at each of four different frequencies (20, 32, 40 and 52 Hz). The projector was operated in a manual mode for 145 hours during the field experiment this spring and was left operating automatically at the end of the experiment. It is still functioning properly.

Signals from the projector buoy are received by two Propagation/Ambient Noise (PAN) buoys. These buoys carry an on-board narrow band spectrum analyser with channels tuned to the four transmitted frequencies. They are clock controlled to integrate received level for five 4 minute periods. These periods are timed so that one of the four minute periods contains signal for the full four minutes at any possible range in the Arctic. The signal level from the measurement window containing the highest level is transmitted. The PAN buoys also carry a SYNARGOS ambient noise 1/3 octave measurement system, allowing computation of both signal and noise levels at the receiver. The initial range between the projector and the PAN buoys was approximately 120 nmi. This range will change depending on relative ice drift. Operation of the buoy array into the summer will provide the first ever summer acoustic propagation data for the Central Arctic.

METEOROLOGICAL SYSTEMS

In addition to environmental acoustic systems, PRL has built a variety of systems for measuring meteorological parameters. These include the work horse Arctic airdrop buoy first built in a NIMBUS/RAMS version (ADRAMS)(7) and

later in a TIROS/NOAA satellite/ARGOS version (TAD)(8) used to measure barometric pressure, average daily temperature and ice drift. This buoy consists of a lexan sphere covered with one inch of foam insulation which is overlaid with fiberglass. It is paraded onto the ice where a crushable pad decelerates the vertical component of velocity. Switches embedded in the pad close on impact firing a cutter for chute release. Horizontal velocity, which is the velocity of the near surface wind, invariably causes the system to roll, but all of the electronics including the battery and antenna are mounted on a pendulous platform that rides on teflon sliders which contact the inside of the sphere. The self erecting internal platform levels the antenna ground plane and also the lithium batteries which must be in an upright position to deliver their rated energy.

A variety of weather stations have been built for use in the Arctic and Antarctic and have performed very well. The version used on pack ice has been built with an eight inch diameter tube base which is inserted in a hole drilled in the ice, as well as in a surface mounting version. The tube provides a compartment for the batteries and electronics that is warmed by the proximity to sea water. This permits use of alkaline batteries rather than the more expensive lithium cells. On-ice stations also carry a compass to provide a magnetic north reference. This has to be corrected for magnetic variation at the station location which can be done very accurately in most Central Arctic areas from published tables. The weather station electronics is currently being converted to PRL's new PTT which allows readout of wind speed and direction or wind vectors.

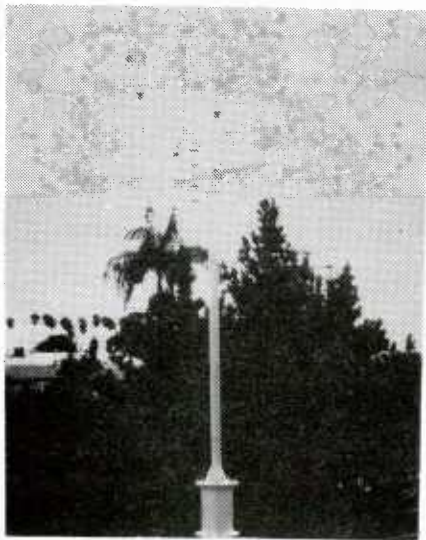


Figure 4. Weather Station for Installation in Arctic Pack Ice

Development of an air deployable version of the station is currently being completed for the Office of Polar Programs, NSF, for use in the Antarctic, but this also may have some Arctic applications. This station is designed to erect itself and raise a mast up to the three meter height after being paraded to the ice. The first phase design and testing work was carried out under an ONR Code 425 Arctic contract with funds from NSF.

At all ice camps in the major Arctic program carried out this spring, PRL utilized small ARGOS units with keypads for reporting weather data in an abbreviated "Ship Code" format. Camp status information was also appended to the message. A PRL Local User Terminal (LUT) positioned at the logistics base in Thule, Greenland received the data. With approximately 28 satellite passes per day available, near real time communications were attained. The weather data and computed positions from the LUT were used for flight operations and were also generally available to meteorologists via the Global Telemetry System through Service ARGOS. This link was felt to be vital because HF communications are interrupted for periods of a week or more at a time by Polar Cap Absorption.

OCEANOGRAPHIC SYSTEMS

A variety of oceanographic sensors have been interfaced to PRL's Arctic platforms. These include thermistor strings (both analog and multiplex), conductivity/temperature/depth strings and current meters at one or more levels.

The initial thermistor string work for both analog and multiplex thermistor strings was carried out under contract to ONR Code 425 Arctic. This work was subsequently carried further on PRL funds and additional improvements were recently made to the multiplex thermistor string under contract to NDBC. The system was refined to utilize the same conductor pair to power the subsurface sensor packages and transmit the digital signals. This system uses up to three two wire buses for redundancy and has been built in 300 meter and 600 meter open ocean versions for use in an NDBC/Naval Oceanographic Office program. These systems carry 15 temperature sensors and one pressure depth sensor (9). The analog strings previously required tedious matching of resistors for linearizing the thermistors, but this is now done via software control. The Arctic versions of the systems are less complex mechanically since they operate in a comparatively benign environment.

The conductivity/temperature string buoy (SALARGOS) was built in several versions for the Polar Science Center, University of Washington, the latest with six sensors pairs distributed over a 300 meter Kevlar string (10). The buoy samples the sensors every 12 minutes and averages the samples over three-hour periods. Averages covering a 24-hour period are transmitted through the ARGOS system during a five-hour transmission window once a day. Recent Arctic deployments suggest that the SALARGOS buoy is capable of

making salinity measurements with accuracies of about 0.02 parts per thousand for periods of at least two months in the Arctic during spring conditions. Biological fouling does not appear to be a problem for these conditions. One of these buoys is currently deployed on the pack ice in a Polar Science Center program.

A current meter version of the buoy was used to collect under-ice current speed and direction data from a pair of Savonius rotor current meters tethered at 100 and 300 feet below the drifting pack ice. They were deployed from a buoy installed 100 miles north of Franz-Joseph Land during the spring of 1982 (11). The data was sampled every two hours after 9 minutes of averaging. The system has a resolution of 0.01 knot with an accuracy of 0.05 knots above 0.1 knot and a rotor threshold of 0.05 knot. By using high stability oscillators to obtain + or -150 meter circular probable error in ARGOS position, it appears to be possible to extract the relative ice drift from the velocity data and extract the true current. After deployment, the buoy drifted under the influence of the East Spitsbergen Current from April of 1982 through January of 1984 providing valuable data from this infrequently studied area. A number of additional units have been built for other users. Other types of current meters have also been interfaced to the system including a spherical instrument that measures current vectors with electromagnetic sensors combined with compass data.

REFERENCES

- 1) Burke, Samuel P. and Beaumont M. Buck, "The SYNRAMS Ice Station", Proc. of the IEEE Oceans 75 Conference, pp 413-417.
- 2) Burke, Samuel P., Beaumont M. Buck and Charles A. Luther, "The SYNARGOS Ambient Noise Measurement Buoy", Proc. of Oceans 82, pp 626-631.
- 3) Buck, Beaumont M. and Daniel W. Jaecks, "Long Term Statistical Measurements of Environmental Acoustics Parameters in the Arctic. AEAS Report No. 1 - Ambient Noise Levels in the West Greenland Sea", Polar Research Laboratory, Technical Report TR53, 13 Dec 1984.
- 4) Anderson, John O., Samuel P. Burke and David W. Iddings, "Deep Ocean Ambient Noise Measurements from the Slack Moored BREAM Buoy", Polar Research Laboratory Technical Report TR59, Feb. 1985.
- 5) Anderson, John O., David W. Iddings, Samuel P. Burke and Lars Pedersen, "Drifting Acoustic Buoy System Design", Polar Research Laboratory Technical Report TR54, 28 Feb. 1984.
- 6) Wilcox, H. A., "Nonresonant Acoustic Projector Project", Naval Ocean Systems Center Technical Report 579, 12 June 1980.
- 7) Brown, Walter P. and Edmond G. Kerut, "Air Droppable RAMS (ADRAMS) Buoy", Oceans 76 IEEE and MIS Conference Proceedings, Sept. 1976, pp. 1401-4.
- 8) Anderson, John O., "Expendable Data Buoys for Oceanographic, Meteorological and Tracking Applications", Proceedings of the Marine Technology Society, Oceans 80.
- 9) Kozak, Ron and John O. Anderson, "Overview of the NOAA Data Buoy Center Drifting Buoy Programs", ARGOS Users Conference Proceedings, May 1984.
- 10) Morrison, James, Samuel Burke, Hermann Steltner and Roger Anderson, "SALARGOS Temperature-Conductivity Buoys", Proceedings of IEEE Oceans 82, Sept 1982, pp. 1255-1260.
- 11) Burke, Samuel P. and John O. Anderson, "Five Years of Arctic Buoy Deployments", ARGOS Newsletter, No. 20, July 1984.

ARCTIC TEMPERATURE-CONDUCTIVITY BUOYS

James Morison

Polar Science Center/Applied Physics Laboratory
University of Washington
Seattle, Washington 98195

ABSTRACT

The SALARGOS buoy system has been designed to make unattended measurements of temperature and conductivity in the Arctic Ocean. Three buoys have been built and used; one with sensors at three depths and two with sensors at six depths down to 300 m.

The units were used at Fram III in 1981, Fram IV in 1982, Pond Inlet, NWT in 1982, MIZEX 83 and AIWEX in 1985. The buoys are capable of producing temperature and salinity measurements of high accuracy for extended periods of time. The results of these experiments and future plans are discussed.

1. INTRODUCTION

Since 1980 three buoys have been designed and built to measure temperature and conductivity in ice-covered oceans. Motivation for this effort has come from three areas. First was the desire to obtain long term hydrographic records from the upper Arctic Ocean in order to study the mixed layer. At present, the best available data sets are a four-year, 1970 to 1973, hydrocast record from ice island T-3 and one year of hydrocast records from the AIDJEX project, 1975-76. The only feasible way of obtaining more year-long hydrographic records is with automated equipment; the maintenance of a manned camp would be prohibitively expensive. The buoys which have been developed so far employ sensors moored at fixed depths beneath an electronics package embedded in the ice cover. The data is telemetered through the ARGOS satellite system, which also determines the buoy position.

Experience has shown that the ARGOS system makes it feasible to recover data in near real time. This presents a second motivation for buoy development. The buoys provide the capability for real time monitoring of oceanographic conditions in much the same way meteorological conditions are monitored. This opens the way for real time reporting and prediction of oceanographic conditions for operational purposes.

The third motivation for the buoy development is to obtain long term records of internal wave energy in the Arctic. The latest buoy samples temperature and conductivity at high frequency, making it possible to collect continuous records of internal wave energy and to see how the energy changes with season, ice conditions and ice motion.

One of the primary concerns in developing the buoys has been achieving accurate moored conductivity measurements. Conductivity measurements are a

necessity in the Arctic Ocean because stratification there is due predominantly to salinity gradients. The conductivity must be measured in order to determine salinity. Historically, the problem in making moored conductivity measurements has been drift, due either to drift in the sensor electronics, or to biological fouling. For this work conductivity sensors were chosen which, experience suggests, yield low inherent drift rates. Also, the Arctic Ocean is a region of relatively low biological fouling because of low light levels and cold temperatures. These factors make the outlook for moored conductivity measurements in the Arctic promising. Nevertheless, much of the development and testing so far has been aimed at evaluating the accuracy of conductivity (or salinity) measurements made with the buoys.

2. THE BUOYS

Figure 1 shows the third and latest of the SALARGOS buoys, all of which have been designed and built by the Polar Research Laboratory (PRL) in Carpinteria, California. In the figure the buoy is shown in cross section as it would appear in the ice. It consists of a 0.2 m diameter tube 5 m long. The tube contains the data acquisition and transmission electronics and enough alkaline batteries to power the buoy for one year. The tube is inserted in a hole in the ice and floats with the antenna about one meter above sea level.

A multi-conductor Kevlar cable is suspended below the tube and six temperature-conductivity sensor pairs are attached to the cable at 15 m, 72 m, 129 m, 186 m, 243 m, and 300 m. The temperature and conductivity sensors are Sea-Bird Electronics SBE-3 and SBE-4 units described by Pederson and Gregg (1979). The Sea-Bird units were chosen for their high accuracy and stability (better than $\pm 0.01^\circ \text{C}$ per six months for temperature and $\pm 0.01 \text{ m mho/cm}$ per month for conductivity are specified by the manufacturer), low power requirements, and convenient frequency output. Irish (1977 and 1981) has used the Sea-Bird sensors in a moored configuration in Puget Sound (Irish, 1977) and on the New England coast (Irish, 1981). He found the SBE-4 conductivity sensors produced good results as long as no severe biological fouling was encountered. In this buoy application the only modifications to the conductivity cells is the installation of light baffles coated with antifouling paint to inhibit biological growth in the cells.

In addition to the temperature and conductivity sensors, a Paroscientific Digiquartz pressure sensor is attached at 300 m. This is used to correct the sensor depths for variation due to motion of the sensor chain.

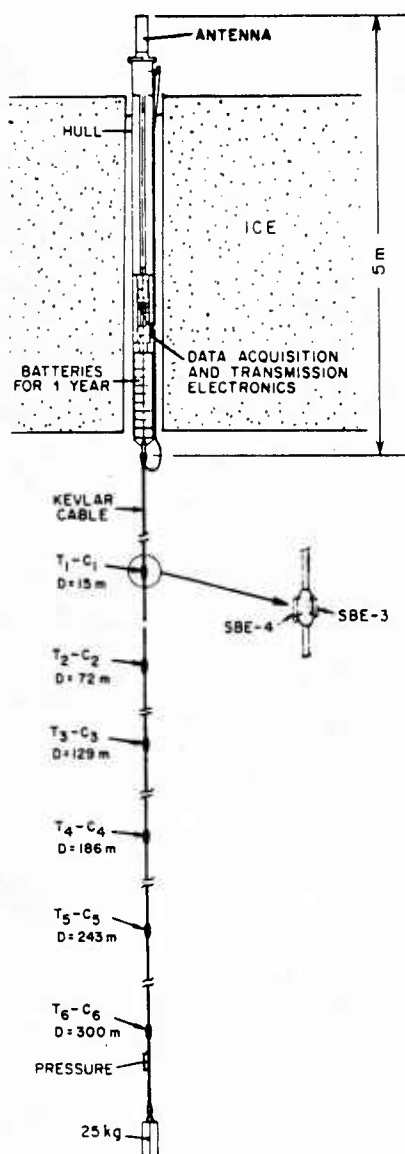


Figure 1.

The SALARGOS temperature-conductivity buoy as it would appear in cross section implanted in sea ice.

The first and second buoys were very similar to the third buoy in physical configuration except that the first buoy had only three sensor pairs down to 50 m and the second had six pairs to 100 m.

The first buoy configuration and electronics design has been described in detail by Morison *et al.*, (1982). The electronics hardware design has remained basically unchanged. In all the buoys the data acquisition, storage and transmission are controlled by a microprocessor. In the first two units, the sensors are turned on and their output frequency is sampled once every twelve minutes and these samples are then averaged over three hours. The three hour averages for the preceding 24 hour period are transmitted through ARGOS during a five hour window.

In the third buoy the sensors are also sampled every 12 minutes but the individual samples are stored in a buffer of nine samples. The buffered data is transmitted one sample at a time, along with a clock signal once per minute continuously. In the Arctic there are enough satellite passes so that each sample is transmitted twice.

3. RESULTS

The first buoy was first used at the Fram III ice camp at 83° N, 10° E in April and May of 1981. During this test the buoy was operated within 40 m of a profiling current meter CTD called the Arctic Profiling System (APS). The experiment provided the first opportunity to compare the performance of the moored sensors with a profiling CTD. The results have been described in detail in Morison *et al.*, (1982). The profiling system and the buoy agreed to within ± 0.013 o/oo and $\pm 0.01^\circ$ C.

The first buoy was next tested over a longer duration by deploying it at Pond Inlet, NWT in the spring of 1982. In this deployment one sensor pair was located at 15 m and two pair were located at 30 m. All the sensors were calibrated at the Northwest Regional Calibration Center before deployment. While the buoy was in place from February to June of 1982, the staff of the Arctic Research Establishment took three hydrocast stations at the buoy site as a check on the long term drift of the sensors. The results have been described in Morison *et al.*, (1982) but are reviewed here for completeness. Figure 2 shows three-hour averages of the buoy salinities from day 57 to day 135 of 1982. Also shown are the hydrocast data taken during the deployment. The top 30 m were fairly well mixed and the buoy and hydrocast data all show a steady increase from about 32.45 o/oo to 32.73 o/oo between day 57 and day 135. This increase is probably due to brine

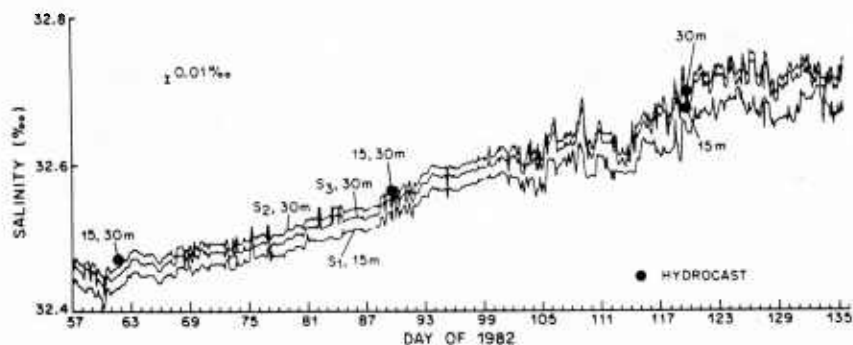


Figure 2.

SALARGOS buoy salinities at Pond Inlet, Northwest Territories plotted versus day of 1982. Salinities measured with hydrocasts at the buoy site are also shown, and agree with the buoy data.

rejection during ice formation. The buoy and hydrocast data agree quite well. The mean difference between the bottle sample salinities and buoy salinities is 0.017 o/oo and the standard deviation of the differences is 0.018 o/oo. The errors in the 15 m values were slightly greater than those at 30 m and the differences were actually less at the end. This, and the fact that all the conductivity sensors exhibited low values for the first 24 hours after deployment, suggest that ice formed in the cells when they were put in the water after being exposed to -46° C air temperatures and that some small ice accretion remained in the 15 m sensor for some time. In any event the accuracies obtained are quite good for a three month deployment.

The second SALARGOS buoy was used at the Fram IV ice camp in the spring of 1982. In spite of numerous sensor dropouts due to faulty underwater connectors, high frequency data was gathered during this experiment by running the buoy in a continuous mode, sampling once per minute, and gathering the data on site with a special receiver and microcomputer. This operation served as an incentive for development of the third buoy which will be discussed below.

The second buoy was also used during MIZEX 1983 in the Greenland Sea at about 81° 7'N, 6° 50'E. It was positioned 6 km from the *M/V Polarbjorn* drifting in the ice. This was done in order that data from the buoy and the ship's CTD could be compared and the horizontal gradients in water properties determined. Figure 3 shows isopycnal depths as determined from the buoy data as a function of time. It shows the tremendous variations in water structure which occur in the Marginal Ice Zone (MIZ). These variations are associated, for the most part, with advection of the ice through fronts created by strong variations in buoyancy flux at the ice edge.

The third SALARGOS buoy, SALARGOS 1947, was deployed at the Arctic Internal Wave Experiment (AIWEX) ice camp in the Beaufort Sea at 74° 04'N, 144° 24'W on April 13, 1985, and is still operating. As mentioned above this buoy uses most of the hardware from the second buoy but with new software which allows samples to be taken every 12 minutes, accumulated, and transmitted through ARGOS. This was done in keeping with the aim of the AIWEX to study the Arctic internal wave field. Specifically the buoy will provide internal wave spectra over an extended period of time so that changes in internal wave energy can be correlated with ice motion and changes in the surface conditions. The actual installation is similar to that shown

in Figure 1 with the addition of an auxiliary battery tube with a VHF homing beacon implanted next to the SALARGOS buoy and a plywood ablation shield laying on the surface around the buoy. The auxiliary battery tube provides an additional one year of power for SALARGOS and the beacon will permit precise location of the buoy by search aircraft in the event of a return to the buoy site. The ablation shield is meant to prevent local radiation melting of the ice during the summer. An ARGOS meteorological buoy has also been installed 70 m from SALARGOS as part of the Coordinated Arctic Buoy Program. The combination of the two buoys should provide much the same data as a small manned camp would provide.

While there is still not a long data record from SALARGOS 1947, data acquired during AIWEX is available along with a few profiles gathered in real time since April 30, 1985. Figure 4 shows salinity and temperature profiles measured with the APS during AIWEX along with the corresponding

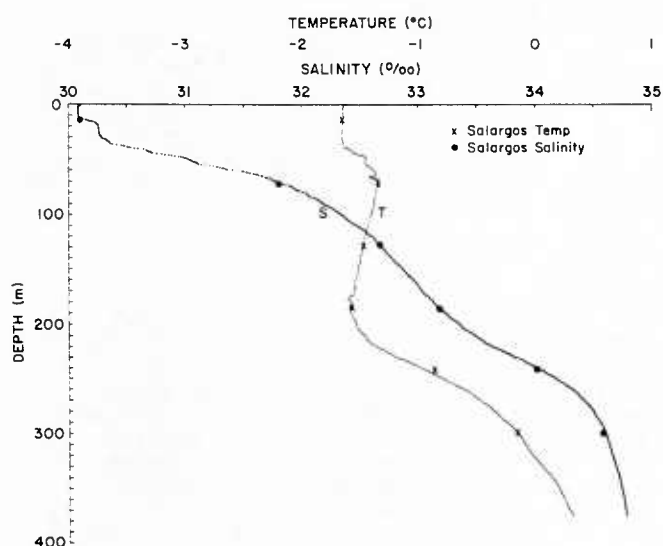
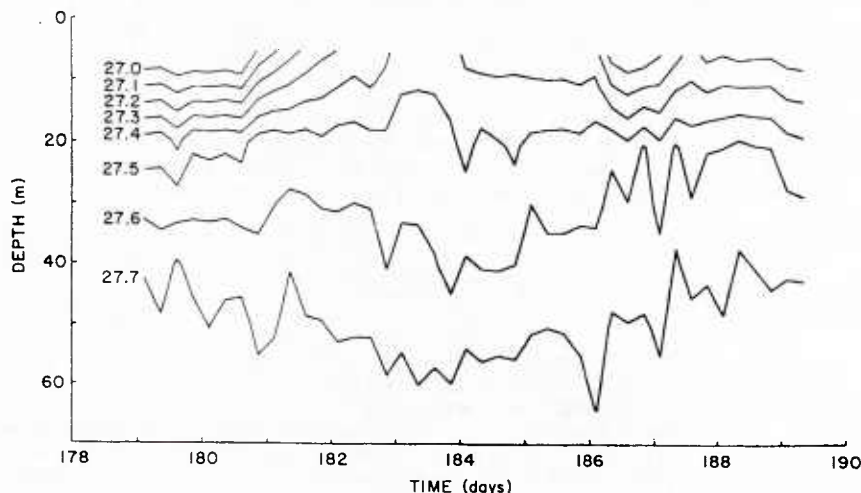


Figure 4.

SALARGOS temperature and salinity data taken at 1818 GMT on 4/19/85 superimposed on APS temperature and salinity profiles measured at 1815 on 4/19/85. Agreement between the two instruments was quite good considering their 600 m horizontal separation.

Figure 3.

Isopycnal depths measured with the SALARGOS during MIZEX 83 at a station 6 km east of the Polarbjorn. The large fluctuations are due to the presence of fronts.



data from SALARGOS 1947. The agreement between the two instruments is quite good, especially considering the buoy and CTD were separated 600 m and some of the measurements are in high gradient areas. Although complete statistics have not been computed, preliminary results indicate buoy salinities average 0.02 o/oo lower, ± 0.01 o/oo, than the CTD salinities and buoy temperatures average 0.01°C higher, $\pm 0.01^{\circ}\text{C}$, than the CTD temperatures. These errors are on the same order as those at Fram III and Pond Inlet.

Figure 5 is an example of some of the largest signal fluctuations we might expect to see in the SALARGOS 1947 data. The figure shows salinity profiles constructed from

survivability and drift of the system. One subject which is worth mentioning is the cost of gathering data with the SALARGOS buoys. The buoys cost on the order of \$50,000 plus an installation cost of about \$10,000. This seems like a lot for an instrument which must be considered expendable. However, the logistical cost of maintaining one scientist in the field is about \$1,200 per day at an ice camp (assuming of course that a large enough camp were maintained year around to achieve economy of size). Thus, a hydrographic program carried out by two people would be more expensive than a SALARGOS buoy after 25 days. Clearly buoy systems are the appropriate way to gather long time series of data in the Arctic.

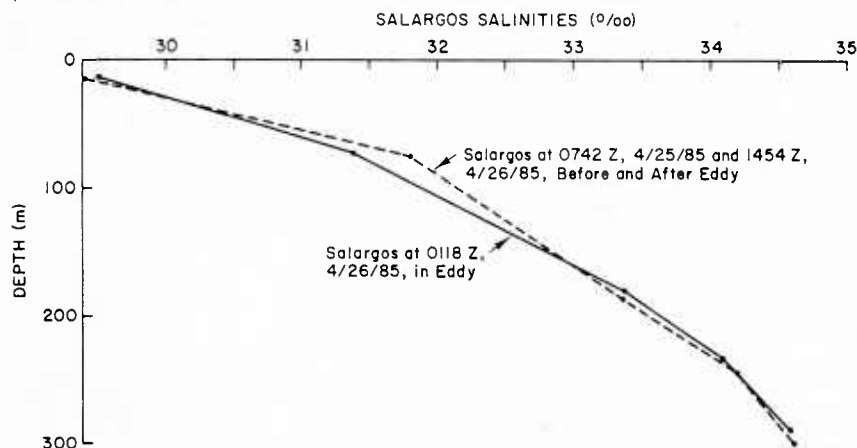


Figure 5.

Profiles of salinity constructed from SALARGOS data gathered before, during, and after an anti-cyclonic eddy passed through the AIWEX area. Salinity values at 129 m are missing because the conductivity sensor at that depth failed. The core of the eddy is between 100 m and 250 m.

data gathered before, during, and after an anti-cyclonic eddy moved through the experimental area. The value at 129 m is missing because the conductivity sensor at that depth failed. The fluctuations are associated with 30 cm/sec currents in the eddy core between 100 m and 250 m. Manley (1981) indicates such eddies may be an important mechanism of vertical momentum transfer in the central Arctic. The data of Figure 5 suggests the detection of eddies over the life of the buoy should be possible. Thus, the buoy data will provide valuable information on the frequency of occurrence and intensity of the eddies.

Figure 6 shows sound velocity profiles computed on the basis of data acquired from SALARGOS 1947 in near real time through the ARGOS data acquisition system. They are presented to demonstrate the type of information which can be recovered by real time monitoring. The ARGOS data center in Toulouse, France disseminates data from SALARGOS monthly on magnetic computer tape but it is also possible to access files of the latest data from the buoy with a computer terminal via phone line. The data of Figure 6 is from the latter source. It indicates a slight increase in sound velocity at 15 m due to a slight increase in salinity.

4. CONCLUSIONS AND FUTURE PLANS

Based on results from Fram III, Pond Inlet, and AIWEX, the SALARGOS buoy concept appears to be a viable means of obtaining long term hydrographic records from the Arctic Ocean. Accuracies are about 0.02 o/oo in salinity and 0.01°C in temperature. Of course experience with SALARGOS 1947 will tell us more about the long term

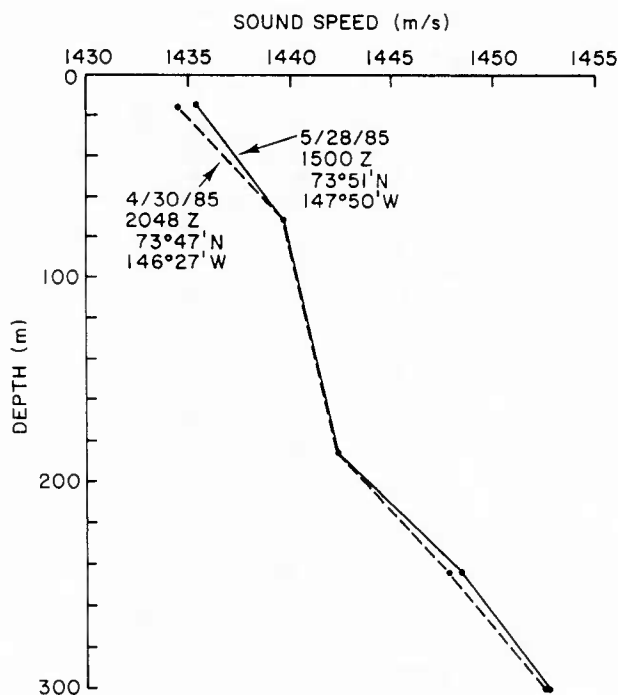


Figure 6.

Sound velocity profiles derived from SALARGOS data gathered on 4/30/85 and 5/28/85 and retrieved in near real time through Service ARGOS. The increase in sound velocity at 15 m is due to an increase in near surface salinity.

Future plans involve three main enterprises. First we hope to return to the SALARGOS 1947 site in six months to a year and perform a hydrocast for a check on instrumental drift. Second we plan on installing more SALARGOS buoys in the Arctic Ocean as part of a long term program funded by CNOC. Finally, we have been funded through a SBIR grant to Flow Research to develop a profiling CTD package suitable for long term use with the SALARGOS system. This will eliminate the cost of using multiple sensor pairs and will provide improved vertical resolution.

ACKNOWLEDGEMENTS

This work has been funded by Office of Naval Research Contracts N00014-79-C-0024, N00014-78-C-0135, and N00014-84-C-0111.

REFERENCES

- Irish, J. D., 1977. Moored temperature and conductivity measurements. *Exposure*, 5 (4), 1-6.
- Irish, J. D., 1981. Water column pressure measurements: CODE. *EOS*, 62 (45), 911. (Abstract of a talk given at the 1981 AGU Fall Meeting, San Francisco, California.)
- Manley, T., 1981. Eddies of the western Arctic--their characteristics and importance to the energy, heat and salt balance. Doctoral dissertation, CU-1-80, Tech. Rep. 1, Lamont-Doherty Geological Observatory, Columbia University, New York.
- Morison, J. H., S. Burke, H. Steltner, and R. Andersen, 1982. SALARGOS temperature-conductivity buoys. *Oceans*, September, 1982.
- Pederson, A. M. and M. C. Gregg, 1979. Development of a small in-situ conductivity instrument. *IEEE Journal on Oceanic Engineering*, OE-4 (3), 69-75.

GENERATION AND MOVEMENT OF ICE ISLANDS NEAR THE CANADIAN ARCTIC ARCHIPELAGO

W.M. Sackinger
M. Yan

Geophysical Institute
University of Alaska
Fairbanks, Alaska 99701

ABSTRACT

A review of ice island generation in the past three decades is presented. For the largest ice island produced in the April 1983 calving from Ward Hunt Ice Shelf, selected episodes of movement are related to conditions of wind and internal pack ice stress. The Department of Energy program to follow the trajectories of eight ice islands using Arctic Buoys is described in detail, and some possible additional uses of ice islands in support of Arctic Naval Operations are also discussed.

1. INTRODUCTION

The discovery of ice islands, which are large tabular icebergs originating from the shelf ice of the north coast of Ellesmere Island, has been largely a matter of chance since 1946, (Koenig, 1951) when the ice island T-1, measuring approximately 15 by 18 nautical miles, was found 300 miles north of Point Barrow. In 1950, the islands T-2 and T-3 were discovered, of dimensions 17 by 18 nautical miles and 4.5 by 9 nautical miles, respectively. The Naval Arctic Research Laboratory maintained a camp for research on T-3 for many years, and in July 1984 the island was sighted near the southern tip of Greenland, having finally been ejected from the Arctic Ocean.

2. HISTORY OF ICE ISLAND GENERATION

Early references to ice islands date back to Parry (1821), who found an immense floe in McClure Strait... "covered with large hummocks, giving to its upper surface the appearance of hill and dale... The thickness of this floe at its nearest edge was 6 or 7 feet above the sea, and... the whole thickness would appear... to have been from forty to fifty feet." It seems likely that this was a very old multi-year hummock field. The ice shelves of Ellesmere Island have long linear melt-pond features, parallel to the coastline, presumably caused by the prevailing wind direction in summer, and ice islands calving from these shelves can be expected to possess these long linear melt-pond features for some years at least. Such features

were noted on drifting islands of ice in 1883 by Greeley, in 1918 by Storkerson, and by others as well. The search of RCAF aerial photos by Greenaway in 1952 yielded 59 possible ice islands and many smaller fragments. A more recent review by Spedding (1977) resulted in an estimate of 3184 km² of ice island area created or discovered in the three decades 1946-1976. This includes the massive calving of five large islands from the Ward Hunt Ice Shelf in February/March 1962, involving an area of approximately 600 km².

An extended series of ice observations made by H. Serson during annual traverses from 1960 to 1980 have led to the consistent conclusion that ice island generation is a sporadic but frequent event. Serson's results have been reported in detail elsewhere (Serson 1984; Sackinger et. al. 1985); the summary of his results are shown in Figure 1, which is a table of ice island generation for 1963-1980. The ice islands produced from the Ward Hunt Ice Shelf in 1962 were observed on an opportunistic basis, and some of them are thought to be responsible for the grounded ice island fragments along the Beaufort Sea coast during 1972-75. The 1972 survey found 433 fragments, with 299 found in 1973, and 27 in 1974 (Spedding 1977). The islands, once created, tend to drift clockwise in the Beaufort Gyre and may circulate for decades before being caught in the trans-Polar drift stream and being finally ejected from the Arctic Ocean. The calving of several islands from the Ward Hunt Ice Shelf in 1983 (Jeffries and Serson 1983) has resulted in similar behavior as discussed below.

3. ICE ISLAND TRAJECTORIES

The largest ice island produced in the 1983 calving was instrumented by Dr. George Hobson of the Canadian Polar Continental Shelf Project, and the trajectory of that island from August 13, 1983 until February 5, 1985 is shown in Figure 2. The average drift towards the southwest along the coast is evident, but the episodes of movement are obviously of at least two types: (1) large daily movements parallel to the coast; (2) small daily movements towards

Year	Ward Hunt	M'Clintock	Nansen	Milne	Ayles	Other	TOTAL
1963	569						569
1964							
1965							
1966		95			85		180
1967				35	(25)	10 _a (15 _c)	45 (40)
1968							
1969							
1970							
1971	4.5		240				244.5
1972	1.5						1.5
1973							
1974	10						10
1975	- - - - -	- - - - -	NO OBSERVATIONS WERE MADE				
1976							
1977-79	- - - - -	- - - - -	NO OBSERVATIONS WERE MADE				
1980	(1)					3 _b	3 (1)
TOTALS	585 (1)	95	240	35	85 (25)	13 (15)	1053 (41)

- a) West of Bromley Island
b) Cape Fanshawe Martin
c) East of Hansen Point

Figure 1. Km^2 Ice Lost (Gain) Since Previous Observation.



Figure 2. Trajectories of Hobson's Ice Island from August 13, 1983 until February 5, 1985.

shore, away from shore, or occasionally towards the east and northeast but parallel to shore. An analysis has been made of the winds which produce these movements; in Figure 3, the example is given of an offshore wind which moved the pack ice away from the shoreline and allowed 3 days of large movements, followed by an on-shore wind which closed the pack ice against the shore and led to small, restricted island movements (Sackinger et. al. 1985). Additional correlation of these movements with geostrophic winds has been carried out (Sackinger et. al. 1985) and the dominant effect upon the trajectory has been shown to be the presence of the adjacent shoreline, the windspeed, and the wind direction in relation to the shoreline. A model for ice island motion which includes these effects has been formulated.

4. RESEARCH PROGRAM OBJECTIVES

The objective of the research program on ice islands, sponsored by the US Department of Energy, is to establish the probability of interaction between an ice island and an offshore oil production structure on the Alaskan Outer Continental Shelf. The approach being taken is to determine the statistics of ice island generation, in time and in space, from historical data and the monitoring of contemporary calving events; these data are used as inputs to a trajectory calculation which contains primarily deterministic elements, but which contains the probabilities of various episodes of crucial wind directions, magnitudes, and durations; the calculated trajectories are to be compared with actual observed trajectory segments; and the combination of the generation and transport calculations is to be used to find the expected paths in the Beaufort Sea coastal regions. Application of geometrical relations (Dunwoody 1983) then yield the interaction probabilities desired. Ice island features, with thicknesses up to 60 meters, represent the most severe ice hazard if they do interact with a structure, and it is important to quantify this problem insofar as possible before production designs are needed in the Arctic offshore.

Eight buoys are to be deployed, each with a projected battery life of six years. Six of these will transmit pressure and temperature; one will transmit windspeed and direction as well, and one will transmit location only. Deployment is in progress, with two buoys presently operating at 82.325°N, 86.68°W and 81.738°N, 93.294°W, and others in various stages of construction, deployment, repair, and redeployment. We anticipate that all will be deployed by October 1985, and that the five major ice islands in the 1983 cluster will be instrumented, with the 1984 minor calving also instrumented with one buoy. Three old ice islands, discovered in 1984 near the Ward Hunt Ice Shelf and the McClintock Ice Shelf, may also be among those chosen to be instrumented. The pressure information from stations that are

relatively near one another should enable a more accurate determination of coastal winds, which in turn will refine the input information for the trajectory calculations.

5. POSSIBLE USES OF ICE ISLANDS FOR ARCTIC NAVAL OPERATIONS

Most of the Arctic operations of the Navy are undersea operations. The difficulties of communications, command, and control are obvious in these situations. The ice island is a very thick, physically hard and extremely durable piece of floating ice with a lifetime measured in decades. It does move, but its position can be known from the satellite positioning techniques currently available. It has a relatively flat undersurface and a gently-rolling upper surface. It can be the base for a remote station which could provide several functions. For example, electromagnetic signals could be received by a station deployed on the island, and translated into acoustic signals to be broadcasted from a suitable transducer beneath the island. Conversely, acoustic signals and/or background noise could be received by hydrophones beneath the island and re-transmitted to satellites or aircraft overhead. The communication, command, and control links might utilize this approach as one of several parallel channel categories. The ice island is of very low salinity ice, so that the electromagnetic loss within the island would not be great, and the island itself could be a dielectric substrate for the support of a large, low frequency electromagnetic antenna which might operate either in the transmitting or the receiving mode, or as an element in an acoustic-to-electromagnetic active conversion station. Finally, the use of an ice island as a physical support station for operations, for research, for emergency logistics of a variety of types, should not be overlooked. Bathymetry, hydrography, and similar studies on an automatic basis may be possible from drifting stations. The essential element to be considered is that perhaps twenty or more ice islands, extremely durable and persistent, inhabit the Arctic ice pack and can serve as a geographically-moving array of bridges between undersea operations and airborne and satellite operations. In order to utilize them, their position must be known and a first step would be a systematic search followed by tagging them with automatic stations.

6. CONCLUSIONS

New ice islands have been created over the past several decades on a sporadic but frequent basis by calving from the ice shelves of Ellesmere Island. The trajectories of islands are dominated initially by the winds and the relatively closed pack ice conditions near the coastline of the Canadian Arctic Archipelago, but the islands eventually enter the Beaufort Gyre and may circulate in it for several

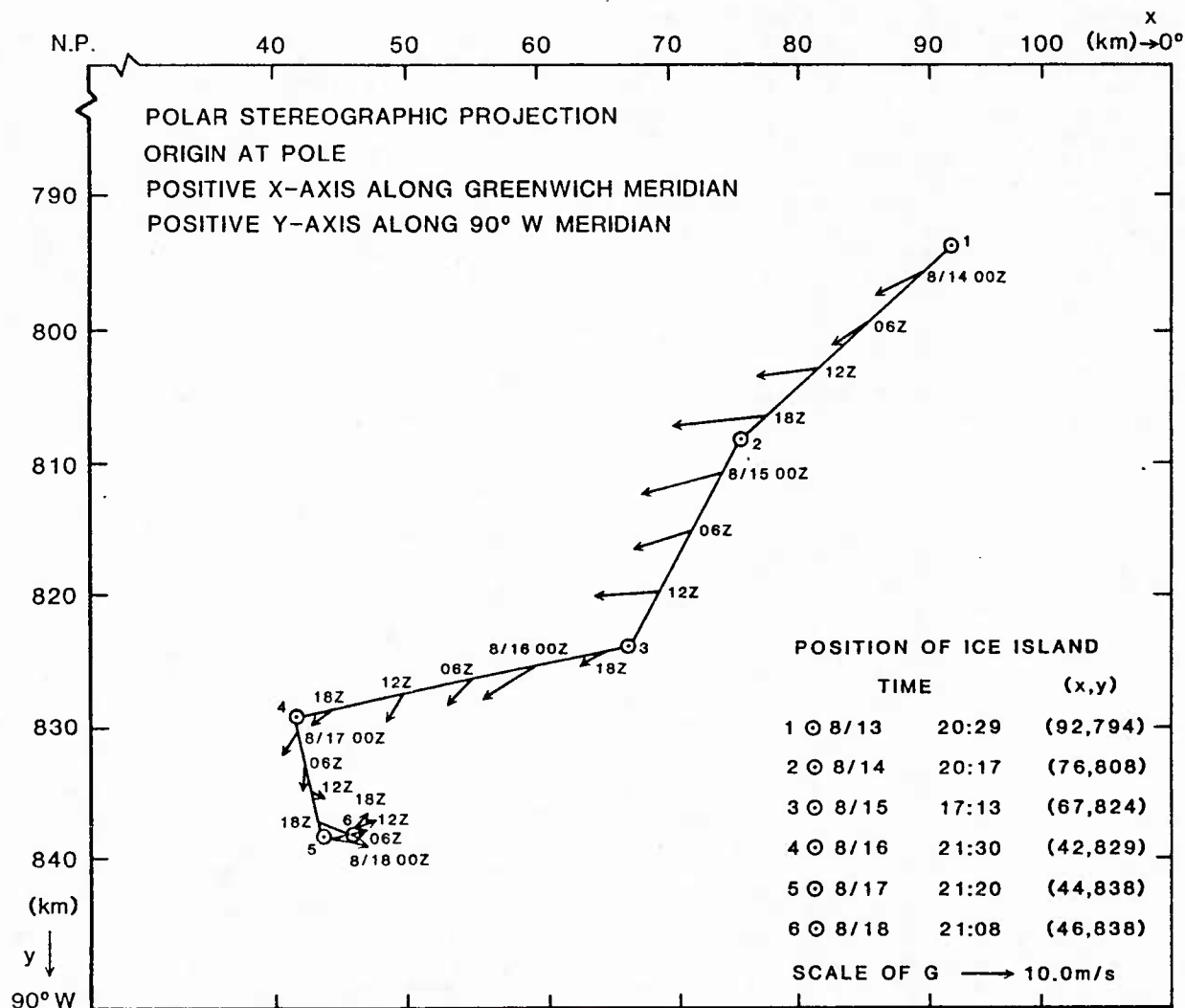


Figure 3. Ice Island Trajectory and Geostrophic Wind.

decades before finally exiting the Arctic through the Fram Strait. A research program is described which is designed to yield the interaction probability between an offshore petroleum production structure and an ice island in the Beaufort Sea. Possible uses of ice islands in support of Arctic naval operations include permanent bases for communication, command, and control functions, as well as research and emergency logistics support.

Jeffries, M.O. and H. Serson, (1983). Recent Changes at the Front of Ward Hunt Ice Shelf, Ellesmere Island, N.W.T. Arctic, Vol. 36, 1983, pp. 289-290.

Dunwoody, A.B. (1983). The Design Ice Island for Impact Against an Offshore Structure. In: Proceedings of the Offshore Technology Conference, (OTC 4550) pp. 325-330.

7. ACKNOWLEDGEMENTS

This research is supported by the US Department of Energy, Arctic/Offshore Program, Morgantown Energy Technology Center. The support of the Canadian Polar Continental Shelf Project is also appreciated. Valuable discussions with Martin O. Jeffries, H. Serson, H.O. Jahns, J. Roederer, G. Weller, and G. Hobson have also been very helpful.

8. REFERENCES

Parry, W.E. (1821). Journal of a Voyage for the Discovery of a North-West Passage from the Atlantic to the Pacific, Performed in the Years 1819-20. London, 310 pp.

Koenig, L.S. (1951). Ice Islands in the Arctic Ocean. In: Proceedings of the 2nd Alaska Science Conference, pp. 263-270.

Greeley, A.W. (1886). Three Years of Arctic Service. An Account of the Lady Franklin Bay Expedition of 1881-84. New York: Vol. 4, 428pp., Vol. 2, 444 pp.

Storkerson, V., (1918). Page 699 In: V. Steffanssen, The Friendly Arctic, New York (1921), 784 pp.

Greenaway, K.R. (1952). Additional Information from Flights and Air Photographs in the Canadian Arctic. Arctic, Vol. 5, No. 2, pp. 75-82.

Spedding, L.G. (1977). Ice island Count of the Southern Beaufort Sea 1976. APOA Project 99-3, IPRT-13ME-77, Imperial Oil Ltd., November 1977, 50 pp.

Serson, H. (1984). Ice Conditions off the North Coast of Ellesmere Island, Nansen Sound, Sverdrup and Peary Channels, 1963 to 1980. Appendix A in Arctic Ice Island and Sea Ice Movements and Mechanical Properties, Second Quarterly Report, US Department of Energy, Morgantown, March 1984.

Sackinger, W.M., H.D. Shoemaker, H. Serson, M.O. Jeffries, and M. Yan, (1985). Ice Islands as Hazards to Arctic Offshore Production Structures. In: Proc. of the Offshore Technology Conference, Houston, Texas, May 6-9, 1985, pp. 399-408 (OTC 4943).

AIWEX FIELD OPERATIONS PLANNING AND EXECUTION

Andreas Heiberg

Polar Science Center/Applied Physics Laboratory
University of Washington
Seattle, Washington 98195

ABSTRACT

Experience in AIDJEX, Fram, MIZEX, CANBARX, etc. has demonstrated the importance of pre-exercise planning and preparation to the success of Arctic research field programs. Early analysis of exercise requirements and objectives must include a systematic study of logistic support factors to determine critical constraints on field operations. Several logistics-related factors are most important in exercise planning and camp siting. These factors include considerations of bases; aircraft; type of mission; weather and ice conditions; navigational aids and location; shelter, heat, food, and power; communications; safety, rescue and survival; and cost and weight. Analysis of some of these factors and their importance in the planning and preparation of AIWEX will be discussed and certain post operations conclusions drawn.

1. INTRODUCTION

The Arctic Internal Wave Experiment (AIWEX) was carried out north of Prudhoe Bay, Alaska during the months of March and April 1985. The 22-25 man camp supported approximately 800 science man-days during the 57-day life of the station. The project enjoyed exceptionally good weather (not enough storms for some of the investigators) and was spared the disruptive consequences of ice breakups. The project was supported throughout by a helicopter and a Twin Otter from ERA Helicopters, Inc. A Bradley of Canada Twin Otter on skis and a MarkAir L-100 Hercules were utilized during deployment.

2. OBJECTIVE

The mission was an internal wave experiment to be carried out in the Beaufort Sea during the spring of 1985. The primary objective was the investigation of the internal wave field with a requirement for deep water and a five to six week measurement period.

3. PLANNING

The planning and preparation of AIWEX were based on experience gained in similar previous projects. Established and to a large degree proven logistics/scenarios from AIDJEX, Fram, MIZEX, CANBARX, etc. were reviewed and adapted to the AIWEX needs.

Geographic Location

Location is dictated by scientific needs (in this case deep water) and logistical constraints which, aside from cost,

are imposed primarily by range/payload limitations of support aircraft and time available to carry out the experiment. In selecting a staging base, Prudhoe Bay was the obvious choice over Barrow and Barter Island. The distance to deep water is the shortest, it has frequent commercial flight connections with Seattle and is accessible by truck year-around, which provides substantial savings with respect to freight costs. Also, various types of aircraft are available for casual charter which would save time and costly positioning from Fairbanks or Anchorage if unscheduled support were to be required.

Medical facilities and a rich assortment of services and supplies are available through the many contractors supporting the oil industry.

The target area for camp deployment was therefore put 250-300 NM northeast of Prudhoe Bay. The northeast starting point of the camp would keep us within reach of Canadian support resources at Tuktoyaktuk and assuming normal ice drift would preclude us from moving into shallow waters or out of aircraft range from Prudhoe during the life of the project.

Timing

The spring months are the best time of the year to operate this type of ice station. The weather is generally good, the surface is cold and firm and is optimal for aircraft operations.

The length of this season is somewhat dependent upon latitude, but is generally eight to ten weeks long, starting in early March with the return of sunlight, and ending in the first part of May with the onset of summer melt and the associated deteriorating flying conditions. Factors that speak against a longer season are cost related: a small and dedicated support crew will perform effectively for eight to ten weeks after which "burn out" symptoms start appearing. In a longer duration project one should either lower the work load by adding personnel or provide for crew rotation. In an extended season the extreme working conditions and shorter working day associated at the start and the deteriorating flying conditions at the end will significantly reduce the efficiency of the operation and jeopardize the evacuation of equipment.

The AIWEX camp was planned to be a nine week field season; March 2 to May 8.

Camp Size

The cost of establishing a research base is obviously not directly proportional to the number of supported investigators. It is more like a step function. The primary

scientific objectives will dictate the minimum number of people in the camp and the type of facilities and support resources required. Once the number of researchers reaches a certain threshold, i.e., 10-12, the camp is going to need a dedicated support staff, comprised of a manager, a cook and a helper. Experience has shown that such a staff when composed of dedicated, versatile and skilled personnel can support a camp of up to 20-25 people. This assumes occasional help from the researchers, particularly during setup and breakdown. Therefore complimentary projects were added to bring the camp up to 24 people. Such a camp can be set up in approximately two weeks and disestablished in a short week, leaving five to six weeks for scientific sampling. A large camp would unfavorably alter this ratio.

Aircraft

Helicopter: Some of the scientific projects required helicopter support and in an effort to come up with the smallest (cost and fuel efficiency) aircraft that would fit our requirements, the Bell-212, Bell-205, Bell-206, A-Star, Alouette III and the MBB-105 were considered. The MBB-105, a relative newcomer to the Arctic, was selected. It is slightly larger compared to the Jet Ranger (Bell-206) with substantially larger cargo hold and more convenient in loading/offloading.

Small Fixed Wing: Such an aircraft was needed for the search and initial deployment of the camp, routine supply flights, and evacuation. Different aircraft and combinations of aircraft were reviewed. Availability and favorable past experience steered us to the Twin Otter in a wheel/ski configuration. It turned out that skis are not readily available in Alaska, neither are pilots with experience in reading ice and doing open field landings on virgin ice. For the search and initial landings we considered this to be essential. Once a site had been selected and a runway maintenance and survey capability existed on the ground, use of a Twin Otter on oversized tires seemed possible. For the search and initial deployment we reviewed different scenarios from small ski-equipped airplanes to a combination of helicopter and fixed wing aircraft deployed using an en route fuel cache. These scenarios were all judged too time consuming or prone to mixups. The solution was to use a long range Twin Otter on wheel/skis with an experienced ice pilot from Tuktoyaktuk for the search and initial landing and then charter a Twin Otter on oversized tires from Prudhoe Bay to provide the subsequent support.

Heavy Airlift: The camp weight was estimated at 222,000-250,000 lbs. and in the interest of a fast and expedient deployment the Hercules was selected for the heavy airlift (5-6 loads). This meant we needed a runway of minimum 4,000' length and 50" thickness with drifts and snow depth within acceptable limits. With a twin-track skidoo as the only motorized means of performing runway improvement we were very much dependent upon finding a natural strip. Although during AIDJEX and CANBARX we had found such ice in the Beaufort, we needed an alternative capability, in case such a site could not be found in our target area or broke up during deployment. Twin Otters would be too slow and costly for the job so a DeHaviland Dash-7 was put on contract as the primary backup with the C46 as an alternative. Both aircraft are in the 50,000 lbs. maximum T.O.W. class requiring a little more than half the ice length/thickness of the Hercules, but doubling the cost and tripling the number of loads needed.

Equipment

The living/working quarters were Manigan and Weatherport structures which we had available and had gained favorable experience with in the Fram programs. Typically, they are 8-16 feet in width and 10-30 feet long. With the availability of the Hercules and in the interest of expediting the erection of the shelters we planned to prefabricate 8'x16' floor sections at Prudhoe Bay.

Power was provided by a series of diesel generators ranging in size from 3 to 12 kw. The 12 kw at approximately 900 lbs. is as big a unit as one would want to move around by manual means.

Runway maintenance was performed by a twin-track Skidoo Alpine pulling a 5' drag which cut and leveled the packed snowdrifts. For marking the runway and centerline extensions we used flags and empty fuel drums as they became available.

Communication/navigation was by standard and established means. The exceptions were an x-band radar which was used to accurately guide the helicopter to specific targets up to 50 miles from camp, and a microcomputer at Prudhoe Bay used for electronic mail (telemail) message traffic and for accessing Service Argos.

Safety

Again, established procedures were followed with recommendation for medical/dental checkups prior to going to the field. Appropriate clothing was discussed and suggested. The medical establishments at Prudhoe Bay and the Search and Rescue Center at Barrow were notified of the project.

Budget

This nine-week camp with approximately 19 investigators, 3 support people, and 2 helicopter crews was budgeted at approximately \$800,000. The cost was comprised primarily of air support, fuel, supplies, salaries, travel and per diem, equipment and shipping costs. The science to support man-day ratio computes to approximately 3:1 with a cost per science man-day of approximately \$1,000.

4. EXECUTION

The project followed closely the plans and schedules laid out in the operations plan. The Bradley Twin Otter from Tuktoyaktuk started the search on March 3; delayed one day by bad weather. Following three more sorties from Tuktoyaktuk a large part of our target area had been surveyed and several possible sites had been spotted. On March 8 the ERA Twin Otter from Prudhoe with project personnel, embryo camp and the Hercules check pilot rendezvoused with the Bradley aircraft for final site evaluation. By evening, the camp was pitched on first-year ice (6-7 feet) adjacent to a 4,500'/72" lead. The check pilot requested some leveling/snow removal on the runway.

Three days later, seven people were in residence and the runway ready for final inspection. The check pilot gave the green light and the Hercules on standby at Prudhoe brought out the first load. The heavily laden aircraft (44,000 lbs.) pushed through the snow cover all the way to the ice and uncovered snow depths in places reaching 10"-12". This posed a potential hazard to the nose gear door, which might have been caught in the hard-packed snow,

started plowing and been torn off. Further flights were suspended. Two remedies were pursued. One was to take the nose gear door off, which the company considered too time consuming and expensive. The other was to bring out a 966 loader with a bucket and remove the snow. This seemed too risky and expensive if the runway were to break up and the vehicle had to be abandoned. The airlift was resumed two days later when the pilot agreed to try it again with a lighter load (25,000 lbs.). On landing, this time from the opposite end, a curb-sized ridge was uncovered by the landing aircraft. This reduced the runway by 1/3. While on the ground, the aircraft taxied several times up and down the runway, breaking up the hard-packed snow, making possible further leveling and grooming by the skidoo pulled drag. Despite the reduced runway length, four more loads brought out the remaining 140,000 lbs. of cargo. By March 20 the camp was operational with several projects installed and collecting data.

Three to five times per week the project Twin Otter made regular service flights to the station, bringing out supplies, parts and rotating short term projects and personnel.

Although the runway remained intact, there was no need to use the Hercules for evacuation. A gradual phase-down of projects started April 25 and with the Twin Otter making two trips a day, a convenient and orderly evacuation was completed on May 4.

Only one good storm and no ice activities spared the personnel the otherwise frequently common chores of digging out or relocating. The project was also spared any medical emergencies. Aside from a few temporarily striking backs and some rope burned hands we experienced no serious injuries, Polar Bears, or personnel falling into leads.

5. POST OPERATIONS REFLECTIONS

Search

Satellite photos were found to be of limited value in assessing the ice condition. When the Twin Otter spends 60-70% of the available fuel getting to and from the search area, there is "looking fuel" left to cover only a small area on each mission. It might prove expedient to start out covering large areas in a fast flying scouting aircraft to define the areas for more detailed examination by the Twin Otter search craft.

In order to take on maximum fuel only the pilot and co-pilot flew as observers. On such long flights (8-9 hours) additional eyeballs are needed to effectively survey the ice, even if it has to be at the expense of flight endurance.

Personnel

A three-man support crew (manager, helper and cook) turned out to be marginally adequate. This was to some degree caused by the camp manager's extensive commitment to helicopter flight following over radio and radar. Under the circumstances we found it necessary to augment the staff by one general hand/cook's helper.

Communications

Two periods of radio blackout of three and five days duration reminded us of the limitations in HF communications. The associated problems were to some extent overcome by relaying via overflying transpolar commercial jets or via Canadian shore stations in Resolute

or Tuktoyaktuk. Although, in this case, the temporary lack of communications did not adversely affect the project, a more reliable link via satellite would be a welcome added assurance of success and safety.

Navigation

The radar installation in camp with an x-band transponder on the helicopter proved very successful. The antenna was mounted on a 40' telescoping mast and allowed accurate and efficient guiding of the helicopter to predetermined survey points up to 50 miles from camp.

Hydroholes

A large number of 36" diameter holes were required for instrument deployment. They were cut using the University of Washington/Applied Physics Laboratory's hot water corer. (The system worked generally very well. It is however, sensitive to improper timing, which leads to the recirculating melt water freezing in the hoses. Ocean Systems, Inc. has developed and demonstrated a closed system melter of similar but smaller and lighter design. It uses antifreeze as the heat carrying medium, has approximately the same melting rate, and appears very attractive.)

Cargo Handling

Aside from the fuel, most camp equipment and scientific cargo was accumulated in Seattle and piece-by-piece loaded into four 27' trailer containers. At Prudhoe Bay it was downloaded and loaded back on the Hercules, some of it after first having been palletized on military C-130 pallets or a long Hercules skid. In the field, individual pieces were manually offloaded. The pallets and skids were winched/pushed off the aircraft and downloaded, so the platforms could be backhauled to Prudhoe. A blow before the cargo has been secured would result in searching, digging and handling boxes an additional time. To avoid having to manipulate the cargo this many times, some thought should be given to a larger size shipping unit that fits into the Hercules. Some type of expendable prefabricated plywood module, maybe 8'x10'x7" high, on a 4'x6' skid could be packed in Seattle, trailered to Prudhoe, and put directly on the Hercules. At the camp these modules would keep the cargo together and protected until it is ready to be used. Once the modules are emptied they would serve nicely as labs, T-houses, warm storage sheds, etc., and might either be dragged or helicopter-lifted to a suitable place of use.

Runway

The substantial effort expended on runway preparation was to a large extent wasted. The lightweight skidoo/drag will do a nice surface job for a Twin Otter size aircraft that rides on top of the general snow cover. Aside from taking out or airdropping heavy duty snow removal and grading equipment, my feeling is that following an inspection the C-130 should come out on the first flight basically empty and spend time taxiing up and down the runway to break up the snow. It might have on board a small size tracked vehicle with a suitable drag that if need be can be deployed to redistribute the broken up snow. Such a vehicle could, depending upon the circumstances, go back out on the subsequent or last load. This first flight should take place as early as possible before too much equipment has been deployed and installed. This would minimize the impact if the Hercules during taxiing exposes surprises that make the site unacceptable.

INTRODUCTION TO SERVICE ARGOS AND DRIFTING BUOY LOGISTICS

R. M. Partridge

National Data Buoy Center
NSTL, MS 39529

ABSTRACT

An overview of Service Argos is discussed including user responsibilities, data handling, distribution, and security. A case is made for optimum distribution of meteorological and oceanographic data to operational forecast centers via the Global Telecommunication System (GTS), and use of the DRIBU/Argos uplink code is discussed. Drifting buoy logistics is addressed. The need for planned procurements, shipping, handling, buoy checkout, data quality control, deployment, and coordination between participants to optimize the most cost-effective use of deployment resources is presented in detail. National Data Buoy Center (NDBC) activities supporting global field experiments using drifting buoys are highlighted. Aerial deployment of drifting buoys is reviewed.

1.0 INTRODUCTION

Environmental data acquisition from remote areas of the globe is simplified through the use of satellite telemetry. Service Argos, in operation since the First GARP Global Experiment (FGGE)¹ in 1978 and 1979 has proven this concept. Large-scale, global experiments, such as the Tropical Ocean Global Atmosphere (TOGA) project and the World Ocean Circulation Experiment (WOCE), will make extensive use of this service through the mid-1990's. Efforts put forth for FGGE and TOGA have resulted in considerable experience in the operation of large-scale data acquisition programs. Coordination among participants is of paramount importance for acquiring the maximum return from monies expended. This covers the spectrum ranging from programmatic and hardware design to the deployment of sensors. Automated, air-deployable devices, such as drifting buoys utilizing satellite telemetry, are particularly beneficial for application in remote areas.

2.0 SERVICE ARGOS

Service Argos is the result of a cooperative venture between NASA, NOAA, and CNES (Centre National d'Etudes Spatiales) and is located at the CNES Space Center in Toulouse, France. The Argos system is primarily intended for applications concerned with environmental data collection through satellite telemetry. The system offers sensor data collection and platform location of fixed or moving platforms located anywhere on the earth's surface.

The system is comprised of three major elements consisting of:

- Two polar-orbiting satellites, each carrying a Data Collection and Platform Location System (DCPLS)
- A user platform equipped with environmental sensors and a Platform Transmitter Terminal (PTT) for telemetry
- Ground-based data processing centers (Toulouse and one programmed for the U.S. in 1987).

The two polar-orbiting satellites carrying the Argos DCPLS are the NOAA/TIROS-N series satellites. These satellites have a sun-synchronous, circular orbit configuration (Figure 1) and are at an altitude of approximately 830 to 870 km above the earth. The satellites have an inclination of 98 degrees, and during each orbit fly over both the North and South poles. The orbital period for each satellite is approximately 101 minutes, with each satellite crossing the poles at an interval of about 45 minutes.

The sun-synchronous orbit of the satellites results in each satellite crossing the equator at the same local solar time each day. Satellite I crosses the equator at 0230 hours (descending) and 1430 hours (ascending), while Satellite II crosses the equator at 0730 hours and 1930 hours. This is important from the user's viewpoint since data telemetered from any platform on the earth's surface will be received at about the same solar time every day, but that time will vary as a function of geographical position. The number of satellite passes or "windows" increases with latitude to a maximum at the poles. Table 1 illustrates the number of passes per day per latitude and the cumulative time of the windows for the two satellites. As the satellites pass over a fixed point on the earth's surface its footprint, or window, covers a circle approximately 5000 km in diameter. Figure 2 depicts tracks of the two satellites and the footprints for the satellites passing over the Mediterranean and Caribbean Seas. At any one time the Argos DCPLS aboard the satellite can acquire and nominally process 920 data-collection-only PTT's (fixed location) and 230 platform-location-plus-data-collection PTT's (variable location) in the footprint of the satellite. The user platform (buoy, ship, etc.) is equipped with a PTT. This device provides the required uplink communication to the satellite DCPLS. All PTT's transmit at a frequency of 401.65 MHz at regular intervals of 40 to 60 seconds.

It has been said that the polar-orbiting satellites do not provide adequate synoptic coverage. In weather forecasting terms, this means that data are not available at the standard synoptic hours of 00, 06, 12, and 18 hours Universal Mean Time (UMT). This may be the case for certain hours at the equator but in the mid-latitudes to the poles there is adequate coverage to meet the synoptic criteria. Figure 3 depicts actual data transmission time and satellite overpasses for a platform located near 35°N and 60°W.

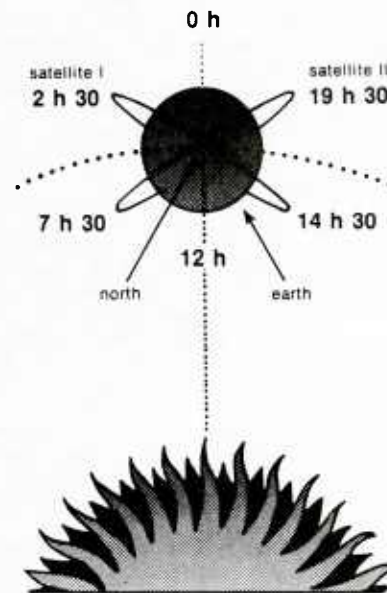


Figure 1. Satellite Orbit Configuration

Table 1. Approximate Satellite Visibility, as a Function of Latitude, for a 24-Hour Period

LATITUDE	CUMULATIVE VISIBILITY TIME OVER 24 HOURS	NUMBER OF PASSES IN 24 HOURS			MEAN PASS DURATION
		MIN.	MEAN	MAX.	
± 0°	80 MIN.	6	7	8	10 MIN.
± 15°	88 MIN.	8	8	9	
± 30°	100 MIN.	8	9	12	
± 45°	128 MIN.	10	11	12	
± 55°	170 MIN.	16	16	18	
± 65°	246 MIN.	21	22	23	
± 75°	322 MIN.	28	28	28	
± 90°	384 MIN.	28	28	28	

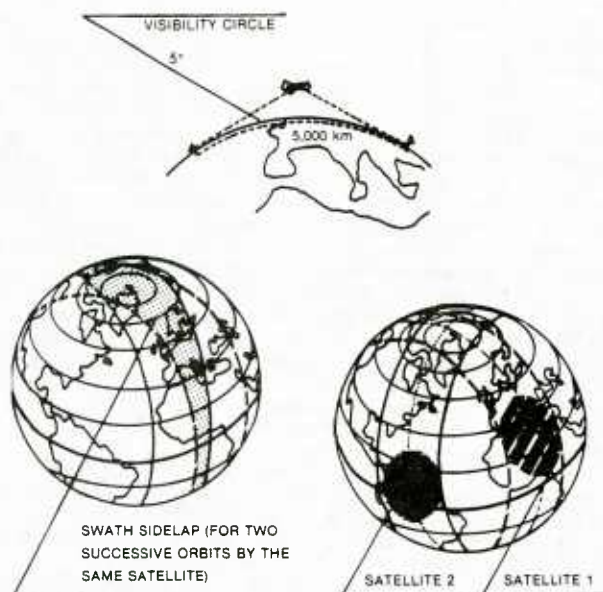


Figure 2. Satellite Visibility Zones

The delay in data reception at the operational forecast centers results from several factors. An inherent time delay due to the satellite orbital period ranging from 0 to 100 minutes will remain. Other time delays that are additions to the basic orbital period are the result of processing and relay times incurred when data are acquired through the main data acquisition stations at Gilmore Creek, Alaska, Wallops Island, Virginia, and Lanion, France. Table 2 summarizes the data delay times incurred at each center.

The use of a Local User Terminal (LUT) eliminates all time delays, except for that incurred as a result of the orbital period of the satellites. An LUT is a small, portable, microprocessor-based receiver capable of receiving transmissions from the polar-orbiting satellite's VHF downlink beacon at 176.77 and 177.77 MHz. The restriction on the use of an LUT is that these systems are regional in data coverage and operate on a line-of-sight basis between the PTT and satellite. This means that the LUT and PTT must be within the footprint of the satellite in order to acquire data. This footprint covers a circle with a diameter of approximately 5000 km (Figure 2).

Argos has the capability to earth-locate these platforms with a high degree of accuracy (normally within 500 meters).² Position-fixing of the earth-based PTT's is accomplished by measuring the Doppler effect on the carrier frequency of incoming messages received by the satellite. Each measurement made by the satellite corresponds to a field of possible positions for the PTT in question. This field takes the form of a cone, with the satellite at the apex and the velocity vector as the axis of symmetry. The satellite altitude is known, and the intersection of several of these cones (each corresponding to a separate PTT transmission/measurement) with the altitude sphere yields the solution of the PTT's position relative to the satellite (Figure 4).

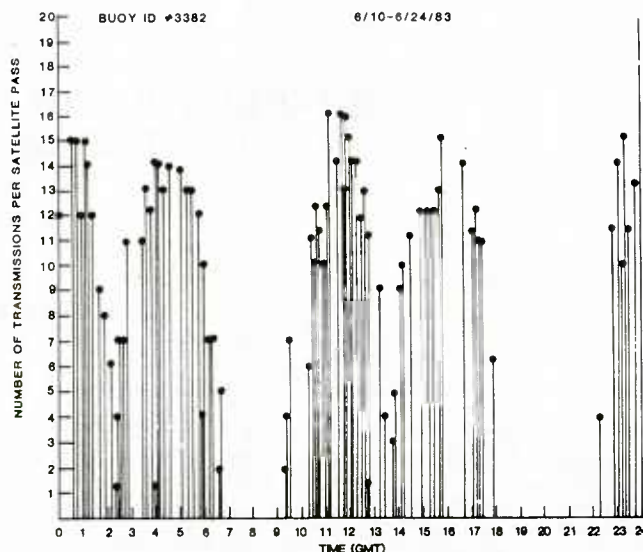


Figure 3. Time and Number of Messages Received by the NOAA Polar-Orbiting Satellites

Each message transmitted through the PTT includes the platform identification number and 32, 8-bit words of sensor information. In the simplest form this allows the transmission of up to 32 unique sensor values per transmission. By alternating inputs to the PTT, as many as 96 unique sensor readouts can be transmitted in three successive transmissions. Sensor processing and data collection on board the user's platform is microprocessor-controlled. This provides considerable flexibility and allows optimum data telemetry to the satellite by maximizing processing of sensor readouts aboard the user platform. Table 3 illustrates an involved uplink format to Service Argos. In this case, up to 4 hours of 30-minute-averaged data from eight different sensors can be telemetered. Although these unique and imaginative formats can be used to transmit a maximum of data for a specific user, they preclude optimum distribution to other potential users of the data.

As a consequence, the World Meteorological Organization (WMO) and Service Argos are encouraging, when possible, the routing of platform data to the global community. Data can be relayed to users in one of several WMO code formats, including DRIBU, HYDRO, SYNOP, and SHIP.³ In order to route data in a WMO-approved code, users must uplink their data to Service Argos in a rigid format. This is necessary since the existing Argos data processing center is not capable of handling variable field transmissions. However, even with this restriction, a tremendous amount of usable environmental data can be acquired and disseminated. Table 4 illustrates the existing Service Argos uplink format specified for GTS distribution. Transmissions received by Argos in this format can thus be encoded in the appropriate code described in WMO Publication No. 306, "Manual on Codes," and routed over the GTS. The GTS is, in turn, monitored by

Table 2. Breakdown of Interval Between Data Collection and Availability

COMPONENT			
ORBITAL INTERVAL		0 TO 100'	
TRANSMISSION TO NESDIS		45'	
TRANSMISSION TO SERVICE ARGOS		20'	
PROCESSING AT SERVICE ARGOS			40'
TOTAL INTERVAL			
MIN.			1 H 45'
MAX.			3 H 25'

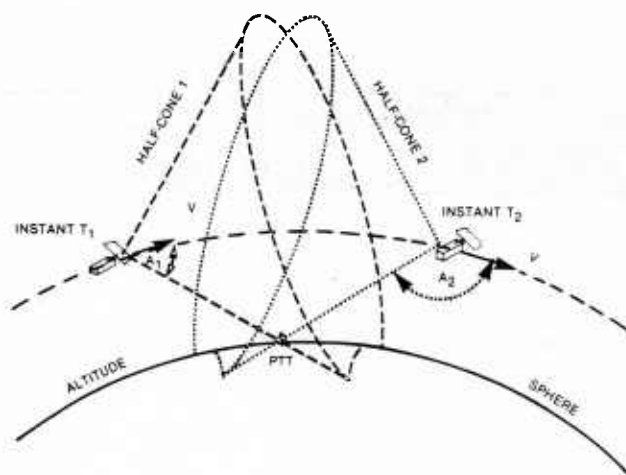


Figure 4. Platform Location

every major environmental data collection center in the world, including NOAA's National Meteorological Center, the Navy's Fleet Numerical Oceanography Center, and the Air Force Global Weather Central.

3.0 LOGISTICS AND OPERATIONS

Regardless of the efficiency of the data telemetry system used to acquire, process, and analyze environmental data from remote areas, platforms capable of sensing the environment must be procured, calibrated, and delivered to regions of the globe that are not easily accessible. Experience with drifting data buoys has shown that the logistics involved to deliver the platforms into remote areas can overwhelm the cost of a program, especially in the case where a single organization must bear the brunt of hardware cost and deployment assets.

3.1 PROCUREMENT

Procurement of hardware and deployment assets are best realized through planned phased buys of large numbers of standardized platforms or buoys. This allows manufacturers to bid competitively on contracts for a significant volume of standard products. This provides cost reduction in the long term through the establishment of assembly line construction and subcontracts for premanufactured components. The problem that arises is when the research community uses nonstandard, highly specialized platforms for data acquisition. However, for the core of basic measurements required to support both operational and postoperational research, the planned procurement of standard platforms is highly desirable. Sharing, or piggy-backing, on deployments by several scientific investigators or organizations greatly reduces the cost per unit for deployment resources.

3.2 DEPLOYMENT

Two methods are proven and are cost-effective for transporting platforms to remote staging areas and for deployments on scene. The two methods are ships and aircraft.

The transportation to and deployment of automated environmental sensing platforms to remote areas is a critical factor in assessing program costs and can overwhelm costs for hardware and data processing. A resource that is free is by far the best. As a second choice, sharing of these costs by the participating agencies is the only viable solution. The common denominator is the cost of platform per unit of time. For example, C130 flying time is typically on the order of \$2000 (U.S.) per hour and covers all expenses of the aircraft and crew. This time starts at the departure point of the aircraft and ends at mission completion and includes transit time. Oceanographic survey vessels often

run \$18,000 to \$20,000 (U.S.) per day for fuel, and availability is often limited due to the high demand for these vessels.

Coordination through a single operational organization is an important factor in minimizing these costs. In more cases than not opportune delivery can be worked out, as in the case for drifting buoy deployments in the Southern Hemisphere. To effect the coordination an organization must be assigned tasking authority, be cognizant of deployment resources, have contacts within participating agencies, and know sensor system delivery schedules as well as when and where the systems are to be deployed. Piggy-backing of experiments in common areas of interest can reduce overall costs since one mission, conducting a variety of experiments, often yields the best results (e.g., activities such as the Space Shuttle and oceanographic surveys). The major concern is saturation, but effective management precludes this possibility.

Other than the factors involved in just sending a sensor package to a site is that of the mechanism of deployment or setting up the observation station. Again coordination in design and deployment technique pays off since a dedicated group can be trained for this task and can, in time, train other individuals. As an example, drifting buoys utilize the same basic packaging assembly, system checkout, and deployment hardware for both ships and aircraft. The major difference is the parachute hardware required for an aerial deployment. An automated common delivery system greatly simplifies field work and ensures successful deployments. Ships are actually a more difficult resource to work with since every ship has different arrangements of deck space, priorities, and equipment. This is true even for vessels of a common class. Aircraft, on the other hand, are more standardized. Delivery from C130 and C141 aircraft is basically the same. Restrictions on these resources are primarily load capacity, range, and cost. In the Arctic region, most areas can be covered by C130 or C141 aircraft. Also, in many Arctic areas other aircraft can be effectively used for smaller payloads.

3.3 SHIPS

Ships are the most expensive asset when used for dedicated deployments. They are also slow, requiring many weeks or months to deliver platforms into remote areas. However, for transportation of large numbers of platforms and for opportune deployments, they are extremely valuable. In this regard, they are the most cost-effective method. Other difficulties that arise when using ships are the wide variation in deck configuration, delivery procedures, and the lack of trained personnel to assemble and deploy the platforms on scene, requiring technicians to assist the ship's crew during deployments.

Deployments from ships follow no basic rule, other than getting the unit safely over the side without damaging the equipment or injuring personnel. Ships have been used with a high degree of success for the deployment of drifting buoys. Weather is the most critical and unpredictable element affecting these deployments. Flexibility in site locations ensures ease in deployment, thereby allowing ships to avoid hazardous conditions and still effect the deployment in a minimum time. This must be considered when tasking resources, and, when possible, deployments should be tailored to the ship's operating schedule. From ships, buoys are usually deployed over the transom or by an overhead crane or davit. Figures 5 and 6 illustrate these two operations. Drifting buoys can survive a free fall from a height of approximately 15 to 20 meters without degradation of function. Complete instructions for deployments from ships and aircraft are contained in the U.S. TOGA Logistics Plan,⁴ published by the National Data Buoy Center.

3.4 AIRCRAFT

Aircraft play an important role in environmental reconnaissance. A variety of aircraft types and classes have been used over the years for oceanographic and geophysical surveys, weather reconnaissance, and logistics.⁵ They are a mainstay of operations in Antarctica and routinely provide data in support of hurricane and typhoon forecasting. The role played by aircraft in the deployment of drifting data buoys has been a large one, beginning with deployments from C141's during FGGE in 1978 and 1979. Recent developments have been in the form of operational experiments to deploy drifting buoy systems in advance of mature hurricanes.⁶ Also, C130's and light aircraft play

Table 3. Hurricane Drifting Buoy Data Format and Transmission Sequence

FRAME NO.	WORD NO.	NO. OF BITS	TYPE SENSOR (30-MINUTE AVERAGE EACH SENSOR)	TRANSMISSION (Tx) SEQUENCE	
				Tx NO. 1 AND EACH SUCCESSIVE ODD Tx (BIT 5 OF WORD 2 = 0)	Tx NO. 2 AND EACH SUCCESSIVE EVEN Tx (BIT 5 OF WORD 2 = 1)
1	1	10	P _B , BAROMETRIC PRESSURE	1st 30 MINUTES OF DATA WITHIN 4-HOUR INTERVAL	5th 30-MINUTE INTERVAL
	2	5	T _O , SEA SURFACE TEMPERATURE		
		1	ODD/EVEN TRANSMISSION INDICATOR		
	3	8	W _G , WIND GUST		
	4	8	W _S , WIND SPEED		
2*	5	10	T ₄₀		
	6	6	T ₆₀		
	7	8	T ₁₀₀		
	8	8	T ₂₀₀		
3	9	10	P _B	2nd 30-MINUTE INTERVAL	6th 30-MINUTE INTERVAL
	10	6	T _O		
	11	8	W _G		
	12	8	W _S		
4	13	10	T ₄₀		
	14	6	T ₆₀		
	15	8	T ₁₀₀		
	16	8	T ₂₀₀		
5	17	10	P _B	3rd 30-MINUTE INTERVAL	7th 30-MINUTE INTERVAL
	18	6	T _O		
	19	8	W _G		
	20	8	W _S		
6	21	10	T ₄₀		
	22	6	T ₆₀		
	23	8	T ₁₀₀		
	24	8	T ₂₀₀		
7	25	10	P _B	4th 30-MINUTE INTERVAL	8th 30-MINUTE INTERVAL
	26	6	T _O		
	27	8	W _G		
	28	8	W _S		
8	29	10	T ₄₀		
	30	6	T ₆₀		
	31	8	T ₁₀₀		
	32	8	T ₂₀₀		

*T_{40,60,100,200} - Subsurface temperature sensors located at 40, 60, 100, and 200 meters below sea surface

a major role in the deployment of ice buoys in the Arctic.

Aircraft are an inherently flexible resource offering speed, standard delivery procedures, trained deployment personnel, and, in some cases, on-scene readout and validation of sensor operation through comparison with baseline data acquired on board the aircraft. For drifting buoys, certification by the U.S. Air Force and procedures have been developed for deployment from C130- and C141-type aircraft (Figure 7). Also, smaller buoys can be air-dropped from the paratroop and/or exit doors on just about any type of aircraft. Present developmental activities are expected to result in an expendable system deployable through standard sized sonobuoy launchers, which will greatly simplify logistical and deployment operations.

Procedures for deployment of buoys and other payloads from aircraft are highly technical and result only after considerable test and evaluation. Not only must crew safety be accounted for, but the flight characteristics for objects deployed must be evaluated. For ice- and FGGE-type drifting data buoys and sonobuoy-type hardware, these evaluations have been completed. FGGE provided the impetus and funding necessary for the larger buoys. The sonobuoy delivery system has been developed and approved over the years as a result of Navy operational usage. An example of the aerial delivery procedures for C130- and C141-class aircraft is contained in the U.S. TOGA Logistics Plan.⁴

The use of aircraft for deployment introduces considerable flexibility along with capability to store, checkout, prepare, transport, and conduct delivery operations for platforms from a common staging area.

Table 4. Argos GTS Distribution Uplink Format

NUMBER OF 32-BIT BLOCKS TRANSMITTED FROM 1 TO 8

BLOCK NUMBER	SENSORS n°	NO. OF BITS	PHYSICAL PARAMETERS MEASURED
1	1	10	ATMOSPHERIC PRESSURE
	2	6	HOUSEKEEPING
	3	8	SEA SURFACE TEMPERATURE
	4	8	AIR TEMPERATURE
2	5	8	PRESSURE TENDENCY
	6	8	WIND SPEED
	7	8	WIND DIRECTION
	8	8	SIGN OF PRESSURE TENDENCY (+ or -)
3	9	8	HOUSEKEEPING
	10	8	HOUSEKEEPING
	11	8	HOUSEKEEPING
	12	8	HOUSEKEEPING
4	13	8	USED TO DEFINE CHARACTERISTICS OF SUBSURFACE TEMPERATURE MEASURING SYSTEM
	14	8	
	15	8	
	16	8	
5	17	8	SUBSURFACE TEMPERATURES AT THREE DEPTHS PLUS ONE EXTRA MEASUREMENT
	18	8	
	19	8	
	20	8	
6	21	8	SUBSURFACE TEMPERATURES AT THREE DEPTHS PLUS ONE EXTRA MEASUREMENT
	22	8	
	23	8	
	24	8	
7	25	8	SUBSURFACE TEMPERATURES AT THREE DEPTHS PLUS ONE EXTRA MEASUREMENT
	26	8	
	27	8	
	28	8	
8	29	8	SUBSURFACE TEMPERATURES AT THREE DEPTHS PLUS ONE EXTRA MEASUREMENT
	30	8	
	31	8	
	32	8	

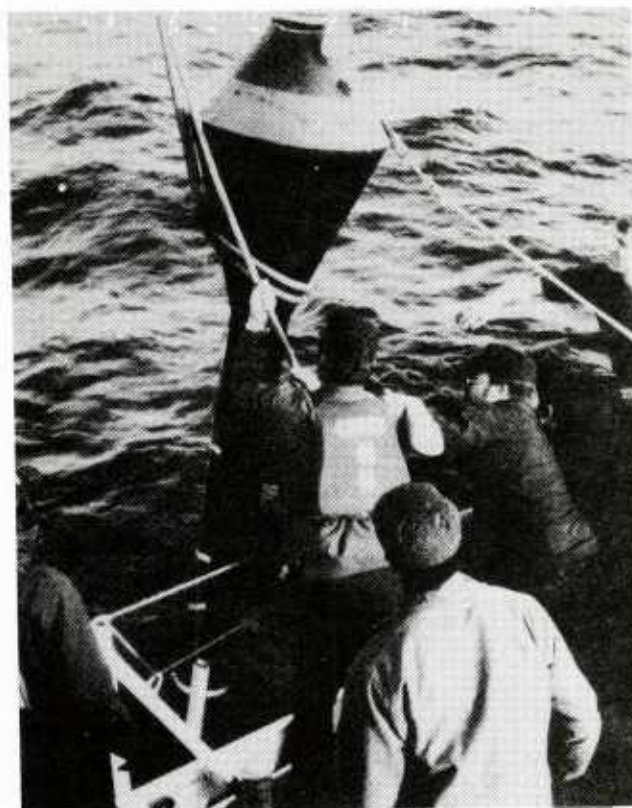


Figure 5. Buoy Being Deployed by Overhead Crane or Davit

4.0 COORDINATION

In all cases, in order to obtain the most effective use of the available deployment resources, rigid coordination of activities and close command and control of the logistical operation from a single source is required. This type of mechanism has been set into motion by NDBC to effect deployment of a large number of drifting buoys throughout the Southern Hemisphere. Figure 8 depicts the status of the drifting buoy array in the southern oceans as of May 1985 that has been established to support the TOGA project. All of the buoys were deployed on an opportune basis utilizing ships from several countries. Prior to initiating the deployments, memoranda of agreement were negotiated with the participating countries. Forward staging areas for the buoys were established in Australia, New Zealand, South Africa, and the United Kingdom. Buoys are delivered to staging areas by commercial surface transport, the Military Sealift Command (MSC) and the Military Airlift Command (MAC). In essence, the entire operation is carried out at minimal cost simply as a result of coordination.

A similar program can be established and operated in the Arctic regions utilizing assets from Canada, Norway, and the U.S. This would allow maximum distribution of sensing platforms, maximum data acquisition, and reduce duplication of effort and funds required for logistics and hardware.

5.0 QUALITY CONTROL

Quality control of data and sensor performance using Service Argos is non-existent at the present time, other than for positioning. Data routed over the GTS are not quality controlled and are the responsibility of the principal investigator or end user. This is unsatisfactory for operational users, and a mechanism for effective quality control of data is needed. NDBC routinely conducts quality control of moored buoys, for drifting platforms used for operational support to the National Weather Service, and when requested by customers.



Figure 6. Buoy Being Deployed over the Ship's Transom

No effective capability is in place to scale or delete bad data from the message traffic routed to users of drifting buoy data. However, NDBC has conducted studies in this regard, and the feasibility is proven.³ Techniques such as those in operation for moored buoys can be applied to drifting buoys. In general, this means monitoring an information data base at one of the primary message centers, such as the National Meteorological Center. Incoming drifting buoy data on the GTS can be quality checked using automated routines, and the message, with appropriate adjustments, can be restructured and routed to U.S. users.

A large environmental observing program, such as the one projected for the Arctic regions, must have an effective quality control plan in place in order to maintain user confidence in the data routed, and to ensure that only information of highest quality is archived for research purposes.

6.0 CONCLUSION

Service Argos is a viable system to acquire and telemeter environmental data for operational and research purposes. At the present time, distribution of data with three hours or greater time delay has a negative impact on operational analyses and forecasts. However, Local User Terminals (LUT's) provide real-time data. In the Arctic, synopticity is not a problem since satellites are overhead virtually every hour. This, plus an LUT capability in Canada, is very attractive. Message routing through the GTS and from Canada to users in the United States is excellent using existing communication networks. Military use of Argos is not prohibited in the agreement with the U.S. so long as data collected are environmental in nature. Provisions are in place to provide protection of proprietary rights of the investigator, but classification in the sense of controlled data distribution is not guaranteed, and "protection" simply refers to withholding data from general distribution. Coordination in all phases relating to the establishment of large environmental observing systems is paramount for effective use of resources ranging from program management to system deployments and data acquisition and distribution.



Figure 7. C130- and C141-Type Aircraft

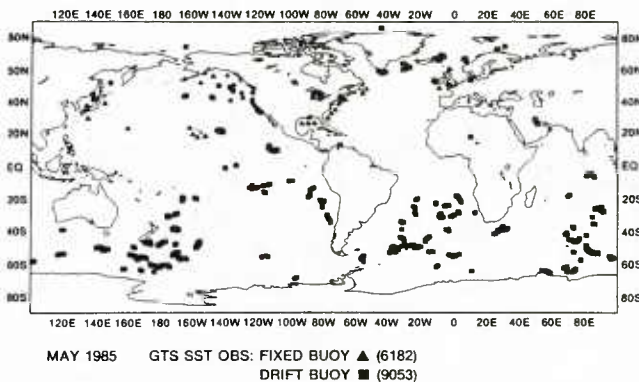


Figure 8. TOGA Drifting Buoy Array

REFERENCES

1. "FGGE Implementation/Operations Plan," The FGGE Special Observation System, Vol. 5, part D, May, 1978.
2. "Service Argos Users Guide," May, 1984.
3. "Guide to Data Collection Services Using Service Argos, World Meteorological Organization, Marine Meteorology, and Related Oceanographic Activities," Report No. 10, 1983.
4. "U.S. TOGA Logistics Plan," National Data Buoy Center, October, 1984.
5. "Tactical Deployment of Satellite-Reporting Drifting Data Buoys for Environmental Data Acquisition," R. M. Partridge and J. J. Shimkus, Proceedings, Argos Users Conference, May, 1984.
6. "Atmospheric Boundary Layer and Oceanic Mixed Layer Observations in Hurricane Josephine obtained from Air-Deployed Drifting Buoys and Low Level Research Aircraft," Dr. Peter Black, et al., NOAA/AOML, May, 1985.

THE EFFECT OF THE PHYSICAL PROPERTIES OF ICE ON THE HIGH FREQUENCY
ACOUSTIC BACKSCATTER FROM AN ICE KEEL MODEL

Stanley A. Chin-Bing

Naval Ocean Research and Development Activity
Numerical Modeling Division Code 221
NSTL, MS 39529

ABSTRACT

The physical properties of ice have been included in a model of an ice keel to predict backscatter. Reflection coefficients for a high frequency (20 kHz) plane wave obliquely incident on a multilayered elastic solid (ice) bounded by two fluid half-spaces (water) have been calculated and included in a modified Ellison model to simulate backscatter (target strength) from an ice keel. The ice keel face is assumed to be composed of many randomly oriented blocks of multilayered ice which act as independent scatterers. Numerical examples are given which show that the plane wave reflection coefficient is dependent upon the frequency, the number of ice layers, the layer thickness, the compressional and shear attenuations, and the presence of a water-to-ice transition layer. The reflection coefficient in turn effects the target strength calculation. It is shown that the magnitude of this effect is highly dependent upon the type of block rotation used.

1. INTRODUCTION

The Ellison ice keel model [1] has been used to study the effect of the physical properties of ice on the backscattered signal from an ice keel. The Ellison model was first modified to accept a plane wave obliquely incident to the individual ice blocks. Then two different types of block rotations were included in the model. The physical properties of the ice were included in the model through the plane wave reflection coefficient. In Section 2 a concise description of the Ellison model and the modifications made to it are presented. A more detailed discussion may be found in the cited references. In Section 3 the plane wave reflection coefficient and the sound velocity profile for the layered ice model are discussed. Section 4 gives the results when this layered ice profile is included in the modified Ellison ice keel model.

2. THE MODIFIED ELLISON KEEL MODEL

One typical ice block, of the many blocks which form the face of an ice keel, is shown in Fig. 1. Each block is rotated through two random angles, one away from the vertical reference axis (y-axis) and the other away from the horizontal reference axis (x-axis). The blocks are packed along the

face of the keel and constitute the surface from which the incident plane wave is scattered.

Fig. 2 shows the geometry for an incident plane wave upon the surface of one of the blocks. The Ellison model [1,2] assumes that the incident wave is in the plane parallel to the long edge of the block and therefore needs only one specified angle. A modification [3] has been made to the original Ellison model which uses two angles to describe the position of the incident signal relative to the block. This gives a more general description since obliquely incident signals can be included. The equations for the backscattered field are calculated using the Helmholtz-Kirchhoff theory and are given in Fig. 2 for the respective incident fields. The target strength, TS, (in decibels) for each block is obtained from the backscatter cross-section and the block's reflection coefficient, R. The target strength for the entire ice keel is obtained by coherently summing the contributions from the individual blocks.

Two possible types of rotation that the blocks may undergo is shown in Fig. 3. In both Rotation I and Rotation II, the block is rotated through the same angle away from its vertical reference axis (y-axis). Similarly, both rotations occur through the same angle away from the horizontal reference axis (x-axis). However, the final orientation of the block's normal axis (z'-axis) is different and thus depends upon the type of rotation. Fig. 4 gives the equations for the reference angles used in Fig. 2. Rotations I and II obviously will give different reference angles even though the rotations away from the respective reference axes were the same. Henceforth, the Ellison model with two reference angles and either Rotation I or Rotation II will be referred to as the modified Ellison model.

3. PLANE WAVE REFLECTION COEFFICIENT

The plane wave reflection coefficient model used in this study is similar to that used by McCammon and McDaniel [4]. The velocity profile for the ice blocks is shown in Fig. 5 and is essentially the same as the one described by Posey, et al [5,6] except that the layered ice blocks are backed by water. Thin transition layers (total thickness of 0.101 meters) are included on the front side of the blocks. These transition layers allow the gradual change from water, which has only compressional velocity and attenuation, to ice

which has both compressional and shear velocity and attenuation. The ice is layered, varying in density, thickness, compressional and shear velocities and attenuations. Table I gives the various values for a typical case. The overall thickness of the ice was varied from one to two meters, but the total thickness of the transition layers remained constant.

4. RESULTS

Fig. 6 shows plane wave reflection coefficients obtained from a plane wave in water incident upon a half-space having homogeneous properties. The solid curve is due to Mayer [7] and does not allow for attenuations (compressional or shear) in the half-space. However, it does allow for shear velocity. The broken curve is obtained if compressional and shear attenuations are included in the half-space. The deviations from Mayer's curve at low grazing angles are due to the inclusion of the shear attenuation and the deviations at the higher grazing angles are due to the inclusion of compressional attenuation. The dotted curve is from the algorithm used in the unmodified Ellison model [1] and is an apparent truncation of the Mayer model.

Figs. 7 and 8 show the target strength versus time for a pulse incident upon the ice keel face at an aspect angle of 45 degrees. Table II gives the complete keel parameters. In Rotation I the largest contributor to the backscatter is block (16,3), i.e. it is the 16th block from the vertical reference edge of the keel and the 3rd block down from the horizontal reference edge of the keel. The incident pulse makes a grazing angle of 79.2 degrees with this block's normal axis. In Rotation II the largest contributors are blocks (11,3) and (16,3); the incident pulse makes grazing angles of 22 and 77.4 degrees, respectively, with these block's normal axis. In Figs. 7 and 8 the broken curve results from using the unmodified Ellison model [1] which uses the truncated form of Mayer's model whereas the solid curve results from using the complete reflection coefficient model for the half-space including compressional and shear attenuations. The peak target strengths using Rotation I are about the same for both curves. This is because the reflection coefficients for the truncated Mayer model and the complete model are the same at 79.2 degrees, which is the grazing angle associated with the block giving the strongest return (refer to Fig. 6). In Fig. 8 the difference between the peak target strength using the unmodified Ellison model and the modified Ellison model is as high as 5 dB. This is because the reflection coefficients from the truncated Mayer model and the complete reflection coefficient model differ significantly at 22 degrees which is the grazing angle associated with the block giving the strongest return for Rotation II.

A comparison of reflection coefficients for ice blocks of different thicknesses is shown in Fig. 9. The broken curve results from 2 meter thick layered ice having the parameters given in Table I but without the transitional "slush" layers. The

solid curve is for 0.98 meter thick layered ice without the transition layers; all of its ice parameters are the same as in Table I except that the 1.07 meter center layer has been shortened to 0.05 meters to give an overall thickness of 0.98 meters. Again, keel parameters are given in Table II. Fig. 9 shows that there is no difference between the two curves in the 0 to 40 degree grazing angle region where shear effects are most dominant. However, in the 50 to 90 degree grazing angle region where compressional effects dominate, the two curves differ. Thus, it would be anticipated that target strength calculations using Rotation I would differ when a keel composed of the 2 meter ice blocks was compared with a keel composed of the 0.98 meter blocks. This would be due to the fact that the reflection coefficient for the 2 meter thick block is larger than that for the 0.98 meter thick block at the grazing angle of 79.2 degrees which is the angle made with the dominant block (16,3). Fig. 10 shows this analysis to be valid. This dominant return block is the main contributor at 67 milliseconds and gives the strongest return from the entire keel. It might therefore be erroneously concluded that the thicker blocks give a stronger return in the keel model. The fact is that the type of rotation chosen can have a strong influence on the keel return. This can be seen in Fig. 11 where the peak returns are essentially the same for the two keels when Rotation II is used. As previously noted, the dominant blocks in Rotation II are (11,3) and (16,3) which make respective grazing angles with the incident signal of 22 and 77.4 degrees. In Fig. 11, block (11,3) contributes at 45 milliseconds and block (16,3) at 67 milliseconds. Fig. 9 indicates that the two reflection coefficients are identical at 22 degrees grazing angle and are approximately the same at 77.4 degrees grazing angle. (Actually, the reflection coefficient from the 0.98 meter block is slightly higher at 77.4 degrees and this is indicated in Fig. 11 where the target strength from the keel composed of 0.98 meter blocks is slightly higher than that from the keel composed of 2 meter blocks.)

Thus, Rotation I implies that the keel with the thicker blocks gives the higher return while Rotation II implies that there is no significant difference in the magnitude of the returns although the return from the keel with the thinner blocks is slightly higher. This type of comparison will now be extended to include blocks with transitional "slush" layers and blocks of equal thickness with and without the transitional layers. It will be seen in each example that while the magnitudes of the reflection coefficients (and therefore the physical parameters of the ice) are important factors in determining the target strength, the type of rotation used can strongly determine the degree of influence of these parameters.

The reflection coefficients for a layered ice block with water-to-ice transitional "slush" layers is shown in Fig. 12. The broken curve is for the 2 meter block (Table I) and the solid curve is for the 0.98 meter block. In the region

where the shear effects are dominant (0-40 degrees) the two curves are identical and almost unity, indicating that for high frequency the transitional layers act as good reflectors at these low grazing angles. The transitional layers are in effect shielding the ice layers where shear is present. At the higher grazing angles the compressional effects dominate and the two curves are slightly different. Therefore, any rotation which has dominant blocks with associated angles in the high grazing angles, such as Rotation I, will show a difference between the target strength calculated for the keel composed of 2 meter blocks and that calculated from the 0.98 meter blocks. Fig. 13 shows this where the return from the 0.98 meter block (solid curve) is approximately 10 dB higher than that from the 2 meter block (broken curve) at 67 milliseconds. This is due to the differences in the reflection coefficients at 79.2 degrees. However, for Rotation II, the target strengths are the same at 45 milliseconds since block (11,3) dominates and has the same value for the reflection coefficient at 22 degrees regardless of the block's thickness. Note that in Fig. 14 the return at 45 milliseconds is much stronger than that at 67 milliseconds due to the reflection coefficient being close to unity at 22 degrees and less than 0.5 at 77.4 degrees.

A comparison of reflection coefficients for 2 meter thick ice with the transitional layers (solid curve) (see Table I) and without the transitional layers (broken curve) is shown in Fig. 15. The corresponding target strengths for rotations I and II are shown in Figs. 16 and 17, respectively. The keel without the transitional layers (broken curve) gives the largest return for Rotation I due the larger reflection coefficient at 79.2 degrees. However, the keel with the transitional layers (solid curve) gives the higher return for Rotation II due to the large value of the reflection coefficient at 22 degrees.

It should be emphasized that the examples presented above were for 20 kHz incident signals. At lower frequencies, the transitional layers are penetrated and absorb energy due to shear resonances. This is shown in Fig. 18 where the reflection coefficients for 2 meter ice without transitional layers (broken curve) and 2 meter ice with transitional layers (solid curve) are shown for a frequency of 8 kHz. Comparing this figure to Fig. 15 shows that the transitional layers are less a factor at this lower frequency. The target strengths at 8 kHz. using the reflection coefficients given in Fig. 18 for rotations I and II are shown in Figs. 19 and 20, respectively. The results in both figures are easily predictable using the analysis presented above. Note that in Fig. 20, the return from the (16,3) block is the largest. Again, this is explained by examining the reflection coefficients. At 77.4 degrees, the difference between the reflection coefficient for the block with the transitional layers and the reflection coefficient for the ice block without the transitional layers is approximately 0.4. This is the largest difference encountered and causes the difference using Rotation II, of approximately 20 dB in favor of the keel with ice blocks

possessing the transitional layers.

Given the results presented, the interesting question arises. Why does the unmodified Ellison model give good results, as has been reported [2], when it does not allow for oblique incidence signals and uses a truncated reflection coefficient model? The answer may be in the type of ice blocks that formed the keels where the data was taken. Fig. 21 compares reflection coefficients from 2 meter blocks without transitional layers (broken curve), 2 meter blocks with transitional layers (solid curve), and the truncated Mayer half-space model used in the unmodified Ellison model (dotted curve). As can be seen, the reflection coefficients for the blocks with transitional layers and for the truncated Mayer half-space model are approximately the same for grazing angles up to approximately 50 degrees. This is the angular range for the dominant blocks using Rotation II at the higher frequency (20 kHz.). While by no means a definitive answer, the existence of transitional layers could help explain the agreement (or lack of agreement) between backscatter predictions and data from ice keels.

5. CONCLUSIONS

The modified Ellison ice keel model presented here extends the range of applicability of the model by allowing for oblique incident signals, inclusion of a wider range of physical ice parameters and a choice of block rotations. In the modified Ellison keel model, physical ice properties (viz. compressional and shear velocities, compressional and shear attenuations, density, and layer thickness) together with frequency effect the backscatter target strength calculations through the plane wave reflection coefficient. The degree of this effect is determined by the type of ice block rotation that is used.

6. ACKNOWLEDGEMENTS

This work was performed for the NAVSEA Arctic USW Environmental Technology Program, NAVSEA 63R, Mr. D. E. Porter, under PE62759N, Subproject SF59-555. This Subproject is block managed by R. L. Martin, NORDA Code 113.

7. REFERENCES

1. W. T. Ellison, "Simulation Studies of Under-Ice Acoustic Scattering (U)," Cambridge Acoustical Associates, Inc. Report C-714-270, 15 October 1980 (Confidential). The sections which describe the model and the computer code are unclassified.
2. G. C. Bishop, L.E. Melberg, C. J. Albanese, S. E. Overdeep, and W. T. Ellison, "A simulation model for high-frequency under-ice acoustic backscattering," J. Acoust. Soc. Am. Suppl. 1 77, S56 (1985).
3. S. A. Chin-Bing "Arctic High Frequency Acoustic Keel Model Study," Naval Ocean Research and Development Activity, NORDA Technical Note 257, July 1985.

4. D. F. McCammon and S. T. McDaniel, "The influence of the physical properties of ice on reflectivity," J. Acoust. Soc. Am. 77, 499-507 (1985).
5. G. H. Branch and J. W. Posey, "High-frequency acoustic reflection from the Arctic ice layer," J. Acoust. Soc. Am. Suppl. 1 77, S56 (1985).
6. J. Posey, G. Branch, S. A. Chin-Bing, and G. Tango, "High frequency acoustic reflection from flat sea ice," Arctic Oceanography Workshop, June 11-14, 1985, NSTL, MS.
7. W. G. Mayer, M. Behraves, and T. J. Plona, "Determination of sonic velocities from reflectivity losses at sea ice/water boundaries," J. Acoust. Soc. Am. 57, 39-46 (1975).

where the shear effects are dominant (0-40 degrees) the two curves are identical and almost unity, indicating that for high frequency the transitional layers act as good reflectors at these low grazing angles. The transitional layers are in effect shielding the ice layers where shear is present. At the higher grazing angles the compressional effects dominate and the two curves are slightly different. Therefore, any rotation which has dominant blocks with associated angles in the high grazing angles, such as Rotation I, will show a difference between the target strength calculated for the keel composed of 2 meter blocks and that calculated from the 0.98 meter blocks. Fig. 13 shows this where the return from the 0.98 meter block (solid curve) is approximately 10 dB higher than that from the 2 meter block (broken curve) at 67 milliseconds. This is due to the differences in the reflection coefficients at 79.2 degrees. However, for Rotation II, the target strengths are the same at 45 milliseconds since block (11,3) dominates and has the same value for the reflection coefficient at 22 degrees regardless of the block's thickness. Note that in Fig. 14 the return at 45 milliseconds is much stronger than that at 67 milliseconds due to the reflection coefficient being close to unity at 22 degrees and less than 0.5 at 77.4 degrees.

A comparison of reflection coefficients for 2 meter thick ice with the transitional layers (solid curve) (see Table I) and without the transitional layers (broken curve) is shown in Fig. 15. The corresponding target strengths for rotations I and II are shown in Figs. 16 and 17, respectively. The keel without the transitional layers (broken curve) gives the largest return for Rotation I due the larger reflection coefficient at 79.2 degrees. However, the keel with the transitional layers (solid curve) gives the higher return for Rotation II due to the large value of the reflection coefficient at 22 degrees.

It should be emphasized that the examples presented above were for 20 kHz incident signals. At lower frequencies, the transitional layers are penetrated and absorb energy due to shear resonances. This is shown in Fig. 18 where the reflection coefficients for 2 meter ice without transitional layers (broken curve) and 2 meter ice with transitional layers (solid curve) are shown for a frequency of 8 kHz. Comparing this figure to Fig. 15 shows that the transitional layers are less a factor at this lower frequency. The target strengths at 8 kHz. using the reflection coefficients given in Fig. 18 for rotations I and II are shown in Figs. 19 and 20, respectively. The results in both figures are easily predictable using the analysis presented above. Note that in Fig. 20, the return from the (16,3) block is the largest. Again, this is explained by examining the reflection coefficients. At 77.4 degrees, the difference between the reflection coefficient for the block with the transitional layers and the reflection coefficient for the ice block without the transitional layers is approximately 0.4. This is the largest difference encountered and causes the difference using Rotation II, of approximately 20 dB in favor of the keel with ice blocks

possessing the transitional layers.

Given the results presented, the interesting question arises. Why does the unmodified Ellison model give good results, as has been reported [2], when it does not allow for oblique incidence signals and uses a truncated reflection coefficient model? The answer may be in the type of ice blocks that formed the keels where the data was taken. Fig. 21 compares reflection coefficients from 2 meter blocks without transitional layers (broken curve), 2 meter blocks with transitional layers (solid curve), and the truncated Mayer half-space model used in the unmodified Ellison model (dotted curve). As can be seen, the reflection coefficients for the blocks with transitional layers and for the truncated Mayer half-space model are approximately the same for grazing angles up to approximately 50 degrees. This is the angular range for the dominant blocks using Rotation II at the higher frequency (20 kHz.). While by no means a definitive answer, the existence of transitional layers could help explain the agreement (or lack of agreement) between backscatter predictions and data from ice keels.

5. CONCLUSIONS

The modified Ellison ice keel model presented here extends the range of applicability of the model by allowing for oblique incident signals, inclusion of a wider range of physical ice parameters and a choice of block rotations. In the modified Ellison keel model, physical ice properties (viz. compressional and shear velocities, compressional and shear attenuations, density, and layer thickness) together with frequency effect the backscatter target strength calculations through the plane wave reflection coefficient. The degree of this effect is determined by the type of ice block rotation that is used.

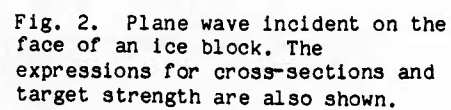
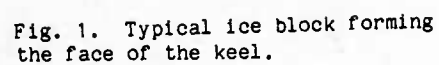
6. ACKNOWLEDGEMENTS

This work was performed for the NAVSEA Arctic USW Environmental Technology Program, NAVSEA 63R, Mr. D. E. Porter, under PE62759N, Subproject SF59-555. This Subproject is block managed by R. L. Martin, NORDA Code 113.

7. REFERENCES

1. W. T. Ellison, "Simulation Studies of Under-Ice Acoustic Scattering (U)," Cambridge Acoustical Associates, Inc. Report C-714-270, 15 October 1980 (Confidential). The sections which describe the model and the computer code are unclassified.
2. G. C. Bishop, L.E. Melberg, C. J. Albanese, S. E. Overdeep, and W. T. Ellison, "A simulation model for high-frequency under-ice acoustic backscattering," J. Acoust. Soc. Am. Suppl. 1 77, S56 (1985).
3. S. A. Chin-Bing "Arctic High Frequency Acoustic Keel Model Study," Naval Ocean Research and Development Activity, NORDA Technical Note 257, July 1985.

4. D. F. McCammon and S. T. McDaniel, "The influence of the physical properties of ice on reflectivity," J. Acoust. Soc. Am. 77, 499-507 (1985).
5. G. H. Branch and J. W. Posey, "High-frequency acoustic reflection from the Arctic ice layer," J. Acoust. Soc. Am. Suppl. 1 77, S56 (1985).
6. J. Posey, G. Branch, S. A. Chin-Bing, and G. Tango, "High frequency acoustic reflection from flat sea ice," Arctic Oceanography Workshop, June 11-14, 1985, NSTL, MS.
7. W. G. Mayer, M. Behraves, and T. J. Plona, "Determination of sonic velocities from reflectivity losses at sea ice/water boundaries," J. Acoust. Soc. Am. 57, 39-46 (1975).



ROTATION I

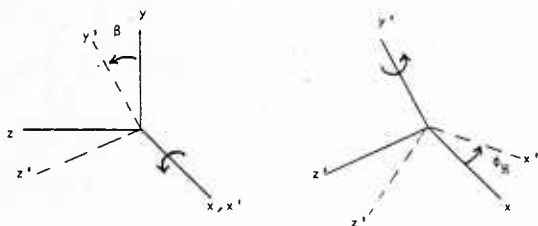
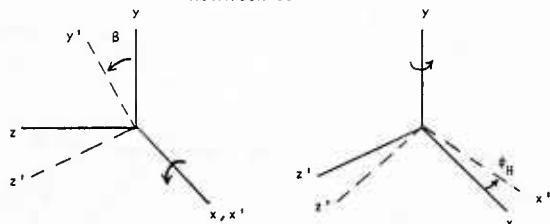


Fig. 3. Rotation sequences for Rotation I and Rotation II.

ROTATION II



$$\beta = \phi_V + \pi/2 - \theta_R$$

ROTATION I

$$\psi = \cos^{-1} [\cos\phi_1 \sin\theta_1 \sin\phi_H + \cos\phi_H (\sin\phi_1 \sin\theta + \cos\phi_1 \cos\theta_1 \cos\theta)]$$

$$\delta = \cos^{-1} [(1/\sin\psi) \{ \cos\phi_H \cos\phi_1 \sin\theta_1 - \sin\phi_H (\sin\theta \sin\phi_1 + \cos\theta \cos\phi_1 \cos\theta_1) \}]$$

Fig. 4. Equations for the reference angles between the incident plane wave and each ice block.

ROTATION II

$$\psi = \cos^{-1} [\sin\phi_1 \sin\theta + \cos\phi_1 \cos\theta \cos(\theta_1 - \phi_H)]$$

$$\delta = \cos^{-1} [(\cos\phi_1 / \sin\psi) \sin(\theta_1 - \phi_H)]$$

VELOCITY PROFILE

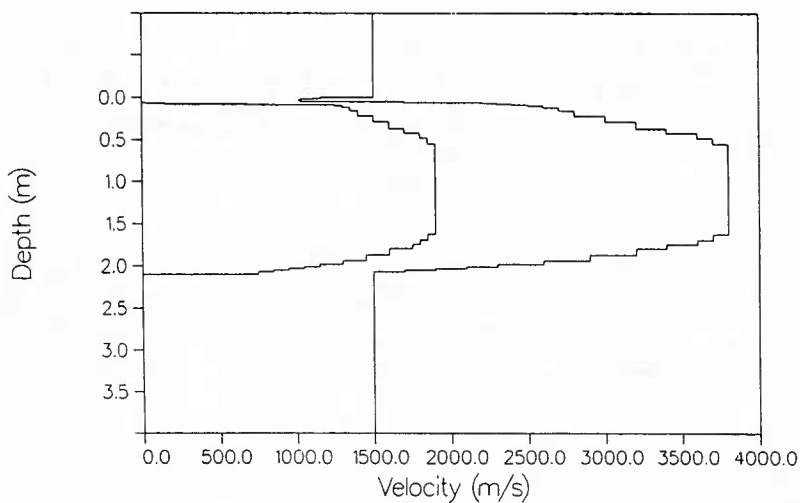


Fig. 5. Compressional and shear velocity profiles for a 2 meter layered ice block with water-to-ice transitional layers.

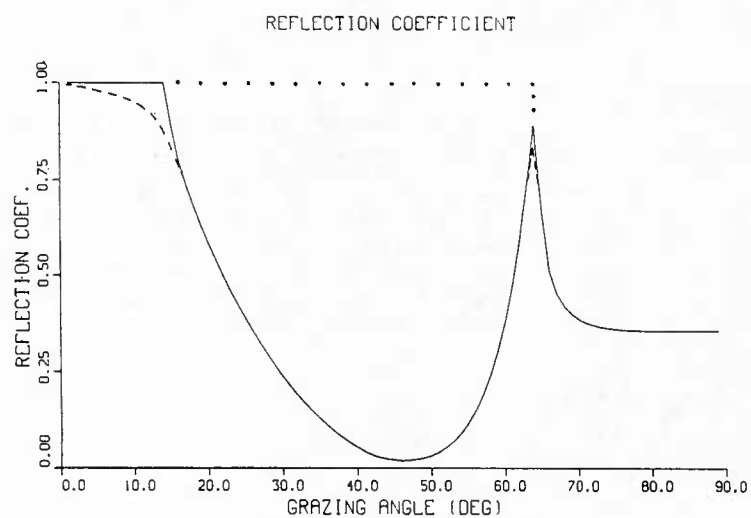


Fig. 6. Reflection coefficients for water over a homogeneous half-space. The solid curve results from using Mayer's model, the dotted curve from using a truncated Mayer model, and the broken curve from using a model which includes compressional and shear velocities and attenuations.

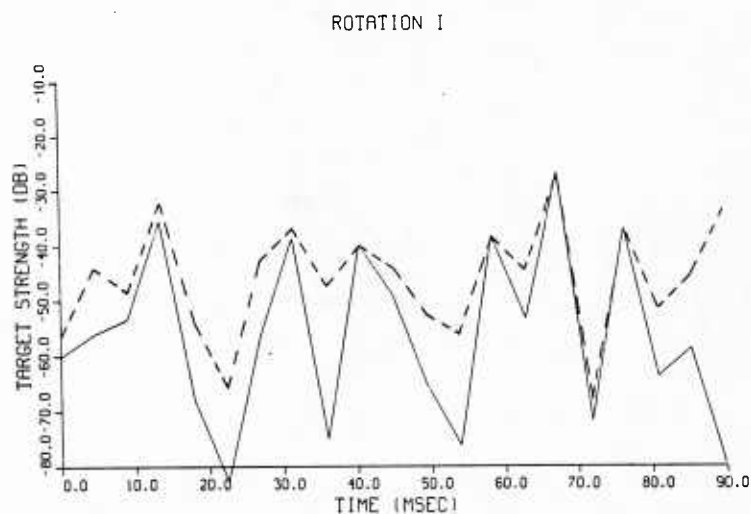


Fig. 7. Target strengths at 20 kHz. using Rotation I. Plane wave reflection coefficients have been calculated by the truncated Mayer model (broken curve) and by the model which includes compressional and shear velocities and attenuations (solid curve).

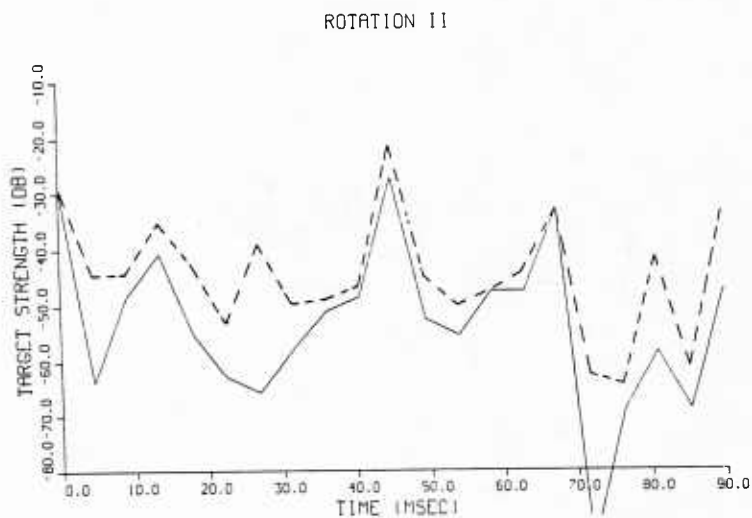


Fig. 8. Target strengths at 20 kHz. using Rotation II. Plane wave reflection coefficients have been calculated by the truncated Mayer model (broken curve) and by the model which includes compressional and shear velocities and attenuations (solid curve).

REFLECTION COEFFICIENT

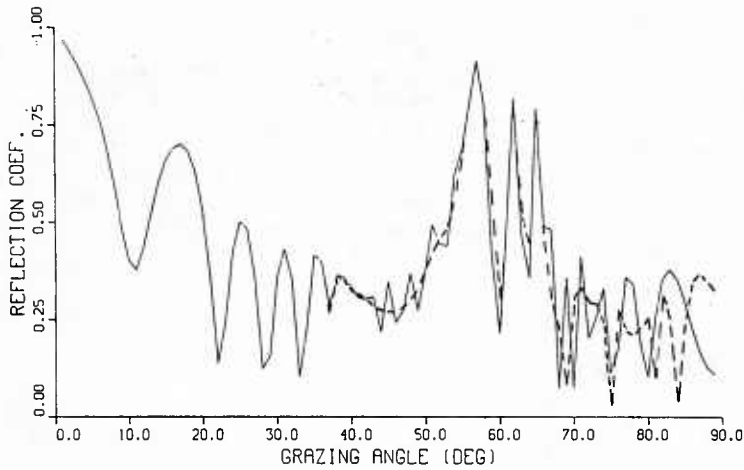


Fig. 9. Reflection coefficients for water backed layered ice at 20 kHz. Total layer thicknesses are 2 meters (broken curve) and 0.98 meters (solid curve). The reflection coefficients are calculated using a model which includes compressional and shear velocities and attenuations.

ROTATION I

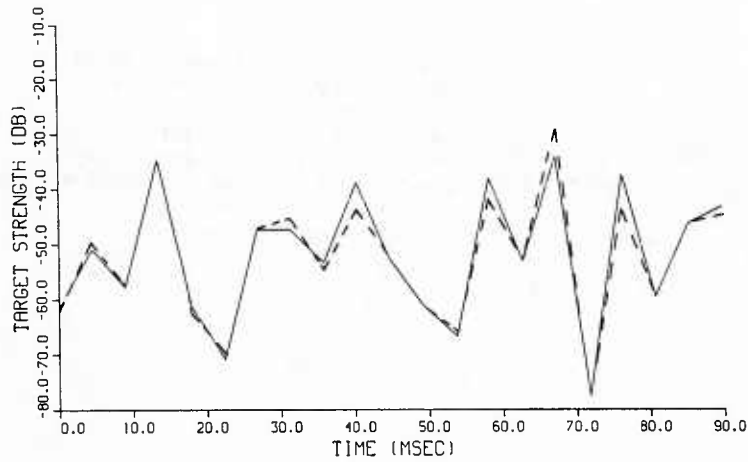


Fig. 10. Target strengths at 20 kHz. using Rotation I. The broken curve is for a keel composed of 2 meter blocks and the solid curve is for a keel composed of 0.98 meter blocks.

ROTATION II

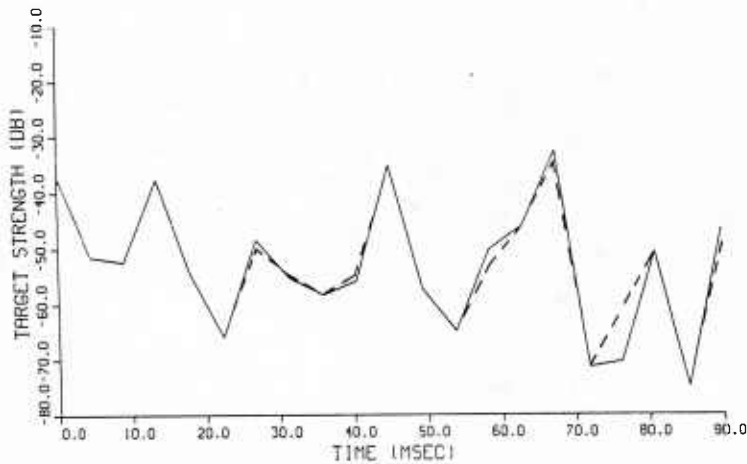


Fig. 11. Target strengths at 20 kHz. using Rotation II. The broken curve is for a keel composed of 2 meter blocks and the solid curve is for a keel composed of 0.98 meter blocks.

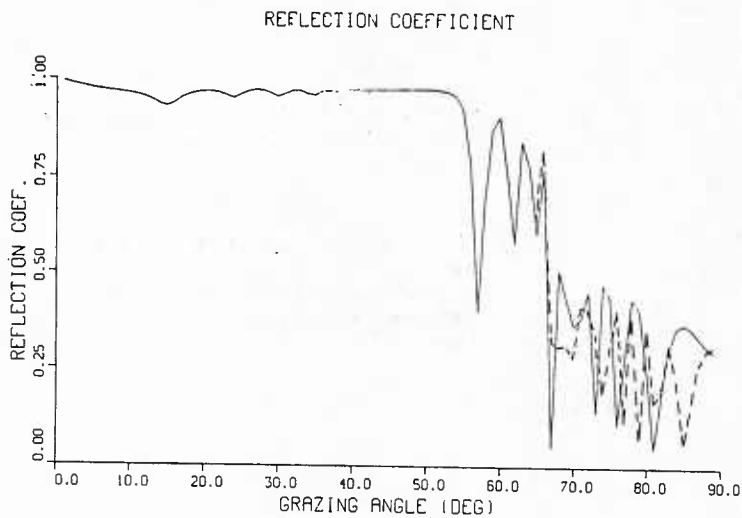


Fig. 12. Reflection coefficients at 20 kHz. for water backed layered ice with the water-to-ice transitional layers on the front surface. Total hard ice layer thicknesses are 2 meters (broken curve) and 0.98 meters (solid curve). The reflection coefficients are calculated using a model which includes compressional and shear velocities and attenuations.

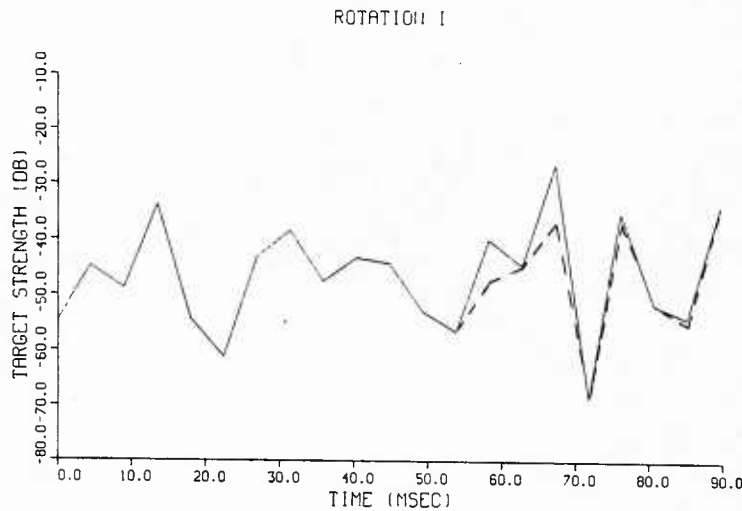


Fig. 13. Target strengths at 20 kHz. using Rotation I. The broken curve is for a keel composed of 2 meter blocks and the solid curve is for a keel composed of 0.98 meter blocks. Each block has the water-to-ice transitional layers on the front surface.

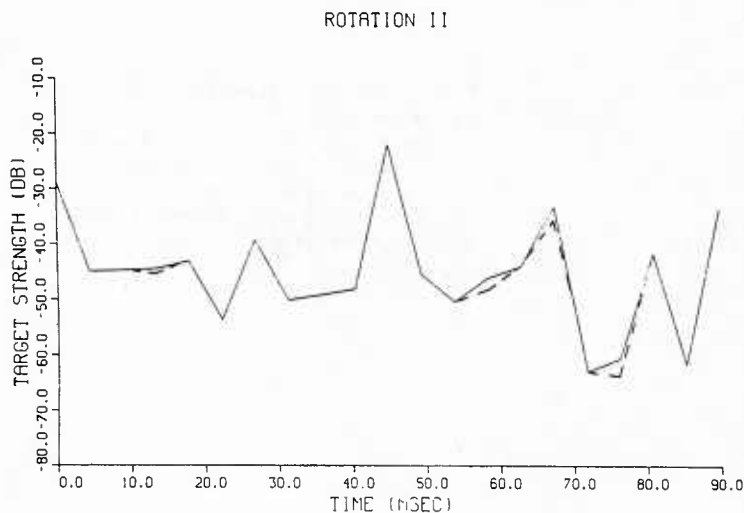


Fig. 14. Target strengths at 20 kHz. using Rotation II. The broken curve is for a keel composed of 2 meter blocks and the solid curve is for a keel composed of 0.98 meter blocks. Each block has the water-to-ice transitional layers on the front surface.

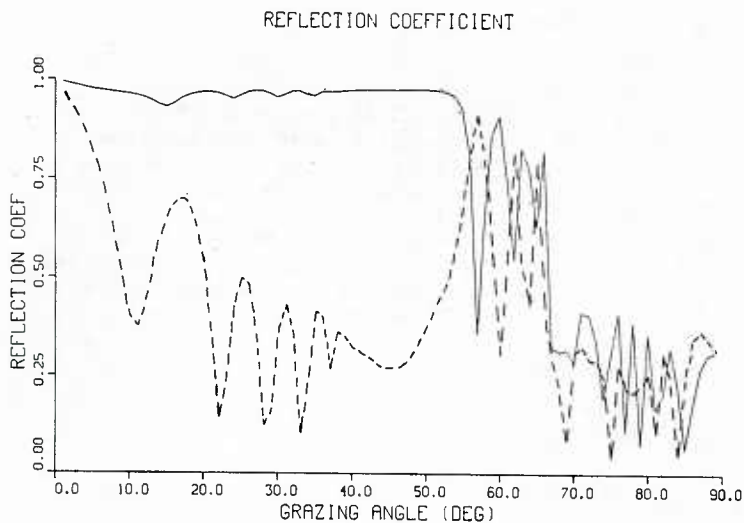


Fig. 15. Reflection coefficients at 20 kHz. for 2 meter water backed layered ice. The solid curve is for the case of the water-to-ice transitional layers on the front surface while the broken curve is for the case of ice without the transitional layers. The reflection coefficients are calculated using a model which includes compressional and shear velocities and attenuations.

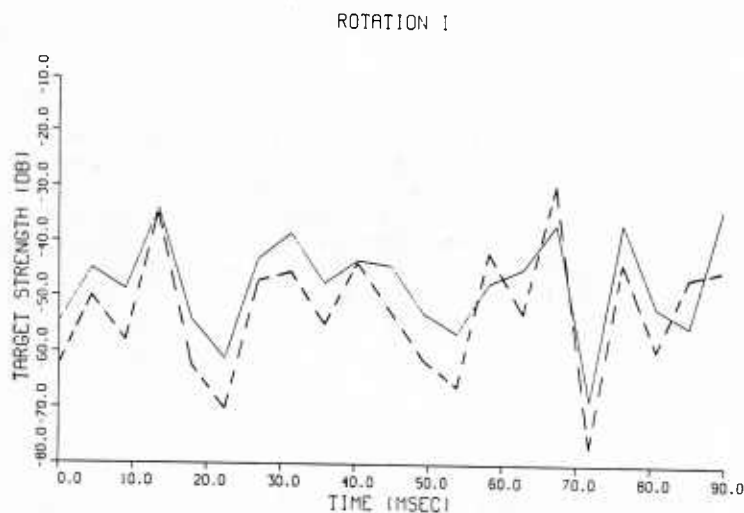


Fig. 16. Target strengths at 20 kHz. using Rotation I. The solid curve is for a keel composed of 2 meter blocks with the water-to-ice transitional layers and the broken curve is for a keel composed of 2 meter blocks without transitional layers.

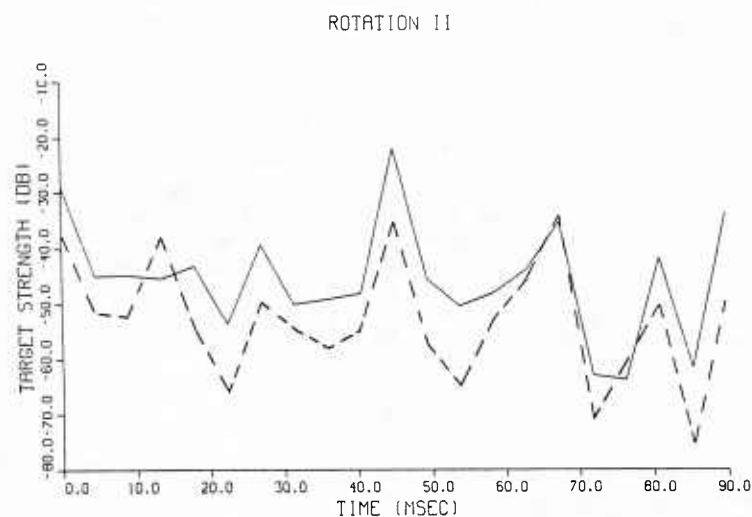


Fig. 17. Target strengths at 20 kHz. using Rotation II. The solid curve is for a keel composed of 2 meter blocks with the water-to-ice transitional layers and the broken curve is for a keel composed of 2 meter blocks without transitional layers.

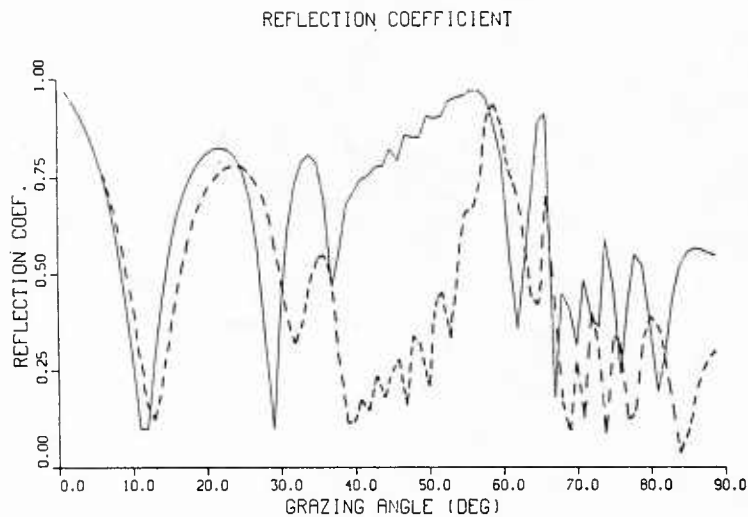


Fig. 18. Reflection coefficients for 2 meter water backed layered ice at 8 kHz. The solid curve is for the case of water-to-ice transitional layers on the front surface while the broken curve is for the case of ice without the transitional layers. The reflection coefficients are calculated using a model which includes compressional and shear velocities and attenuations.

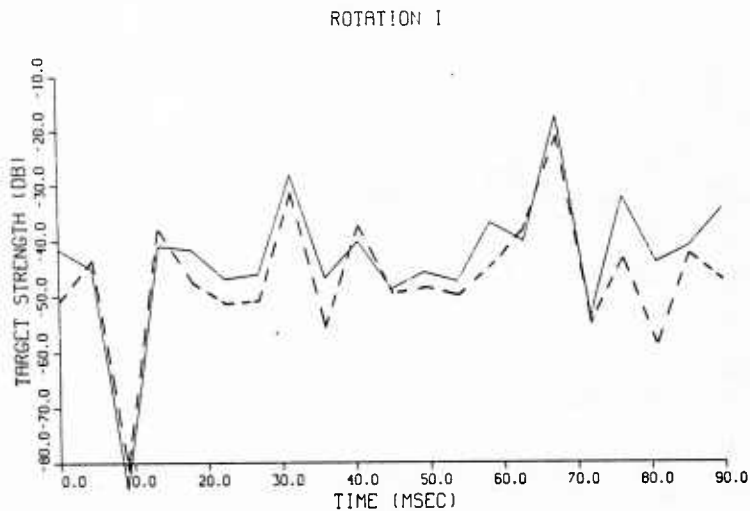


Fig. 19. Target strengths at 8 kHz. using Rotation I. The solid curve is for a keel composed of 2 meter blocks with the water-to-ice transitional layers and the broken curve is for a keel composed of 2 meter blocks without transitional layers.

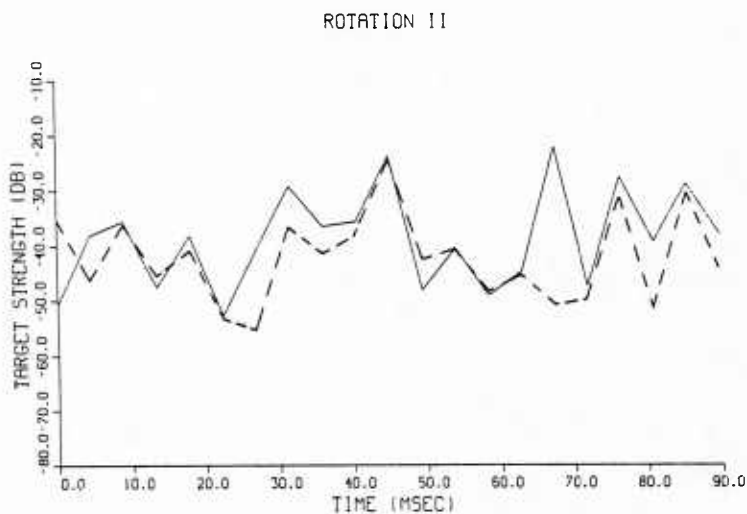


Fig. 20. Target strengths at 8 kHz. using Rotation II. The solid curve is for a keel composed of 2 meter blocks with the water-to-ice transitional layers and the broken curve is for a keel composed of 2 meter blocks without transitional layers.

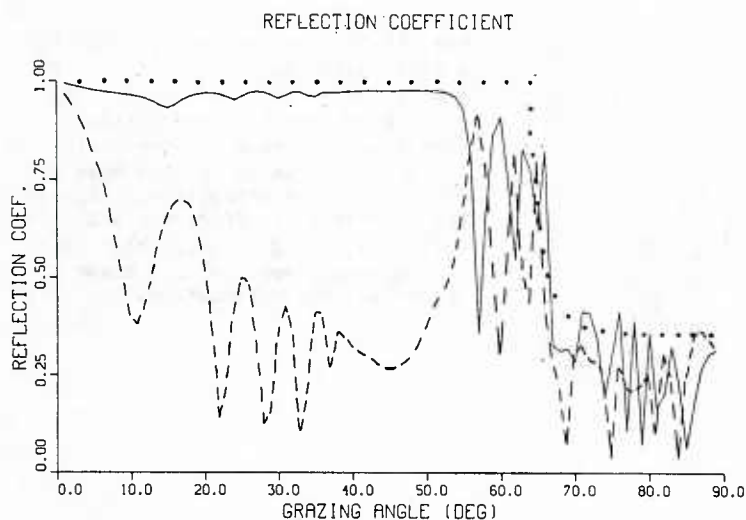


Fig. 21. Reflection coefficients at 20 kHz: for the cases of 2 meter blocks without the water-to-ice transitional layers (broken curve), 2 meter blocks with the water-to-ice transitional layers (solid curve), and truncated Mayer model for a homogeneous half-space (dotted curve).

TABLE I

LAYER TYPE	LAYER THICKNESS (M)	DENSITY (GM/CC)	COMPRES. SPEED (M/SEC)	SHEAR SPEED (M/SEC)	COMPRES. ATTENUATION (DB/M-KHZ)	SHEAR ATTENUATION (DB/M-KHZ)
WATER	INFINITE	1.02	1500.0	0.0	0.00	0.00
ICE	0.015	0.75	1300.0	650.0	0.06	0.22
ICE	0.015	0.88	1500.0	750.0	0.06	0.28
ICE	0.020	0.90	1700.0	850.0	0.06	0.29
ICE	0.020	0.90	1900.0	950.0	0.06	0.30
ICE	0.025	0.90	2100.0	1050.0	0.06	0.31
ICE	0.030	0.90	2300.0	1150.0	0.06	0.32
ICE	0.040	0.90	2600.0	1300.0	0.06	0.33
ICE	0.065	0.90	2900.0	1450.0	0.06	0.34
ICE	0.080	0.90	3200.0	1600.0	0.06	0.35
ICE	0.050	0.90	3400.0	1750.0	0.06	0.36
ICE	0.050	0.90	3600.0	1800.0	0.06	0.36
ICE	0.070	0.90	3700.0	1850.0	0.06	0.36
ICE	1.070	0.90	3800.0	1900.0	0.06	0.36
ICE	0.070	0.90	3700.0	1850.0	0.06	0.36
ICE	0.060	0.90	3600.0	1800.0	0.06	0.36
ICE	0.050	0.90	3400.0	1700.0	0.06	0.36
ICE	0.085	0.90	3200.0	1600.0	0.06	0.36
ICE	0.070	0.90	3000.0	1500.0	0.06	0.36
ICE	0.055	0.90	2800.0	1400.0	0.06	0.36
ICE	0.040	0.90	2700.0	1350.0	0.06	0.36
ICE	0.020	0.90	2600.0	1300.0	0.06	0.36
SLUSH	0.015	0.91	2500.0	1250.0	0.06	0.10
SLUSH	0.010	0.92	2400.0	700.0	0.06	0.04
SLUSH	0.010	0.93	2300.0	150.0	0.06	0.01
SLUSH	0.005	0.93	2200.0	20.0	0.06	0.00
SLUSH	0.005	0.94	2000.0	0.0	0.06	0.00
SLUSH	0.002	0.94	1700.0	0.0	0.06	0.00
SLUSH	0.002	0.95	1400.0	0.0	0.06	0.00
SLUSH	0.001	0.96	1150.0	0.0	0.06	0.00
SLUSH	0.003	0.98	1060.0	0.0	0.06	0.00
SLUSH	0.004	0.99	1030.0	0.0	0.06	0.00
SLUSH	0.005	1.00	1020.0	0.0	0.06	0.00
SLUSH	0.008	1.00	1015.0	0.0	0.06	0.00
SLUSH	0.006	1.01	1030.0	0.0	0.06	0.00
SLUSH	0.005	1.01	1040.0	0.0	0.06	0.00
SLUSH	0.005	1.01	1060.0	0.0	0.06	0.00
SLUSH	0.005	1.01	1100.0	0.0	0.06	0.00
SLUSH	0.005	1.01	1160.0	0.0	0.06	0.00
SLUSH	0.005	1.01	1200.0	0.0	0.06	0.00
WATER	INFINITE	1.02	1500.0	0.0	0.00	0.00

TABLE II

FREQUENCY: 20 KHZ
 KEEL DEPTH: 9.3 M
 KEEL SLANT HEIGHT: 15.2 M
 KEEL ANGLE OF REPOSE, θ_R : 38 DEG.
 PULSE LENGTH: 2 MILLISEC.
 INCIDENT DECLINATION/ELEVATION ANGLE, ϕ_i : 5 DEG.
 TOTAL KEEL LENGTH: 100 M
 KEEL SAIL HEIGHT: 1.0 M
 KEEL (BLOCK) THICKNESS: 1.0 - 2.0 M
 INCIDENT ASPECT ANGLE, θ_i : 45 DEG.
 TOTAL NUMBER OF BLOCKS: 21 X 3 = 63

SIMULATION MODELS FOR HIGH FREQUENCY UNDER-ICE ACOUSTIC BACKSCATTERING

Garner C. Bishop, Leonard E. Mellberg, Carl J. Albanese, Suzanne E. Overdeep (Naval Underwater Systems Center, Newport, RI 02841), William T. Ellison (Marine Acoustics, Cotuit MA 02635)

Models have been developed to synthesize a three dimensional under-ice canopy characteristic of pack ice regions of the interior Arctic and to evaluate the backscatter of a high frequency acoustic pulse from the under-ice canopy model. The canopy synthesis model (CHOOSKL) utilizes measured two dimensional under-ice profile data and several empirical results to identify and classify ice features and to construct a three dimensional bimodal under-ice canopy consisting of first year ice keels and sloping flat ice regions. The backscattering model synthesizes the small scale roughness of first year keels that is produced by the constituent ice blocks of the keel. Reverberation is calculated and compared with measured reverberation data and excellent agreement is obtained.

1. INTRODUCTION

The under-ice environment is a unique environment in which to propagate acoustic waves. The ice canopy causes sound speed to vary with depth in a manner that causes acoustic waves to refract upward toward the under-ice surface. The under-ice surface exhibits large scale roughness produced by more or less distinct relief features e.g. ice keels and small scale roughness produced by the constituents of the relief features e.g. ice blocks. At the smallest length scales, the surface of ice blocks exhibits roughness as well. The under-ice surface acts as an acoustic scatterer whose scattering properties are poorly known. In this work a model is described that has been developed to evaluate the backscatter of a high frequency acoustic pulse from the under-ice canopy. The model consists of two major components; 1) a model that synthesizes a three dimensional under-ice canopy from two dimensional acoustic profile data (CHOOSKL) and 2) a backscattering model that evaluates the reverberation produced by the scatter of a high

frequency acoustic pulse from the three dimensional canopy synthesized by CHOOSKL. The backscattering simulation model is a significantly enhanced and improved version of a similar model developed by W.T. Ellison [1980].

2. CANOPY SYNTHESIS MODEL (CHOOSKL)

The canopy synthesis model is an ensemble of models. The models are used systematically to examine measured two dimensional under-ice acoustic profile data and to identify and classify discrete relief features, to determine various morphological and geometrical parameters and to synthesize a three dimensional canopy from two dimensional acoustic profile data.

A. Feature identification

It is assumed that the under-ice canopy is composed of two distinct types of ice regions, deformed and undeformed ice, and that these regions are composed of and may be modeled by discrete relief features. In this work, regions of deformed and undeformed ice are modeled as first year keels and sloping flat regions respectively. However, there exists no universally recognized criteria or definitions that may be used to identify and classify relief features based on the acoustic profile they project onto a vertical plane oriented randomly with respect to the vertical plane of the feature. Therefore it is necessary to define and/or adopt more or less arbitrary criteria that may be used to identify and classify relief features and to determine their important geometric parameters from their projected acoustic profiles. Three criteria are necessary and sufficient to identify a discrete relief feature: 1) It is necessary to distinguish a feature from surface irregularities and/or undulations that exist frequently on the under-ice surface. 2) It is necessary to resolve or distinguish between adjacent features (Rayleigh criterion). 3) The lateral extent of a feature must be determined. The quantitative expressions of these criteria are given by

$$H_{KR} \geq H_{KRM/N} \quad (2.1a)$$

$$H_R(r) \leq H_{RR} \quad (2.1b)$$

and

$$\frac{dH_R(r)}{dr} = 0 \quad (2.1c)$$

with

$$H_{KR} = H_K - H_0 \quad (2.2a)$$

$$H_{RR} = (1 - C_e) H_{KR} \quad (2.2b)$$

and

$$H_R(r) = H(r) - H_0. \quad (2.2c)$$

The conditions given in Eqs. (2.1a) - (2.1c) are referred to as the condition of minimum relief, the condition of resolution and the end condition respectively. The parameters used in Eqs. (2.1a)-(2.2c) are shown in figure 1.

H_K is the draft of the feature measured from the sea-water surface and is different for each relief feature. H_0 is the average thickness of the parent ice floe and is constant for a given geographic location. In this work the value $H_0 = 2.5$ m was used. H_{KR} is called the feature relief and provides a measure of the amount by which the feature extends downward from the surface of the ice sheet. H_{KRMIN} is an arbitrary parameter that specifies the minimum feature relief and in this work the value $H_{KRMIN} = 2$ m was used. A feature is distinguished from surface irregularities when its relief is greater than the arbitrary minimum value H_{KRMIN} .

C_e is an arbitrary parameter used to determine the Rayleigh Relief and is such that $0 < C_e < 1$. In this work the value $C_e = .5$ was used. H_{RR} is the Rayleigh relief and is the maximum relief at

which the feature is resolved i.e. a feature is resolved when its relief at any range r , $H_R(r)$, decreases to the Rayleigh relief. Once a feature has been identified and resolved, the lateral extent of its acoustic profile remains to be determined. In this work the lateral extent of a keel is reached when the relief $H_R(r)$ is such that $H_R(r) < H_{RR}$ and the condition given in Eq. (2.1c) is met.

2.2 Slope angle model and feature classification

The transverse geometry of ice keels has been studied by many researchers and it has been shown that it may vary from triangular to semicircular or semielliptical or to even more complex shapes. Indeed the leading edge of a keel may be highly irregular and composed of many linear and curvilinear segments. In order to effect a compromise between computational simplicity and physical accuracy the acoustic profile data is used to partition the leading edge of a relief feature into two straight line segments. The point at which the leading edge is partitioned is fixed for all features and is determined by examining the average feature profile and determining, in a subjective manner, the best two line fit to the leading edge of the mean feature profile. The point at which the feature is partitioned is expressed as a fraction of the left crossing width. In this work, the value of the partition fraction, X_F was determined to be $X_F = .3$.

It is evident that in order to describe accurately the leading edge of a relief feature, it is necessary to specify the slope angles that describe the slopes of the straight line

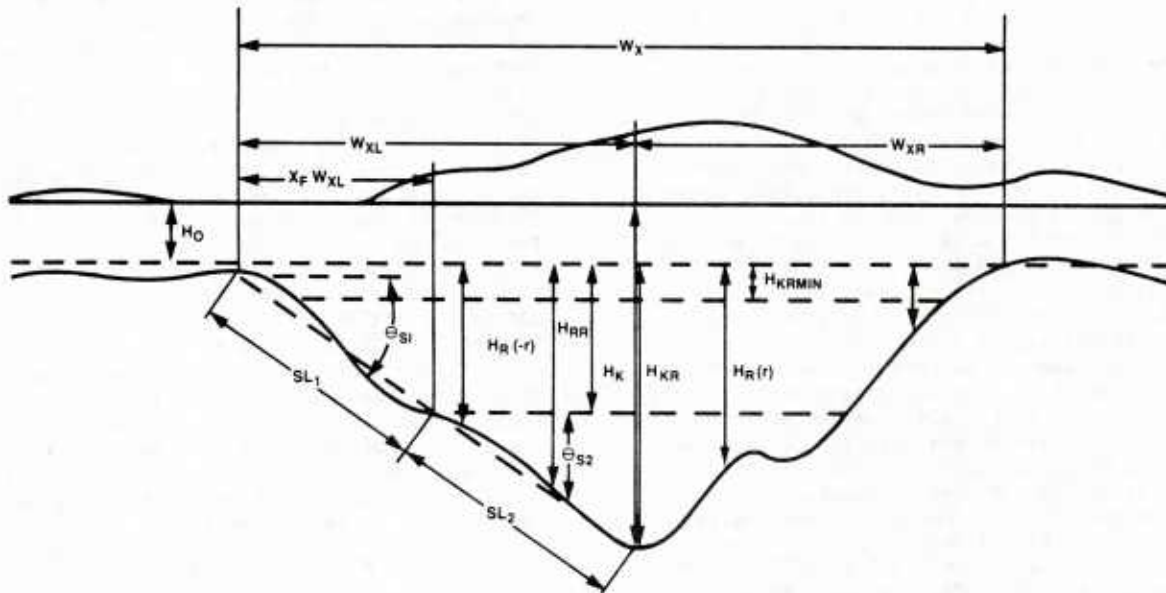


Fig. 1. Keel geometry and parameters.

segments used to model the upper and lower portions of the leading edge of the feature. These slope angles are called the upper and lower slope angles respectively. It should be noted that this slope angle model differs from previous slope angle models that characterize the leading edge of a relief feature by a single slope angle.

Once a relief feature has been identified and its acoustic profile modeled, the following geometric parameters may be determined: location on the track; draft (H_L); left and right crossing width; (W_{XL} , W_{XR}) upper and lower slope angles (θ_{s1} , θ_{s2}). A sloping flat ice region is modeled as a relief feature whose average slope angle is less than some critical angle. In this work a value of 1.4° was used for the critical slope angle θ_{SC} . This angle corresponds to a relief feature whose draft to width ratio is $1/40$. θ_{SC} is used to partition the ensemble of discrete relief feature into a set containing first year keels and a set containing flat ice features.

C. Synthesis of a three dimensional canopy: Ridge length and aspect angle models

A two dimensional acoustic profile of the under-ice surface does not provide information about the spatial orientation of relief features out of the plane of the profile. However, a three dimensional canopy may be synthesized. Parameters necessary to describe and/or model the three dimensional canopy may be defined. Data from other work may be used to obtain mean values and distribution functions for these parameters from regions that are similar to those from which specific profile data is available and used to supplement the two dimensional acoustic profile data. In this work two parameters are necessary and sufficient to synthesize a three dimensional canopy from the two dimensional acoustic profile data and they are ridge length and aspect angle. Ridge lengths have been measured by Hibler and Ackley [1975] and this data forms the basis of the model that synthesizes ridge lengths. The ridge length model selects ridge lengths in a random manner from an exponential distribution of ridge lengths. The exponential distribution of ridge lengths has a mean value of 580.9 m and the maximum allowed ridge length is 3750 m. The mean ridge length was determined by varying the mean ridge length until the frequency distribution of ridge lengths produced by the model agreed with that of the Hibler-Ackley data.

Aspect angle (θ_A) is defined conventionally as the angle measured from the normal to the longitudinal center line of the ridge to an arbitrary datum line. This definition is used in this work and the track line is chosen as the arbitrary datum line. Aspect angles vary in the range $-90^\circ < \theta_A < 90^\circ$. θ_A is positive when measured clockwise when the ridge is viewed from above and negative otherwise. It should be noted that since the orientation of a ridge is

characterized by a single aspect angle, the ridge is assumed implicitly to be linear. This approximation is made in order to simplify calculations. Field observations have shown that ridges are only approximately linear and in some cases may be highly non-linear. There is a paucity of data for the frequency distribution of aspect angles of pressure ridges along a linear track. However Mock, Hartwell and Hibler [1972] obtained several sets of aspect angle data and analyzed spatial aspects of pressure ridges. They showed that the observed aspect angle frequency distributions did not correspond to those of a randomly oriented population of ridges. However, they concluded that the observed aspect angle frequency distributions were very complex and that despite their results suggested that the best aspect angle model is one in which the ridges are oriented randomly in aspect and is the model adopted in this work.

3. PROPAGATION LOSS AND GRAZING ANGLE MODELS

Since sea water attenuates and refracts acoustic waves, it is essential to model these acoustic properties of sea water and to obtain a quantitative description of these phenomena to serve as input to the backscattering model. It is assumed that quantitative descriptions of the dissipative and refractive properties of sea water are given sufficiently by the propagation loss and source-grazing angle tables respectively which are included as input to the backscattering model.

Sound velocity data was obtained by a submarine expendable sound velocity profiler (SSXVP). The CONGRATS [WEINBERG, 1981] ocean sound speed model is used to fit a curve to the measured sound velocity data, plot the sound velocity profile and a ray diagram. Then the sound velocity profile is used by the FACT eigenray model [Weinberg, 1981] to calculate acoustic eigenrays at various target ranges for a fixed source depth. An eigenray table is obtained that lists the following for each eigenray: target range; travel time; source angle; target angle; level (dB); phase and the number of surface and bottom reflections. The acoustic eigenrays at each range are summed incoherently and a sound pressure level table is constructed. The propagation loss table is constructed from the sound pressure level table by regarding negative pressure levels as positive losses. A source-grazing angle table is constructed from the eigenray table in the following manner. At each range for which the eigenrays are calculated the eigenrays of maximum amplitude is identified. The source and grazing angles at each range are those of the eigenray of maximum amplitude.

4. UNDER-ICE ACOUSTIC BACKSCATTERING MODEL

The high frequency under-ice acoustic backscattering model consists of the following

three major components: 1) modeling the microscopic structure or small scale roughness of ice keels and canopy features; 2) calculating the target strength for ice blocks, ice keels and then the entire under-ice canopy and 3) computing reverberation using the sonar equations.

A. Modeling the microscopic structure of an ice keel

The macroscopic structure of an ice keel and indeed the entire canopy is modeled by CHOOSKL. However at high frequencies the microscopic structure or small scale roughness produced by the constituent ice blocks of a keel is important and must be considered. It is assumed that all keels are first year keels and are formed from rectangular blocks of ice. Modeling the small scale roughness of a keel is accomplished in two steps: First an array of ice blocks is constructed using a combination of measured data and empirical and theoretical relationships. Then the blocks are placed on the lateral plane of the keel defined by the keel parameters determined by CHOOSKL.

An ice block is described by its geometric parameters i.e. thickness, length and width as well as its spatial orientation on the lateral plane of the keel. The following describes the manner in which these aspects of an ice block are modeled. The mean ice thickness and area for all ice blocks on a keel are given by

$$T = .0029 H_K^2 \quad (4.1)$$

and

$$\langle A \rangle = 10.2 T^2 \quad (4.2)$$

respectively where H_K is the keel draft [Mellberg, Tucker and Connors 1985; Tucker et. al., 1984]. It should be noted that data from field observations has shown that keels may contain ice blocks of several thicknesses. However, in this work all the ice blocks of a keel have the same thickness given in Eq. (4.1). This model is adopted as an approximation to simplify calculations. The distribution of block areas is assumed to be a truncated Gaussian with the average block area given by Eq. (4.2) and $A_{\min} = .064 \text{ m}^2$, $A_{\max} = 37.73 \text{ m}^2$ and $\sigma_A = 1.33 \langle A \rangle$, where A_{\min} , A_{\max} and σ_A refer to the minimum, maximum and standard deviation respectively of the block area Gaussian distribution. Similarly the distribution of the width to length ratio, ϵ , is assumed to be a truncated Gaussian with $\langle \epsilon \rangle = .646$, $\epsilon_{\min} = .146$, $\epsilon_{\max} = .981$ and $\sigma_\epsilon = .077$ where ϵ_{\min} , ϵ_{\max} and σ_ϵ are the minimum, maximum and standard deviation respectively of the ϵ Gaussian distribution. The block area A and the ratio ϵ are chosen randomly from their respective distribution functions. After A and ϵ are determined, the length and width of the rectangular scattering surface may be determined and are given by

$$L = \sqrt{A/\epsilon} \quad (4.3)$$

and

$$W = A/L \quad (4.4)$$

respectively.

Since the target strength of an ice block depends on its spatial orientation with respect to the incident sound wave, it is important to consider carefully the spatial orientation of the block. Therefore three coordinate systems

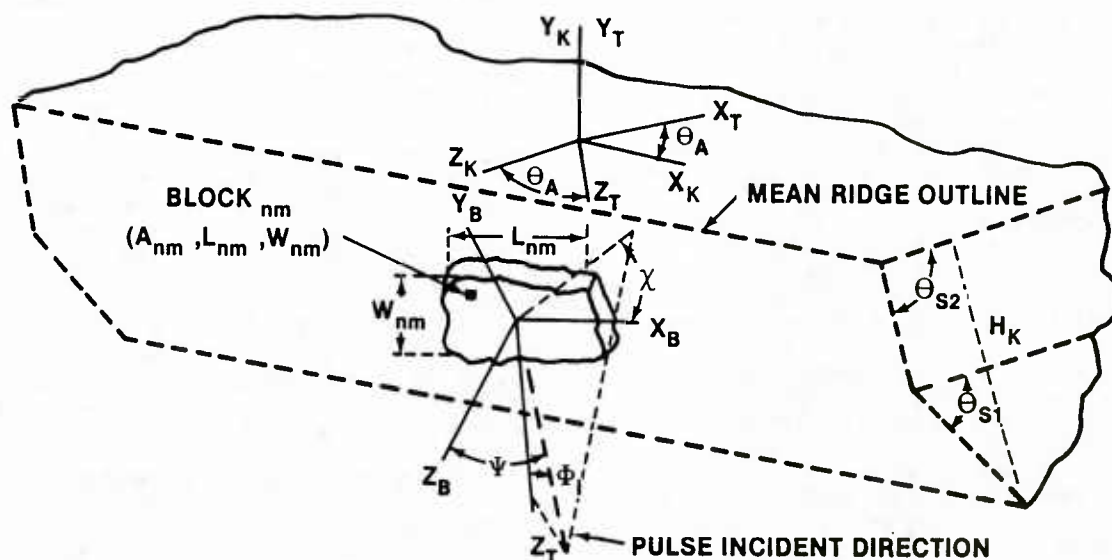


Fig. 2. Keel, track and ice block coordinate systems.

are considered; 1) a coordinate system fixed on the track of the under-ice profile (X_T, Y_T, Z_T), 2) a coordinate system fixed on the keel (X_K, Y_K, Z_K) and 3) a coordinate system fixed on the constituent ice blocks of the keel (X_B, Y_B, Z_B). These coordinate systems are shown in figures 2 and 3. The coordinate system fixed on the track has its origin at the track origin, its positive Z_T -axis oriented along the track in the direction of the track origin so that Z_T is the range to the keel. The Y_T -axis is oriented vertically and the X_T -axis is perpendicular to the Y_T - Z_T plane and forms a right hand coordinate system. The coordinate system fixed in the keel has its origin at the location of the keel on the track and Y_K parallel to Y_T . However the X_K and Z_K axes are rotated about the Y_K axis by the keel aspect angle. The X_K -axis is oriented along the longitudinal axis of the keel and the Z_K -axis is normal to the vertical plane of the keel. The origin of the block coordinate system is at the center of the block and initially the X_B, Y_B and Z_B axes are parallel to the X_K, Y_K and Z_K axes respectively.

The Z_B -axis is normal to the block face, the Y_B -axis is parallel to the block width and X_B -axis is parallel to the block length. The orientation of a block is determined by a sequence of three counter-clockwise rotations. The block is rotated about the X_K axis by an angle β , about the Y_K -axis by an angle ϕ_h and then about the resultant Z_B -axis by an angle ϕ_r . This sequence of rotations describes the orientation of the block and the unit vectors X_B, Y_B and Z_B are given by

(4.5a)

$$\begin{aligned}\hat{X}_B = & (\sin \phi_v \sin \beta \sin \phi_h + \cos \phi_v \cos \phi_h) \hat{X}_K \\ & + \sin \phi_v \cos \beta \hat{Y}_K \\ & + (\sin \phi_v \cos \phi_h \sin \beta - \cos \phi_v \sin \phi_h) \hat{Z}_K\end{aligned}$$

(4.5b)

$$\begin{aligned}\hat{Y}_B = & (\cos \phi_v \sin \beta \sin \phi_h - \sin \phi_v \cos \phi_h) \hat{X}_K \\ & + \cos \phi_v \cos \beta \hat{Y}_K \\ & + (\cos \phi_v \cos \phi_h \sin \beta + \sin \phi_v \sin \phi_h) \hat{Z}_K\end{aligned}$$

and

(4.5c)

$$\hat{Z}_B = \cos \beta \hat{X}_K - \sin \beta \hat{Y}_K + \cos \phi_h \cos \beta \hat{Z}_K.$$

In order to include the fact that the lateral plane of the keel is inclined by the slope angle, the angle β is given by $\beta = \pi/2 - \theta_s + \phi_v$ where ϕ_v is an angle measured from an axis normal to the lateral plane of the keel. The angles ϕ_h and ϕ_r are selected randomly from a uniform distribution of angles between $-\pi/4$ and $\pi/4$. $\pi - \beta$ is selected randomly from a truncated Gaussian distribution with $\langle \pi - \beta \rangle = 36.6^\circ$, $(\pi - \beta)_{\min} = 0$, $(\pi - \beta)_{\max} = 90^\circ$ and $\sigma_{\pi - \beta} = 22.2^\circ$. Finally the projections of each block along the horizontal and vertical directions of the keel are calculated. This is necessary to pack the blocks on the keel. The blocks are packed on the keel beginning at one end and along the uppermost horizontal row. The row is packed with blocks until the sum of the horizontal projections of the blocks equals the ridge length. Then blocks are packed along the first vertical column until the sum of the vertical projections of the blocks equals the sum of the upper and lower slant ranges. The numbers of blocks along the horizontal row and vertical

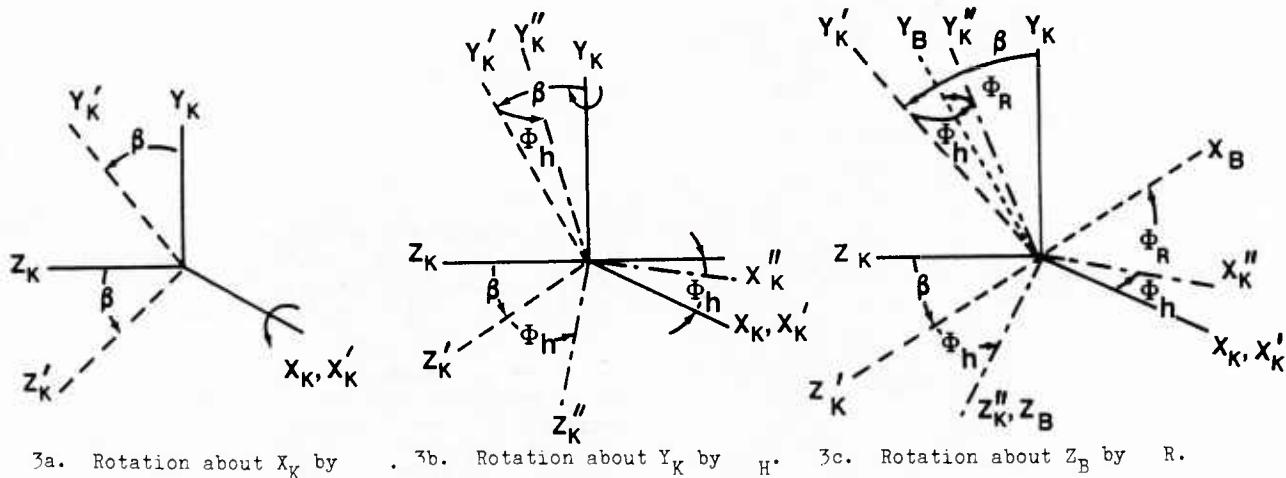


Fig. 3. Block rotation angles.

column are noted. The remaining rows and columns are packed with the same number of blocks as the first row and column. The position of each block on the keel is given by the horizontal and vertical coordinates that are obtained by summing all the horizontal and vertical block projections respectively that precede and are on the same row and column as the block of interest. All block parameters and coordinates are stored in N by M arrays, when N and M are the numbers of blocks along the horizontal and vertical rows respectively.

B. Ice block target strength model

In this work it is assumed that an acoustic source is located at some depth below the ice canopy, that all ice blocks are in the far field of the acoustic source, and that the far field may be approximated by a plane wave travelling down the track along the Z_T axis. The plane wave is refracted upward and makes an angle ϕ_i with the horizontal in the Z_T - Y_T plane.

The unit vector in the direction of propagation of the incident plane wave \hat{k} , is given by

$$\hat{k} = -\cos\phi_i \sin\theta_A \hat{x}_k + \sin\phi_i \hat{y}_k - \cos\phi_i \cos\theta_A \hat{z}_k. \quad (4.6)$$

When a plane wave is incident upon a rectangular scatterer, it is necessary to specify two angles to describe uniquely the incident direction. The two angles of incidence are ψ and χ and are the angles the plane wave makes with the Z_B -axis and the X_B -axis in the X_B - Y_B plane respectively. ψ and χ are given by

$$\psi = \cos^{-1} [\cos\phi_i \cos\beta \cos(\theta_A - \phi_h) + \sin\phi_i \sin\beta] \quad (4.7a)$$

and

$$\chi = \cos^{-1} \left\{ \frac{1}{\sin\psi} [\cos\phi_i \cos\phi_r \sin(\phi_h - \theta_A) - \cos\phi_i \sin\phi_r \sin\beta \cos(\theta_A - \phi_h) + \sin\phi_i \sin\phi_r \cos\beta] \right\}. \quad (4.7b)$$

It has been assumed that the shape of the scattering surface of an ice block is rectangular. Therefore the target strength of an ice block is modeled as that of a rectangular piston and for the n,m block on the ridge is given by

$$TS_{nm} = 20 \log \frac{A_{nm}}{\lambda} \frac{\sin\chi_{nm}}{\chi_{nm}} \frac{\sin\psi_{nm}}{\psi_{nm}} \cos\psi_{nm} R_{nm} \quad (4.8)$$

with

$$\chi_{nm} = k L_{nm} \sin\psi_{nm} \cos\chi_{nm} \quad (4.9a)$$

$$\psi_{nm} = k L_{nm} \sin\psi_{nm} \sin\chi_{nm} \quad (4.9b)$$

$$R_{nm} = [G_{nm} (P_I/P_W) \cos\psi_{nm} - (V_W/V_L) \cos\beta_{nm}] / \quad (4.10a)$$

$$G_{nm} (P_I/P_W) \cos\psi_{nm} + (V_W/V_L) \cos\beta_{nm}$$

$$G_{nm} = 1 - 2 \sin\chi_{nm} \sin(2\chi_{nm}) \cdot \quad (4.10b)$$

$$(\cos\chi_{nm} - (V_S/V_L) \cos\beta_{nm})$$

$$\chi_{nm} = \sin^{-1} [(V_S/V_W) \sin\psi_{nm}] \quad (4.10c)$$

and

$$\beta_{nm} = \sin^{-1} [(V_L/V_W) \sin\psi_{nm}] \quad (4.10d)$$

is the wave length of the incident acoustic plane wave. L_{nm} , W_{nm} and A_{nm} are the length, width and area respectively of the n,m block. V_S and V_L are the shear and longitudinal wave velocities in the ice and V_W is the sound velocity in water. ρ_i and ρ_W are the densities of ice and water respectively. The expression for target strength of a rectangular piston was obtained by evaluating the Helmholtz-Kirchoff integral in the Kirchoff approximation. The quantity R_{nm} is the plane wave amplitude reflection coefficient from a water-ice boundary [Mayer et al., 1975]. It should be noted that R_{nm} as given in Eq. (4.10a) does not include any effects produced by

scattering from small scale roughness that may be present on the surface of the ice block or effects produced by the finite thickness of the ice block. Further it is assumed that the ice block is homogeneous and isotropic. Eq. (4.10a) is recognized as a rather crude approximation for the reflection coefficient of an individual ice block, however when the backscatter from $\sim 10^3$ ice blocks is combined to determine the backscatter from the entire canopy, Eq. (4.10a) is assumed to be an adequate approximation.

B. Keel and canopy target strength models

The target strength of a keel is obtained from the target strengths of its constituent ice blocks. The pulse width is projected onto the lateral plane of the keel. The target strengths of all blocks in all columns contained within one half the projected pulse width are added coherently and the results are stored in target strength bins. The target strength bins are updated as necessary by contributions from subsequent keels as the pulse proceeds down the track.

The process described above yields the target strength of a canopy composed of acoustically independent keels. However all the keels in the canopy are not acoustically independent. The target strength of a keel may be reduced by acoustic shadowing produced by the preceding keel. It is assumed that all the target strength bins within the geometric shadow of the previous keel are reduced or shaded. The number of target strength bins that fall within the geometric shadow of the previous keel is given by

$$m_s = 2000 H_k / \theta_0 \sqrt{w} T / 2 \quad (4.11)$$

where τ is the pulse width. The target strength of the m^{th} shaded target strength bin is given by

$$TSS_m = 10 \log \left[\left(10^{TSS/10} \right) \frac{m}{m_s} \right] \quad (4.12)$$

where $1 \leq m \leq m_s$.

5. REVERBERATION CALCULATION

The sonar equation is used to calculate the reverberation at each target strength bin and is given by

$$RL = TS - 2TL - DI_R - DI_T - DBW + SL$$

DI_R and DI_T are losses due to the receiver and transmitter beam patterns respectively, DBW is the beam width correction factor and SL is the source level. The model was used to calculate the reverberation produced by three separate pings along a track beneath a high Arctic pack

ice site. The modeled reverberation is plotted and compared with measured reverberation in figures 4a-c. In each case the average modeled and measured reverberation are in excellent agreement. However it is evident that while there are some areas for which the modeled and measured reverberation levels are in excellent agreement there are areas where they differ significantly. It is conjectured that this is due to significant scatterers that are present in the under-ice surface but are not present in the plane of the acoustic profile data and therefore not presently in the simulation model either.

6. CONCLUSION

The above results indicate that the bimodal simulation and three dimensional synthesis of the under-ice canopy is not only a morphologically and geometrically reasonable model of the under-ice canopy but also an acoustically reasonable model. Although the canopy synthesis model has two arbitrary parameters C_e and H_{KRMIN} , careful analysis and comparison with data from field observation has shown that for a physically reasonable canopy model, C_e and H_{KRMIN} may be restricted to the ranges $.4 \leq C_e \leq .5$ and $2 \text{ m} \leq H_{KRMIN} \leq 3 \text{ m}$ respectively. When the backscattering model is used to compute the reverberation levels for C_e and H_{KRMIN} in these ranges, it is found that the reverberation levels are essentially independent of the values of C_e and H_{KRMIN} .

However, it should not be assumed that the scattering model is independent of the canopy model. In fact it has been observed that poor canopy models and/or parameter values that differ significantly from experimentally measured values are reflected in poor model reverberation. Present work in this area is directed towards identifying those morphological and geometrical parameters that most strongly influence the backscatter.

It is evident from figures 4a-c that although some of the approximations and models included in the backscattering model are rather crude, they are indeed sufficiently accurate to produce reasonable results. It is concluded that this is a direct consequence of the enormous number of the scatterers that contribute to the final result. As a consequence it is concluded that the model is a useful tool to investigate high frequency under-ice acoustic backscattering. The model may be used to study reverberation levels produced by various acoustic sources and canopies, as well as to study target strength frequency distributions and echo characteristics of ice blocks.

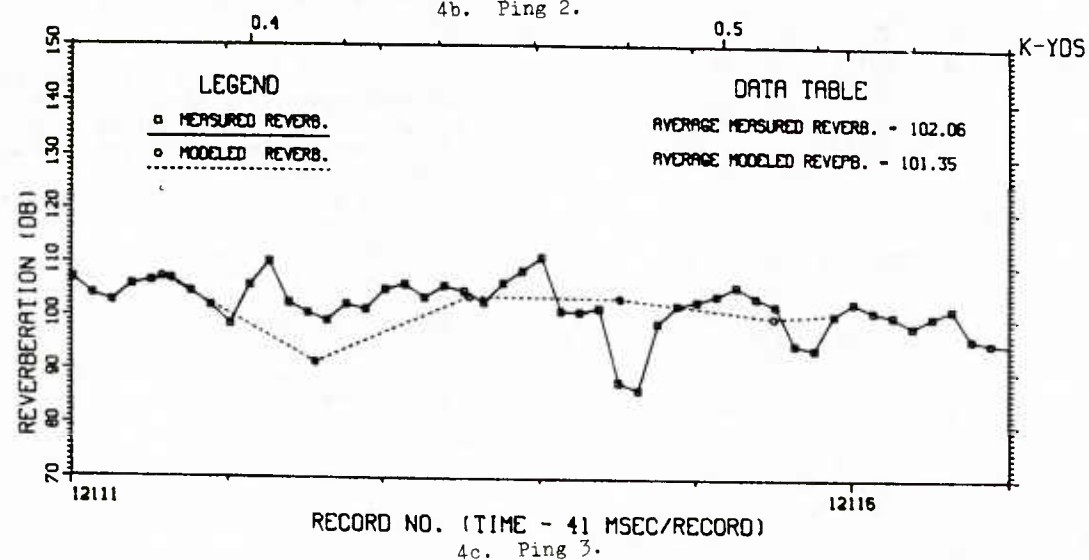
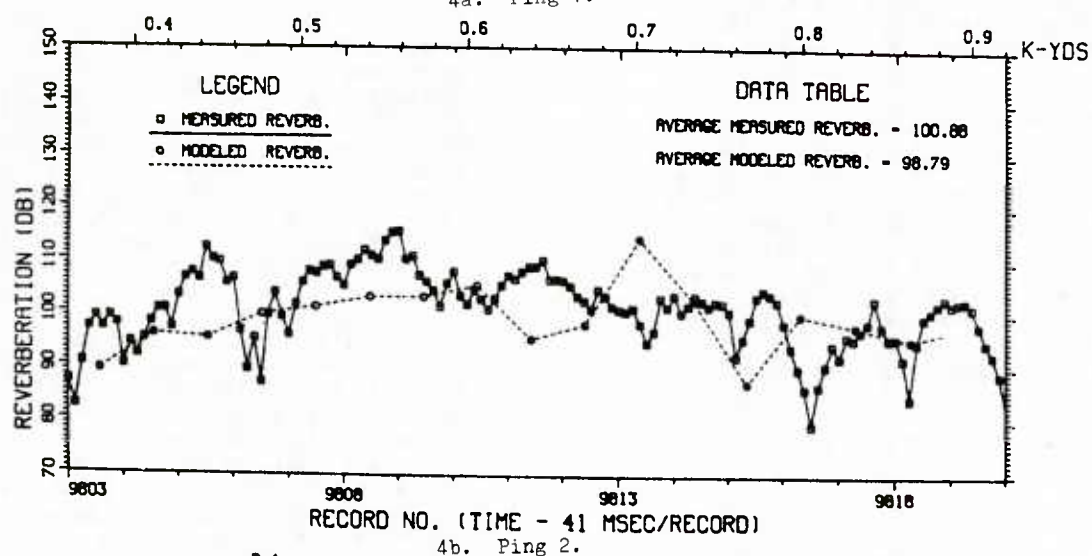
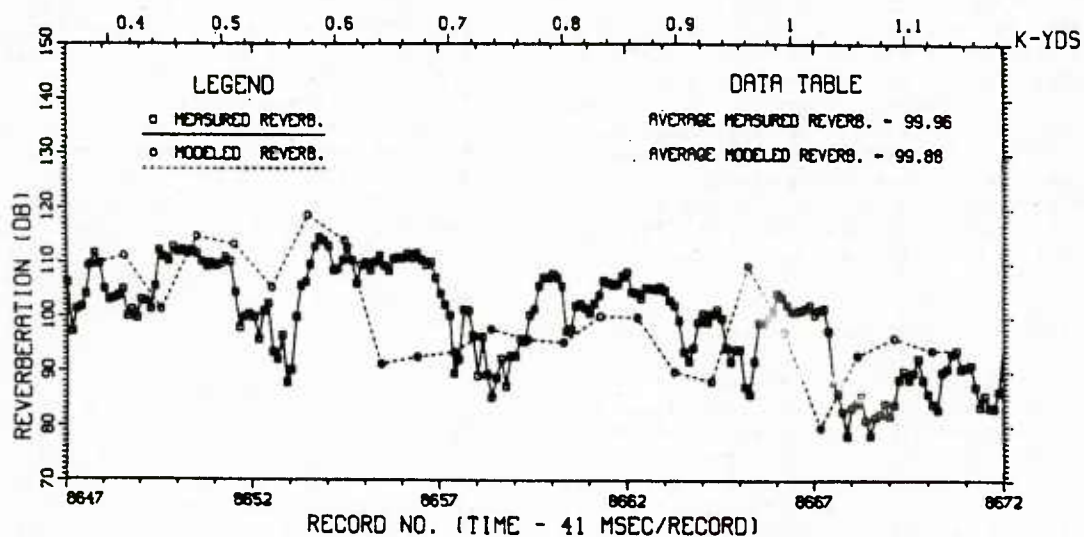


Fig. 4. Modeled and measured reverberation for three pings along a track beneath an under-ice surface of the high Arctic.

References

Ellison, W. T., Simulation studies of under-ice acoustic scattering, CC-714-270, Cambridge Acoustical Associates, Inc., Cambridge, MA 02140, 1980 (CONFIDENTIAL).

Hibler, W. D., III, and S. F. Ackley, A sea ice terrain model and its application to surface vehicle trafficability, CRREL-314, U.S. Army Cold Regions and Research and Engineering Laboratory, Hanover, NH 03755, 1973.

Mayer, W. G., M. Behraves and T. J. Plona, Determination of sonic velocities from reflectivity losses at sea ice/water boundaries, J. acoust. Am., 57, 39-46, 1974.

Mellberg, L., W. B. Tucker III and D. Connors, private communication (All parameters have been calculated from this data set unless otherwise noted.)

Mock, S. J., A. D. Hartwell and W. D. Hibler III, Spatial aspects of pressure ridge statistics, J. Geophys. Res., 77, 5945-5953, 1972.

Tucker, W. B., III, D. S. Sodhi and J. W. Govoni, Structure of first year pressure ridge rails in the Prudhoe Bay Region, in The Alaskan Beaufort Sea: Ecosystems and Environment, P114-135, 1984.

Weinberg, H., Generic sonar model, NUSC TD 5971C, Naval Underwater Systems Center, Newport, RI 02841.

HIGH FREQUENCY ACOUSTIC REFLECTION FROM FLAT SEA ICE

J. W. Posey, G. H. Branch, S. A. Chin-Bing
Naval Ocean Research and Development Activity
NSTL, MS 39529

and

G. Tango
ODSI Defense Systems, Inc., 6110 Executive Blvd.
Rockville, MD 20852

ABSTRACT

The plane-wave cw reflection coefficient for water-borne acoustic waves incident upon a stratified ice cover is calculated for all grazing angles and for frequencies from 5 to 30 kHz. The ice is modeled as an elastic solid composed of homogeneous, isotropic layers. The effects of features such as ice thickness, snow cover and an ice-water transition region are studied by using parameters appropriate to a typical 3 meter winter ice cap as a baseline condition and varying only one feature at a time from this baseline. Calculations show that near normal incidence, the reflection coefficient is completely dependent upon the compressional wave parameters of the ice since coupling with shear modes is inefficient at these angles. Away from normal, the reflection coefficient exhibits strong dependence upon frequency, grazing angle and structure of the ice-water interface. This sensitivity to model inputs is due to the dispersive nature of various propagation modes in the ice.

1. INTRODUCTION

An excellent review of previous studies of the reflection of water-borne sound from flat arctic ice is given by McCammon and McDaniel (ref. 1), who extended that work by including stratification within the ice, absorption of shear and compressional waves, and a snow cover. The present paper addresses similar issues, but for a higher frequency range (5 to 30 kHz) than does the McCammon and McDaniel paper (0.5 to 3 kHz). The acoustical significance of the transition region at the ice-water interface is considered here for the first time.

The reflection coefficient, R , defined as the ratio of the amplitude of the specularly reflected wave to the amplitude of the incident plane wave, is calculated in this paper in the same way used by McCammon and McDaniel. That is, the ice is modeled as being composed of a series of horizontal, homogeneous layers, each characterized by constant values for density, shear and compressional wave speeds, and shear and compressional wave attenuations. Each layer is assumed to contain up-going and down-going waves in response to excitation by an incident plane wave. Imposition of

the causality condition in the air and of continuity of vertical displacement and pressure at the layer interfaces results in a matrix equation for the wave amplitudes, or specifically for the amplitude of the water-borne reflection.

In section 2, we calculate R for a homogeneous half space of ice and for a single homogeneous layer of ice between air and water. Examination of the results for these simple physical models facilitates the interpretation of the results presented in section 3 for more realistic ice models.

2. FUNDAMENTAL CONCEPTS

In this section, we examine R as a function of grazing angle for two highly simplified physical models of the ice. The purpose of this discussion is to establish vocabulary and to remind the reader of some fundamental acoustical principles which are used in the next section to interpret calculation results for more realistic ice models.

The reflection coefficient from a homogeneous half space of ice is shown in figure 1. This configuration was studied in great detail by Mayer, Behraves and Plona (ref. 2). Throughout this paper, the speed of sound in water is assumed to be 1450 m/s. The shear wave speed in the half space of ice is 1900 m/s and the compressional wave speed is 3800 m/s. The attenuation constants are 0.36 dB/m/kHz for shear and 0.06 dB/m/kHz for compression.

The concept of trace velocity is useful in the physical interpretation of figure 1, as well as in the interpretation of the results to follow. Consider the horizontal trace velocity, v , of the incident wave; that is, the apparent phase velocity along the horizontal ice-water interface. For a grazing wave, v is simply the speed of sound in water. For normal incidence, v is infinite, since there is zero time delay between the pressure observed at any two points on the interface. In general, v is equal to the speed of sound in water divided by the cosine of the grazing angle of the incoming wave. Equivalently, v could be defined as the radial acoustic frequency divided by the horizontal wave number. Since there is no mechanism for changing the horizontal wavenumber in a horizontally stratified, linear medium, the horizontal trace velocity must be preserved as the disturbance propagates into the ice. It follows

that in any layer with wave speeds higher than v , a propagating wave cannot be excited; that is, even in the absence of attenuation, any excited disturbance would decay exponentially in the vertical direction through this layer. Nonetheless, such a layer may transmit a significant amount of energy if it is relatively thin and is backed by a low-velocity medium.

For the half space of ice used here, v is less than either of the wave speeds in the ice for grazing angles less than 40 degrees. Thus, little wave energy can be transferred to the ice, and R is near unity for these angles (see fig. 1). At 40 degrees, coincidence occurs between v and the shear speed, so that propagating shear waves can be excited at this and higher grazing angles. Figure 1 shows a large drop in R near 40 degrees due to the transfer of a significant fraction of the incoming energy to shear waves in the ice.

At normal incidence, there is no mechanism for exciting shear waves in a perfectly stratified ice sheet. Hence, the normal incidence reflection coefficient depends only upon the compressional behavior of the ice. Since R is nearly constant from just above the compressional coincidence angle (68 degrees in this case) up to 90 degrees, we surmise that shear waves are not significantly excited over this range of angles.

Note that the lack of any vertical scale length in the model composed of two half spaces results in frequency independence of the reflection calculations.

Next, consider a finite thickness of ice between water and air. Figure 2 shows R at 15 kHz for a 0.8 m thick, homogeneous layer of ice. The ice properties are the same as for the ice half space discussed above, and the speed of sound in air is 331 m/s.

In figure 2, R reaches an absolute minimum near 40 degrees, but significant loss begins to occur below 30 degrees. Apparently, the ice is thin enough, about 6 shear wavelengths, to transmit energy into the low-velocity air, even below the shear coincidence angle. The bumpy nature of the reflection plot is due to the presence of many propagation modes in the ice. Each mode obeys a different dispersion relation, which can be expressed as horizontal trace velocity vs frequency. As the grazing angle of a constant-frequency incident wave increases, v increases and coincidence with the trace velocities of the various modes is achieved in turn. Coupling of the incident wave with any given mode is optimized at that mode's coincidence angle, producing a relative minimum in the plot of R vs grazing angle. The irregular pattern of the curve near 60 degrees implies significant coupling between shear and compressional waves in the ice for these angles.

The high value of R at normal incidence for the finite ice layer is the result of the large impedance discontinuity between ice and air.

3. VERTICALLY INHOMOGENEOUS SEA ICE

Now we look at ice which has variable properties in the vertical direction. First, we define a baseline acoustic profile and then vary one characteristic of the profile at a time to determine the importance of that characteristic in the calculation of R . The wave speeds for shear and compression used in the baseline model, as shown in figure 3, are intended to be representative of a 3 m thick arctic ice cap in winter. Gavrilov, Gusev and Nikitin (ref. 3) give measured wave speed profiles for the main portion of the ice, which we call hard ice, and Bogorodskii, Gavrilov and Nikitin (ref. 4) measured sound speeds in formative ice, which makes up the ice-water transition region. The vertical extent of the sound speed minimum in the ice skeletal layer is exaggerated in figure 3 to emphasize its existence. In the calculations, the sound speed in the ice is below that of water for the first 0.9 cm, and no shear is permitted in the ice for the first 2.8 cm.

For the sake of simplicity, the attenuation constants for shear and compressional waves are taken to have the constant values of 0.36 and 0.06 dB/m/kHz, respectively. These are the values used by McCammon and McDaniel (ref. 1) for a temperature of -6 degrees Celsius. Calculations not reported here indicate that the relaxation of this assumption would not affect the qualitative conclusions which follow.

Calculation results for the baseline model are presented in figure 4 as a waterfall display of R vs grazing angle with frequency going from 5 to 30 kHz in 0.2 kHz steps. The bottom curve, for 5 kHz, shows characteristics of both infinite and finite ice. The 3 m thickness is sufficient at this frequency that little energy is transmitted through the ice for grazing angles well below the shear coincidence angle associated with the fastest part of the ice (40 degrees). The oscillations of R just above 40 degrees indicate that many shear modes are cut on in the ice slab. A large dip in R at 68 degrees clearly marks the compressional coincidence angle, and several compressional or mixed ice slab modes cause subsequent dips as normal incidence is approached.

As the frequency increases, the modal coincidence angles migrate downward because of the dispersive nature of the ice slab modes. Also, the effects of the shear modes die out because of the large shear attenuation, which increases with frequency. It is paradoxical that an increase in wave attenuation in the ice causes less reflection loss. The explanation for this is that large attenuation effectively eliminates interaction between the top and bottom of the ice so that modes no longer exist. If shear modes are absent, then the incident wave cannot transfer energy into them. Thus, an important contributor to reflection loss is eliminated.

Two other effects of increasing frequency are observed. First, the effective fundamental shear and compressional coincidence angles decrease as more wavelengths are contained within the slower

transition layers. Also, new modes appear below the fundamental coincidence angle which must be edge modes propagating in the ice-water transition region.

With a 20 cm layer of snow added to the top of the baseline ice model, there is no qualitative change in the waterfall display of R (not shown for the sake of brevity). At the highest frequencies, the curves are identical, and at the lower frequencies, the only change is in the details of the dispersion of the modes above the compressional coincidence angle.

In another calculation (fig. 5), the air-ice transition and the air are eliminated, with the fastest ice layer becoming a half space. As expected, all the features previously identified with the finiteness of the ice are no longer present. We still see the effects of the fundamental coincidence angles for shear and compression and of the modes associated with the ice-water transition.

Figure 6 shows the results for the baseline model minus the ice-water transition region. Here, the compressional wave speed jumps from 1450 m/s in water to 3300 m/s in the adjacent ice layer instead of transitioning more gradually over several layers. The shear wave speed in the bottom ice layer is 1650 m/s. The coincidence angle for transmission from the water into a half space with a 1650 m/s wave speed would be 29 degrees, and the observed coincidence for shear drifts down toward this value as the incident wavelength decreases (frequency increases). However, the absence of the soft ice, arbitrarily defined as ice having a compressional wave speed below 3300 m/s, results in the disappearance of the more dispersive transition modes. Also, shear modes seem to couple better with the incident wave around 60 degrees in the absence of the transition.

In the baseline model, the shear speed is zero in the bottom 2.8 cm of ice, and it then jumps up to 1250 m/s. We feel that there is some ice near the interface which does not support shear, but we do not know what a representative thickness is or how to transition from no shear to hard ice. Therefore, a case is presented (fig. 7) in which the baseline model is modified only in that the shear speed is zero in the bottom 1.4 cm of ice and then increases in steps to 200, 600 and 900 m/s. Above 2.8 cm, the model is unchanged from the baseline. Comparing the calculated values of R for this model (fig. 7) with those for the baseline model (fig. 4), we see no difference above compressional coincidence, but a large difference below it. Not only do the transition modes exhibit very different dispersion, but the presence of the very low velocity layers seems to greatly impede coupling of the incident wave into the shear modes that propagate primarily in the hard ice. Thus, how shear is modeled in the relatively small transition region can have a tremendous impact on the calculated values of R, especially at small grazing angles and high frequencies.

4. OTHER CONSIDERATIONS

There are, of course, many important ice features which have been ignored in the above calculations. These include anisotropy, inhomogeneity and departures from perfect stratification (roughness). The inclusion of anisotropy would produce only slight shifts in the dispersion curves for the various ice plate modes (ref. 5) and would not change the qualitative observations of the previous sections. On the other hand, inhomogeneities and roughness could be such strong scatterers that coupling into the ice modes would be virtually eliminated. The consideration of such inhomogeneities as brine pockets, drainage channels and air bubbles is beyond the scope of this paper, but a preliminary look at roughness follows.

We report here on the initial results of a study of the effects of ice roughness on the R. These calculations are made using a fast field program developed at the NATO SACLANT ASW Research Center (ref. 6). This computer code permits the specification of an rms roughness at any or all of the layer interfaces.

First, we take the baseline ice model but eliminate all of the layers in the ice-water interface region which have compressional wave speeds below 2600 m/s. The solid line in figure 8 is the reflection loss vs grazing angle for an 8.5 kHz excitation and no roughness. (Note that the ordinate in figures 8 and 9 is reflection loss in dB rather than the linear plot of reflection coefficient used in previous figures: $\text{loss} = -20 \log R$.) The dashed curve is for the same case except that an rms roughness of 0.5 cm is imposed at the ice-water interface. The effect of this slight roughness is to increase the loss at most angles below the compressional coincidence angle for the fastest ice layer (68 degrees). The largest increase in the loss is just below 30 degrees, where the incident plane wave couples into an edge mode in the ice. Larger loss with roughness is as expected, since it seems reasonable that the primary effect of the roughness would be to scatter the incident wave.

A curious result is shown in figure 9, where the addition of roughness greatly reduces the loss at shallow grazing angles. In this case, all layers of the baseline ice model are included, and the shear wave speed is tapered gradually. The last ice layer which supports shear has a shear speed of 20 m/s and a compressional wave speed of 2200 m/s. A roughness of 0.5 cm rms is imposed on the bottom of this layer, not on the softer ice below it. Apparently, the roughness works in some unknown way in this particular case to impede the coupling of the incident wave with both of the transition modes evident in the zero roughness case of figure 9. Because these are preliminary calculations, we draw no conclusions about their typicality.

5. DISCUSSION

The effect of the ice-water transition region on the plane-wave reflection coefficient of flat sea ice is considered here for the first time. The fundamental nature of the reflection process is unchanged by the presence of the transition. That is, only compressional waves are excited in the ice when the incident wave is near normal, but shear properties dominate the process at grazing angles below compressional coincidence for the hard ice. Also, dips in the plot of R vs grazing angle occur when the horizontal trace velocity of the incoming wave matches that of some propagation mode in the ice plate. Since the ice modes are dispersive, their horizontal trace velocities, and therefore the positions of the dips in the plot of R , may be sensitive to small changes in frequency, ice thickness and wave speed structure in the ice. Thus, in general, precise knowledge of ice properties is required to accurately predict R for a given frequency and grazing angle.

Even though the transition region does not change the nature of the reflection process, it does have a profound influence on it in two ways. First, new modes are introduced which propagate primarily within the transition region. Since the shear speed is less than the sound speed in water over much of the transition, these transition modes may be excited all the way down to zero grazing angle. Second, the transition region may enhance or impede the coupling of the incident wave with the thickness modes of the ice. Both of these effects are very sensitive to the details of how the shear speed is tapered. We feel that the skeletal layer (the bottom two cm or so of the ice) does not support shear, but we do not know the appropriate shear speed profile to represent the soft ice between the skeletal layer and the hard ice. The results presented here show that such knowledge is required to determine the effects of the transition

region on the plane wave reflection coefficient. Since these effects may be large, knowledge of the shear properties of the soft ice should be sought.

ACKNOWLEDGEMENT

This work was performed for the NAVSEA Arctic USW Environmental Technology Program, NAVSEA 63R, Mr. D. E. Porter, under PE62759N, Subproject SF59-555. This subproject is block managed by Mr. R. L. Martin, NORDA Code 113.

REFERENCES

1. D. F. McCammon and S. T. McDaniel, "The Influence of the Physical Properties of Ice on Reflectivity," *J. Acoust. Soc. Am.*, v. 77, 499-507, 1985.
2. W. G. Mayer, H. Behravesch and T. J. Plona, "Determination of Sonic Velocities from Reflectivity Losses at Sea Ice/Water Boundaries," *J. Acous. Soc. Am.*, v. 57, 39-46, 1975.
3. V. P. Gavrilov, A. V. Gusev and V. A. Nikitin, "Seasonal Changes Affecting the Elastic Properties of Sea Ice Cover," *Transactions of AANII*, v. 374, 73-74, 1980.
4. V. V. Bogorodskii, V. P. Gavrilov and V. A. Nikitin, "Sound Propagation in Ice Crystallized from Salt Water," *Soviet Physics - Acoustics*, v. 22, 158-159, 1976.
5. D. L. Anderson, "Elastic Wave Propagation in Layered Anisotropic Media," *Bull. Seismol. Soc. Am.*, v. 43, 17-34, 1961.
6. G. Tango and H. Schmidt, "SAFARI: The SACLANTCEN Fast Field Program for Range Independent Environments, Introduction and Basic User's Guide," NORDA-SACLANTCEN Memorandum, to be published.

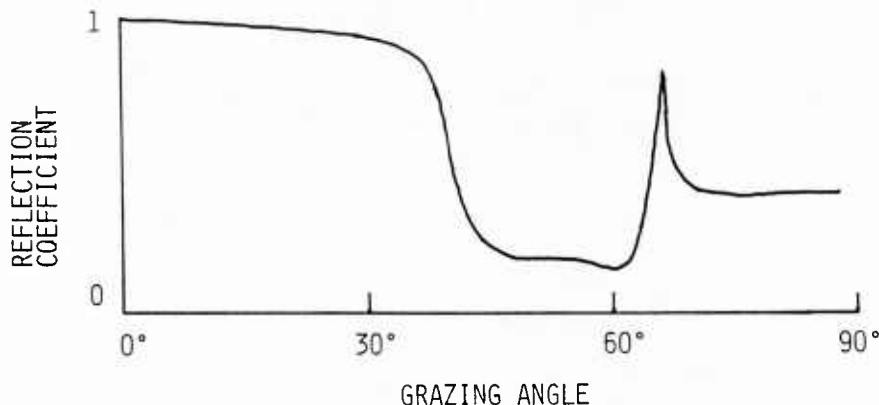


Figure 1. Reflection Coefficient vs grazing angle for a water-borne plane wave incident upon a half space of ice. Ice-to-water density ratio = 0.9, water sound speed = 1450 m/s, ice compressional wave speed = 3800 m/s, ice shear speed = 1900 m/s.

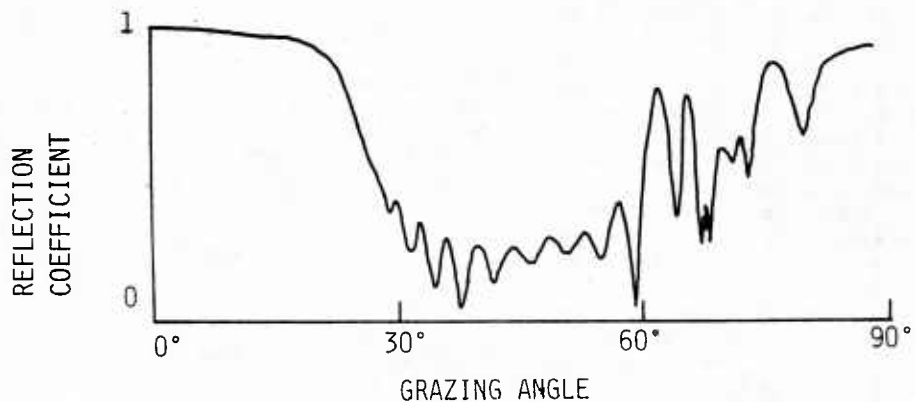


Figure 2. Reflection coefficient vs grazing angle for a water-borne, 15 kHz plane wave incident upon a 0.8 m thick homogeneous ice plate bounded above by a half space of air. The water and ice properties are the same as for figure 1, and the speed of sound in air is 331 m/s.

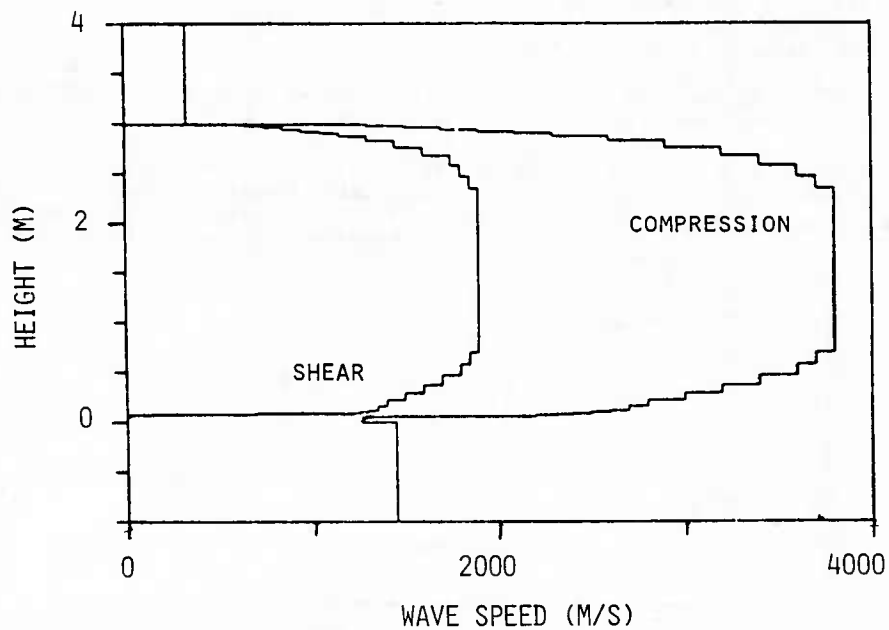


Figure 3. Wave speed profiles for the baseline ice model, representative of 3m thick sea ice in the winter. The vertical extent of the sound speed minimum in the skeletal layer is exaggerated. See the text for a full explanation.

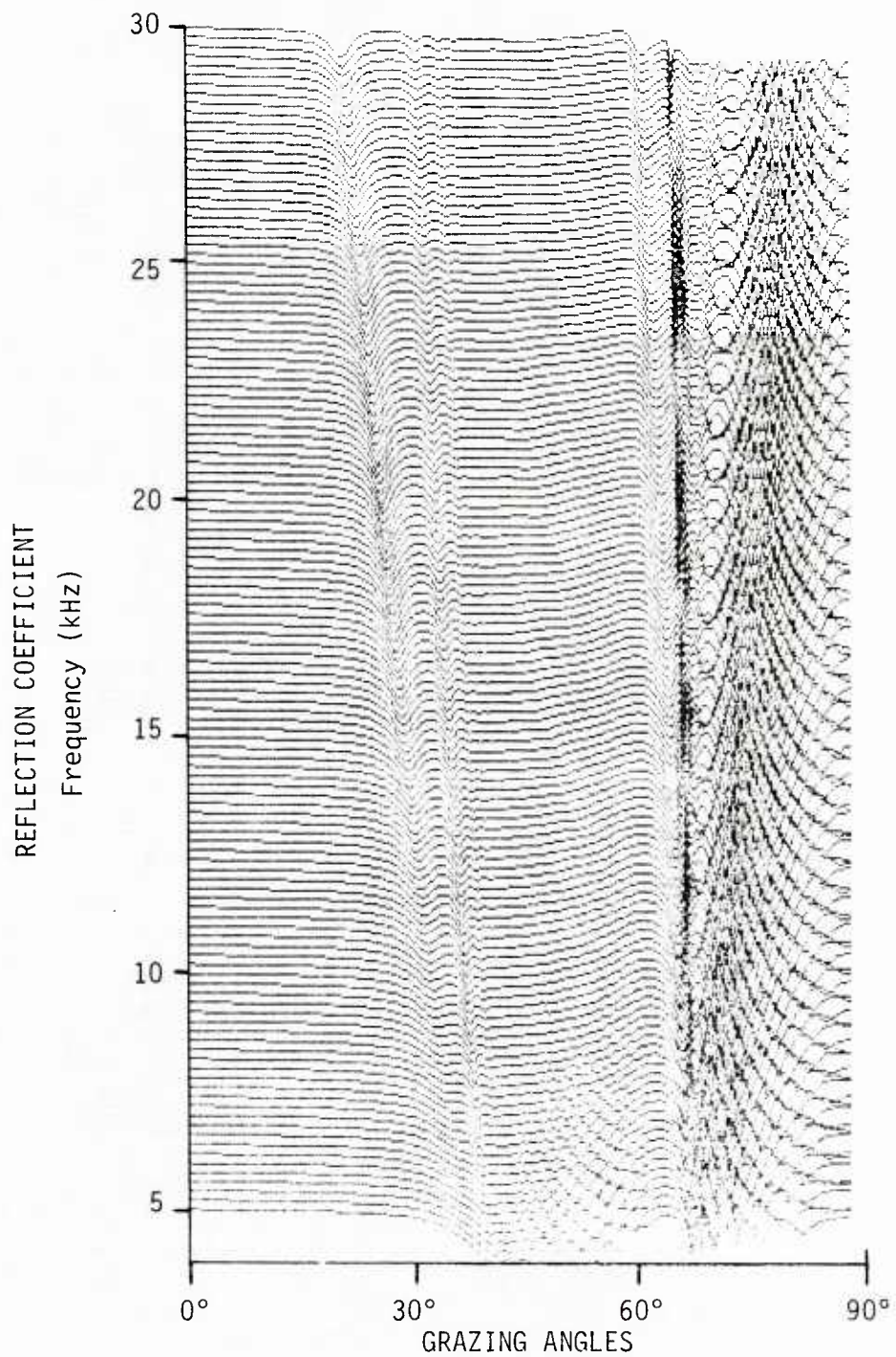


Figure 4. Waterfall display of reflection coefficient vs grazing angle for the baseline ice model shown in figure 3. Frequency is the offset parameter, with a curve shown for every 0.2 kHz interval between 5 and 30 kHz.

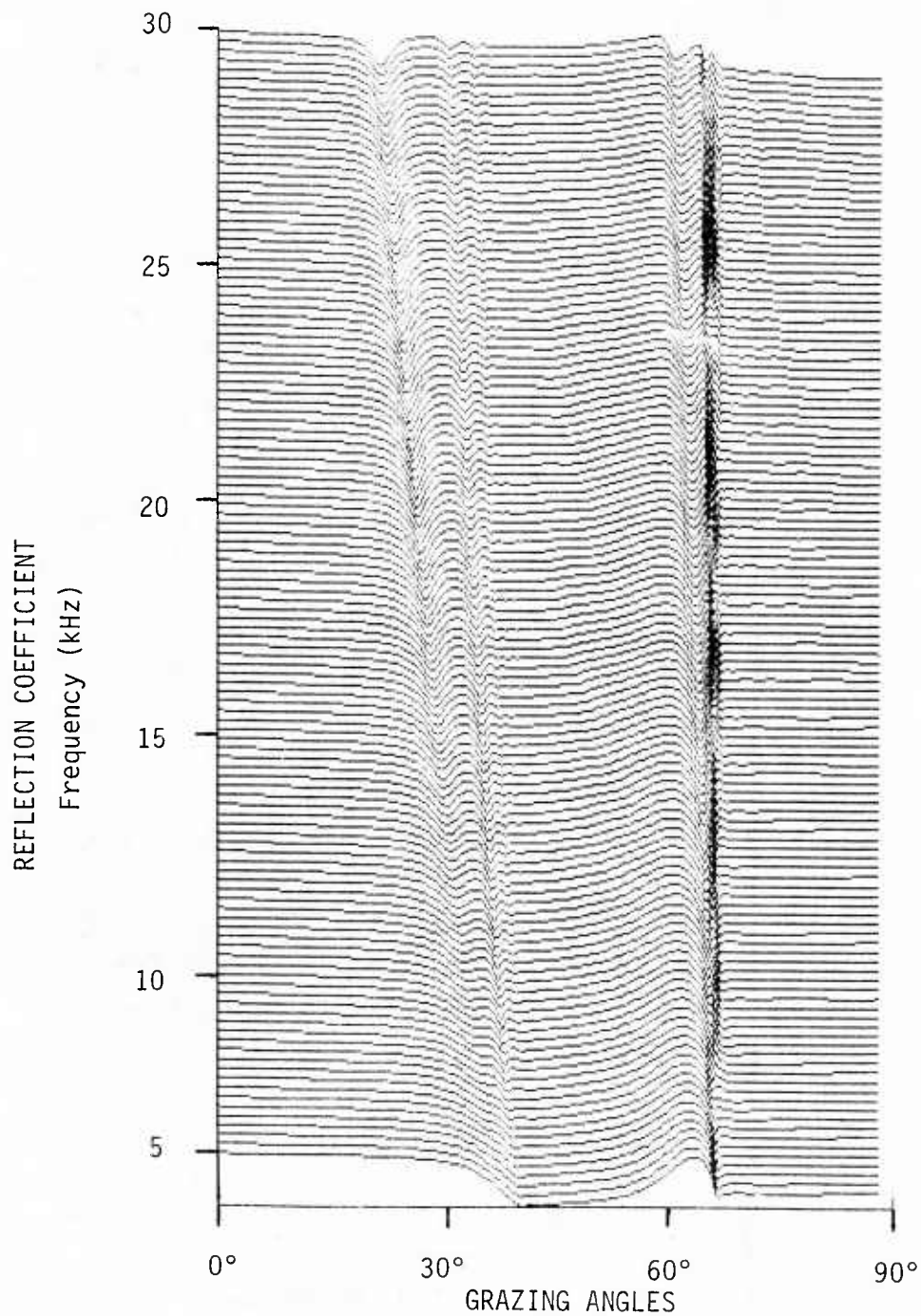


Figure 5. Waterfall display of reflection coefficient vs grazing angle for an ice model identical to the baseline model of figure 3 up to the layer with the maximum compressional wave speed (3800 m/s). Above that level, this model consists of a homogeneous half space of ice having the same properties as that layer.

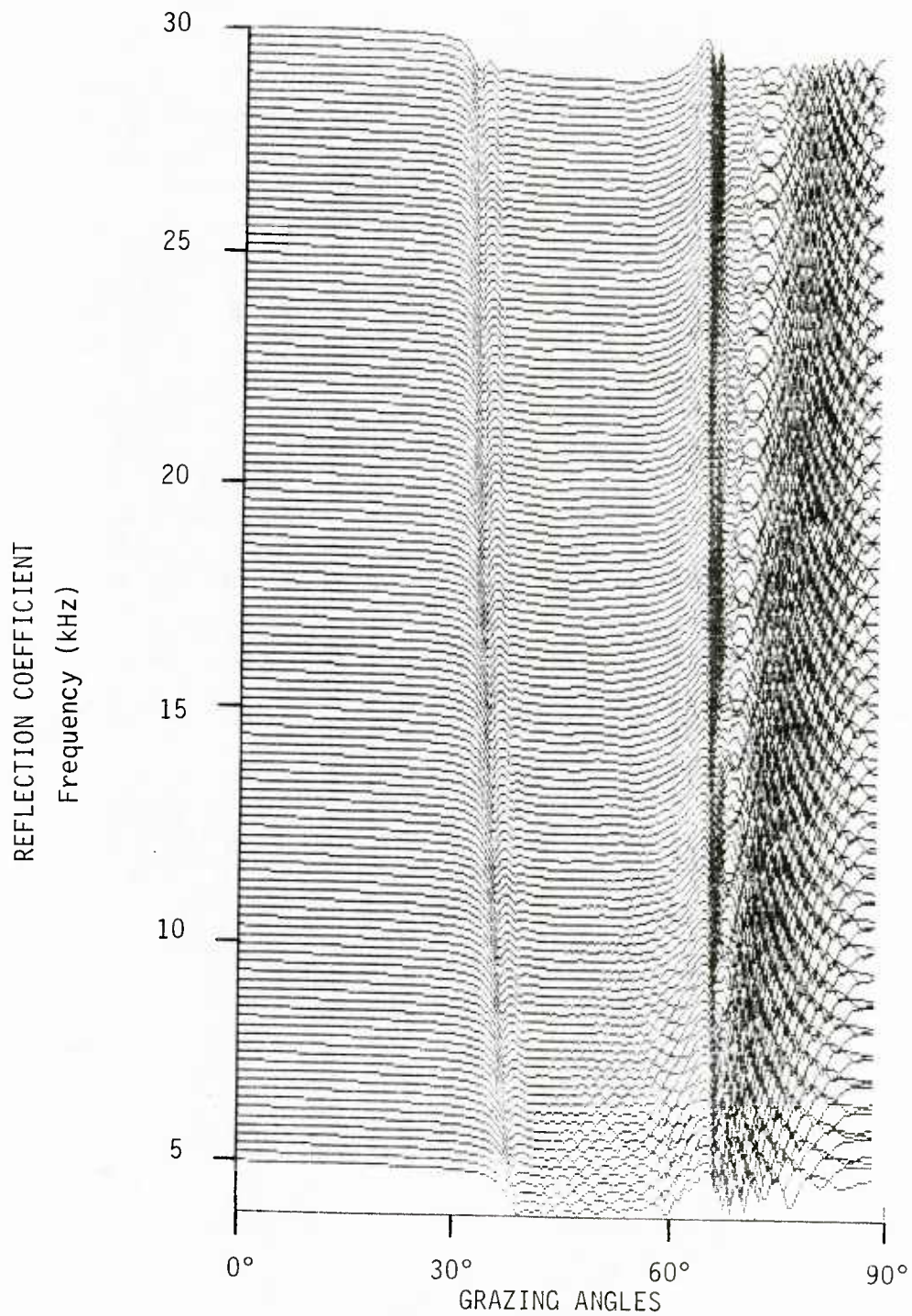


Figure 6. Waterfall display of reflection coefficient vs grazing angle for an ice model identical to the baseline model of figure 3 except that the ice layers in the ice-water transition region having compressional wave speeds below 3300 m/s are omitted.

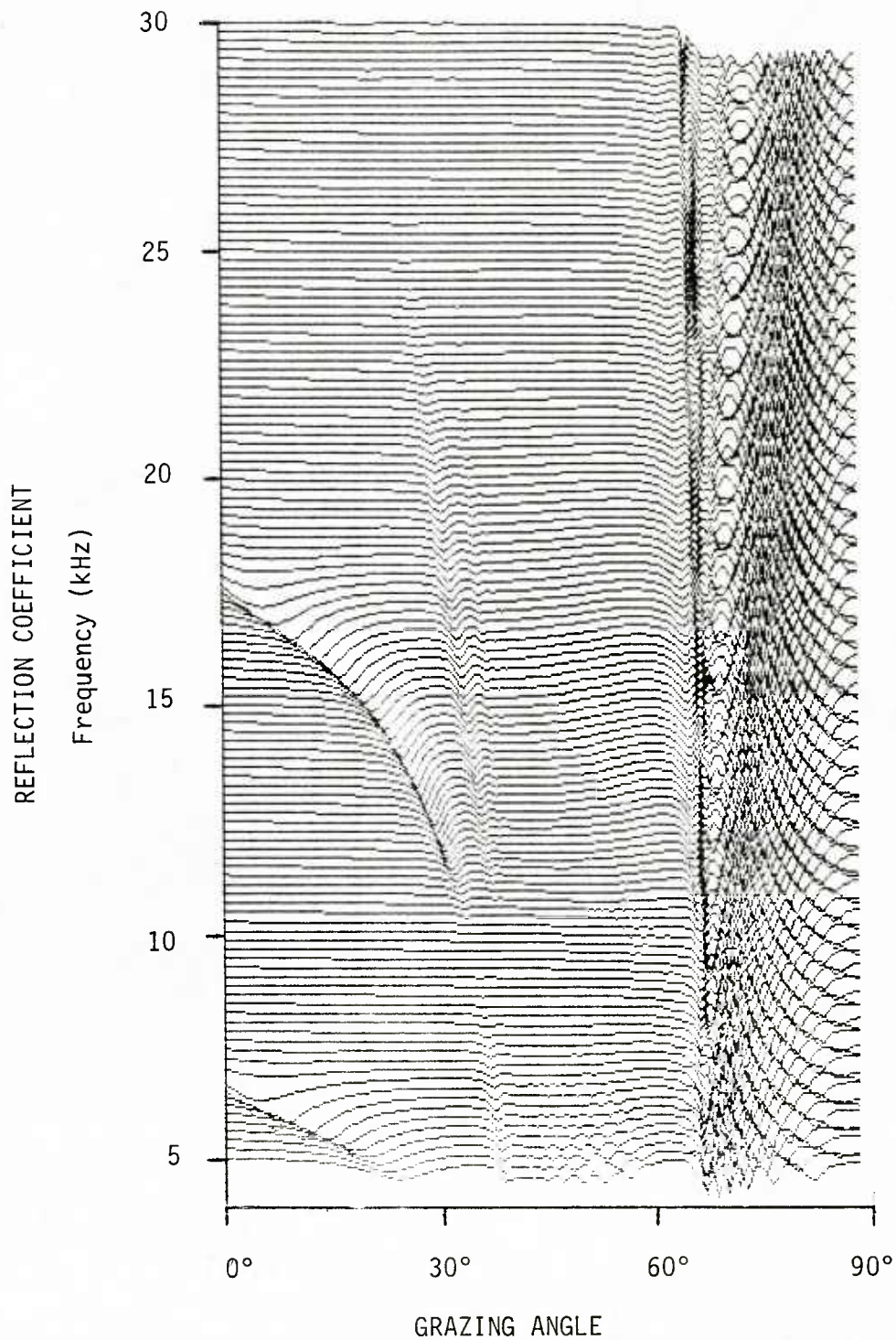


Figure 7. Waterfall display of reflection coefficient vs grazing angle for an ice model identical to the baseline model of figure 3 except that an additional 1.4 cm of the ice-water transition region is allowed to support shear.

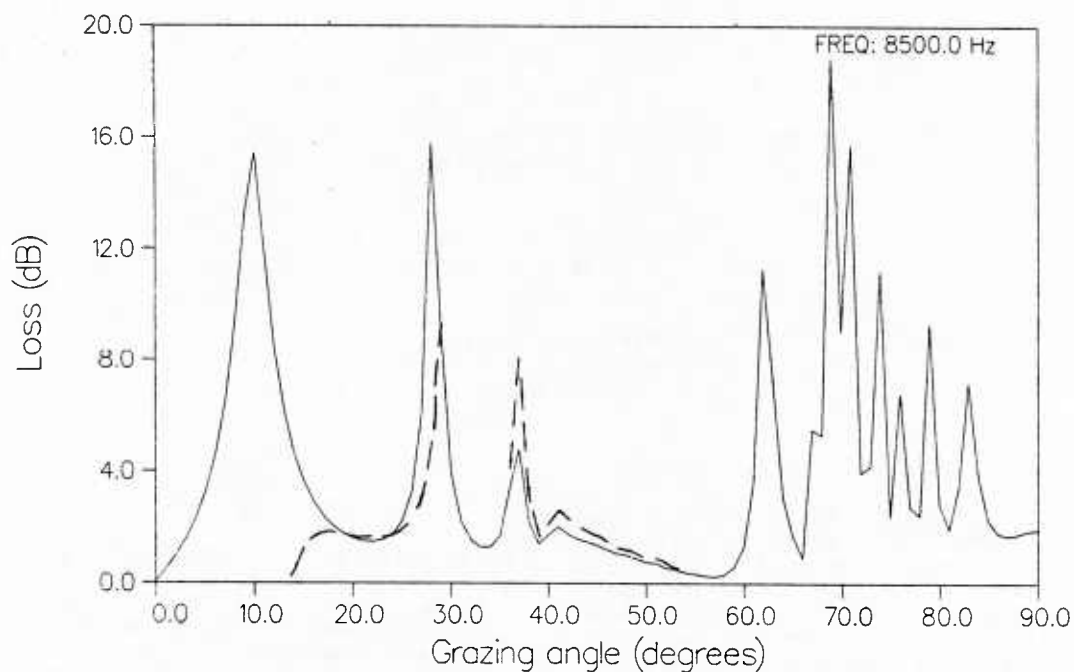


Figure 8. Reflection loss vs grazing angle at 8.5 kHz for an ice model similar to the baseline model of figure 3 except that the ice layers in ice-water transition region having compressional wave speeds below 2600 m/s are omitted. Results are shown with (---) and without (—) a roughness of 0.5 cm rms at the ice-water interface.

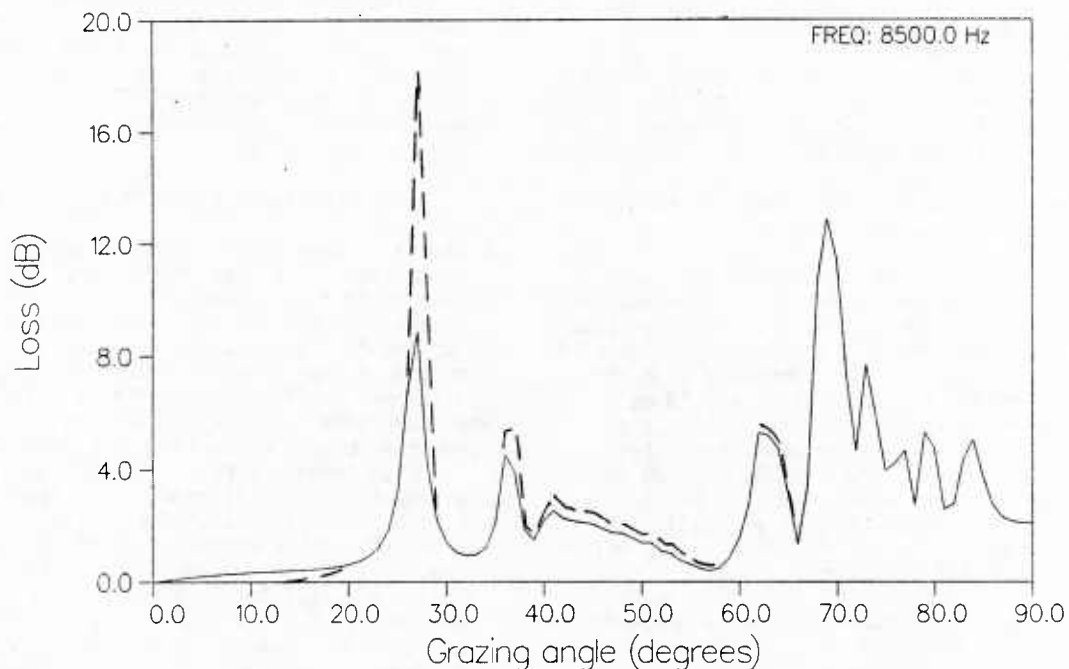


Figure 9. Reflection loss vs grazing angle at 8.5 kHz for an ice model similar to the baseline model of figure 3, with (---) and without (—) a roughness of 0.5 cm rms imposed on the lowest shear-supporting layer.

USE OF PENETRATORS TO ESTIMATE THE PROPERTIES OF ICE IN THE ARCTIC REGION

Ching H. Yew

Applied Research Laboratories
The University of Texas at Austin
Austin, Texas 78713

ABSTRACT

The use of penetrators for making in-situ measurements of ice properties in the Arctic region is studied in this paper. Methods of generating, monitoring and analyzing waves in the ice layer are presented and discussed in detail. Mathematical analysis on the use of measured waves to estimate the acoustic impedance distribution in the ice layer is also presented. Our analysis shows that it is feasible to use a group of penetrators for in-situ measurements of the ice properties.

1. INTRODUCTION

The objective of this project is to study the feasibility of using penetrators for in-situ measurements of the acoustical properties of ice in the Arctic region. Due to the severe environment and the remoteness of the region, it would be uneconomical and impractical to send teams to conduct frequent measurements. This prompts the idea of using a group of remotely controlled penetrators as an alternative means of performing the required in-situ measurements.

A group of instrumented ice penetrators can be deployed by air to the region to be studied. The penetrator can be designed so that it penetrates several feet into the ice mass leaving an antenna section on the surface to communicate with the control station. The penetrators should be equipped with an acoustic (or seismic) signal generator and a receiver for conducting the required experiments. They should also be equipped with a radio signal receiver and transmitter for receiving signals from the control station to start the experiment, and to transmit data back to the station for analysis.

Using penetrators to make in-situ measurements has the following advantages.

- 1) It is more economical than sending teams to the site.
- 2) Since the instruments inside the penetrator are below the ice surface, they are protected from the severe Arctic environment. The penetrator can thus be left at the site

for long periods of time allowing data collection over several seasons.

The design of the ice penetrators, either based on impact or heating, has been a much studied subject,¹ and will not be repeated here. Instead, in this paper, the discussion will focus on the means of generating a proper signal, and on the data analysis method for deducing the desired ice properties via the measured wave motion.

A brief description of the penetrators and their deployment is presented in Section 2. Methods for generating the proper signals for measuring the material properties are presented in Section 3. Procedures for data analysis are presented in Section 4. An analytical study regarding the use of measured wave motion to determine the acoustic impedance distributions in a non-homogeneous medium, such as ice, is presented in Section 5. Finally, a brief discussion regarding the feasibility of using penetrators for making the in-situ measurements is presented in the concluding section, Section 6.

2. PENETRATORS AND THEIR DEPLOYMENT

Figure 1 shows a conceptual sketch of an impact penetrator and a heat penetrator. Both penetrators have their instrument sections buried in the interior of the ice mass leaving an antenna at the surface for communication. Using the pulse-echo method, a single penetrator should be, in principle, sufficient for the material property measurements. The ice is, however, known to be a non-homogeneous and anisotropic material;² and in the high frequency range, the ice is also known to attenuate acoustical waves. To illustrate this attenuative property of ice, a plot of wave amplitude attenuation versus frequency is reproduced in Fig. 2.³ In view of these properties, it is clear that, for obtaining a complete description of the properties in a region, a group of penetrators will be required. Figure 3 shows the deployment of a group of penetrators. A near-surface penetrator is used as the wave (or signal) generator. The receiving penetrators are deployed at different depths and distances for receiving waves emitted from the generator. The distance between penetrators should be designed so that they are consistent with the frequency range and attenuation of the waves to be studied.

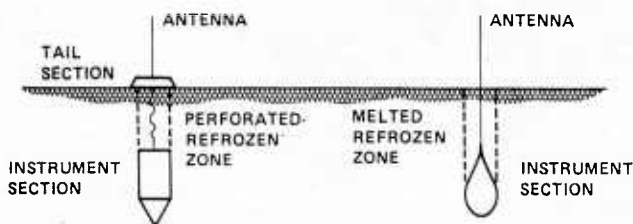


FIGURE 1
IMPACT AND HEAT ICE PENETRATORS

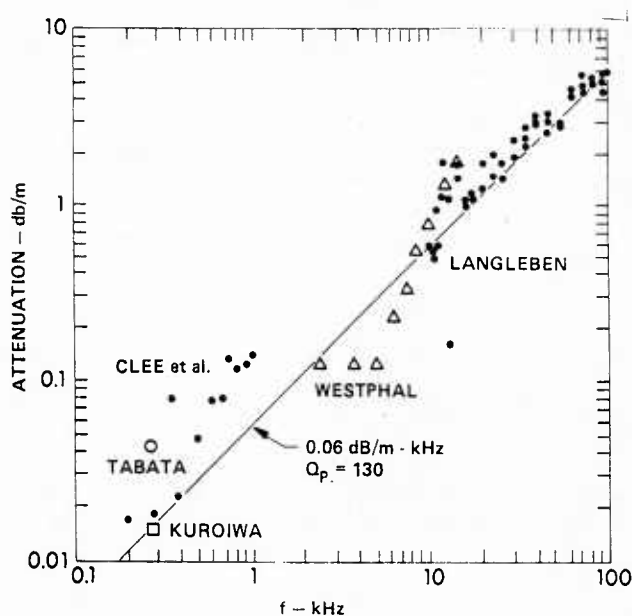


FIGURE 2
COMPRESSIONAL WAVE ABSORPTION IN NATURAL AND
LABORATORY GROWN SALINE ICE AT -6°C AND IN
GLACIAL ICE NEAR ITS PRESSURE MELTING POINT

3. METHOD FOR GENERATING AND RECORDING SIGNALS

After the penetrators are properly deployed, the experiment can be started by a command signal. Since ice is an attenuative medium, signals of sufficient strength are required. The required compressional (P), horizontal shear (SH), and surface waves (R) can be generated by the following arrangements.

1) Referring to Fig. 4, the compressional (P) and surface waves (R) can be generated by igniting an electric spark, or by bursting an air bubble at the nose tip of the penetrator. The pulse generated by a spark, in general, contains many high frequency waves. The center frequency of a pulse generated by a spark of 2000 Vdc is approximately 80 kHz depending upon the distance between the spark gap. The center frequency of a pulse generated by bursting an air bubble is, however, much lower than that generated by an electric spark. By bursting a dental rubber bubble in a water tank, this author has recorded a pulse with center frequency near 1 kHz. We estimate that, by bursting the bubble by different means, one should be able to generate a pulse with center frequency ranging from 500 Hz to 1.5 kHz. Referring to Fig. 3 again, the so-generated pulse is received as a compressional wave by the penetrators located at position P_1 and P_2 . The pulse will be received as a surface wave (with P and S precursors) by the penetrators deployed at R_1 and R_2 . Furthermore, the motion recorded by receivers S_1 and S_2 , placed at a distance from the sources, are the plate waves in the ice layer.

2) In the petroleum industry, horizontal shear (SH) waves in a rock mass are generated by impacting the wall of a shallow pit on the surface with a hammer or with explosives. In an ice penetrator, such shear waves can be generated by impacting the ice wall horizontally with a plunger activated by an electrical solenoid as illustrated in Fig. 4. The motion monitored at position H_1 and H_2 by the receivers with their sensitive axis aligned horizontally are the SH-waves in the ice mass.

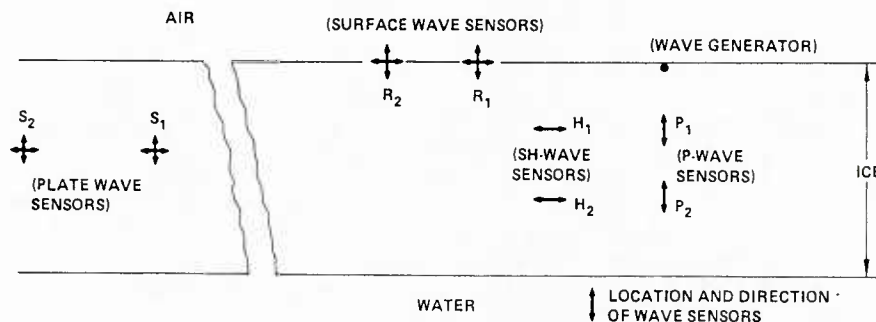


FIGURE 3
DEPLOYMENT OF A GROUP OF PENETRATORS

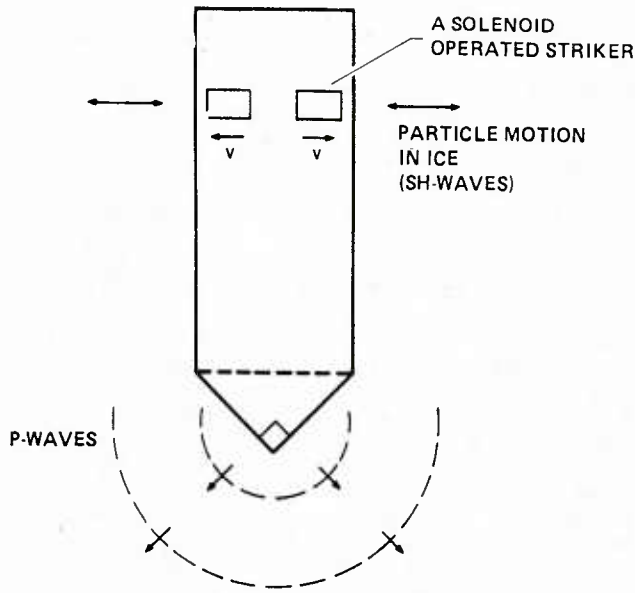


FIGURE 4
WAVE GENERATING PENETRATOR

4. ANALYSIS OF THE RECORDED WAVES

The recorded waves can be accelerations or pressures. The sensitive axis of the wave sensors should be carefully aligned according to the characteristics of the waves to be measured. For example, the sensitive axis of the transducer should be aligned in the horizontal direction for the SH-wave measurement, while its sensitive axis should be aligned in the vertical direction for the P-wave measurements.

Two wave transducers are used to monitor the wave motions. Assume that an impulsive motion of form $f(t)$ is generated at the point of impact. The pulse, after traveling distances x_1 and x_2 , is monitored by transducers placed at these positions. The wave amplitude and phase velocity relationship between these two measured waves can be written as⁴

$$\text{Amplitude ratio} = \left| \frac{F_2(\omega, x_2)}{F_1(\omega, x_1)} \right| \quad (1)$$

and

$$v(\omega) = \frac{\omega(x_2 - x_1)}{\tan^{-1}\left(\frac{I_2}{R_2}\right) - \tan^{-1}\left(\frac{I_1}{R_2}\right) + 2n\pi} \quad (2)$$

In the equations above, ω is the angular frequency, $R(\omega, x)$ and $I(\omega, x)$ are the real and imaginary components of the Fourier transform of the measured wave motion $f(t, x)$, and the integer n must be so chosen that Eq. (2) yields a continuous phase velocity and frequency relationship. With proper digital recording instruments, the Fourier transform of the recorded waves and the necessary com-

putations for the construction of the attenuative and dispersive relationship of the medium can be performed with a high speed computer. This method was applied successfully by this author in the study of dispersion of the longitudinal and bending waves in a circular rod as well as the dispersion of surface waves in a layered medium.⁵

A proper mathematical model regarding the acoustical properties of the medium can thus be constructed based on these measured wave characteristics. A procedure of analyzing is suggested in Fig. 5. An iterative process on the material properties must be employed so that the wave's characteristics predicted by the mathematical model is in reasonable agreement with that deduced from the measured wave motion.

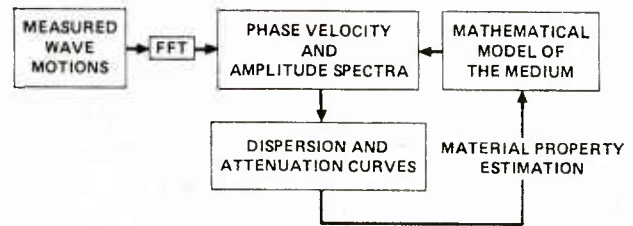


FIGURE 5
FLOWCHART OF ANALYSIS

5. ESTIMATION OF THE IMPEDANCE DISTRIBUTION IN A MEDIUM USING THE REFLECTED WAVES

In the following analysis, the medium is regarded as one made of many thin layers, as shown in Fig. 6.

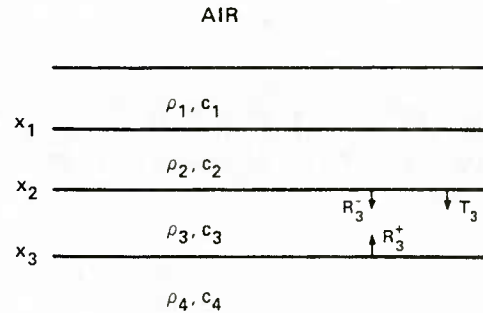


FIGURE 6
A LAYERED MEDIUM

For plane wave motions, the equation of motion in the i th layer can be written as:

$$c_i^2 u_i'' + \omega^2 u_i = 0 \quad (3)$$

where c_i is the wave speed and ω is the angular frequency. The solution of this equation has the form:

$$u_i = A_i e^{ik_i x} + B_i e^{-ik_i x} \quad (4)$$

where k_i is the wave number, and A_i and B_i are the integration constants.

The continuity requirement of displacements and stresses at the interface between the $(i-1)$ th and the i th layer yields the following equations:

$$A_{i-1} e^{ik_{i-1} x_i} + B_{i-1} e^{-ik_{i-1} x_i} = A_i e^{ik_i x_i} + B_i e^{-ik_i x_i} \quad (5)$$

$$\begin{aligned} \rho_{i-1} c_{i-1} (A_{i-1} e^{ik_{i-1} c_i} - B_{i-1} e^{-ik_{i-1} x_i}) \\ = \rho_i c_i (A_i e^{ik_i x_i} - B_i e^{-ik_i x_i}) \end{aligned} \quad (6)$$

where ρ_i is the mass density of the i th layer. By letting

$$\begin{cases} R_i^- = \frac{B_i}{A_i} e^{-2ik_i x_i} & \text{reflection coefficient at} \\ & \text{the upper endpoint of the} \\ & \text{ith layer} \\ R_i^+ = \frac{B_i}{A_i} e^{-2ik_i x_{i-1}} & \text{reflection coefficient at} \\ & \text{the lower endpoint of the} \\ & \text{ith layer} \\ T_i = \frac{A_i}{A_{i-1}} e^{i(k_i - k_{i-1})x_i} & \text{transmission coef-} \\ & \text{ficient from (i-1)th} \\ & \text{to the ith layer} \end{cases} \quad (7)$$

the following identities can be obtained:

$$\begin{cases} R_{i-1}^+ = \frac{r_i + R_i^-}{1 + r_i R_i^-} \\ T_i = \frac{1 + r_i}{1 + r_i R_i^-} \end{cases} \quad (8)$$

$$r_i = \frac{1 - \mathcal{P}_i}{1 + \mathcal{P}_i} \quad (9)$$

$$\mathcal{P}_i = \frac{z_i}{z_{i-1}} = \frac{\rho_i c_i}{\rho_{i-1} c_{i-1}} \quad (10)$$

Using the assumptions that the layers are thin, and the material property differences between adjacent layers are small, Eqs. (9) and (10) can be expressed by the following differential forms after dropping the higher order terms:

$$\mathcal{P}_i = 1 + \frac{1}{z_{i-1}} \frac{dz}{dx} \Delta x \quad (11)$$

$$r_i = -\frac{1}{2z_i} \frac{dz}{dx} \Delta x \quad (12)$$

Substituting Eqs. (11) and (12) into Eq. (8), one obtains the following Ricatti's equation after some algebraic manipulations:

$$\frac{dR^+}{dx} + \frac{1}{2z} \frac{dz}{dx} R^{+2} + 2ikR^+ - \frac{1}{2z} \frac{dz}{dx} = 0 \quad (13)$$

We now assume that the layer thickness is so thin, and that the material property differences between the adjacent layers are so small that the medium may be regarded as a continuum with a varying property in one direction. One can, thus, replace R^+ with $R(x)$ in Eq. (13).

In order to simplify the analysis, we note that R is the amplitude ratio of the reflected and transmitted waves. For a medium such as ice, we expect R to be a small number. We thus drop the R^2 term in Eq. (13), and rewrite the equation as follows:

$$\frac{dR}{dx} + 2i \frac{\omega}{c(x)} R = \frac{1}{2z} \frac{dz}{dx} \quad (14)$$

Introducing a new variable

$$\tau = \int_0^x \frac{dx}{c(x)} \quad (15)$$

Eq. (14) can be transformed to the form

$$\frac{dR}{d\tau} + 2i\omega R = \frac{1}{2z} \frac{dz}{d\tau} \quad (16)$$

The solution of this equation is

$$R(\omega, \tau) = e^{-i2\omega\tau} \left[\int_0^\tau e^{i2\omega\tau} \frac{1}{2z} \frac{dz}{d\tau} d\tau + D \right] \quad (17)$$

where D is an integration constant to be determined from the boundary condition.

Taking a special case, we assume that at $x=L$ the waves are transmitted into the slurry between the ice layer and the water. This implies that there is no wave reflection at $x=L$, i.e., $R=0$ at $x=L$. Applying this condition, Eq. (17) becomes

$$R(\omega, \tau) = -e^{-i\omega\tau} \int_0^{\tau_L} e^{i2\omega\tau} \frac{1}{2z} \frac{dz}{d\tau} d\tau \quad (18)$$

where

$$\tau_L = \int_0^L \frac{dx}{c(x)} \quad (19)$$

At $x=0$ (i.e., $\tau=0$), $R(\omega, \tau)$ can be written as

$$R(\omega, 0) = - \int_0^{\tau_L} e^{i2\omega\tau} \frac{1}{2z} \frac{dz}{d\tau} d\tau \quad (20)$$

An equation relating the amplitude of the reflected and the incident waves at $x=0$ to $R(\omega, 0)$ can be obtained by setting $x=0$ in Eq. (7), i.e.,

$$R(\omega, 0) = \frac{B(\omega, 0)}{A(\omega, 0)} \quad (21)$$

The displacement at the surface $x=0$ caused by the reflected wave therefore has the form

$$u_R(t, 0) = \frac{1}{2\pi} \int_{-\infty}^{\infty} B(\omega, 0) e^{i\omega t} d\omega \quad (22)$$

Substitution of Eqs. (20) and (21) into (22) yields

$$\begin{aligned} u_R(t, 0) &= -\frac{1}{2\pi} \int_{-\infty}^{\infty} A(\omega, 0) R(\omega, 0) e^{i\omega t} d\omega \\ &= -\frac{1}{2\pi} \int_0^{\tau_L} \frac{1}{2z} \frac{dz}{d\tau} d\tau \\ &\quad \times \int_{-\infty}^{\infty} A(\omega, 0) e^{i\omega(t-2\tau)} d\omega \\ &= - \int_0^{\tau_L} \frac{1}{2z} \frac{dz}{d\tau} v_i(t-2\tau, 0) d\tau \quad (23) \end{aligned}$$

Equation (23) relates the reflected waves to the incident waves at $x=0$. Thus, by measuring the reflected and incident waves at that surface, i.e., $u_p(0, t)$ and $u_i(0, t)$, the impedance distribution of the layer can be determined from this equation.

The following case is studied to test the accuracy of the prediction from Eq. (23). We consider a medium which has the following properties:

$$\rho(x) = c(x) = (1+2x)^{1/2} \quad \text{for } x > 0 \quad (24)$$

The impedance distribution of the medium is therefore

$$z(x) = \rho(x) c(x) = 1 + 2x \quad (25)$$

For a unit impulse

$$u_i(t, 0) = \delta(t) \quad (26)$$

applied to the surface $x=0$, the reflected wave at $x=0$ can be calculated.⁶ It has the form

$$u_R(t, 0) = -\frac{1}{2} e^{-t/2} H(t) \quad (27)$$

Substituting Eqs. (26) and (27) into Eq. (23), the impedance distribution of the medium can be calculated. The results are plotted with the exact distribution, Eq. (25), in Fig. 7. The agreement is good.

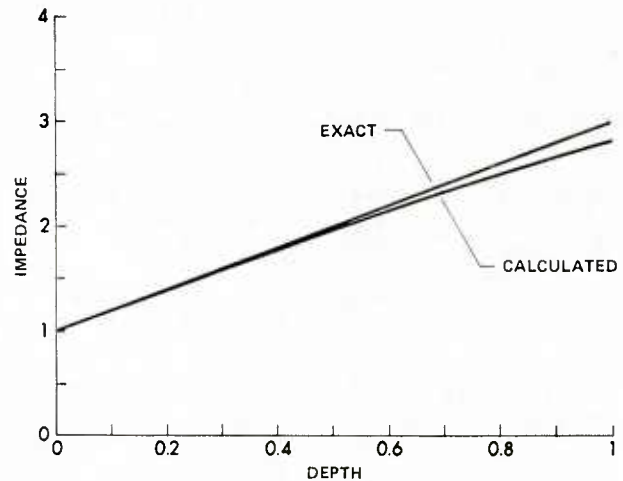


FIGURE 7
COMPARISON OF THE CALCULATED
AND THE EXACT IMPEDANCE DISTRIBUTION

6. CONCLUDING REMARK

Based on the preliminary study presented in the above sections, it appears entirely feasible to employ penetrators as a means of performing the required in-situ experiment. The method used to generate, to monitor, and to analyze the wave motion, in this case, is identical to that which would be used in a laboratory test. The advantage of using penetrators, in addition to those listed in Section 1, is that there is no limitation on the size and condition of the sample, as would be the case in a laboratory experiment on cored samples. The penetrator thus offers the possibility of conducting experiments under realistic conditions and with great freedom in designing the experiment.

ACKNOWLEDGMENT

This study was supported by the Office of Naval Research. The author is indebted to Dr. Paul Vidmar for his interest and encouragement while this study was being made.

The study was carried out while the author was with Applied Research Laboratories, The University of Texas at Austin, in the summer of 1985. The hospitality of the Laboratory is gratefully acknowledged.

REFERENCES

1. USACRREL, Hanover, New Hampshire, Workshop on "Ice Penetration Technology", CRREL Special Report 84-33, June 1984.
2. E. R. Pounder, "The Physics of Ice" (Pergamon Press, New York, 1965).

3. D. F. McCammon, and McDaniel, "The Influence of the Physical Properties of Ice on Reflectivity", ARL/PSU Report, Applied Research Laboratory, Pennsylvania State University, University Park, Pennsylvania.
4. Y. Sato, "Analysis of Dispersed Surface Waves by Means of Fourier Transform, I, II, and III", Bulletin, Earthquake Research Institute, Vol. 33, No. 33, 1955; Vol. 34, No. 9, 1956.
5. C. H. Yew and C. S. Chen, "Study of Linear Wave Motions Using FFT and Its Potential Application of Non-destructive Testing", International Journal of Engineering Science, Vol. 18, No. 8, 1980, p. 1027.
6. J. A. Ware and K. Aki, "Continuous and Discrete Inverse Scattering Problem in a Stratified Elastic Medium, I. Plane Waves at Normal Incidence", The Journal of the Acoustical Society of America, Vol. 45, No. 4, 1965, p. 911.

Acoustic Bottom Interaction Considerations in the Arctic

⁽¹⁾ W.H. Geddes and ⁽²⁾ J.E. Matthews

(1) Planning Systems Inc.

(2) Naval Ocean Research and Development Activity

Predictions of acoustic propagations in certain areas of the Arctic region are critically dependent upon a knowledge of the interaction of acoustic energy with the sea floor. There are several approaches to applying the sea floor environmental information to the acoustic models. Each approach has a specific requirement for information and has application in the Arctic. Preliminary geoacoustic investigations indicate three clearly defined sea floor environments for the continental shelves and upper slopes of the Arctic Ocean. The acoustic implications of this simple geoacoustic classification may be significant to experiment planning and system performance prediction.

Today we plan to present some of the factors to be considered in the interaction of acoustic energy with the bottom. First, why worry about bottom loss in the Arctic when the real problem is reflection of acoustic energy from the underside of the ice? The answer is of course, some times of the year, in some places, a knowledge of the acoustic properties of the bottom becomes critical to the prediction of weapon performance in the Arctic.

Figure 1 shows the marginal seas where bottom loss may be critical to acoustic prediction and the deep water areas where the bottom loss can perhaps become important under certain circumstances. The boundary between these two areas is defined in a general way by the shelf edge. As our exploration of the Arctic region increases, it is reasonable to assume that a corresponding increase in information on the bottom will be required. For example, bottom loss may become important on marginal plateaus such as the Yermak Plateau.

There are several techniques currently in use to apply our knowledge of the bottom to the prediction of acoustic propagation. Table 1 shows some of the widely used bottom loss models.

Table 1. BOTTOM LOSS
CLASSIFICATION SYSTEMS

NAVOCEANO HIGH FREQUENCY	
BOTTOM LOSS UPGRADE	(BLUG)
GEOACOUSTIC MODEL	
INTERIM BOTTOM LOSS UPGRADE	(IBLUG)

The NAVOCEANO high frequency model is a set of nine curves that relate bottom loss, grazing angle and acoustic province. The model is based on a statistical analysis of bottom loss measurements. The NAVOCEANO system treats the ocean floor as a boundary with a reflected component and a loss component of acoustic energy. Therefore, this approach is most useful at high frequencies.

Bottom Loss Upgrade (BLUG) is a model developed by Spofford also based on measurements. The model uses the measurements to assign acoustic properties to the bottom and sub-bottom. The Bottom Loss Upgrade model assumes propagation through the sediments and is most useful at lower frequencies.

The Geoacoustic Model was developed by Hamilton and is based on the relationship of the physical properties to the acoustic properties of the sediment. The Geoacoustic Model treats the ocean floor as a part of the propagation medium and application of the model is only limited by the amount of information required to establish the model. That is, high frequency application of the model requires more detail and knowledge on the composition and structure of the sediments than low frequency application.

All three of these bottom loss models have application to the Arctic. However, while these three models are in wide use in the North Atlantic and North Pacific, the information required to construct these models for the Arctic region has not been assembled nor analyzed. Therefore, an interim model has been developed to improve the solution of bottom loss by using sediment thickness as the primary environmental factor. This Interim Bottom Loss Upgrade (IBLUG), consists of a family of bottom loss curves and a chart that assigns a bottom loss classification to each one degree square in the North Atlantic (Spofford, 1980). This procedure was intended to be used until such time as the Bottom Loss Upgrade (BLUG) is completed and tested. IBLUG was principally designed for deep ocean areas and the model included classification of shallow water areas such as the Barents Sea only for the sake of completeness. The Barents Sea was arbitrarily assigned a Class 3 as a part of the analysis of the North Atlantic. However, the requirements for acoustic predictions in the Arctic make it necessary to extend the IBLUG classification into the Arctic Ocean and marginal seas.

An analysis of a relatively large amount of geophysical data has been conducted to extend the IBLUG bottom loss classes to the Barents Sea. The information available for this analysis included acoustic measurements, seismic reflection profiles, sonobuoy reflection and refraction data, sediment type, bathymetry, and geophysical extrapolation from land areas to the underwater areas. Geophysical information for other regions of the Arctic is much less available for analysis and the assignment of IBLUG classes was accomplished by extrapolation of bottom loss from known provinces in the Barents Sea and North Atlantic Ocean to similar geomorphic provinces in other areas. In general the classification of the provinces follows the system of Heezen, Tharp, and Ewing (1959) and the geographic names and boundaries of the provinces follow the analysis of Perry and Fleming (1985).

A chart of low frequency bottom loss for the Arctic was compiled by PSI. Construction of this chart followed the classification criteria of Spofford (1980). A bottom class was assigned to each bottom province as follows:

Class 1

- a. Sediment thickness greater than 0.4 sec
- b. Sediment thickness 0.2 to 0.4 sec but known very low loss

Class 2

- a. Sediment thickness 0.2 to 0.4 sec
- b. Thicker but either rough seafloor or known higher-than-average loss

Class 3

- a. Sediment thickness less than 0.2 sec
- b. Thicker areas which include high-relief terrain (seamounts, etc.)

The family of curves for Class 1 is shown in Figure 2, Class 2 in Figure 3, and Class 3 in Figure 4.

The bottom loss chart was digitized by assigning a charted bottom class index number to each 1° square. In those 1° squares that have more than one bottom class, the index number of the bottom class with the largest area within the square was assigned to the square.

Principal geomorphic elements of Barents Sea are relict highlands and valleys. The action of the Pleistocene glaciers has eroded the highlands into low lying islands on broad, flat platforms. Material from the highlands has been deposited in the valleys to form an almost flat continental shelf. The platforms consist of a crystalline complex of metamorphic rocks covered by a few centimeters of sediment. Gravel and large boulders make up a significant component of sediment cover on the platforms.

Since on the platforms the sediment is extremely thin and acoustic basement is crystalline rock, the low frequency propagation is expected to be poor. High impedance contrast combined with the rough surface leads to the expectation of high bottom reverberation levels. Indeed, one measurement on the Svalbard Platform near Bear Island showed large time spreading in the acoustic signal and relatively poor low frequency acoustic propagation. This interpretation is consistent with similar environments in other areas.

Areas between the platforms are relict valleys filled in with thick layers of glacial deposits composed of sand, mud, and gravel. The sand and gravel appears to be common near islands and continental land areas. Mud appears to be the principal sediment in the troughs, depressions, and near the shelf edge. Acoustic propagation then, is expected to be moderate on the shelf and excellent in the troughs. Limited data indicates that these acoustic characteristics are typical of similar provinces throughout the marginal seas. Figure 6 presents the provinces and IBLUG class for the Kara Sea, Figure 7 the Laptev Sea; Figure 8 the Siberian Sea; and Figure 9 the Chukchi Sea.

These bottom loss assignments are intended to be used as interim solutions

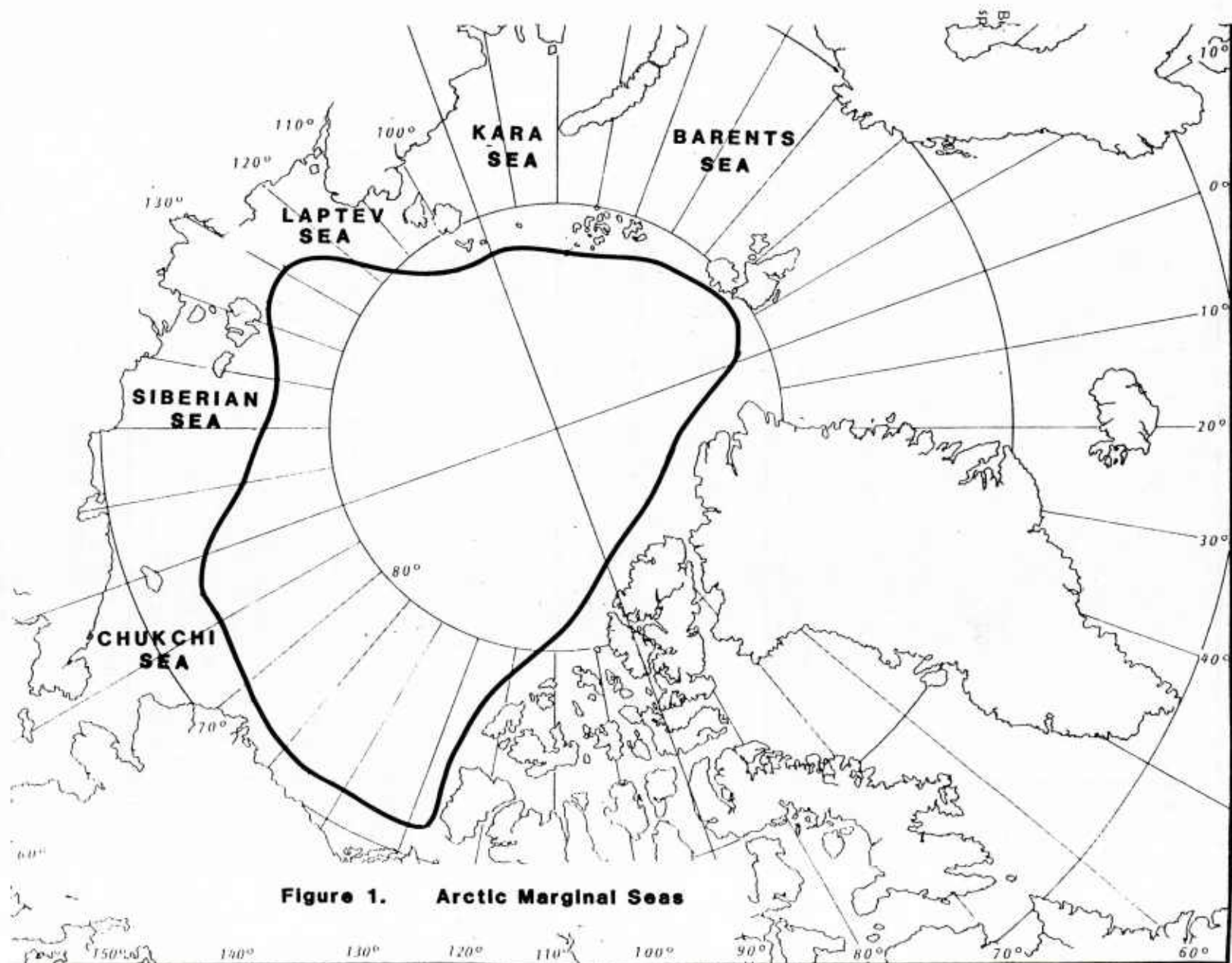
until a more thorough analysis is completed.

Conclusions

There are two aspects of bottom interaction to be considered in the Arctic: 1. Propagation of low frequency acoustic energy through the sediments is expected to be good on the outer shelf and in the troughs and poor on the platforms and rises. 2. Bottom reverberation is expected to be high on the platforms and rises.

References

- Akal, T., S. Fiori, O. Hastrup and A. Parisotto, "Acoustic Transmission Loss Data for Some Selected Shallow Water Areas", SACLANT ASW Research Center Report SR-33, 1979, NATO CONFIDENTIAL.
- Aubell, A., "Some Acoustic Measurements in the Middle Region of the Barents Sea", Norwegian Defense Research Establishment Technical Note U-275 REF11QWOP, 1972.
- Eldholm, O. and M. Talawani, "Sediment and Distribution and Structural Framework", Geological Society of America Bulletin, pp. 1015-1029, July 1977.
- Eldholm, O. and J. Ewing, "Marine Geophysical Survey in the Southwestern Barents Sea", Journal of Geophysical Research, Vol. 76, No. 17, pp. 3832-3840, 1971.
- Gregory, L.A., "Ambient Noise in Norwegian Coastal Waters of Barents Sea", Office of Naval Research, ONR Report DR-160, 1971, CONFIDENTIAL.
- Hamilton, E.L., "Geoacoustic Modeling of the Sea Floor", Journal of Acoustical Society of America, 68(5), 1980.
- Heezen, B.C., M. Tharp, and M. Ewing, "The Floors of the Oceans", The Geological Society of America Special Paper 65, 1959.
- Hinz, K. and H.U. Schuluter, "The Geological Structure of the Western Barents Sea", Marine Geology, Vol. 26, pp. 189-230, 1978.
- Houtz, R. and C. Windisch, "Barents Sea Continental Margin Sonobuoy Data", Geological Society of America Bulletin, pp. 1030-1036, 1977.
- Houtz, R.E., "Seafloor and Near-surface Sound Velocities from Barents Sea Sonobuoy Data", Journal of Geophysical Research, Vol. 85, No. 89, pp. 4838-4844, 1980.
- Perry, R.K., H.S. Fleming, "Bathymetry of the Arctic Ocean", Naval Research Laboratory, Washington, D.C., 1985.
- Spofford, C.W., "Interim Bottom Loss Values and Geographic Assignment Based on Sediment Thickness", Science Applications, Inc., Report No. SAI-81-303-WA, 1980.
- Sundvor, E., "Seismic Refraction and Reflection Measurements in the Southwestern Barents Sea", Marine Geology, Vol. 16, pp. 255-273, 1974.
- "Final Report on Operation LEVEL OCEAN of Project ROUGH START, CINCEASTLANT Report CHEL 4335/3 Ops, 1978, NATO CONFIDENTIAL.
- GEBCO Chart No. 5-17, The Arctic, Canadian Hydrographic Service, Ottawa, Canada, 1979.
- "The Ocean Basins and Margins", Vol. 5, Edited by Alan E.M. Nairn, Michael Churkin, Jr. and Francis G. Stehli, Plenum Publishing Corporation.



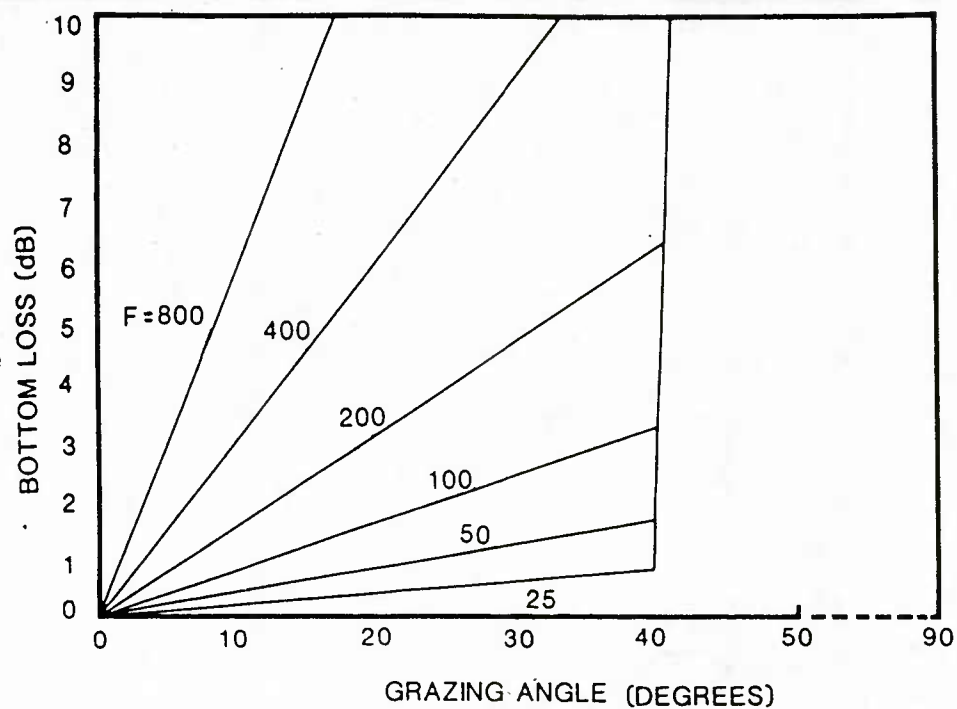


Figure 2. Bottom Loss Curves for Bottom Class 1.

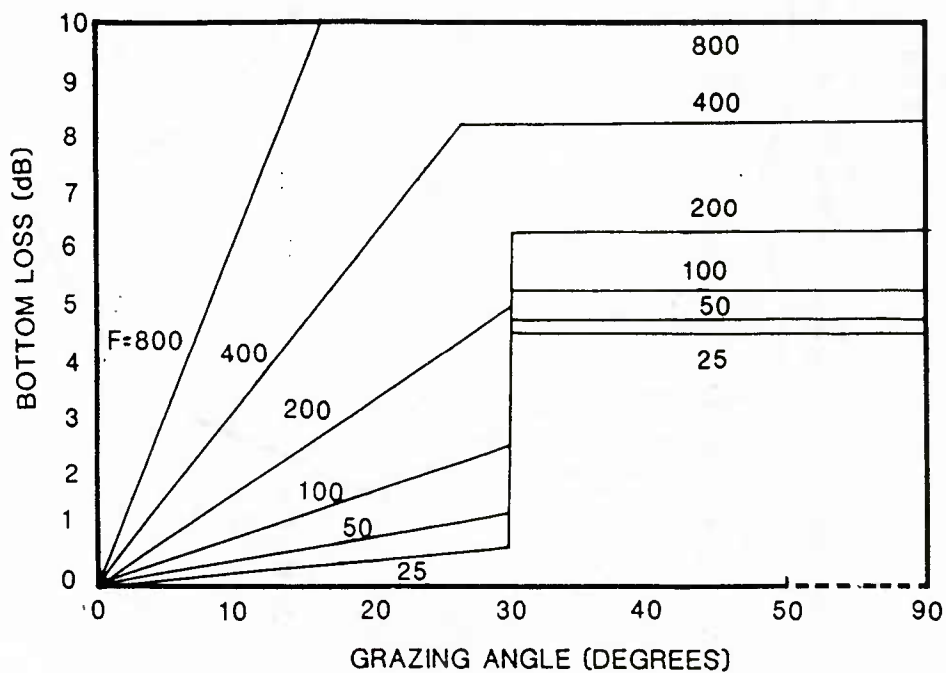


Figure 3. Bottom Loss Curves for Bottom Class 2.

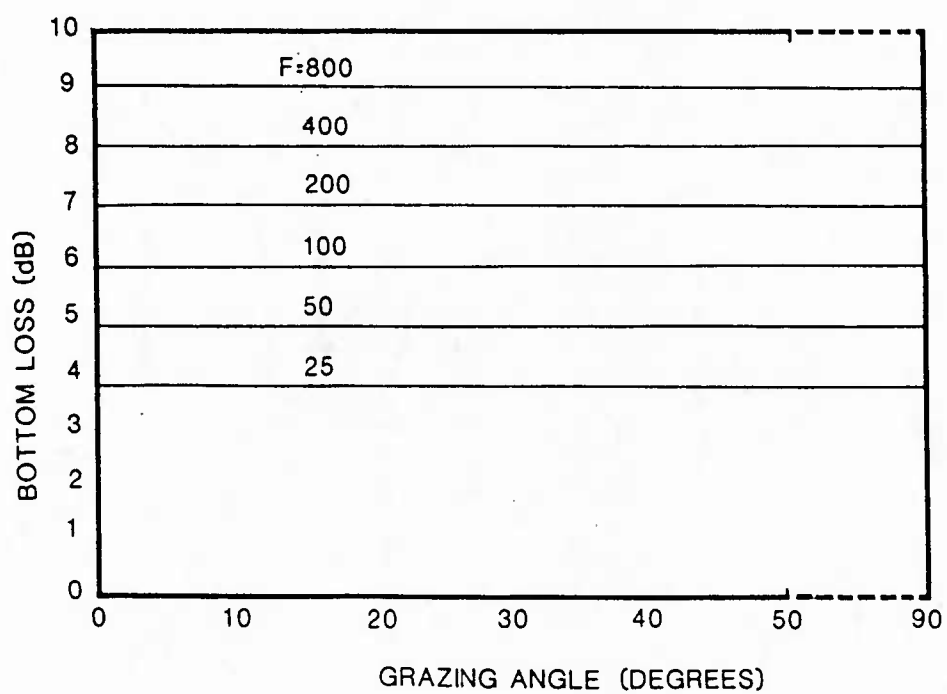


Figure 4. Bottom Loss Curves for Bottom Class 3.

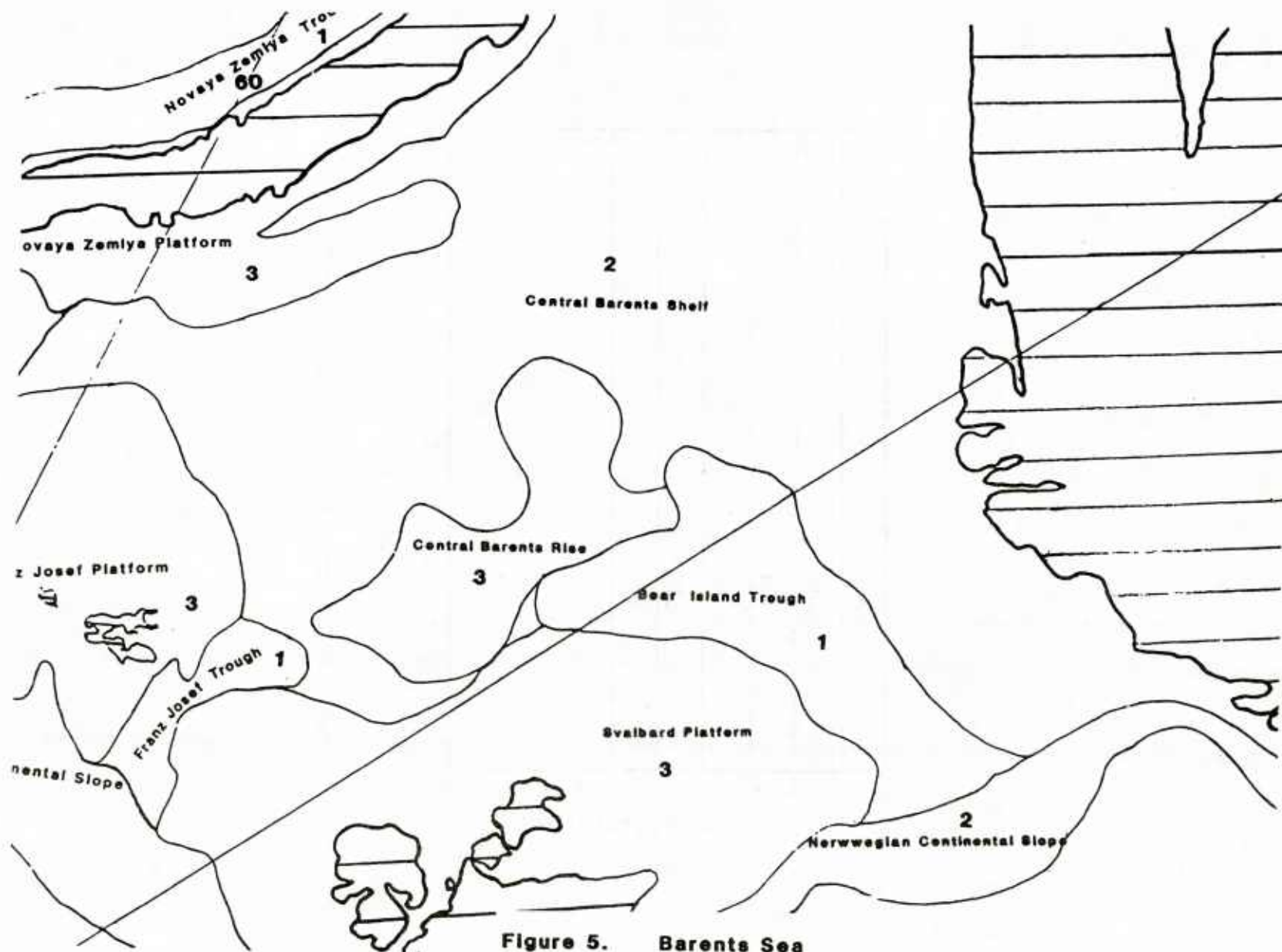
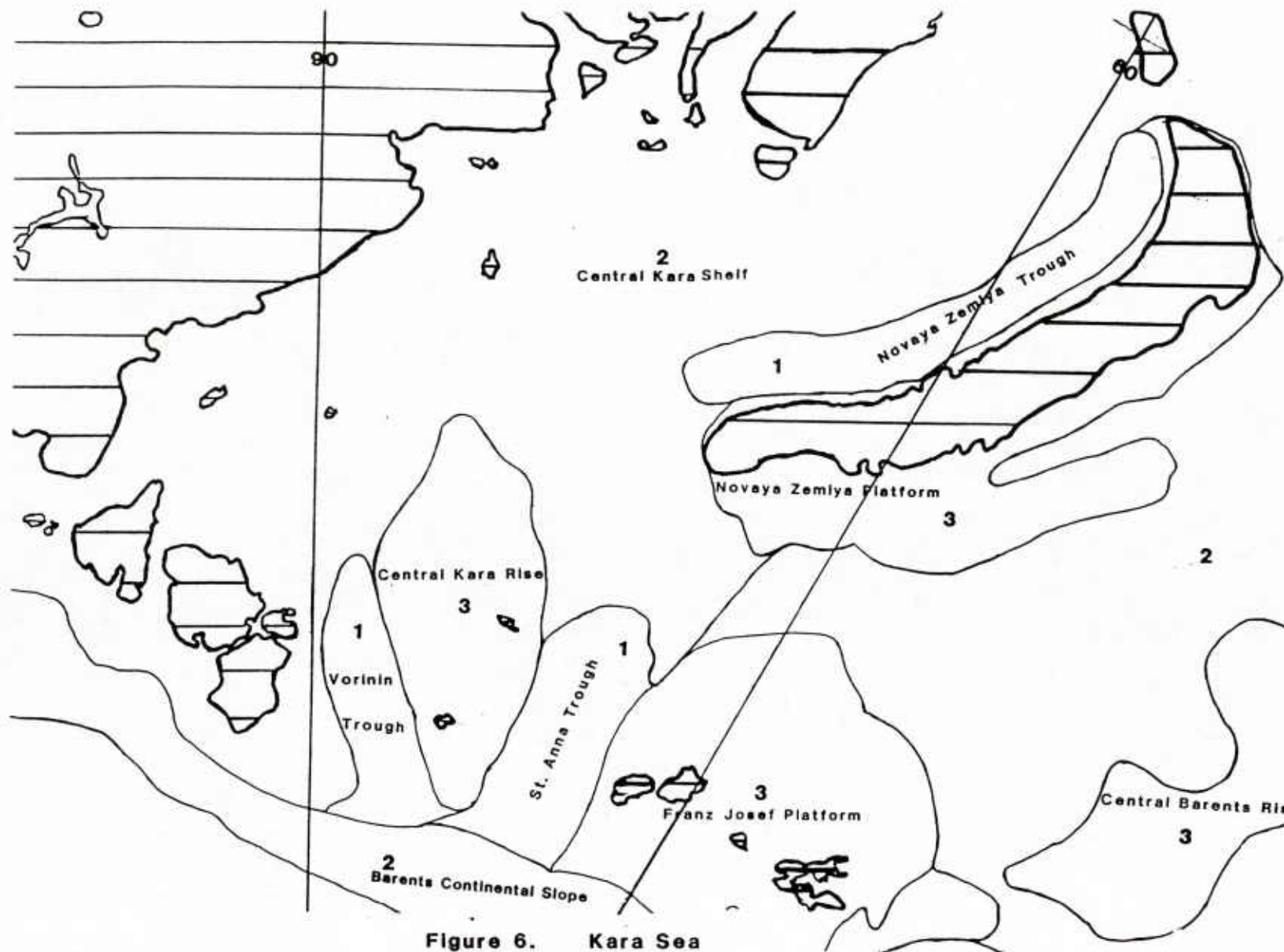
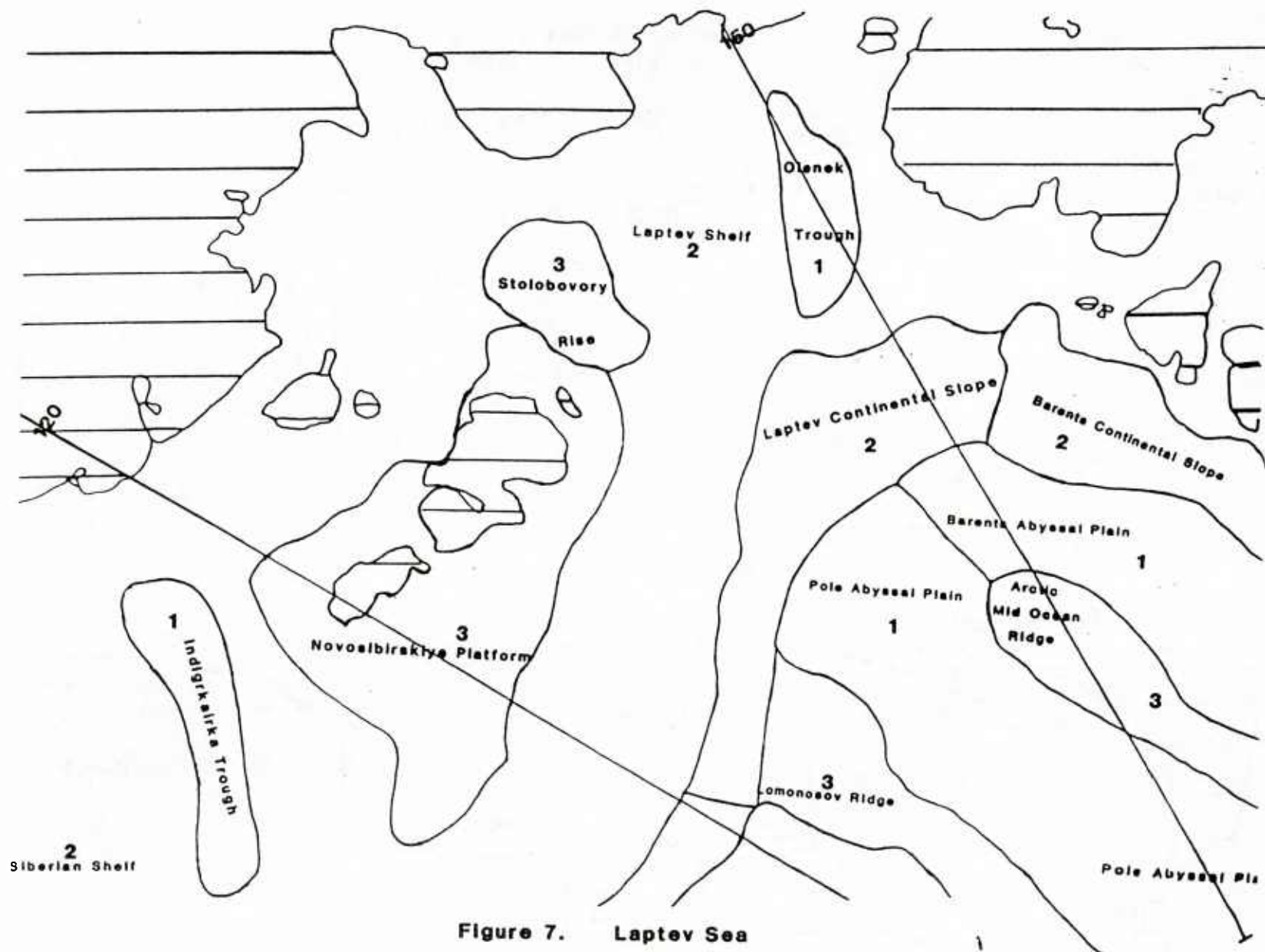


Figure 5. Barents Sea
Bottom Loss Provinces



**Figure 6. Kara Sea
Bottom Loss Provinces**



**Figure 7. Laptev Sea
Bottom Loss Provinces**

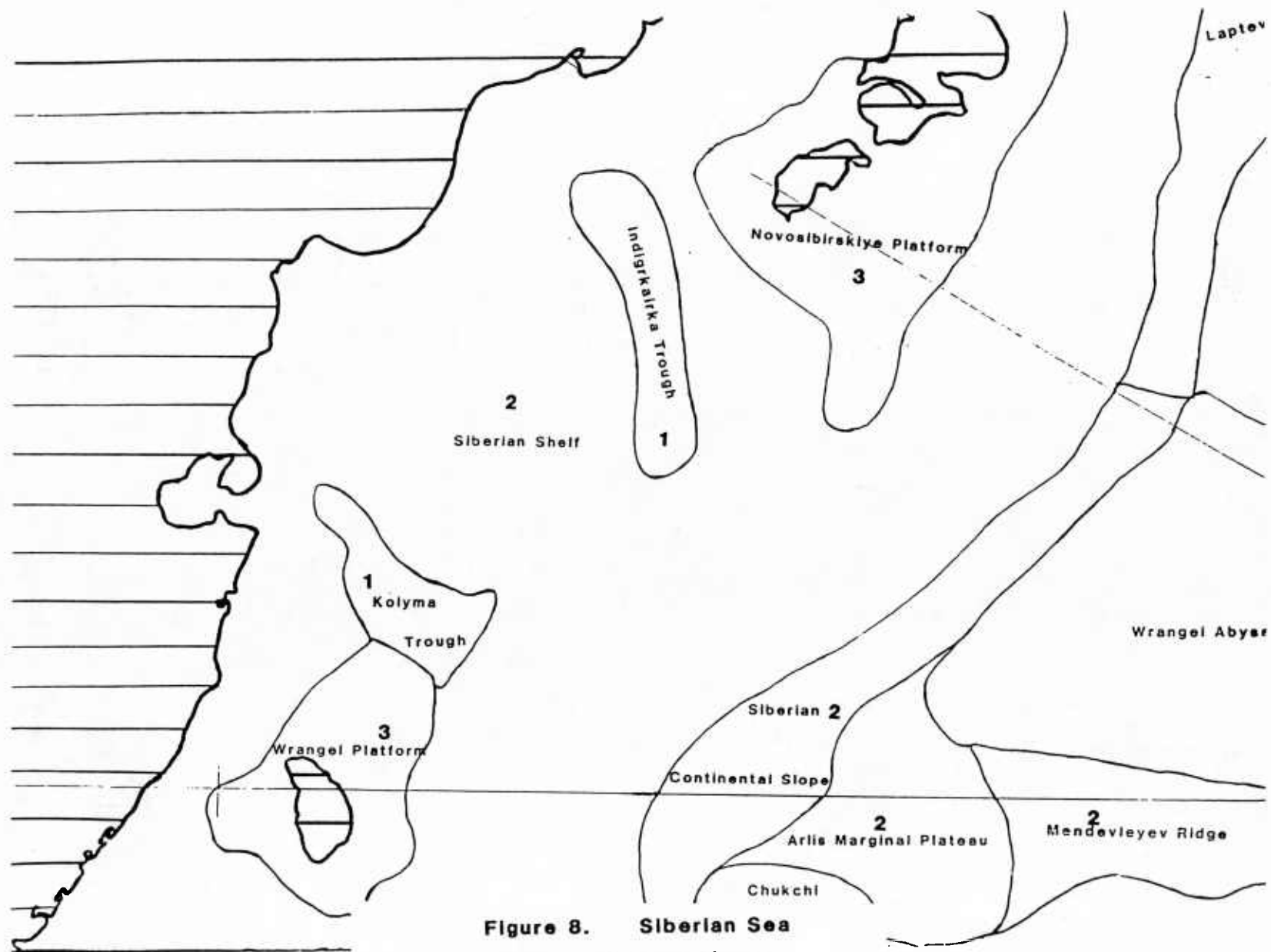


**Figure 8. Siberian Sea
Bottom Loss Provinces**

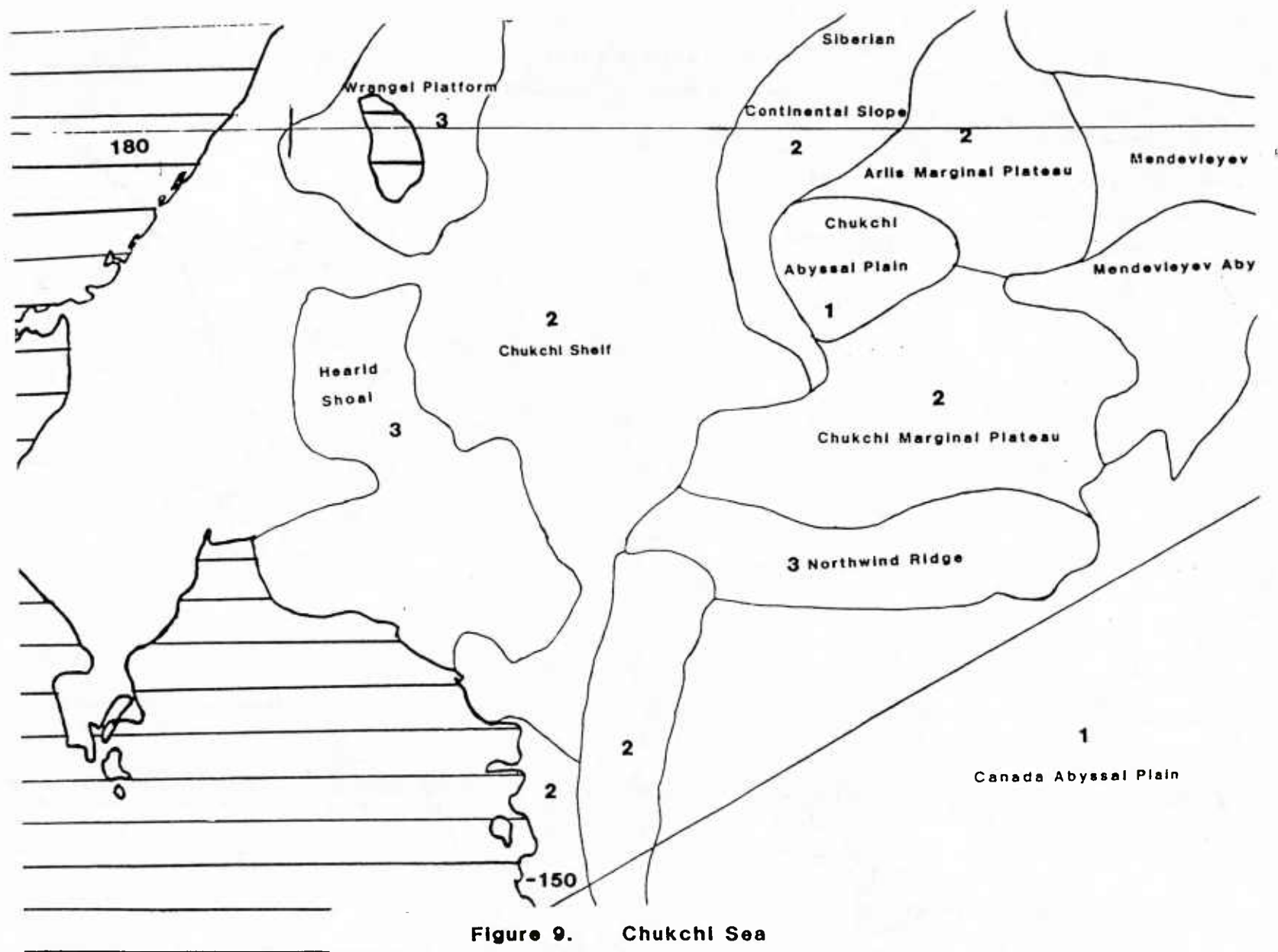


**Figure 9. Chukchi Sea
Bottom Loss Provinces**

ENVIRONMENTAL ACOUSTIC DATA BASE DEVELOPMENT IN THE ARCTIC

George A. Kerr

Naval Ocean Research and Development Activity
Code 223
NSTL, MS 39529-5004

ABSTRACT

Until recently, most computerized environmental data bases used in making underwater acoustic predictions have had less than worldwide coverage. In particular, the polar regions have often been neglected except by those intimately involved with studies of the surface ice-cover, iceberg movement, or world-wide weather prediction. With interest in Arctic acoustics growing, it is important that the best available environmental-acoustics data be made available for acoustic model predictions. This paper describes such a data base currently under construction by the Naval Ocean Research and Development Activity (NORDA). The paper describes some of the data sets which will be used for low-frequency, range-independent acoustic model input. The data base management system used to store and retrieve information from the various data sets is also briefly described.

INTRODUCTION

The Naval Ocean Research and Development Activity (NORDA) has been tasked by the Basic Acoustic Users Service (BAMUS) program to build and maintain an Arctic Environmental Acoustic Data Base (AEADB). One of the prime functions of the BAMUS program is to respond to requests from throughout the acoustics community for acoustic predictions using the models and data bases resident at NORDA. With interest now high in the Arctic, it was decided to increase BAMUS coverage to include all ocean areas in the northern hemisphere which are seasonally ice-covered. The first applications for this data base will involve low-frequency, range-independent, acoustic modeling applications. NORDA's first phase of data base development will involve the collection, storage, and retrieval of data to meet this requirement.

DATA BASE DESIGN

NORDA plans to design AEADB around the INGRES relational data base system resident on NORDA's VAX 11/780 minicomputer. Using such a relational based data base will permit the use of similar data base management systems resident on other computers without extensive software revision. A major benefit of a relational data base system is

that it permits interaction between the various data sets comprising the data base. For example, depth excess can be determined from the combined use of bathymetry and sound speed data sets, or keel parameters can be determined from the information provided by under-ice roughness and ridge frequency data. Another benefit of using such a system is that it greatly simplifies the tasks normally associated with data base design and maintenance. A majority of the data files residing in the data base will be indexed sequential access mode files built around tables created from the individual data sets. One of the goals to be met in the design of the data base is to permit rapid retrieval of information at the expense of disk storage space. A 300 megabyte removable disk pack is presently being used for data base development.

The data base will consist of two major elements; a gridded data base and an ungridded data base. Each of these elements will be contained on a separate removable disk pack. Some data sets resident in the gridded data base will consist of data with area-wide coverage. For example, seasonal sound speed profiles representative of relatively large areas will be contained in a gridded sound speed data set. This type of information will be queried by testing the data set for the grid which surrounds the location at which data is desired. Other types of gridded data sets, (e.g. bathymetry, ice parameters, etc.) will contain information located at grid lines intersections. Information contained in these data sets will be extracted using two dimensional linear interpolation. The ungridded data base will contain information gathered at a particular location and time. For example, the Marginal Ice Zone Experiment-West (Bering Sea) Conductivity-Temperature Depth data soon to be obtained from the National Snow and Ice Data Center or future acoustic experimental data will be included as a data set within the ungridded data base. The ungridded data base will provide the raw information from which updates or new gridded data sets can be formed.

The system will include a series of menus which will provide the user with an overview of the contents of the data base, and permit menu driven queries to be exercised. Some of these menus will perform specific functions, such as defining the default data sets to be included in a users sessions with the system. Another menu will allow the user to view the spatial and temporal bounds

of each data set. Extensive use of graphics terminals is expected for this and other data base functions. Other menus will allow the user to extract information from the data base, and reformat the data for his or her own particular application, or to perform simple statistical analyses or plotting of retrieved data sets. Magnetic tape output of extracted data according to user's specifications will also be included as a future menu item.

Contouring routines have been acquired for use within AEADB. These routines can be used to provide maps of the various gridded data set variables or any parameter derived from them. For example, charts of the ocean bottom can be obtained from the bathymetry data set, and depth excess can be obtained from the combined use of the bathymetry and sound speed profile data sets.

DATA SETS INITIALLY INCLUDED

The AEADB will have a geographical coverage from 40° N to the North Pole for all 360° of longitude. At the present time there are several in house data sets which were obtained for inclusion in the AEADB. These include the National Ocean Data Center's (NODC's) Climatological Atlas of the World Ocean, Fleet Numerical's Master Oceanographic Observation Data Set (MOODS), the Naval Oceanographic Office's (NAVO's) Digital Bathymetric Data Base (DBDB), NAVO's Standard Ocean data sets for the North Pacific and North Atlantic Oceans, the Naval Polar Oceanography Center's (Suitland, Md.) Arctic ice field data set, NORDA's AUTOOCEAN data set, a gridded LeSchack's surface ice roughness standard deviation data set, a monthly ice extent and thickness data set derived by NORDA through the use of Hibler's model, and a low frequency (IBLUG) bottom loss data set.

Some of the above data sets include portions of the ocean which cannot be considered as belonging to the Arctic or other seasonally ice covered areas. Therefore, those portions of the above mentioned data sets which do not reside in areas which have the potential of being ice covered may be excluded from AEADB disk if disk storage capacity is exceeded.

The NODC Climatological Atlas of the World Ocean

This digital atlas of the world ocean contains a synthesis of all temperature, salinity, and oxygen data available from NODC's Oceanographic Station Data, Mechanical Bathythermograph, and Expendable Bathythermograph files. The data were analyzed in a consistent, objective manner at standard oceanographic depth levels on a one-degree latitude-longitude grid between the surface and ocean to a maximum depth of 5500 m. The four seasonal data sets contain information at 24 standard depths between the surface and 1500 meters. The annual data set will be used to extend the seasonal data sets to deeper depths.

Sound speed profiles will be formed from the resulting temperature and salinity profiles. Both temperature and salinity profiles will be retained in the gridded disk data base. The sound speed profiles can be made available for acoustic model input through an application of any of the sound speed equations. The salinity profiles can be used to provide an estimate of salinity for use in constructing sound speed profiles from bathythermograph profiles.

As with any oceanographic profiles formed by an averaging process, important gradient information may be averaged out. This is especially important in the shallow portions of the profiles where variability is high and surface ducting can take place. A further examination of acoustic ramifications brought about by this and other objective analysis derived data bases (Standard Ocean) must take place before total confidence can be assured.

FLEET NUMERICAL'S MOODS

MOODS was intended primarily for the storage of profile data taken by mechanical bathythermographs; ship-dropped, air-dropped and submarine-launched expendable bathythermographs (XBTS); Nansen casts and the Salinity Temperature Depth (STD) class of instruments used in a depth profile mode. The MOODS data set not only includes the holdings of NODC but also includes Japanese, Korean, British, French, and Norwegian data not included in the NODC data set. The next update of MOODS, expected during FY 85, should also include portions of the Naval Oceanographic Office's data holdings. MOODS is most probably the most extensive set of raw oceanographic data available today. The MOODS data set will be separated into two data sets; XBT type and STD type. The STD data file will remain on the disk system for extractions of representative sound speed profiles and other oceanographic analyses. The XBT data file will be stored on magnetic tape, but will be made accessible through the disk based system if desired.

NORDA's AUTOOCEAN

AUTOOCEAN is a digital data base residing at NORDA which contains all those parameters normally required for input into the acoustic models. Sound speed profiles and wave heights are available on a seasonal 5 degree grid from 60° S to 60° N. Portions of the Barents Sea have also recently been included. Smith-Menard bathymetry, Bassett-Wolff low-frequency bottom-loss, NAVO high-frequency bottom-loss, and the Synthetic Bathymetric Profiling System bathymetry are also available in the Northern Hemisphere. A new non INGRES VAX 11/780 version of AUTOOCEAN has recently been made available by Ocean Data Systems, Inc.. In the future a new INGRES based AUTOOCEAN will be developed within the AEADB.

At the present time only the sound speed profiles obtained from the AUTOCEAN data set are being incorporated into AEADB. With the exception of the wave height and high-frequency bottom-loss data sets, all other AUTOCEAN data sets have been replaced by higher quality data within AEADB. High-frequency bottom-loss will be incorporated within AEADB when a high-frequency, under-ice acoustic model becomes available.

Additional sound speed profile selection analyses have been performed for all 5 degree square areas north of 60° N. Additions to the AEADB AUTOCEAN sound speed profile data set will be made on the basis of these analyses. Most of the new additions will be made in the relatively data rich areas near Greenland. It is expected that the soon to be released version of the MOODS data base may provide additional data in areas which are now data void. In addition, information from recent experiments in the Arctic will be used to update the existing AEADB AUTOCEAN data.

For Arctic applications, wind speed data will probably be of more direct value than wave height. Wave heights, if required can be obtained from wind speed. We are currently seeking to obtain the wind-field data set used in Hibler's ice model. Unlike similar data sets derived from objective analyses, AUTOCEAN sound speed profiles have been measured in situ. These sound speed profiles were selected from the subset of all available profiles in a given area for a given season. The selection process involves the testing of each profile for closeness to the mean sound speed profile in addition to closeness to the average layer depth and average depth of the deep sound channel axis.

Interim Bottom Loss Upgrade

The Interim Bottom Loss Upgrade (i.e. Interim Spofford-Hanna) data base contains a set of loss versus grazing angle curves (types 1, 2, and 3) that are based upon sediment thickness. The data base presently covers essentially the entire world's oceans. In the Northern Hemisphere the data base contains information to 80° N. Planning Systems Inc. has been tasked to extend the data base to 90° N.

Naval Polar Oceanography Center Data

Monthly digital data of 15 nautical mile minimum resolution, from 45° N to the North Pole has been made available for the area from 90° W to 90° E. The remaining half of the data base will not be available until later in FY 85 or early FY 86. Some of the data which can be extracted from this data set includes maximum-mean-minimum ice edges, probability of occurrence of any ice, mean ice concentration, and predominant ice type. These data are the result of analyses of data spanning from 2 to 11 years.

NORDA's Polar Ice Prediction System

(Preller (1985))

NORDA has implemented Hibler's dynamic/thermo-dynamic sea ice forecasting model at FNOC. Results from the spin-up of this model, the climatology, have been output for use in the AEADB. Parameters include ice drift velocity, ice thickness, ice concentration, ice growth, ice strength, and ice convergence/divergence. These variables have been made available on a monthly basis. The model currently includes the Arctic Basin plus the Barents and East Greenland-Norwegian Seas. The model output is of a 127 km spatial resolution. In the future regional ice models beginning with the development of a regional Barents Sea model during FY 85 will be available.

NUSC Norwegian Sea Sound Speed Profiles

Podeszwa (1979) has analyzed acoustic and environmental data for the Norwegian Sea, Baffin Bay, Davis and Denmark Straights, Greenland, Barents and North Seas, and has produced a series of sound speed province charts for these areas. For each province, monthly sound speed profiles are available. The province charts have been digitized to one half degree spatial resolution so that the monthly sound speed profiles may be extracted by latitude and longitude rather than by province number.

LeSchack's Surface Ice Roughness Standard Deviation

LeSchack's (1977) updates chart contains annual surface ice roughness standard deviation contours for the Arctic from approximately 70° N to the North Pole. Green's (1984) algorithm will be used to convert these data, with the addition of Wittmann and Schule's (1966) ridge frequency data, to determine keel parameters required by the under ice low frequency acoustic models now under development.

NAVO Standard Ocean

This seasonal, 1 degree square spatial resolution, objective analysis produced data set consists of temperature, salinity, and sound speed profiles for the North Atlantic and North Pacific Oceans. The available Mediterranean Sea data base will not be included in AEADB. While these data sets do not now extend into the Arctic Ocean, they do cover several important seasonally ice covered marginal seas.

Future Data Base Acquisitions and Capabilities

After the requirement to provide an Arctic low frequency acoustic modeling capability has been met, the data base will be expanded to include data available from recent experiments in the

Arctic. Data from the various marginal ice zone experiments (MIZEX) available from the National Snow and Ice Data Center, Boulder, Colorado, will probably be one of the first new data acquisitions. A bibliography of available references pertaining to underwater acoustics in the Arctic will also be constructed using those compiled by Planning Systems Incorporated's, Slidell, Louisiana office as the first version. Buck's Arctic noise models will also be included in the near future.

References

Green, R. R., 1984. SAI Interim Scattering Model/Ice (SISM/ICE). Science Applications Inc., McLean, Virginia, SAI-84/1100, April.

LeSchack, L. A., 1977. Arctic Under-ice Roughness. Development and Resources Transportation Co., Technical Report.

Podeszwa, E. M., 1979. Sound Speed Profiles for the Norwegian Sea. Naval Underwater Systems Center, New London, Connecticut, NUSC Td 6035, June.

Preller, R. H., 1985. The NORDA/FNOC Polar Ice Prediction System (PIPS) - Arctic: A Technical Description. Naval Ocean Research and Development Activity, NSTL, Mississippi, NORDA Technical Report 108, May.

Wittmann, W. I., J. J. Schule, 1966. Comments on the Mass Budget of Arctic Pack Ice. Proceedings of the Symposium on the Arctic Heat Budget and Atmosphere Circulation, Rand Corp., RM-5233-NSF.

UNDER-ICE AMBIENT NOISE VARIATIONS AS RELATED TO OBSERVABLE ICE MOTION PARAMETERS

James K. Lewis
Warren W. Denner

Science Applications International Corporation
1304 Deacon
College Station, TX 77840

ABSTRACT

Under-ice ambient noise is discussed in terms of the generation of the noise by the five basic modes of motion. Ice translation is used as an indicator of turbulent energy plus the ice rushing through the water column. Divergence of an ice parcel is used as the indicator of lead/ridge formation plus a method for damping floe/floe interaction during the summer. Ice parcel deformation is discussed in terms of noise generation as floes move past one another during a rearrangement process. Preliminary analysis of summer data show that ice parcel translation speed and divergence can account for up to 70% of the variance of the noise at 10 Hz. The correlation between these two kinematic parameters and the 10 Hz signal is 0.84, and the noise is positively correlated with the divergence.

energy increases, one can expect a corresponding increase in turbulent energy. Thus, $|\vec{U}|$ can be an indicator of noise increases due to the ice rushing through the water plus greater floe/floe bumping as a result of turbulence.

Divergence is a direct measure of lead and ridge formation. Spreading within an ice field ($D > 0$) can cause the ice to fault under tension, and one would expect a corresponding increase in noise. As the ice converges ($D < 0$), one of two things can happen, depending on the season. During the summer when it is not cold enough to produce new ice, ice convergence can act as a method for damping floe/floe interaction, and the noise level falls. However, if new ice forms in the leads, convergence can cause noise increases as the young ice is crushed.

1. INTRODUCTION

A majority of the lower frequency ambient noise variations in the Arctic is a direct result of the response of sea ice to wind forcing, given the strength of the ice. Buoys drifting with the ice give kinematically the response of the ice to the wind, so one might expect a relationship between the under-ice noise variations and the kinematics of the ice. The kinematics of ice can be described by the 5 basic modes of motion (Figure 1):

- \vec{U} - translation (net displacement per unit time),
- ζ - vorticity (the change in the orientation of the ice without a shape or size change),
- D - divergence (the change in size of a parcel of sea ice, without an orientation or shape change),
- N - normal deformation rate (the change in the shape of an ice parcel due to forces normal to the sides of the parcel, without a size or orientation change), and
- S - shear deformation rate (the change in the shape of an ice parcel due to forces acting parallel to the sides of the parcel, without a size or orientation change).

These 5 modes of motion are related to the generation of under-ice noise in distinct and independent ways. The translation of the ice can be used as a measure of kinetic energy. As this kinetic

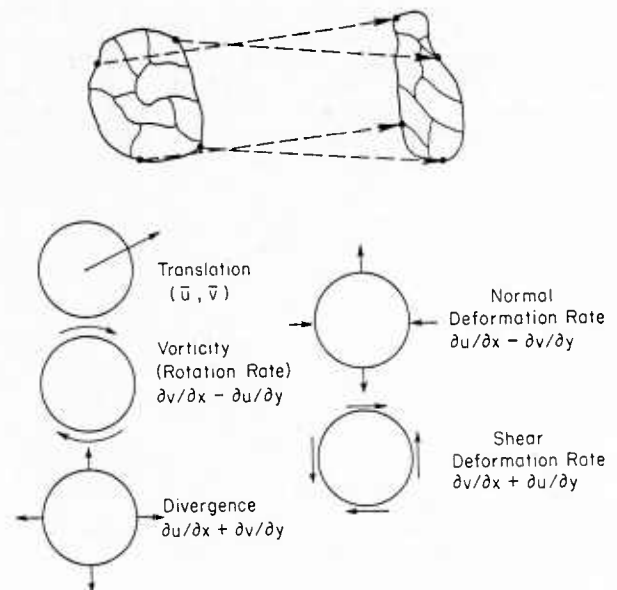


Fig. 1. Mathematical and physical definitions of the five basic components of the motion of a parcel of ice.

Deformation of an ice field can be thought of as a shape change only, with no area change. Thus, a rearranging of the individual floes is all that may be required to take on the new shape configuration. This rearrangement will result in the breaking of any bonds between adjacent floes plus the movement of floes past one another. Thus, one would expect an increase in under-ice noise with an increase in $|\dot{N}|$, $|\dot{S}|$ or $N^2 + S^2$ (total deformation).

Vorticity ζ (rotation rate) is an interesting parameter when the ice takes on the movement of the inertial oscillation. This motion is highly coherent in space, a result of the scales of the atmospheric forcing which triggers the motion. As a result, D , N , and S tend to oscillate at the inertial frequency (approximately 12 hrs in the Arctic). The end result is a strong inertial signal in the noise variations.

2. UNDER-ICE NOISE AND ICE KINEMATICS

A preliminary analysis of the relationships between ambient noise and associated ice kinematics has been made using data collected during the summer of 1975 during the Arctic Ice Dynamics Joint Experiment (AIDJEX). Figure 2 shows the AIDJEX study area, including Buoy 10 at which an omnidirectional hydrophone measured ambient noise in one-third octave bands centered at 3.2 Hz, 10 Hz, 32 Hz, and 1000 Hz. Figure 3 shows the 10 Hz and 1000 Hz noise variations at 3 hr intervals during August 1975. Since noise generated by lead and ridge formation is typically found in the 10-20 Hz band¹, only the 10 Hz data (referred to as S_{10}) are considered here.

We first note that there are two distinct periods of noise variations which oscillate at close to the inertial frequency (days 221-225 and 229-232). Secondly, note that the first set of these variations correspond well with inertial oscillations in the translation speed $|\dot{U}|$ of the manned camp

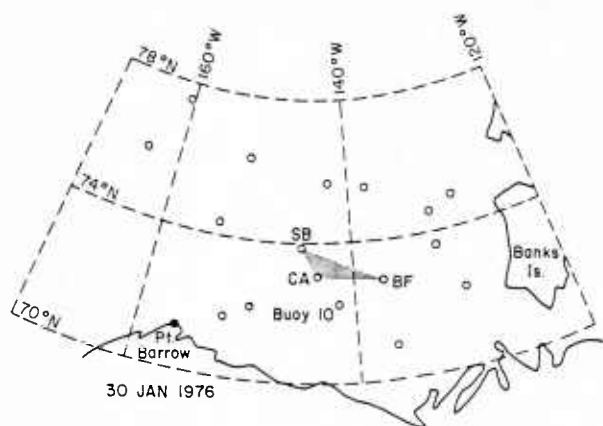


Fig. 2. Locations of a number of AIDJEX data buoys and manned camps (SB, CA, and BF) for 30 January 1976. Acoustic data discussed in this paper were collected at Buoy 10.

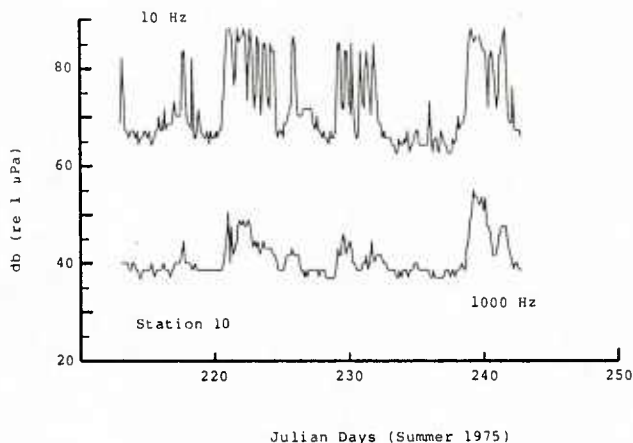


Fig. 3. Ambient noise variations, 10 Hz and 1000 Hz, Buoy 10, during August 1975.

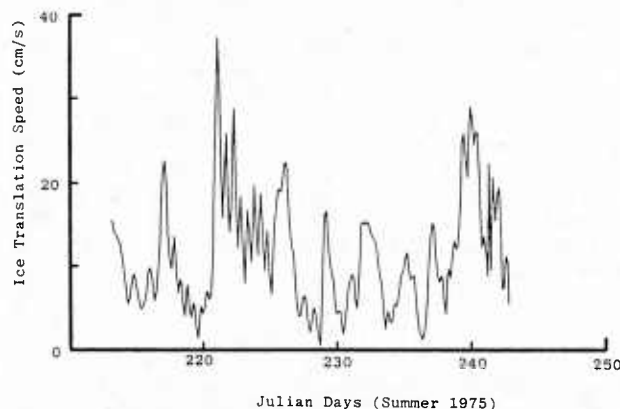


Fig. 4. Variations in the speed of the manned camp array during August 1975.

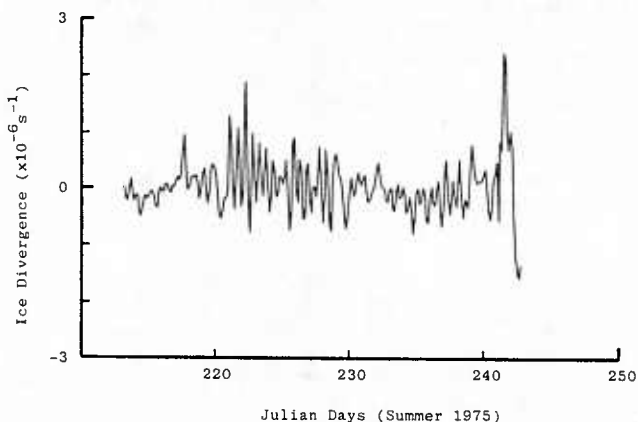


Fig. 5. Variations in the ice divergence between the manned camps during August 1975.

array (Figure 4), some 50 km north of Buoy 10. The general relationship between S_{10} and $|\vec{U}|$ is that peaks in S_{10} tend to occur during peaks in $|\vec{U}|$. Figure 5 shows the spatially averaged divergence between the manned camps. Once again, the first set of inertially-varying S_{10} data corresponds well to inertially-varying D . In this case, S_{10} tends to increase with D .

We performed a preliminary regression analysis using the 40 hr low-passed versions of these data sets. Considering only S_{10} and $|\vec{U}|$, the results were

$$S_{10} = 78.82|\vec{U}| + 63.4$$

with a correlation of 0.72, 52% of the variance accounted for, and a mean error of 3.38 dB. When divergence was incorporated into the regression formula, the results were

$$S_{10} = 60.65|\vec{U}| + 1.23 \cdot 10^{-8}D + 65.0$$

with a correlation of 0.84, 70% of the variance accounted for, and a mean error of 2.5 dB. These results are encouraging considering the distance between the manned camp array and the exclusion of the deformation rates N and S .

Research is continuing into the relationships between the ice kinematics and ambient noise variations. In particular, we are concentrating on the raw data (as opposed to the low-pass filtered versions) to determine which ice parameters are of greater importance and how this varies with season.

ACKNOWLEDGEMENTS

The authors wish to acknowledge the continued support of this research by the Office of Naval Research. We would also like to thank Dr. Ira Dyer for his most helpful suggestions and comments.

REFERENCES

- Dyer, I.: The Song of Sea Ice and Other Arctic Ocean Melodies. In Arctic Technology and Policy (I. Dyer and C. Chrysostomidis, eds.), Hemisphere Publ. Corp., New York, 1984, 11-37.

HORIZONTAL DIRECTIONALITY OF ICE EDGE NOISE

T. C. YANG, C. W. VOTAW, G. R. GIELLIS AND O. I. DIACHOK

Naval Research Laboratory, Washington, D.C. 20375

ABSTRACT

A ship-towed horizontal array experiment was performed by the Naval Research Laboratory in 1982 in the vicinity of the ice-water boundary in the East Greenland Sea. The array was towed approximately normal and parallel to the ice edge. Analysis of beam-formed acoustic data revealed that a few localized "hot spots" (with dimensions less than 5 km) were the dominant noise sources. These sources persisted for at least several hours. The nominal separation between the hot spots was about 30 km. The spectrum of the hot spots decreased by 12 dB per octave between 100 and 500 Hz, compared with the 6 dB per octave spectrum of typical sea noise.

1. INTRODUCTION

Ambient noise at some Arctic ice-open ocean boundaries is characterized by anomalously high levels, hypothetically generated by the interaction of ocean swell with ice floes. Representative data for diffuse and compact edges are shown in Figure 1. Also shown are expected levels for central Arctic and open ocean conditions at the same wind speed. No ice-edge peaks have been observed in the Denmark Strait (low swell) and in the Alaskan North Slope shore lead (no swell).

The data shown in Fig. 1 were collected with sonobuoy hydrophones in the Greenland Sea. Several interesting questions were

raised by this data set, namely, 1) are noise sources uniformly distributed along the ice edge (i.e., a line source), 2) what is the noise radiation pattern, and 3) what are the physical mechanisms for noise generation. A towed array experiment, specifically designed to help resolve these questions was conducted by the Naval Research Laboratory in the Spring of 1982. The array consisted of 64 hydrophones grouped into three sub-arrays with design frequencies of 100, 200, and 300 Hz. The aperture was 300 m; the array was towed at a depth of 100m, 60m behind the ship. The data reported in this paper was collected in a 24-hr period at a site north of Jan Mayen Island. The ship tracks are shown in Fig. 2.

The noise directionality measurements with this array reveal that ice edge noise is more nearly characterized as emanating from a few localized sources rather than as a continuous line. These "hot spots" were clearly resolvable from the towed array data at ranges of 15 or more miles from the ice edge; they persisted as dominant sources for many hours. The mechanisms of noise generation have not been identified, but a spectral slope of 12 dB per octave separated these sources from typical sea noise, which has a spectral slope of 6 dB per octave. The hot spot noise is hypothesized to be generated by ocean swell interaction with highly concentrated floes.

DATA ANALYSIS

Whether ice edge noise is distributed over a continuous line or concentrated at a few hot spots can be distinguished by spatial distributions of the received noise levels. In the case of a continuous line noise source, noise levels will decrease with distance between the receiver and the ice edge. This decrease of noise level can be measured with an array towed either away from or toward the ice edge. On the other hand, if the array is towed parallel to the ice edge, little variation of the noise level should be expected during one tow, assuming that the average source level remains constant throughout the experiment. The noise should be spread across many beams in the beamformed output when the array is parallel to the ice edge, but concentrated near end fire directions when the array is normal to the ice edge.

If the ice edge noise is concentrated at a few localized hot spots, beam noise levels will not follow the pattern described above; instead the noise should peak at a few dominant beams. The relative bearings of high power noise beams should change as the array changes location and orientation, always pointing toward the hot spots. In other words, the noise can be treated as target-like and can be localized using standard analysis involving towed array data of different tow locations/orientations.

The resultant data were subdivided into 3.2 minute segments, Fourier transformed with a window of 3.2 sec, and beamformed at several frequencies in the frequency range 100 to 500 Hz. Beam outputs for each 3.2 min. data sample were plotted, and bearings of the high noise power peaks were logged.

One of the major unwanted noise sources was tow-ship generated noise. The ship generated noise always appeared at fixed beams whereas ice edge noise moved to different beams as the array changed location and orientation. The direct arrival of the ship noise was dominant in the near endfire direction of the towed array (pointing toward the ship); bottom reflected ship generated noise was evident near 5 deg from broadside, consistent with geometrical considerations. These two noise sources were readily identified in the beam output data and were excluded from analysis.

The bearings of the dominant noise level peaks for the major runs in Fig. 2 are plotted in Fig. 3. The left-right ambiguity of the beam output was resolved with towed array data of different heading directions. Analysis of sequential beam power vs angle data displays revealed that noise level peaks in two or three directions consistently pointed to spatially well defined hot spots. The spatial extent of these spots was less than 5 km., and the nominal separation between spots was about 30 km. The hot spots illustrated in Fig. 2 persisted over at least several hours. Noise peaks which appeared only temporarily are not shown.

The array heading was not measured; it was assumed to coincide with the ship's heading. Azimuthal wander of the array would spatially smear the hot spots. Hence, the estimated dimension of these spots should be considered upper bounds.

The location of the ice edge (Fig. 2) was surveyed by the tow ship about 10 hours prior to the acoustic measurements. Since

the ice edge moves with a nominal speed of one half knot in unknown directions, the locations of the hot spots relative to the ice edge are uncertain by about ± 8 km. This implies that hot spots occur in close proximity to the ice edge, but not necessarily just within the ice boundary as Fig. 2 might suggest.

Aerial photographs can provide a more accurate determination of the ice edge location. Unfortunately, the very limited set of aerial photographs obtained during this experiment did not cover the points where the ice was noisiest. Currently available satellite information is of insufficient resolution to be useful.

The spatial extent and nominal separation of the noise generators resemble the dimensions of eddies in the East Greenland Sea², suggesting a possible link between noise hot spots and ocean eddies (a subject beyond the scope of this paper).

The spectral shape of ice edge noise associated with the hot spots is clearly distinct from typical sea noise. The beam output in the 100 to 500 Hz range showed a spectrum of 12 dB per octave, as compared with typical sea noise of 6 dB per octave. This result not only distinguishes ice edge noise from typical sea noise, but also provides a clue to the generating mechanism. Additional analysis will hopefully provide an estimate of the vertical radiation pattern.

SUMMARY

High resolution towed array measurements reveal that noise in the vicinity of the ice edge is horizontally anisotropic; noise level peaks emanate

from widely separated, spatially well defined hot spots. Ice edge noise is characterized by a 12 dB per octave spectrum, compared with the 6 dB per octave spectrum of typical sea noise.

REFERENCES

1. O.I. Diachok, "Arctic Hydroacoustics: Cold Region Science and Technology, 2, 185, 1980.
2. O.M. Johannessen et al., "Oceanographic Conditions in the Marginal Ice Zone North of Svalbard in Early Fall 1979 with an Emphasis on Mesoscale Processes". Jour. of Geophys. Research, 88, 2755, 1983.

FIGURE CAPTIONS

1. Ambient noise at compact and diffuse ice edge vs distance for comparison with noise levels under ice-free and totally ice-covered conditions.
2. Locations of ice edge, ship tracks and observed high noise areas (hot spots).
3. High level noise beams pointed to the noise hot spots.

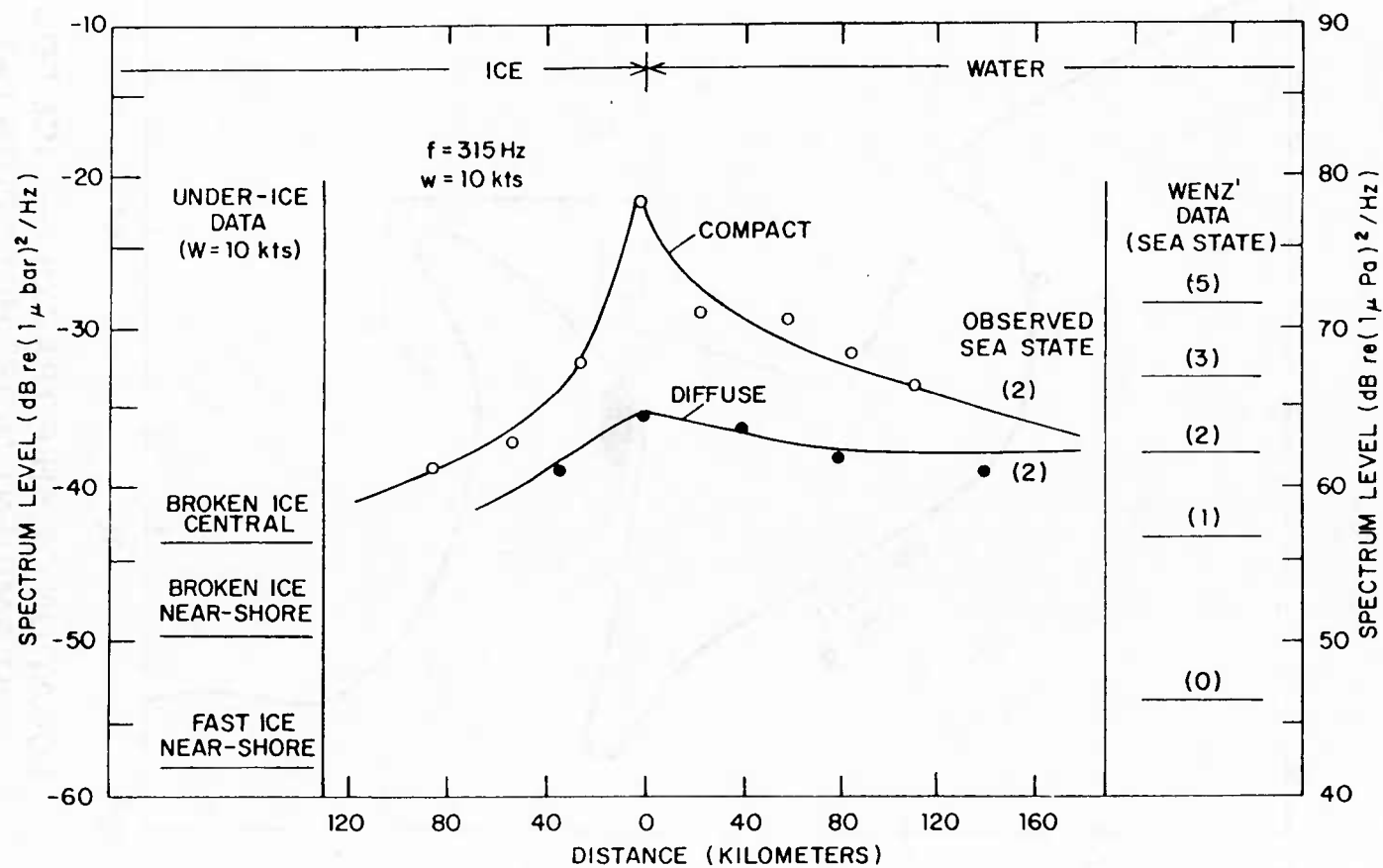
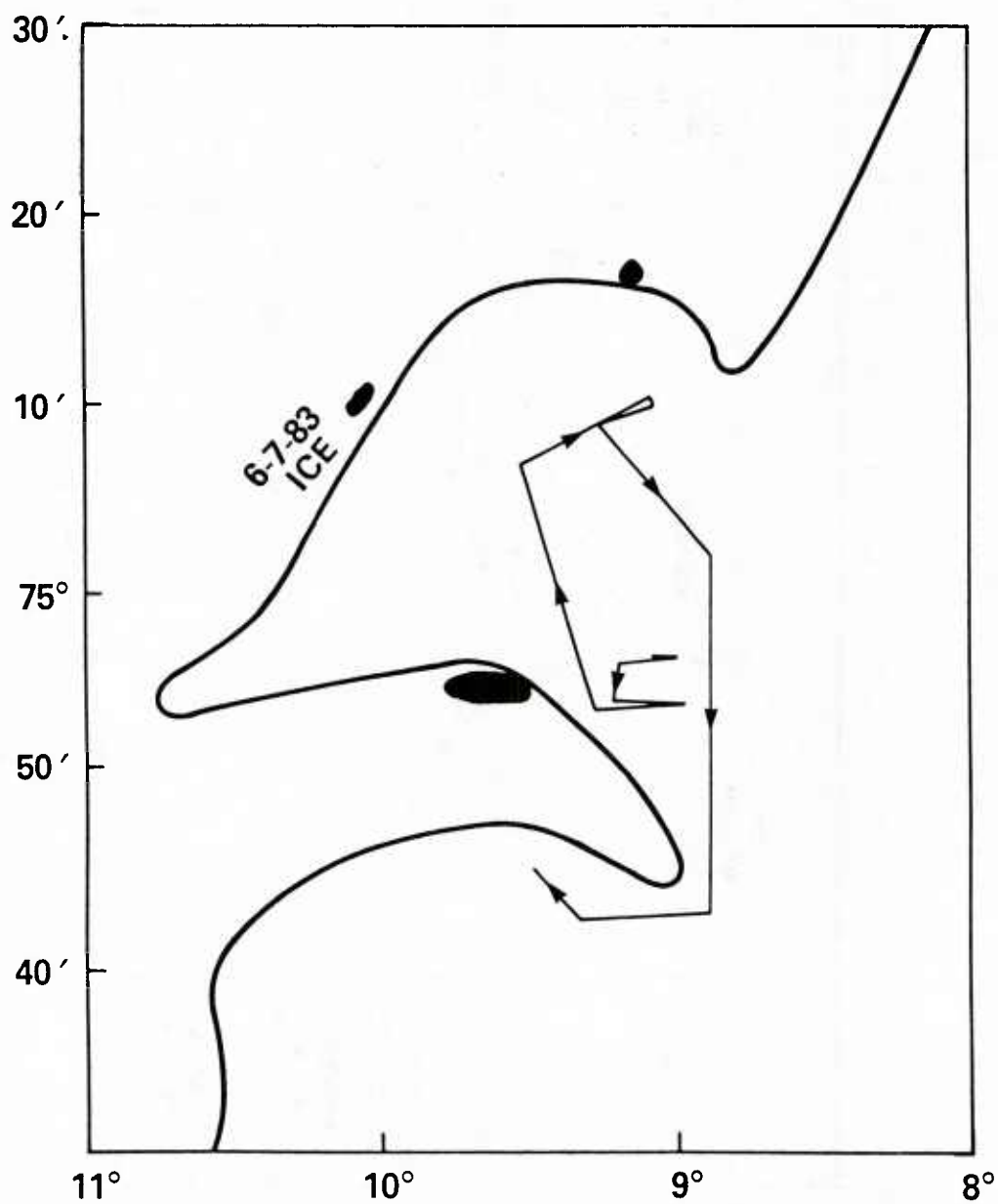


Fig. 1



LOCATION OF SHIP TRACKS (—), ICE EDGE,
AND AMBIENT NOISE HOT SPOTS (●)

Fig. 2

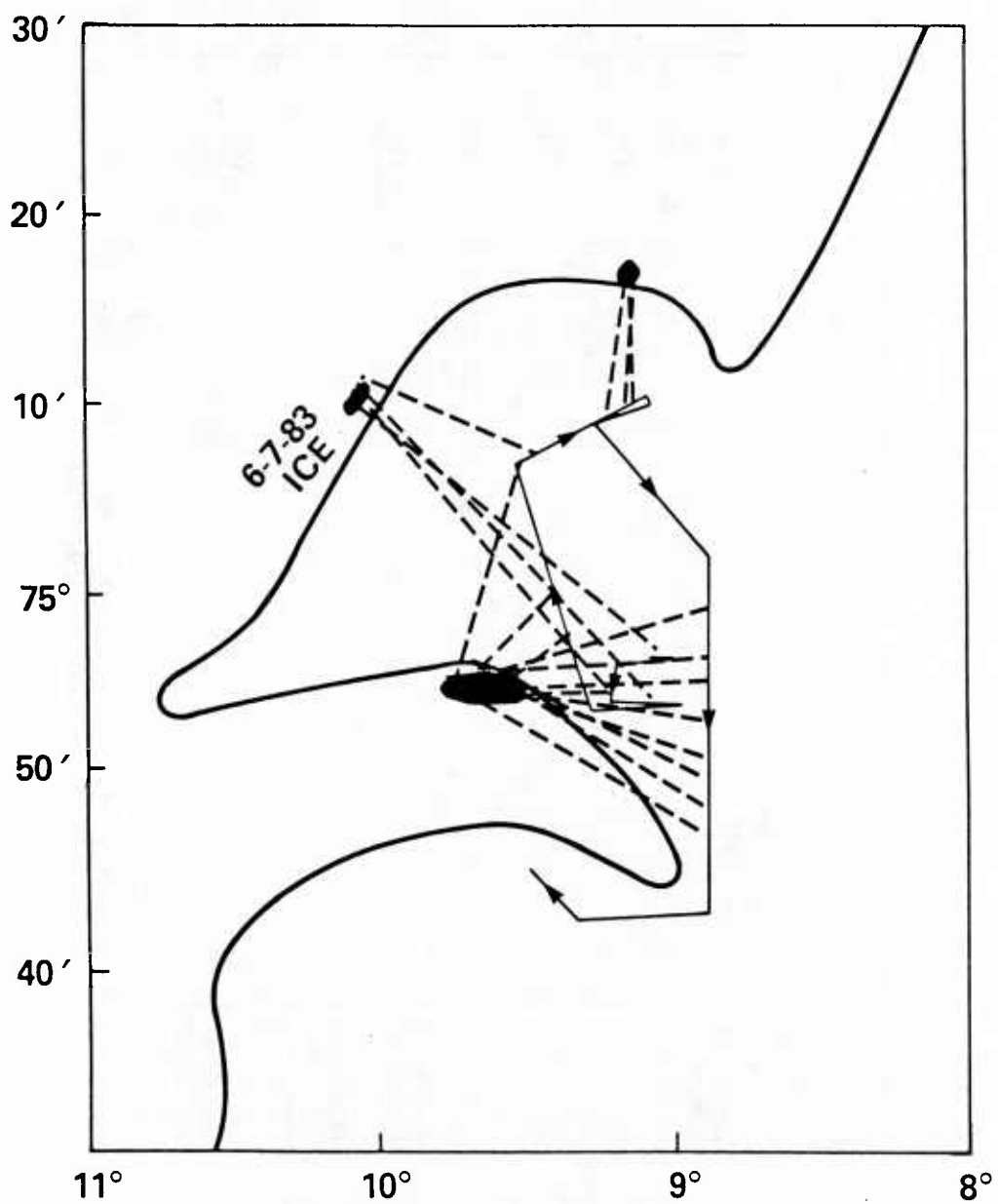
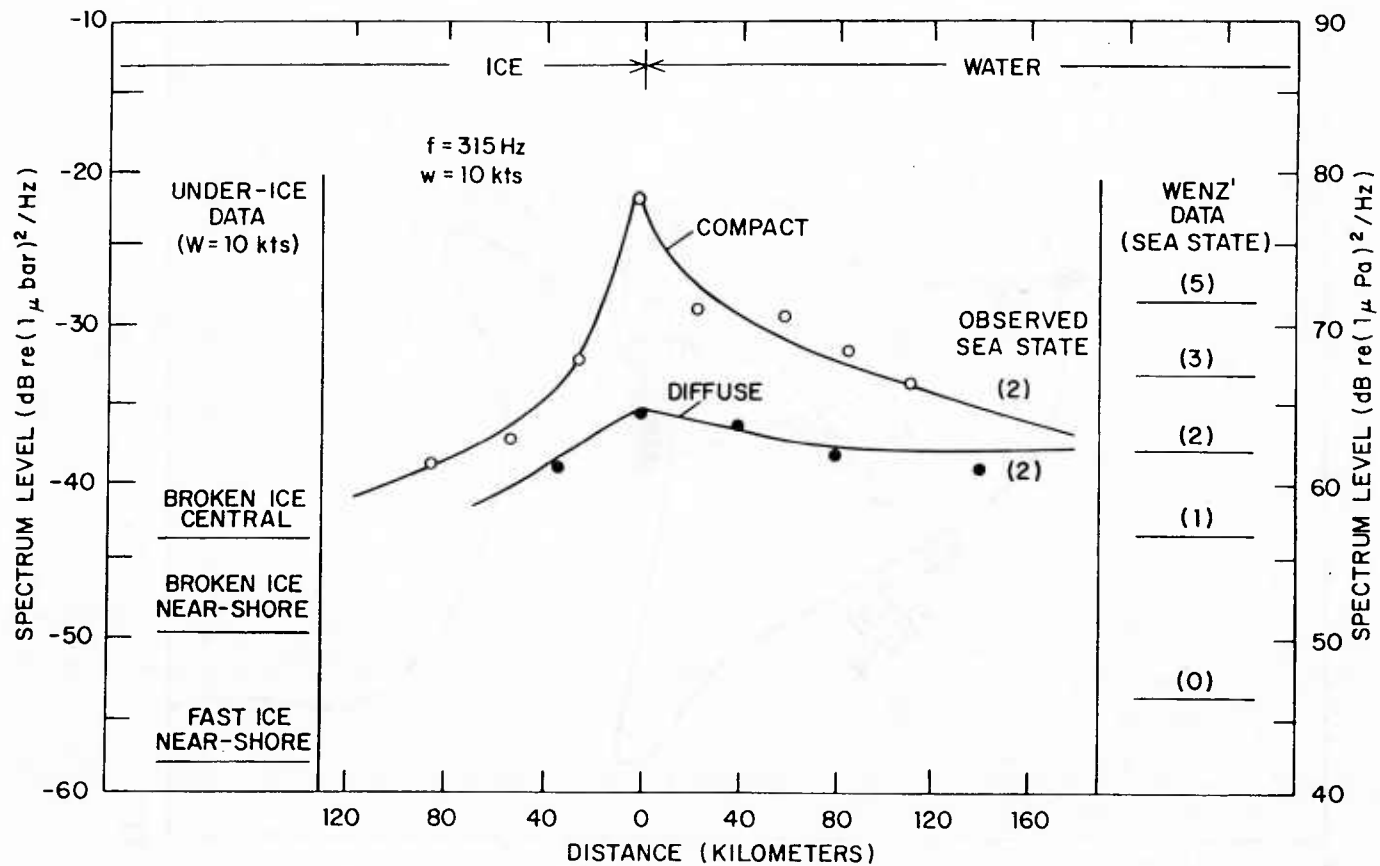
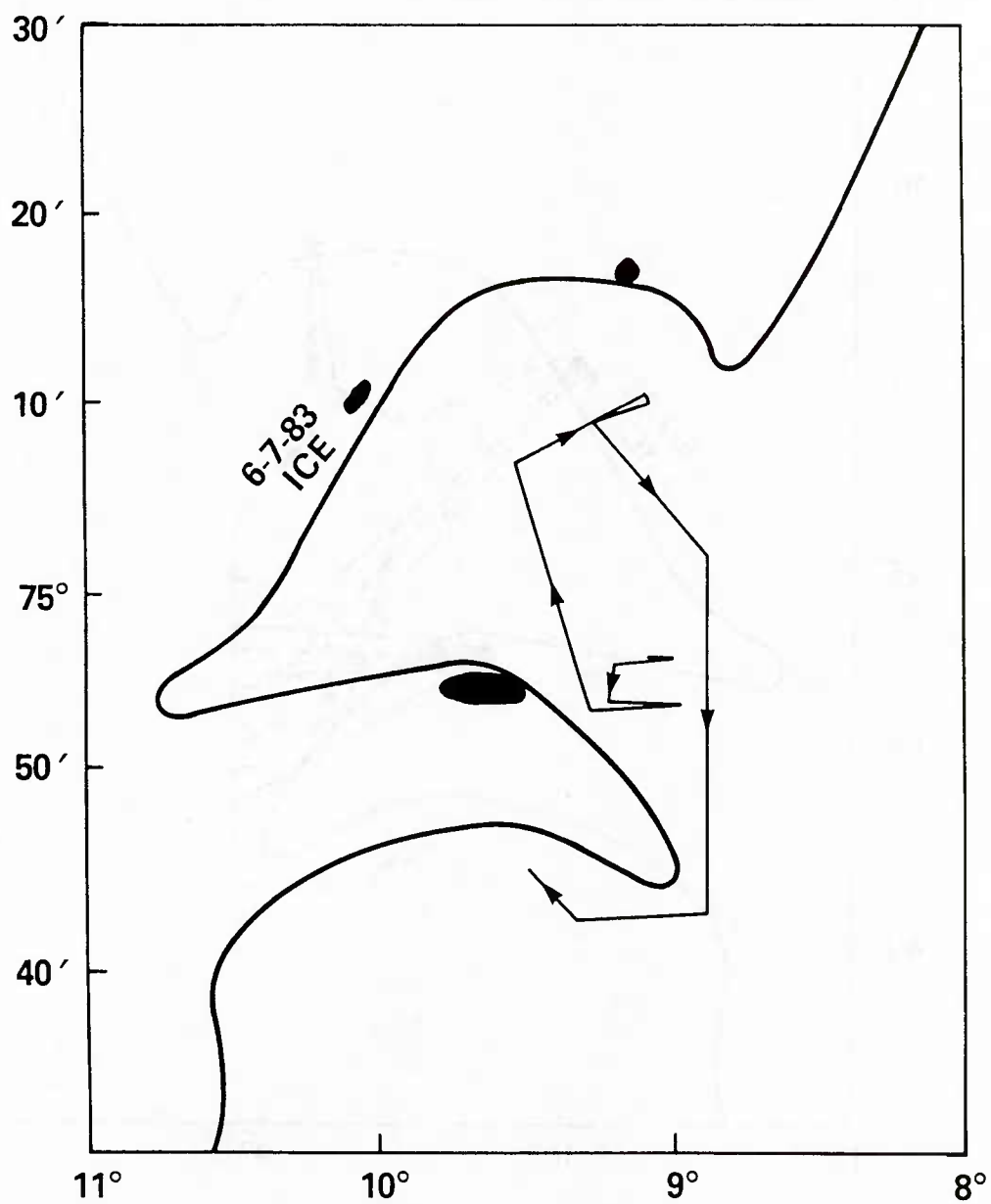
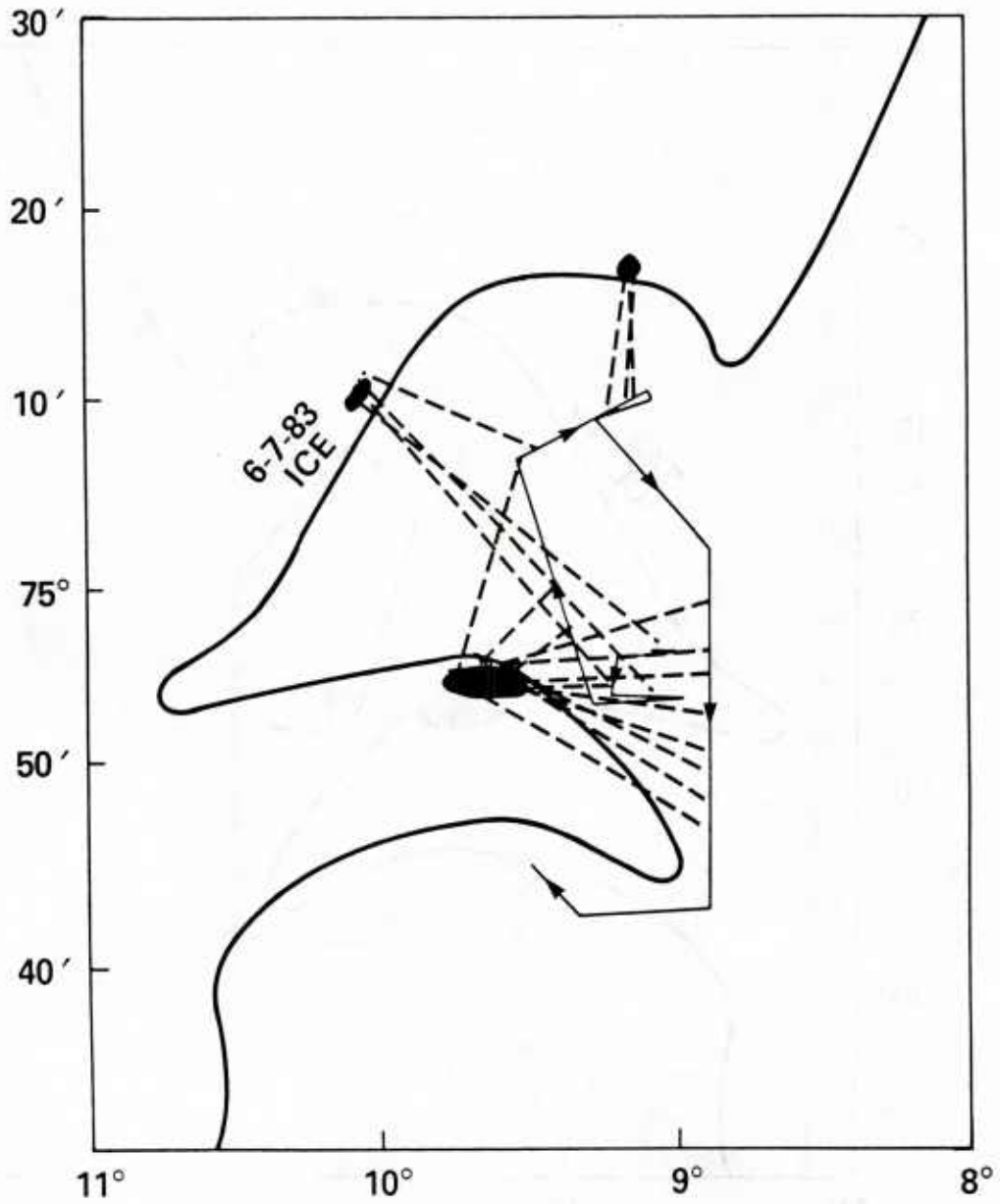


Fig. 3





LOCATION OF SHIP TRACKS (—), ICE EDGE,
AND AMBIENT NOISE HOT SPOTS (●)



CHARACTERISTICS OF INDUSTRIAL SOUNDS IN THE SHALLOW BEAUFORT SEA

Charles R. Greene, Jr.

Greeneridge Sciences, Inc.
5276 Hollister Avenue, Suite 408
Santa Barbara, California 93111

ABSTRACT

Oil industry activities in the Beaufort Sea north of Alaska and Canada are increasing, and some of the attendant sounds will propagate into the deep water of the Arctic Ocean. Each August from 1980 to 1984 we measured ambient and industrial sounds in the shallow waters (generally <50 m) of the eastern Beaufort Sea. The sound sources included drillships, hopper and transfer dredges, crew boats, supply boats, fixed wing aircraft and helicopters, and marine seismic survey sources like airgun arrays. Analysis results include waveforms and waterfall spectrograms of transient sounds, like seismic survey signals, and power spectra spanning 20-1000 Hz, 1.7 Hz resolution, and 80-8000 Hz, 27.2 Hz resolution, of continuous sounds. [Work supported by the Minerals Management Service, U.S. Department of the Interior.]

INTRODUCTION

The Department of Interior leases offshore areas for oil and gas exploration and development. Among the areas of special interest are Alaskan coasts along the Bering, Chukchi, and Beaufort Seas.

The Department is also responsible for environmental concerns in offshore lease areas, and the Alaskan natives living along the western and northern coasts have expressed strong concern about the possible effects of industrial activities on marine mammals, especially bowhead whales.

Bowheads are considered to be the most endangered of the whale species. Wintering near the ice edge in the Bering Sea, they swim north through the Bering Straits to Pt. Barrow in late April and May each year. From Pt. Barrow they swim through the ice of the deep Beaufort Sea to the Canadian Islands. They summer in the eastern Beaufort, feeding. In September and early October, they migrate westward across the north coast of Alaska, where oil and gas exploration are accelerating.

Among the perceived problems industry activity may provide bowheads, only concern about oil spills exceeded the concern about the possible effects of industrial noise. To study such noise and bowheads, the Minerals Management Service (MMS) contracted with LGL, Inc. for a study of bowheads and industrial noise. The study included field experiments during August each year from 1980-84. This field work took place in the shallow waters of the Canadian Beaufort Sea and was based at Tuktoyaktuk, North West Territories, Canada. (See Figure 1.) Canadian oil companies have been active with seismic surveys, drillships, and dredges building artificial islands since the mid 1970's, providing a wide range of noise types. With bowheads summering in the same area, circumstances were close to ideal for the study.

A crew of five biologists studied bowheads from a twin-engine Britten-Norman Islander flying 1500 or 2000 ft above the sea. (At lower altitudes there was evidence the airplane disturbed the whales.) Sonobuoys were dropped with each group of whales to determine the levels and qualities of the sounds to which they were exposed. The sounds radioed back to the airplane were tape recorded for later analysis.

An acoustician and two biologists worked from a chartered 12.5 m fishing boat to make sound measurements and whale observations. They also deployed an underwater sound projector for controlled playback experiments of previously recorded industrial noise (drillship and dredge).

This paper presents results of noise measurements from the boat and the sonobuoys. Examples are presented of ambient noise, aircraft sounds, boat and ship sounds, seismic survey signals, and the sounds of drillships, dredging, and artificial island operations. We conclude with a summary of all these sound sources and a discussion of possible transmission into the deep water of the Arctic Ocean.

RESULTS

Ambient Noise

The project did not include a systematic study of ambient noise, but many recordings and analyses were made when industrial noise was not present or was only incidental. Figure 2 presents six sound pressure spectra. The dashed curves correspond to Knudsen's Sea State Zero noise spectrum extended to 20 Hz and are presented for comparison. (A) is a sample of noise recorded near melting ice floes. The three narrowband components are from the Islander. (B) is the same noise sample analyzed to 8000 Hz. (C) and (D) were recorded from the drifting boat and show spectra for a quiet time. They also show that ambient sounds at depth 3 m are lower in level than those at depth 18 m, in accordance with theory for waterborne sound near the air-water interface. (E) and (F) provide a comparison of sonobuoy- and boat-measured sounds recorded 8 hours apart. (F) includes some strong tones from an unknown source at low frequencies.

Aircraft Noise

All the spectra in Figure 3 were computed from recordings made on the boat. The tones corresponded to propeller blade rates and, in the case of the Islander, cylinder firing rates. The Sikorsky 61, the Bell 212 and the Bell 214ST were used routinely to support offshore work from Tuktoyaktuk. The waterfall spectrogram in (F) corresponds to the averaged spectrum in (B).

Boat and Ship Sounds

Figure 4 presents sound pressure spectra for several vessels underway. (A) is the spectrum for 'Imperial Sarpik', a 21 m twin-engine crewboat. The dip in the low frequency portion of the spectrum is an effect of the shallow water sound propagation. The bow thrusters on 'Supplier III', Figure 4B, provided tones in a harmonic family extending to 1 kHz. (C) is the spectrum of a supply boat with twin engines totaling 2200 SHP. (D) is the spectrum for a hopper dredge, capacity 8000 m³ underway with a full load. This dredge, 'Geopotes X', was the noisiest vessel we measured during the five year project. We were later told that the ship was operating with a damaged propeller, which was repaired before the following year. 'Cornelis Zanen', Figure 4E, was for another large hopper dredge underway. 'Gulf Beaufort', a 153,000 ton supertanker, was anchored when the sounds were recorded leading to Figure 4F.

Figure 5 summarizes the sound levels in the 20-1000 Hz band vs range for several vessels. The strongest sounds came from 'Geopotes X', as previously stated. The weakest sounds came from 'Arctic Sounder', a survey boat anchored and running only a housekeeping generator.

Seismic Survey Sounds

The highest amplitude industrial sounds recorded were those from geophysical survey ships, but they were short-lived transients, repeating at 8 to 15 s intervals. Sources were arrays of airguns, sleeve exploders, or open-bottom gas guns. Examples are presented in Figure 6 of signals from the open-bottom gas guns on 'Arctic Surveyor' operating in water 11-13 m deep. (A) and (B) are the time and frequency signatures of a signal at range 0.9 km; the energy is concentrated at frequencies below 100 Hz. (C) and (D) are for range 3.7 km, for which the low frequencies arrive first, via bottom paths, and the waterborne energy is found at frequencies above 200 Hz. (E) and (F) are for range 14.8 km, for which only the higher frequency waterborne energy remains. We believe we crossed a geological discontinuity between the 3.7 and 14.8 km range stations, where the low frequency bottom traveling energy was severely attenuated.

Drilling Sounds

'Explorer II' was one of four drillships operating in the Beaufort Sea; Figures 7 (A) and (B) are spectra for near and far ranges, respectively. 'Kulluk' was a conical drilling unit (CDU) operating for Gulf Canada. Spectra for various hydrophone depths and ranges are presented in (C) - (F).

Figure 8 presents a summary of drilling vessel sounds in the 20-1000 Hz band vs range. 'Kulluk', the largest such vessel, also appears to be the noisiest, although there were support boats operating in the vicinity and contributing to the noise. Drillship 'Explorer I', during logging, was the quietest drilling vessel measured. For comparison, the sound levels are presented for a caisson retained island (CRI) recorded during drilling at Amerk (See Fig. 1).

Dredging Sounds

Figure 9 presents spectra of sounds from dredges recorded during dredging operations. 'Beaver Mackenzie' was a transfer dredge. (A) and (B) present spectra including a tone from 'Beaver Mackenzie' at 1775 Hz, an unusually high frequency for a machinery tonal sound. Three years later, in 1983, the dredge had been refurbished and the spectrum levels changed (Fig. 9c). (D) is for 'Cornelis Zanen' picking up a load. (E) and (F) are for transfer dredge 'Aquarius' at near and far ranges.

Figure 10 presents a summary of dredge sounds, 20-1000 Hz band levels vs range. 'Cornelis Zanen' picking up a load was the strongest source of dredging noise, while transfer dredge 'Beaver Mackenzie' in 1983 was the weakest.

Island Operations

Figure 11 presents spectra for sounds recorded near three caisson retained islands. (A) and (B) are for 'Tarsiut', where drilling had been completed and testing was underway, and there were several support vessels operating in the vicinity. (C) and (D) are for 'Kadluk', which was under construction at the time although most of the sounds probably were from nearby vessel operation. (E) and (F) are for 'Amerk', where drilling was taking place.

SUMMARY

Figure 12 represents an attempt to present summary levels for all the different types of sound sources except aircraft. The format is 20-1000 Hz band levels vs range. The strongest levels were those from the transient seismic survey signals, especially the airgun array on 'GSI Mariner'. The received levels of signals from the sleeve exploders on 'Arctic Surveyor', ranges 8-28 km, fit a model with two range-dependent terms: $-10 \log(R) - 1.4R$, where R was in km. The first term is the cylindrical spreading loss term and the second is an absorption/scattering loss term. 'Geopotes X' was the strongest noise source. The weakest source presented here was 'Imperial Adgo', a 16 m crewboat.

Also presented on Figure 12 are the 20-1000 Hz band levels expected for Sea State Zero and Sea State Two. The median levels of the ambient noise samples from both the sonobuoy and the boat recordings in 1984 were within 1 dB of the Sea State Two band level. It should be noted that because neither the boat nor the airplane could operate during storms and severe weather, the computed median levels are probably biased below the actual median levels.

DISCUSSION

Navy research and operations in the deeper waters of the Arctic Ocean may be affected by sounds from the continental shelf areas of northern Alaska and Canada. In particular, seismic survey sources and noisy ships may transmit sounds into deepwater during the months from July into October while the ice is sufficiently thin to permit navigation. For example, unmanned drifting data buoys in the Beaufort Gyre collecting ambient noise data in summer and fall could easily be affected by the arrival of seismic signals, but no one would know that sources other than ice, wind, and seals accounted for observed levels.

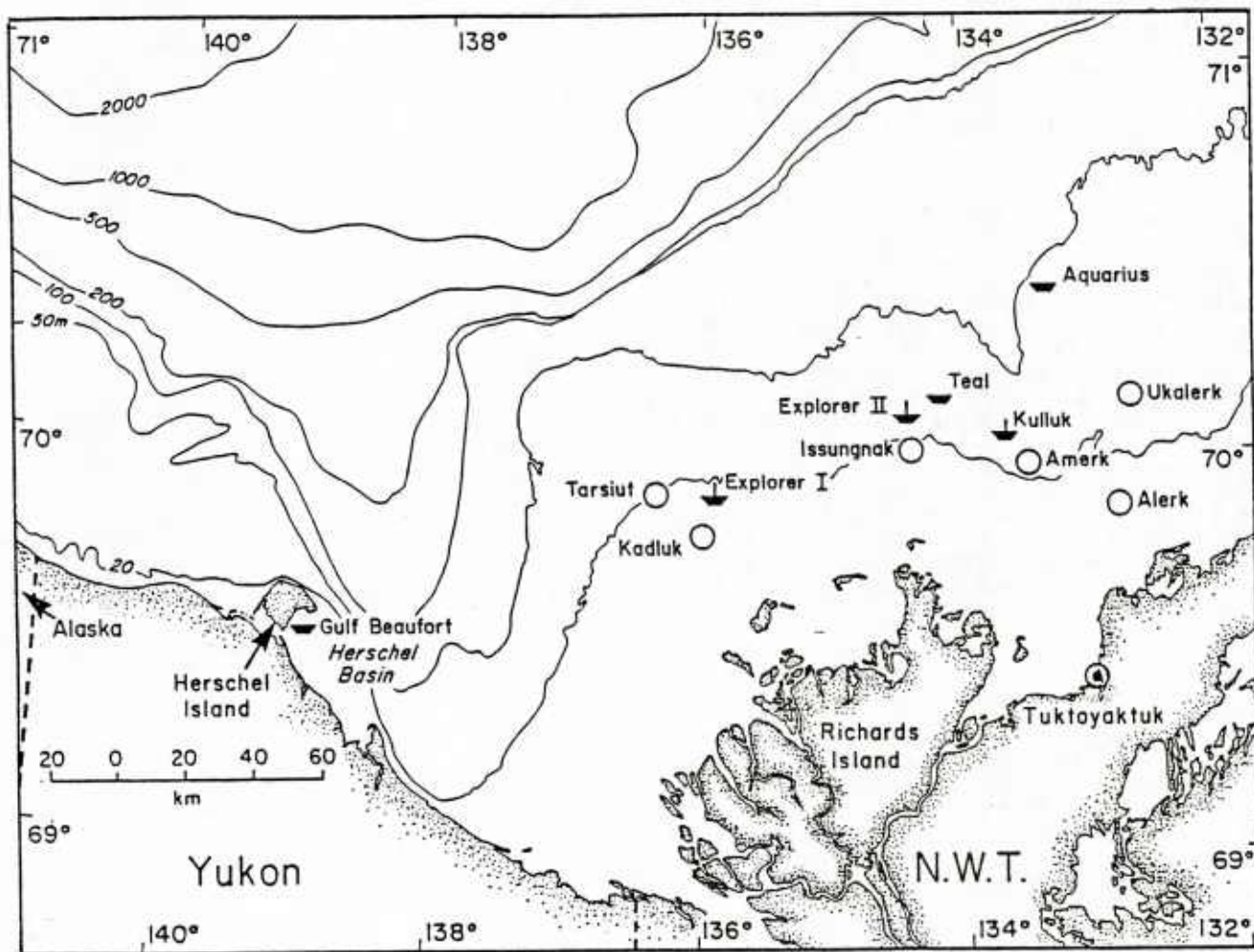


FIGURE 1. Map of the study area, east-central Beaufort Sea, showing recording sites mentioned in text.

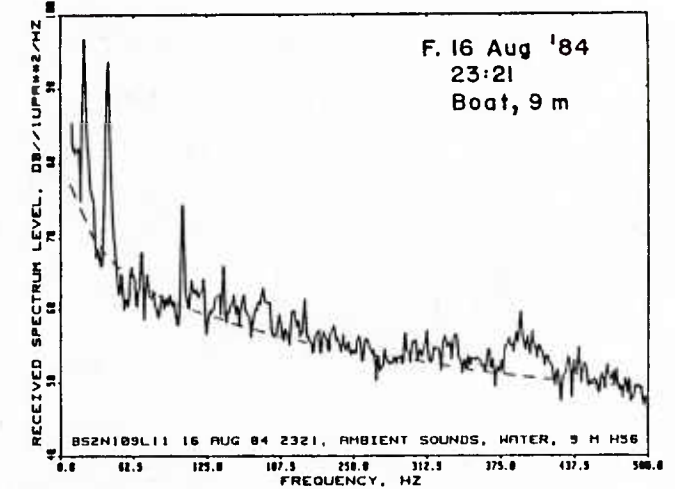
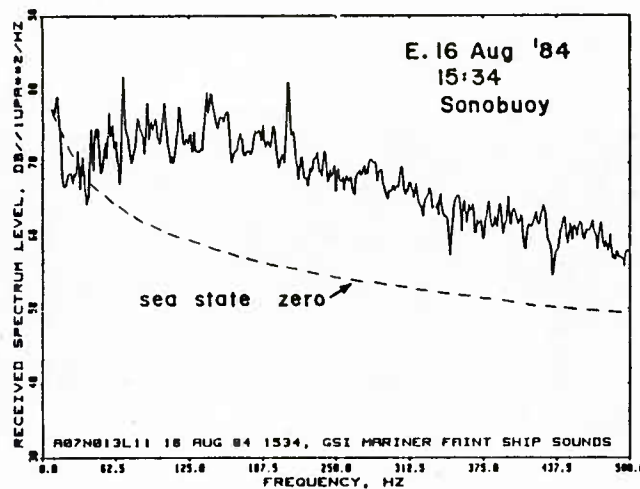
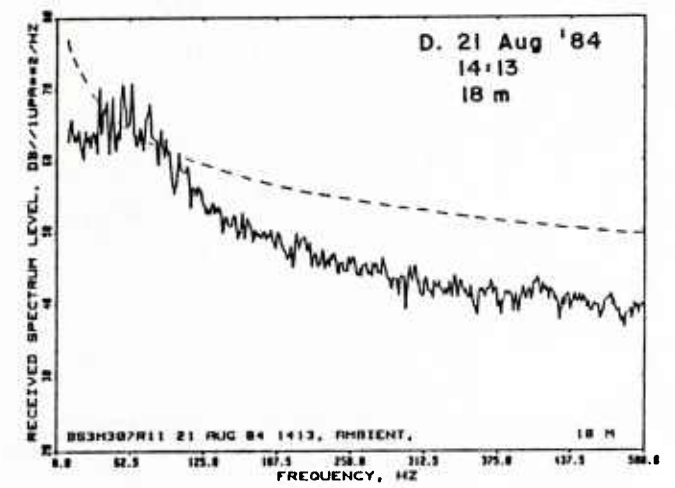
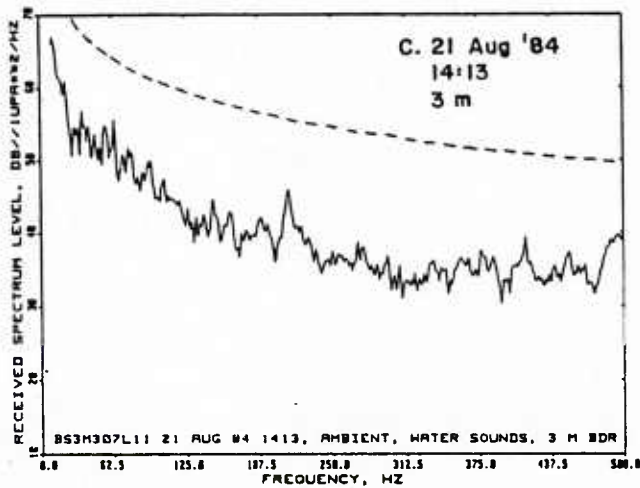
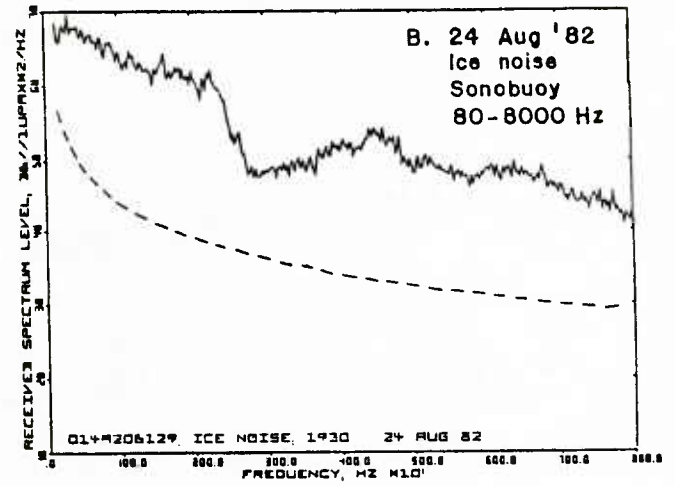
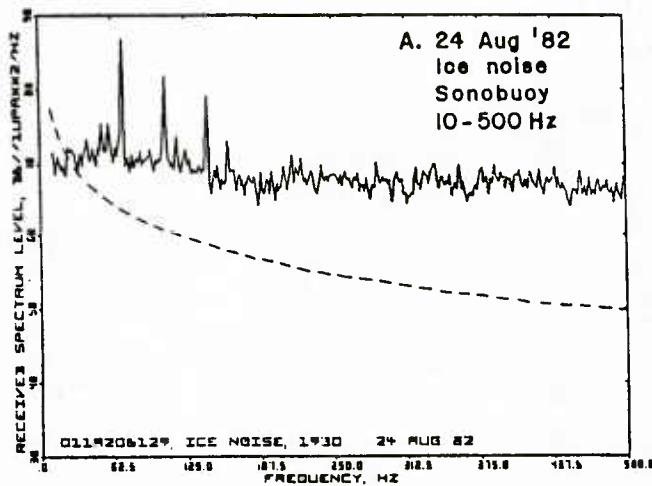


FIGURE 2. Examples of ambient noise sound pressure spectra. The extended sea state zero spectrum has been added for reference.

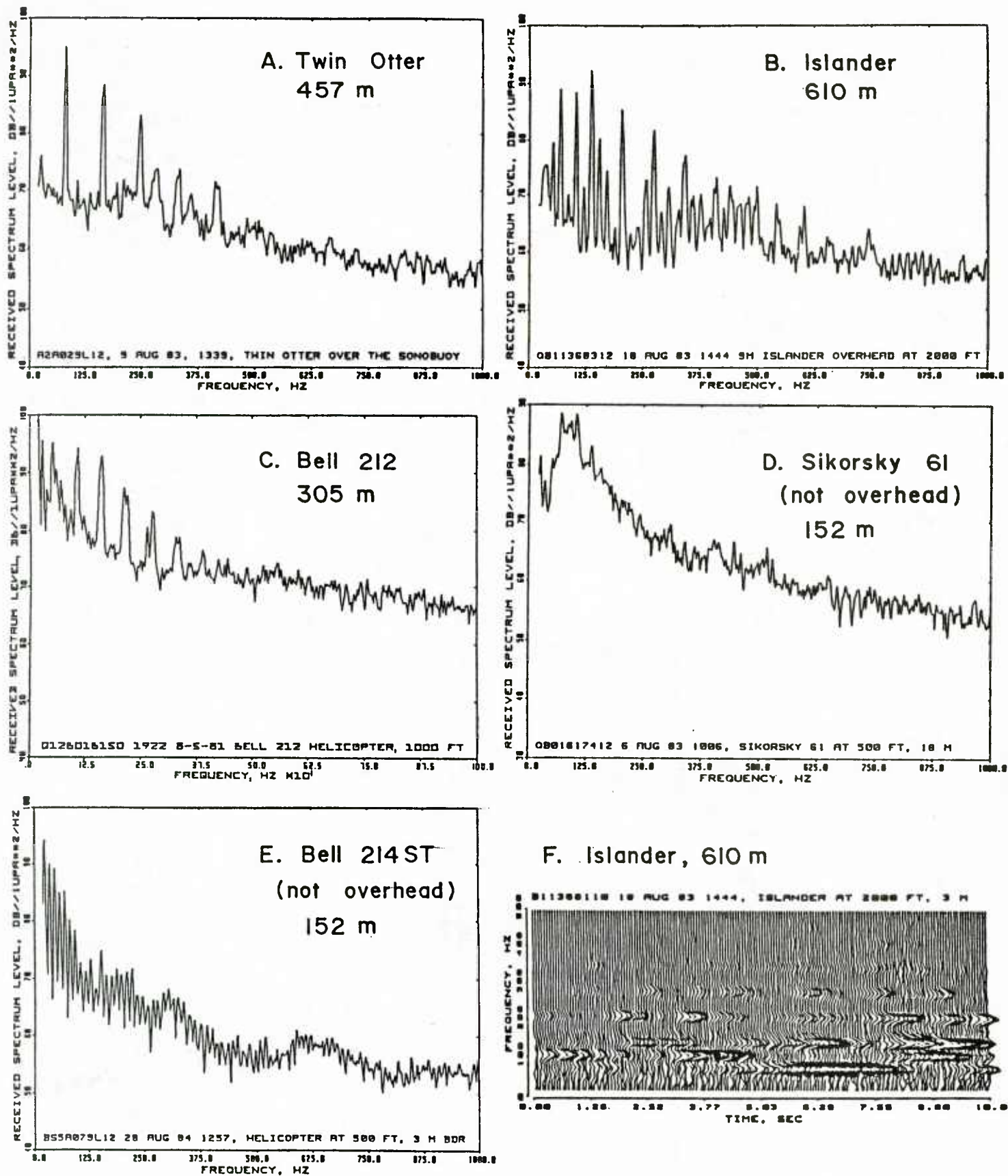


FIGURE 3. Aircraft spectra: (A) deHavilland Twin Otter overhead at altitude 457 m; (B) Britten-Norman Islander overhead at altitude 610 m; (C) Bell 212 helicopter overhead at altitude 305 m; (D) Sikorsky 61 helicopter about 20° from overhead, altitude 152 m; (E) Bell 214ST helicopter about 55° from overhead, altitude 152 m; (F) waterfall spectrogram of the Islander overhead at 610 m.

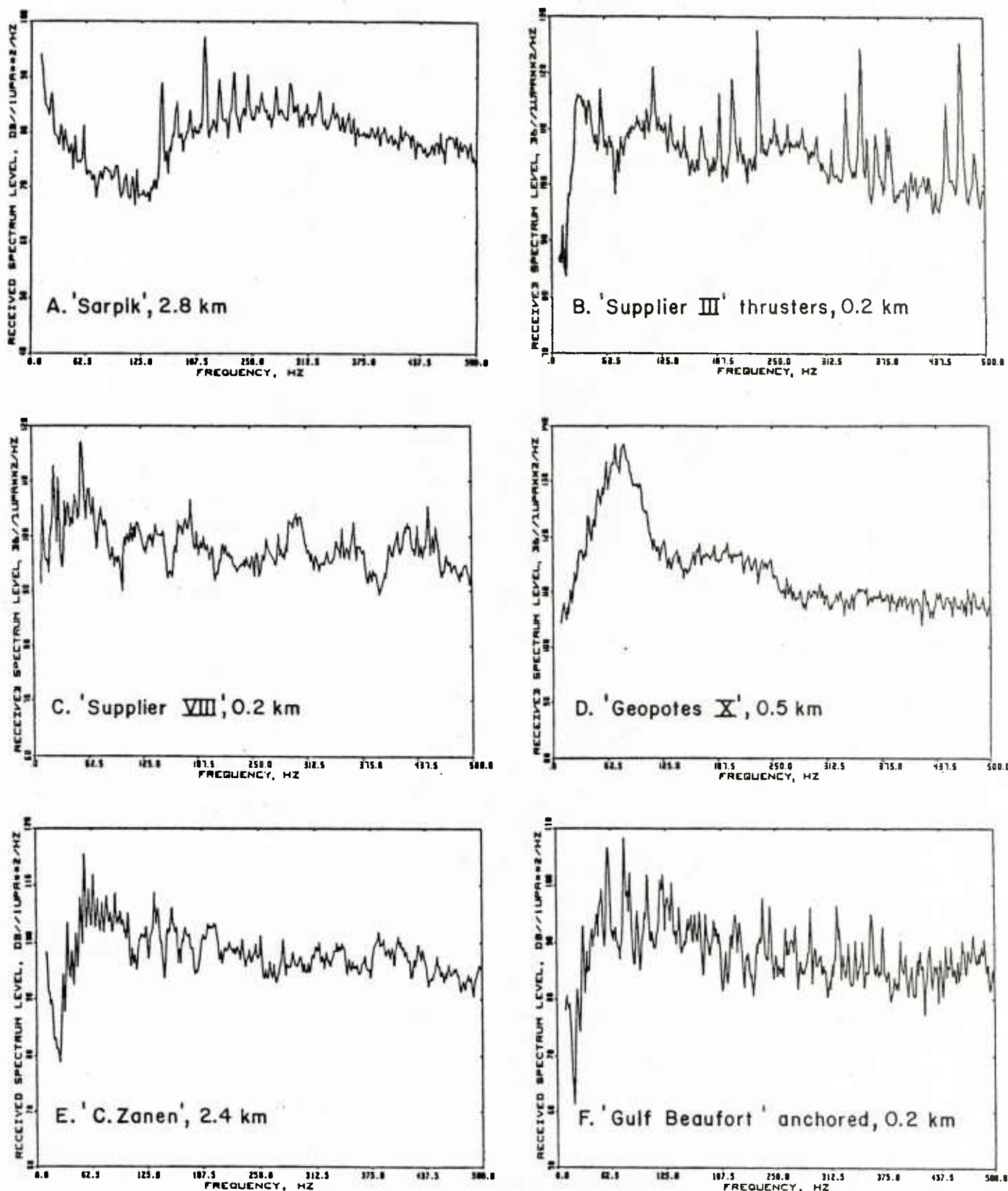


FIGURE 4. Representative boat and ship sound spectra. (A) is for crewboat 'Imperial Sarpik' at range 2.8 km. (B) is for the bow thrusters on 'Canmar Supplier III' at range 0.2 km. (C) is for 'Canmar Supplier VIII' at range 0.2 km. (D) is for hopper dredge 'Geopotes X' at range 0.5 km. (E) is for hopper dredge 'Cornelis Zanen' at range 2.4 km. (F) is for anchored tanker 'Gulf Beaufort' at range 0.2 km. Hydrophone depth was 9 or 18 m in each case.

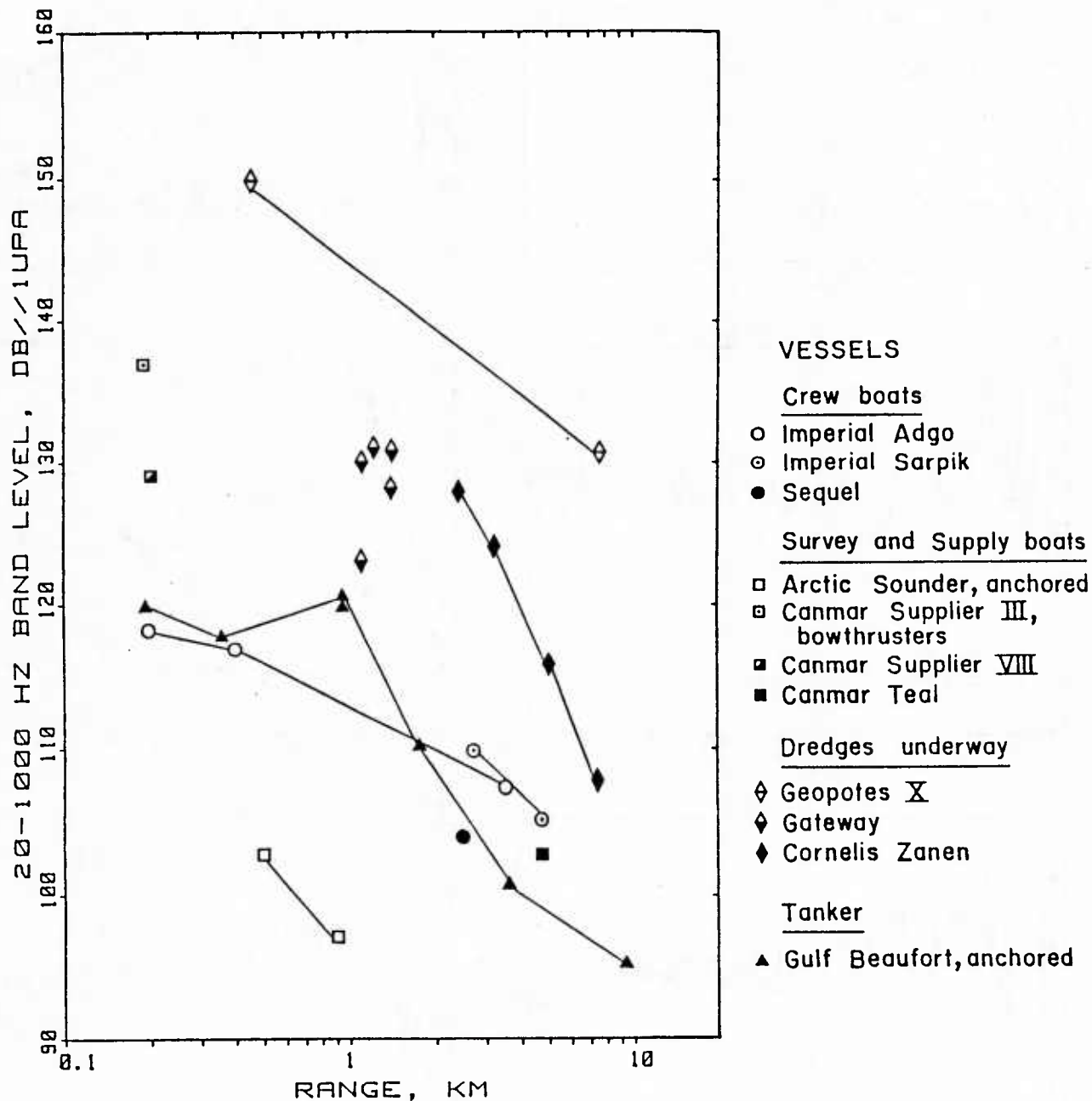


FIGURE 5. Boat and ship sound levels in the 20-1000 Hz band, in dB/1 μ Pa, vs. range. All values are from hydrophones at depths 18 or 9 m. These data are also presented in Table 5.

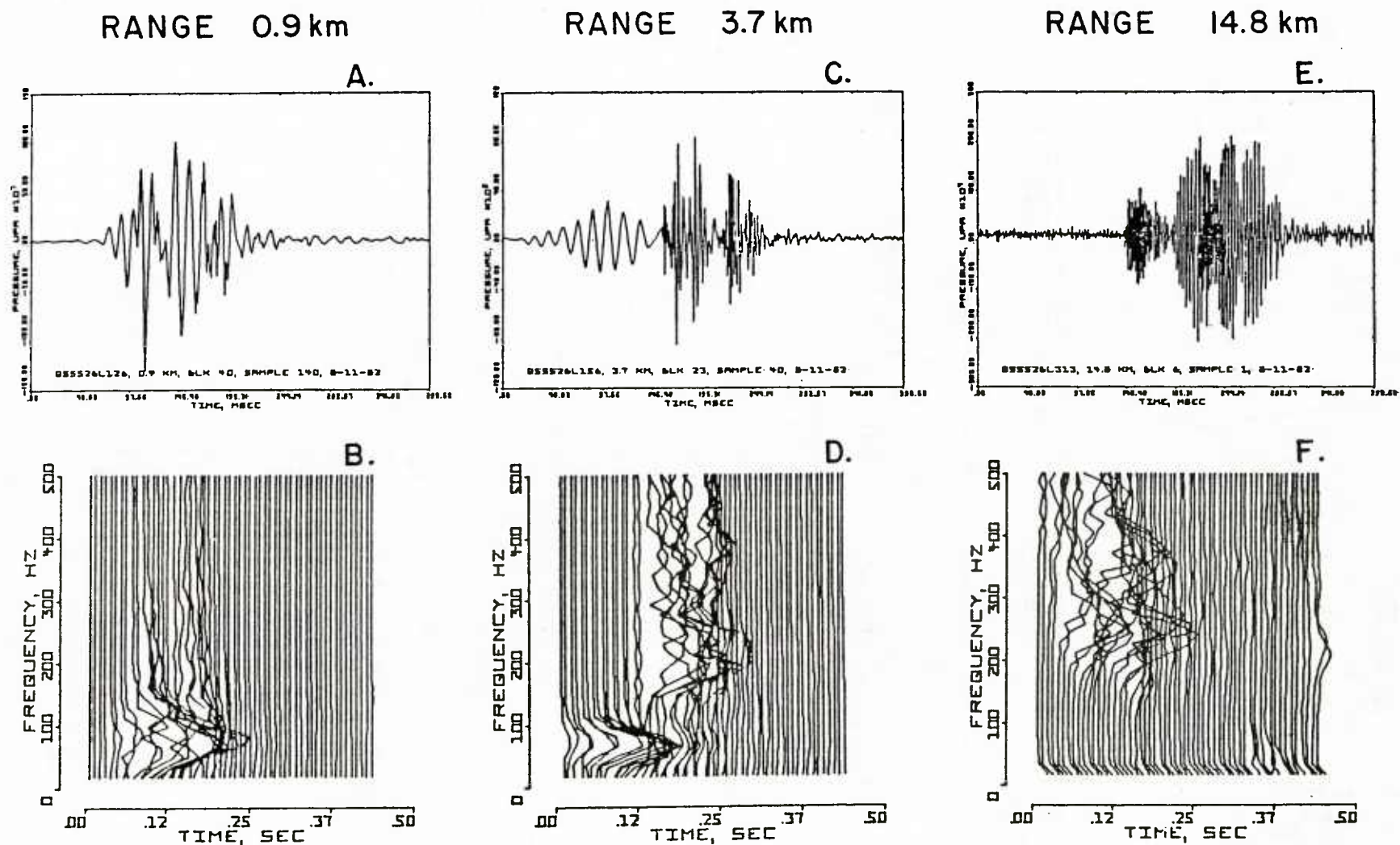


FIGURE 6. Waveforms and waterfall spectrograms of signals from open-bottom gas guns at ranges 0.9, 3.7, and 14.8 km. Water depth was 9-11 m; hydrophone depth was 8 m.

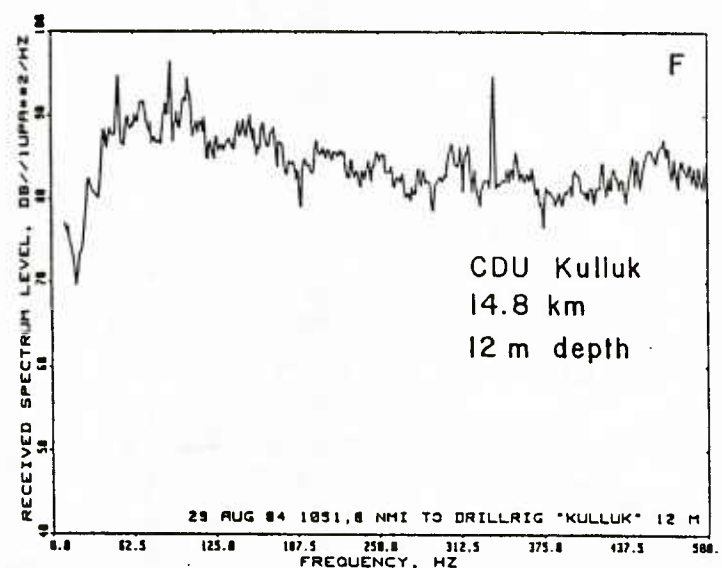
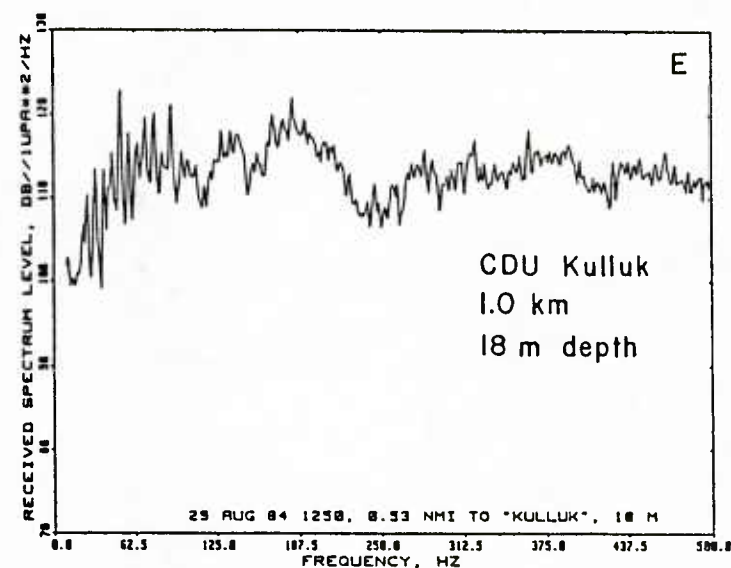
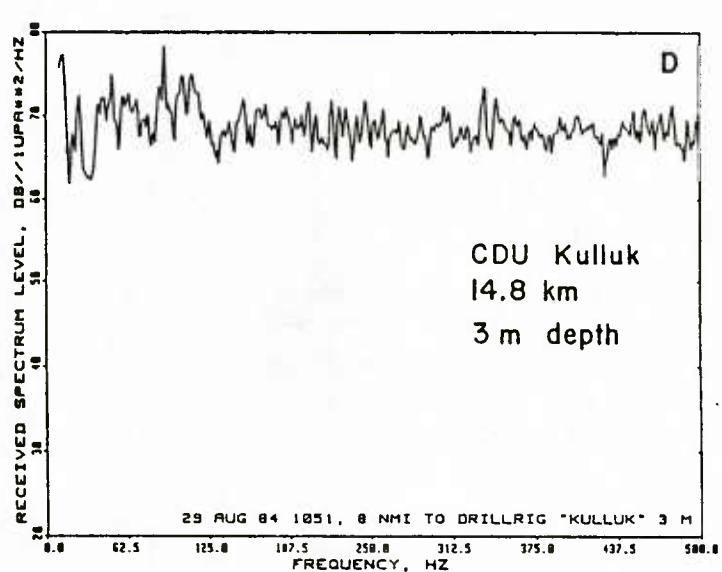
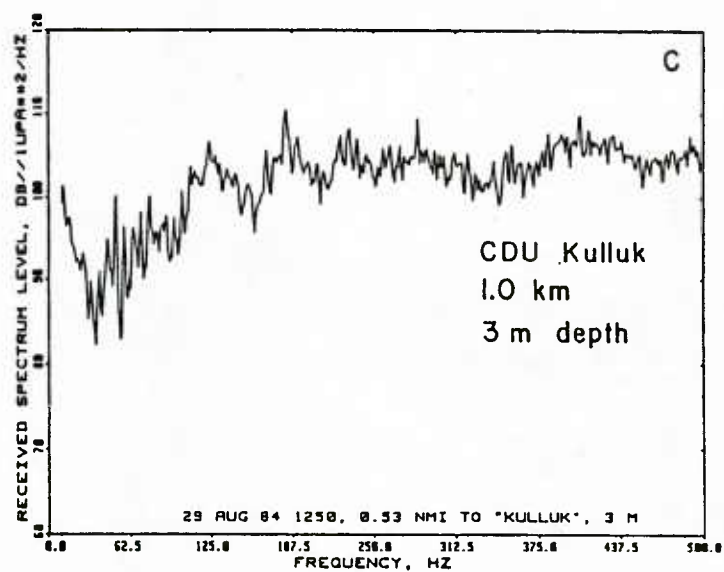
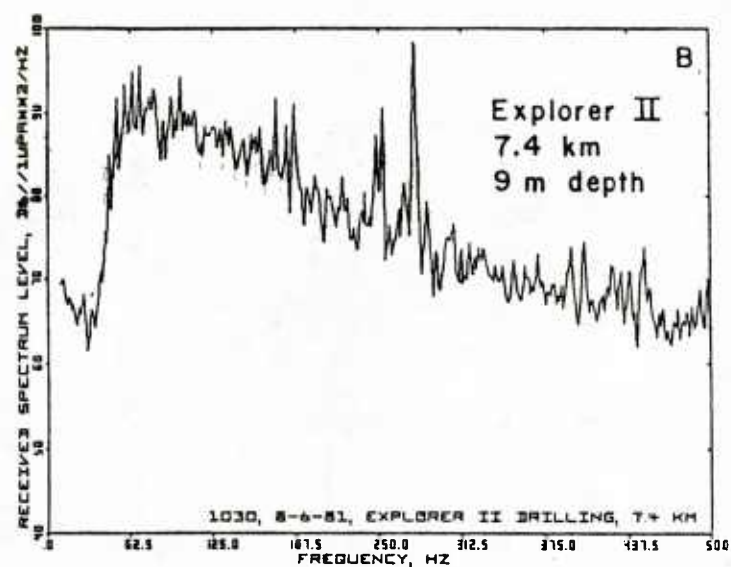
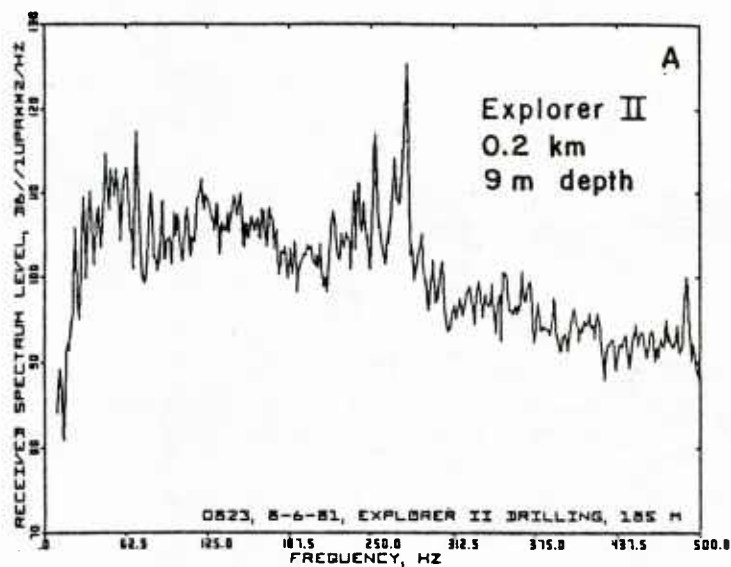


FIGURE 7. Sound pressure spectra for drillships 'Explorer II' and Conical Drilling Unit 'Kulluk' from recordings made while drilling.

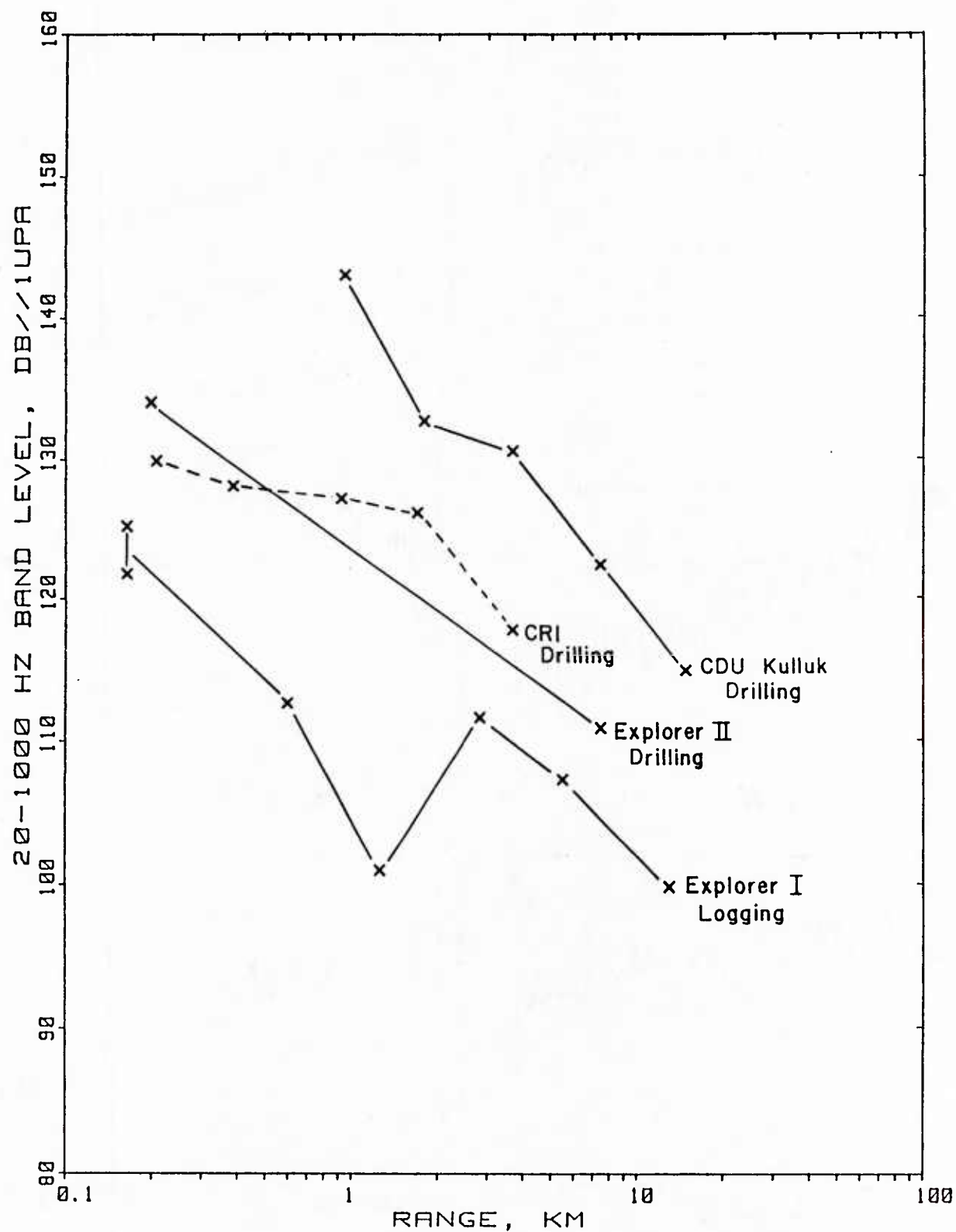


FIGURE 8. Drillship sound levels in the 20-1000 Hz frequency band vs. range for three drilling vessels. Levels near a drilling operation on a caisson-retained island are also shown for comparison. The hydrophone depth was 9-18 m in each case.

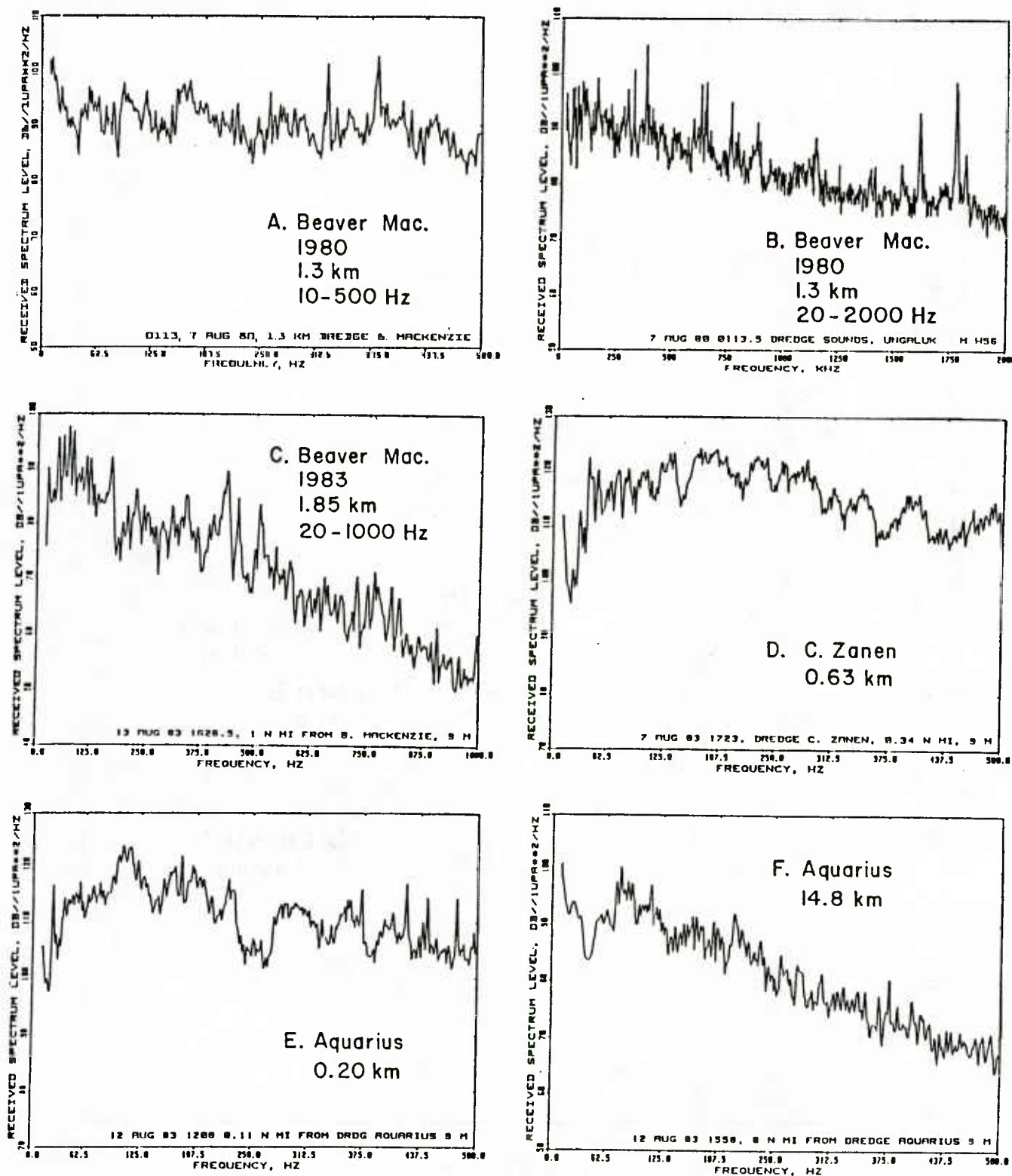


FIGURE 9. Sound pressure spectra from working dredges.

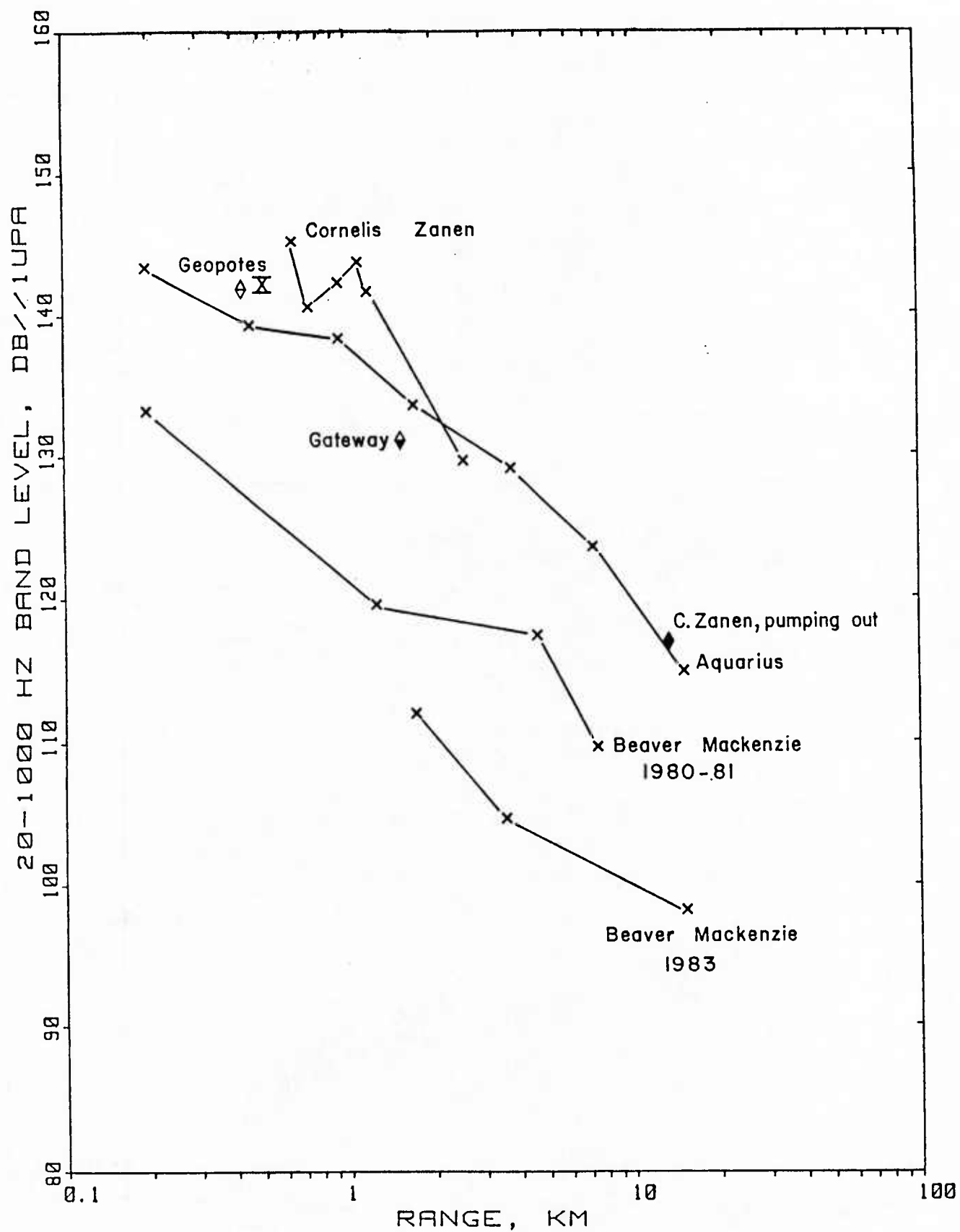


FIGURE 10. Dredge sound levels in the 20-1000 Hz frequency band vs. range for dredges that were actively dredging; hydrophone depths 9-18 m.

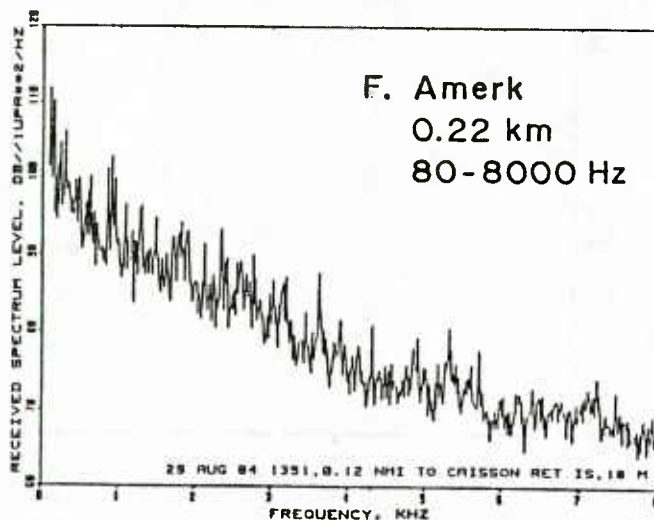
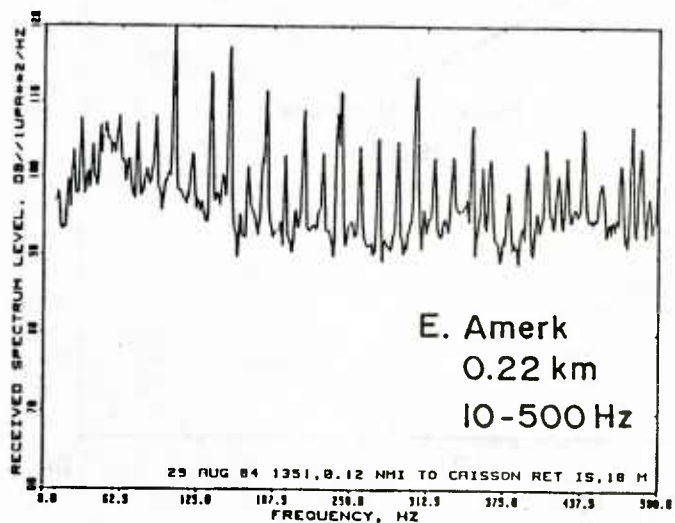
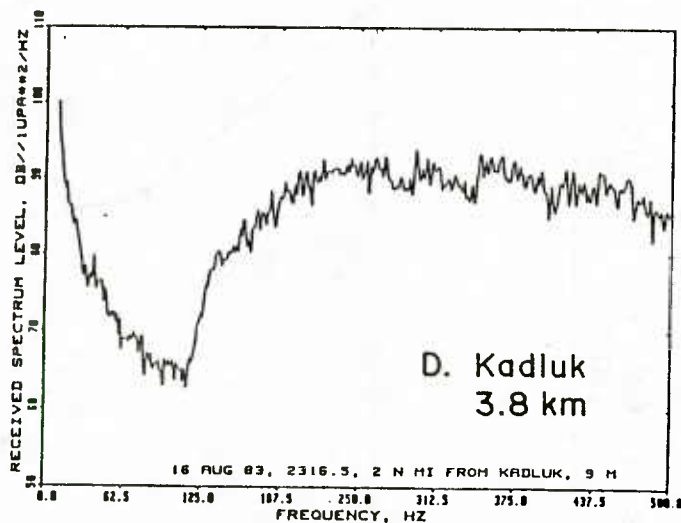
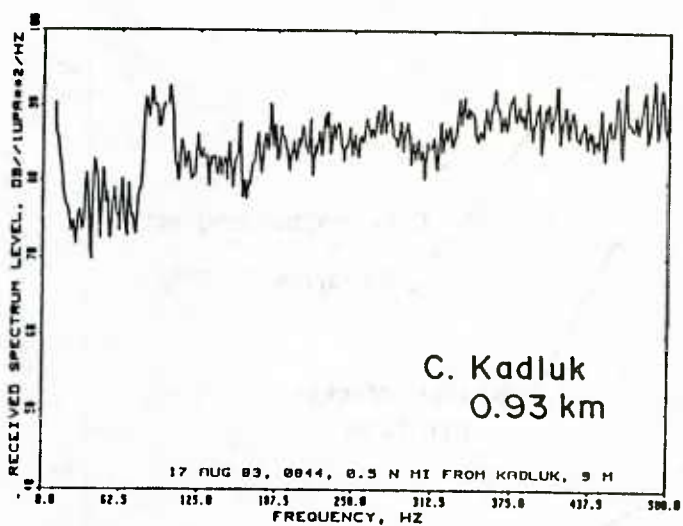
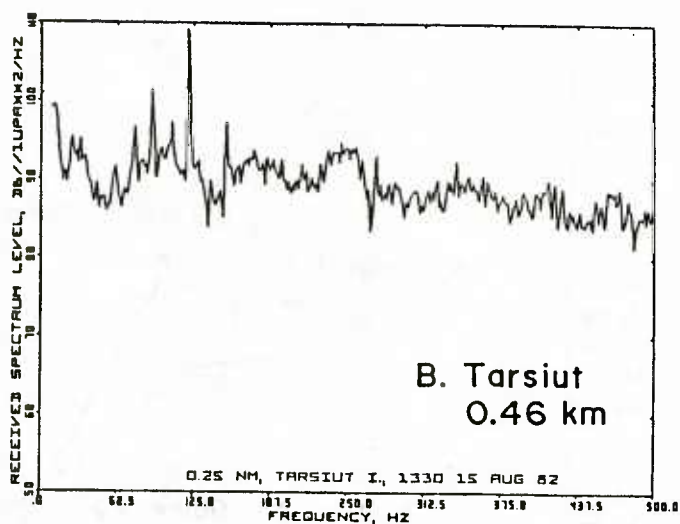
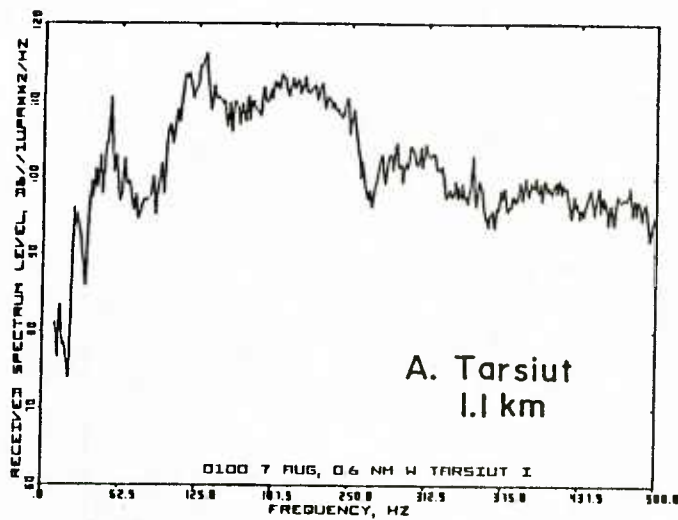


FIGURE 11. Sound pressure spectra from operations at caisson islands.

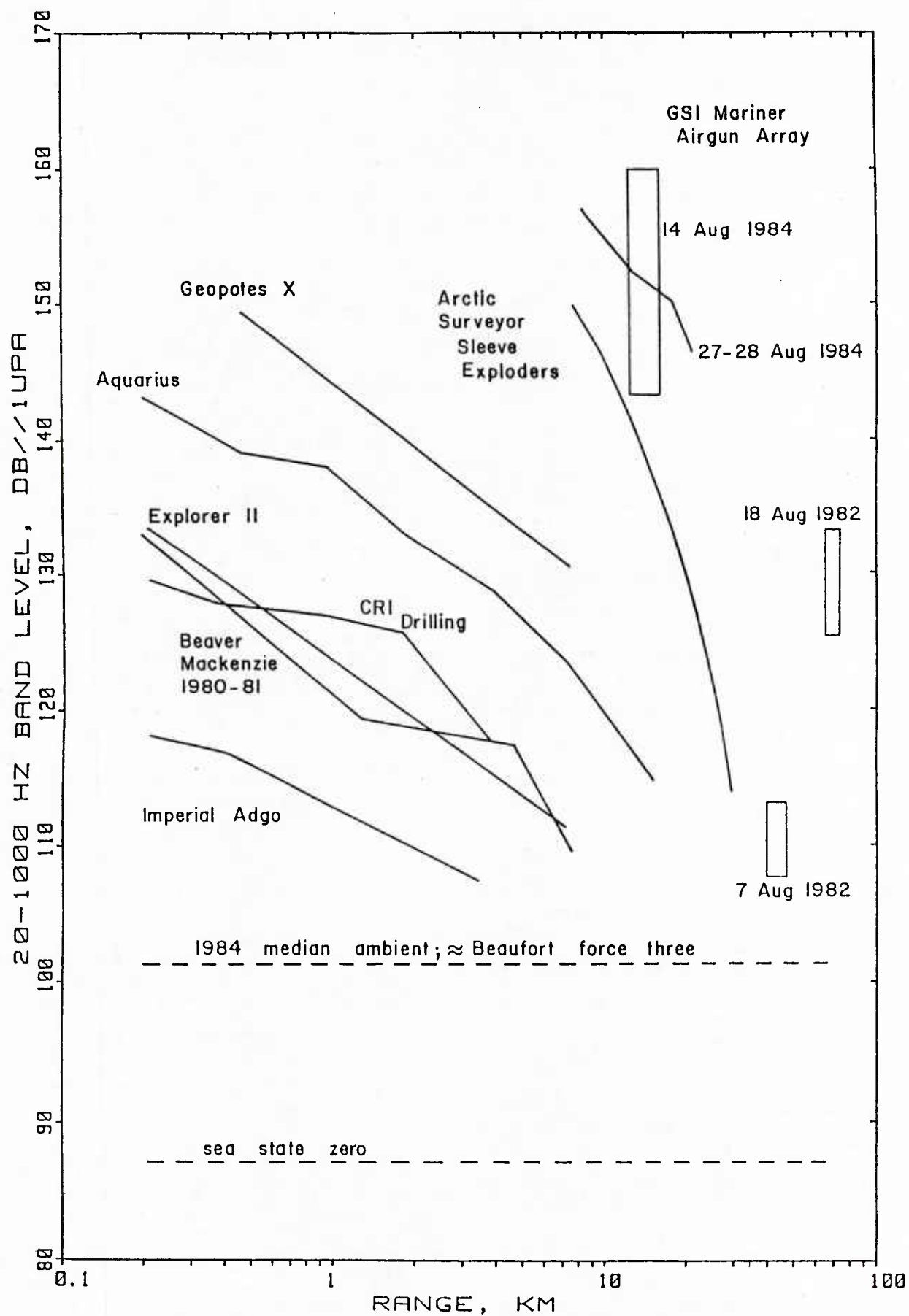


FIGURE 12. Summary of levels vs. range for various industrial sounds.

Numerical Modeling of Acoustic
Ice Interaction in the Arctic

Thomas N. Lawrence
Naval Ocean Research & Development Activity

and

G. Tango
ODSI Defense Systems Inc.

ABSTRACT

Propagation of acoustic waves in an ocean waveguide bounded above by plane ice layers can be readily modeled using a Fast Field Program (FFP). The direct global matrix FFP formulation embodied in the SAFARI algorithm of Schmidt and Jensen [1] permits rapid computation of transmission loss from a continuous wave point source as a function of receiver range for multiple source and receiver depths. Various shear and compressional velocity models of Arctic sea ice were investigated to show the effects of physical parameters on reflectivity and net transmission loss below 5 kHz. Special attention is given to the effect of the ice-water interface and how the existence of this layer is important to accurate acoustic prediction in the Arctic.

1. INTRODUCTION

Acoustic propagation in the Arctic is distinguished by the interaction of sound with an ice cover which in most cases is treated as a rigid scatterer of that sound. Arctic ice is not a homogeneous body, but a porous one, the cells and capillaries of which are filled with brine, silt and air. Mayer, et al [2], have shown that if ice is treated as a non-fluid half space over water, then changes in the physical parameters (sound speed, density, etc.) can significantly affect reflection from ice of a water-borne sonic signal. McCammon and McDaniel [3], using a five layer model of several overall thicknesses showed the effects on reflectivity when physical parameters are varied. In this presentation we will consider what physical properties of Arctic sea ice will affect, in a significant way, the propagation of sound in a typical Arctic underwater sound channel.

Calculations of reflection loss from sea ice can be made provided we know the sound speed and attenuation, both compressional and shear, the density, and the variation of these parameters with depth. We have considered such ice models from measurements by Bunney and Hanse [4], and from Bogorodskii and his co-workers of the Arctic and Antarctic Scientific Research Institute (AANII) in the Soviet Union [5,6,7]. These ice models show a fine structure which we feel is not atypical of what would be found in nature, but clearly could not represent the depth and breath of all sea ice for which variations are quite wide. Arctic sea ice can be characterized by parameters such as: 1) the age of the ice, first-year, second-year, and multi-year, 2) the season, winter ice having for example quite a different structure from summer ice, 3) snow cover, 4) location, and 5) the water-ice interface, which we will refer to as formative ice. These parameters are not independent. For example, season will affect snow cover. We will focus on the final parameter, formative ice, and how this layer affects the reflection loss from sea ice when it is ensonified from the water at low grazing angles.

2. METHOD OF SOLUTION

The SAFARI Fast Field Program (FFP) of Schmidt and Jensen [1], as with other FFP algorithms due to DiNapoli [8,9], and Kutschale [10], is based on a direct numerical evaluation of the Bessel-Hankel integral, obtained by solving for the multi-layer depth-dependent Green's function. Numeric integration is accomplished by employing the FFT with the transform variables from horizontal wavenumber to range to evaluate complex pressure.

The difference in SAFARI with respect to other FFP models is its approach to the acoustic field. The total field is considered as a superposition of two fields, one field produced by sources in the absence of boundaries, and an unknown field satisfying the homogeneous wave equation. The unknown field is determined from boundary conditions which are satisfied at each interface. This approach is equivalent to the method of Ewing, et al [11]. In this approach

3. ICE MODELS

Two models of Arctic sea ice are used in this study. The first, the Bunney-Hanse [4] profile was chosen because it represents direct measurements of first year ice made in the Chukchi Sea in 1973. This profile lacks some of the very fine structure we would hope to consider, but we feel that it does help in placing our conclusions on a firm foundation. The second, the Bogorodskii AANII [5,6,7] ice profile, is a generic type of profile incorporating many of those attributes that could be found in "typical" Arctic sea ice.

Figure 1 shows the Bunney-Hanse profile, where the solid line indicates the compressional sound speed, and the dotted line the shear speed. A relationship for attenuation is derived from experimental data, and is the same as that used by McCammon and McDaniel [3], where,

$$\alpha = 0.06 f (-6/T)^{2/3}$$

$$\beta = 0.36 f (-6/T)^{2/3}$$

- α - compressional attenuation in dB/m
- β - shear attenuation in dB/m
- f - frequency in kHz
- T - temperature in degrees centigrade, for temperatures between -2°C and -20°C .

Bunney and Hanse measured the temperature gradient in the ice to be about -20°C at the surface, and -2°C at the water-ice interface with an approximate linear gradient in between. The density was taken to be 0.9 gm/cm^3 in the ice with a slight increase to 1.0 gm/cm^3 at the water-ice interface.

The Bogorodskii AANII profile is shown in figure 2. We used the same temperature with depth dependency that was used in the Bunney-Hanse profile, and the density is treated the same except for a decrease to 0.75 gm/cm^3 in the snow layer. The bottom 10 cm of the AANII profile is plotted in figure 3, showing about a 2 cm formative ice layer. It is this layer which takes on some importance in propagation loss in Arctic waters. We will present modeling results which show that this layer acts as a sound channel permitting acoustic energy to enter the ice when that sound interacts at the small grazing angles, typically found in Arctic propagation. The Bunney-Hanse measurements do not show this formative ice layer to the extent that is seen in the AANII profile. It is clear that the spacial resolution was such that Bunney and Hanse could not detail this part of the ice. However, the curve in figure 1 which shows shear, does indicate some tendency towards a formative layer. In both cases just discussed the ice layers are backed by air.

4. REFLECTION LOSS

The Bunney-Hanse profile was modeled using 16 layers, and figure 4 shows reflection loss versus grazing angle at 500 Hz for that profile. The solid line is the reflection loss with the full profile used in the calculation, while the dashed line represents the result for reflection loss obtained when only the average value of all parameters are used, that is sound speed, density, and attenuation, of single homogeneous ice layer backed by air. We see that at low grazing angles there is less loss for homogeneous ice. We feel that this difference is due primarily to the decrease in sound speed, in particular shear speed, at the water-ice interface. This interface is a channel which enables sound to enter the ice, were as its absence does not permit such penetration.

Figure 5 shows a transmission loss model calculation in an Arctic sound channel (here a deep water Beaufort Sea sound speed profile was used). The solid line shows a result obtained with no surface loss considered. The dashed line is the same calculation with the reflection loss as determined from the full Bunney-Hanse profile in flat ice. Using the averaged Bunney-Hanse profile reflection loss, a transmission loss result was obtained that was little different from the result with no surface loss. The difference in the two curves in figure 5 suggests that a formative ice layer does have some affect on propagation loss.

The Bogorodskii AANII profile was then modeled using 41 layers. Figure 6 is a plot of our results showing reflection loss versus grazing angle for all frequencies under 5000 Hz. The frequency and grazing angle are in the X-Y plane, with the reflection loss upward in the Z direction. At low grazing angles there is considerable reflection loss indicated. If the effect of the formative ice layer is neglected there is an absence of such reflection loss at low grazing angles as seen in figure 7. The figure 7 results were obtained with the same AANII profile model, except the formative ice layer has been removed, and the parameters which are at 10 cm from the water ice interface are extended to that interface. The results in figure 8 are for a homogeneous ice layer of the same thickness using the parameters at the center of the AANII profile. Both figure 8 and figure 7 show a very flat region at low grazing angles, i.e. the formative ice layer is not present to allow energy to enter the ice. Figure 9 shows the reflection loss versus grazing angle for 4500 Hz. The solid line is the full AANII profile, while the dashed line is the same profile with the formative ice layer removed. At the low grazing angles the difference in transmission loss is quite significant, as can be seen in figure 10 when transmission loss is modeled for the full AANII profile (dash), and for a case with no

reflection loss (solid).

5. THE FORMATIVE LAYER

In section 4 we showed that the presence of a formative ice layer has a significant enough effect on propagation that the question of its existence and nature is of considerable importance. E. R. Pounder [12] writes of the water-ice interface as being between 1 and 2 cm, consisting of pure ice platelets with layers of brine between them. W. L. Weeks [13] has confirmed that the formative ice layer is about 2 cm and is considered to be uniform throughout most of the Arctic. Bogorodskii's model of formative ice was our only available source, and although based on careful measurements is subject to verification.

The thickness of the formative ice we feel is a matter of some importance since our calculations show that reflection loss is affected by that thickness in two ways: 1) the level of reflection loss, and 2) the frequency at which large losses or modal peaks can occur. Figure 11 shows reflection loss plots for various thicknesses of formative ice. In these examples the 2 cm formative ice layer has been shrunk uniformly to 75% (figure 11b) and 50% (figure 11c) of the original thickness. Figure 11a is the original AANII reflection loss plot shown in figure 6. The levels of reflection loss are down in figures 11b and 11c. Furthermore, the modal peaks which occur at low grazing angles in 11a have shifted in frequency. The behavior of reflection loss in the presence of formative ice is clearly complex, representing a very important factor in determining reflectivity and transmission loss.

6. CONCLUSIONS

The formative ice layer as constructed in the Bogorodskii AANII model is sensitive parameter in the determination of reflection loss. Our results using the Bunney and Hanse measurements confirm that their empirical ice parameters do yield results consistent with the Bogorodskii model even in the absence of measured fine structure. Also, variation in the details of the formative ice layer can cause significant variation in the reflection loss both in intensity and frequency. It may be predicted that if surface loss due to ice-sound interaction is present, then further experimental results should show a frequency dependence similar to what appears in our reflection loss results in figure 6.

We feel that Arctic ice models currently used require additional refinement, in order to model the frequency dependence of reflection loss at low grazing angles with sufficient accuracy. For example, the values we used for sound attenuation were of necessity extrapolated from higher frequencies values because there exist few, if any, direct measurements of sound attenuation in Arctic ice in the frequency ranges of our interest, due to the inherent difficulties of working at such low frequencies.

We hope that these results will encourage further experimental work on ice-sound interaction, particularly to confirm the affects of the formative ice layer.

7. REFERENCES

1. Schmidt, H., and F. B. Jensen, A Full Wave Solution for Propagation in Multilayered Viscoelastic Media with Application to Gaussian Beam Reflection at Fluid-Solid Interfaces, JASA, 77, 3, 1985.
2. Mayer, Walter G., Mohamad Behravesh, and Thomas J. Plona, Determination of Sonic Velocities from Reflectivity Losses at Sea Ice/Water Boundaries, JASA, 57, 1, pp 39-46, 1975.
3. McCammon, Diana F., and Suzanne T. McDaniel, The Influence of the Physical Properties of Ice on Reflectivity, JASA, 77, 2, pp 499-507, 1985.
4. Bunney, R. E., and J. E. Hanse, Acoustic Velocity Profiles in Annual Sea Ice, Unpublished.
5. Bogorodskii, V. V., V. P. Gavrillo, and V. A. Nikitin, Characteristics of Sound Propagation in Snow, Soviet Physics-Acoustics, 20, 2, pp 121-122, 1974.
6. Bogorodskii, V. V., V. P. Gavrillo, and V. A. Nikitin, Sound Propagation in Ice Crystallized from Salt Water, Soviet Physics-Acoustics, 22, 2, pp 158-159, 1976.
7. Gavrillo, V. P., A. V. Gusev, and V. A. Nikitin, Seasonal Changes Affecting the Elastic Properties of Sea Ice Cover, Transactions of the AANII, 374, pp 37-41, 1980.
8. DiNapoli, F. R., Fast Field Program for Multilayered Media, Rep 4103 Naval Underwater Systems Center, New London, CT, 1971.
9. DiNapoli, F. R., and R. L. Deavenport, Theoretical and Numerical Green's Function Solution in a Plane Multilayered Medium, JASA, 67, pp 92-105, 1980.

10. Kutschale, H. W., Rapid Computation by Wave Theory of Propagation Loss in the Arctic Ocean, Rep. CU-8-73 Columbia University, Palisade, NY, 1973.

11. Ewing, W. M., W. S. Jardetsky, and F. Press, Elastic Waves in Layered Media, McGraw-Hill, New York, 1957, Chapter 4.

12. Pounder, E. R., The Physics of Ice, Pergamon Press, New York, 1965, Chapter 2, page 23.

13. Weeks, W. L., U. S. Army Cold Regions Research and Engineering Laboratory, personal communication.

Sea Ice Sound Speed Profile

Bogorodskiy RANII Profile

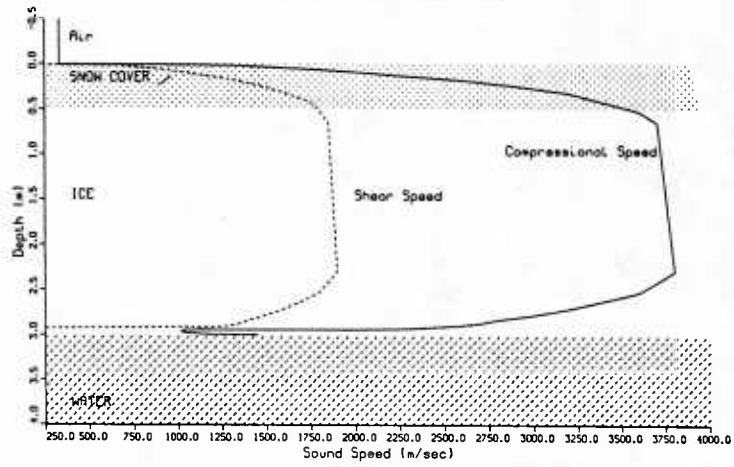


Figure 1

Sea Ice Sound Speed Profile

Bunny-Honse Profile

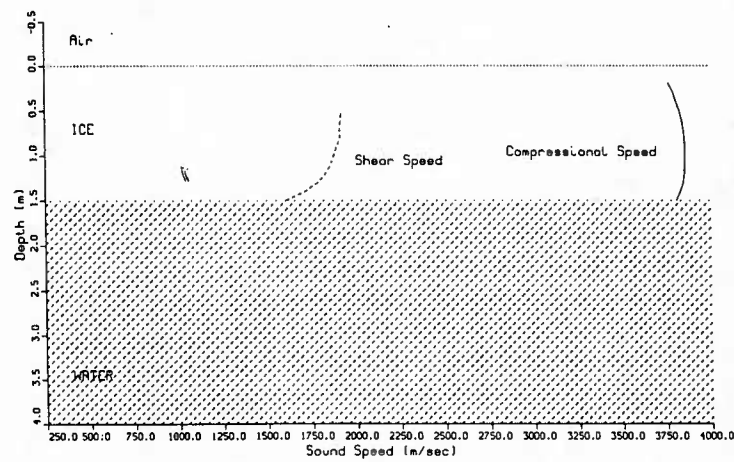


Figure 2

Formative Ice Sound Speed Profile

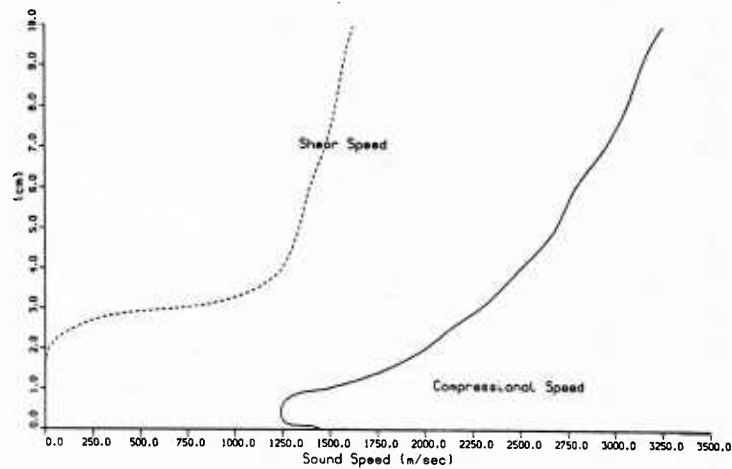


Figure 3

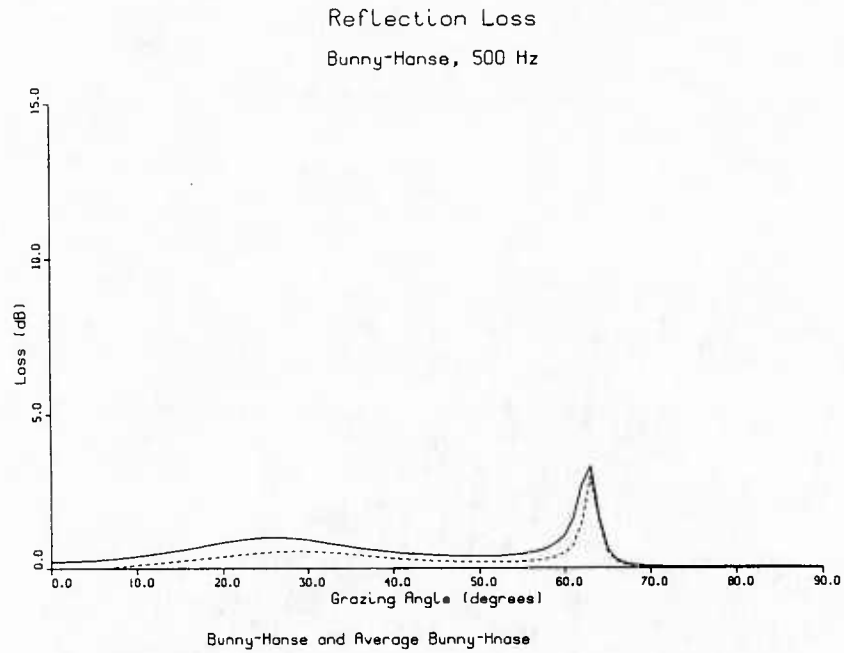
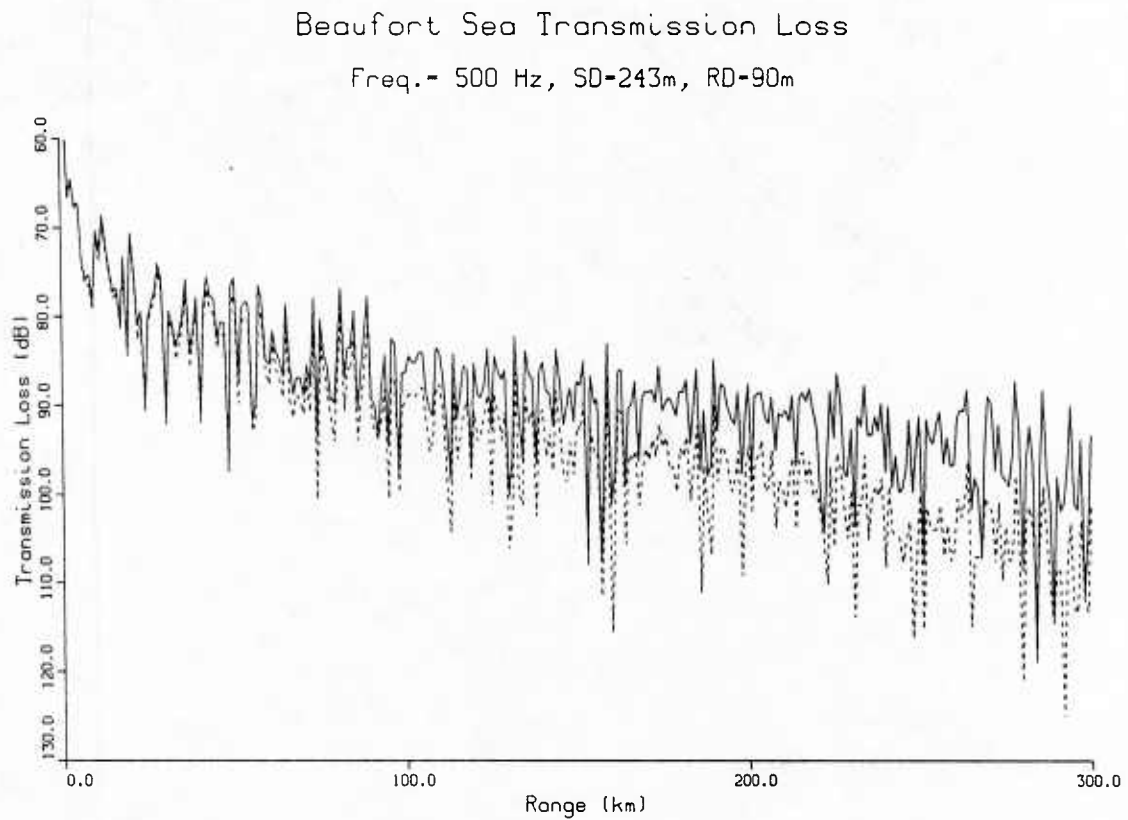


Figure 4



With (dash) and without (solid) Bunney & Hanse ice Loss

Figure 5

Reflection Loss

Bogorodskii RANII Profile

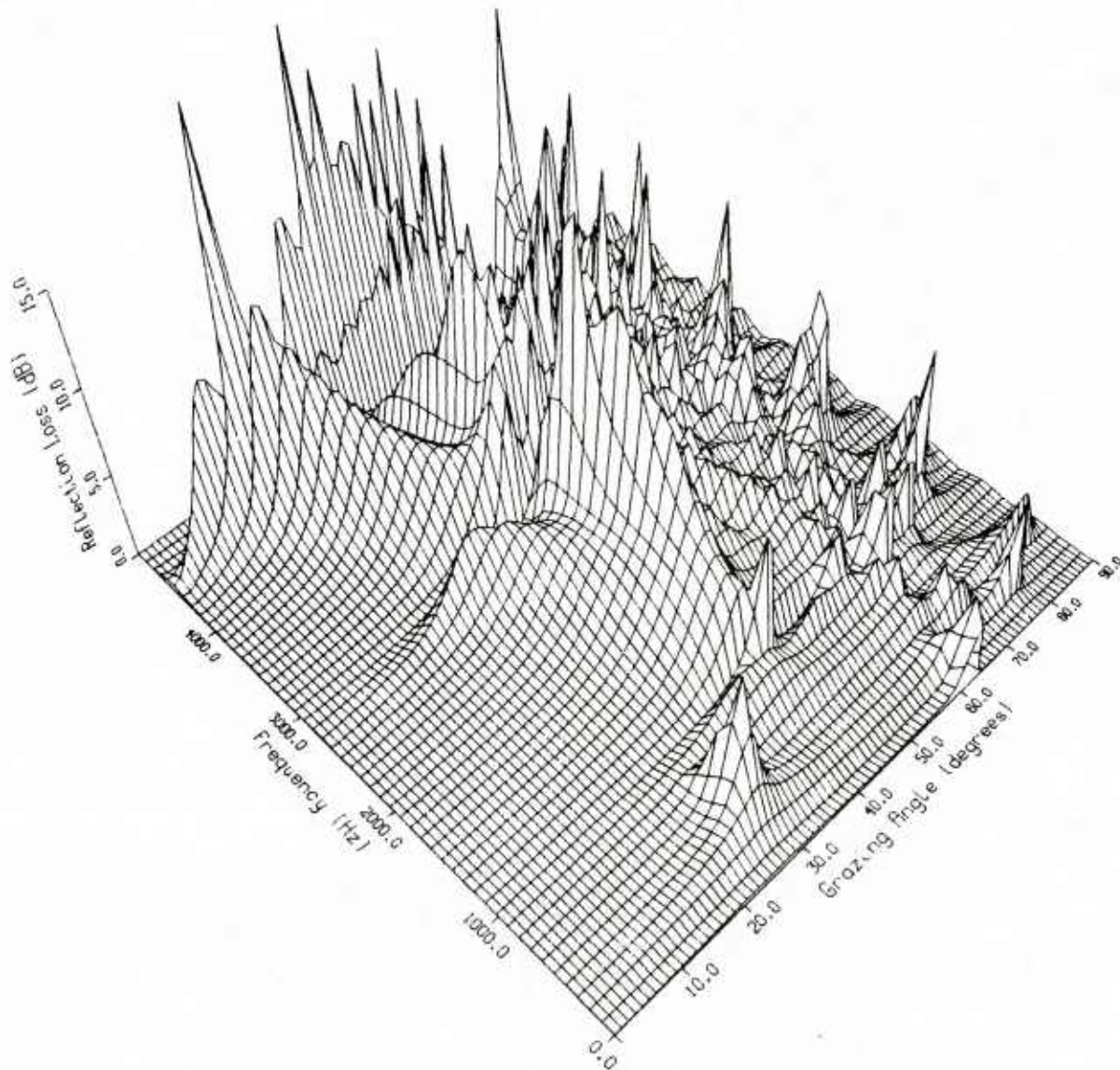


Figure 6

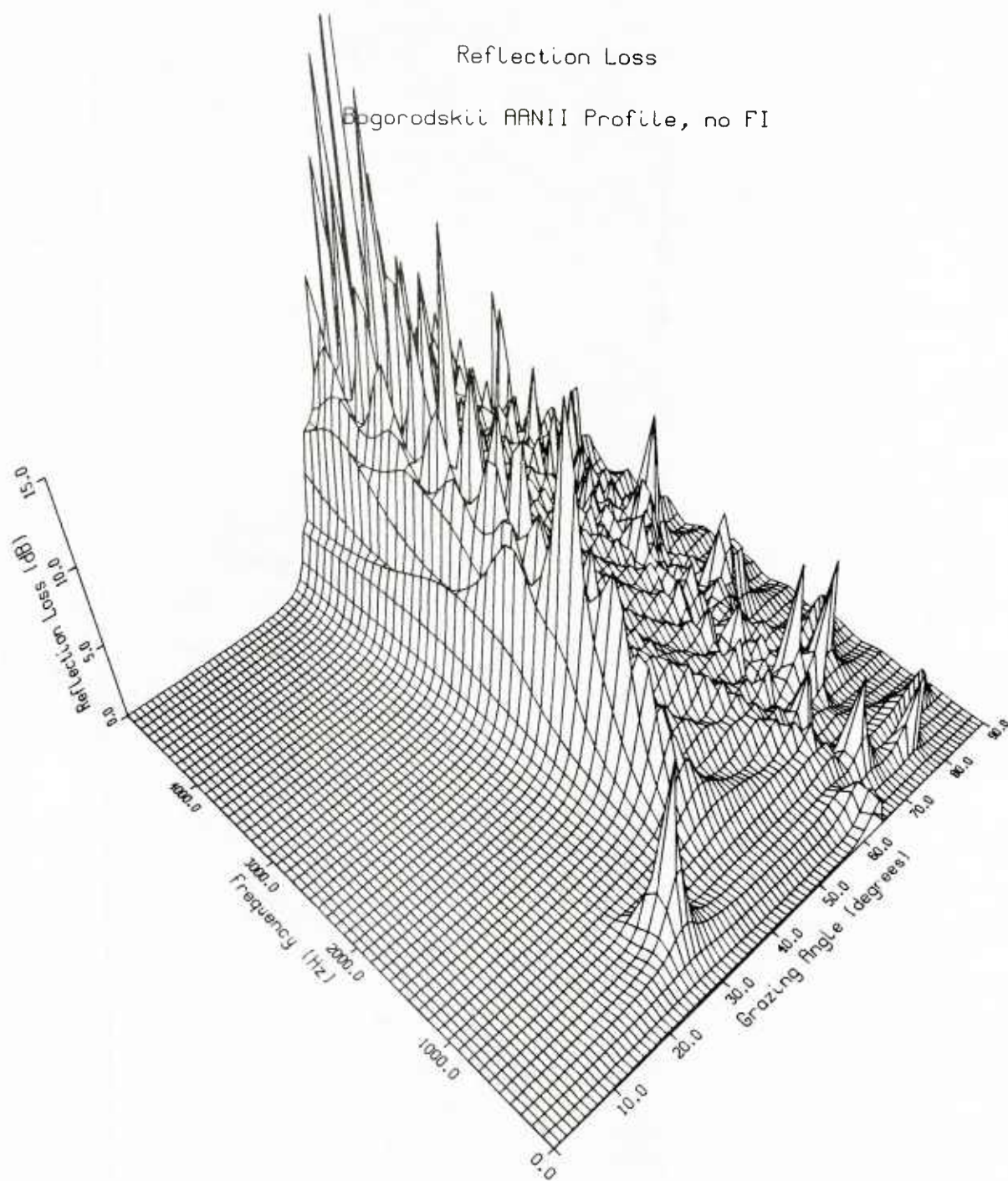


Figure 7

Reflection Loss

Bogorodskiy AANII Median Profile

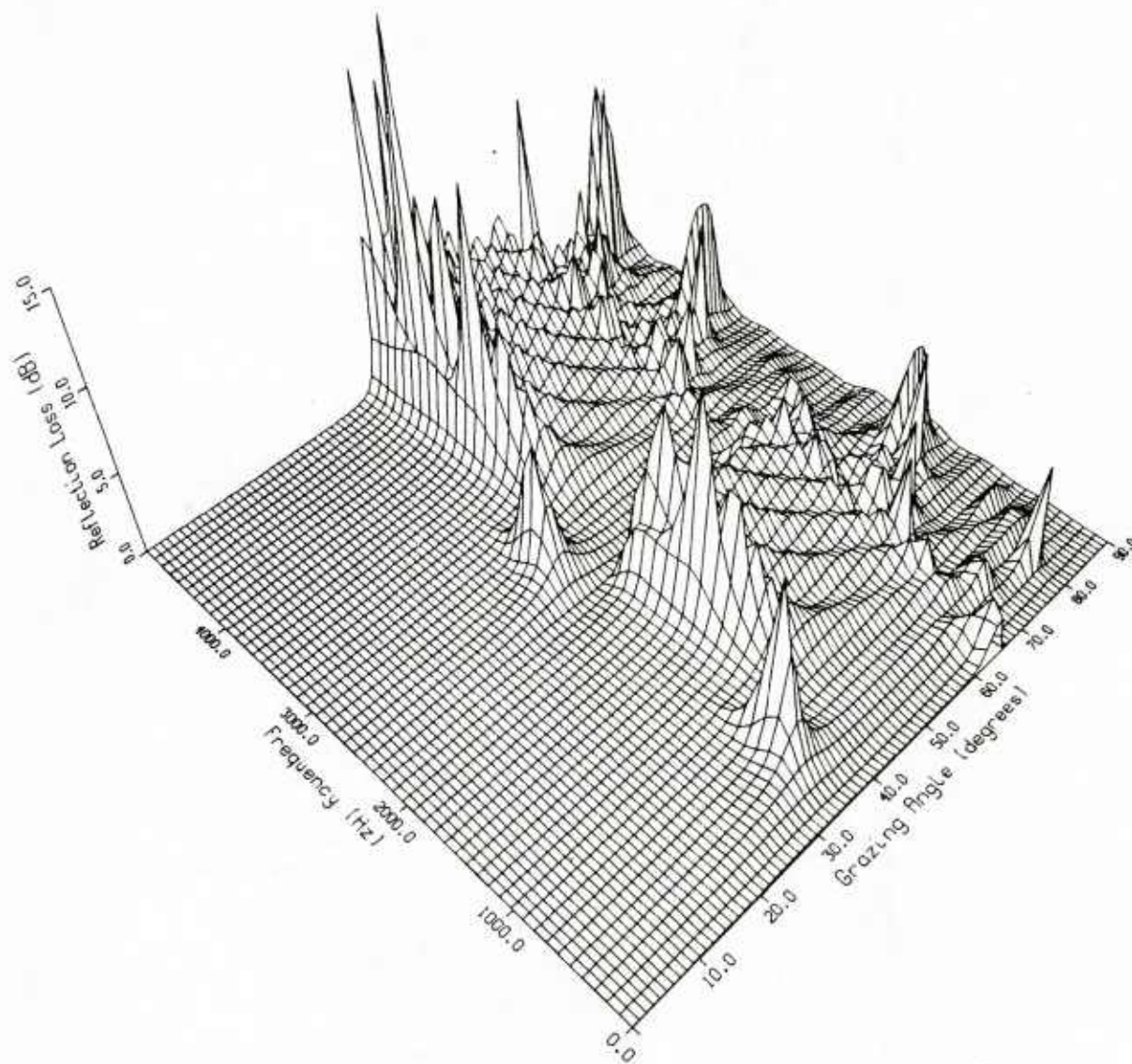


Figure 8

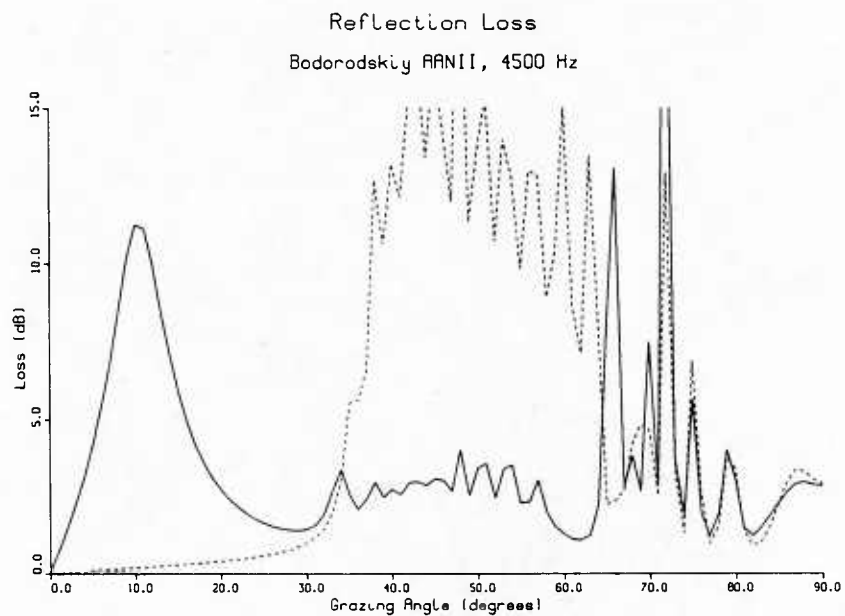


Figure 9

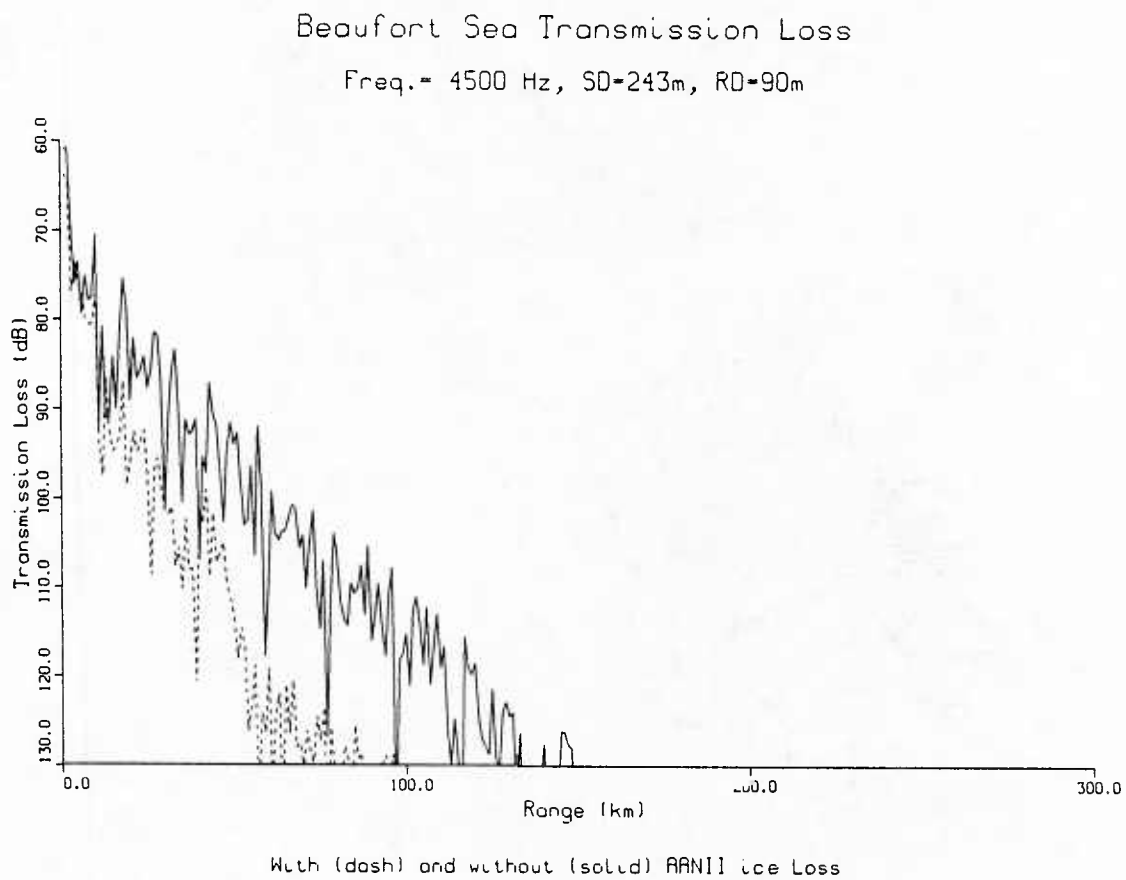


Figure 10

Reflection Loss Various Formative Ice Layers

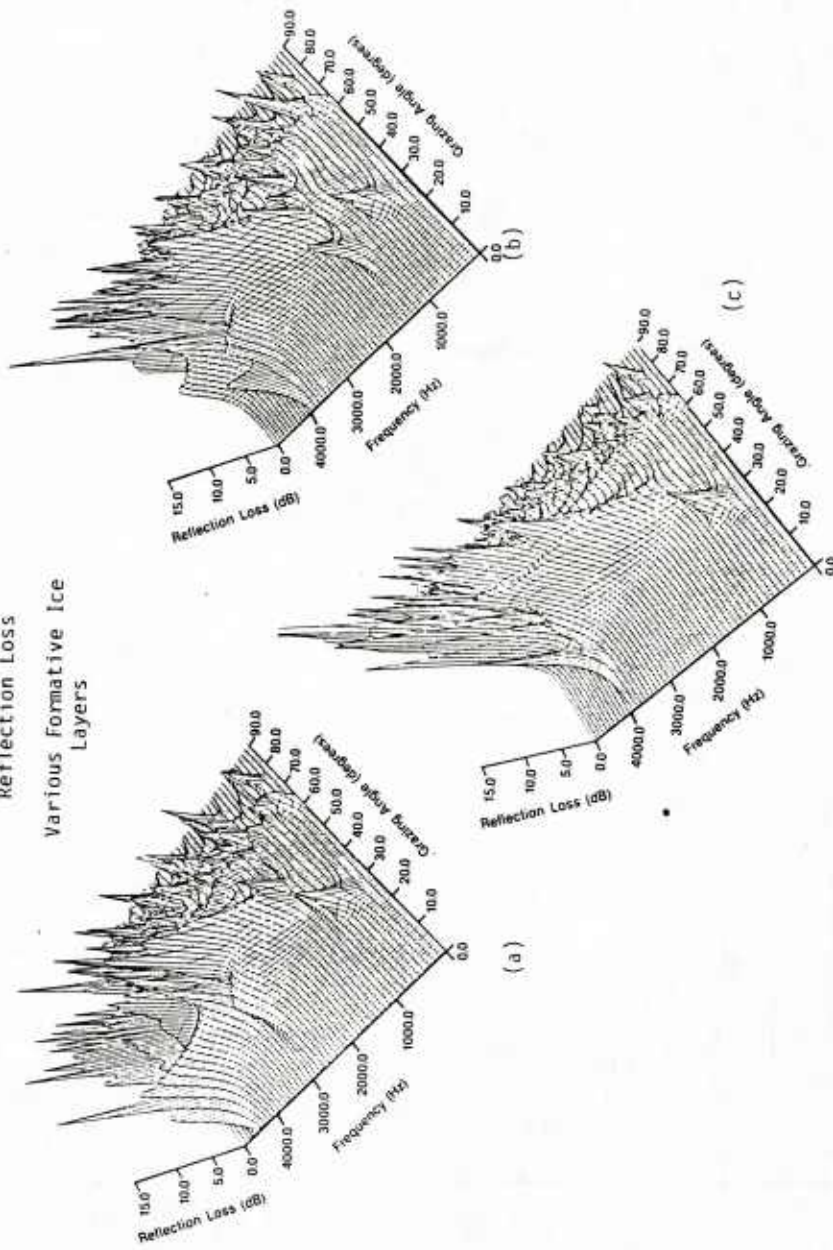


Figure 11

A MULTI-BOUNCE, SINGLE-SCATTER RAY THEORETIC MODEL FOR UNDER-ICE PREDICTIONS

A. Tolstoy, D. H. Berman, E. B. Wright, and R. N. Baer

Naval Research Laboratory, Washington, D.C. 20375-5000

ABSTRACT

This study describes the propagated and scattered acoustic field from a point source to a point receiver in an approximate under-ice environment characteristic of the deep Arctic Ocean. Our model considers both the azimuthal and vertical redistribution of scattered energy caused by a rough surface overlying an upwardly refracting, linear sound-speed profile. The model considers one non-specular surface scattering per path (connecting the source with the receiver) coupled with any number of specular interactions, each of which suffers losses due to scattering into non-specular directions. The propagation model is based on ray theory while the scattering model uses Twersky's scattering cross section for hard or soft planar surfaces roughened by hard or soft, hemispherical bosses. Results at all frequencies show that for the hard and soft surfaces the strongest scattered field is produced directly above the submerged source, that the total scattered energy levels increase as frequency increases while specular levels decrease, and that at high frequency both hard and soft surfaces have similar scattering levels and character.

1. INTRODUCTION

A problem of continuing interest in underwater acoustics is that of the scattering of acoustic energy by a rough surface. Such behavior is important, for example, when sound interacts with the rough bathymetry present in large ocean areas in shallow to moderate depths, with ocean ridges, as well as with the air-water interface, and with the water-ice interface in the arctic. In many cases the energy can interact with both a rough bottom and a rough ocean surface. Here we shall be particularly concerned with deep-water arctic studies where the upward refracting profile causes under-ice interactions to be of major significance.

The full problem of under-ice scattering coupled with the propagation of energy in a realistic 3-D environment is analytically intractable. Hence, models for solving this problem require significant approximations, and even for simplified models only various components of the full problem have been examined. Nevertheless, important insights can and have been made in situations where the study focus is sufficiently well-defined as to allow a segment of the whole problem to be isolated. In this vein the purpose of this study is to ascertain:

- o the manner and the degree to which single and multiple scatter are significant in the arctic environment;
- o when important, are there patterns in the scattering behavior which lead to efficient computation of effects and which point toward methods and regimes where multiple-scattering effects can be treated practically;
- o frequencies for which change in boundary conditions (hard versus soft) becomes important.

These questions are addressed by considering the azimuthal and vertical redistribution of energy caused by a single non-specular interaction (scattering event) per path, while allowing for any number of specular reflections, with losses, on the remainder of the path connecting the source and the receiver. This approach reveals the possibility of taking advantage of the sharply peaked azimuthal character of the scattering cross section at high frequency to compute multiple-scattering effects efficiently in future efforts.

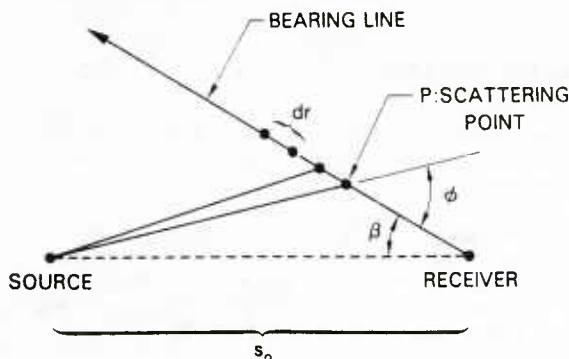
2. THE MODEL

The immediate aim of the calculations is to determine the azimuthal distribution of total energy, scattered or direct (specularly reflected) at a point receiver arising from a point source (Fig. 1). It is assumed that there is only one non-specular interaction of sound with the surface at some arbitrary point P. All surface interactions from the source to P and from P to the receiver are regarded to result in specular reflections only. Losses are incurred upon these reflections as a result of the scattering. However, the energy not scattered into bearing β at point P is not considered in calculating the energy arriving at the receiver along bearing β . At the point P all rays θ^R which scatter azimuthally into bearing angle β , including those scattered vertically, are considered in the family of rays which subsequently propagate to the receiver (Fig. 2). For $\beta = 0$ (the direct bearing) paths consisting of all specular interactions (with losses) are also considered. Finally, the energy arriving at the receiver should be regarded as a sum of the energy from all single scattering and specular interactions.

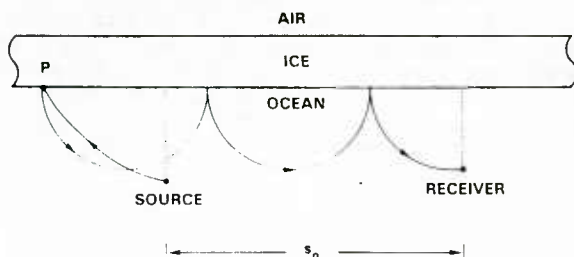
The propagation model used in this study is ray theoretic [1] with the source and receiver separated horizontally and each allowed to be located at an arbitrary depth below the surface. The acoustic intensity incident at the receiver is computed as a function of incremental distances dr from the receiver to P

1. Geometry of source and receiver configuration.

a. Top view of ice surface with geometry of source location and receiver location, and bearing line at angle β for energy incident to receiver. The non-specular interaction point P of scattering lies on the bearing line. The angle of azimuthal scattering is φ .



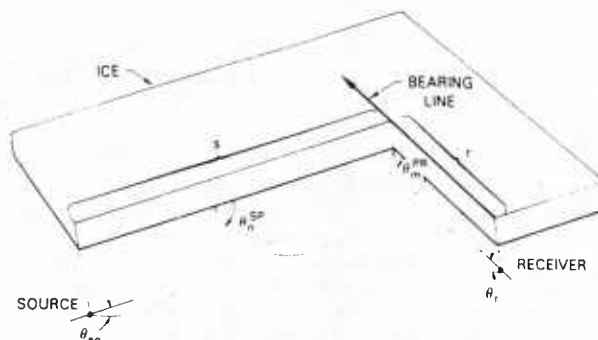
b. Side view of ice surface with $\beta = 0$. Ray shown goes from source to P to receiver and is backscattered. For P between source and receiver such rays are forwardscattered. Source is at range s_0 from the receiver.



along the specified bearing line (Fig. 1). The non-specular, single-point-of-scattering interaction lies within the wedge of angular width $d\beta$ centered on the line of bearing β from the receiver.

The sound-speed profile $c(z)$ is assumed to be an increasing, linear function of depth measured from the under-ice rough surface. It is independent of horizontal position: $c(z) = c_0 + pz$ where $p > 0$. This profile (representative of an arctic environment) results in rays which are circular arcs and allows for the rapid computation of all rays of interest connecting the source to the receiver via the scattering point P. All eigenrays from the source to P and from P to the receiver are computed unless the source and/or receiver are located on the ice surface. In that case a minimum angle must be specified (equivalent to specifying a maximum number of bounces). For a source and receiver below the surface there are two rays [2] which propagate from the source to P at range s with n surface reflections (not including one at P) and two rays from P to the receiver at range r with m surface reflections. For the parameters of Table 1 there is an average of 10 to 20 rays computed from source to P and 10 to 20 rays from P to receiver along the 10° bearing line resulting in a total of 1,036,181 rays from source to P to receiver from 0 to 200 km in steps of 0.1 km increments.

2. Oblique view of Fig. 1. The surface eigenangle from source to P having n bounces is denoted by θ_n^{sp} . At P the ray scatters azimuthally while the angle of vertical scatter at the surface having m bounces from P to receiver is denoted by θ_m^{rk} . Since the sound speed profile is assumed to be an increasing, linear function of depth, the ray paths are circular arcs.

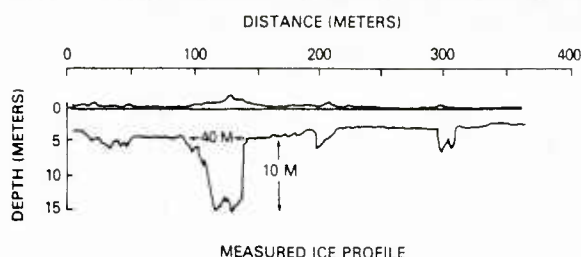


3. A planar surface with randomly distributed hemispherical bosses. Inverting this figure we have the idealization of the under-ice roughness considered in the Twersky scattering formulation which is used in this model.



A scattering cross section is required to compute the scattered intensity at P in the direction (θ_m^{rk}, φ) from the direction θ_n^{sp} where φ is the azimuthal angle of scattering ($\varphi = 0$ for forward scattering; $\varphi = 180^\circ$ for backscattering). The cross section which we incorporate is based upon Twersky's [3] scattering cross section σ which assumes that the rough surface can be described in terms of hard or soft, hemispherical bosses distributed on a hard or soft plane by means of a uniform probability law (Fig. 3). By definition a hard surface is one on which the normal component of acoustic velocity is zero with no phase change to the coherent pressure field upon reflection while a soft surface is one on which the pressure field is zero with a subsequent phase change of 180 degrees upon reflection. Figure 4 shows a typical under-ice profile [4], with height equal to half the radius (note the 5:1 scale of the figure). The small ice ridges have heights of about 5 m and occur about every 100 m. While the keels beneath the ice ridges might be better approximated by hemicylindrical bosses having elliptical cross sections, there is at present no theory which can deal with such anisotropic scatterers for energy incident at oblique angles. Hence, we have used hemispherical shapes which approximate short ridges. Twersky's cross section was selected primarily because the bossed surface resembles the discrete character of the ice, and because Twersky's cross section is unrestricted in frequency (unlike perturbation or Kirchhoff theories). The size (radius a), spatial distribution density ρ of the hemispherical bosses, and the frequency f of the acoustic signal are the parameters of the model and are given in Table 1.

4. A measured under-ice profile (by R.E. Francois and W.E. Nodland of APL Univ. of Wash.). Note the 5:1 (range:depth) scale of the figure. For a 1:1 scale like that of Fig. 3 we would see that the ice ridge heights are approximately half of their radii.



3. COMPUTATIONS

This model currently gives two types of results:

- o calculations and plots of acoustic intensity $I(r)$ at the receiver from areas of the surface $rdrd\beta$ as a function of distance along a bearing line from the receiver to the non-specular scattering event;
- o calculations of total intensity, $\int I(r)rdr$, per degree of bearing angle at the receiver where the energy has scattered once into this bearing.

For both of these computations a range window (such as the 0 to 200 km used in these results) or a time window must be specified to account for the range or time interval over which the receiver examines the signal. See Table 1 for complete parameter values. The time window allows only those rays which take a specified time from source to P to receiver. We selected the range window in order to isolate and study the surface regions where the strong single-scattering is occurring.

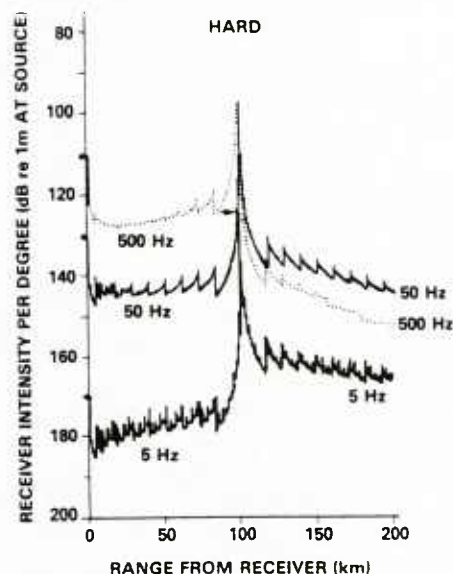
3.1 Hard surface

Consider the scattered energy incident at 0° direct path bearing from a source 100 m below the hard, rough surface to a receiver 10 m below the surface. The lower solid curve of figure 5 representing low frequency results shows this scattered energy as a function of range from the receiver while excluding all completely specular paths. We notice a number of features for this curve.

First, there is a strong energy peak of -125 dB located over the source (distance = 100 km). The source peak is about 30 dB higher than the energy scattered from other regions along the bearing wedge. This peak indicates that for a simple, non-directional source the strongest single-scattered signal occurs over the source where the scatterer is only 100 m from the source. This result is the consequence of the high intensity nearly vertical rays.

Second, the distant backscattered energy (coming from distances greater than 100 km) is stronger than the nearby forward scattered energy (from 0 to 100 km) by approximately 15 dB. This is an effect of the scattering cross section. In particular, we note that at low frequencies ($ka = 0.1$) and at shallow grazing

5. Intensity of energy scattered by hard surface into 0° bearing at various frequencies as a function of range from receiver. Note how all levels of forward scattered intensity increase as a function of frequency. However, the backscatter levels ($r > 100$ km) relative to the forward-scatter levels are strongly reduced by reflection losses as frequency increases. Note how at 500 Hz all forwardscatter levels are larger than the backscatter levels. Both 50 and 500 Hz signals peak over the receiver at -97 dB.

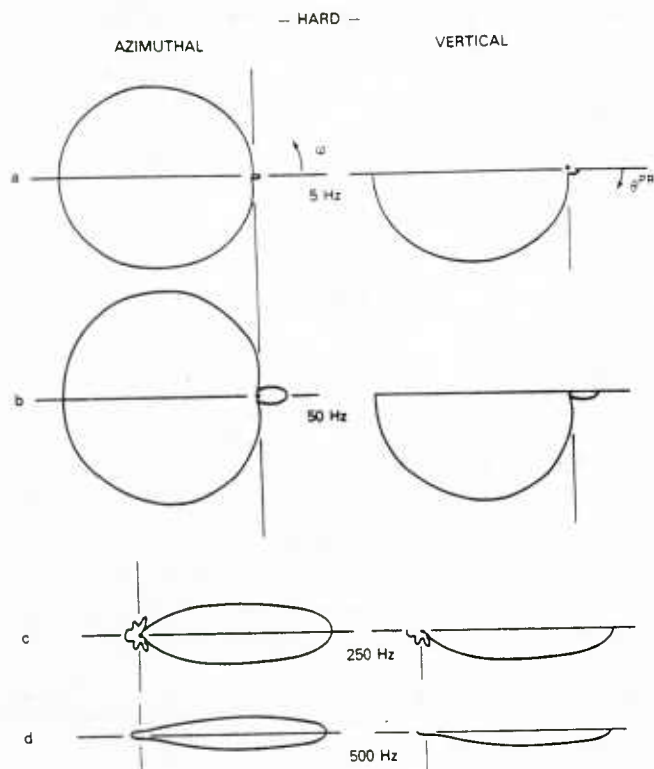


angles $< 15^\circ$ the scattering cross section for a hard sphere has a broad maximum in the backscattered direction $90^\circ < \theta < 270^\circ$ (Fig. 6).

Third, we notice the gradual decay of the backscattered energy which is the result of specular losses accumulating as the contributing paths require more surface interactions and also of larger spreading losses for these long distance rays. Hence, the incoming scattered energy will decrease beyond some range (consistent with intuition). The total scattered intensity per degree for this bearing and these ranges (0 - 200 km) is -133 dB while the all specular energy level is approximately -77 dB. Thus, the single-scattered energy in a 1 degree wedge about 0° bearing is about 56 dB down from specular.

Consider the mid frequencies as represented by 50 Hz ($ka = 1$) with scattering into 0° bearing shown by the middle curve in Fig. 5. Comparing these results to those at 5 Hz ($ka = 0.1$) shown by the lower curve we see 20-40 dB higher intensity levels at the higher frequency where the total levels for scattered energy within 200 km of the receiver are approximately -102 dB versus -129 dB. Hence, we conclude that there is significantly more scattering occurring at each interaction at the higher frequency. We note that more scattering will result in less specular energy and greater specular losses for the rays. The total all-specular energy level for the 50 Hz signal is -86 dB compared to -83 dB at 5 Hz.

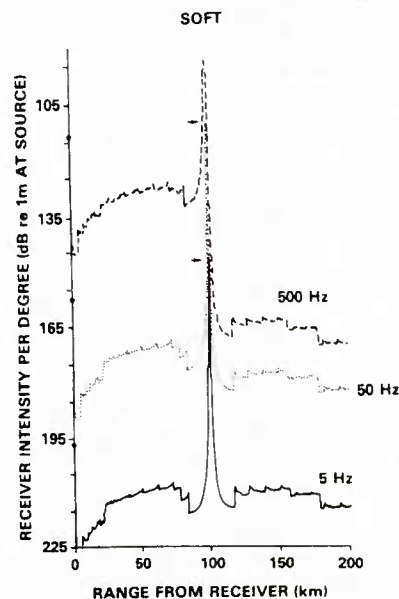
6. A polar plot of Twersky's scattering cross section for the hard surface ($ka = 0.1, 1, 5, 10$) representative of shallow grazing angles $< 15^\circ$ as a function of azimuthal angle φ (vertical angles in θ^{SP} and out θ^{PR} of the rough surface are 1°) and as a function of vertical scattering angle θ^{PR} where $\varphi = 0$ and the vertical angle into the surface $\theta^{SP} = 1^\circ$.



Also we see that the distant (at distances greater than 100 km) backscattered signal is no longer substantially stronger than the nearby forward scattered signal, and it decays more rapidly than at the lower frequency. This is the result of strong specular losses reducing the strength of the distant rays. The scattering cross section given in Fig. 6 for rays incident at < 15 degrees still shows backscattering to be quite strong relative to forward scattering.

For the high frequencies as represented by 500 Hz ($ka = 10$, upper dashed curve) we find that the forward scattered energy dominates the backscattered energy which in turn decays very rapidly. This is consistent with the behavior of the scattering cross section as seen in Fig. 6 which show that for shallow grazing angles as frequency increases the scattered energy increasingly concentrates into the forward direction. Furthermore, as frequency increases, the total level of scattered intensity continues to increase (total intensity from 0 to 200 km is -96.5 dB for 500 Hz, -129 dB for 50 Hz) while specular levels continue to decrease (total specular intensity is -90 dB for 500 Hz, -83 dB for 50 Hz).

7. Intensity of energy scattered by soft surface into 0° bearing at various frequencies as a function of range from the receiver. Note how all levels of scattering increase as a function of frequency. Note also the peak intensities indicated by arrows with corresponding dB values.



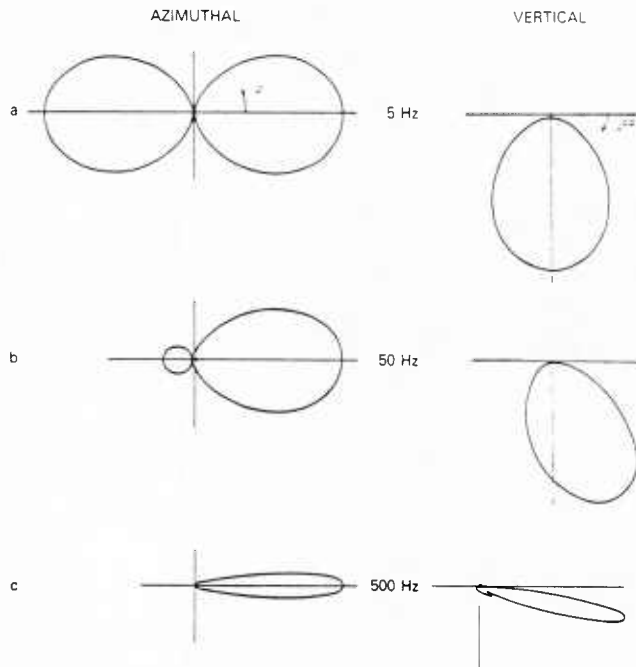
3.2 Soft Surface

Similar to the hard surface results, we again see a very high intensity signal scattered from the rough surface above the source. Examining Fig. 7 we see that at 5 Hz (solid curve) the peak intensity reaches -146 dB versus -133 dB for the hard surface (Fig. 5). Considering the scattering cross section representative of shallow grazing angles we see a generally weaker scattering cross section for the soft bossed surface (compare the maximum strength, $R_{MAX} = 9.23 \times 10^{-16}$ of Fig. 8 with that of Fig. 6 where $R_{MAX} = 6.87 \times 10^{-7}$). For forward azimuthal scattering ($\varphi = 0$) we see in Fig. 8 that the maximum vertical angle scattering strength is 3.01×10^{-10} for energy incident at 1° vertical and scattered directly downward versus a strength of 1.1×10^{-7} for the same situation with the hard surface as seen in Fig. 6. From such estimates we would expect differences of about 30 dB in the scattered levels. However, peak levels are the result of energy vertically incident to the surface with a range of scattered angles. For the soft surface the scattering strength for energy incident at 90 degrees vertical angle (figure not shown but behavior has same character as Fig. 8) increases from 2.7×10^{-9} scattered into 3 up to a maximum of 2.49×10^{-7} scattered directly downward while it remains at 1.1×10^{-7} for all vertical rays to the hard surface. Thus, the soft and hard surface peak levels differ by much less than 30 dB, i.e., by ~ 13 dB.

Consistent with the generally weaker soft surface scattering cross section at low frequency we see that away from the source region (before and after 100 km from the receiver in Fig. 7) the soft surface scattering levels at 5 Hz are 20 to 40 dB lower than the hard surface levels (Fig. 5), i.e., average -210 dB versus -190 to -170 dB. Moreover, the soft surface does not

8. A polar plot of Twersky's scattering cross section for the soft surface ($ka = 0.1, 1, 10$) representative of shallow grazing angles $< 15^\circ$ as a function of φ (θ^{SP} and θ^{PR} are 1°) and as a function of θ^{PR} where $\varphi = 0$ and $\theta^{SP} = 1^\circ$.

- SOFT -

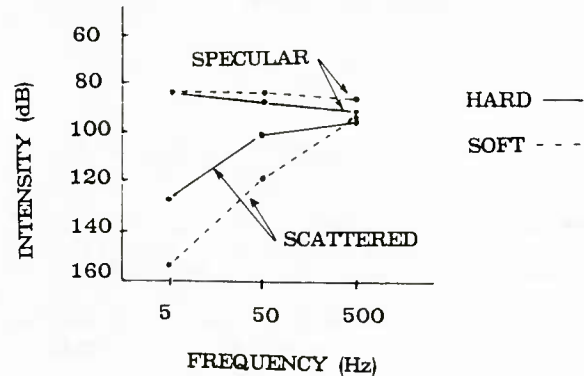


show predominant backscattering at low frequency. This is evident in both the cross section itself where scattering is predominantly downward and in the distant (beyond 100 km) scattered intensity at the receiver where the distant (backscattered) energy is of comparable intensity to the nearer (forwardscattered) energy. At increasing distance this is the result of more eigenrays over a larger integration area ($rdrd\beta$) competing against smaller individual intensities (greater spreading losses) and smaller scattering strengths (shallower rays to the receiver).

Increasing signal frequency we see in Fig. 7 leads to results which are similar to those for the hard surface in Fig. 5. That is, all scattering levels increase with frequency while distant backscattered energy drops below the forwardscattered levels. Examining the scattering cross sections of Fig. 8 we see that as in the hard surface case when frequency increases the scattering increases and concentrates in the forward direction both azimuthally and vertically. In addition we see in Fig. 9 that concurrent specular levels decrease gradually as scattering increases. At 500 Hz the total scattering incident at 0° bearing and within 200 km has intensity -95 dB while specular intensity is only 10 dB higher at -85 dB.

We also note that the general scattering levels for the soft surface are below those for the hard surface. These results are consistent with the generally smaller scattering strengths evident in the soft surface cross sections.

9. Plot showing specular energy levels and total scattering levels for energy incident to receiver (from $\varphi = 0$, from 0 to 200 km, 100 m source, 10 m receiver) for hard and soft surfaces. Note how scattering levels increase with frequency while specular levels decrease until at 500 Hz they are comparable, i.e., within 10 dB.



4. CONCLUSIONS AND RECOMMENDATIONS

Using rays to propagate between scattering points plus Twersky's scattering cross section for a hard and soft surfaces roughened by sparse, hard and soft, hemispherical bosses we have computed the directional intensity resulting from single-scattered energy from a point source located below the surface to a point receiver below the surface. We have included the effects of multiple specular encounters and have shown that for ice parameters (boss height of 5 m, one boss per 10,000 m^2):

1. For both the hard and soft surfaces and at all frequencies the strongest contribution to the scattered field is produced directly above the source with peak levels of -97 dB for the hard surface, -90 dB for the soft surface at 500 Hz.
2. At low frequency the scattered levels are 45 to 60 dB below the specular levels indicating that very little scattering is occurring and that the signal should be highly coherent for both the hard and soft surfaces.
3. As the source frequency increases from 5 to 500 Hz, the total scattered energy levels (along 0° bearing to a receiver at 10 m and within ranges 0 to 200 km) increase from -129 dB to -97 dB for the hard surface, from -155 dB to -95 dB for the soft surface. Concurrently, specular interactions suffer higher losses with total specular levels decreasing from -83 dB to -90 dB for the hard surface, from -83 dB to -85 dB for the soft surface.
4. At low and mid frequencies the hard surface shows strong backscatter relative to forwardscatter with levels 25 to 40 dB above soft levels.
5. At high frequency both hard and soft surfaces have similar scattering levels.

Finally, we found that for both hard and soft surfaces as frequency increases, the scattered energy becomes more concentrated in the forward direction. This indicates that high frequency multiple scattering might be computed by iterating the approach presented in this model and densely sampling forward scattering points near the source and receiver.

REFERENCES

1. L. Tolstoy and C.S. Clay, Ocean Acoustics (McGraw-Hill, 1966).
2. M. J. Jacobson, "Analysis of spreading loss for refracted/reflected rays in constant-velocity-gradient media," *J. Acoust. Soc. Am.* 36 (1964), 2298-2305.
3. V. Twersky, "On scattering and reflection of sound by rough surfaces," *J. Acoust. Soc. Am.* 29 (1957), 209-225.
4. O.L. Diachok, "Effects of sea-ice ridges on sound propagation in the arctic ocean," *J. Acoust. Soc. Am.* 59 (1976), 1110-1120.

TABLE 1

Model Parameters

$$k = \begin{array}{ll} 0.02 \text{ m}^{-1} & (f \approx 5 \text{ Hz}, \lambda = 314 \text{ m}) \\ 0.20 \text{ m}^{-1} & (f \approx 50 \text{ Hz}, \lambda = 31.4 \text{ m}) \\ 2.00 \text{ m}^{-1} & (f \approx 500 \text{ Hz}, \lambda = 3.1 \text{ m}) \end{array}$$

$$a = 5 \text{ m}$$

$$\rho = 0.0001 \text{ bosses per m}^2$$

$$c(z) = 1.5 + 0.01 z \text{ km/sec (with depth } z \text{ in km)}$$

$$\text{Source-Receiver separation distance} = 100 \text{ km}$$

$$\text{Incremental distance} = 0.1 \text{ km}$$

$$\text{Source depth} = 0.1 \text{ km}$$

$$\text{Receiver depths} = 0.01 \text{ km}$$

THE CALCULATION OF AN EFFECTIVE THICKNESS TERM FOR SEA ICE USING LAGRANGIAN DATA

James K. Lewis
Warren W. Denner

Science Applications International Corporation
1304 Deacon
College Station, TX 77840

ABSTRACT

A methodology is presented which allows one to calculate an ice thickness term using observed ice motion and wind data. Since the wind data can come from atmospheric pressure fields or numerical models, the methodology is in fact a remote-sensing capability which relies on ice motion data from satellite imagery, buoys drifting on the ice, etc. The thickness term is shown to be an effective ice thickness which reflects the strength of the ice as a result of the true ice thickness plus the added mass effect of internal ice stresses. Examples of the temporal variations of the effective ice thickness are presented, and these variations are explained in terms of the compactness of the ice field as the motion is toward or away from the ice pack.

1. INTRODUCTION

In this paper, we consider a parcel of pack ice which consists of a number of individual floes plus a variable percent of open water. As wind blows over the ice parcel, the energy of the wind is distributed down through the ice, and the ice moves according to the geophysical balances of forces. In other words, $f=ma$, which implies that an ice parcel of greater thickness (mass) is accelerated less for a given wind stress. However, this concept of the relationship between wind forcing and ice thickness is complicated by the fact that the internal stresses of pack ice can be considerable, and an ice parcel under greater compression is also accelerated less for a given wind stress. In this case, the internal ice stresses make the ice parcel appear thicker than it actually is.

Here we present a methodology which provides a basis for calculating an effective ice thickness, which is the summation of the true ice thickness plus the added mass effect of the internal ice stresses. In essence, we take the wind forcing and the observed ice response and force f to equal ma . The resulting mass parameter, \bar{H}_e , is the effective ice thickness, a vector as a consequence of the internal ice stresses.

This methodology is based upon observed ice speed \vec{U} , corresponding wind stress $\vec{\tau}$, and the analytical solutions to the appropriate equations of motion. As such, it provides the basis for a remote sensing capability for measuring the strength of pack ice in terms of its true ice thickness plus the effect of internal ice stresses. Ice motion data from buoys drifting on the ice or synthetic aperture radar (SAR) can be used with wind stress as determined from atmospheric pressure fields or numerical models to calculate \bar{H}_e . Two-dimensional contour maps of \bar{H}_e can be generated at regular time intervals to provide operationally-valuable information with respect to true ice thickness plus internal ice stresses.

2. THEORETICAL AND TECHNICAL CONSIDERATIONS

The governing equations for ice motion can be expressed as

$$d\vec{U}/dt + f\vec{k} \times \vec{U} = (\vec{\tau} - KR\vec{U} + \vec{I})/H\rho \quad (1)$$

where f is the Coriolis parameter, \vec{I} is the gradient of pressure and internal stresses, H is the ice thickness, ρ is the ice density, and KRU represents the drag between the ice and the underlying water with K =drag coefficient, $R_x=1-|V_x|/|U_x|$, $R_y=1-|V_y|/|U_y|$, and V is the speed of the water. Consider the situation such that, at some time $t=0$, $\vec{I}=\vec{U}=0$. In this situation, Lewis et al.¹ have shown that the solutions to the above expression are

$$\begin{aligned} U_{x,t} &= \int_0^t e^{-\Gamma_x \delta} \left[\tau_x \Big|_{t-\delta} \cos f \delta + \right. \\ &\quad \left. \tau_y \Big|_{t-\delta} \sin f \delta \right] d\delta / (H_x \rho) \\ U_{y,t} &= \int_0^t e^{-\Gamma_y \delta} \left[\tau_y \Big|_{t-\delta} \cos f \delta - \right. \\ &\quad \left. \tau_x \Big|_{t-\delta} \sin f \delta \right] d\delta / (H_y \rho) \end{aligned} \quad (2)$$

where

$$\bar{H}_e = (H_x, H_y) = H \left((1 + U_{I_x}/U_{\tau_x})^{-1}, (1 + U_{I_y}/U_{\tau_y})^{-1} \right)$$

and \vec{U}_I and \vec{U}_T are the ice velocities induced by the pressure/stress gradients and the wind stress, respectively. Also,

$$\vec{T} = (\tau_x, \tau_y) = K(Rx/Hx, Ry/Hy)/\rho.$$

Equations (2) express the wind-induced ice motion as the summation of inertial oscillations that are modified by (a) the water stress under the ice (\vec{T}) and by (b) the internal ice stresses (\vec{H}_e). As previously mentioned, the effective ice thickness \vec{H}_e reduces to the actual ice thickness H as $\vec{I} \rightarrow 0$ (i.e. the added mass effect of \vec{I} goes to zero).

In using our analytical solutions to determine \vec{H}_e , we note that \vec{U} and $\vec{\tau}$ may be calculated using actual ice motion and wind data. But we still must determine \vec{I} , and this is done empirically as outlined in Figure 1. Over a given time interval of n hours, various values of τ_x and τ_y are used to calculate series of theoretical ice transports ($U_T H$) using $\vec{\tau}$ in the RHS of equations (2) after multiplying by \vec{H}_e^2 . Each series of theoretical transports for each τ are then correlated with the corresponding observed ice speeds. The τ 's of the series which give the highest correlations between the observed speeds and the theoretical transports are used as estimators of the true τ 's. The \vec{H}_e terms are then calculated by determining the least squares slope of $U_T H$ versus U ($H = d(U_T H)/dU$; see Figure 2).

This method results in an average effective ice thickness over the n hour period. Fluctuations in \vec{H}_e can be a result of variations of \vec{I} or H . However, one would expect that the true ice thickness H would vary over a considerably longer time scale than that of \vec{I} . Thus, the shorter term fluctuations in \vec{H}_e will most likely be the result of variations in \vec{I} , and this information can be used to calculate the variations in the forces which result from horizontal pressure gradients and internal ice

stresses. Moreover, minimum values of \vec{H}_e will tend to reflect the actual ice thickness H since the tensile strength of pack ice is relatively small with respect to its compressive strength³.

3. EFFECTIVE ICE THICKNESSES IN THE BEAUFORT SEA

Wind speed and ice motion data from the manned camps of the Arctic Ice Dynamics Joint Experiment (AIDJEX) were used to calculate \vec{H}_e . Wind stress was calculated following Amorochio and DeVries⁴. Six hour averages of the observed ice speeds and theoretical ice transports were correlated over 15 day periods by varying τ such that

$$e^{-\tau t} = 0.1 \text{ for } \begin{cases} t=3 \text{ hr} \\ t=4.5 \text{ hr} \\ t=6 \text{ hr} \\ t=9 \text{ hr} \end{cases}$$

These values of τ will be referred to as τ_3 , $\tau_{4.5}$, τ_6 , and τ_9 , respectively.

The maximum linear correlations for 16 May-21 July 1975 at 15 day intervals are shown in Figure 3. All the correlations are ~ 0.85 or greater. The corresponding \vec{H}_e are also shown in Figure 3. During 16-30 May and 7-21 July, H_y is significantly greater than H_x , the implication being that the y component of \vec{I} has a greater decelerating effect than the x component of \vec{I} . Thus, the ice appears thicker in the y direction during the 16-30 May and 7-21 July periods.

The linear correlations for 24 July-18 September 1975 at 15 day intervals are shown in Figure 4. Once again, the correlations are ~ 0.85 or greater. Also, during this period H_y is larger than H_x . These and the May-July variations of \vec{H}_e can be associated with the direction of movement of the ice. During 16 May-21 July 1975, most of the

Start With the Analytical Solution:

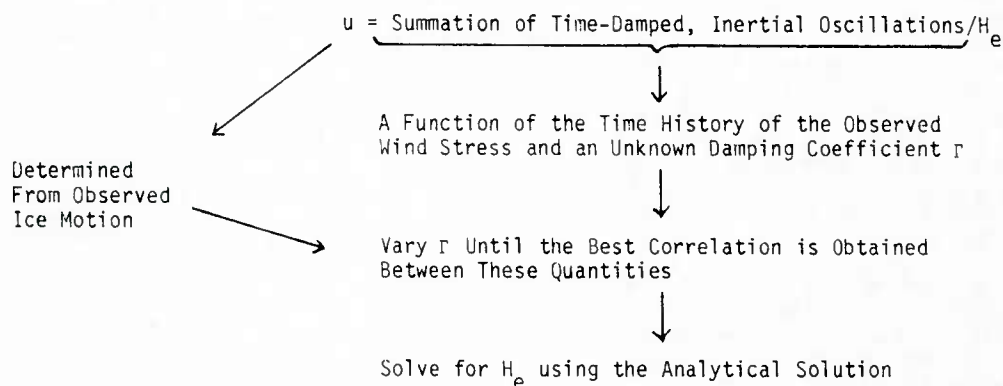


Fig. 1. Method for calculating \vec{H}_e .

motion was in the y direction (approximately east/west), and this motion of the ice was most likely restricted by adjacent ice in the pack (Figure 5). This would lead to a general increase in H_e , especially in the y direction. For the period of 29

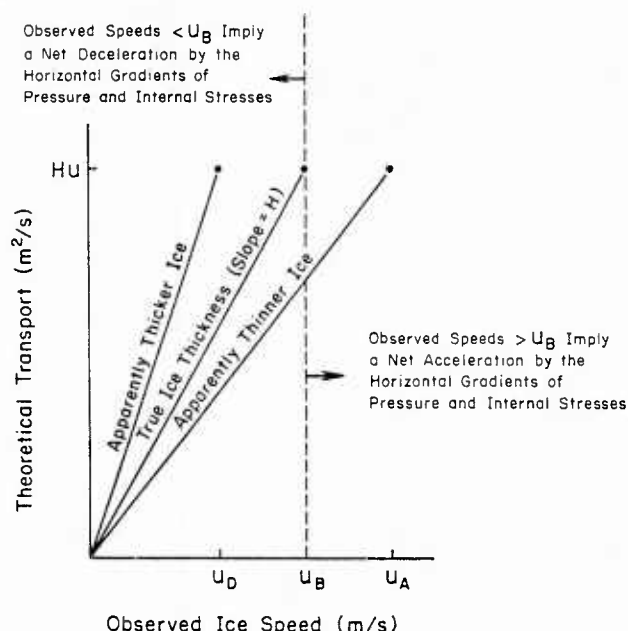


Fig. 2. The effect of the horizontal gradients of pressure and stress on the determination of the effective ice thickness. For the observed ice speed U_D (U_A), the effect is a net deceleration (acceleration) which makes the ice appear thicker (thinner) than it actually is.

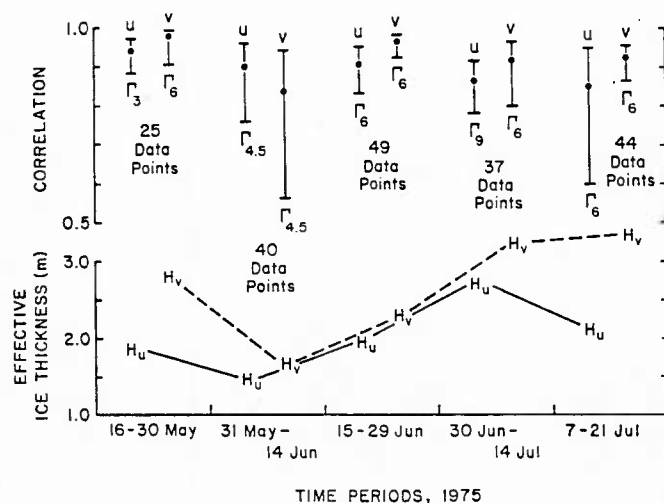


Fig. 3. Linear correlations (top) between observed ice speeds and theoretical ice transports, $\pm 90\%$ confidence limits. The r factor which gave the best correlation and the number of data points (at 6 hr intervals) used to calculate the correlation are also given. Effective ice thickness components (bottom) were determined using a least squares fit.

July-18 September 1975, the motion was primarily southeastward toward coastal regions which are typically ice free (Figure 5). Thus, one would expect less internal ice stresses, and H_e does tend to decrease during the 29 July-18 September period (Figure 4), especially the H_v term. By the end of August, $H_u \approx 2.2$ m, in good agreement with an average ice thickness of 2.3 m measured during August 1975 at the most centrally located AIDJEX manned camp. This would imply $I_x \approx 0$.

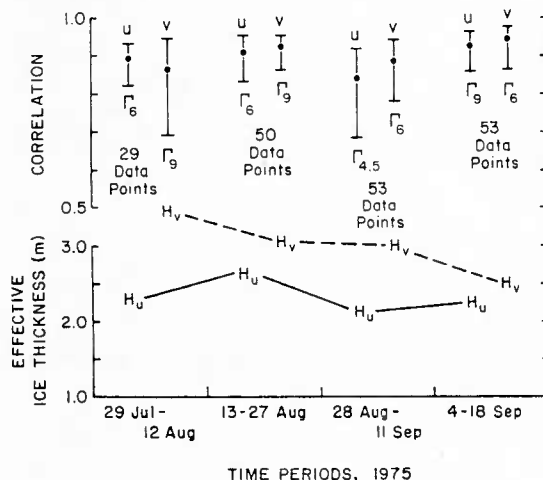


Fig. 4. Linear correlations (top) between observed ice speeds and theoretical ice transports, $\pm 90\%$ confidence limits. The r factor which gave the best correlation and the number of data points (at 6 hr intervals) used to calculate the correlation are also given. Effective ice thickness components (bottom) were determined using a least squares fit.

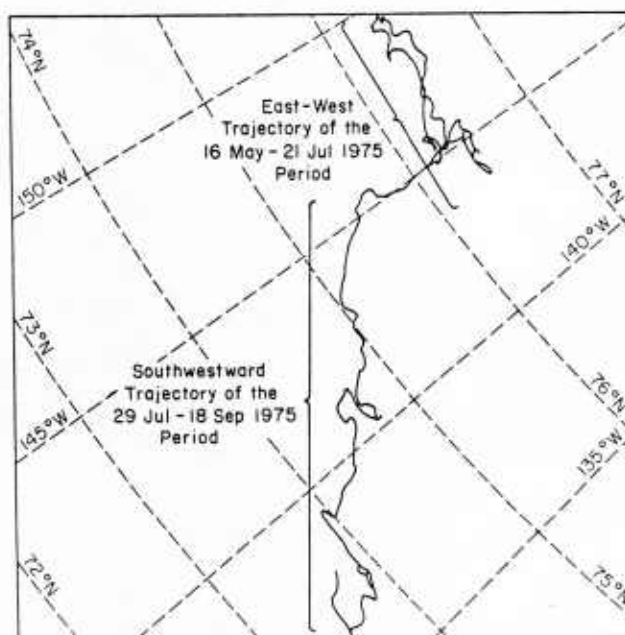


Fig. 5. Motion of the AIDJEX manned camp "Big Bear" for the period of 16 May-18 September 1975.

ACKNOWLEDGEMENTS

This research was supported in part by Gulf Oil Exploration and Production Company, Frontiers Division, Houston, Texas

REFERENCES

1. Lewis, J.K., R.D. Crissman, and W.W. Denner; Kinematics and Dynamics of Pack Ice in the Beaufort Sea. Submitted to Dyn. of Atms. and Ocns., 1985.
2. Lewis, J.K., and W.W. Denner; A Theoretical Response of a Wind-Driven Oceanic Surface Layer and Its Application to the Analysis of Lagrangian Measurements. J. Geophys. Res., 89(C2), 1984, 2101-2103.
3. Mellor, M.; Mechanical Behavior of Sea Ice. Cold Regions Res. and Eng. Lab., Monograph 83-1, 1983, 105 pp.
4. Amoroch, J., and J.J. DeVries; Reply to "Comment on a New Evaluation of the Wind Stress Coefficient Over Water Surfaces." J. Geophys. Res., 86(C5), 1981, 4308.

CURIOUS PLUMES FROM BENNETT ISLAND

Pierre St. Amand, USNWC, James Clark, USGS, Michael Matson, USNOAA

ABSTRACT

Plumes, hundreds of kilometers long and tens of kilometers wide are often noted coming from the sea in the vicinity of Bennett Island. These plumes are not volcanic. They are often at low altitude and appear colder on infrared photographs than the surrounding air. The plumes are probably produced by release of a light gas, most likely methane. Sighting of these plumes in 1810 and 1886 gave rise to the rumor of Sannikov Land, an undiscovered continent in the Arctic Ocean.

INTRODUCTION

Bruce Webster of the Anchorage, Alaska office of the National Weather Service called the attention of personnel at the Geophysical Institute of the University of Alaska at Fairbanks to peculiar airborne plumes that had been noted on 18 February 1983 on imagery from the NOAA 6 Satellite, Photo 1. The plumes, several hundred kilometers in length and several tens of kilometers in width at the source, came from the vicinity of Bennett Island in the East Siberian Sea, Figure 1. The temperature of the plumes, at their coldest, as determined by infrared imagery, suggested that they started at an altitude of either 7 or 13 kilometers. The longest plume was pulsed in what were described as explosions. A preliminary analysis was published in EOS by Kienle, Roederer and Shaw, 1983.

Such plumes are of scientific interest in view of the tectonic implications. The possibility of a volcanic or geothermal origin for the plumes in a region in which no volcanism has taken place for perhaps 80,000,000 years is exciting. The implications for cloud physics in studying the growth and dispersion of such a plume in very cold, atmosphere offers opportunities for valuable scientific research.

Michael Matson and Bruce Needham began a search of the archives of NOAA satellite imagery to see if other similar events had occurred. Vertical profiles of atmospheric temperature, humidity, wind velocity and direction taken at Zhokhova Island, about 130 kms to the east were collected for the days on which emissions were noted from the vicinity of Bennett Island. A search for

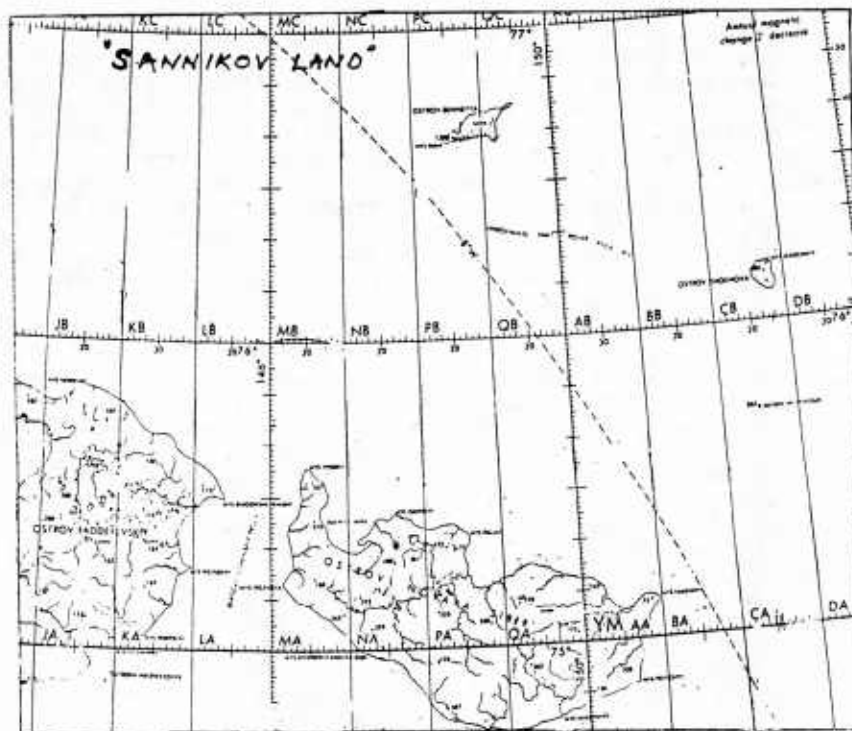
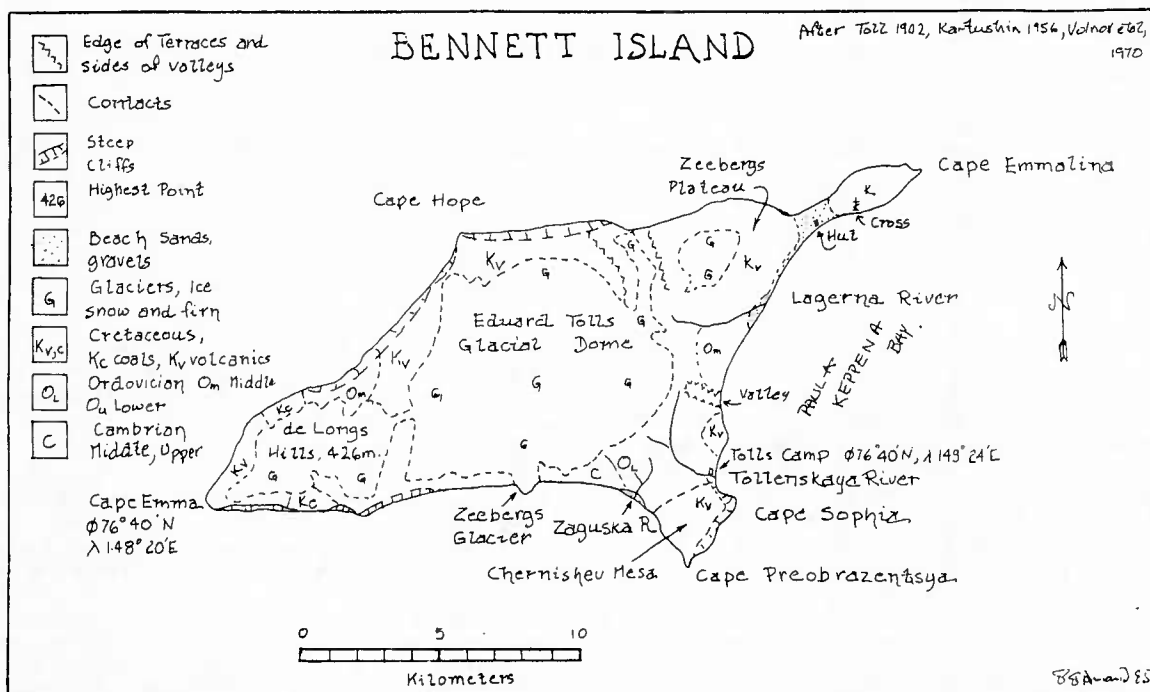
seismic activity was conducted by Robert Engdahl and Waverly Pearson of the Denver Office of the Geological Survey. None were found although they would have been detectable.

Prof. Jurgen Kienle wrote to Prof. S. A. Fedotov, describing the event and asking if any information was available about the eruption. Prof. Fedotov replied that a group of volcanologists had overflown the island (presumably between the end of April and the end of July 1983) but could not see any evidence of recent volcanism. He supposed that it was a "moderate fissure eruption at shallow water to the east from Bennetta Island." A visit to the island was planned. Subsequently an interview with Yu. Masurenkov of the Institute of Volcanology of the Far Eastern Scientific Center of the USSR Academy of Sciences was published in Izvestia, 31 May 1984. In August of 1983 he and his party went by sea and were on the island in September 1983. He regretted that no evidence for a recent eruption could be found and commented that between February and September that "arctic blizzards could very well have covered over the effects of the eruption." He reported finding evidence that the mountain rocks on the island have been geothermally altered. He reported that an underwater cone with a diameter of 4 kilometers and a height of 10 to 15 kilometers was found. He did not say just where, but he did say that, as compared with the "old map" of the bottom that the underwater cone had grown considerably during the past years. A noticeable excrescence had appeared on it that reminded him of a huge lava field. He noted that samples from the bottom of the East Siberian Sea turned out to be similar to that which falls out of contemporary thermal waters; the location of the sample was not given. He mentioned that the "mysterious trail" was noted again in November 1983 and in March and April 1984. No published record of a bathymetric map except for some soundings by de Long in 1881 have reached our attention.

This preliminary report summarizes this and other information and speculates as to the cause of the plumes.

OBSERVATIONS OF THE PLUMES BY SATELLITE IMAGERY

As of May 1985, the staff at NOAA/NESDIS has compiled a list of 104 images that contain plumes



from Bennett Island. We will not try to reproduce this mass of information here. The plumes are not a rare occurrence and this list is by no means complete. They have been noted mainly in the winter months with a pronounced peak in November and December. None were observed between the end of June and the first of September. The number peaked sharply in November and December with a gradual decrease through the months of springtime. The diurnal variation is also marked, the events were rarely noted between 1600 and 0200 local time but the number of sightings increased rapidly to a maximum at 1500 local time from which it dropped abruptly to almost nothing in the late afternoon. Although these results are suggestive, it would not be well to place much faith in the reality of the diurnal and annual variations noted here because of the way in which the archives were searched and the time of day at which a satellite could be over the island. Most of the searching was done in connection with studies of sea ice and was therefore concentrated in the winter months, although some searching was done during the summer months. In summer, the weather is often overcast and the chances of the island being obscured by clouds is much greater than in winter.

If the plumes were composed of water, or of ice, they would be more apt to propagate in the wintertime than in the summer because it is colder then. It is dark there a large part of the time in the winter and thus the main bulk of the observations are in the infrared.

Another observation is that the plumes are most often noted when the wind is blowing at right angles to the long axis of the island, either from the ESE or the WNW. This may however be more indicative of the direction of the prevailing winds at the time the observations were made than of any mechanism for generation of the plumes.

COMPOSITION OF THE PLUMES

None of the satellite imagery showed any dirt or discoloration on the ice following the discovery of the plume of 18 February 1983, nor for that matter on any of the other occasions. The Russian expeditions both by air and by sea did not notice any evidence of volcanic ash upon the island or the ice. On the other hand, Landsat photos from 16 March 1973 and 29 April 1984 show plumes present over the island with what appears to be fresh snow on the darker ice beneath a portion of the plume and a little to one side of it as well.

Fogs abound on Bennett Island, as reported by the explorers who have visited the place. LT CDR de Long camped on the ice foot at Cape Emma (see Figure 1) for a week in the fall of 1883. He was only able to take one solar observation for position in all that time. Baron Eduard von Toll was on the island in 1902 but in the time there he was not able to complete a map of the outline (Vittenburg, 1960), Kartushin (1968) was on the island from May to October 1956 and although he

did not take much notice of the fogs per se, he did make some comments about the growth of glaciation on the hills. He claims that the fogs which often occur at the summits of the glacial domes preserve the firm and cover it with new snow. Much new snow, or rather neve resulted from the deposition of hoar frost, most notably in the summer. On 16 June 1956 he noted that while pausing to rest on the larger glacier that rosettes of hoar frost crystals were growing upwind at the rate of several millimeters a minute. It seems that nearly a meter of "snow" accumulated on the summit during a period in which there were no snow storms, and indeed, the lower reaches of the glaciers were melting rapidly.

This visible portions of the plumes are almost certainly of water, be it liquid or solid.

TEMPERATURE OF THE PLUMES

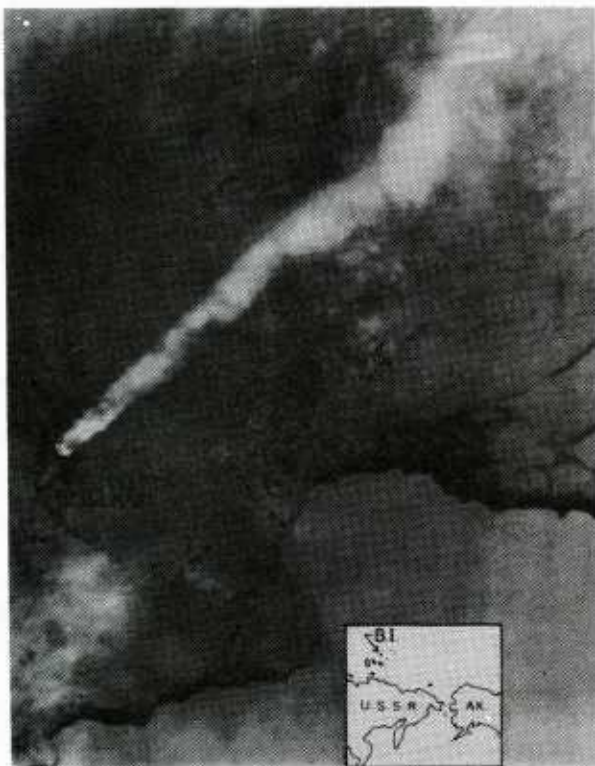
The infrared pictures of the plumes indicate that the plumes are very cold. The temperature of the plume of 18 February 1983 was estimated to be -45°C . The plumes usually appear to be colder than the surrounding clouds, and much colder than the sea or the sea ice.

ALTITUDE OF THE PLUMES

The observations of the temperature as deduced from the infrared leads to the conclusion that they are quite high in the atmosphere; altitudes of 7 to 13 kms were estimated for the plume of 18 February 1983. A number of other observations however are at variance with this idea, making it seem that the plumes are much lower than that.

On many occasions, the direction of the plumes coincide closely with that of the darker grey streaks of arctic sea smoke. A comparison of the wind directions, as observed on Zhokhova Island, 130 kms to the southeast shows that most of the plumes in the winter time have almost the same direction as the winds below 500 feet. On some occasions, the plume rises and can be seen to mix with higher clouds. On 10 September 1983, a plume seen in the infrared appears much colder than the surrounding clouds. One would assume that it lay above them. In the visual photograph taken at the same time, the plume is less dense than the overlying clouds and can clearly be seen to be overlain by them because the structure of those clouds continue right across the plume. After about 100 kms the plumes merge and the upper cloud becomes much whiter, indicating that it has changed from super-cooled water to ice.

The plume of 18 February 1983, 0614Z, shows no wind shear with distance, the coldest appearing part of the cloud being right over the source. However an isothermal region existed between 9,000 and 16,000 feet with a wind shear at about 10,000 feet. The photograph taken at 0047Z shows a double plume which has the direction of the winds at or below 2750 feet for 107 kms, after which it shifted to the direction of the higher winds. This indicates a rise rate of about 90 feet per minute for the plume.



AREA

Photo 1-A. NOAA Infra-red image of plume of 0616Z 18 Feb 1983. Courtesy Geoph. Inst. U. of Alaska.

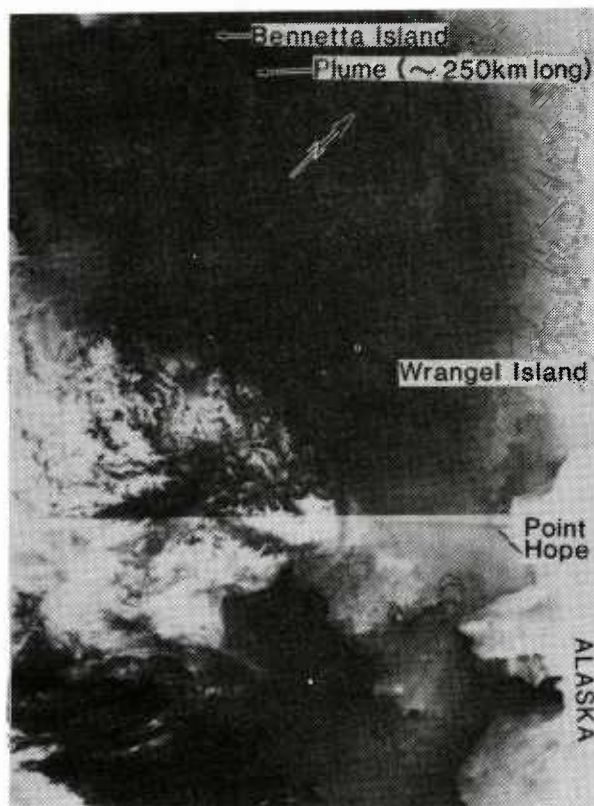


Photo 1-B Same plume showing location and scale of the affair. Geoph. Inst. U. of Alaska.

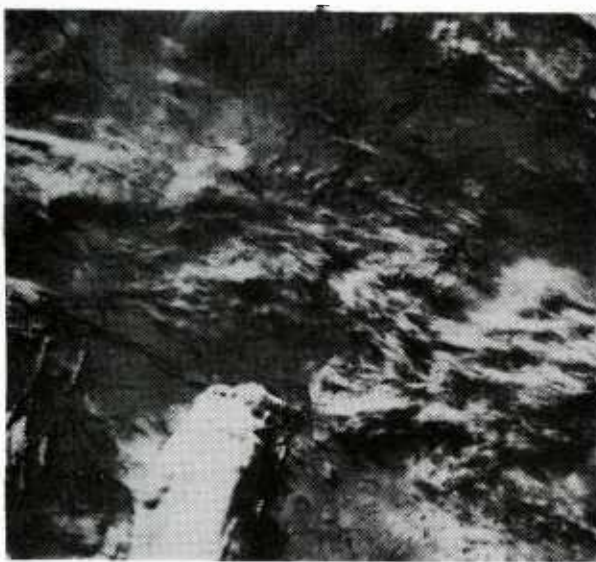


Photo 3. Landsat of plume of 29 April 1984. Wind from north. Note new snow on ice to west of island.

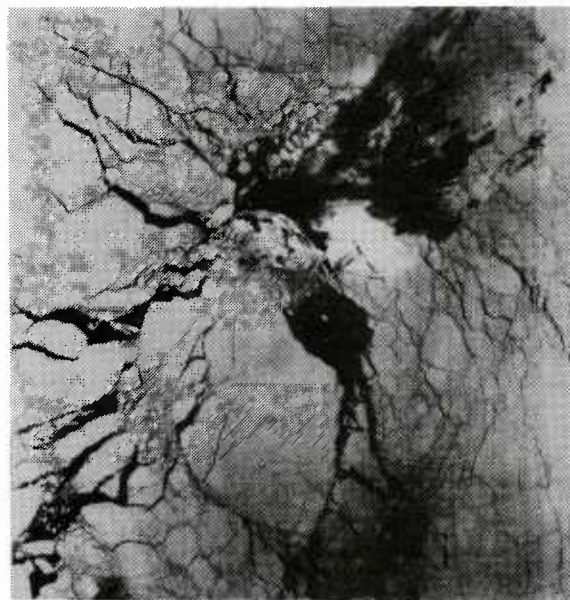


Photo 2. Landsat of plume of 16 March 1973. Note new snow on ice to northwest of island. Wind and sun from due south.

Several of the visual photographs from the meteorological satellites show shadows from which the height of the plumes can be determined, albeit with no great precision. The heights derived from these photographs are all 10,000 feet or below.

The two Landsat photographs mentioned earlier give much more information about the heights of the plumes. The photographs for 16 March 1973 shows clouds lying upwind of the island at heights of 9,800 feet, in one case the shadow of one of these clouds touches the ice and another cloud, right at sea level, Photo 2. The second of these clouds rises to about 10,000 feet in a short distance. The altitudes of the rest of the clouds downwind of the island are about the same. The material, whatever it is, is coming out of the sea from beneath the leads in the ice and from open water upwind of the island.

The photograph of 29 April 1984 shows the entire northern shore of the island shrouded with cloud arising directly from the sea and being driven over the island in a vertically oscillating wave cloud, Photo 3. The material is arising from along the shore in a curtain of rising jets. The cloud nearest the origin reach altitudes of 5,000 to 6,000 feet, the cloud then descends but rapidly rises again to 12,000 feet or so and goes down and back up to about 18,000 feet a few tens of kilometers downwind of the island.

A thin broken layer of stratus clouds covers the sea to the north of the island for at least the width of the picture. For 50 or more kilometers upwind of the island, however, the air is virtually cloud free as if a gigantic downdraft had caused the clouds to evaporate. The clouds are at an altitude of 4000 feet. Indeed, one can see streaks of the remnants of these clouds as they are drawn downward and into the plume over Bennett Island. Lines of small cumulus have formed at places, over leads in the ice. Near Bennett Island, some of the clouds on the upwind side are very near sea level, while clouds in the same line farther downwind seem to have risen to about 2000 feet. The critical data for these two days is not yet available but when it is it will be possible to calculate the rise rate and perhaps the density of the gases in the plume.

The apparent discrepancy between the temperature of the plumes as seen on the infrared photographs and the height as observed by measurement of shadows and by comparison with the tracks of the arctic sea smoke and with the lower level winds as measured at Zhokhova Island must be resolved. Either the plumes are colder than the surrounding air, or the measurement of the temperature of thin cirrus clouds by infrared techniques is in doubt, or perhaps a little of both.

While approaching the island in 1881, LT CDR de Long noted that the fog was quite cold, as compared with ambient outside the fogs. He cites a case where the air temperature in the fog was at 27°F while all around the ice was melting and the air temperature well above freezing

(de Long, 1883). Kartushin did not discuss this point.

Marshunova, in several references, points out that the emissivity of ice is a function of temperature. This matter has also been addressed by the Air Force Cambridge Labs (Kern, 1983). It appears that at -4°C and warmer that the emissivity of ice is 1.00 but that it gradually decreases to 0.85 at -24°C. Good physical reason exists to explain why small ice particles of the range 1 to 10 microns might have emissivity differing from that of bulk ice because of edge effects.

It is thus possible, that the plumes are not only colder near the ground than is the surrounding air when the plume is first emitted, but that the temperatures as determined by infrared observation may appear to be too low when the ambient air is quite cold.

SITUATION OF BENNETT ISLAND

Bennett Island, 67°38', 148°21'; rises out of shallow water in the East Siberian Sea. LT CDR de Long made several soundings while approaching the island over the ice. The water is only 20 fathoms deep for several tens of miles from the shore.

Geologic observations have been made for that portion of the island not covered by ice, by Dr. J. Ambler, USN, by Baron Eduard von Toll, by members of Kartushin's party and by Volnov and Sorokov (1961). The latter have published a good enough description to prepare the geologic comments on Figure 1. Briefly summarized, the island is covered for the most part by glacial domes, some of the glaciers reaching to sea level. The glacial ice rests for the most part upon Cretaceous basalts. The basalts lie unconformably upon Cretaceous argillites and lignitic coal. These rest unconformably upon siltstones, argillites and sandstones of paleozoic age.

No evidence exists for holocene or tertiary volcanism anywhere near the island. No earthquakes occur within several hundreds of kilometers. The area may be rising slowly from the sea, as evidenced by some terraces and upraised beaches, but otherwise appears to be tectonically inactive at present.

DID THE PLUMES JUST BEGIN, OR HAVE THEY BEEN THERE AWHILE?

Our earliest satellite photographs of the plumes are in 1973. It is likely that they were also present during 1956 when Kartushin was on the island. Uspensky (1959) shows a photograph of the beach with a cloud rising out of the sea in the middle distance and draping over a hill. Baron von Toll encountered fogs the whole time he was on the island.

Earlier still, while on the New Siberian Islands in 1886, von Toll thought he saw a continent to the north, with snow covered mountains

visible in the distance (Vittenberg, 1960). The view was somewhat ephemeral, but Toll for a while became convinced that he had seen Sannikov's Land--he later concluded that it maybe did not exist. In 1810 Jacob Sannikov, also from the New Siberian Islands saw what he thought was a continent to the north (Uspenskiy 1959A, 1959B, Obruchev 1935, 1946). The direction in which he saw this was not exactly towards Bennett Island but a little to the west thereof. It is likely that both men saw the plumes from Bennett Island.

More recently, 1881, during his heroic but tragic trek from the spot where his ship was lost, to Bennett Island, LT CDR de Long and some of his crew saw, from time to time, a large land mass and they diverted their march to arrive at it. While it is hard to tell exactly where they were during this phase of the march, they were at least 130 kms away from Bennett Island when they first decided to go for it (de Long, 1883). The highest point on the island is on the southwest end and is only 246 ms high. Even allowing generously for refraction, it does not seem possible that they could have spotted the island from that distance. Nor would one expect any special miraging or other phenomena that would have raised the image of the island far enough to have made it visible because at that time of year, the atmosphere and the ice would be at about the same temperature. The constantly changing images that the explorers saw was probably a plume raised over the island. To one not used to the arctic it might seem as if such a thing were unlikely, but towering cumulus are very rare in those climes and ones imagination will do anything to present him with some relief from the monotony of the landscape.

It therefore seems that the phenomenon has been going on for at least a 175 years. It is also probable that it gave rise to the rumors of Sannikov Land and thus greatly encouraged exploration in an effort to find a hypothetical continent that many geographers at the time thought reached all the way across the pole. Had de Long's party not detoured to the island, they might have reached shelter and safety in the Lena Delta without the loss of life that they endured. Baron von Toll went to Bennett Island to make preparations for a further trip north to seek Sannikovs Land and he too perished.

WHAT CAUSES THE PLUMES

Without some more concrete source of information and without visiting the island and perhaps using aircraft surveillance, or some form of more detailed remote sensing as well, we are not likely to discover the cause of this phenomenon. We will for the moment have recourse to the method of multiple hypotheses--the last resort of those who have information.

To this end, we can dismiss, out of hand, hypotheses invoking volcanism, radioactivity or human intervention as sources for these plumes. Other explanations might include orographic effects--but then one would expect such plumes from every large land mass in the arctic. Nearby

polynia may be dismissed because they are rarely present during the events. Warm surface water seems unlikely because of the presence of ice over the areas from which the plumes come; submarine and terrestrial hotspots would surely have been noted, thus they may also be dismissed. Orography obviously plays some role in the development of the wave-like motion often noted in the plumes.

It has been proposed by Prof. Clark that the plumes are initiated by the release of methane gas from beneath the sea. The methane would be derived from the coal beds that are very extensive under all of the Siberian Platform. Indeed, the world's largest natural gas fields occur in this general area. A layer or layers of permafrost underlies most of the East Siberian Sea because during the Pleistocene this whole area was uncovered for the better part of almost 3 million years, the sea having withdrawn to the edge of the continental shelf by removal of water to form the ice caps (Grosswald, 1980, 1983, Vetichko et al. 1984). This layer of permafrost could easily form a caprock that would retain, at depth, the methane produced by decomposition of the lignite. At sufficient depth, the methane would react with the water present in the formations and with the permafrost to form a methane hydrate which would further seal the formation, thus allowing methane to accumulate in large quantities and high pressures at depth.

With the return of the sea to the area, the ocean water protects the land from the extreme cold of the arctic winter and heat derived from the sea and from the interior of the earth would eventually begin to melt the permafrost. Once melted, the methane hydrate would no longer be in its stability field and would break down releasing the methane as a gas which would eventually escape through the overlying formations and reach the surface. A very similar process is now taking place on land in the Copper River Basin of Alaska where mud volcanoes, several hundred feet high, that emit salt water and methane gases are now developing. Methane seeps, large enough to be detected by geophysical seismic sounding techniques, have been observed in the Navarin Basin (Carlson and Malow, 1984).

The release of the methane could cause cooling because of adiabatic expansion of the gas, which would eventually cause some of the hydrate to reform or the water to freeze, giving rise to the episodic character of the plumes.

The gas would be expected to come out of the ocean a little bit cool because of the expansion. Once in the atmosphere, the methane would rise rapidly because it has a density of only 0.55 that of air. The methane would be relatively pure with perhaps 20 or so percent of nitrogen mixed with it. The rising column would entrain air which in that part of the world is usually near saturation with respect to water and often saturated with respect to ice. Thus any ice particle that formed would grow from the deposition of atmospheric water vapor; this would give rise to the long lived plumes.

The Landsat image of 1973 shows clearly that a mass of gas is rising right over the island without much condensation or freezing of water within it. A zone around the rising column is however marked by what appears to be frozen water particles.

Several of the satellite images show that the plumes rise through or into an overcast and after a few tens of kilometers cause the overcast to disappear. This is not unexpected if the overcast consists of supercooled water because the ice particles from the plume would then seed the supercooled stratus and cause it to precipitate--a technique commonly used to clear fog in the arctic.

It is true that the coal beds on Bennett Island are only a few tens of meters thick and this mitigates against the hypothesis. On the other hand, the island is at the crest of what is called the de Long Arch, giving gas an opportunity to migrate up dip to any fractures that may have formed at the crest of the gigantic dome.

CONCLUSIONS

With what little we now know about the situation it is fairly clear that the plumes are of liquid water or of ice, depending upon the air temperature. The plumes emerge from the ocean somewhat colder than the rest of the air at the surface. The plumes rise rapidly, much more so than if they were simply convective. The best hypothesis for the moment, one that is not at variance with the physical facts, is that the plumes are caused by release of a light gas from the ocean around the island for a distance of tens of kilometers. The gas is most likely methane.

The matter will not be resolved without further field work and the application of remote sensing. Because the island is now held by Russia, even though it was discovered and claimed by the United States Navy in 1881, some sort of a joint research project will have to be devised, and really should be, if we are to learn more about this interesting situation. The opportunities for large scale outdoor research into cloud physics and meteorological processes is too good to ignore. Let us hope that some scientific cooperation in this interesting matter can result. Some economic advantages might some day ensue considering that there must be an awful lot of whatever is coming out of the ocean.

ACKNOWLEDGEMENTS

The personnel of the U.S. Geological Survey have helped in many ways, Jack Rachlin made a short study of the seismicity and tectonics of the region. The people at NOAA have made weather records available, the NASA folks have helped us find Landsat pictures. The Director of the Geophysical Institute, Dr. Juan Roederer has been very open handed and helpful, as has Prof. Kienle. Prof. Glenn Shaw has done his very best to put up with our numerous questions and theoretical

suggestions and has helped enormously in assembling information. Mrs. J. Triplehorn of their arctic library has helped us search out references to the literature on Bennett Island and the New Siberian Islands. COL Lloyd Smith, U.S. Air Weather Service, retired, has helped with meteorological and cloud physics suggestions. Deborah Shafer did much Russian translation. The Fleet Numerical Weather Facility at Monterey has been most helpful in the collection of weather data and in the interpretation. The Oceanographic detachment at China Lake has helped by plotting and interpreting tephigrams.

This report is, we hope, the beginning of a more thorough investigation into this interesting phenomena; may it be an international effort.

REFERENCES

- Carlson, P. R. and W. S. Malow, 1984. "Discovery of a Gas Plume in Navarin Basin," Oil and Gas Journal, V. 82, No. 14, April 2, pp. 157-158.
- De Long, George Washington, 1883. "The Voyage of the Jeannette, the Ship and Ice Journals of George W. de Long, LT CDR, USN and Commander of the Polar Expedition of 1879-1881," edited by his wife, Emma de Long, Boston, Houghton, Mifflin and Company, N.Y., 11 East Seventeenth St., The Riverside Press, Cambridge, two volumes.
- Grosswald, M.G., 1983. "Pokrovnie Ledneke Kontinentalnic Schelfov (Ice Sheets of the Continental Shelves), Nauk, Moscow 1983, 216 pp.
- Grosswald, M. G., 1980. "Late Weichselian Ice Sheet of Northern Eurasia," Quaternary Research, V. 13, No. 1, pp. 1-32.
- Kartushin, V. M., 1963. "Fiziko-Geograficheskii Ocherk Ostrova Benneta (Physical-Geographic Outline of Bennett Is.), Sibirskii Geograficheskii Sbornik, 1963, No. 2, pp. 69-99, Tables, Profiles, Maps, eleven references.
- Kartushin, V. M., 1963. "Ozedenenie O. Benneta (Glaciation of Bennett Islands), Leningrad, Arkticheskii i Antarkticheskii n.-i Inst., Trudy 1963, V. 224, pp. 166-176, Tables, Illustrations.
- Kern, Dr. Clifford, 1983. Personal Communication.
- Marshunova, M. S., 1959. "O Raschete Balansa Dlenovolnovoe Radiashii pre Pasmurnom Nebe v Arktiki (Calculation of the Longwave Radiation Balance during an Overcast Sky in the Arctic), Trudy Arkticheskoto Nauchno-Issled. Inst., 226, pp. a09-112. Trans by American Meteor. Soc. T.R. 304.

- Kieule, J., J. G. Roederer and G. E. Shaw, 1983. "Volcanic Event in the Soviet Arctic EOS, Transactions American Geophysical Union," Vol. 64, No. 20, May 17, 1983, p. 377.
- Marshunova, M. S., 1961. "Principal Characteristics of the Underlying Surface and of the Atmosphere in the Arctic." Source: Trudy Arkticheskovo i Antakticheskovo Nauchno-Issledovatel'skovo Instituta, Radiatsionniy i Teplovoy Balans Arktiki, TOM 229, pp. 5-53, Leningrad, 1961. Translation by the Rand Corp. Memo RM-5003-PR, pp. 51-131.
- Obruchev, B. A., 1946. "Zemlya Sannikova Suschestvovala (The Existence of Sannikovs Land)." Preroda No. 10, 1946.
- Obruchev, B. A., 1935. "Zemlya Sannikova--Nereshennaya Problema Arktiki (Sannikovs Land--Unsolved Problem of the Arctic)." Preroda, No. 11, 1935.
- Uspenskiy, S. M., 1959A. "Unter Robben und Eis-moewen, . Espedition zur Bennett-Insel," Leipzig, Urania-Verlag, 150 p.
- Uspenskiy, S. M., 1959B. "Na Predele Zesne, Eksedisiu na Ostrov Bennetta. (Limits of Life)," Gosudarstvennoe Esdatelstvo, Moscow (probably same text as Uspenskie 1959A).
- Velichko, A. A., L. O. Isayeva, V. M. Makeyev, G. G. Matishov and M. A. Faustova, 1984, "Late Pleistocene Glaciation of the Arctic Shelf, and the Reconstruction of Eurasian Ice Sheets," Chapter 5, In Late Quaternary Environments of the Soviet Union, A. A. Velichko, editor; H. E. Wright, Jr. and C. W. Barnosky, editors of English version.
- Vittenburg, Pavel Vladimirovich, 1960. "Zhizn i Nauchnaiya Deyatlnost E. V. Tollya (Life and Scientific Works of E. V. Toll)," Akademiya Nauk SSSR, Moskva 1960, 245 pp.
- Volnov, D. A. and D. S. Sorokov, 1961. "Geologicheskoye Stroyeniye Ostrova Bennetta (Geology of Bennet Island)," Trudy Nauchno-Issledovatel'skogo, Instituta Geologii Arktiki, V. 123, pp. 5-18.
- Wright, H. E. and C. W. Barnosky, 1984. "Late Quaternary Environments of the Soviet Union." A. A. Velichko, editor, University of Minn. Press, Minneapolis, Minn. 327 pp., Num. drawing and photos.

FREQUENCY-DOMAIN ELECTROMAGNETIC ICE-SOUNDING

I. J. Won and K. Smits

Naval Ocean Research and Development Activity
NSTL, Mississippi 39529-5004

ABSTRACT

A pair of coils acting as transmitter and receiver of a harmonic electromagnetic (EM) wave acts as an excellent high-resolution altimeter at low altitudes over ocean regions. Due to high seawater conductivity, the altimetric determination from a received signal is computationally simple. The method can be applied to determining the sea-ice thickness: since ice is transparent to EM waves up to several tens of kilohertz, determining sea-ice thickness is reduced to an EM altimetry problem involving the distance up to the ice-seawater boundary. Since the distance to the air-ice boundary can be easily measured by a radar (or laser) altimeter, the difference between the EM and the radar altitudes constitutes the ice thickness.

INTRODUCTION

The Naval Ocean Research and Development Activity (NORDA) has been investigating a possible application of the airborne electromagnetic (AEM) method to the bathymetric charting in the shallow ocean. The first test survey was conducted in the Cape Cod Bay during a 3-day period in June 1984. The AEM system used was a commercially available Digheem III (described in detail by Fraser, 1978, 1979, and 1981). The system was equipped with two horizontal coplanar coil pairs operating at 385 Hz and 7200 Hz, both having an 8-m coil separation. A Sikorsky S58T twin-engine helicopter towed the sensor platform or, simply, bird, which maintained an altitude ranging from 40 m to 50 m above the sea level. Bathymetric results derived from this experimental survey data showed excellent agreement with ground truth data. The results have been reported by Won and Smits (1985).

Bathymetric determination by an AEM method requires a very accurate (hopefully better than a 1% resolution) altitude information for the sensor coils. For the Cape Cod Bay experiment, we employed a radar altimeter (Sperry Model 220) that had a manufacturer-specified accuracy of 5%. At our survey altitude of 40-50 m, the possible altitude error amounts to more than 2 m. It became evident, therefore, that the radar altitude cannot be trusted for the bathymetric interpretation. Instead, a new algorithm has been developed to utilize the 7200-Hz response data to derive the electromagnetic altitude. The computed altitudes thus derived show fairly random zero-biased differences with respect to the radar altitudes.

This method should be applicable to determining the sea-ice thickness. Since ice is transparent to EM waves up to several tens of kilohertz, determining sea-ice thickness is reduced to an EM altimetry problem

involving the distance up to the ice-seawater boundary. If the distance to the air-ice boundary can be measured by a radar (or laser) altimeter, the difference between the EM and the radar altitudes represents the ice thickness.

MATHEMATICAL CONSIDERATIONS

Fundamental equations for the magnetic field generated by a vertical magnetic dipole located at or above the surface of a layered earth are given by Kozulin (1963) and Frischknecht (1967). The mutual coupling ratio for a horizontal coil configuration used for the present system is defined as the ratio of the total magnetic field (H_z) to the primary field (H_z^p). The primary field, however, is usually bucked out during measurements, and only the ratio Q of the secondary field to the primary field is measured (customarily in a part per million (ppm) unit):

$$Q = H_z/H_z^p - 1 = -a^3 \int_0^{\infty} \lambda^2 R(\lambda) J_0(\lambda a) d\lambda \quad (1)$$

The kernel function R corresponding to a uniform half-space whose geometry is shown in Figure 1 can be expressed as

$$R(\lambda) = \frac{\lambda - \sqrt{\lambda^2 + i2\pi\mu\sigma f}}{\lambda + \sqrt{\lambda^2 + i2\pi\mu\sigma f}} e^{-2\lambda b} \quad (2)$$

where

f : transmitter frequency (Hz),
 b : sensor altitude,
 a : coil separation,
 σ : water conductivity,
 μ : magnetic susceptibility of free space,
 λ : integration variable, and
 J_0 : the zeroth order Bessel function.

The integral in Equation (1) can be efficiently evaluated by the linear digital filter method (Koefoed et al., 1972). We used the filter coefficients published by Anderson (1979) for the Hankel transform integral. The ice conductivity is assumed to be negligible.

Figure 2 shows the computed inphase (real part of Q) and quadrature (imaginary part of Q) responses in ppm for sensor altitudes of 30 m, 45 m, 60 m, 75 m, and 90 m for a 4-mho/m seawater conductivity

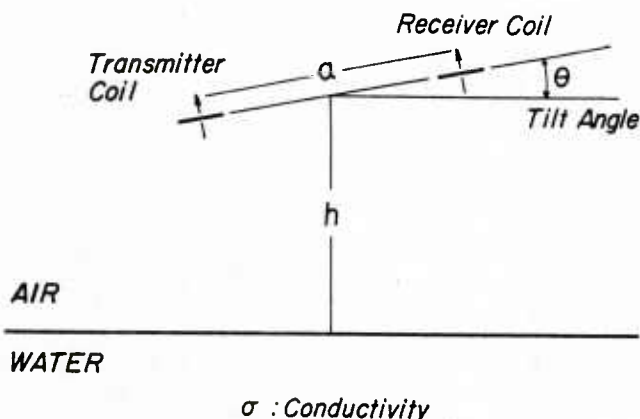


Figure 1. The mathematical ocean model for EM altimetry.

and a 8-m coil separation. The response is approximately proportional to the cube of the coil separation. We note that, for a given altitude, the inphase response is dominant over the quadrature response. Also, the total response decreases rapidly with an increasing sensor altitude.

The response gradient at an altitude, say 45 m, is about -76 ppm/m at 10 kHz. Since the measurement error of most commercial airborne EM systems is generally claimed to be less than 1 ppm, we can achieve, at least theoretically, an altimeter accuracy better than 1.3 cm at the 45-m altitude. This corresponds to a 0.03% altimeter resolution. Due to the decreasing response with increasing altitude, the resolution is degraded at high altitudes. This limits the usable range of the EM altimeter up to several hundred meters.

For the case when the sensor platform is not horizontal, an expression for a tilted platform (Fig. 1) has been derived by Son (1985) and is shown to be

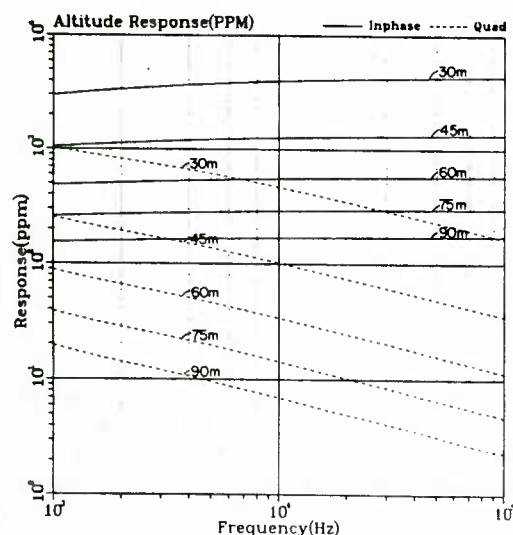


Figure 2. Inphase (solid lines) and quadrature (dashed lines) responses of seawater for various sensor heights. Water conductivity is fixed at 4 mho/m and the coil separation at 8 m.

$$Q = -a^2 \int_0^{\infty} [\lambda a J_0(\lambda a) - \sin\theta \tan\theta J_1(\lambda a)] R(\lambda) e^{-2\lambda h} d\lambda. \quad (3)$$

Equation (3) is used to compute the response error (Fig. 3) due to the tilt angle ranging from 0° to 30° . The ocean response at $\theta = 0^\circ$ for each altitude has been subtracted so that this graph shows only the response difference due to the tilt. If we assume a 1-ppm measurement accuracy, the tilt effect is essentially negligible when the altitude exceeds 60 m. Even for a 30-m altitude, the sensor may tilt up to 5° within the measurement accuracy.

If the tilt information is available (using an electronic inclinometer mounted on the sensor platform), this may be incorporated into the altitude calculation through Equation (3). For the Cape Cod experiment we did not have the capability to measure the tilt. Since the average survey altitude was about 45 m, it is clear from Figure 3 that data are not affected up to about an 11° tilt. In most data, the tilt is believed to be less than this amount.

At each data point we measure the value Q in Equation (1) consisting of an inphase and a quadrature part. The only unknowns in Equation (1) are the altitude (h) and the water conductivity (σ). Using a numerical method similar to the classical Newton-Raphson method, we may solve the two simultaneous nonlinear equations expressed by Equation (1) for h and σ .

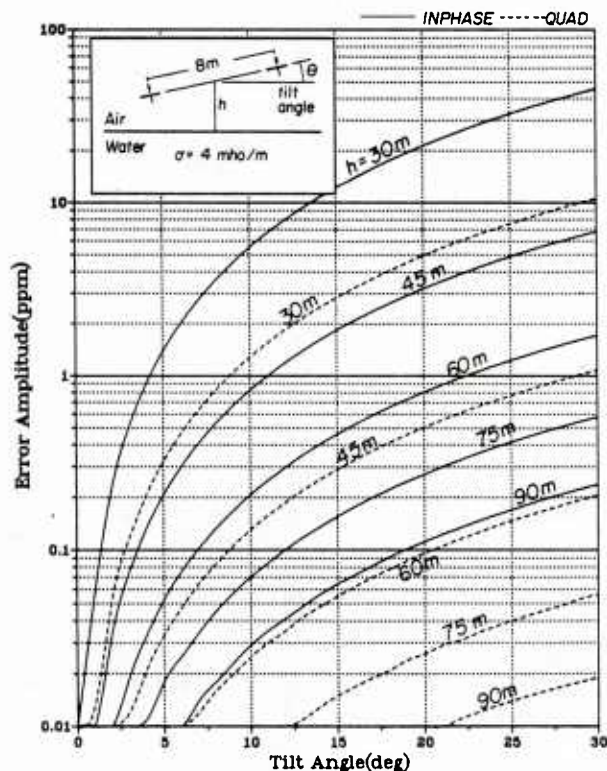


Figure 3. Effect of sensor platform tilt for various altitudes. A 1 ppm error is considered to be negligible. Water conductivity is fixed at 4 mho/m and the coil separation at 8 m.

EXPERIMENTAL RESULTS

A total of about 200 line-km data consisting of 13 segment profiles was obtained during the Cape Cod experiment (Fig. 4). The sampling rate was 1 sec corresponding to about 50 m along the ground track. Figures 5-7 show some of the results obtained from the Cape Cod experiment. In each figure, we show from bottom to top:

- (1) raw data consisting of inphase (solid line) and quadrature (dashed line) responses in ppm at 7200 Hz,
- (2) computed water conductivity (σ) profile,
- (3) raw radar altitude (solid line) and computed EM altitude (dashed line) profiles, and
- (4) differences between the radar altitudes and the EM altitudes.

Spot measurements of water conductivity were made at eight locations along Flight Line 5031 at a 3-m depth. They ranged from 4.0 mho/m to 4.12 mho/m. These are shown in Figure 5 as solid circles along with the computed water conductivity profile. Since the Bay has no fresh-water inlets, we may expect a fairly uniform water conductivity in the neighborhood of 4 mho/m. While the measured values may be fairly representative for deep water, there are considerable uncertainties over very shallow water over the shoal (location is shown in the figures) and toward the beach where the water depth is less than 3 m. Water temperature may rise significantly during the day over shallow water (particularly during a sunny day in June as in this case). A mere 4°C difference at a given salinity can cause as much as a 10% change in water conductivity. While this offers a possible explanation for some high water conductivities over shoal and beach, no ground truth data are available to confirm this possibility.

Clearly the 7200-Hz response is overwhelmingly correlatable with variations in the sensor altitude. A 1-m altitude change corresponds to an approximately 75-ppm change in the inphase response at this frequency (Fig. 2). Data on the right end of each profile should be disregarded because the interpretative ocean model fails due to extremely shallow water and beach. The 7200-Hz signal has a skin depth of about 2.9 m and thus feels the effect of shallow water bottom. The water depth must exceed about two skin depths to render this effect negligible. Since some portions of the survey area could not meet this requirement, we adopted a two-layer ocean model that had finite water depths. These water depths are determined from additional 385-Hz response data (for details on the water depth determination, see Won and Smits, 1985). Had we employed a higher frequency, say 50 kHz or more, the water depth data would not have been necessary. In the future experiments, we plan to use such a high frequency for altimetric determination.

Careful inspection of the altitude profiles show that (1) the EM altitudes are generally smoother than the radar altitudes, and (2) differences between the two altitudes are generally less than 1 m except near the beach. The altitude differences from the entire 13 flight lines,

consisting of about 4500 data points, are compiled and shown in a histogram in Figure 8. The differences are obviously of a zero-biased, random, Gaussian-type distribution.

The cause for the differences cannot be ascertained at this time. We may only surmise that they are due to either measurement error of the radar altimeter or to possible differential motions between the aircraft (on which the radar altimeter is mounted) and the towed EM sensors. An indirect proof of the superiority of the EM altimetry comes from the fact that, when combined with the 385-Hz data, the EM altitude produced far more satisfactory bathymetric results than the radar altitude.

DISCUSSIONS AND CONCLUSIONS

An EM loop pair operating at a low frequency is shown here to be potentially an excellent altimeter over the ocean. It appears to be superior in resolution to a radar altimeter. Furthermore, owing to its wide beamwidth, an EM altimeter is free of the nadir-pointing error of a laser altimeter. Further considerations for improvements may be given in the following areas:

- (1) The operating frequency must be sufficiently high so that the ocean would appear infinitely deep. This condition is satisfied when water depth exceeds about two skin depths. A frequency in the 100 kHz-10 MHz range appears to be appropriate. Beyond this range, the dielectric effect of water should be incorporated in data reduction.
- (2) The towed sensor platform is not necessary, particularly at high frequencies. The transmitter and receiver coils can be attached directly on the aircraft with an adequate separation. The primary field bucking can be achieved electronically instead of using a separate bucking coil. Noise due to moving parts of aircraft (such as aileron, rudder, elevator, propeller, etc.) can be reduced through precision tuning and filtering, which should be electronically effective at high frequencies.
- (3) Because of the dipolar radiation pattern of the transmitter coil and, thus, a wide beamwidth, the EM altimeter measures the distance to the instantaneous mean sea level and ignores ripples and waves. This may be considered advantageous for most purposes over a laser altimeter which, having a small beamwidth, is susceptible to noise caused by small surface fluctuations.
- (4) An essentially similar method can be applied to determine the sea-ice thickness. Since ice is transparent to EM waves up to several tens of kilohertz, determining sea-ice thickness is reduced to an EM altimetry problem involving distance up to the ice-seawater boundary.

ACKNOWLEDGMENTS

Airborne electromagnetic data used in this report were obtained under a NORDA contract by Carson Geoscience Co., Perkasié, Pennsylvania, employing a Dighem III AEM system furnished by Dighem, Inc., Mississauga, Ontario, Canada.

AEMB FLIGHT LINES

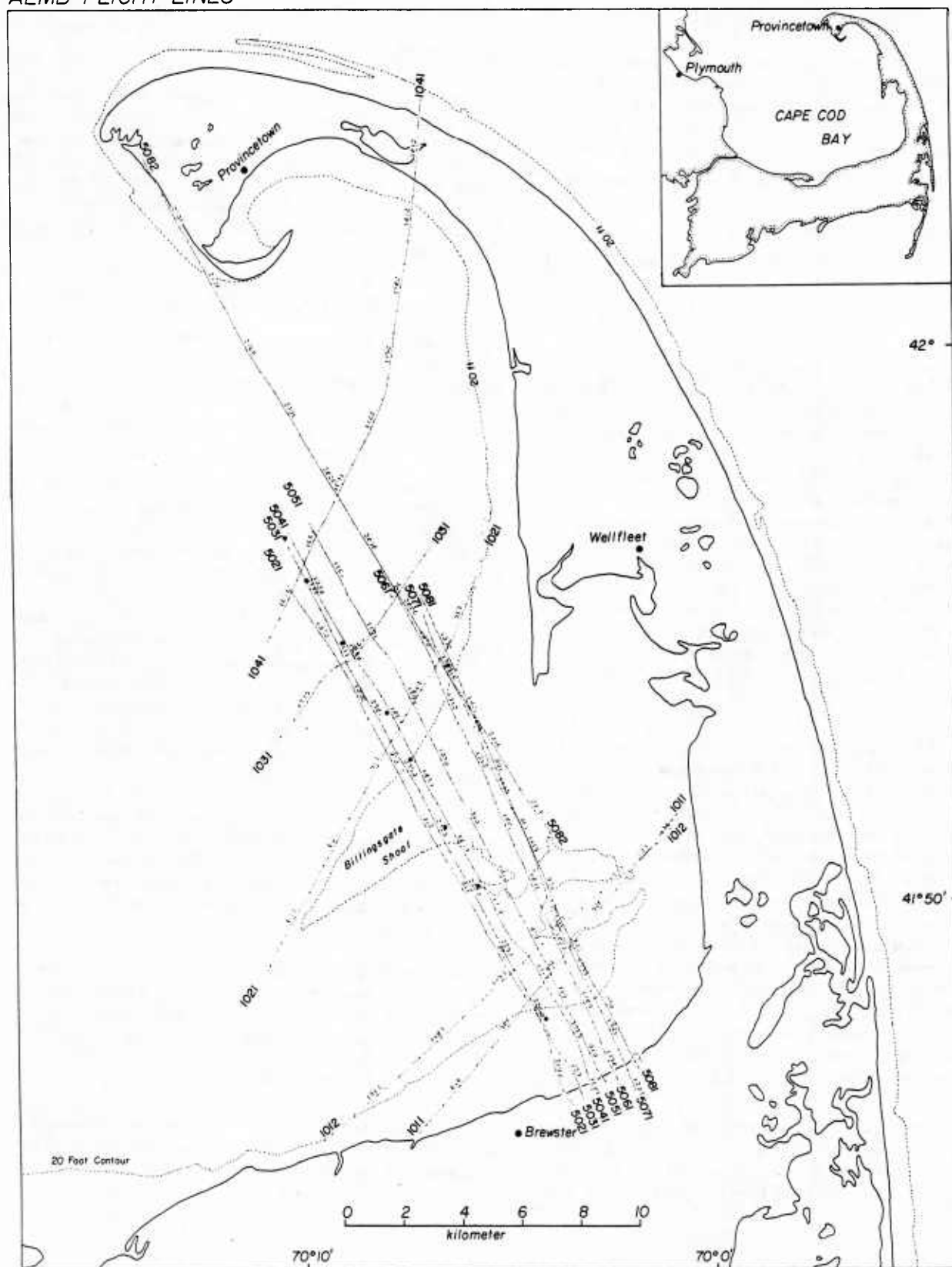


Figure 4. The Cape Cod Bay test area and AEM flight lines. Small solid circles along Flight Line 5031 represent locations where water conductivity is measured

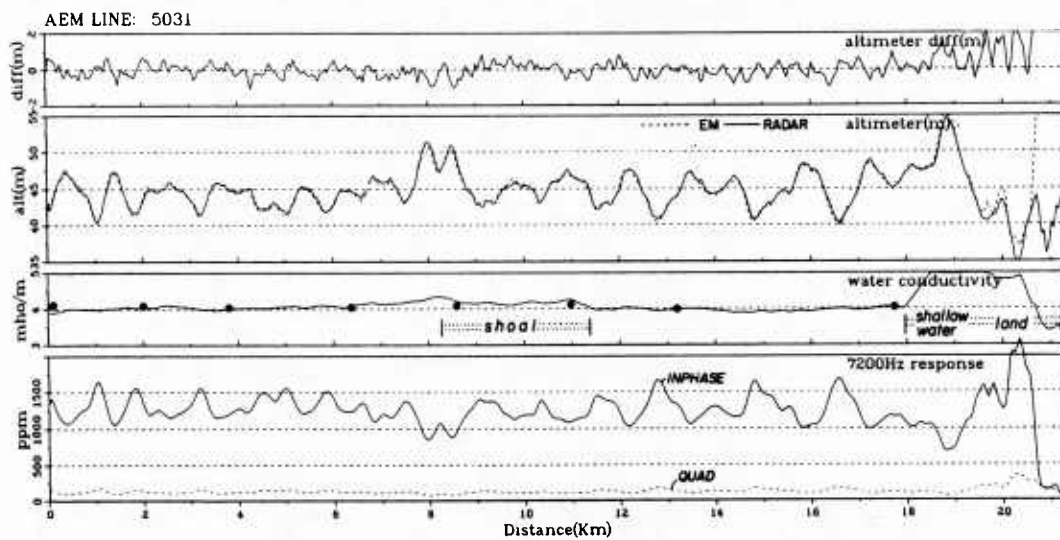


Figure 5. Data and interpretation results for Flight Line 5031. Solid circles represent water conductivities measured at a 3-m depth.

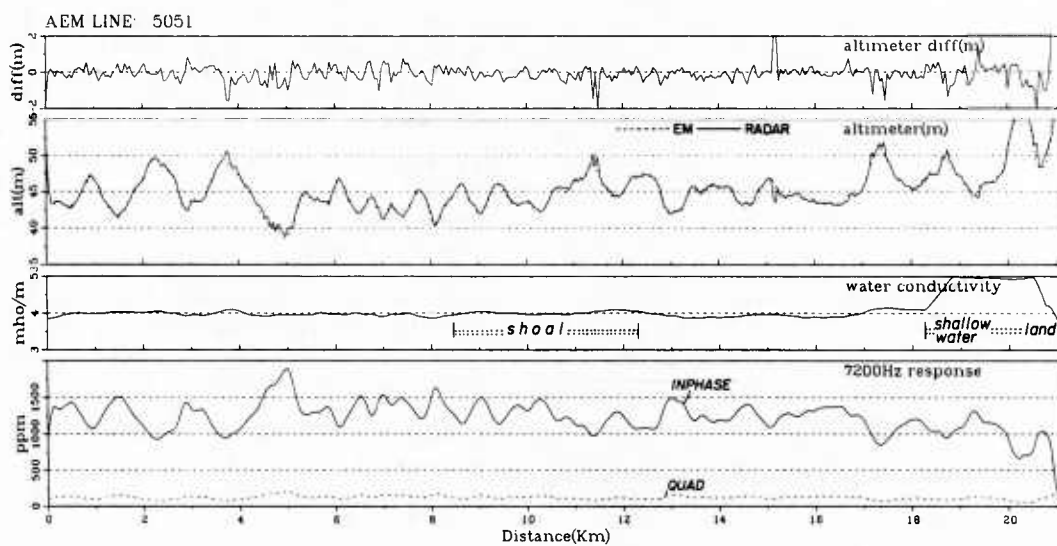


Figure 6. Data and interpretation results for Flight Line 5051.

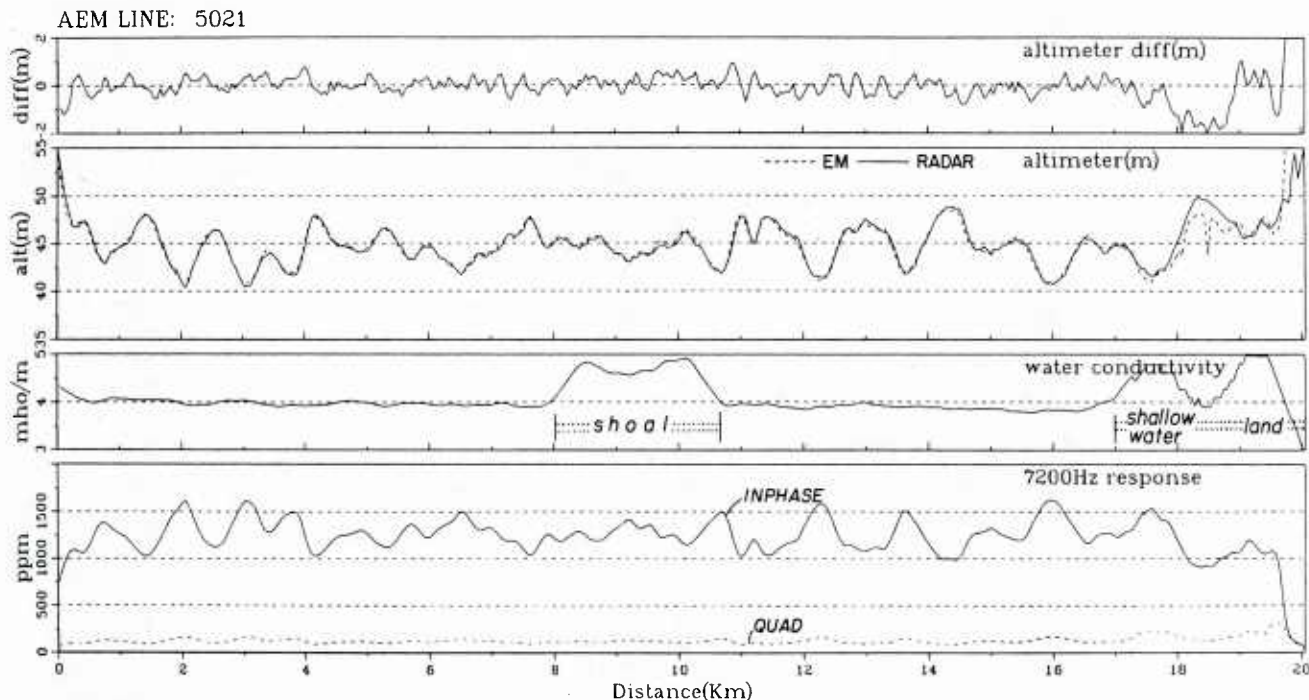


Figure 7. Data and interpretation results for Flight Line 5021.

REFERENCES

- Anderson, W. L. (1979). Numerical Integration of Related Hankel Transforms of Order 0 and 1 by Adaptive Digital Filtering. *Geophysics*, v. 44, pp. 1245-1265.
- Fraser, D. C. (1978). Resistivity Mapping with an Airborne Multicoil Electromagnetic System. *Geophysics*, v. 43, pp. 144-172.
- Fraser, D. C. (1979). The Multicoil II Airborne Electromagnetic System. *Geophysics*, v. 44, pp. 1367-1394.
- Fraser, D. C. (1981). Magnetic Mapping with a Multicoil Airborne Electromagnetic System. *Geophysics*, v. 46, pp. 1579-1593.
- Frischknecht, F. C. (1967). Field about an Oscillating Magnetic Dipole Over a Two-layer Earth and Application to Ground and Airborne Electromagnetic Surveys. *Quarterly of the Colorado School of Mines*, v. 62, n. 1, Golden.
- Koefoed, O., D. P. Ghosh, and G. J. Polman (1972). Computation of Type Curves for Electromagnetic Depth Sounding with a Horizontal Transmitting Coil by Means of a Digital Linear Filter. *Geophysical Prospecting*, v. 20, pp. 406-420.
- Kozulin, Y. N. (1963). A Reflection Method for Computing the Electromagnetic Field above Horizontal Lamellar Structures. *Izvestiya, Academy of Sciences, USSR, Geophysics Series (English Edition)*, n. 3, pp. 267-273.
- Son, K. H. (1985). *Interpretation of Electromagnetic Dipole-Dipole Frequency Sounding Data over a Horizontally Stratified Earth*. Ph.D. thesis, North Carolina State University, Raleigh.
- Won, I. J. and K. Smits (1985). *Airborne Electromagnetic Bathymetry*. Naval Ocean Research and Development Activity, NSTL, Mississippi, NORDA Report 94.

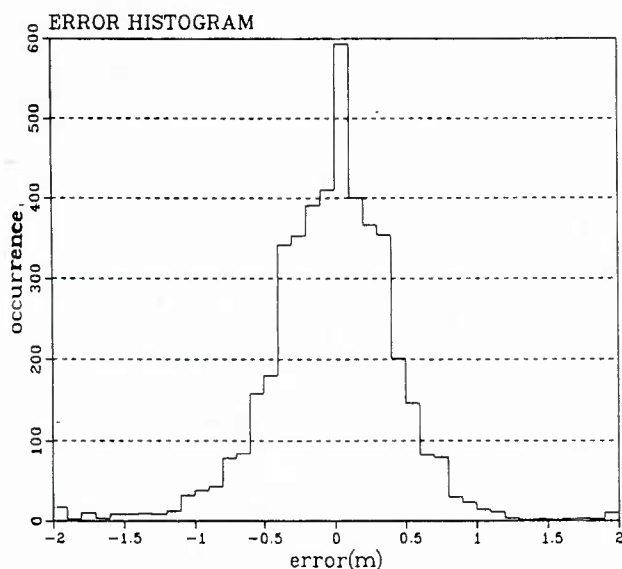


Figure 8. Histogram for differences between radar altitudes and EM altitudes for the entire 7200-Hz data collected during the Cape Cod experiment.

RADIOMETRIC IMAGERY OF SEA ICE

James P. Hollinger and Mary Ruth Keller

Space Sensing Branch, U.S. Naval Research Laboratory
Code 7781, Washington, D.C. 20375-5000

ABSTRACT

The Naval Research Laboratory (NRL) has conducted a series of flights over the eastern Beaufort Sea and the Mould Bay area during October 1981 and over the marginal ice zone in the Greenland Sea in November 1981 and July 1983. Airborne millimeter-wave imagery at 90, 140, and 220 GHz and nadir microwave measurements at 19, 22, 31 (1981), and 37 (1983) GHz were made from the NRL RP-3A aircraft. A 130 km by 130 km area was mapped at 90 GHz from high altitude in July 1983 to obtain a time sequence of the marginal ice zone. The 1981 imagery, obtained at 90 and 140 GHz from several altitudes through both clear and heavy cloud conditions, can be used to delineate the ice edge, locate polynas and leads, measure ice concentration, and determine ice type and age (from which thickness can be inferred). The 1983 time sequence of imagery was also used to determine the motion of the ice edge and of individual floes within the ice pack.

1. INTRODUCTION

Microwave scanning radiometry has proven to be of great value for the remote sensing of the environment and for the remote surveillance of man-made objects against the environmental background. It has the advantage of being completely passive and emitting no signals; thus, it is covert, difficult to jam, and uses relatively little power compared to active microwave devices. Further, it offers several potential advantages for remote surveillance over passive sensors operating at infrared, optical, and ultraviolet wavelengths. Perhaps most important, it allows all-weather, day and night operation, providing the capability to observe surface features and to detect and track objects moving on or near the surface below a cloud cover.

Microwave radiometry offers a broad range of applications and a wealth of information due to the wide variation of the emission, absorption, and reflection properties of matter with the observational frequency, polarization, and viewing angle. The microwave radiation received from the earth's surface is composed of the radiation emitted by the surface, the radiation emitted by the atmosphere between the observer and the

surface, and the downwelling atmospheric and cosmic background radiation reflected or scattered from the surface to the observer. Further, the radiation emitted and reflected from the surface is attenuated by the atmosphere between the surface and the observer.

Millimeter-wave radiometry is ideally suited for remote sensing in the arctic regions because of the high signal contrast between open water and sea ice, and between different sea ice types. Also, millimeter waves provide the highest spatial resolution for a given aperture size while still readily penetrating the relatively dry arctic air and low lying fog and ice clouds which perennially cover the marginal ice zone and polar regions. They, thus, enable all-weather day or night observations and are the ideal compromise between low-resolution, longer wavelength microwaves and high-resolution infrared and optical sensors which are blinded by weather much of the time.

The location of the sea-ice edge, polynyas, and leads, determination of ice thickness, and measurement of ice type and concentration in the polar regions is of major importance for shipping and for military operations. Ice concentration greatly affects the dynamics of ice-ocean circulation and air-sea interaction processes and is thus fundamental to accurate long-term weather prediction. It is therefore of great importance to measure the characteristics and properties of sea ice at millimeter wavelengths and to develop the techniques and technology for an all-weather, high-resolution remote sensing system for the arctic regions.

2. MICROWAVE MEASUREMENTS OF SEA ICE

The Naval Research Laboratory (NRL) has developed an airborne millimeter-wave imaging system to investigate the all-weather applications of millimeter wavelength radiometry to polar regions. Measurements have been conducted at 90, 140, and 220 GHz during a wide range of atmospheric conditions of all types of sea ice both during frozen, winter conditions and during summer melt^{1,2,3,4}.

The atmospheric transmission coefficient versus frequency for the average meteorological

conditions during the November 1981 flight² is given in Figure 1. It was calculated using the NRL environmental model⁵ and the atmospheric conditions measured at the time of the flights. It is typical for the atmospheric conditions encountered in all of the flights where the transmission was either similar to that in Figure 1 or higher. The high transmissivity allowed detailed high-quality images of sea ice to be obtained through heavy clouds at both 90 and 140 GHz from which quantitative information on ice type, location, and concentration was derived. An example is given in Figure 2 which shows a high-altitude image of the ice edge observed through heavy clouds at 90 GHz and at 140 GHz at a different time. The images are 11 km wide and show a diffused and spread ice edge in each case, with large areas of open water in the ice more than 30 km away from the ice free ocean. There were rain clouds over the ocean which are visible in the 90 GHz image on the left. The bright region on the left of the 140 GHz image is also due to increased radiation from regions of heavier clouds. Observations at 220 GHz were masked by high radiometer noise more than by atmospheric interference but surface images were only obtained under cloud free conditions².

A low altitude 90 GHz image, with corresponding 35 mm strip film photography, obtained near Prince Patrick Island is shown in Figure 3³. It shows a 32 km section of 90 GHz imagery and corresponding strip film photography taken over Fitzwilliam Strait. This image is included here specifically to illustrate the great diversity of microwave ice signatures discernible with the 16 m by 16 m surface resolution of the 90 GHz imager. The strip film photograph is good, but not optimum, because of the dim and diffuse light resulting from overcast skies above the aircraft. The microwave brightness temperature (T_B) ranges from 180 to 260 K. The original image is in color which provides a greater dynamic range and hence more detail than is shown here in black and white. The width of the image is 1880 m, equal to twice the altitude. Despite the poor conditions for photography, the correlation between ice features in the microwave imagery and the photography is clear. The photography shows apparently open water, new ice, and thicker snow-covered floes. In contrast the passive microwave 90 GHz imagery shows a far greater variety of ice types, including new ice (nilas), gray-white ice, second year (SY) and multiyear (MY) ice, as well as open water. The open water areas in the photography can only be identified positively with the aid of the microwave imagery, since water and unrafted thin ice are similar in the photography.

Ice type can be determined unambiguously from millimeter-wave imagery. This is shown in Figure 4 which gives the measured T_B distribution curves for various ice types and for open water at both 90 and 140 GHz. Each curve is derived from an individual ice floe and from a single contiguous area. Values of the mean and standard deviation are given. Note that the standard deviation for open water, a homogeneous microwave scene, is

approximately equal to the instrument noise of 1.4 K at 90 GHz and 3.5 K at 140 GHz. Thus a significant portion of the spread in the microwave signal for a single ice type is due to instrument noise. In particular, the higher instrument noise at 140 GHz increases the apparent spread of T_B for the various ice types compared to 90 GHz. The broadening, as a result of instrument noise, may be removed to obtain the standard deviation in the ice T_B alone or 1.4 and 2.8 K for young ice, 2.2 and 3.1 K for SY ice, and 3.7 and 3.4 K for MY ice at 90 and 140 GHz, respectively. The inherent T_B distribution of all ice types are sufficiently well separated at both frequencies to allow each ice type to be easily distinguished by its microwave signal.

Millimeter-wave imaging can provide detailed, high-quality mesoscale maps of surface ice conditions through complete cloud cover from which quantitative information about ice types, ice concentration, flow size, and ice kinematics can be determined. Three such maps, collected during July 1983, are shown in Figures 5, 6, and 7. The 90 GHz ice maps cover an area approximately 130 km by 130 km extending from open ocean deep into the ice pack interior with a surface resolution of 133 m. Water, first year (FY), and MY ice are clearly distinguishable in the imagery. The general shades of the different ice types in the imagery are as follows: water is usually light grey with lighter or darker patches, FY ice appears uniform and is medium to dark grey, MY floes are mottled light grey and black. The original images are in color, which provides a greater dynamic range and facilitates interpretation, but are reproduced here in black and white. The area was cloud-free on 1 July, but was cloud-covered on 4 and 11 July. Although the presence of clouds does not affect the ability of radiometry to distinguish between water, FY, and MY ice, it does decrease the measured brightness temperature contrast of all three and slightly modifies their appearance in the imagery.

The brightness contrast between water, FY, and MY ice allow the ice edge and several dozen MY floes on 1, 4, 11 July to be easily located in the imagery. Fifty-two floes were tracked from 1 to 11 July to determine ice drift for the period. Figure 8 shows that the ice edge remained relatively stationary from 1 to 4 July, but by 11 July it had changed considerably. In general, ice motion is a product of many factors including wind, ocean current, size and roughness of the floes, coriolis force, and the compactness of the ice field. Motion of ice at the edge and, to some extent, into the marginal ice zone (MIZ) is greatly influenced by the ice-ocean boundary where mechanisms of wave-floe interactions and oceanic processes such as fronts and eddies, and the effects of storms can have a significantly greater impact than at locations further from the edge. Some local correlations can be seen between the translation vectors of large floes in the upper half of the figure, which corresponds to the 50-100 km interior of the MIZ. Likewise, some general correlations can be seen between the translation vectors in the bottom half of the

figure in the areas nearest the edge. Interestingly, in the area nearest the edge, where the influence of wave interaction and other oceanic processes on the ice floes is greatest, the direction of the floe movement for the period 1-4 July is somewhat counter to the direction of movement in the interior. The dynamics of the ice edge environment is evidenced by the apparent loss of the major floes at the edge southward across the open ocean boundary sometime between 4 and 11 July. An off-ice wind, generated during a storm which was located at approximately 76°N 0°E on 10 July, is the probable cause for the floe movement into the open ocean.

3. REFERENCES

1. Troy, B.E., Hollinger, J.P., Lerner, R.M., and Wisler, M.M., "Measurement of the Microwave Properties of Sea Ice at 90 GHz and Lower Frequencies," *J. Geophys. Res.*, Vol. 86, pp. 4283-4289, 1981.
2. Hollinger, J.P., Troy, B.E., Jr., and Hartman, M.F., "All-Weather Millimeter Wave Imagery in the Marginal Ice Zone," *Radio Science*, Vol. 19, No. 3, pp. 8562-8570, May-June 1984.
3. Hollinger, J.P., Troy, B.E., Jr., Ramseier, R.O., Asmus, K.W., Hartman, M.F., and Luther, C.A., "Microwave Emission from High Arctic Sea Ice During Freeze-Up," *J. Geophys. Res.*, Vol. 89, No. C5, pp. 8104-8122, September 1984.
4. Hollinger, J.P., Keller, M.R., Luther, C.A., and Ramseier, R.O., "Millimeter Wave Radiometric Images of the Marginal Ice Zone," *IGARSS '84*, ESA-SP-215, Vol. 1, pp. 353-358, August 1984.
5. Wisler, M.M. and Hollinger, J.P., "Estimation of Marine Environmental Parameters Using Microwave Radiometric Remote Sensing Systems," Memo Report 3661, Naval Res Lab., Washington, DC, 1977.

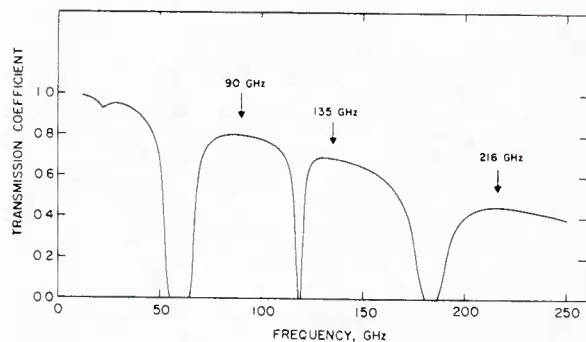


Figure 1. Atmospheric Transmission Versus Frequency for Atmospheric Conditions During November 1981 Flights.

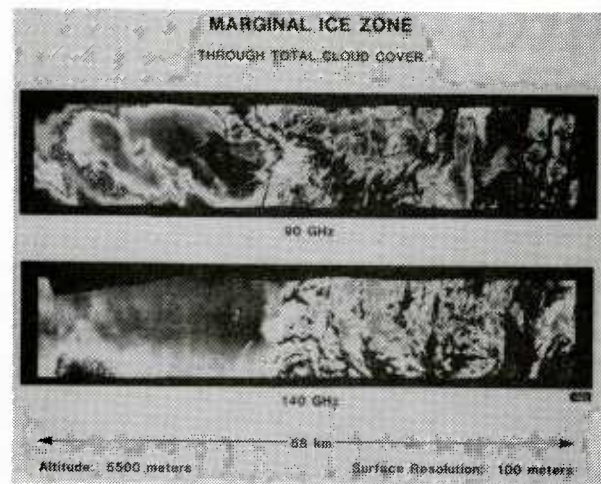


Figure 2. Two Different High Altitude Millimeter-Wave Images of a Diffuse Ice Edge.

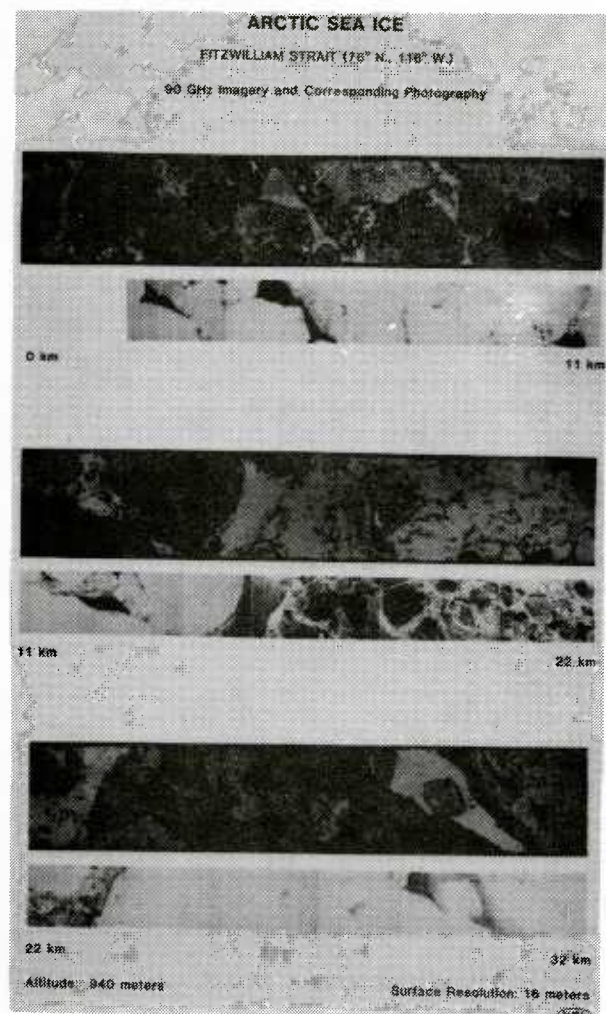


Figure 3. Low Altitude Imagery of the Fitzwilliam Strait and Corresponding Photography.

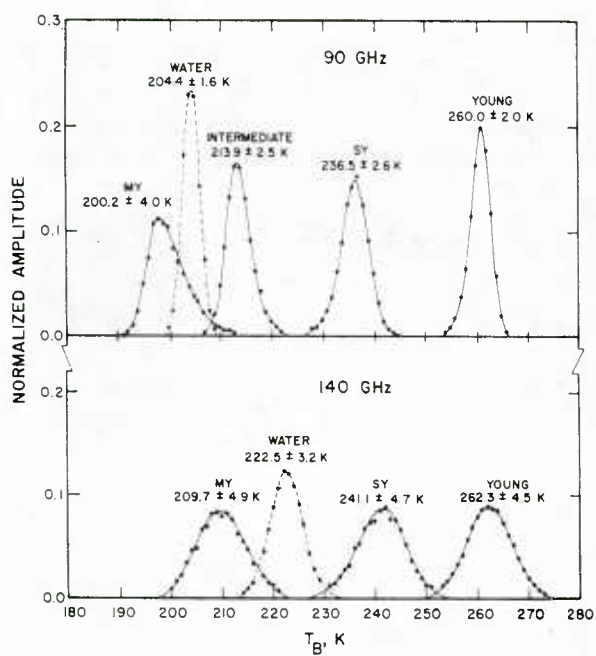


Figure 4. 90 GHz and 140 GHz Distribution Curves of Several Ice Types and Open Water.

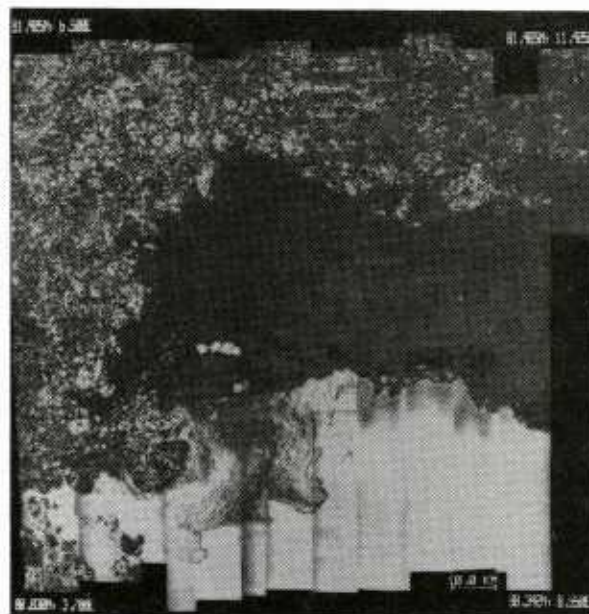


Figure 6. 4 July 1983 90 GHz High Altitude Ice Map.

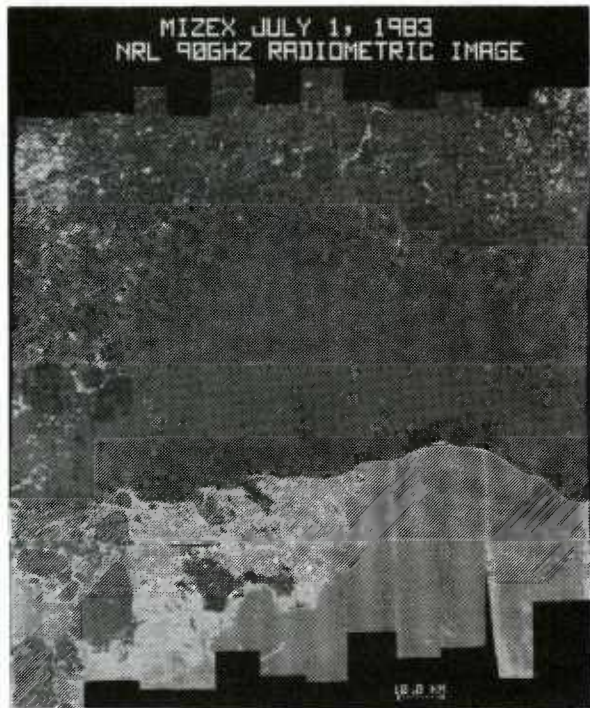


Figure 5. 1 July 1983 90 GHz High Altitude Ice Map.

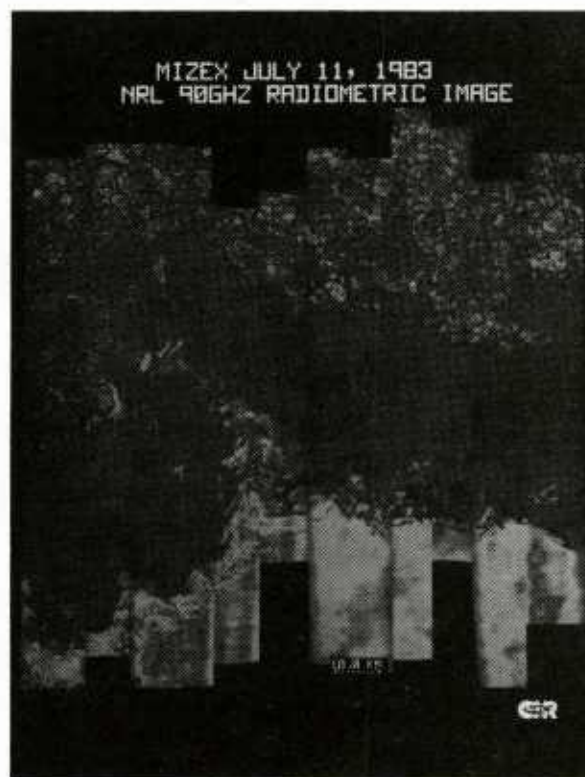


Figure 7. 11 July 1983 90 GHz High Altitude Ice Map.

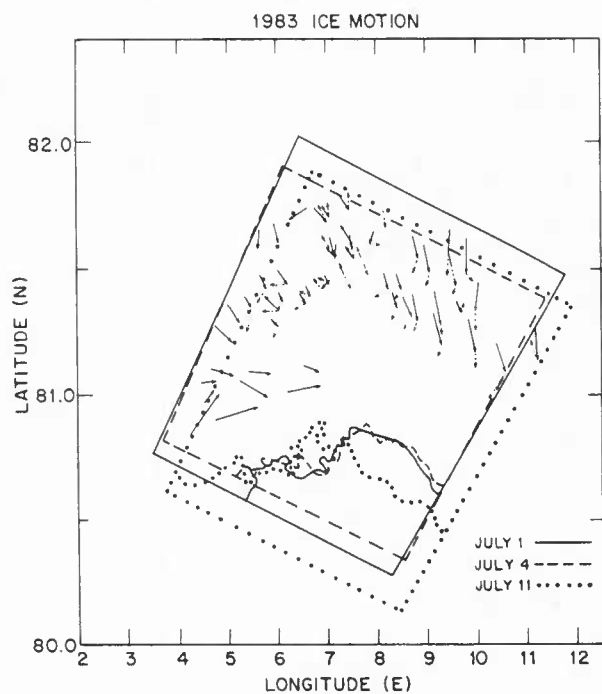


Figure 8. Ice Edges and Drift of Multiyear Ice Floes From 1, 4, and 11 July 1983 Ice Maps.

REMOTE SENSING OF THE MARGINAL ICE ZONE DURING MIZEX 83 AND 84

R.A. Shuchman and B.A. Burns

Radar Science Laboratory
Environmental Research Institute of Michigan (ERIM)
P.O. Box 8618
Ann Arbor, Michigan 48107

ABSTRACT

The remote sensing techniques utilized in the Marginal Ice Zone Experiment (MIZEX) 1983 and 1984 to study both the physical characteristics and geophysical processes of the Fram Strait Region of the Greenland Sea are described. The studies, which utilized satellites, aircraft, helicopters, and ship- and surface-based remote sensors, focused on the use of microwave remote sensors since they permit observation of ocean and ice surfaces through clouds, rain and snow which frequently occur in the marginal ice zone. Preliminary MIZEX results indicate that remote sensors can provide marginal ice zone characteristics which include ice edge and ice boundary locations, ice types and concentration, ice deformation, ice kinematics, gravity waves and swell (in both the water and the ice), location of internal wave fields, location of eddies and current boundaries, surface currents and sea surface winds. The emphasis of this paper is on the results obtained with the synthetic aperture radar (SAR) active microwave sensor.

Keywords: Remote Sensing, Marginal Ice Zone, Microwave Sensors, Synoptic Coverage, Eddy Formation, Ice Kinematics, Concentration, Ice Type

1. INTRODUCTION

The Marginal Ice Zone (MIZ) is the region of the outermost extent of the Polar Ice Field. In the MIZ, strong interactions between the atmosphere, sea ice, and ocean occur. Current scientific interest in the Arctic marginal ice zone results from the important influence this air-sea-ice interaction has on both local and hemispheric weather and climate. A central problem to MIZ studies is the definition of those oceanic and atmospheric processes which determine the location of the ice edge, ice morphology, and deformation within the marginal ice zone. Clearly, advances in the understanding of these processes are of practical as well as scientific importance. The results of such studies will lead to more accurate short-range forecasts of sea ice movements which will contribute toward resource management, exploration, and exploitation. For these reasons, an internationally coordinated deep-water Marginal Ice Zone experiment in the Fram Strait Region of the Greenland Sea has been

organized for the purpose of studying mesoscale air-ice-ocean interactions in the Arctic MIZ^{1,2}. This experiment, begun in the summer of 1983 and continued in the summer of 1984, offers a comprehensive array of coordinated mesoscale ocean, ice, and atmospheric measurements involving icebreakers, oceanographic vessels, ice and ocean buoys, remote sensing aircraft and spacecraft.

The focus of the MIZEX remote sensing studies is on the use of microwave sensors since they permit observation of ocean and ice surfaces through clouds, rain, and snow which frequently occur in this region of the world. Several of the phenomena to be studied in the MIZ, such as oceanic fronts and eddies, internal and gravity waves, ice concentration and ice types, have distinct surface signatures that can be observed by active and passive microwave sensors. Remote sensing is the only way to obtain mesoscale, synoptic, coverage of these phenomena at sufficiently high spatial resolution to provide useful information on ice, ocean and atmospheric parameters in the MIZ. The remote sensing data therefore can be used to not only identify the ice and ocean characteristics of the MIZ, but to also better understand the physical processes that control the MIZ.

In spite of much research conducted with respect to microwave detection of sea ice during the last decade, i.e., BESEX³, AIDJEX⁴, and NORSEX⁵, very little work has been done during the summer season. Many ambiguity problems are known to exist in this season due to snow melt and continual freezing and refreezing of ice surfaces. For example, passive microwave techniques yield good estimates of ice concentration when the ice is frozen⁶, but it is uncertain how well this technique will work for wet ice. Another example is the imaging radar observations. This technique presently provides information about the ice edge and its structure, as well as surface and internal waves in the ocean. However, we have not yet shown how useful the SAR is for estimating ice concentration and floe size distribution during summer and for locating fronts and eddies in the open ocean off the ice edge.

The purpose of this paper is to describe the remote sensing techniques utilized in MIZEX 83 and 84 to study both the physical character and

the geophysical processes of the MIZ. Presented in this paper is a background section that discusses the remote sensing systems utilized in MIZEX, as well as the integrated measurement plan for aircraft, helicopter, and in situ surface-based measurements. The background section is followed by a discussion of the preliminary results of the remote sensing analysis of the MIZEX data and a summary and recommendations section. Special emphasis is given to the SAR results obtained in the experiment.

2. BACKGROUND

The study of the microwave remote sensing of sea ice and oceans was initiated by NASA in the late 1960's with the objective of discovering an all-weather and day-or-night means of observing the oceans and polar sea ice canopies. Since that time, a series of international sea ice remote sensing experiments have been conducted that have improved the understanding of the microwave properties of sea ice and oceans: AIDJEX (Arctic Ice Dynamics Joint Experiment) Pilot Experiment, 1971 and 1972; Joint U.S.S.R. Bering Sea Experiment, 1973; AIDJEX Main Experiment, 1975-76; Norwegian Remote Sensing Experiments (NORSEX), 1978 and 1979; Bering Sea MIZEX, 1983. This microwave research has, for example, enabled investigators to utilize Nimbus-5 ESMR and Nimbus-7 SMMR satellite observations to obtain the first synoptic views of the entire Arctic and Antarctic sea ice covers and to derive spatial and temporal variations of sea ice parameters⁷⁻¹¹. During the last decade an intensive effort has been made to improve the accuracies in the measurement of these ice parameters. The above-mentioned experiments have also enabled researchers to utilize the Seasat SAR to obtain ice type, kinematic, and concentration information of summer ice in the Arctic^{12,13}.

For MIZEX there are two specific objectives of the remote sensing program:

1. Remote sensing as a tool — to provide baseline information on various ocean and ice characteristics required by MIZEX investigators, e.g., ice edge position, ice-ocean eddy location, positions of large leads and polynyas.
2. Remote sensing as a science — to improve our knowledge of the microwave signatures of different geophysical parameters of the MIZ in summer. This will comprise the following elements:
 - a. To develop improved algorithms for extracting geophysical ocean and ice parameters from aircraft and spacecraft (where available) remote sensing observations. This requires an extensive surface-based microwave program to relate scattering and emission characteristics to sensor frequency, ice type, and physical ice properties (surface roughness, snow cover, dielectric characteristics, temperature, salinity, crystal size).

- b. To determine whether certain ice parameters such as ice concentration, ice type and ice roughness can be reliably extracted from the outputs of a combination of active and passive microwave sensors, especially for the MIZ in summer.
- c. To develop new applications of remote sensors in this zone, such as the detection of gravity waves as they propagate into the ice and the evolution of melt ponds.
- d. To develop models that adequately explain and predict remotely-sensed electromagnetic radiation signatures of both ice and ocean features.

Remote sensors have a proven ability to detect these geophysical parameters; however, to determine the ultimate accuracy with which they can do so is a prime objective of MIZEX.

Both active and passive, microwave and visible remote sensing systems were utilized during MIZEX. The sensors included: imaging radar (both SAR and SLAR), microwave scatterometers, visible, infrared, and microwave radiometers, AXBTs, aerial photography, CODAR, and dielectric constant measuring devices. Tables 1-3 lists the satellite, aircraft, helicopter, and surface-based remote sensing instrumentation utilized in MIZEX 83 and 84. Also included on the tables is the frequency of the remote sensing instrument along with the MIZ characteristic it directly or indirectly measures. The MIZ characteristics include ice edge position, ice types and concentration, ice deformation, ice kinematics, gravity waves and swell both in the water and the ice, location of internal wave fields, location of eddies and current boundaries, surface currents, and sea surface winds. Table 4 summarizes the present status of algorithms that utilize remote sensor data to extract ice and ocean parameters such as those mentioned above. This table shows which sensor has a demonstrated or potential capability to observe each phenomenon.

The satellite systems which proved most useful during MIZEX were the NOAA AVHRR imagery with its 1 km resolution and the microwave SMMR data from Nimbus-7. The NOAA visible and IR data coverage was dependent on cloud cover, while the passive microwave data with its 25 km resolution was collected on alternate days regardless of weather conditions.

The aircraft listed on the table were utilized in two types of flight plans: high-altitude with imaging radars and scanning passive microwave sensors to acquire the mesoscale sequential synoptic images of the entire MIZEX test area, and low-altitude with active and passive microwave instruments to acquire high-resolution transect data in selected locations within the test area. Thus, two types of remote sensing products were generated: composite mosaic maps of the entire test area and transect images and profiles. The active and passive microwave

TABLE 1
MIZEX 83 AND 84 REMOTE SENSING INSTRUMENT ENSEMBLES

Name	MIZEX Participation	Satellite Sensors		Resolution and Coverage	MIZ Characteristics Provided
		Instruments	Type		
NOAA-7/8 (US/NOAA)	1983 and 1984	AVHRR	Visible and Infrared	1 km entire Fram Strait	Meteorology Ice Motion Ice Edge Location Eddy Structure
Meteor (Soviet)	1983 and 1984	OLS	Visible and Infrared	5 km entire Fram Strait	Meteorology Ice Motion Ice Edge Location Eddy Structure
DMSP (US/DOO)	1983 and 1984	OLS	Visible and Infrared	1 km entire Fram Strait	Meteorology Ice Motion Ice Edge Location Eddy Structure
LANDSAT-D (US/NASA)	1983 and 1984	MSS	Visible and Near Infrared	80 m 100 km frames	Meteorology Ice Motion Ice Edge Location Eddy Structure
NIMBUS-7 (US/NOAA/NASA)	1983 and 1984	SMMR	Microwave	25 km entire Fram Strait	Meteorology Ice Motion Ice Type

NOAA = National Oceanic and Atmospheric Administration
DOO = Department of Defense
NASA = National Aeronautics and Space Administration
DMSP = Defense Meteorological Satellite Program
AVHRR = Advanced Very High Resolution Radiometer
OLS = Optical Line Scanner
MSS = Multispectral Scanner
SMMR = Spectral Scanning Microwave Instrument

TABLE 2
MIZEX 83 AND 84 REMOTE SENSING INSTRUMENT ENSEMBLES

Platform	MIZEX Participation	Aircraft Sensors		Resolution and Coverage	MIZ Characteristics Provided
		Instruments	Frequency (GHz)		
CCRS CV-580 (CCRS/ERIM)	1983 and 1984	Imaging radar (SAR) Scatterometer Microwave radiometer Aerial Cameras	9.8, 5.3, 1.3 13.3 19.4 Visible	3 m, 10 km swath width 70 km mosaics Profiler Profiler	Ice Edge Location Eddy Structure Ice Type Mapping Ocean Wave Spectra Flow Size Distribution Ice Concentration Ice Kinematics
RDAF C-130 (Denmark/Air Force)	1983	Imaging radar (SLAR) Passive microwave imager 35-mm photography	10 1.3, 5, 17, 34 Visible	25 m, 40 km swath width Profiler	Ice Edge Location Eddy Structure Ice Type Ice Concentration
USA-NRL P-3 (USA)	1983 and 1984	Passive microwave imager SSM/I radiometer PRT-5 infrared profiler INS winds Environmental sensors 60 mm photography - Hasselblad Stepped-frequency radiometer	90, 140, 220 19, 22, 31, 37 11 (microns) NA NA Visible 4.5-7.2	15-120 m, 2-15 km swath width 100 km mosaics Profiler	Ice Edge Location Ice Concentration Ice Type Ice Kinematics
Norwegian Air Force P-3 (Norway/Air Force)	1983 and 1984	AXBT	NA	Point measurements	Ocean Temperature
ARA Baron (US)	1983	Atmospheric boundary layer parameters Survey photography	Visible	Profiler Mosaics	Meteorology Ice Edge Location Flow Size Distribution
CV-990 (NASA//USA)	1984	Radar altimeter Passive microwave imager Radiometer PRT-5 and camera	13.7 92, 19 10.7, 18, 21, 37 11 μ m, visible	1 km profiler 100 m, 100 km mosaics Profiler	Wave height, ice edge location Ice type Ice concentration
NOAA P-3 (USA)	1984	SLAR Laser profilometer Gust probe	35 GHz Visible	10 m, 20 km swath width Profiler Profiler	Ice edge Flow size distribution Ice concentration Ice type Ice roughness Eddy structure
B-17 (CNES/France)	1984	SLAR Photography	9.3 GHz Visible	25 m, 20 km swath width 90 km mosaics	Ice edge location Flow size distribution Ice concentration Oceanographic information
Falcon 20 (DFVLR/W. Germany)	1984	Meteorology air samples	NA	Profiler	Cloud drop size distribution Aerosol samples Scattering coefficient

CCRS = Canada Centre for Remote Sensing
ERIM = Environmental Research Institute of Michigan
NRL = Naval Research Laboratory

ARA = Airborne Research Associates
NASA = National Aeronautics and Space Administration
NOAA = National Oceanic and Atmospheric Administration

CNES = Centre National d'Etudes Spatiales
DFVLR = Deutsche Forschungs- und
Versuchsanstalt für Luft- und Raumfahrt

TABLE 3
MIZEX 83 AND 84 REMOTE SENSING INSTRUMENT ENSEMBLES

Platform	MIZEX Participation	Ship- and Surface-Based Sensors			Frequency (GHz)	Resolution and Swath	MIZ Characteristics Provided
		Instruments	Instrument Platform				
Drifting-Ice Ship Station (Polarbjorn or Polarqueen)							
Univ. of Kansas	1983	Microwave Step Frequency Scatterometer	Helicopter	1 to 18 selected	Profiling	Ice Type, EM Properties EM Ice Properties (reflection, penetration, etc.)	
		Dielectric Constant Measurements	Ground	1 to 4	Point Measurements		
Univ. of Washington	1983 and 1984	Passive Microwave Radiometer	Ground	10, 18, 37 and 90	Point Measurements	Ice Type, EM Properties	
Ice-Strengthened Ship (Polarstern)							
Univ. of Kansas	1984	Microwave Step Frequency Scatterometer	Helicopter	1 to 18 selected	Profiling	Ice Type, EM Properties EM Ice Properties (reflection, penetration, etc.)	
		Dielectric Constant Measurements	Ground	1 to 4	Point Measurements		
Switzerland/Univ. of Bern	1983	Passive Microwave Radiometer	Ship-Mounted	10.4	Point Measurements	Ice Type/EM Properties Thermal Ice Properties	
		Microwave Scatterometer	Ship-Mounted	4.9, 10.4, 21, 36 and 94.6	Point Measurements		
		Infrared Radiometer		8 to 14 (microns)			
		Resonant Cavity (Dielectric Constant Measurements)	Ground	1.0	Point Measurements	EM Ice Properties	
France/CNES	1983 and 1984	RAMSES Microwave Active Radiometer (ERASME Scatterometer)	Ship-Mounted	8-18 Selected (9, 13.5 Used Extensively)	Point Measurements	Ice Type/EM Properties	
			Helicopter	5.35	Trnsects		
ERIM	1984	Resonant Cavity (Dielectric Constant Measurements) Incident Power Measurements Snow Free Water Measurements	Ground	1, 10, 100 MHz	Point Measurements	EM Ice Properties X-C-L SAR Calibration Microwave Penetration	

CNES = Centre National d'Etudes Spatiales
ERIM = Environmental Research Institute of Michigan

TABLE 4
SEA ICE AND OCEAN PARAMETERS AND SENSORS

1 -- Demonstrated Capability 2 -- Potential Capability 3 -- Ancillary Capability

	Imaging Radar	Radar Altimeter	Passive Microwave	Scatterometer	Photography	Infrared Imager	Laser Profilometer	Infrared Profiler	AXBT
Deformation of ice boundary	1	3	1	2	1	--	--	--	--
Location and shape-size of ocean ice studies	1	--	2	2	3	2	--	--	--
Floe size distribution	1	--	3	--	1	--	--	--	--
Ice type	2	--	1	1	3	--	--	--	--
Ice roughness	2	2	--	2	--	--	1	--	--
Ocean wave spectra	1	1	--	2	--	--	2	--	--
Surface wind over water	2	1	2	1	--	--	--	--	--
Sea surface temperature	--	--	1	--	--	1	--	1	2
Ocean temperature profiles	--	--	--	--	--	--	--	--	1
Ice temperature (surface)	--	--	2	--	--	1	--	1	1
Ice concentration	1	2	1	--	3	--	--	--	--

instrumented aircraft were flown coincidentally for the purpose of sensor performance comparison and validation.

In order to validate the satellite and aircraft remote sensors, multispectral microwave measurements were made by helicopter, ship, and surface-based sensors. Measurements included brightness temperature, radar backscatter cross sections, and dielectric properties for water and various types of ice during different weather conditions. Measurement groups were located on both the ice drifting ships and the ice edge ships. On the former, their task was to concentrate on detailed temporal studies of selected ice types. On the latter, it was to study different ice types as the ship made transects into the ice. Helicopter-borne instruments linked both mesoscale programs and provided high mobility to study ice conditions within the experimental region.

Surface measurements were made of physical-electrical properties of various ice and snow types present at the active-passive remote sensing test sites to help in understanding the microwave interaction processes involved. Physical property information acquired included small-scale surface roughness, snow wetness, grain size, salinity distribution, temperature, snow thickness, ice thickness, and scatterers in the ice. Dielectric constant measurements were made to describe various ice types at X-L-C bands and 13.7 GHz. Scenes of special interest included surfaces which had melted and refrozen, ice ridges, multi-year, first-year and thin ice of various thicknesses, and melt ponds and open water under calm and windy conditions.

During both the MIZEX 83 and 84 field programs, emphasis was given to coordinating the aircraft, helicopter, ship-based, and surface-based (in-situ) measurements. To meet the objectives outlined above required helicopter, ship-based and in situ measurements to be made during all remote sensing aircraft flights and active SAR data to be collected coincidentally with the passive microwave data. Table 5 summarizes the MIZEX 84 aircraft operations for remote sensing and meteorology.

3. PRELIMINARY RESULTS

Remote sensing imagery obtained during MIZEX from both aircraft and satellite sensors provided synoptic information on ice location, ice edge features, and the regimes of ice conditions within the MIZ. Scanning Multichannel Microwave Radiometer (SMMR) and Advanced Very High Resolution Radiometer (AVHRR) images from satellite show the general location of the ice edge and ice edge features in the entire Greenland Sea. This imagery is invaluable for monitoring the temporal evolution of the MIZ and providing a synoptic context for phenomena observed in the field. The AVHRR data were also useful in determining meteorological conditions over the experiment area as well as discriminating large ice floes (i.e., 5 km or larger).

Passive microwave and radar imagery from aircraft sensors also provide a synoptic view, but on the 100-200 km scale of the experiment itself. By collecting this imagery over a period of days, it is possible to also monitor temporal changes and increase the spatial extent of ice edge observations. High resolution SAR (i.e., 3 m x 3 m resolution) can give ice edge and feature location to within 1 km, which is sufficient for ships to subsequently locate and investigate a given feature.

A comparison of the satellite-derived ice edge to that obtained by the higher resolution aircraft data for 29-30 June 1984 is presented in Figure 1. Shown on the figure is the NIMBUS-7 SMMR edge (i.e., 10 and 35 percent ice concentration), that from the NOAA-7 AVHRR along with the ice edge extracted from the SAR and SLAR data. Also, for comparison, the ice edge, as provided by NAVOCEANO is presented on the figure. Given the respective resolution of the AVHRR (1 km), SMMR (25 km), SAR (3 m), and SLAR (100 m), the sensors all appear to provide accurate ice edge information. The NAVOCEANO prediction which is based on NOAA-7 and DMSP AVHRR data also appears to be quite accurate.

In addition to the general character of the MIZ, satellite, aircraft, and surface remote sensing data from MIZEX have collectively produced significant information on MIZ processes and geophysical parameters under summer conditions. Preliminary results are available from studies of eddy formation at the ice edge, propagation of gravity waves into the ice, ice kinematics, ice concentration, floe size distribution and ice type discrimination.

AVHRR imagery has served as a context for observations of oceanic eddies made during MIZEX. Surface patterns on the imagery indicate the presence of ice edge eddies over and near the vicinity of the Molloy Deep, a topographic feature (depression) at approximately 79°15'N 0°E, as well as the ice drift and ice edge deformation due to combined effects of waves and eddies. Eddies in this area have been observed previously^{14,15} and appear to be topographically controlled and baroclinic in nature.

Eddies seen in AVHRR imagery also have been observed on the SAR images of the MIZ. Figure 2 is a mosaic of the L-band (23.5 cm wavelength) data collected on 5 July 1984. The three eddies clearly observed on the mosaic (see Figure 3 for an interpretative key) were also observed on the 4 July AVHRR infrared image. Note from the blow-up on the figure that individual ice pieces can be resolved on the 3 m resolution radar data. These eddies are visible on the SAR data because surface currents associated with the eddy align and consolidate (due to current shear) small 50-500 m pieces of ice. These small floes which were broken up from larger floes due to wave action, are in effect, surface current drifters that are very bright radar reflectors to the SAR.

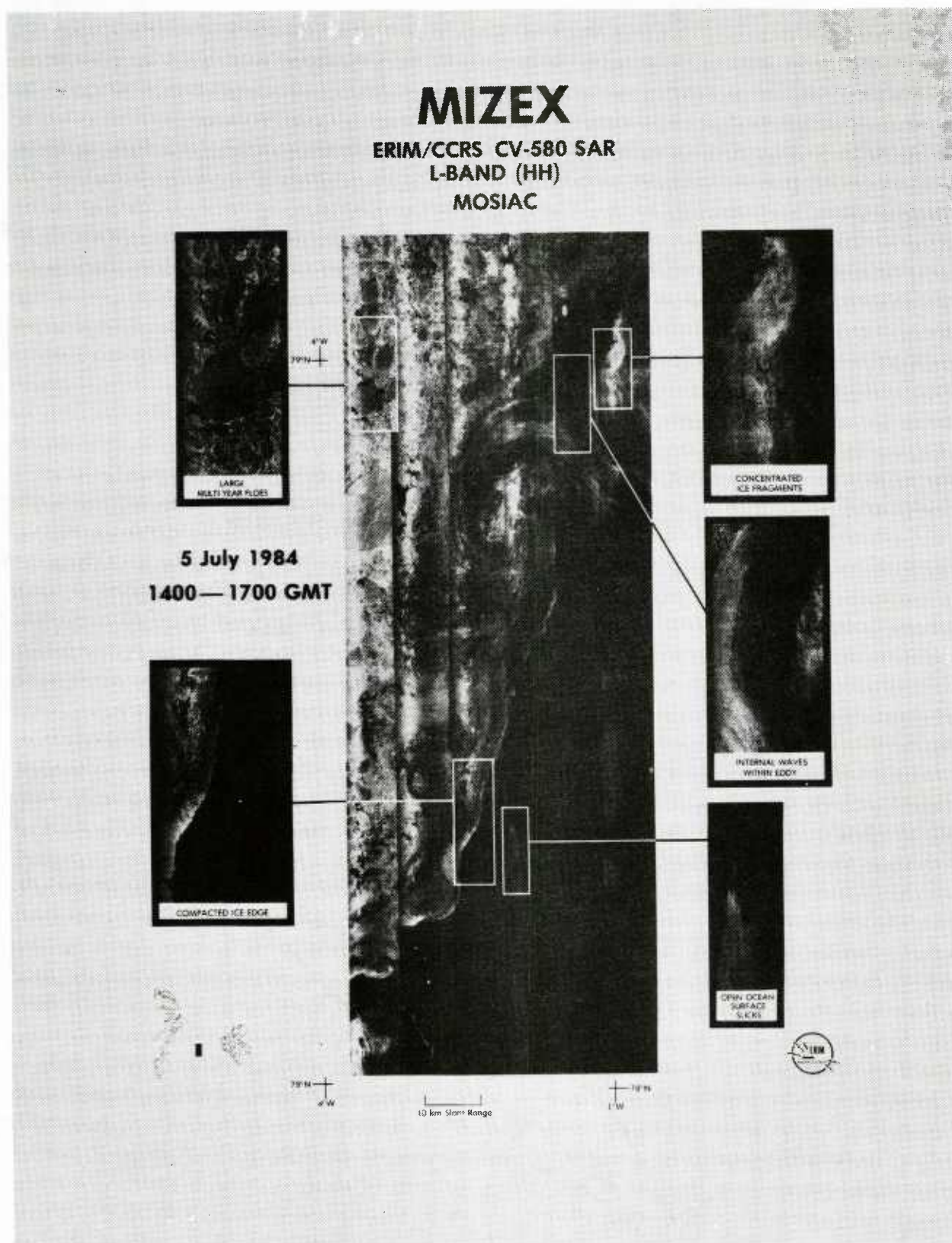




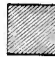


Figure 2. SAR mosaic for 5 July 1984. Note the eddy clearly visible in the center of the image.

ICE INTERPRETATION

5 July 1984
1400 — 1700 GMT

CV-580 SAR

MIZEX

-  — LARGE INDIVIDUAL FLOES
-  — POLYNYAS AND ICE FREE OCEAN AREAS
-  — APPROXIMATELY 30% CONCENTRATION WITH ICE FLOE SIZE RANGING FROM 10m TO 500 m WITH A MEDIAN FLOE SIZE OF 125 m • INDICATES INCREASED LOCAL ICE CONCENTRATION DUE TO SURFACE CURRENTS
-  — APPROXIMATELY 80% CONCENTRATION WITH ICE FLOE SIZE RANGING FROM 10m TO 1.3 km WITH A MEDIAN FLOE SIZE OF 150 m
-  — APPROXIMATELY 80% CONCENTRATION WITH ICE FLOE SIZE RANGING FROM 10 m TO 6 km WITH A MEDIAN FLOE SIZE OF 1 km



R-85-148

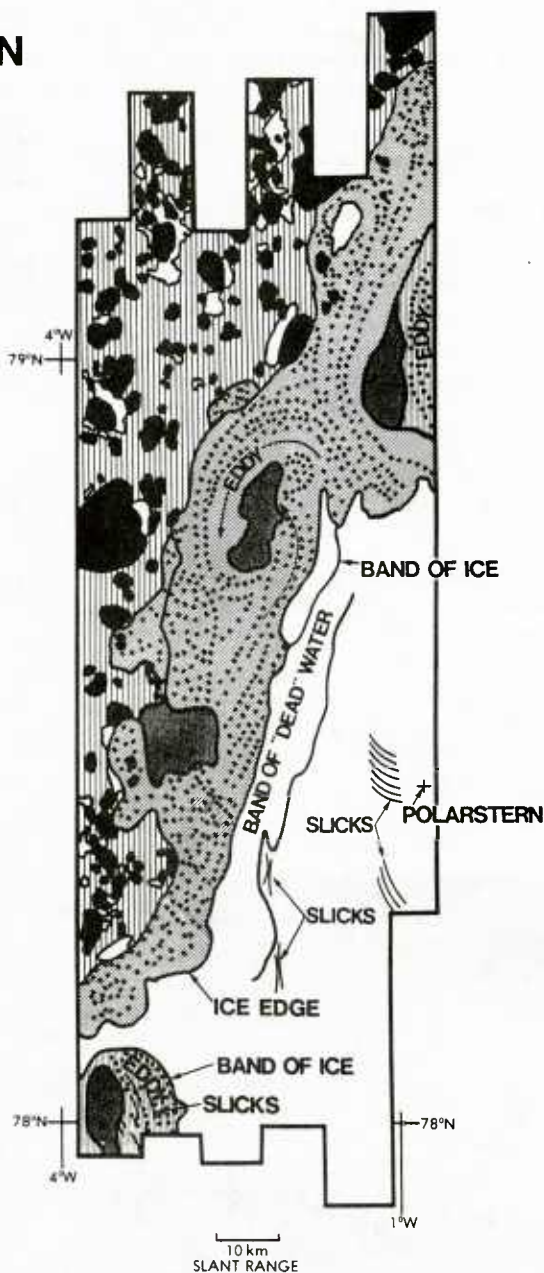


Figure 3. SAR interpretation key for the 5 July mosaic.

Figure 4 is an oblique photograph taken from 23,000 ft of the SAR imaged eddy located at approximately 78°40'N and 2°W. Remote sensing instruments as well as in situ observations indicated this cyclonic eddy has a lifetime of approximately 30 days. The diameter of the eddy is 30-40 km. ARGOS buoys deployed within the eddy indicated a counter-clockwise orbital velocity flow of 0.5 m/s. The convergence of the ice floes in the center of the eddy clearly suggest that ageostrophic effects are important.

The eddies were extensively "sea truthed" during MIZEX with the aid of SAR imagery. Using the SAR real-time output images to locate the center of the eddies, complete temperature, salinity, and density profiles were obtained from ships and AXBT observations.

In addition to the SAR providing mesoscale information on ice edge and eddy formation, the SAR has also been used to provide detailed high-resolution information on MIZ characteristics. This information was obtained through manual interpretation, machine-assisted manual analysis or fully digital analysis of the SAR data.

Manual interpretations done on the mosaics from each day were based on features observed in the X-band (3-cm wavelength) and L-band data. The 5 July interpretation is shown in Figure 3. These channels provide complimentary information: the X-band gives better ice/water contrast and therefore good floe definition, whereas the L-band provides more detail on features within the floes and on ocean wave features.

The interpretation consisted of three parts. The first was the identification of unique features: eddies, large floes, polynyas, and internal waves. The second step was to segment ice covered regions into areas with the same signature, that is the same perceived overall tone and texture. In general, each area or class appears to be associated with a different combination of ice concentration and floe size distribution which is responsible for the perceived texture. The number of classes so defined ranged from 3, as in the 5 July interpretation, to 7.

Step three was to quantify ice concentration and median floe size associated with each class. To do this, representative subareas for each class were selected from the mosaic and located on the image strips from the real-time processor. Floe boundaries for all floes within each subarea were then transferred to clear acetate for digitization. Digitizing was done on a DIGI-PAD 5 digitizer interfaced to a Z-100 micro-computer. A software package for the digitizer, developed at ERIM, converts the image into an array of cartesian coordinates and stores the information on floppy disk. Once on disk, the data are manipulated to obtain area, perimeter, and diameter of each floe and total ice concentration of the subarea.

Values of ice concentration and floe size obtained in this way appear in the interpretation key (see Figure 3). The accuracy of this procedure was determined by repeating it on coincident aerial photographs obtained simultaneously with SAR data on 30 June by the CV-580. Discrepancy

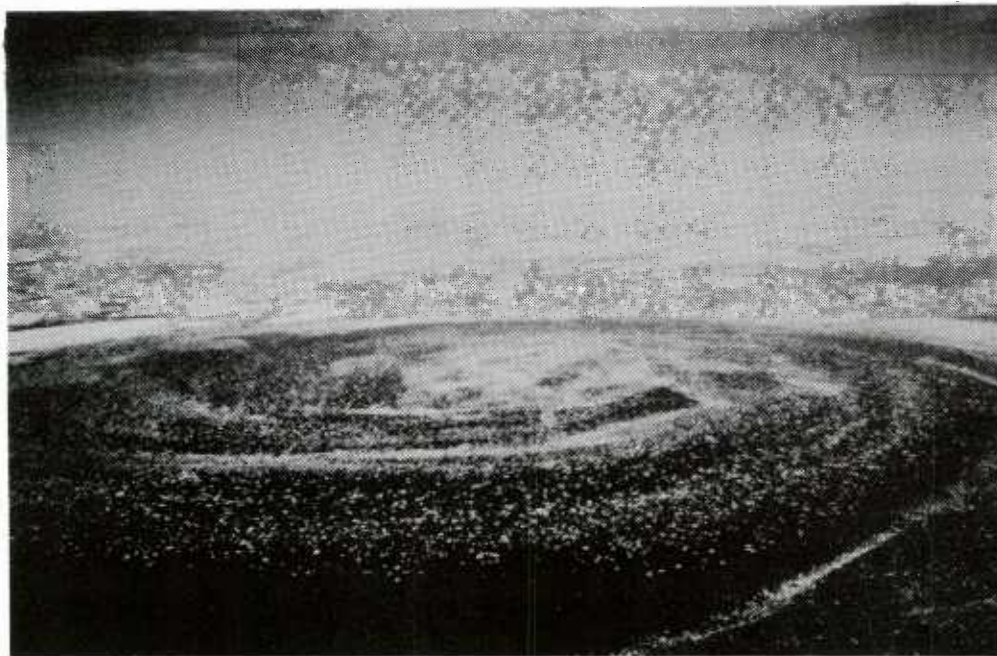


Figure 4. An oblique photograph of an ice eddy observed during MIZEX '84.

between SAR-derived and aerial photo concentration estimates was at most 5 percent for concentrations ranging from 30 percent to 80 percent. Correspondence between floe sizes measured on SAR imagery and aerial photos was also evaluated and found to be within 10 percent on average.

A more automated procedure for obtaining total ice concentration estimates from digital SAR data has been recently implemented but was not used in the manual interpretations. The algorithm developed is similar to that used with passive microwave data in that it assumes the image intensity given at each pixel is linearly related to the ice concentration in the surface area represented by that pixel (Figure 5). However, unlike its application to the relatively low resolution passive microwave data, the general mixed pixel relationship

$$I = C \bar{I}_{ICE} + (1 - C) \bar{I}_{WAT},$$

where C = total ice concentration, I = pixel intensity, \bar{I}_{ICE} and \bar{I}_{WAT} are mean intensity values for ice and water in the image, is applied not to the entire range of the SAR image intensities but only to those where $\bar{I}_{WAT} < I < \bar{I}_{ICE}$. This is appropriate not only because of the higher, approximately 3 m, resolution of the SAR imagery, but also because SAR ice backscatter intensities have a wide distribution about the mean due to natural variability and coherent speckle. At present, \bar{I}_{WAT} and \bar{I}_{ICE} must be determined manually with the aid of an image display device, but pattern recognition routines are being investigated to automate this step also.

This algorithm has been applied to image data of a relatively high ice concentration (80-90 percent) area in the vicinity of the MIZEX 84 drift station and to imagery of a low concentration diffuse ice edge area. Both areas had coincident, near simultaneous aerial photography coverage. Total ice concentration estimates derived from the digital SAR data agreed to within 5 percent with those derived manually (as described above) from the aerial photography.

The high resolution SAR also provided information on gravity waves. Wind-generated sea and swell gravity waves were observed on both the X- and L-band SAR MIZEX data. Figure 6 is an example of gravity waves imaged by the SAR as these waves propagated into the ice pack. Initial examination of the data set indicates the wave energy is dissipated quite quickly due to the small individual ice floes colliding with each other. No gravity waves were observed in the ice by the SAR that were more than 25 km from the ice edge.

Internal waves located both in ice free areas of the MIZ and within the pack were observed by the SAR. The open water internal waves are observable due to surface current straining of the SAR ocean Bragg wave¹⁶, while the internal waves within the ice are visible via the same mechanism as the eddies; that is, differential surface

currents cause small ice floes to align themselves to the surface current field.

Ice kinematics also were studied during MIZEX using satellite located buoys, radar transponders deployed on ice floes and by synthetic aperture radar. The ERIM/CCRS SAR aircraft produced images of the ice with a sufficiently high resolution for individual ice features to be recognized.

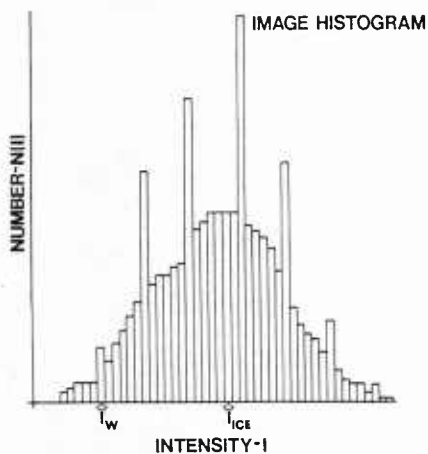
A SAR-derived two-dimensional vector field representing ice movement between 4 July and 6 July 1983 is shown in Figure 7. These are movements of recognizable ice features which persisted in their shapes during the two-day interval. Sixty-seven ice features were identified and their positions measured on transparent image film in a slant-range representation. Algorithms were implemented to convert these measurements to actual distance on the scene, to convert these in turn to latitude-longitude coordinates, and to plot automatically the vector field of ice movement. The feature coordinates on the two days were based upon the flight altitude, the inertial navigation system data, and the location of the imaged research vessel, which was fixed by satellite positioning. Account was also taken of the spherical earth geometry in which the separate N-S flight lines making up the data are skewed at these high latitudes, the angle between them being only slightly smaller than their difference in longitude.

Examination of the diagram indicates that the area was subject to both shear and deformation during this period. These motions are consistent with ARGOS buoy and ship displacements shown for comparison in the figure. The sources of the observed variation in ice drift in the area, however, still need to be investigated through a careful comparison of wind and current data with the SAR imagery.

4. SUMMARY AND RECOMMENDATIONS

An ensemble of satellite, aircraft, helicopter, ship, and surface-based remote sensors were utilized in MIZEX to study the physical characteristics and geophysical processes of the Fram Strait Region of the Greenland Sea. To date, the sensors that have proved most useful for Marginal Ice Zone (MIZ) studies include the NOAA-7/8 AVHRR and NIMBUS-7 SMMR satellite sensors and the active SAR and passive microwave aircraft systems. The satellite systems provide synoptic coverage of the entire Greenland Sea with specific details on the ice edge location, and in the case of SMMR additional information pertaining to ice type and concentration. The higher resolution AVHRR data were useful in providing meteorology as well as mapping out the structure of ice edge features.

The aircraft data provide 100-200 km synoptic coverage with significantly more detailed ice information than the NOAA-7/8 and NIMBUS-7 satellites. The aircraft data have been shown useful in providing information for ice edge location,



TOTAL ICE CONCENTRATION

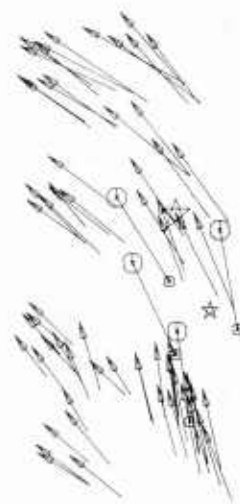
$$= \frac{I}{N_{TOT}} \sum_{I=0}^{I_{MAX}} f_i \cdot N(I)$$

f_i = FRACTION OF PIXEL AREA COVERED BY ICE

Figure 5. SAR ice concentration algorithm where

$F_I = 0$ for $I < I_W$; $\frac{I - I_W}{I_{ICE} - I_W}$ for $I_W < I < I_{ICE}$; and

$F_I = 1$ for $I > I_{ICE}$.



ICE MOVEMENT FROM SUCCESSIVE SAR IMAGES
49-HOUR INTERVAL 7/4 - 7/6, 1983

Figure 7. Vector field of ice movement derived from successive SAR images indicated deformation and shear in the ice during a 49 hour interval between 4 and 6 July. Motions of four Argos buoys and Polarbjorn are also shown.

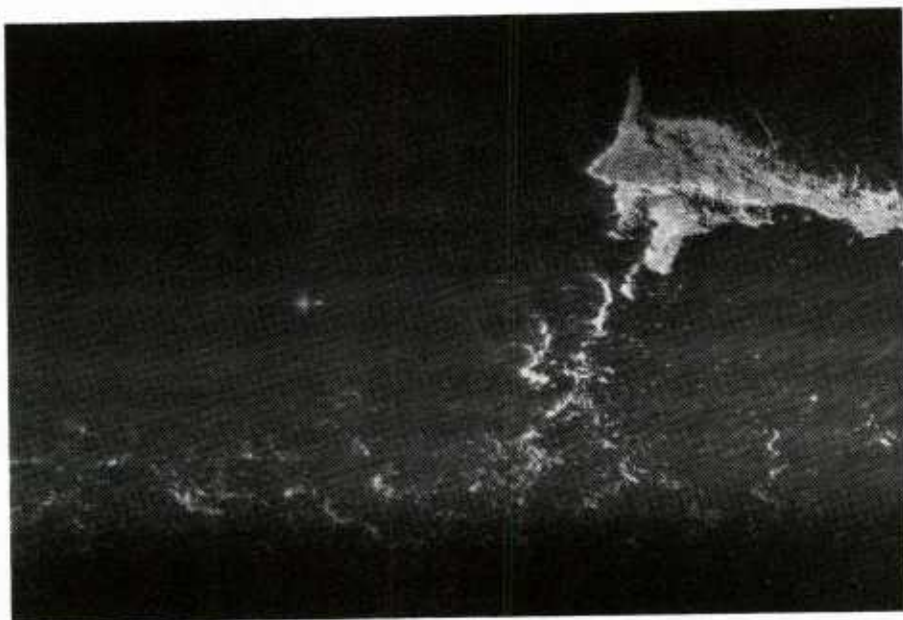


Figure 6. Gravity waves propagating into the ice as observed by SAR.

ice type identification, detection of gravity waves in the ice, ice morphology as a function of distance from the ice edge, location and areal extent of melt ponds, ice roughness, ice concentration, ice temperature, and ice dynamics. Ocean information that can be provided by the aircraft remote sensors includes: ocean eddy and frontal mapping, gravity wave measurements, synoptic measurement of currents, sea surface temperature, and measurement of small-scale ocean surface roughness.

The ship and surface-based measurements were extremely useful in validating the satellite and aircraft data by determining the physical basis for features observed by the remote sensors, as well as determining optimum active and passive microwave sensor system parameters for future MIZ data collections. The focus of the MIZEX remote sensing was on microwave sensors because they permit observation of the MIZ through clouds, rain, and snow independent of solar illumination.

The analysis to date has not addressed the central question of the ultimate accuracy with which the individual remote sensors can detect MIZ characteristic nor has the analysis intercompared the active and passive microwave aircraft sensor and aerial photography. The active and passive microwave data have also not been combined to assess whether a combination active/passive approach yields more detailed and accurate MIZ characteristics.

5. ACKNOWLEDGEMENTS

The Marginal Ice Zone Experiment (MIZEX) is primarily supported by the Arctic Program Office of the Office of Naval Research (ONR). The ONR technical monitors for MIZEX are Dr. Leonard Johnson and Mr. Charles Luther. The Environmental Research Institute of Michigan (ERIM) is supported to participate in MIZEX under ONR Contracts N000-14-83-C-0404 and N000-14-82-C-0063. These contracts are monitored by Mr. Charles Luther.

6. REFERENCES

1. Wadhams P et al, MIZEX, A Program for Mesoscale Air-Ice-Ocean Experiments in Arctic Marginal Ice Zones. I. Research Strategy, CRREL Special Report 81-19, 1981, 20 pp.
2. Johannessen O M et al, MIZEX, A Program for Mesoscale Air-Ice-Ocean Interaction Experiments in Arctic Marginal Ice Zones. II. A Science Plan for a Summer Marginal Ice Zone Experiment in the Fram Strait/Greenland Sea: 1984, CRREL Special Report 83-12, 1983, 47 pp.
3. Gloersen P et al, Variation of Ice Morphology of Selected Mesoscale Test Areas During the Bering Sea Experiment, in USSR/US Bering Sea Experiment: Proceedings of the Final Symposium on the Results of the Joint Soviet-American Expedition, Leningrad, 12-17 May 1974, K. Ya. Kondratyev, Yu. I. Rabinovich, and W. Nordberg, eds., 1975, pp. 196-218.
4. Campbell W J et al, Microwave Remote Sensing of Sea Ice in the AIDJEX Main Experiment, Bound. Layer Meteor., 13, 1978, pp. 309-337.
5. NORSEX Group, The Norwegian Remote Sensing Experiment in a Marginal Ice Zone, Science, 220, 1983, pp. 781-787.
6. Svendsen E et al, NORSEX II: Evaluation of the Nimbus 7 Scanning Multifrequency Microwave Radiometer for Sea Ice Research, J. Geophys. Res., 88, 1983 pp. 2781-2792.
7. Gloersen P et al, Time-Dependence of Sea Ice Concentration and Multiyear Ice Fraction in the Arctic Basin, Boundary-Layer Meteorol., Vol. 13, 1978, pp. 339-360.
8. Campbell W J et al, Aspects of Arctic Sea Ice Observable by Sequential Passive Microwave Observations from the Nimbus-5 Satellite, in Arctic Technology and Policy: An Assessment and Review for the Next Decade, Hemisphere Publishing Corp., Cambridge, Mass., 1983, pp. 197-222.
9. Gloersen P et al, A Summary of Results from the First Nimbus-7 SMMR Observations, submitted to J. Geophys. Res., 89, 1984, pp. 5335-5344.
10. Cavalieri D J et al, Determination of Sea Ice Parameters with the Nimbus-7 SMMR, submitted to J. Geophys. Res., 89, 1984, pp. 5355-5369.
11. Zwally H J et al, Antarctic Sea Ice Cover 1973-1976 from Satellite Passive Microwave Observations, NASA SP-459, 1983.
12. Carsey F D, Summer Arctic Sea Ice Character from Satellite Microwave Data, J. Geophys. Res., 90, 1985, pp. 5015-5034.
13. Luther C A et al, Synthetic Aperture Radar Studies of Sea Ice, International Geoscience and Remote Sensing Symposium Digest, Munich, Germany, 1982 pp. TA-8, 1.1-1.9.
14. Vinje, Sea Conditions in the European Sector of the Marginal Seas of the Arctic, 1966-75, Norsk Polarinstitutt Arbok 1975, 1977, pp. 163-174.
15. Wadhams P and V A Squire, An Ice-Water Vortex at the Edge of the East Greenland Current, J. Geophys. Res., 88, 1983, pp. 2770-2780.
16. Alpers W, Theory of Radar Imaging of Internal Waves, Nature, 314, 1985, pp. 245-247.

SOME RESULTS OF THE MIZEX WEST ICE OBSERVATION PROGRAM

Robin D. Muench*, Donald J. Cavalieri**
and Gilbert R. Stegen*

*SAIC, 13400B Northup Way, Bellevue, WA 98005

**NASA/GSFC, Greenbelt, MD 20771

ABSTRACT

The Bering Sea Marginal Ice Zone Experiment (MIZEX West) obtained extensive field observations of atmospheric, sea ice and oceanographic conditions over the central Bering Sea shelf. The remote sensing portion of this experiment compared satellite, aircraft and surface sea ice data in order to evaluate the remote sensing methods used and to provide real-time ice monitoring capability. The results verified that AVHRR data are useful for determining sea ice concentration and floe drift trajectories during clear weather periods. Satellite SMMR data were demonstrated to correctly locate ice edge position and areas of low ice concentration under all weather conditions. In addition, it was found that dual-polarized SMMR radiances can differentiate among new, young and first-year ice and can correct ice concentration biases in regions of thin ice cover. Combined AVHRR and SMMR data can provide excellent quality information on ice distribution and motion.

1. INTRODUCTION

1.1 The MIZEX West Program

MIZEX West was an integrated, interdisciplinary program which simultaneously observed winter atmospheric, sea ice and oceanographic processes in the central Bering Sea Marginal Ice Zone (MIZ). A summary program description has been provided by the MIZEX West Study Group (1), and in-depth descriptions of selected aspects of the program have been presented in Volume VI of the MIZEX Bulletin (2) as well as in various scientific publications. Meteorological studies addressed transfer of wind stress through an ice cover and development of the atmospheric boundary layer at an ice edge. Sea ice studies examined the dynamic processes which control ice movement, floe interactions and melting. Oceanographic studies focused on the frontal structure and circulation associated with the ice edge. Remote sensing data were used for real-time monitoring of sea ice conditions during the experimental program, contributed to our knowledge of ice character and distribution, and allowed for evaluation of the remote sensing methods used.

MIZEX West took place along the centr

Bering Sea MIZ in the vicinity of and north of St. Matthew Island (Figure 1) on 5-27 February 1983 when the ice was at its maximum extent. Field observations were obtained using two surface vessels, two aircraft and recording current/temperature/conductivity instruments which were deployed on moorings in the study area through the winter. These field data were supplemented by satellite imagery which provided data on larger-scale sea ice characteristics, distribution and motion. Both vessels, the U.S. Coast Guard Icebreaker WESTWIND and the NOAA Ship DISCOVERER, were equipped with instrumentation for measuring oceanic temperature and salinity and for making meteorological observations. Sea ice observations were made visually from these vessels and through in situ sampling of the floes by personnel deployed on the ice. Ice drift was measured using satellite-tracked (Argos) and radar-tracked buoys which were deployed on the ice from the vessels or from helicopters based on the icebreaker.

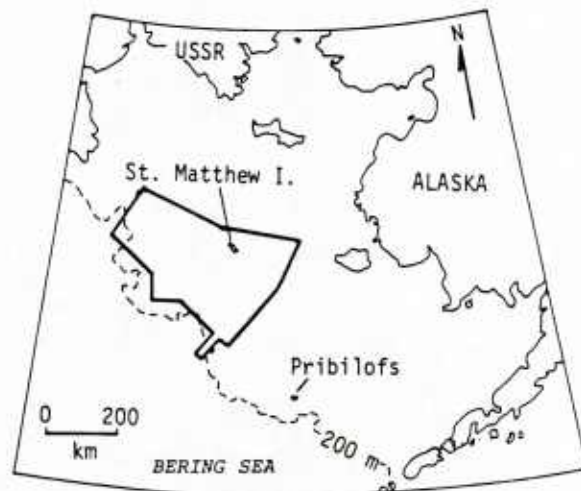


Figure 1. Geographical location of the MIZEX West study region (closed polygon).

The aircraft were equipped to measure meteorological and sea ice parameters. Specifically, the NOAA WP-3D Research Aircraft measured atmospheric turbulence and used a side-looking air radar (SLAR), laser profilometer and cameras to

observe ice distribution and properties. The NASA CV-990 Airborne Laboratory used passive microwave radiometers, an infrared radiometer, two cartographic cameras and a version of the radar altimeter planned for the ERS satellite to observe the ice.

Visible and infrared AVHRR data from the NOAA satellites were used to determine ice distribution and to estimate ice types during the experiment when no clouds were present. These data were used to track individual ice floes during cloud-free periods, hence, to provide information on regional ice motion. Passive microwave data from the scanning multichannel microwave radiometer (SMMR) on the Nimbus 7 satellite were used to determine ice distribution and type during both cloud-free and cloudy periods.

1.2 The Study Region

The Bering Sea ice cover varies seasonally from none between late June and November to more than 80% of the shelf at the time of maximum coverage which typically occurs in February-March. The ice is almost entirely first-year with thicknesses of 0.5-2.0 m (3, 4). Most of this ice is formed along leeward (south-facing) coasts on the northern shelf, is wind-driven toward the south by the prevailing north-northeasterly winter winds, then melts along the ice edge (4, 5). The pattern of southward motion is interrupted at frequent intervals by cyclones which propagate through the region (6).

Water circulation on the Bering shelf is dominated by a mean northward volume transport

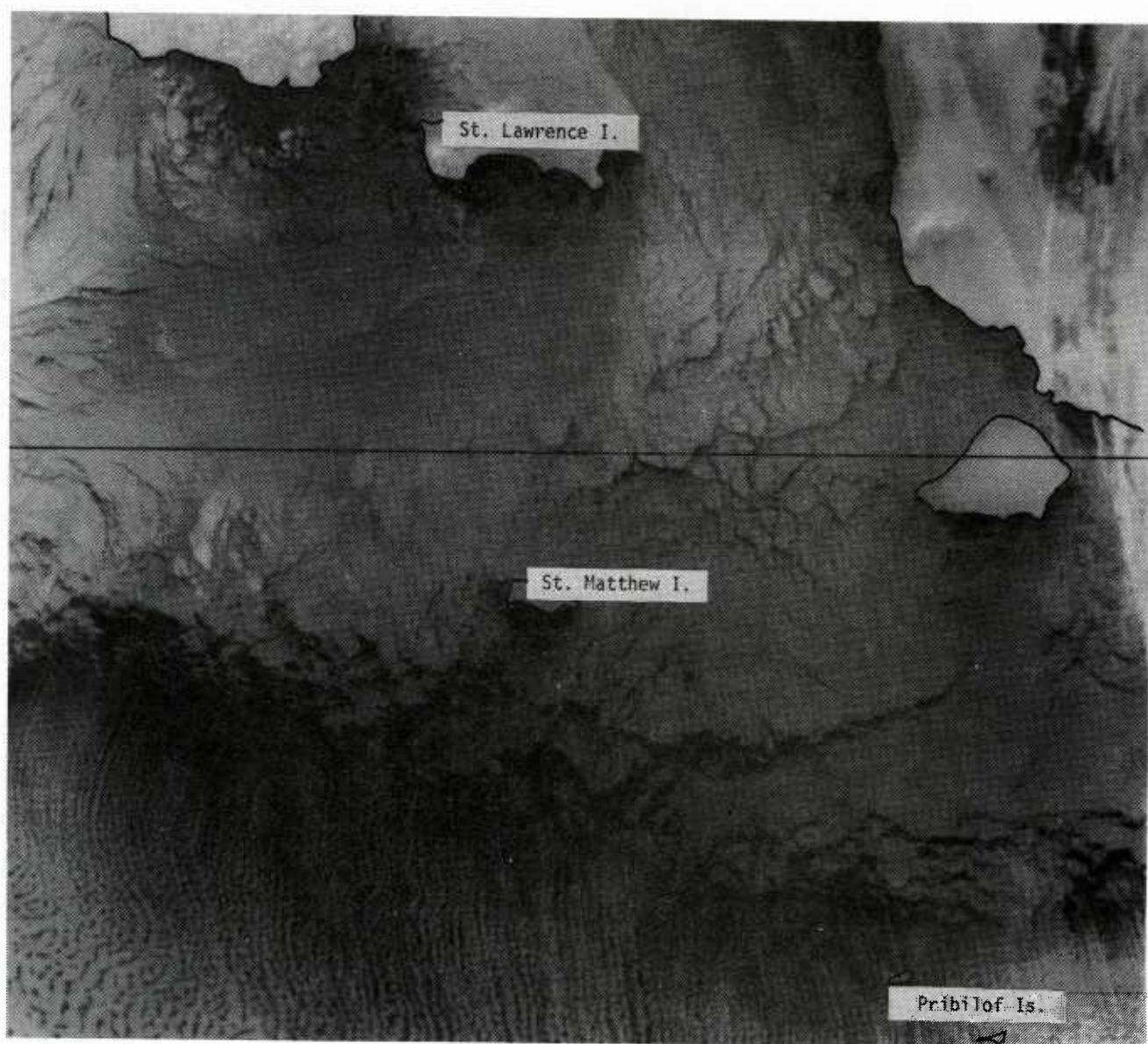


Figure 2. Example of IR imagery obtained on 10 February 1983 from the NOAA satellite AVHRR.

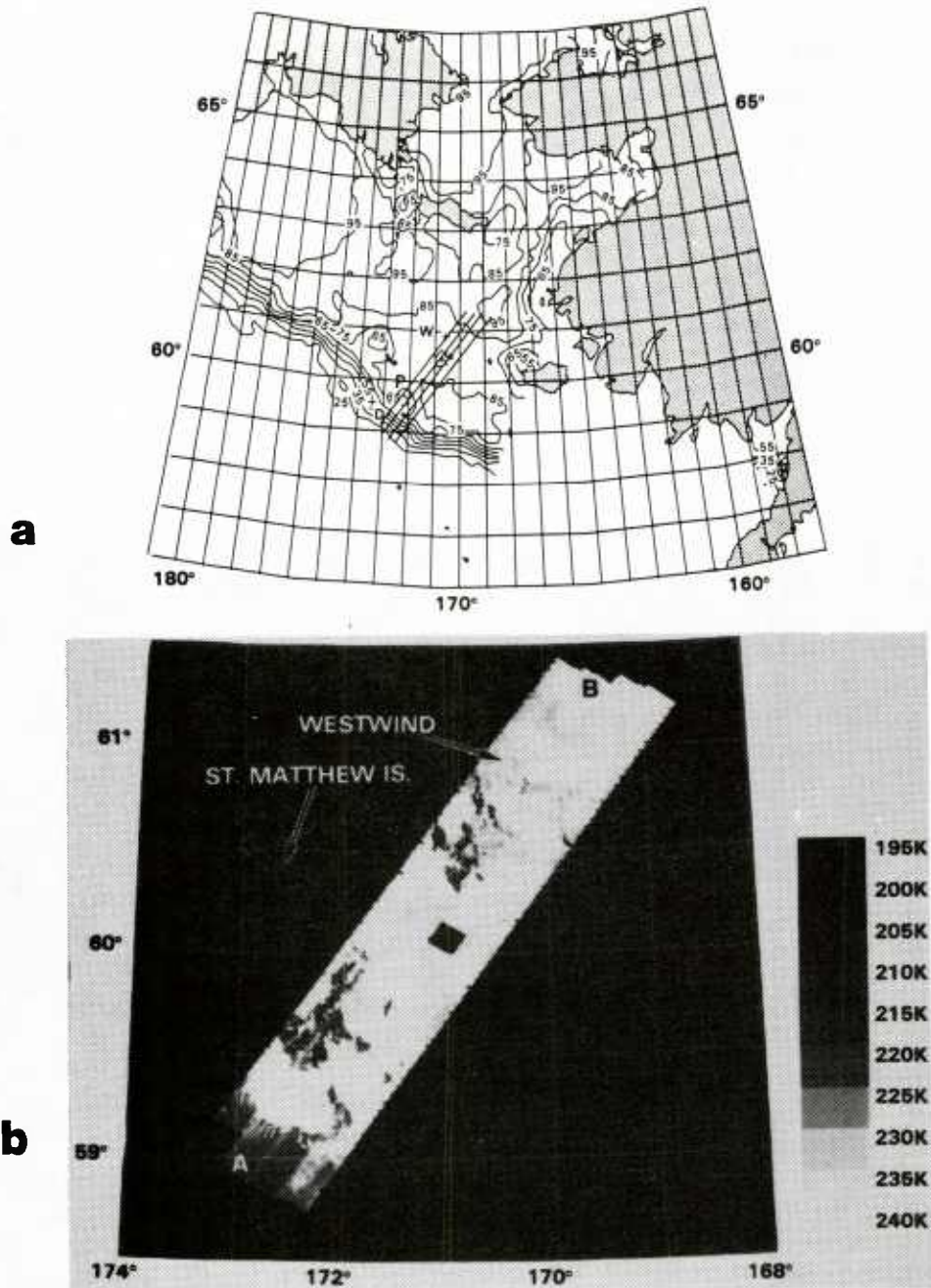


Figure 3. Ice concentration contours for 10 February 1983 derived from the Nimbus 7 SMMR (a) and mosaic constructed using data acquired by the NASA CV-990 Airborne Laboratory (b). Straight lines (middle of 3a) indicate locations of flight tracks used in constructing 3b.

through the Bering Strait to the Arctic Ocean. This flow is driven by regional sealevel differences and persists through the year (7, 8, 9). In winter, the central Bering shelf is dominated by a temperature-salinity front which coincides approximately with the ice edge and has an associated northwestward current (10). The ice edge location is maintained through the mid-winter

period of maximum ice extent by a balance between southward advection of ice toward the edge by the prevailing north-northeast winds and melting at the edge. The heat needed to melt ice at the edge is provided almost entirely by the regional northward transport of relatively warm water from the oceanic regions farther to the south (10).

1.3 The Bering Sea As A Natural Sea Ice Laboratory

The Bering Sea ice cover can be characterized as a "conveyor-belt" with ice forming in the north, being advected toward the south and melting along the edge. During the advective phase, the ice is subjected to compressive forces leading to ridging and rafting. Thickening also occurs during this advective phase due to freezing from below. As the ice nears the edge, the larger floes are fractured by swell which propagates beneath the ice from the stormy ice-free ocean areas to the south. The individual floes become progressively smaller nearer the edge, as wave action becomes more energetic. At the edge, the highly fractured floes become divergent under the influence of winds and currents and move rapidly into warmer water seaward of the edge where they melt.

The ice moves southward quite rapidly (speeds exceeding 0.5 m/s were not unusual during the MIZEX West program), consequently, over a 2-3 week period a specified ice floe might make the complete transition from formation in the north through melting at the edge, all the while undergoing deformation and accretion. It is therefore possible, on the Bering shelf, to observe a wide variety of stages of ice development within a relatively short time frame and over distances spanning a few hundred kilometers. The remainder of this paper briefly describes some of the remote and *in situ* sea ice observations which were made during the MIZEX West program and discusses these within a remote sensing context.

2. RESULTS

2.1 Satellite and Aircraft Data

The MIZEX West remote sensing program was designed to provide coordinated observations from surface-based, airborne and space-borne sensors for the purpose of providing for the first time a comprehensive study of the Bering Sea ice cover. The aircraft data provided a degree of detail impossible to duplicate with the satellite data and yielded areal coverage far greater than could be obtained from the surface vessels. The satellite sensors however were able to provide nearly instantaneous data over a much larger region. For instance, the NOAA AVHRR covers the entire Bering Sea shelf in a single overpass (see for example Figure 2), and the Nimbus 7 SMMR covers almost the entire region on a single pass, but more importantly provides ice concentration information even under cloudy conditions. Figure 3a, for example, shows ice concentration contours derived from the SMMR using a single pass over the Bering Sea on February 10, a day with heavy cloud cover resulting from a storm in the southern Bering Sea. The position of the WESTWIND is indicated, as is the location of a large polynya within the MIZ. The four parallel lines crossing the ice edge indicate the NASA aircraft flight tracks during the time of the SMMR overpass. Figure 3b shows a mosaic image made with the 92 GHz imaging radiometer on the NASA CV-990 for the flight tracks shown in Figure 3a. In addition to detailed information on the structure of the MIZ, the mosaic also confirms the

existence of the polynya labelled "P" on the SMMR ice contour plot (Figure 3a). Finally, satellite data have been available since the early 1970's, hence, there is a historical base of internally compatible data for construction of time series and detection of interannual trends. For these reasons, this paper focuses upon the use of satellite data within the context of sea ice studies.

2.2 AVHRR Imagery

Both visible and infrared (IR) AVHRR imagery from the NOAA satellites were used to determine ice distribution and motion in the MIZEX West study region during the experiment. An example of this imagery is provided in Figure 2. Because daylight hours were short, the IR data were of more use than the visible, particularly since the thermal signature separating sea ice from open water is clearly evident on the IR imagery. The approximately 1 km resolution of the imagery was adequate to accurately determine the ice edge location and to pinpoint areas of ice divergence (signified by a preponderance of open leads). The satellite imagery indicated, for example, a region of low ice concentration south-southwest of St. Matthew Island. This feature, which was a reflection of southwesterly advection of ice past the island, was corroborated by *in situ* observation and was of significant operational use to the vessel which was operating along the ice edge. The AVHRR data were used, when weather conditions permitted, in conjunction with aircraft, shipboard and satellite SMMR (see below) observations, during the experiment to prepare charts showing the ice distribution. These charts were somewhat more detailed than those routinely provided by the Navy-NOAA Joint Ice Center.

The 1 km resolution of the AVHRR data allowed identification, from day-to-day during clear weather periods, of individual ice floes. These could then be tracked over a period of time to provide individual floe trajectories. An example of a plot of such trajectories is shown in Figure 4; these compare favorably with those of the Argos buoys which were deployed on individual ice floes (1). The trajectories plotted using individual floes identified with satellite data are in general of shorter duration than those obtainable with buoys, because clouds truncate the satellite-derived time series. The satellite data allow, however, construction of a field of ice motion for the entire shelf. This information is invaluable when used within the context of, for example, a numerical model of ice motion.

2.3 Scanning Multichannel Microwave Radiometer (SMMR) Data

Passive microwave instruments have the ability to provide useful sea ice observations both through darkness and cloud cover. The utility of microwave sensors derives from the contrast in thermal microwave emission between areas of ice-free ocean and ice-covered waters. Further, the microwave brightness temperature maps do not have to be subjectively analyzed, but lend themselves to objective computer analysis. Lastly,

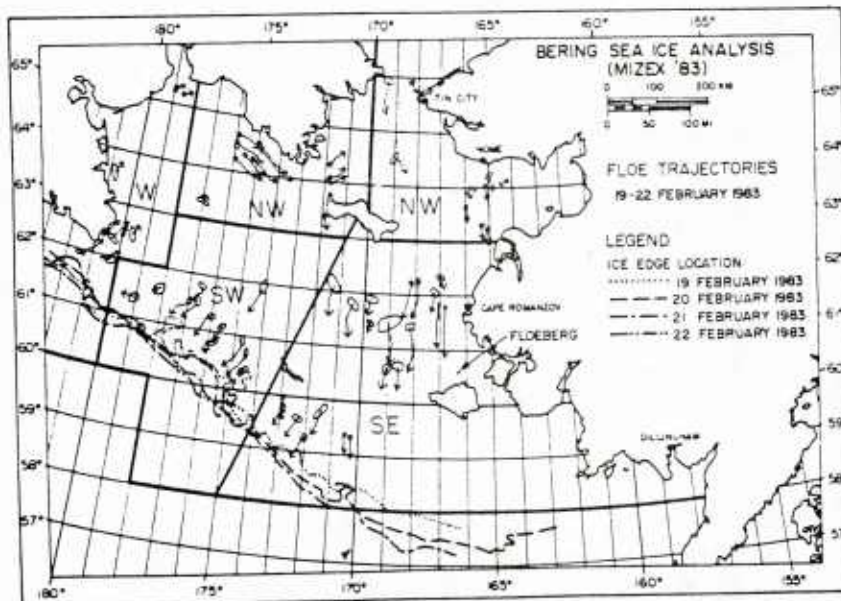


Figure 4. Ice floe trajectories for 19-22 February 1983 derived from the NOAA satellite AVHRR imagery (courtesy of C.H. Pease, PMEL/NOAA).

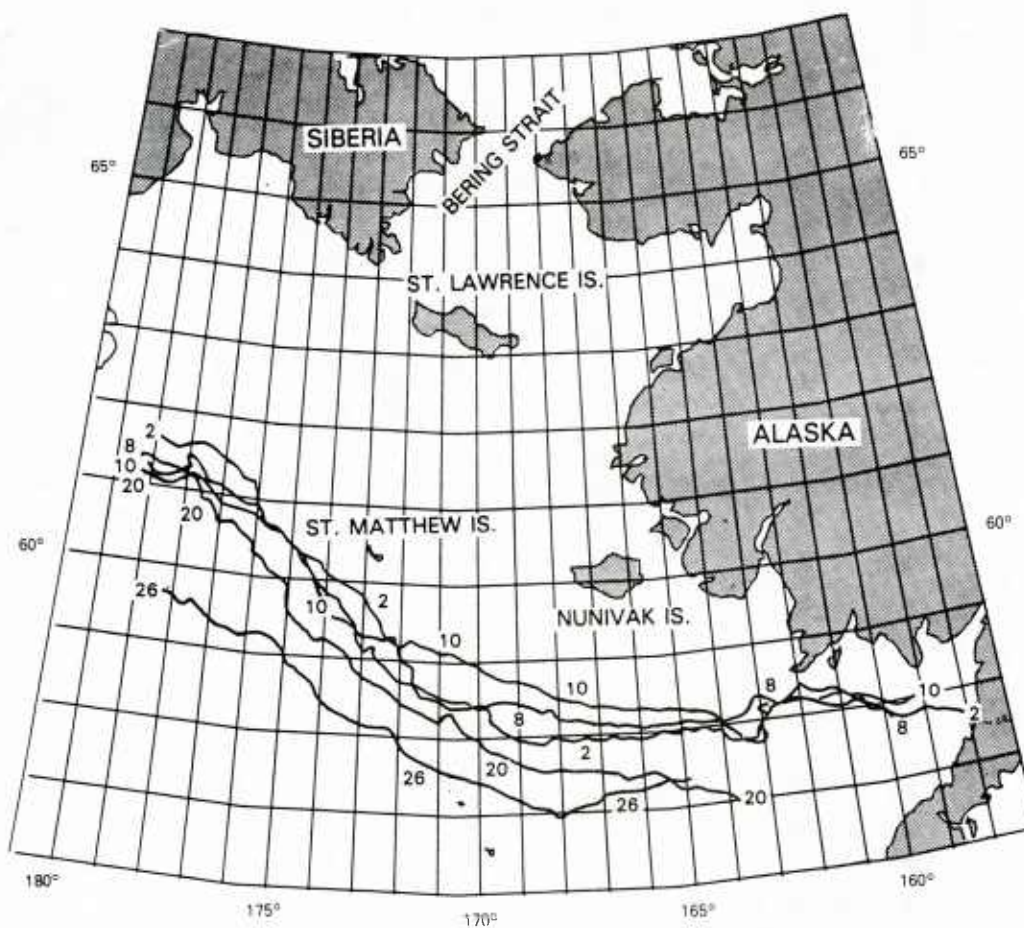


Figure 5. Sequential ice edge locations, indicated by date during February 1983, derived using Nimbus SMMR data.

although the satellite passive microwave sensors are currently limited to a spatial resolution of about 30 km, they do provide an integrated measure of ice concentration or open water amount without having to resolve small floes or polynyas. For these reasons, they are in many ways more useful than the AVHRR data which are limited by cloud cover, available daylight for the visible bands, and require visual interpretation. Conversely, their poor resolution when compared to the AVHRR data limit their use to identifying larger-scale features.

Data from the scanning multichannel microwave radiometer (SMMR) aboard the Nimbus 7 satellite were used in conjunction with AVHRR and in situ data to determine ice distribution during MIZEX West. The SMMR data were invaluable, in particular, for filling in data gaps when cloud cover was present. For example, Figure 5 shows the ice-edge position for selected days during the experiment period regardless of weather conditions.

Although current SMMR algorithms locate correctly the ice edge and the regions of low ice concentration associated with lee-shore polynyas in the Bering Sea (11), a significant fraction of the concentration gradients within the interior pack results from spatial variations of thin ice types. This problem is particularly serious in the Bering Sea MIZ which is characterized by rapid ice growth creating large areas of new and young ice. Figure 6 shows, for example, ice concentration contours derived from SMMR observations as well as the distribution of the dominant ice types based on visual observations made from the NASA aircraft. A comparison of the computed SMMR ice concentrations with the visual observations of ice type shows that there is an association between ice type and ice concentration. For example, areas of 85% or greater ice concentration are associated with first-year thin or medium ice cover; 65%-85% concentrations are associated with young ice; and concentrations of less than 55% reflect new ice. Part of this association, of course, is real, but

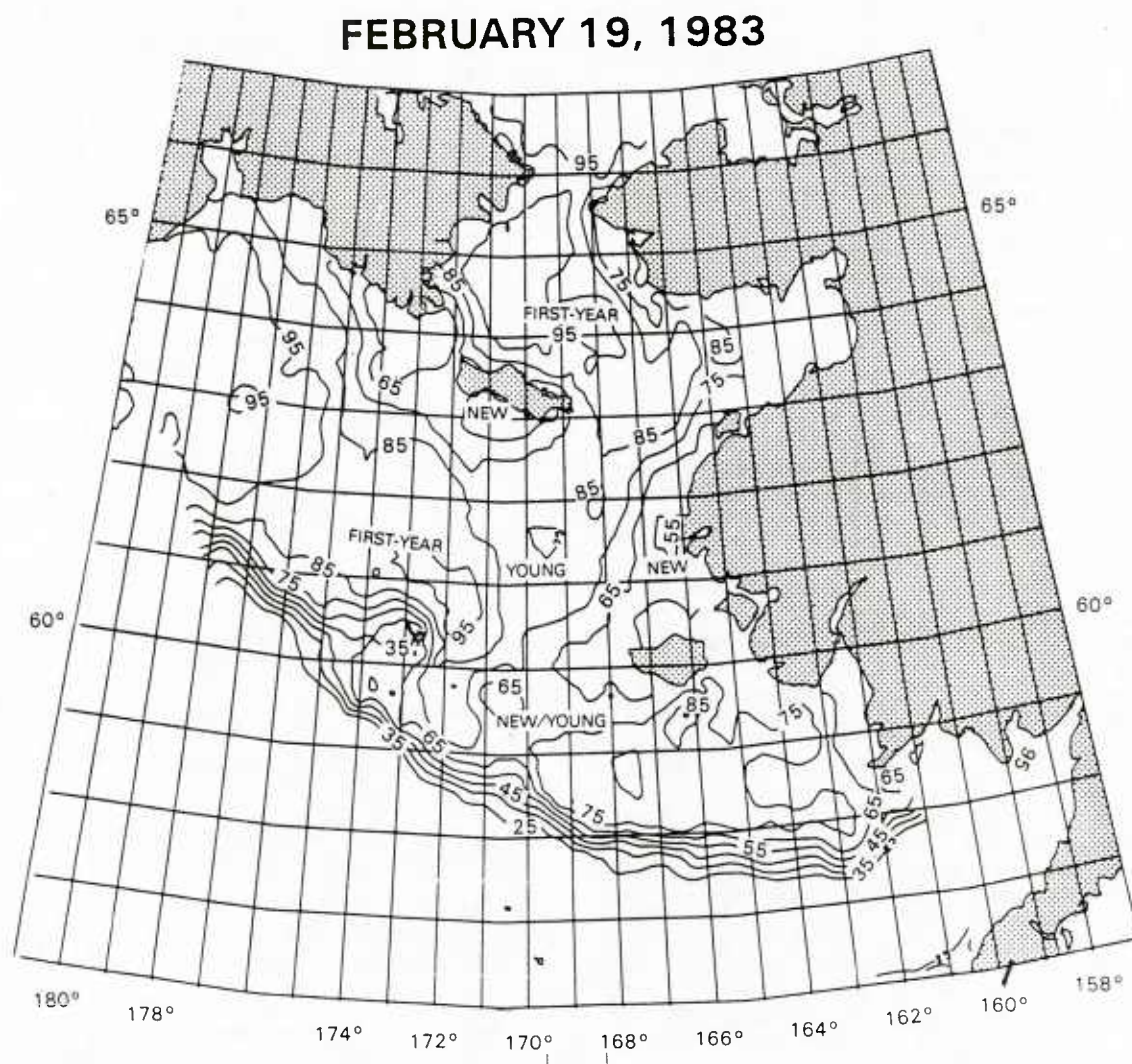


Figure 6. Chart derived from Nimbus 7 SMMR data and showing ice concentration and type.

a significant portion is in error as indicated by the visual ice concentration estimates made from the aircraft. This bias toward low ice concentration results from the use of horizontally-polarized SMMR radiances in computing ice concentrations in areas of young and new ice and has been noted previously (11). In sharp contrast, SMMR ice concentrations in regions of medium and thick first-year ice agree to within 5% of ice concentration observations from the USCG WESTWIND (12).

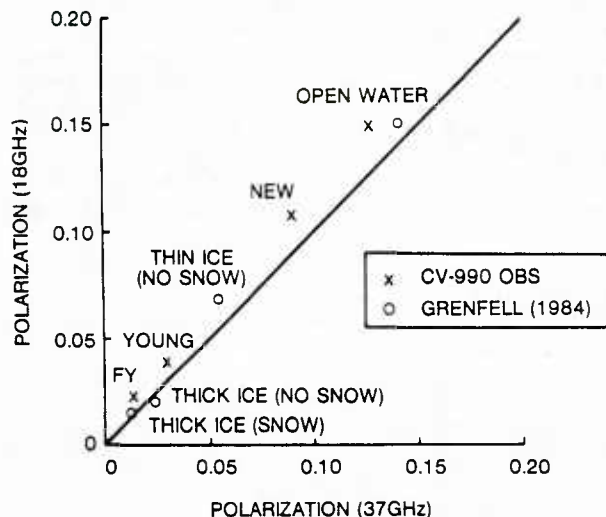


Figure 7. Graph illustrating the relationship between polarization at two frequencies and ice type (see text for details).

A key result from the analysis of the coincident NASA aircraft, Nimbus 7 SMMR, and surface-based data set was that the sensitivity of the horizontally-polarized microwave radiances to the variation of ice type may be used to discriminate among new, young, and first-year sea ice. Figure 7 illustrates the variation between the polarization (defined by $(TBV-TBH)/(TBV+TBH)$) at both 18 and 37 GHz with ice type and open water based on the NASA CV-990 aircraft radiometric data. Data obtained from surface radiometric measurements are also shown for comparison (13). The first-year ice sample corresponds to snow-covered thick ice, the young ice sample to snow-free grey ice, and new ice to areas of frazil and grease ice in the polynya south of St. Matthew Island. The agreement between the CV-990 and surface measurements for both the open ocean and thick ice samples demonstrates some consistency in the absolute calibration of the radiometers and more importantly confirms the observation that the radiometric properties of the ice types were spatially homogeneous (13). This latter result is particularly encouraging for the development of algorithms for mapping the distribution of thin ice from passive microwave satellite data.

3. CONCLUSIONS

The MIZEX West program obtained a large coordinated set of remote sensed sea ice data, and also acquired valuable *in situ* sea ice data for comparison with the remote data. Results of comparisons between these two data sets indicate that:

- o AVHRR satellite data are useful for determining sea ice concentration and floe trajectories during periods of cloud-free weather.
- o Satellite SMMR data correctly locate ice-edge positions and regions of low ice concentration associated with lee-shore polynyas even under adverse weather conditions.
- o Dual-polarized SMMR radiances can be used to differentiate among new, young and first-year ice types and to correct ice concentration biases in regions of thin ice cover.
- o A combination of high resolution AVHRR data and SMMR data having a lower resolution can provide excellent information on the field of ice distribution and motion, as determined through comparison between the *in situ* and remote sensed sea ice data obtained during MIZEX West.

4. ACKNOWLEDGEMENTS

This research has been carried out under contract N00014-82-C-0064 between Science Applications International Corporation (SAIC) and the Office of Naval Research (RDM and GRS). DJC gratefully acknowledges the support of NASA's Oceanic Processes Branch. This is SAIC publication No. 995-50.

5. REFERENCES

1. MIZEX West Study Group, MIZEX West: The Bering Sea Marginal Ice Zone Experiment, EOS 64, 1983, 578-579.
2. Various Authors, The Bering Sea Marginal Ice Zone Experiment, MIZEX Bulletin VI, CRREL, Hanover, NH, 1985, in press.
3. Niebauer, H.J., Sea ice and temperature variability in the eastern Bering Sea and the relation to atmospheric fluctuations, J. Geophys. Res. 85, 1980, 7507-7515.
4. Pease, C.H., Eastern Bering Sea ice processes, Mon. Weather Rev. 108, 1980, 2015-2023.
5. Muench, R.D. and K. Ahlnas, Ice movement and distribution in the Bering Sea from March to June 1974, J. Geophys. Res. 81, 1976, 4467-4476.
6. Overland, J.E. and C.H. Pease, Cyclone climatology of the Bering Sea and its relation to sea ice extent, Mon. Weather Rev. 110, 1982, 5-13.

7. Coachman, L.K., K. Aagaard and R.B. Tripp, Bering Strait: The Regional Physical Oceanography, Univ. of Washington Press, Seattle, WA, 1975, 172 pp.

8. Coachman, L.K. and K. Aagaard, Reevaluation of water transports in the vicinity of Bering Strait, in The Eastern Bering Sea Shelf: Oceanography and Resources, Vol. I, edited by D.W. Hood and J.A. Calder, Univ. of Washington Press, Seattle, WA, 1981, 95-110.

9. Stigebrandt, A., The North Pacific: a global-scale estuary, J. Phys. Oceanogr. 14, 1984, 464-470.

10. Muench, R.D. and J.D. Schumacher, On the Bering Sea Ice Edge Front, J. Geophys. Res. 90, 1985, 3185-3197.

11. Cavalieri, D.J., S. Martin and P. Gloersen, Nimbus 7 SMMR observations of the Bering Sea ice cover during March 1979, J. Geophys. Res. 88, 1983, 2743-2754.

12. Cavalieri, D.J., P. Gloersen, and T.T. Wilheit, Aircraft and satellite passive microwave observations of the Bering Sea ice cover during MIZEX West. Submitted to IEEE Transactions on Geoscience and Remote Sensing, March 1985.

13. Grenfell, T.C., Surfaced-based brightness temperatures of sea ice in the Bering and Greenland seas, IGARSS'84 Symposium Proceedings, 1984.

VARIATIONS IN THE BERING SEA ICE COVERAGE RELATED TO LARGE-SCALE ATMOSPHERIC CIRCULATION PATTERNS

Ronald E. Englebreton

Science Applications International Corporation
205 Montecito Avenue
Monterey, CA 93940

ABSTRACT

It has been shown that significant relationships exist between dominant modes of forcing atmospheric and responding sea ice coverage variability. The tracks of synoptic scale storms are frequently used to depict atmospheric variability. These storm tracks are known to be determined by the larger scale long-wave patterns of the atmosphere.

The 500 mb SL patterns, routinely produced by Fleet Numerical Oceanography Center, Monterey, CA represent the centers of the long-wave circulation pattern at the mid-tropospheric level. A unique data base of 500 mb SL data, generated by SAIC, is used for correlation studies with the monthly and seasonal Bering Sea ice coverage extent. The results of the study suggest potential prediction skill for periods of several months.

INTRODUCTION

A number of studies have been made in the recent years that relate Arctic region sea ice conditions and large-scale atmospheric patterns. Walsh and Johnson (1979) provide a bibliography of authors, through the late 1970's, who have described interannual sea ice fluctuations on the order of hundreds of kilometers in high-latitude seas surrounding the Arctic Ocean. They show year-to-year ice extent fluctuations exceeding 5 degrees latitude on nearly all seas surrounding the Arctic Ocean during the years 1953-1977. However, they found the largest deviations from monthly mean areal extent of sea ice on the Bering shelf along 170°W, as compared with other high-latitude seas. In a later study Walsh and Sater (1981) found significant lag correlations of sea ice fluctuations with atmospheric forcing over antecedent periods of 3-4 months in the Bering Sea, and as much as 9 months in the northern Alaskan waters.

The interannual variability of the Bering Sea ice extent has been shown to be highly correlated with variations of seasonal storm tracks (Overland and Pease, 1982). They concluded that, "On the basis of the high correlation between ice extent and storm track location, that meteorological steering of cyclones determined primarily external to the Bering Sea (Walker and Bliss, 1932; Rogers, 1981), is the primary factor in determining interannual variability of sea ice extent". These studies generally establish the relationship between interannual variations in regional sea ice extent, cyclone storm tracks, and large-scale circulation patterns.

Large scale atmospheric climate oscillations, on a regional or hemispheric spatial scale and a temporal scale of several years, are known to exist. Wallace and Gutzler (1981) describe the Pacific/North American (PNA) pattern and its influences on the hemispheric circulation. Rogers (1984) discusses the North Atlantic Oscillation (NAO) and the Southern Oscillation (SO) and their association with northern hemisphere mean circulations at the surface and 500 mb. The variations in these climatic oscillations influence the interannual changes in the synoptic scale storm tracks.

A general theme is found in the literature on Arctic ice conditions and atmospheric forcing that says in general: Large scale ice variations respond to large scale atmospheric forcing, the large scale ice variations lag the large atmospheric variations, and the cold season atmospheric variations have the strongest persistence, however, the local ice variations in summer reflect small scale local wind and temperature variations.

This paper addresses an approach to explaining the variations in the Bering Sea ice coverage through correlations with the large-scale atmospheric circulation patterns. The development and utilization of a unique data base developed by this author under Science Applications International Corporation (SAIC) Independent Research and Development (IR&D) funding is discussed in the Data section. A following section on Procedures and Results illustrates the methodology developed during the IR&D work and some findings relative to the Bering Sea. A final section, Future Applications addresses the long-range forecasting potential of this approach with emphasis on direct applications to existing Navy arctic ice condition forecasts.

DATA

The approach presented in this paper is designed to correlate the centers-of-action of the large-scale atmospheric circulation pattern with an index of any other environmental parameter, in this case, the extent of annual Bering Sea ice coverage. During the IR&D project addressed earlier a 32 year data base of the "SL" centers of action was developed. The "SL" field is routinely produced at the Fleet Numerical Oceanography Center (FNOC), Monterey, California by a pattern separation program.

The pattern separation program decomposes a two-dimensional scalar field into three additive range of scale components. The 500 mb field is decomposed into components defined as: (1) the planetary vortex (SV); (2) the large-scale disturbances (SL); and, (3) the small-scale disturbances (SD). Mathematically, the three components can be expressed as: $Z(500) = SD(500) + SL(500) + SV(500)$

The pattern separation program has been a part of the FNOC operational procedures since the 1960's. See Holl (1963) for a complete description of the pattern separation procedure.

The SAIC large-scale atmospheric circulation data base contains pertinent information on the SL centers including: type, position, intensity, life duration, and movement. The SAIC format reduces the original daily fields of about 4000 computer words each, to about 40 words. The entire 32 year data set, representing over 11,000 daily analyses, can be interrogated in seconds by computer.

The ice condition data set (Table 1) was taken from Overland and Pease (1982). It represents the average February and March ice extent in the Bering Sea along a vector extending southwestward from the Alaskan coast near 65°N 165°W through the center of the Bering Sea to near 55°N 178°W, as shown in figure 1.

PROCEDURES AND FINDINGS

The intent of this paper is to illustrate that the distribution of 500 mb SL centers over the Arctic region is closely related to the sea ice extent of the Bering Sea. The approach used is extracted from a more generalized procedure developed by SAIC for use in an Applied Statistical and Climatological Ice Model (ASCIM).

For this demonstration, years of "heavy and light ice extent" as described by Overland and Pease (1982) were used to condition the 500 mb SL climatology. The distribution of 500 mb SL high pressure centers was summarized for both Februarys and Marchs of the five heaviest and five lightest ice extent years. The years used were those designated as heavy (1958, 61, 64, 76, and 77) and light (1959, 66, 67, 78, and 79) by Overland and Pease (1982) and as indicated in Table 1. Difference charts between the two extreme summary charts were then produced to aid in illustrating the variations of SL high center distribution during the contrasting ice extent years.

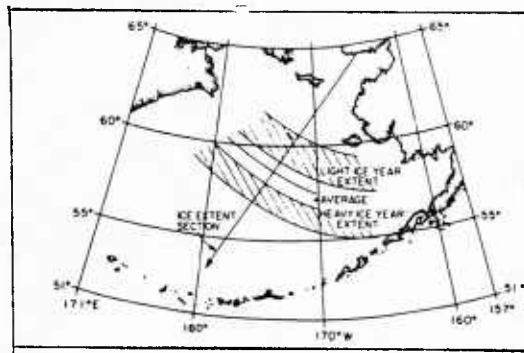


Fig. 1. Section along which maximum ice extents are computed and range of five minimum and maximum ice extents for 1958-80 relative to the section. (from Overland and Pease 1982)

Table 1. Average February and March ice extent in the Bering Sea along the section shown in Fig. 1. (after Overland and Pease, 1982).

Year	February extent (km) ¹	March extent (km) ¹	Confidence in extent (km)	Heavy or light ice
1958	930	660	±100	H
1959	550	670	±100	L
1960	700	800	±100	
1961	960	970	±100	H
1962	760	770	±200	
1963	770	810	±100	
1964	1030	930	±100	H
1965	800	800	±100	
1966	465	540	±100	L
1967	660	430	±100	L
1968	860	720	±100	
1969	670	770	±50	
1970	690	800	±50	
1971	870	870	±50	
1972	780	890	±30	
1973	680	870	±30	
1974	800	790	±30	
1975	770	790	±30	
1976	940	910	±30	H
1977	890	830	±30	H
1978	670	750	±30	L
1979	560	650	±30	L
1980	750	780	±30	

¹February \bar{x} = 763.4, S.D. = 141.9; March \bar{x} = 774.1, S.D. = 126.5 Maximum, either month: \bar{x} = 812.2, S.D. = 114.5.

The results are illustrated in figures 2 through 6. Before addressing the summary and difference charts, figures 2 and 3 are provided for orientation purposes. The vertical and horizontal numbered scale extending from the lower left corner of figure 2 represents the I,J indices of the FNOC 63x63 grid. The north pole is located at 32,32 and is indicated by a circle in each figure. Figure 2 represents the land/sea table of the FNOC 63x63 northern hemisphere numerical grid, grid points located over land are indicated by dots. The north pole is located at the center of figure 2, North America is in the lower center sector,

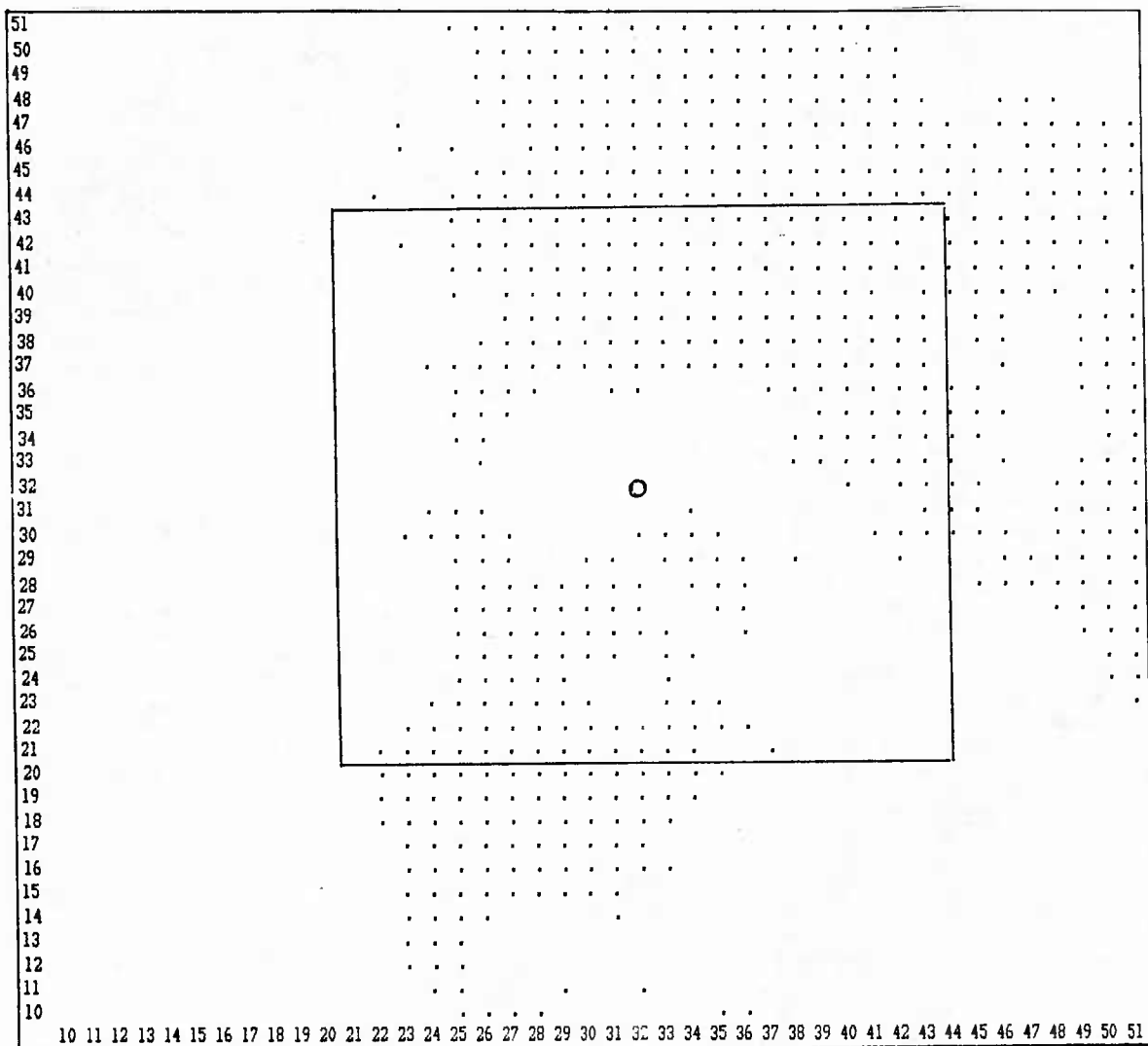


Fig. 2. The portion of the Fleet Numerical Oceanography Center's 63x63 grid used for the Science Applications International Corporation 500 mb SL data base. The data base includes all centers north of 20°N. The North Pole is located at grid point 32,32. The dots represent grid points located over land. The boxed portion defines the area that will be used in illustrated cases of varying 500 mb SL patterns during extreme periods of Bering Sea sea ice extent.

Europe to the right, and the Pacific Ocean to the left. Figure 3 provides a landmass outline on the same projection and scale. Only the area within the boxed region of figures 2 and 3 will be shown in the following illustrative cases.

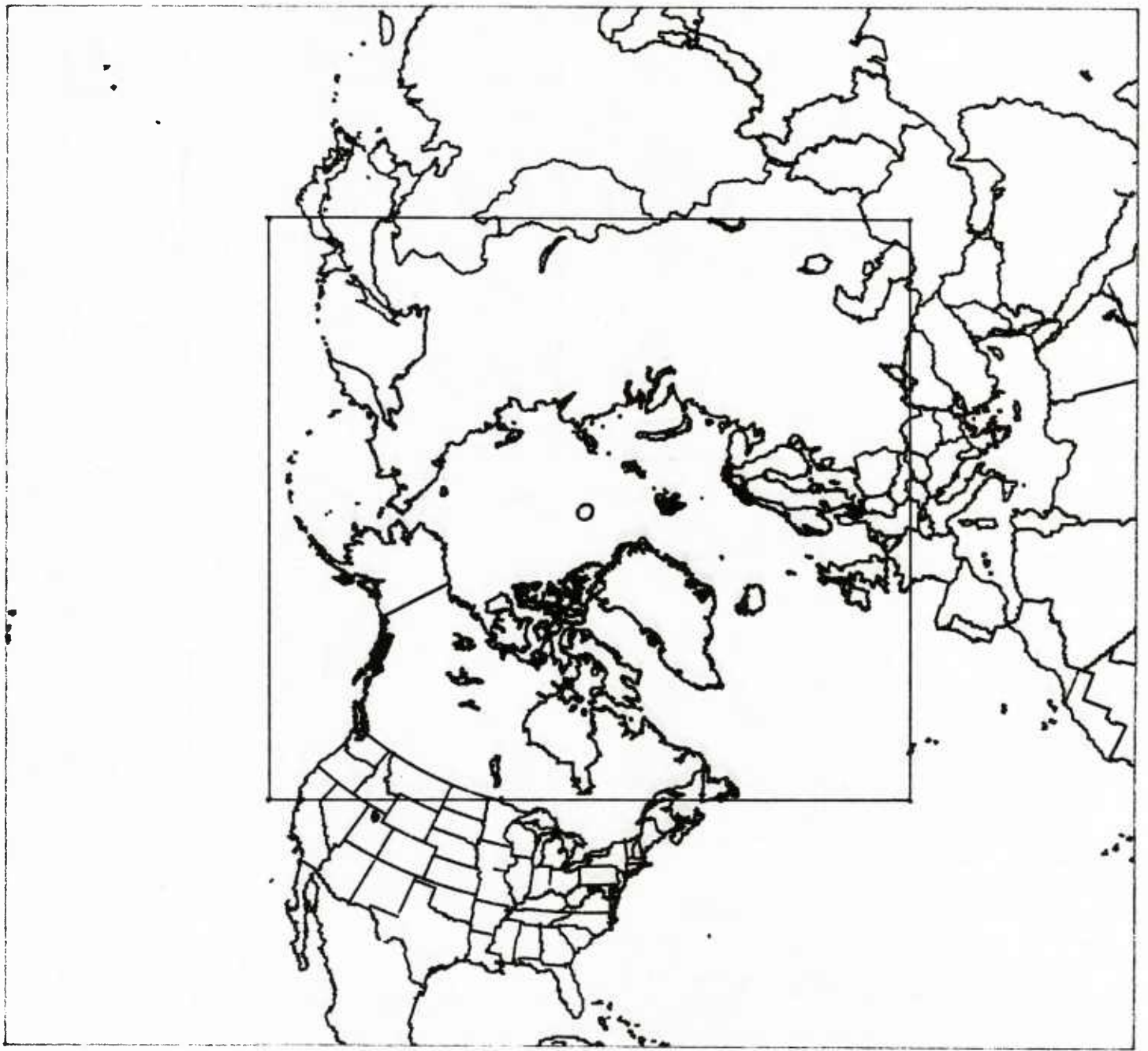


Fig. 3. A land mass outline on the same projection and scale as in figure 2. The inter box defines the area that will be used to illustrate the 500 mb SL pattern variations during periods of extreme Bering Sea sea ice extent.

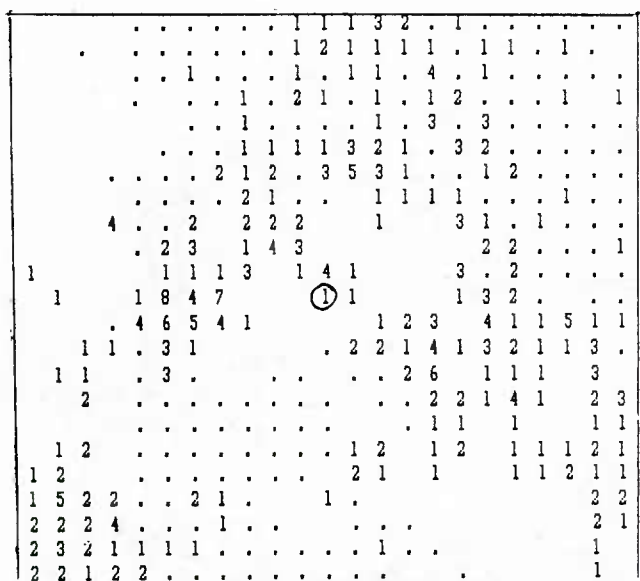


Fig. 4. February Bering Sea heavy ice extent years of 1958, 61, 64, 76, and 77. The numbers represent the total number of 500 mb SL high centers that was located at each grid point during the subject period. The North Pole position is indicated by the circled value/grid points.

The distribution of 500 mb SL high centers, summarized for the five Februarys of heavy and light Bering Sea ice extent years are shown in figures 4 and 5 respectively. During the heavy ice extent period (figure 4) the SL center patterns over the Arctic region show a maximum frequency of high centers extending westward from the Bering Straits towards north central Siberia. In comparison, the center patterns during February of light ice years show the maximum frequency extends southeastward from the central Bering Sea to southeastern Alaska.

Interpreting these two large-scale center distributions relative to steering pattern indicates that during the heavy ice extent periods there is a general northerly mid tropospheric flow over the Bering Sea and a reversal to southerly flow during light ice extent periods. These are the patterns one would expect during the contrasting ice extent conditions. The northerly flow during heavy years, plus the general large scale high pressure region northwest of the Bering Sea, forces the migratory cyclone paths (storm track) to remain south of the Bering Sea area with west to east zonal movement, and pass into the Gulf of Alaska region. During the light ice extent periods the large-scale high pressure over Alaska and to the southeast, with the accompanying southerly flow over the Bering Sea, will block the eastward progression of migratory cyclones and steer them northward through the Bering Sea region. These are the general conditions described by Overland and Pease (1982) as being responsible for the variation in the Bering Sea ice extent.

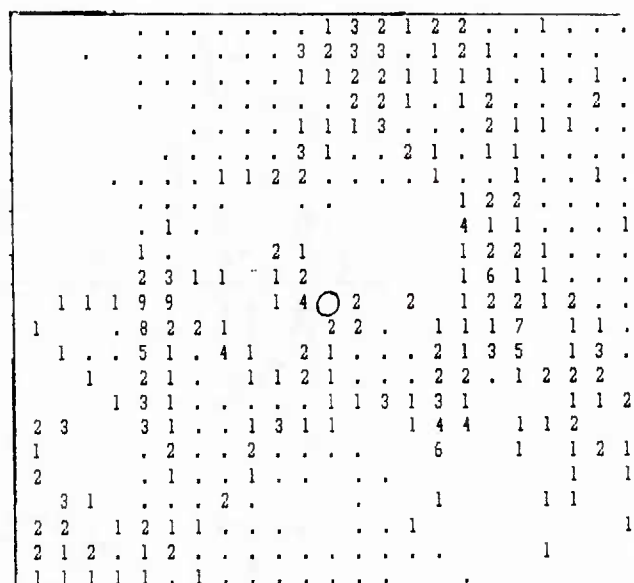


Fig. 5. February Bering Sea light ice extent years of 1959, 66, 67, 78, and 79. Values and labels as in figure 4.

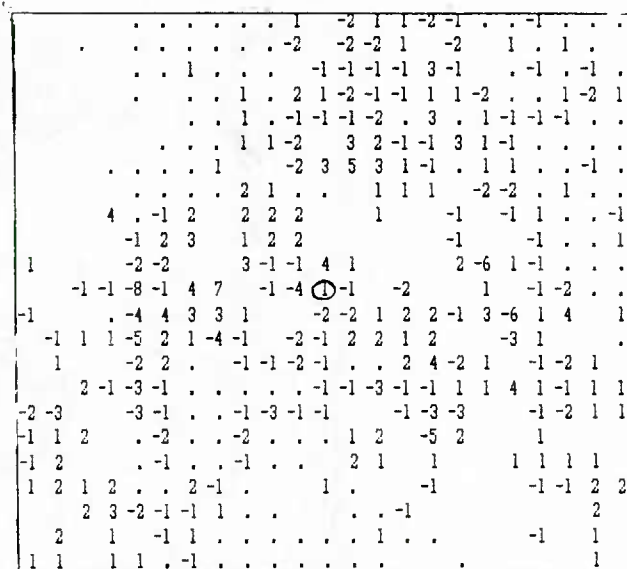


Fig 6. Difference chart of 500 mb SL high centers (centers during heavy years minus centers during light years). The values are the difference between figure 4 minus figure 5. Positive values reflect dominant distributions during Februarys of heavy ice years and negative values represent dominance during Februarys of light ice years.

Figure 6 is a simple difference chart between figure 4 (heavy) and 5 (light) periods. The positive values reflect dominant distribution during heavy years and negative values dominance during light years. The total number of cases involved were nearly equal for the two conditions (1050 heavy and 1071 light) so the differences can be used with some confidence.

Similar summaries for March heavy and light years (not shown) reflect the same general patterns. However, the light year pattern of high centers over the Alaskan area is the more dominant feature. During the heavy years there is a preference for high centers at higher latitudes over the Arctic Ocean. These March patterns could be interpreted as indicating that the normal pattern is for generally heavy ice conditions to exist in March, and significant variations on the low side occur when blocking patterns are dominant over the Alaskan region.

Further illustration of the correlation between the 500 mb SL high center distribution and Bering Sea ice extent is found when shorter time periods, during which large ice extent fluctuations occur, are examined. Figures 7 through 9 show the 500 mb SL high center distribution for half month periods during February and the first half of March for 1973. This corresponds with the largest ice extent growth (190 km) between February and March during the 1958-1980 period (Table 1). During January of 1973 there were no SL high pressure centers over the Bering Sea or that portion of the Arctic Ocean which directly influences the Bering Sea ice extent. This resulted in the February ice extent being relatively light (680 km extent versus an average of 763 km). The 1-15 February distribution (figure 7) shows evidence of SL high center activity dominance over and south of Alaska, a non-growth pattern. Figure 8 displays the 16-28 February 1973 distribution of 500 mb SL high centers. Some indication of a shift of high centers to the north and west is seen. Figure 9 illustrates the 1-15 March 1973 summary of 500 mb SL high centers which corresponds with the period of rapid growth of the Bering Sea ice extent. The centers are now clustered to the northwest of the Bering Sea and would be interpreted as resulting in a northerly flow over the Bering Sea and blockage of cyclonic storms into that area.

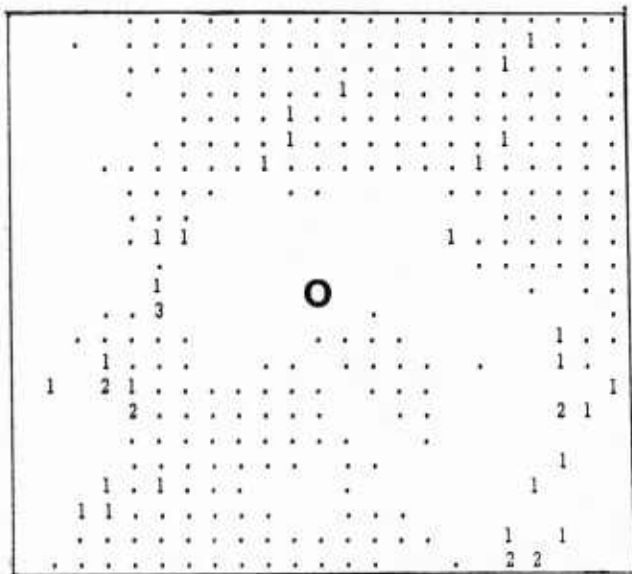


Fig. 7. Distribution of 500 mb SL high centers for 1-15 February 1973. Values and labels as in figure 2.

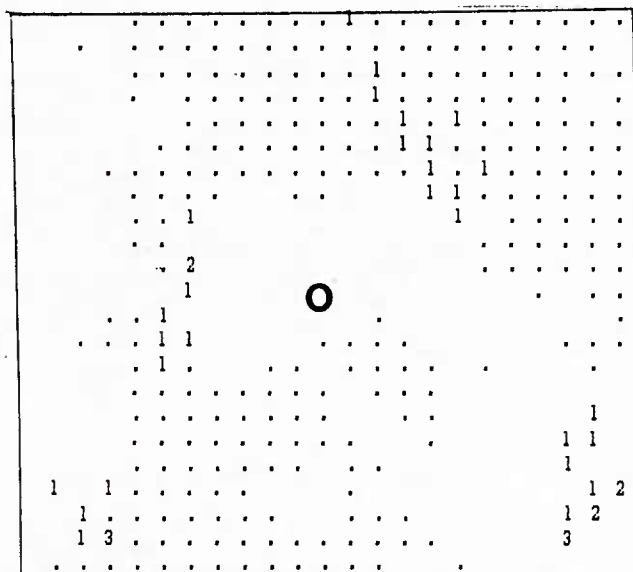


Fig. 8. Distribution of 500 mb SL high centers for 16-28 Feb 1973. Values and labels as in figure 2.

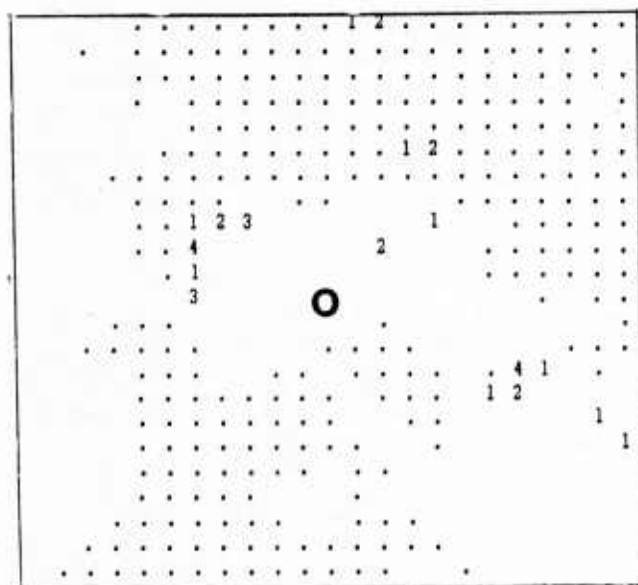


Fig. 9. Distribution of 500 mb SL high centers for 1-15 March 1973. Values and labels as in figure 2.

These examples have been used to illustrate the use of the SL patterns in depicting the large-scale atmospheric steering patterns and the correlation between the SL high center distribution and Bering Sea ice extent. In earlier work with the SAIC 500 mb SL center data base other very interesting characteristics of SL center variations on annual, seasonal, and monthly time scales have been noted. A few of these characteristics, and their predictive potential are addressed in the following section.

FUTURE APPLICATIONS

Establishing the relationship between large-scale atmospheric circulation patterns, as depicted by 500 mb SL centers, and Bering Sea ice extent patterns is of interest from the standpoint of overall understanding of the atmosphere-ocean-ice relationships. It does not in itself provide any predictive procedure. However, because the SL center patterns reflect the atmospheric longwave circulation, which exhibits both large spatial and temporal persistence over periods of 1 to 2 weeks, some promise of forecast potential on similar area and time scales appears to exist. Availability of this type of statistic would be useful in support of the current operational weekly ice condition forecasts.

Prior SAIC investigation found evidence of even longer term forecast potential through analysis of the SL center data base. A tendency has been noted for annual variations of SL center distribution to persist for several months. This agrees with the findings of Walsh and Sater (1981) and others who have noted tendencies for large-scale atmospheric anomalies to persist for months at a time once established. The variations of the SL center distribution include patterns which reflect such general circulation features as strong zonal flow, enhanced meridional flow, blocking patterns, and frequent or infrequent SL center activity in the polar region. The variations tend to become established during the fall/early winter and persist at various degrees until into the following spring/summer period. This persistence has been found to be strongest in the polar and/or tropical regions.

The ASCIM approach utilizes this persistence characteristic of the SL patterns. It has been used to produce probabilistic forecasts for sea ice conditions both within the Arctic Ocean and for several high latitude seas. The interannual variability of the large-scale circulation pattern has been related to such regional fluctuations as the Pacific North American pattern (PNA), the North Atlantic Oscillation (NAO), and North Pacific Ocean SST (Namias, 1982) patterns. On larger scales much recent interest has been paid to the El Nino Southern Oscillation (ENSO) patterns. All of these large-scale forcing patterns have an impact on the general circulation and therefore on the SL pattern signature. Investigation of the SL patterns using climatic records that are conditioned to account for the larger-scale climatic regimes would appear to be a reasonable next step in refinement of the ASCIM or similar models. Additional information gained through such investigations will improve the understanding of the atmosphere-ocean-ice relationships which in turn should result in prediction potential of long-range forecast models.

REFERENCES

1. Holl, M.M., 1963: Scale-and-Pattern Spectra and Decompositions. FNOC Tech. Memo No. 3, Contract N228-(62271)-60550, M.I.I., Monterey, CA.
2. Namias, J., 1982: Case Studies of Long Period Air-Sea Interactions Relating to Long-Range Forecasting. Paper, Study Conference on the Physical Basis for Climate Prediction on Seasonal, Annual and Decadal Time Scale. Leningrad, USSR, 13-17 September 1982. Collected Works of J. Namias 1975 through 1982, Vol III., U of Calif., San Diego, CA
3. Overland, J.E., and Pease, C.H., 1982: Cyclone Climatology of the Bering Sea and Its Relation to Sea Ice Extent. Mon. Wea. Rev., 110, 5-13
4. Rogers, J.C., 1981: The North-Pacific Oscillation. J. Climatol., 1, 39-57.
5. Rogers, J.C., 1984: The Association Between the North Atlantic Oscillation and the Southern Oscillation in the Northern Hemisphere. Mon. Wea. Rev., 112, 1999-2015.
6. Walker, G.T., and E.W. Bliss, 1932: World Weather V. Mem. Roy. Meteor. Soc., 4, 53-84.
7. Wallace, J.M. and D.S. Gutzler, 1981: Teleconnections in the Geopotential Height Field During the Northern Hemisphere Winter. Mon. Wea. Rev., 109, 784-811.
8. Walsh, J.E., and Johnson, C.M., 1979: Interannual Atmospheric Variability and Associated Fluctuations in Arctic Sea Ice Extent. J.G.R., 84, 6915-6928.
9. Walsh, J.E., and J.E. Sater, 1981: Monthly and Seasonal Variability in the Ocean-Ice-Atmosphere Systems of the North Pacific and the North Atlantic. J.G.R., 86, 7425-7445.

A METHOD FOR DETERMINING SEA ICE TYPE AND INFERRED ICE THICKNESS DISTRIBUTIONS FROM AERIAL PHOTOGRAPHS

L. D. Farmer and D. T. Eppler

Naval Ocean Research and Development Activity
Code 332
NSTL, MS 39529-5004

INTRODUCTION

Since 1962 Naval Ocean Research and Development Activity (NORDA), in conjunction with the Naval Oceanographic Office (NAVOCEANO), has accumulated a substantial archive of remotely sensed (airborne) data in Arctic regions. These data show ice conditions in the central Arctic and in waters adjoining the United States, Canada, Greenland, Iceland, and Norway. Most data are in the form of aerial photographs and laser profiles, though limited sequences of infrared, passive microwave, and radar images also are available.

Individual records in the archive have been used for specific projects, but the data set has never been analysed as a whole for the synoptic information it contains. Insofar as these data depict ice conditions over a wide range of geographic regions in most seasons over more than twenty years, information concerning annual variation in ice conditions is present in the NORDA-NAVOCEANO data archive.

Our objective in conducting this study is to reduce aerial photographic data in the archive to a form in which it can be used to study regional and seasonal variation in ice type, thickness, and concentration. In the course of this work we have developed image processor programs that measure the abundance of different surface types in a photograph with minimal human intervention. The end product is an environmental data base of histograms, one for each photographic frame in the archive. Each histogram gives the distribution of ice types and the percentage of open water present at a specific time and place in the Arctic. Extraction of this information provides baseline data that will benefit acoustic, oceanographic, and meteorologic models of the Arctic marine environment.

The following discussion is divided into five sections. First, we present the basis for inferring ice type and thickness from albedo. The ice classification scheme used and a description of surface types measured in the analysis are provided. Second, we describe the aerial photographic archive and discuss the method by which data are screened and selected for inclusion in the data base. Third, we discuss the hardware and software system used to reduce the data and the processing sequence followed for each frame. Fourth, we present the format in which reduced data are stored and describe rudimentary programs developed to access

the data base. Fifth, we discuss briefly possible applications both for the data reduced here and for the NORDA-NAVOCEANO archive as a whole.

SEA ICE THICKNESS CLASSIFICATION

Thickness categories used here are those defined by the World Meteorological Organization (WMO) classification system (WMO, 1970). Each WMO ice category corresponds to a range of ice thicknesses (Fig. 1). Categories are defined primarily by albedo, a parameter measured directly from aerial photographs. Albedo can be used to discriminate between ice in most categories, enabling machine classification of ice type from aerial photographs. A review of the WMO ice classification scheme is presented below and in Figure 1.

OPEN WATER

Ice-free areas (open ocean, polynyas, leads, and interstices between ice flows) constitute open water. Ice thickness here is zero and albedo typically is lower than that of any other Arctic surface. Open water can occur anywhere in the Arctic in any season.

NEW ICE

New ice consists of unconsolidated accumulations of frazil, commonly agglomerated as slush in spongy clumps, streamers, and tadpoles. When light winds push dispersed clumps of frazil into a concentrated mass, a soupy unconsolidated layer of grease ice up to a meter thick may form on the sea surface (Weeks and Ackley, 1982). Water content of most new ice forms typically is greater than 60% by volume (Martin and Kauffman, 1981). This high water content makes dispersed frazil and thin accumulations of grease ice practically indistinguishable from open water in most vertical aerial photographs. Streamers and tadpoles of slush and thick accumulations of grease ice display higher albedo than surrounding water, however, and commonly are identifiable in winter scenes of open water.

NILAS

Nilas is a thin, elastic crust of ice, less than 10 cm thick, that bends under waves and swell. Under compression, nilas rafts, typically

FIGURE 1

Relationship Between Albedo, Ice Type, and Thickness

- A. open water
 - 1. absence of ice
 - 2. thickness = 0 cm
- B. new
 - 1. includes frazil, grease, slush, shugga
 - 2. unconsolidated ice spicules or plates
 - 3. thickness up to several cm
- C. dark nilas
 - 1. thin elastic crust of ice
 - 2. bends on waves and swell
 - 3. rafts in fingers under compression
 - 4. dark in tone
 - 5. 0 to 5 cm thick
- D. light nilas
 - 1. like dark nilas but thicker, more rigid
 - 2. lighter in tone than dark nilas
 - 3. 5 to 10 cm thick
- E. grey
 - 1. less elastic than nilas
 - 2. breaks on swell
 - 3. lighter in tone than nilas
 - 4. usually rafts under compression
 - 5. 10 to 15 cm thick
- F. grey-white
 - 1. thick enough to sustain snow cover
 - 2. almost white to white in tone
 - 3. more likely to ridge than raft
 - 4. 15 to 30 cm thick
- G. first-year
 - 1. ice of not more than one winter's growth
 - 2. white in tone
 - 3. floes commonly angular in shape
 - 4. ridges when present appear fresh
 - 5. inter-ridge areas are smooth
 - 6. 30 cm to 2 m thick
- H. old = 2 to 4 meters
 - 1. survived at least one summer's melt
 - 2. white in tone
 - 3. floes commonly rounded in shape

in fingers, rather than forming ridges. Nilas will not sustain snow-cover, probably due to a combination of surface brine and insufficient thermal insulation against the near melting temperature of underlying sea water. Nilas is divided into two categories, dark nilas and light nilas, based on thickness and albedo. Dark nilas is less than 5 cm thick, is very dark in tone (nearly as dark as open water), and represents the thinnest consolidated type of ice. Light nilas ranges in thickness from 5 cm to 10 cm and is lighter in tone than dark nilas.

YOUNG ICE

Young ice ranges in thickness from 10 cm to 30 cm, is less elastic than nilas, and breaks (rather than bends) under swell and wave action. It may raft or ridge under compression depending on thickness. Young ice is divided into two categories, grey ice and grey-white ice, based on thickness, albedo, and ability to sustain snow cover. Grey ice ranges in thickness from 10 cm to 15 cm, displays higher albedo than nilas, generally will not sustain snow-cover, and typically rafts rather than forming ridges under compression. Grey ice appears grey in aerial photographs. Grey-white ice ranges in thickness from 15 cm to 30 cm, displays higher albedo than grey ice (but slightly lower albedo than first-year ice), and sustains snow-cover. When snow-cover is present, discrimination between grey-white ice and thin first-year ice is difficult if deformational features (rafting, ridges) are absent.

FIRST-YEAR ICE

First-year ice is ice of not more than one winter's growth that ranges in thickness from 30 cm to 2 meters. First-year ice is white in tone and sustains snow-cover. Under compressive stress it forms ridges that commonly appear fresh and sharp. Undeformed ice between ridges is smooth. Drifted snow supplies whatever surficial texture is present.

OLD ICE

Old ice is ice that has survived at least one summer's melt. At the beginning of winter old ice thickness may be thinner than 2 meters due to the effect of summer melt. By winter's end old ice has grown to total thickness that commonly ranges from 2 meters to 4 meters. Under compressive stress old ice forms ridges. Although new ridges appear fresh and blocky, relict ridges that survive from past years are rounded and form hummocks of lower relief. Frozen meltponds that form in summer months commonly are present between ridges and hummocks. Old ice sustains snow-cover and displays high albedo similar to that of first-year ice as a result. Old ice is distinguished from first-year ice primarily by differences in roughness of the ice surface and rounded shapes of floes.

ICEBERGS

Icebergs are massive chunks of fresh-water ice that break (calve) from the terminus of a glacier or ice shelf. They are distinguished from floes of sea ice by their size, large freeboard (typically greater than 5 meters for large icebergs (WMO, 1970)), high relief, and, in some cases, their irregular shape.

NORDA ARCHIVE OF AERIAL PHOTOGRAPHS

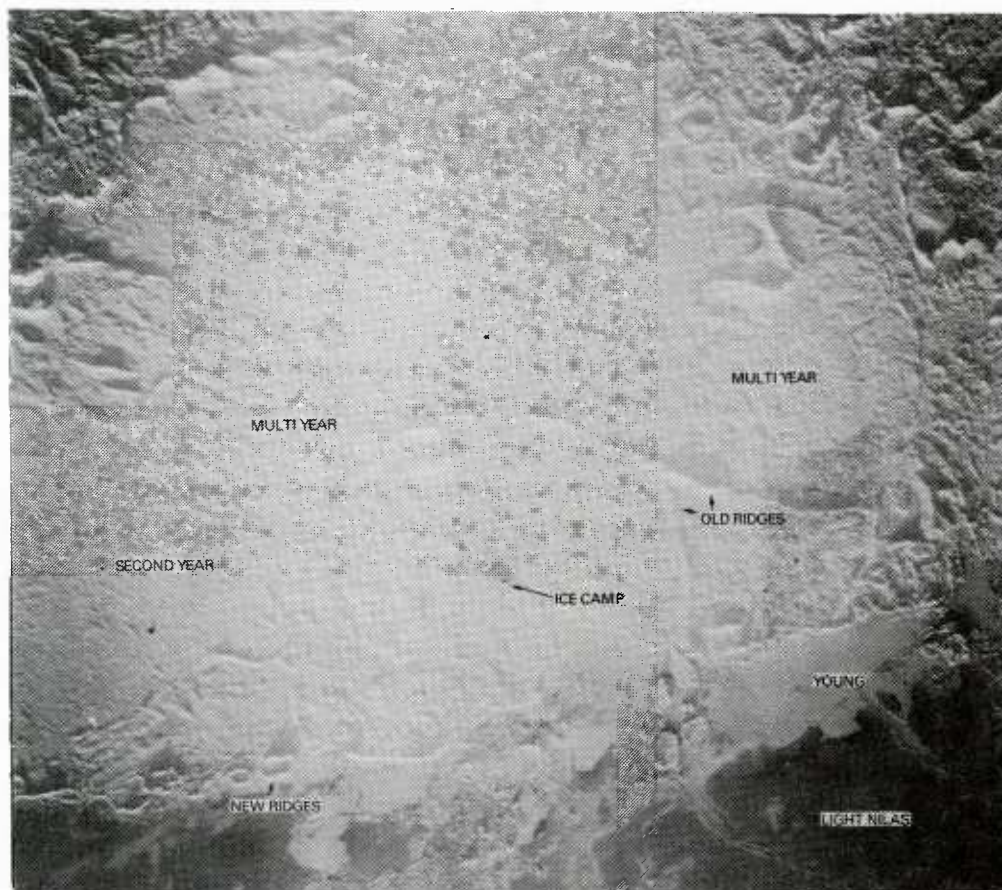
The NORDA Arctic film archive consists of approximately 250 rolls of black and white aerial photographic film. Most images are on 9 inch film and are of quality comparable to Figure 2. Cameras used to obtain the most recent images include the Wild RC-10 and RC-8. Earlier images were made using the Fairchild CA-14, T-11, and KC-1B series, and the CAI (Chicago Aerial Industries) KA-50. The images were collected between 1962 and 1984 in the course of Arctic field experiments and reconnaissance flights, primarily aboard P-3 aircraft. Images made between 1976 and 1984 were acquired by NORDA; those made prior to 1976 were acquired by the Naval Oceanographic Office (NAVOCEANO). A typical example is given in Figure 2.

EXTEND BELOW

Seasonal ice conditions in waters bordering the United States, Canada, Greenland, Iceland, and Norway are documented in the archive. Tracks flown are of two types: mapping and transit. Mapping tracks provide detailed photographic coverage of confined areas. Photographs are taken at altitudes that are typically less than 5000 feet. Overlap between frames is sufficient to provide stereographic coverage in many cases. Almost without exception mapping tracks coincide with field camps that are associated with Arctic experiments such as AIDJEX. Transit tracks provide photographic coverage along flight lines that extend between two widely separated points. Coverage is not always continuous between frames and between different segments along the track. Typical transit tracks extend from Thule to the North Pole, from Barrow to the North Pole, and from the site of Arctic field experiments to landfall.

SCREENING PROCEDURES

The overall usefulness of data in the archive is a function of image quality and the completeness of associated flight logs. Each roll of film in the archive is screened manually and evaluated with respect to image quality and



completeness of navigation logs prior to digital analysis. Although clouds and ground fog, poor lighting, camera malfunctions, and inconsistent film processing degrade some images, image processing programs applied to reduce the archived photographic data are designed to compensate for some of these factors. Data quality is deemed acceptable in all but the most severe examples as a consequence.

Incomplete flight logs present a more significant problem, particularly with older data in the archive. Flight logs represent the most accurate source of information concerning location of an imaged scene. In many cases logs are recorded poorly and in some cases they are missing altogether. Way points that are needed to document image locations along flight tracks often are not recorded with ample regularity. If flight logs are poorly documented, incomplete, or missing altogether, usually it is not possible to reconstruct flight tracks and image locations with precision.

Adequate flight logs exist for most recent data in the archive, but logs are missing for much of the older data. In the absence of logs, acceptable frames are digitized only if reasonable location data can be inferred from alternative sources such as mission reports, associated correspondence, or workers who participated in the experiment for which the data were gathered. In such cases, the general region in which data were acquired sometimes can be inferred but precise ground tracks followed can not be reconstructed.

DATA REDUCTION

The end product of the data reduction effort is a set of histograms, one for each frame analysed. Each histogram gives the abundance of surface types present in a particular scene. Histograms are produced by classifying a random selection of pixels on the basis of their intensity. The classification is static. That is, it takes into account single pixel intensities without regard to the values of adjacent pixels. Textural characteristics of the scene thus are not considered.

The particular category into which a given pixel intensity falls is determined by a series of interval boundaries. Interval boundaries are set after visual inspection of the negative defines the range of values that are characteristic of the set of surface types present in a scene. Interval boundaries can be adjusted from frame to frame to compensate for differences in lighting, exposure or cloud cover, or changes in the assemblage of surfaces present. The accuracy with which a given set of interval boundaries classifies a scene can be checked visually by segmenting the scene into a series of grey tones, each of which corresponds to a given histogram interval. Misclassified pixels show as anomalous patches or isolated specks in areas that otherwise are uniform in tone.

In some scenes two different surfaces of similar albedo, such as first-year ice and multi-year ice, display ranges of pixel intensities that overlap. Discrimination based

on static pixel value is not possible in such instances. Instead, the two surfaces initially are classified into a single combined category. Then, the areal extent of one surface is outlined (blotched) manually on the screen. The percentage of pixels in the scene that are enclosed by the blotch is computed and subtracted from the percentage of pixels in the combined category.

When an acceptable histogram is obtained, associated header information that consist of frame and can number, location data, and camera focal length is updated. The header is appended to the histogram array and both are written to hard disk. Other programs can be used subsequently to correct erroneous entries in the file, add missing location data, plot flight tracks, or manipulate the data as required for further analysis.

IMAGE PROCESSING SOFTWARE

Software used to reduce photographic data to histograms of surface type abundance was written specifically for this project. A detailed description by Eppler and Farmer is in preparation. A discussion of functions performed by the program and philosophical considerations around which the program is written follows.

A program named ALBEDO serves as an interface between the operator and image processing hardware. ALBEDO runs in an interactive mode and gives the operator maximum control and flexibility over image processing operations. Eight basic imaging functions permit the user to perform operations necessary to classify (segment) scenes and to produce histograms of the abundance of Arctic surface types: 1) calibrate the intensity of video input, 2) view live video images, 3) capture (store) images in frame buffers, 4) measure the range of intensities displayed by groups of pixels, 5) set histogram interval boundaries, 6) construct histograms that display abundances of surface types present in an image, 7) set look-up tables (LUTs) to display negative images, positive images, or images segmented by histograms surface types, and 8) determine the percentage of a scene that falls within a designated boundary.

1. Calibrate Video Input Intensity: The problem overcome by calibration is one of saturation of the digitized image. In order to avoid saturation at either end of the digitized grey scale, video input levels must be adjusted such that the full range of video intensities is digitized within the range of 256 digital levels allowed by hardware. Both the range of negative densities by which images are depicted and the film base density vary between rolls of film. Calibration permits the operator to compensate for differences in film characteristics between rolls of film by adjusting the intensity of light reaching the television camera.

Calibration is performed once for each roll of film by measuring changes in the digitized pixel intensity of the film base in response to changes in light intensity. A section of unexposed film between frames is positioned at

the center of the field of view. Light intensity is changed by adjusting the iris diaphragm on the digitizing camera lens. The scene is digitized after each intensity change and pixel values that corresponds to a 9-pixel square of film base at the image center are noted. Light level is set such that film base digitizes just below 255, the maximum value allowed by hardware. Digitized values for other surfaces in the image are allowed by fall between this calibrated film base intensity and 0.

Three assumptions underlie this procedure. First, we assume that no part of the image is more transparent than film base. Film base will digitize with the highest intensity possible for a given roll of film as a consequence. In no case will images of open water, the surface with the lowest albedo, or images of any other surface be less dense than film base. Second, we assume that sensitivity of the vidicon tube is greatest near the center of the field of view. Experience with cameras used in our imaging system confirms this assumption. The digitized value of film base will be greater here than at other points across the field of view. For this reason film base is calibrated at image center. Third, we assume that if film base is set near 255, then digitized intensity of the densest part of the negative will fall above 0. Experience confirms this assumption.

2. View Live Video: Live video is used to position film correctly within the field of view. Only the central portion of each frame is analysed for surface type distribution so frames must be centered in the field of view before digitization.

3. Store Images: Images must be captured in frame buffers before they are processed. When an image is stored, it is converted from an analog video signal to digital pixel intensities. Artifacts in the imaging system that persist from image to image and that are independent of the digitized scene (burn spots on the vidicon, uneven light table intensity) are removed as the image is digitized. An artifact image that consists of mean deviations of pixel intensities from a normalized background of zero is subtracted from each digitized image before it is stored. The artifact image is created by making ten images of the bare light table at maximum illumination and then computing the mean value of each pixel in the image. The mean image is normalized by subtracting the mean value computed for all pixels within the mean image from the mean image.

4. Measure Pixel Intensities: Measurements of pixel intensity are required to set histogram interval boundaries. The intensity of single pixels is obtained by moving a cursor across the screen. Cursor location is displayed on the console in terms of column-row coordinates of the screen along with the pixel value at that point. Summary statistics of pixels enclosed by a box also can be obtained. The cursor is used to mark two corners of a square or rectangle. The range, mean, variance, and standard deviation of pixels enclosed by the box are computed and displayed on the console.

5. Set Histogram Interval Boundaries: Interval boundaries define the classification scheme on the basis of which histograms are computed. Initial boundary values are determined from cursory examination of pixel values that characterize each surface in the scene. Final boundaries are set through an interactive process by which bounds that define each class are adjusted. A given interval is selected and pixels that fall within that class are illuminated brightly on the monitor. Pixels that fall outside the class are displayed in subdued tones of grey. As boundaries are moved up or down via keyboard commands, the collection of pixels that falls within the interval is updated and displayed in real time on the monitor. When acceptable boundaries are achieved, the routine is exited and a histogram is constructed.

6. Construct Histograms: Histograms are constructed from a random sample of pixels in the scene. Approximately 3% of the pixels enclosed in a 250-pixel square box centered in the 512-pixel square field of view are selected randomly. Pixel intensities are compared with interval boundaries established previously and the results displayed on the console. Pixels that fail to fall in any category are counted as unclassified and indicate errors in interval boundary settings. When an acceptable histogram is achieved, header information is updated and the histo-header pair is written to disk.

7. Set Look-Up Tables (LUTs): LUTs control grey scales into which pixel intensities are mapped when the image is displayed. For example, a negative image (such as is obtained by imaging a photographic negative) can be displayed as a positive image by inverting digitized pixel intensities such that 0 (black) is displayed as 255 (white), 1 (very dark grey) is displayed as 254 (very light grey), 2 is displayed as 253, . . . , 254 (very light grey) is displayed as 1 (very dark grey), and 255 (white) is displayed as 0 (black). LUTs also can be set such that scenes are displayed according to the classification scheme defined by histogram boundary intervals. This provides a means of checking interval boundaries and studying the areal extent and spatial relationships of different surface types.

8. Count Pixels Within a Boundary: Areas of interest within an image can be outlined with the cursor via commands entered from the keyboard. The percentage of pixels in the 250-pixel square sample box that are included in the resulting blotch then is computed.

IMAGE PROCESSING HARDWARE

Reduction of images to histograms of surface-type abundance is performed using conventional image processing hardware. Imaging Technology Incorporated's (ITI) IP-512 system of imaging boards are used for image processing operations. Specifically, analog video images are converted to digital images using an RGB-512 board or an AP-512 board, images are stored in FB-512 frame buffers, and images are manipulated using an ALU-512 arithmetic logic unit. Although programs described here are tailored to

characteristics of ITI boards, imaging boards offered by other manufacturers probably can be used if they provide similar image processing functions.

Image processing hardware is controlled by a Cosmos Systems Inc. STARFIELD LYRA/40 computer. The computer, which uses a Motorola 68000 CPU, employs a UNIX Version 7 operating system. Online storage is provided by a 40 megabyte Winchester hard disk. Images are acquired using a JVC KY-2700 television camera mounted over a Richards light table. Virtually any television camera can be used as long as two requirements are met. First, the camera should be equipped with an iris diaphragm so that light intensity reaching the imaging can be controlled. Second, automatic gain control circuits, if they are present, must be disabled.

DATA FORMAT

Data recorded for each frame consist of header values and histogram percentages. An explanation of these data and, where appropriate, the manner in which they are encoded follows. Archived data are available in tabular form as printed output and in digital form on magnetic tape. Formats used for the tape product are discussed following Header and Histogram Discussions.

HEADER DATA

Header data are provided for each frame and give 1) can and frame number, 2) latitude and longitude coordinates at the frame center, 3) a numeric code that signifies the Arctic region in which the frame is located, 4) the date on which the image was made, and 5) aircraft altitude and focal length of the camera lens.

1. Can and Frame Number: Record of identification consists of the combination of can and frame number, which identifies each image in the archive uniquely. Individual images from which histogram data are derived can be retrieved from the film archive as a result.

2. Latitude and Longitude: Latitude and longitude coordinates of image centers as determined from flight logs are given in decimal degrees. Latitude ranges from -90.0° to $+90.0^{\circ}$. Longitude ranges from -180.0° to $+180.0^{\circ}$. Negative latitudes signify southern hemisphere data. Negative longitudes signify western hemisphere data. Entries of 999 indicate missing location data.

Most locations given represent interpolations between way points recorded in flight logs. In making interpolations we make assumptions concerning the flight path followed, and the interval at which successive frames are made. First, we assume that flight paths travelled between adjacent way points are straight lines. Where transit flights are concerned, experience suggests strongly that this is true. Continuity of photography is checked during the screening process. Navigators commonly record way points only when course changes are made during transit tracks.

Second, we assume that the distance between successive frame centers is constant over the interval between way points. In most cases inspection of the film provides evidence that this assumption is correct. Overlap between successive images verifies that the ground distance between successive frames is constant. Where the interval is such that overlap does not occur, the camera clock, which is imaged in each frame, provides a means of verifying the interval.

3. Arctic Region: Figure 3 is a map that shows numeric region codes and the Arctic seas to which they correspond. Boundaries between regions are somewhat arbitrary and are based partly on geography, partly on convenience, and partly on preconceived notions of regions within ice characteristics are similar. This crude regional classification is intended to be used both as a rapid means of determining the general location of a particular frame or roll of film and as a means of specifying the general location of images that lack latitude-longitude coordinates.

4. Date: The date on which images were acquired is given by month, day, and year (mddy). For example 030577 is March 5, 1977. Leading zeroes commonly are truncated on printed output. In such case the above data appears as 30577.

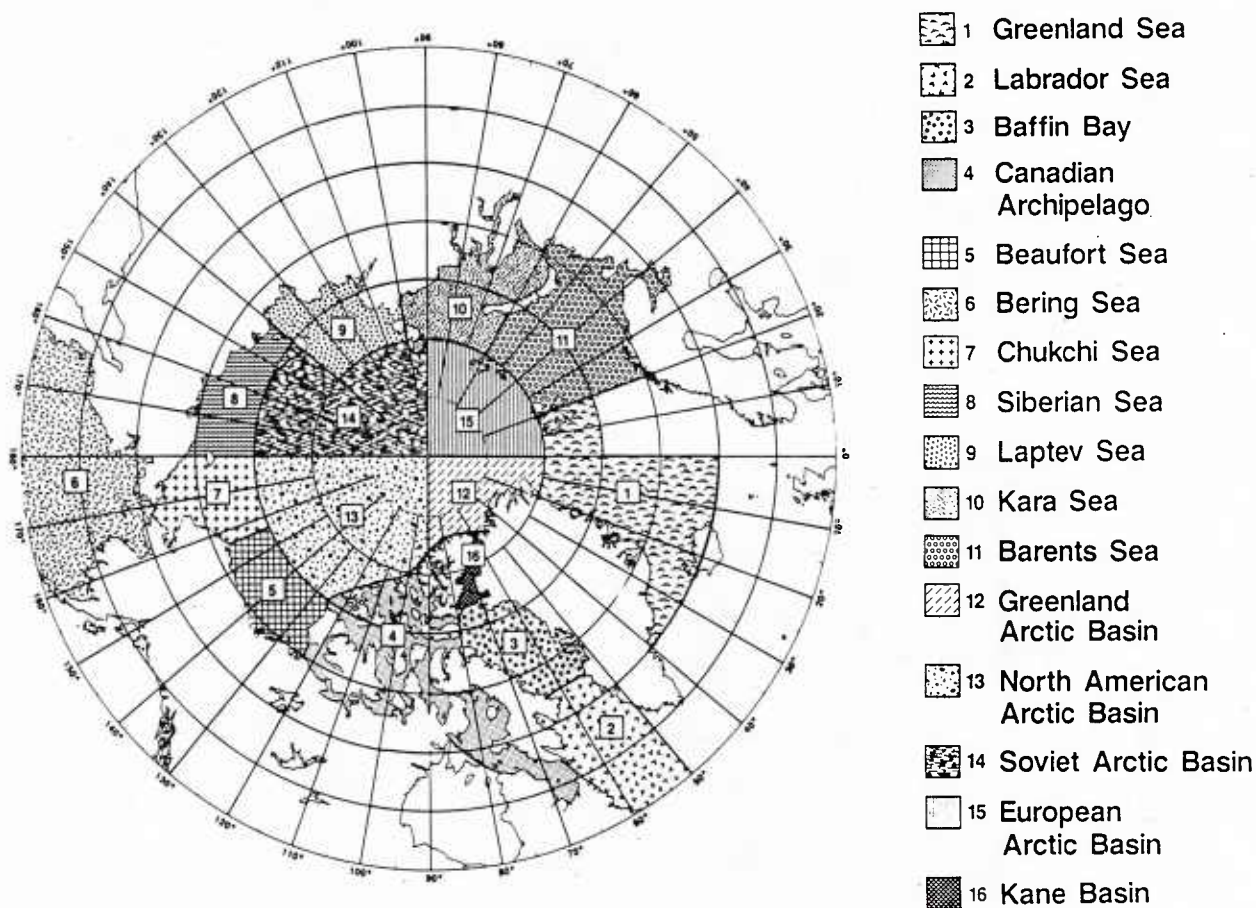
HISTOGRAM DATA

Percentages of the abundance of each of 13 surface types in a given scene are recorded for each histogram. Figure 4 is an example of the reduced data. The location of digitized photography is shown as figure 4a with a plot of the distributions of ice types along the track are illustrated in figure 4b. Categories as defined by the WMO classification scheme for open water, new ice, dark nilas, light nilas, nilas (undifferentiated), grey ice, grey-white ice, first-year ice, old ice, ridges, melt ponds, ice bergs, and land are used. Explanation of the derivation and use of data in some categories is in order.

Nilas (undifferentiated) includes both dark and light nilas. Percentages for nilas (undifferentiated) are set to 0.0 unless discrimination between dark nilas and light nilas is not possible by programs discussed above. Therefore, listings of 0.0% nilas (undifferentiated) does not necessarily mean that nilas is not present in the scene. Dark nilas, light nilas, and nilas (undifferentiated) must all be checked to determine total percent nilas in a given scene. Percentages for nilas (undifferentiated) can be computed, if required, by adding percentages given for dark nilas and light nilas.

Ridges includes estimates of the areal extent of ice in ridges in the scene. Ridges can not always be classified completely, however, using software described above. Several points must be considered as a consequence if ridge data are used. First, 0.0% ridges does not necessarily mean that there are no ridges in the

FIGURE 3



scene. More often than not 0.0% ridges indicates that ridges could not be classified as a group separate from ice in which they are observed. Second, ridge percentages, when given, are conservative estimates of the actual percentage of ridged ice in a scene. Actual percentages of ridged ice present probably exceed percentages given in all cases. Third, ridge data, if not needed, should be combined with percentages of the most abundant thick ice (first-year ice or old ice) in the scene to give more accurate measures of ice abundance.

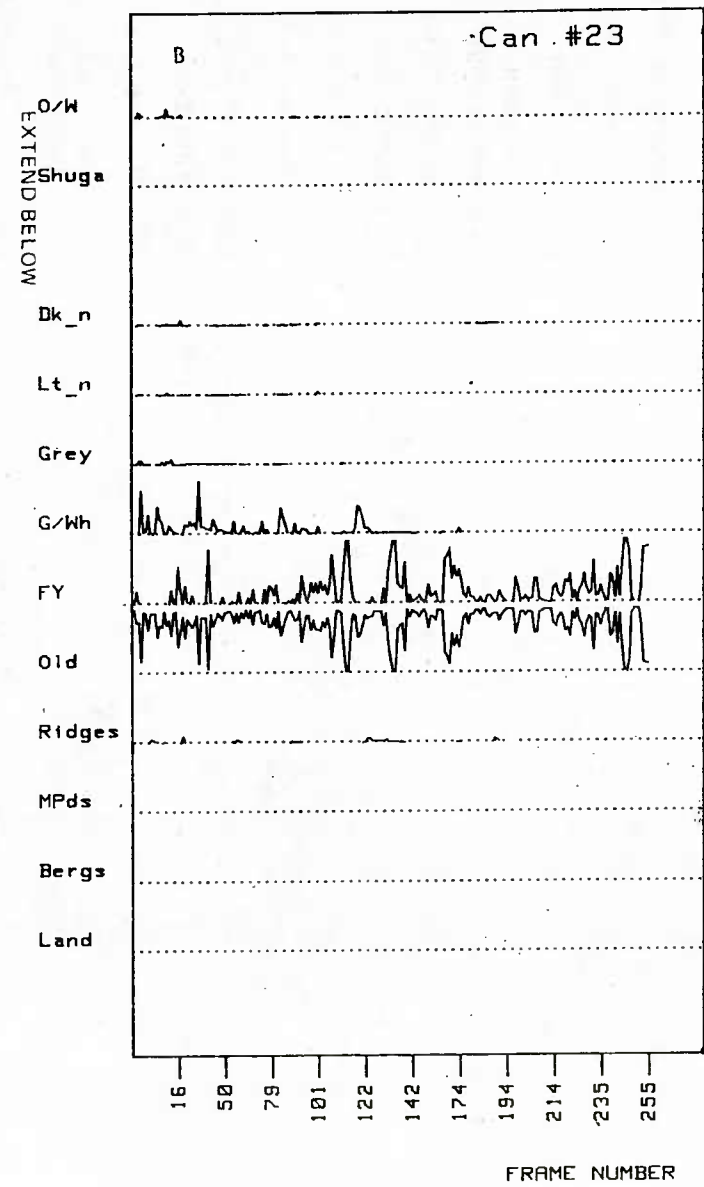
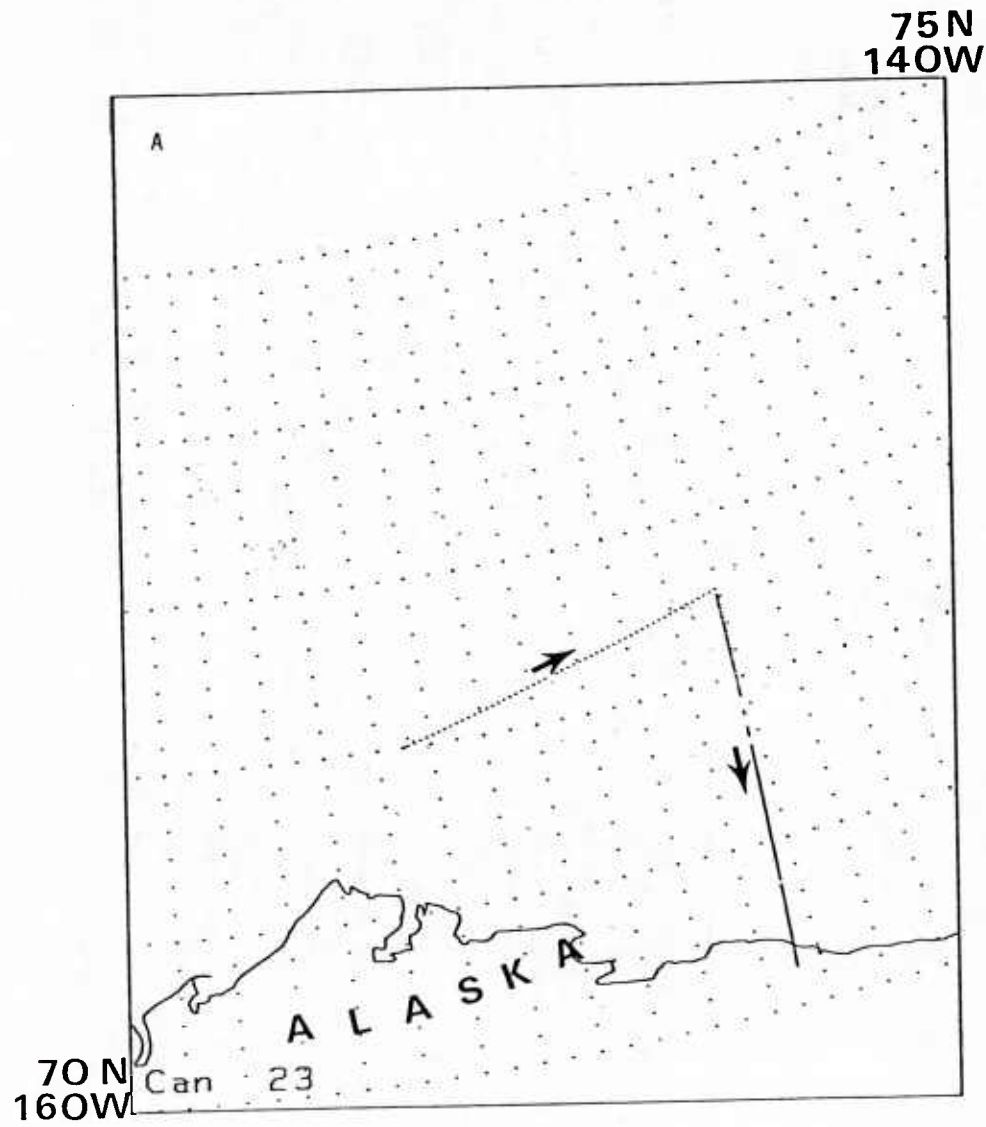
Meltponds represent the areal extent of pooled water on the ice surface during summer months. Percentages given represent conservative estimates of meltpond development. Most meltpond data come from summer images. However, the percentage of multi-year ice surfaces comprised of frozen meltponds in winter months probably can be estimated with reasonable accuracy from percentages measured in late summer images (late August, September). Meltpond percentages should be added to first-year ice and old ice percentages if not needed.

Unclassified pixels are those pixels that fail to fall into any of the categories defined by interval boundaries used. The presence of unclassified pixels indicates that, as a result of operator error, histogram boundaries used to classify a scene failed to include the full range of pixel intensities that were present. The unclassified percentage is zero for most frames in the archive. For those frames that do have unclassified pixels, note that percentages of surface types given in the scene are normalized to 100.0% without taking into account the percentage of unclassified pixels. Depending on applications for which these data are used, the user might choose either to recompute surface type percentages to account for the unclassified percentage, or to remove the few frames that include unclassified pixels from the archive.

TAPE FORMAT

Archived data can be provided on 9-track tape at 1600 bpi either as a series of ASCII files or as a structure of UNIX directories and

FIGURE 4



files. In either format, each file contains histogram and header data for all frames on a given roll of film. Data are given in the following order: 1) can, 2) frame, 3) date, 4) region, 5) latitude, 6) longitude, 7) altitude, 8) focal length, 9) open water, 10) new ice, 11) dark nilas, 12) light nilas, 13) nilas (undifferentiated), 14) grey ice, 15) grey-white ice, 16) first-year ice, 17) old ice, 18) ridges, 19) melt ponds, 20) ice bergs, 21) land, and 22) unclassified pixels.

APPLICATIONS

The data set of histograms is generally applicable to problems that Arctic processes, whether they describe climatologic, acoustic, oceanographic, or ice dynamics phenomena. The histograms represent sets of conditions that are known to have occurred at given points and at given times in the Arctic. As such, they form a points to the real world. The role of these data in modelling applications is two-fold. First, they provide ground truth data with which models that describe ice dynamics can be tested. Effective models must be able to predict ice conditions documented in the data set, given meteorologic and oceanographic boundary conditions that existed when the data were acquired. Accordingly, existing models can be verified by comparing predicted conditions with actual conditions that the data set documents. For example, Nimbus ESMR and SMMR data, and SEASAT SAR and SMMR data in many instances are inadequately ground truthed. Data in the archive that coincides with archived satellite images can be used to verify ice products derived from these satellite platforms. This is an especially important function in projects that seek to develop new algorithms for new sensors from archived satellite data.

The data set also can be used to set boundary conditions for models that predict other Arctic phenomena. Models of heat exchange, for example, are dependent on the concentration of

open water in the pack and on the abundance of thin ice types that transmit heat well. Histograms of ice abundance, if analysed in conjunction with figure 1, set limits on the abundance of ice of critical thicknesses that have occurred historically at specific points in the Arctic. Use of these data as inputs to climatological models should provide more reliable results than are now possible. In another example, acoustic models commonly require estimates of roughness elements that catter, absorb, and otherwise attenuate distant signals. Insofar as ice roughness and ice type are related, estimates of ice abundance contained in the data set provide baseline data with which estimates of regional scattering characteristics can be developed.

SUMMARY

In the end, the nature of problems at hand not only determine the degree to which these data are applicable but also dictate the manner in which they should be applied. The NORDA-NAVOCEANO data set represents a historical record of ice conditions at specific times and places in the Arctic. Histograms of ice abundance contain a wealth of information concerning seasonal, regional, and annual variation in ice conditions that has occurred over the past twenty years. In many instances these data are recorded nowhere else.

The data base established at NORDA is rather extensive and quite detailed. However, there are obvious areas where coverage (high resolution imagery) is limited or non-existent. Therefore, there is opportunity for other researchers, with archived imagery or collection capabilities to contribute. Also, efforts will be made to gather data where need exists.

The digitizing and processing method developed at NORDA is simple, easy to operate and reliable. Thus, additional data sets could be digitized and added to the digital data base with minimum effort and cost, allowing greater emphasis on end product analysis.

PRESSURE RIDGE MORPHOLOGY AND PHYSICAL PROPERTIES
OF SEA ICE IN THE GREENLAND SEA

W.B. Tucker III, A.J. Gow, W.F. Weeks

U.S. Army Cold Regions Research and Engineering Laboratory
72 Lyme Road, Hanover, New Hampshire 03755-1290

ABSTRACT

Field investigations of pressure ridge sails have shown that ridge height is limited by the thickness of the ice that deformed. Sail height and width can be conveniently expressed as functions of the thickness of the ice blocks contained in the ridge. Surface dimensions of the blocks are also related to ice thickness. Ridge height may be determined by the ability of the parent sheet to support the loading imposed by the ridge or by the type of failure occurring. Some insight into the structure of ridge keels may result from detailed study of the sails.

The physical properties of sea ice in the Fram Strait region of the Greenland Sea were examined as part of the MIZEX field program in 1984. The properties measured at each sampling site included salinity, temperature, thickness, crystal structure and snow depth. The measured salinities agreed well with those measured elsewhere in the Arctic during summer. Crystal texture analysis indicated that about 75% of the ice consisted of columnar type crystal structure. The remaining 25% consisted of granular ice.

1. INTRODUCTION

This paper will focus on two aspects of sea ice morphology. First, we will describe the results of our extensive investigations of the structure of first-year pressure ridge sails in the Alaskan Beaufort Sea. This study focused on establishing relations between ridge sail size and the geometry of the ice blocks composing the sail. We will then move to a much smaller scale and completely different area of the Arctic and describe ice physical properties investigations. These latter studies were conducted in the Fram Strait and consisted of the examination of small-scale properties, including temperature, salinity and structural profiles observed in cores obtained from a variety of first-year and multi-year ice floes.

Although these two aspects are of different scales, they are more closely related than might be obvious. Ridges are composed of ice blocks, which taken individually, may have highly variable small-scale properties. The larger scale characteristics of the ridge, such as mechanical, acoustic or electromagnetic properties, are determined not only by its size but also by the geometry and consolidation of the blocks and by the physical properties of the

individual blocks. If the ridge survives the summer, its properties are modified considerably. For instance, the sail is largely desalinated and the original blocks are ablated and consolidated by ice formed from meltwater freezing in the voids. These changes cause the ridge to have an independent set of small-scale properties which are different from those of the adjacent undeformed ice. In other words, some of the variation of small-scale properties observed in Arctic sea ice is attributable to ridges.

2. PRESSURE RIDGE MORPHOLOGY

Sea ice ridges are an important consideration to Naval operations in the Arctic. They impede surface and marine transportation because of their size and strength. Their often deep keels can be hazards to subsurface navigation and they significantly affect the underice acoustic environment. The keels act as scatterers, absorbers and reflectors of acoustic energy and a significant amount of ambient noise can be generated when the ridges are forming. For these reasons, the study of ridges can only help to enhance Naval Arctic operations.

Ridges have been the subject of considerable study since the 1960's. Early field measurements concentrated on thickness investigations to establish sail-to-keel ratios and on ice coring to provide temperature, salinity and density profiles through the ridge. Examples of these types of measurements for multi-year ridges are given by Kovacs⁴. The other aspect of ridges which has been addressed in some detail is the frequency distribution of sail heights and keel depths. Laser profiles have been used to obtain regional distributions of sail heights and upward-looking submarine sonar profiles have provided similar distributions of keel depths. Wadhams¹⁰ presents an excellent review of previous work regarding ridge frequency distributions.

Three types of ice features will be identified as ridges in the analysis of laser or sonar profiles. Two types of newly formed deformational features, called first-year ridges, are distinguished by their formative forces. Pressure ridges are formed primarily by compressive forces on the ice, which cause the ice to fail in bending or buckling, resulting in piles of ice blocks of various sizes. Shearing forces dominate in shear ridges, which are characterized by their linearity, vertical walls and the generally pulverized ice which composes



Figure 1. Typical pressure ridge.

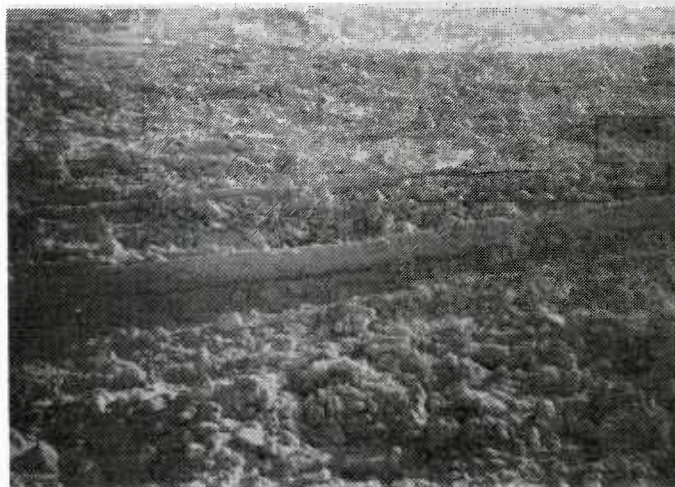


Figure 2. Typical shear ridge.

them. Examples of these two types of ridges are shown in Figures 1 and 2. Pressure ridges are far more common than shear ridges in the Arctic because deformational incidents where shearing forces dominate are generally infrequent except near coastlines. The third type of ridge is distinguished solely by its age rather than its structure. Multi-year ridges are features which have survived a summer. The melting has smoothed the surface and filled the internal voids with water which has subsequently frozen. Even though the topography of these ridges has been reduced by melting, they can be quite large and are considerably stronger than first-year ridges because they are more consolidated and contain lower-salinity ice. Figure 3 shows a large grounded multi-year ridge.

Field Studies

We have extensively studied the structure of first-year pressure ridge sails. The majority of these

investigations took place in 1980 and 1981 off the Beaufort Sea coast of Alaska. Detailed methodology and results have been previously described⁹.

Briefly, the geometry of the ridge sail and the dimensions of some of the larger blocks in the ridge were measured. We made these measurements along a short section of the ridge that usually included the maximum sail height of the ridge. Over 80 ridges were studied in this manner. One major goal of these investigations was to measure the thickness of the ice blocks in the ridge because it indicates the thickness of the ice that deformed to create the ridge.

Ridge and Ice Block Geometry

Figure 4 shows the ridge sail height plotted against the mean block thickness. The most obvious feature demonstrated by this figure is that ridge height seems to be a function of block thickness.

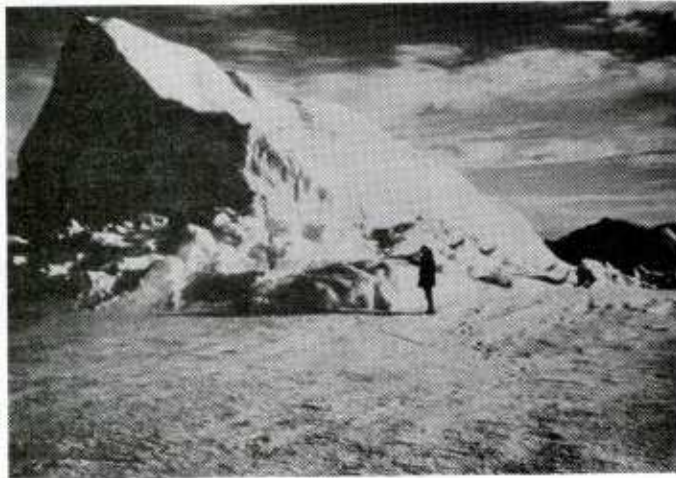


Figure 3. Large grounded multi-year ridge.

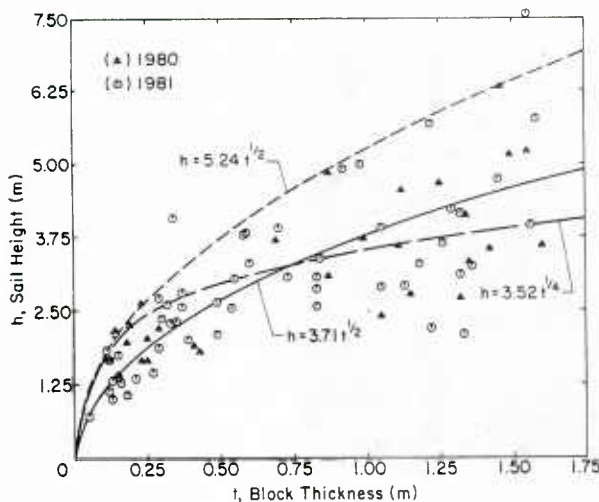


Figure 4. Sail height as a function of ice thickness.

Such a relationship was first hypothesized by Parmeter and Coon⁵ in an ice ridging model. Their basis for the limiting height concept is that the parent ice sheet, which is being loaded both above and below by ice rubble, eventually fails and the ridge subsequently grows wider rather than higher. Other height-limiting possibilities are discussed below. Another important finding pointed out by this figure is that thick ice (> 1 m) deforms to create ridges. The implication is that if environmental driving forces are sufficient, thick ice will be ridged after all thin ice in the area has been consumed by the ridging process.

The curves which are fitted to the data shown in Figure 4 are derived from energetic arguments that consider the two major forces involved in ridge building; potential energy and friction. Functional relations between ridge height and ice thickness

were established when these forces were compared to bending and buckling modes of ice failure. The buckling failure analysis results in sail height being a function of the square root of ice thickness. This accounts for two of the curves shown in Figure 4, the best fit relation to all data, where the constant is 3.71, and a type of limiting height curve, where the constant is 5.24. This latter curve originated from fitting the square root relationship to sail heights which exceeded the best fit curve by more than one standard deviation. Bending failure analysis results in sail height being a function of the fourth root of ice thickness. It appears that the buckling failure curve provides the best fit to thinner ice while bending failure fits the thicker ice categories best. Theory and laboratory experiments verify that thin ice is more prone to buckling, while bending failure dominates in thick ice. The curves point out that the mode of ice failure taking place during ridging may ultimately determine the limiting ridge height.

Other aspects of pressure ridge geometry and structure are also interesting. As might be expected, ridge width also scales well with sail height. This is reasonable in that slopes of first-year ridges have been found to average around 26 degrees without excessive scatter. Regarding the variation of ice thicknesses found in single features, some ridges contained as many as three distinct block thicknesses. This probably indicates that the ice in a small refrozen lead was totally consumed in ridge formation. Subsequently, driving forces were sufficient to continue ridging the ice sheets that were adjacent to the lead. Thick multi-year ice blocks were also observed in ridges on an infrequent basis.

Block surface dimensions also scale with thickness. Figure 5 shows the length of the major surface dimension plotted against thickness. The curves shown give the best least squares linear fit as well as the best fit to the three-quarters power of ice thickness. The motivation for the power law



Figure 1. Typical pressure ridge.

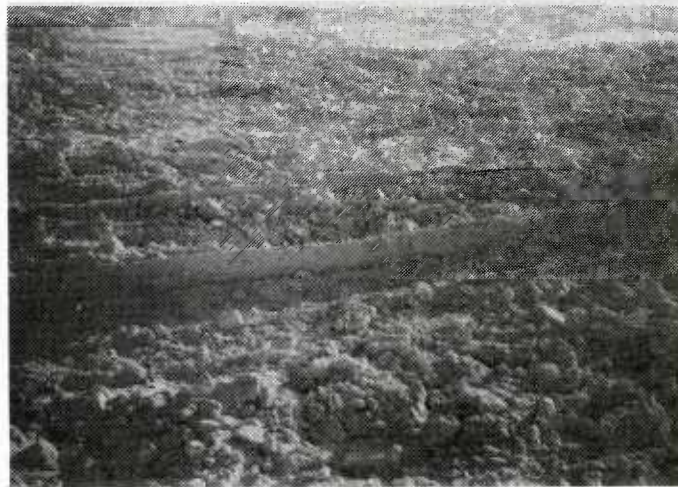


Figure 2. Typical shear ridge.

them. Examples of these two types of ridges are shown in Figures 1 and 2. Pressure ridges are far more common than shear ridges in the Arctic because deformational incidents where shearing forces dominate are generally infrequent except near coastlines. The third type of ridge is distinguished solely by its age rather than its structure. Multi-year ridges are features which have survived a summer. The melting has smoothed the surface and filled the internal voids with water which has subsequently frozen. Even though the topography of these ridges has been reduced by melting, they can be quite large and are considerably stronger than first-year ridges because they are more consolidated and contain lower-salinity ice. Figure 3 shows a large grounded multi-year ridge.

Field Studies

We have extensively studied the structure of first-year pressure ridge sails. The majority of these

investigations took place in 1980 and 1981 off the Beaufort Sea coast of Alaska. Detailed methodology and results have been previously described⁹.

Briefly, the geometry of the ridge sail and the dimensions of some of the larger blocks in the ridge were measured. We made these measurements along a short section of the ridge that usually included the maximum sail height of the ridge. Over 80 ridges were studied in this manner. One major goal of these investigations was to measure the thickness of the ice blocks in the ridge because it indicates the thickness of the ice that deformed to create the ridge.

Ridge and Ice Block Geometry

Figure 4 shows the ridge sail height plotted against the mean block thickness. The most obvious feature demonstrated by this figure is that ridge height seems to be a function of block thickness.

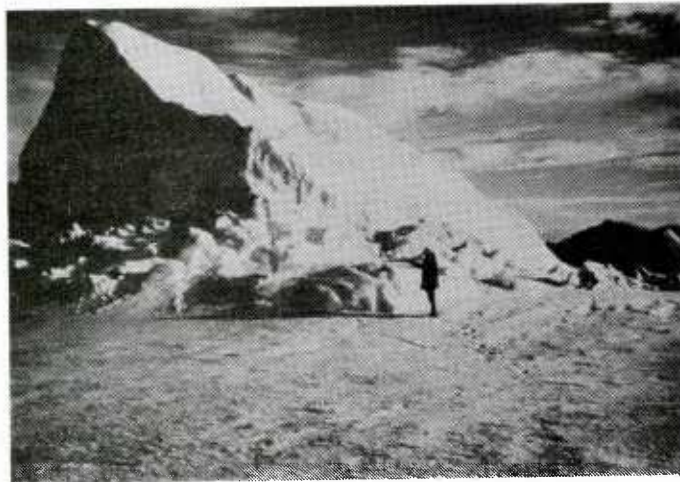


Figure 3. Large grounded multi-year ridge.

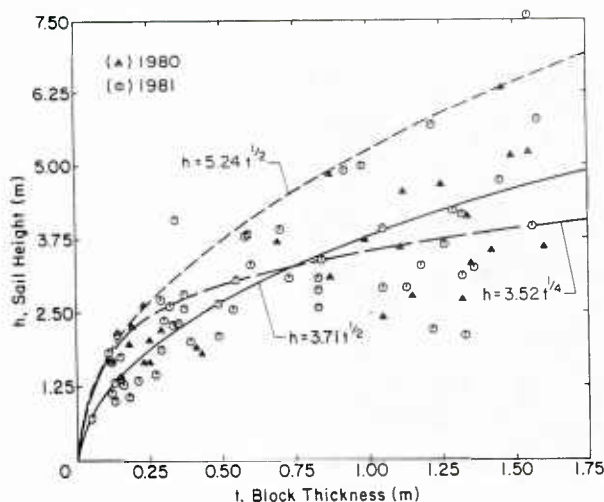


Figure 4. Sail height as a function of ice thickness.

Such a relationship was first hypothesized by Parmerter and Coon⁵ in an ice ridging model. Their basis for the limiting height concept is that the parent ice sheet, which is being loaded both above and below by ice rubble, eventually fails and the ridge subsequently grows wider rather than higher. Other height-limiting possibilities are discussed below. Another important finding pointed out by this figure is that thick ice (> 1 m) deforms to create ridges. The implication is that if environmental driving forces are sufficient, thick ice will be ridged after all thin ice in the area has been consumed by the ridging process.

The curves which are fitted to the data shown in Figure 4 are derived from energetic arguments that consider the two major forces involved in ridge building; potential energy and friction. Functional relations between ridge height and ice thickness

were established when these forces were compared to bending and buckling modes of ice failure. The buckling failure analysis results in sail height being a function of the square root of ice thickness. This accounts for two of the curves shown in Figure 4, the best fit relation to all data, where the constant is 3.71, and a type of limiting height curve, where the constant is 5.24. This latter curve originated from fitting the square root relationship to sail heights which exceeded the best fit curve by more than one standard deviation. Bending failure analysis results in sail height being a function of the fourth root of ice thickness. It appears that the buckling failure curve provides the best fit to thinner ice while bending failure fits the thicker ice categories best. Theory and laboratory experiments verify that thin ice is more prone to buckling, while bending failure dominates in thick ice. The curves point out that the mode of ice failure taking place during ridging may ultimately determine the limiting ridge height.

Other aspects of pressure ridge geometry and structure are also interesting. As might be expected, ridge width also scales well with sail height. This is reasonable in that slopes of first-year ridges have been found to average around 26 degrees without excessive scatter. Regarding the variation of ice thicknesses found in single features, some ridges contained as many as three distinct block thicknesses. This probably indicates that the ice in a small refrozen lead was totally consumed in ridge formation. Subsequently, driving forces were sufficient to continue ridging the ice sheets that were adjacent to the lead. Thick multi-year ice blocks were also observed in ridges on an infrequent basis.

Block surface dimensions also scale with thickness. Figure 5 shows the length of the major surface dimension plotted against thickness. The curves shown give the best least squares linear fit as well as the best fit to the three-quarters power of ice thickness. The motivation for the power law

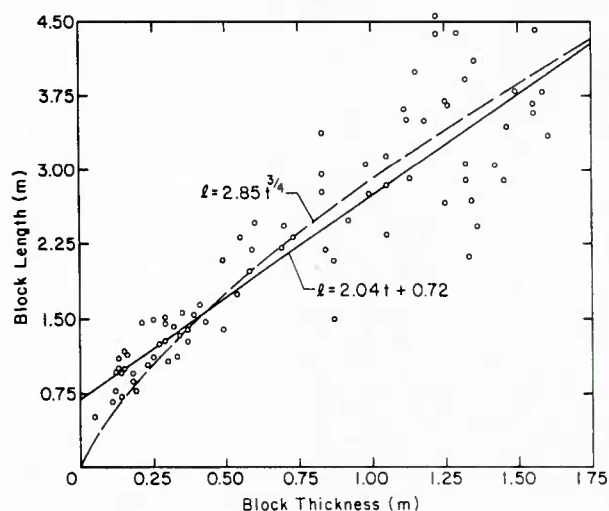


Figure 5. Block length as a function of block thickness.

fit was to assess the relation of the block length to the characteristic length of the ice, which is partially a function of the three-quarters root of thickness. The mean ratio of the measured block length to the characteristic lengths is 1:4.5. This is somewhat less than the ratio expected when ice fails in bending⁵ and thus may be indicative of secondary failure of the blocks occurring during ridging. Secondary failure can include blocks breaking when tumbling from the pile or breaking under their own weight if they are forced into cantilevered positions. If either of these mechanisms contributes to the size reduction of the blocks, then blocks in ridge keels would be expected to be larger because the buoyant force rather than gravity dominates.

Ridges are continuing to be studied when appropriate opportunities become available. Recent measurements, carried out in conjunction with investigators from the Naval Underwater Systems Center, Newport, Rhode Island, have included measuring as many blocks as possible along a given ridge section. This results in the distribution of block sizes for the ridge. Measurements of vertical orientation of the blocks have also been made. These measurements, in addition to those discussed above, have been used to describe the scattering faces of ridge keels in the NUSC weapons frequency acoustic scattering models. The structure of keels, however, may be quite different from that of sails. Serious investigations of ridge keels are now necessary to establish the relationships between sail and keel structure. These will be logistically very difficult and we cannot hope for the quantity or quality of measurements that exist for sails. However, using a combination of high resolution sonar, divers, and perhaps submersible vehicles, we should be able to obtain enough basic information to adequately characterize ridge keel structure.

3. PHYSICAL PROPERTIES

The physical properties of sea ice in the Fram Strait region of the Greenland Sea were investigated on the Marginal Ice Zone Experiment (MIZEX), which took place in June and July 1984. These studies were conducted from the FS Polarstern, a well-equipped icebreaking research vessel. Because this vessel visited many different locations within the Fram Strait during MIZEX, it provided an ideal platform for obtaining ice samples over a relatively large area.

The Fram Strait is the major ice outflow region of the Arctic Basin. Modeling studies³ have indicated that ice discharging through the Strait can originate in essentially any part of the Arctic Basin. Ice that formed in the western Arctic arrives at the Strait via the Transpolar Drift Stream, while that from the Lincoln, Barents or Kara seas can take a more direct approach to the Strait. Thus, the ice examined in the Fram Strait or Greenland Sea could have originated in any number of different areas within the Basin. This suggests that if ice properties are strongly influenced by area of origin, then a large variation in properties might be observed in this small area. A disadvantage, of course, is that exact areas of origin of individual floes would be unknown.

Very few studies have examined the crystal structure of sea ice in addition to the more standard properties of temperature and salinity. The crystal texture has been shown recently to have significant influence on ice strength¹, and thus is of interest in studying practical Navy problems dealing with the penetration of ice. In addition, the small scale structure has recently been shown to affect high frequency acoustic scattering from the ice underside⁸. Thus variations in small-scale properties of sea ice should be assessed for ice throughout the Arctic.

Field Sampling

The locations of our ice sampling sites are shown in Figure 6. The sampling program was conducted between 15 June and 13 July 1984. Individual sites were reached either directly from the ship or by helicopter. Using the helicopter we were able to effectively extend the sampling area as well as choose representative floes for investigation. Forty individual floes, ranging in diameter from 30 m to several kilometers, were sampled. Occasionally the same floe was sampled at more than one location. At each site, two cores were obtained, one for salinity analysis and the other for structural analysis. Ice temperatures were measured on one of the cores immediately after removal from the ice.

On board Polarstern the salinity samples were melted and allowed to warm to room temperature (20°C). Salinity values were then obtained from conductivity measurements of the resulting solutions. Structural analysis of the ice cores was much more involved. First, we documented significant stratigraphic features of each core. The locations of banded structure, sediment or algae layers, bubbles

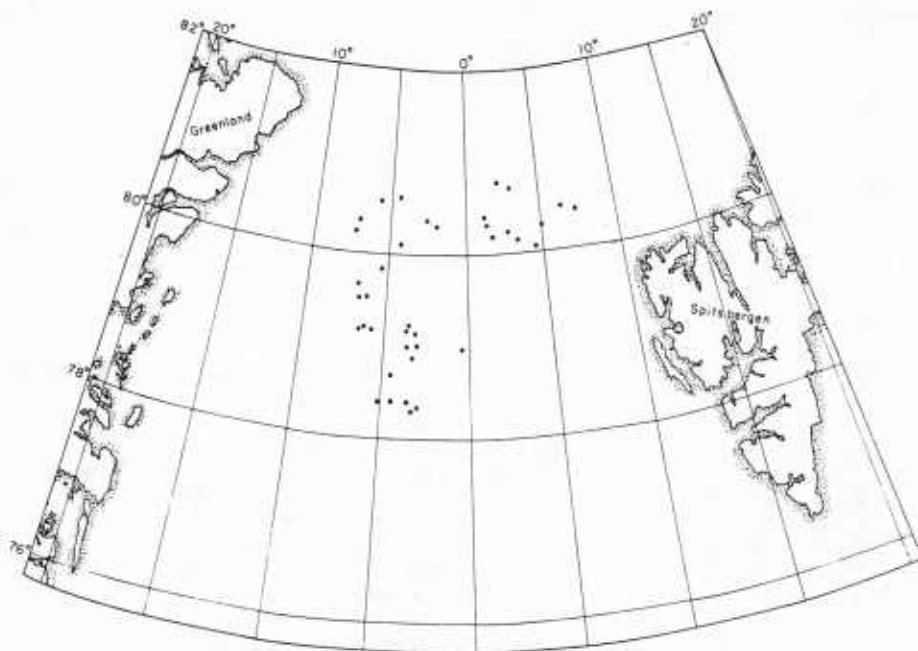


Figure 6 . Ice properties sampling locations.

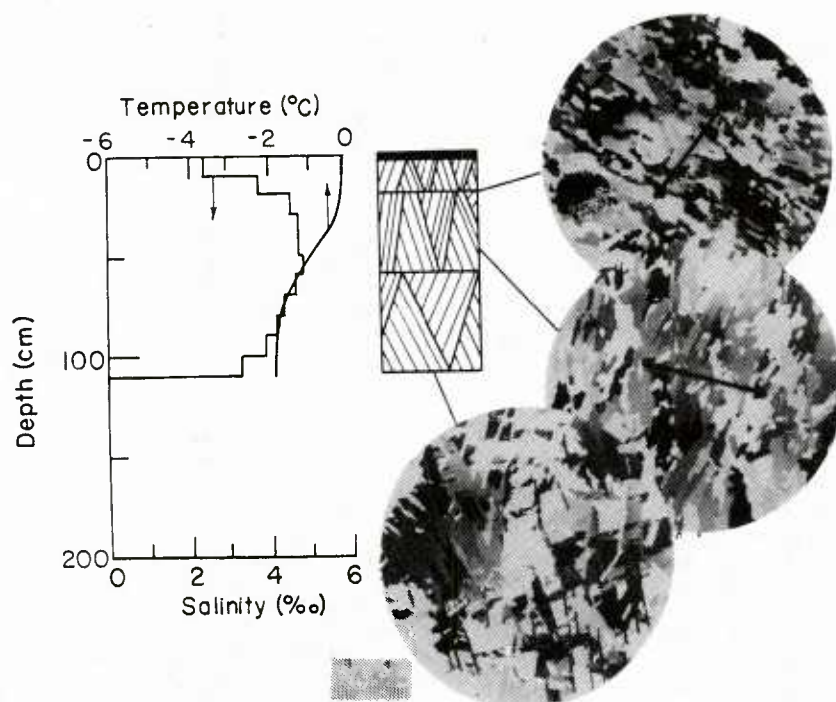


Figure 7. Structural schematic of undeformed first-year ice. Arrows indicate preferred c-axis direction.

and variations in the translucence were among the features noted. Then a 0.5-cm vertical thick section was cut from along the entire length of the core with a bandsaw. We examined this thick section through crossed polaroids to determine the overall nature of the crystal structure along the length of the core. This structural description of the cores included observations on crystal type (columnar or granular), grain size, degree of preferred orientation and the location of transition zones. This analysis dictated from where in the core vertical and horizontal thin sections would be selected for more detailed structural investigations.

The thin sections were prepared by sawing a 0.5-cm-thick section from the core, freezing it to a glass slide and further thinning the section to about 1

mm on the bandsaw. Finally a microtome was used to reduce the final thickness to between 0.2 and 0.5 mm. At this thickness, grain boundaries and brine lamellae/ice platelet structure of the crystals are clearly revealed when the section is viewed between crossed polaroids. A total of approximately 300 thin sections were prepared and photographed. A schematic description of the crystalline texture, along with temperature and salinity profiles and thin section photographs, has been prepared for each core. Examples of this type of ice core characterization are shown in Figures 7 and 8 for undeformed first-year and multi-year ice respectively.

Results

Of the 40 individual floes that were sampled, 27 were multi-year, 9 were first-year, and 4 were com-

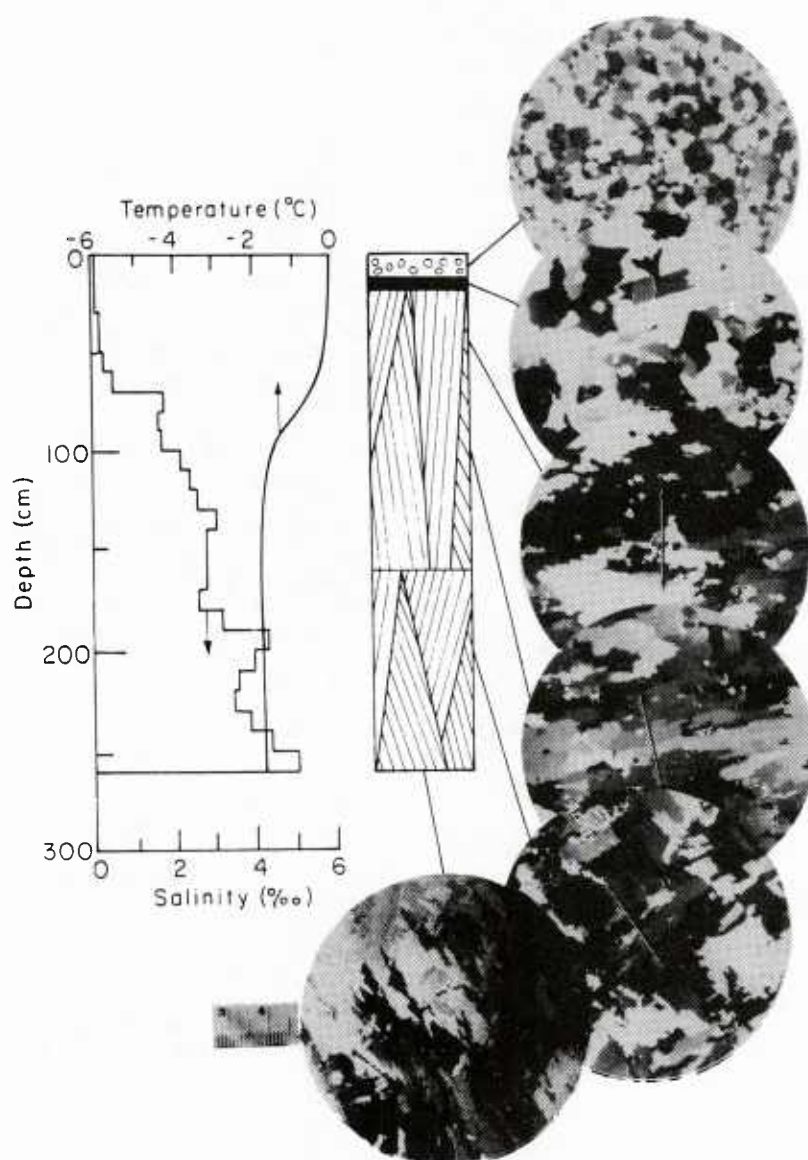


Figure 8. Structural schematic of undeformed multi-year ice.

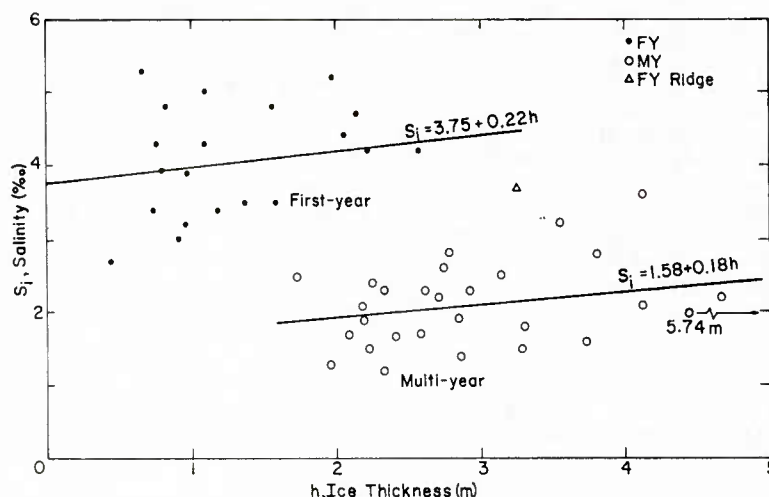


Figure 9. Bulk salinity as a function of ice thickness for first-year and multi-year ice.

posites. The composite floes generally consisted of multi-year floes with undeformed first-year ice attached. The percentage of first-year ice sampled was higher than the relative concentration of first-year ice in the region because we sampled first-year ice whenever possible. From the amount of ridging observed, it appeared that most first-year ice was deformed prior to entering Fram Strait. The first-year ice we sampled ranged from 38 cm in a newly frozen lead to a maximum floe thickness of 236 cm. Multi-year thicknesses varied from 174 to 536 cm, but where thicknesses exceeded 350 cm the ice was usually associated with old pressure ridges. Excessive snow depths often masked multi-year ice ablation features, making ice type identification difficult. Depths on the multi-year ice ranged from 3 to 65 cm and averaged 28.5 cm. Snow on the first-year ice averaged 8 cm in depth and never exceeded 20 cm.

The salinity profiles positively identified the ice as either first-year or multi-year in cases where the thickness may have indicated otherwise. Multi-year ice had a mean salinity of 2.1 ‰ and the salinity was generally very low (< 1 ‰) in the upper layers. We found the mean salinity of first-year ice to be 4.0 ‰, with salinities usually greater than 2 ‰ in the upper layers, although a few exceptions were noted. As the melt period progressed from mid-June to mid-July the mean salinity of the first-year ice decreased about 1 ‰, while the multi-year ice showed an increase of about 0.3 ‰. Figure 9 shows the variation of mean salinity with ice thickness for both ice types. Both show a slight salinity increase with thickness. For multi-year ice, the best fit regression line of salinity, S_1 , to thickness, h , is

$$S_1 = 1.58 + 0.18h \quad (1)$$

This least squares fit is in excellent agreement with that found for warm, predominantly Beaufort Sea ice².

In a few cases, salinities indicative of fresh ice (near zero) were observed in the upper 10 cm of first-year ice. The fresh ice structure was also verified by the crystal analysis. The implication is that either warming earlier in the year melted some of the snow cover or rain fell on the ice. In either case the fresh water subsequently refroze on the ice surface. In contrast, high surface salinities of 3 to 5 ‰ were occasionally observed in multi-year ice. These high salinities were probably caused by seawater flooding of the surface of the floe.

Analysis of the crystal structure indicates predominantly columnar (congelation) ice structure in both multi-year and first-year ice floes. Combining all cores gave a total of 74% congelation ice and 26% granular ice. Figure 10 shows that small amounts of granular ice were found in nearly every core. This is not surprising in that sea ice growth generally initiates as grease or slush ice¹¹. The majority of the granular ice that we observed, however, was associated with old ridges. Within ridges, granular ice occurred both in voids between blocks of columnar ice and near the bottoms of the ridges.

Substantial amounts of granular ice in multi-year ridges have also been observed in the Beaufort Sea⁵. An example of the ice structure in an old ridge fragment is shown in Figure 11. We found a mixture of inclined blocks of columnar ice with granular ice between those blocks in the upper meter. The lower part of the ridge contained more granular ice underlain by columnar ice representing recent growth on the bottom. In only one multi-year ice floe lacking evidence of ridging did we find substantial amounts of granular ice.

Another interesting structural feature observed was the variation of the alignment of the horizontally oriented c-axes of the columnar crystals. We found every conceivable orientation, ranging from an entire core containing randomly oriented crys-

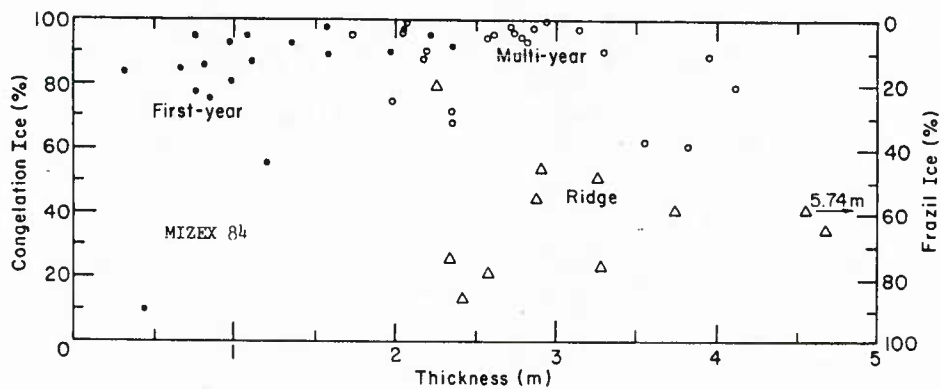


Figure 10. Percentages of congelation and frazil (granular) ice versus ice thickness.

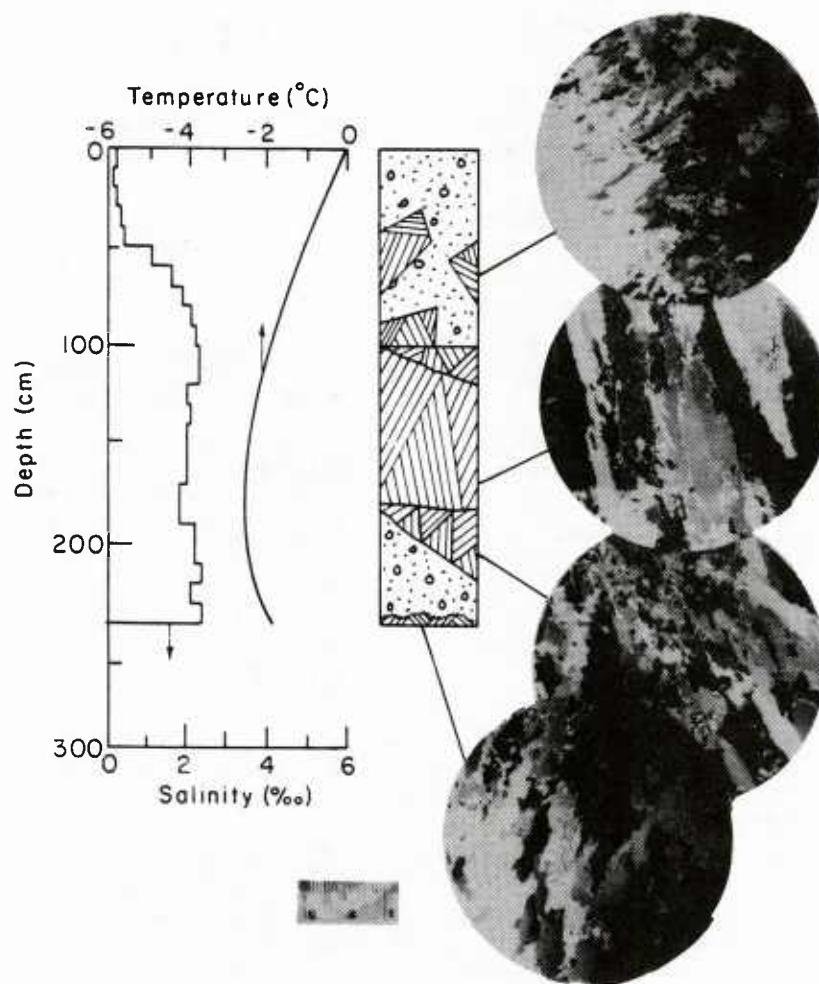


Figure 11. Structural schematic of a multi-year ridge fragment.

tals to cores with preferred alignment which remained constant throughout the ice thickness. Among the most interesting, however, were those cores exhibiting preferred alignments which changed with depth. Figure 7 shows such an example where the c-axes were well aligned, with the alignment direction changing with depth except at the bottom where no alignment is evident. Strong c-axis alignments are believed to indicate a stable growth environment in which the c-axes are oriented parallel to the current direction at the growth interface^{12 13}. Accordingly, changes in alignment direction with depth reflect relative changes of the orientation of the ice with respect to the currents. Lack of preferred orientation, as on the bottom of the core in Figure 7, probably indicates continual rotation of the floe on its passage through Fram Strait.

4. CONCLUSIONS

Ridge Morphology

The studies of the structure of first-year pressure ridges have resulted in several significant conclusions.

Ridge height and width have been found to be a function of the thickness of the ice that deformed, indicating a limiting height mechanism.

Ice thicker than 1 m was observed in pressure ridges. This indicates that environmental driving forces are sufficient to deform thick ice if all thin ice in the area has been consumed.

In addition to ice failure in bending, the buckling mode of failure is indicated by an analysis which considers functional arguments of the major forces involved in ridging.

Block lengths in the sails are less than those expected for bending failure. The indication is that secondary failure of the blocks in the sail is taking place during ridge building.

Ice Properties

Our observations of sea ice in the Fram Strait during June and July 1984 lead to the following conclusions:

The amount of multi-year ice in the Fram Strait greatly exceeded the amount of first-year ice.

Snow as deep as 65 cm was observed on multi-year ice while little (generally less than 10 cm) was evident on first-year ice.

The ice salinities measured here agree well with salinities of warm sea ice measured elsewhere in the Arctic.

The ice structure consisted primarily of columnar-type crystals. Granular ice was found in small amounts in surface layers and in much larger amounts in old ridges.

Preferred alignments of horizontally oriented c-axes were commonly observed, indicating a stationary environment with regard to the currents during the growth of the ice layer. This alignment frequently changed direction with depth, indicating episodes of movement and immobilization of the floe during its growth history.

5. ACKNOWLEDGMENT

This work has been supported by the Arctic Programs Office of the Office of Naval Research.

6. REFERENCES

1. Cox, G.F.N., Richter-Menge, J.A., Weeks, W.F., Mellor, M., Bosworth, H., Durrell, G. and Peron, N., Mechanical properties of multi-year sea ice, Phase II: Test Results. U.S. Army Cold Regions Research and Engineering Laboratory, CRREL Report in press, 1985.
2. Cox, G.F.N. and Weeks, W.F., Salinity variations in sea ice. *Journal of Glaciology*, vol. 13, no. 67, 1974, 109-120.
3. Hibler, W.D. III, A dynamic-thermodynamic sea ice model. *Journal of Physical Oceanography*, vol. 9, no. 4, 1979, 815-846.
4. Kovacs, A., Characteristics of multi-year pressure ridges. *Proceedings of The Seventh International Conference on Port and Ocean Engineering Under Arctic Conditions*, vol. 3, 1983, 173-182.
5. Parmeter, R.R. and Coon, M.D., Mechanical models of ridging in the Arctic sea ice cover. *AIDJEX Bulletin* No. 19, 1973, 59-112.
6. Richter-Menge, J.A. and Cox, G.F.N., Structure, salinity and density of multi-year sea ice pressure ridges. *Proceedings of ASME Offshore Mechanics and Arctic Engineering Symposium*, Dallas, Texas, in press, 1985.
7. Richter-Menge, J.A. and Cox, G.F.N., The effect of sample orientation on the compressive strength of multi-year pressure ridge ice samples. *Proceedings of ASCE Arctic 85 Conference*, in press, 1985.
8. Stanton, T. and Jezek, K., Acoustic scattering measurements from the underside of laboratory grown sea ice. *These proceedings*, 1985.
9. Tucker, W.B. III, Sodhi, D. and Govoni, J.G., Structure of first-year pressure ridge sails in the Prudhoe Bay region. *The Alaskan Beaufort Sea: Ecosystems and Environments* (P.W. Barnes, D.M. Schell and E. Reimnitz, eds.), 1985, 115-135.
10. Wadhams, P., Arctic sea ice morphology and its measurement. *Arctic Ice Technology and Policy* (I. Dyer and C. Chrysosostomidis, eds.), 1983, 179-193.

11. Weeks, W.F. and Ackley, S.F., The growth, structure and properties of sea ice. U.S. Army Cold Regions Research and Engineering Laboratory, CRREL Monograph 82-1, 1982, 130 pp.
12. Weeks, W.F. and Gow, A.J., Preferred crystal orientation along the margins of the Arctic Ocean. Journal of Geophysical Research, vol. 83, no. C10, 1978, 5105-5121.
13. Weeks, W.F. and Gow, A.J., Crystal alignments in the fast ice of arctic Alaska. Journal of Geophysical Research, vol. 85, no. C2, 1980, 1137-1146.

COHERENCE ESTIMATES OF UNDER-ICE PROFILES IN THE BEAUFORT SEA - AN
INDICATOR OF THREE DIMENSIONAL STRUCTURES.

E.R. LEVINE
S.E. OVERDEEP
D.N. CONNORS

Naval Underwater Systems Center
Code 3632, Newport, R.I. 02841

ABSTRACT

Under-ice profiles obtained in the fall in the Beaufort Sea with an upward looking sonar were used to examine three dimensional structures in a variety of ice environments. Parallel tracks, 2km in length, with separations from 10-1000m, were examined for coherence and phase in the wavenumber band from $0.005-0.5 \text{ m}^{-1}$. Significant coherence (0.90 level), was estimated at a wide range of wavenumbers at the three sites, corresponding to ridge spacing, width, and variability, and individual large block dimensions. For lower wavenumbers, coherence did not necessarily decrease monotonically with increased track separation. A reasonable comparison can often be made between triads of coherence peaks for block wavenumbers, and results of a model relating ice thickness to block dimensions.

1. INTRODUCTION

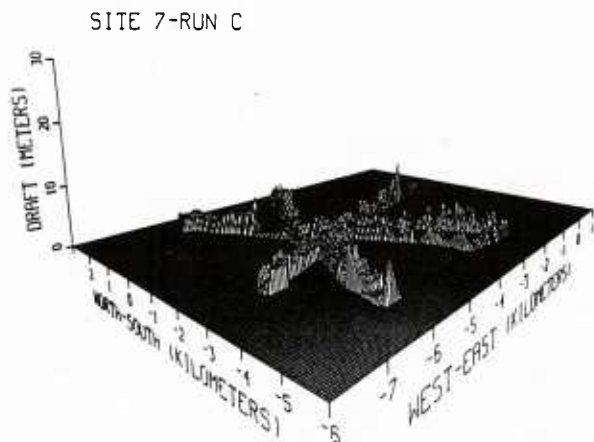
Previous studies of the three dimensional character of the underside of Arctic sea ice have included analysis of individual track statistics in a complex pattern¹, and mapping of small scale structures with an upward-looking sonar deployed through a hole in the ice. Three dimensional structures and their spatial orientation have been inferred using a geometric argument applied to autospectra obtained from orthogonal track segments², and two-dimensional power spectra have been estimated for ice upper surface data obtained using a laser profiler³. In this latter study, anisotropy was observed over a range of scales including structures from snow dunes to ridge sails.

In the present study, under-ice profiles of approximately 2km length were obtained in starlike patterns at three diverse sites in the Beaufort Sea during Fall 1982. Data were obtained with a high

resolution upward-looking sonar mounted on a submarine transiting at speeds of 6-11 kt and a depth of approximately 70m. This sampling mode acquires data with a footprint of about 2m at track intervals of 0.5-1.5m length. Autospectra estimated from these high resolution data⁴ show a wavenumber dependance closer to k^{-2} , rather than the k^{-3} dependance previously estimated⁵. In our paper, we take the next step with these data and present a coherence and phase analysis of all parallel track segments in order to evaluate correlations of structure with wavenumbers from $0.005-0.5 \text{ m}^{-1}$, at separations from 10-1000m. In this wavenumber band under-ice features include structures such as keel spacing and width, and rubble fields ($0.05 \text{ m}^{-1} < k$), ridge variability and large blocks ($0.05 < k < 0.25 \text{ m}^{-1}$), and blocks and rubble ($k > 0.25 \text{ m}^{-1}$).

The three areas of study in the Beaufort Sea were designated as Sites 7, 8, and 9, respectively. A summary of the individual runs taken at these sites is presented in Table 1, including ice environment, and a description of all of the parallel legs. Both Sites 7 and 9 are within the Offshore Province and Site 8 in the Central Arctic Basin Province⁶ in a region of transition between the two major drift features in Arctic circulation, the Pacific Gyral and the Transpolar Drift Stream. Site 7 (Figure 1) can be characterized as being made up of thin first year ice with imbedded second/multi-year ice floes from the presence of long stretches of undeformed ice with thicknesses of 0.3m and also ice greater than 2.5m thick. Site 8 (Figure 2) can be characterized as heavily ridged multi-year pack ice, due to the prescence of rugged ice topography in a field of undisturbed ice with a minimum thickness of approximately 2.5m. Site 9 (Figure 3) can be characterized as heavily ridged medium first year ice due to the prescence of many small ridges within a field of undisturbed ice of approximately 1.0m thickness. For the three sites, 7, 8, and 9, the

average number of ridges/km was 6.5, 14.3, and 8.6, respectively, based on a Rayleigh criteria for resolving individual ridges⁷.



2. METHODOLOGY

Ice profile data from the upward-looking sonar and relative position data from the submarine self-tracking system were obtained at the rate of 5.9 and 1.0 samples/sec, respectively. The individual tracking sequences run at each site were combined into a two-dimensional spatial pattern by superimposing a fixed point in space common to the individual patterns, and properly orienting the patterns with respect to north. The three-dimensional ice morphology diagrams presented above (Figures 1,2,3) were prepared by mapping all data at a particular site to a 50m x 50m grid using a scheme in which data points contributing to a grid value are weighted inversely as the square of their distance from the grid point. The sloping sides of each sampled region and flat topography in unsampled regions are artifacts of the chosen mapping procedure.

In preparation for the coherence/phase analysis, data taken at a constant temporal sampling rate, but variable transit velocities, were interpolated into constant spatial interval samples. This procedure was particularly important for a comparison of inbound and outbound legs, whose transit speeds could differ by several knots. The sampling interval chosen for the interpolated space series was based on the more poorly resolved outbound leg.

Parallel track segments of interpolated data, sampled at approximately 1m intervals, were chosen

for the coherence/phase analysis. Space series of 2048 points were input to a FFT⁸ based program which removed the mean, multiplied the data by a Hanning function to reduce leakage in wavenumber space, compute raw Fourier amplitudes in data segments, and ensemble averaged these coefficients to compute autospectra, cross-spectra, coherence (squared), and phase. For the 16 degrees of freedom of these results, the significance level at the 0.90 confidence level is 0.14⁹. Error bars on the individual coherence estimates, a function of the number of degrees of freedom and the coherence estimate, itself, were also obtained. Combining the significance level with error bar tables indicates that coherences greater than 0.31 are significant at the 0.90 confidence level for this study. The sign convention for phase used in this study is that if the second (lower) space series lags the first (upper) space series the phase has values between 0- π radians, while if the second space series leads the first the phase has values between π - 2π radians.

3. RESULTS

The most complete example of parallel track segments obtained at a fixed azimuth at a given site are from the 306° azimuth at Site 8 (Figure 2). Here, separations from 0.04-0.39km were available for coherence estimation. Space series for the 0.04km separation, interpolated as previously described, are presented in Figure 4. Inspection of the two records shows a similarity of structures over a range of scales from ridges with 12-14m drafts to small scale variability with several meter drafts. Indeed, coherence estimates obtained from these data (Figure 5) indicate significant coherence (at the 0.90 confidence level) in each of the three generic wavenumber bands. In the lowest wavenumber band, significant coherence is found for $k < 0.01\text{m}^{-1}$, corresponding to a wavelength $L > 100\text{m}$, with phase decreasing from 0 to $-\pi/2$ with increasing k . In the midrange wavenumber band several significant peaks were found, with maximum coherence at 0.19m^{-1} ($L = 5.3\text{m}$), and corresponding positive phase ($\sim \pi/2$). In the high wavenumber regime, significant coherence is found at approximately 6 wavenumber bands, with maximum coherence for $k = 0.41\text{m}^{-1}$ (wavelength, $L = 2.4\text{m}$). Summarizing these results, the occurrence of significant coherence over a wide range of wavenumbers from ridges to blocks, at a separation of 0.04km, was not expected. The question arises

whether these results, at lower coherence values are typical for other separations at the same azimuth, at other fixed azimuths at Site 8, and at the other Sites 7 and 9.

First, the above analysis was repeated for track segments also taken at 306° azimuth for separations of 0.09, 0.12, 0.19, 0.31, and 0.36km, respectively. While coherence estimates for the 0.09km separation (not shown) generally agree qualitatively with the 0.04km separation results, although at lower coherence levels, results for the 0.12km separation (Figure 6) show a decreased number of significant coherence values and lower estimates in the three generic wavenumber regimes. For the low and midrange regimes, only marginally significant values were obtained. For the high wavenumber regime four significant peaks were observed, with a maximum estimated at 0.34m^{-1} ($L = 2.9\text{m}$) and 0.49m^{-1} ($L = 2.0\text{m}$), comparable to the maximum obtained for the 0.04km separation results obtained above. This comparison suggests that the block-like scales at the larger separation remains coherent, although the ridge variability and ridges themselves are incoherent. Thus at 0.09km separation we may have left the particular ridge structure which was coherent at 0.04km separation.

Coherence estimates for the 0.19km separation (Figure 7) show an increased number of significant coherence values and higher estimates than for the 0.12km separation. For the low wavenumber band significant coherence is found at 0.04m^{-1} ($L = 25\text{m}$), while for the midrange the maximum occurs at 0.21m^{-1} ($L = 4.8\text{m}$). For the high wavenumber band, the maximum coherence occurs at 0.34m^{-1} ($L = 2.9$). For this case, the sampling interval was too large to resolve scales greater than $k = 0.43\text{m}^{-1}$, and thus the $0.46\text{--}0.47\text{m}^{-1}$ estimates obtained above could not be made. These results show that the 0.19km separation was in a region in which the midrange and low wavenumber components more closely resembled the 0.04km than the 0.09km separation results, and suggests that the ridging structure and variability may occur at approximately 0.2km spacing.

At the next largest separation, 0.31km, fewer significant peaks and generally lower coherence values were estimated than at 0.19km separation. The low wavenumber maximum occurs at 0.01m^{-1} , the midrange maximum at 0.07m^{-1} , and the high

wavenumber maximum occurs at 0.40m^{-1} . This pattern is repeated at 0.36km, where the number of significant points and the estimates, themselves, are further reduced. Here, the only large coherence estimates occur in the midrange, with a maximum at 0.08m^{-1} .

Another look at coherence, for a variety of ranges, at a different azimuth at Site 8, is provided by data taken at 90° at 0.06, 0.29, and 0.44km. Coherence estimates for the 0.06km separation show significant coherence in each of the three wavenumber bands, similar to results previously shown for the 0.04km separation described above. In the lowest wavenumber band, significant coherence is found for a range of scales with peak value at 0.02m^{-1} ($L = 50\text{m}$). In the midrange wavenumber band four significant peaks are found, with the maximum at 0.11m^{-1} (9.1m). In the high wavenumber range, four significant peaks are found, with the maximum found at 0.27m^{-1} (3.7m). Results for the 0.29km separation also show multiple coherent peaks in each of the three generic wavenumber bands, but in contrast, the number of peaks and coherence values, themselves, are reduced for the 0.44km separation estimates.

In order to consider the effects of different ice regimes on coherence, two examples will be considered which compare similar track separations at different sites. For this comparison, azimuth will be ignored due to the rotational motion possible in the ice canopy. Results for a Site 7, 0.22km separation (Figure 8) and a Site 9, 0.22km separation (Figure 9) closely resemble the Site 8, 0.19km separation results described above. For the Site 7 data, significant coherence was found in the low wavenumber band at 0.045m^{-1} (22.2m). In the midrange, three significant peaks were found with maximum at 0.20m^{-1} (5m). For the high wavenumber band, five peaks are found, with a maximum at 0.28m^{-1} ($L = 3.6\text{m}$). For the Site 9 data, significant coherence was also found in the low wavenumber band at 0.045m^{-1} ($L = 22.2$). For this site, in the wavenumber midrange three peaks were observed with the maximum at 0.24m^{-1} ($L = 4.2\text{m}$). For the high wavenumbers, three peaks were observed, with the maximum occurring at 0.44m^{-1} ($L = 2.3\text{m}$). The similarity of results between the three sites at approximately the same separation is another unexpected result given the different ice regime and ridge formation processes at the sites. This result

is further reinforced considering another Site 7 run at 0.09 km separation. Similar to the 0.09km results obtained for Site 8 above, the coherence was low in value and few peaks occurred in any of the generic wavenumber bands.

4. DISCUSSION

In the low wavenumber band corresponding to $k < 0.5\text{m}^{-1}$, coherence did not monotonically decrease with increasing separation as expected. This band includes ridge spacing, ridge widths, and such phenomena as rubble fields and multi-year ice floes imbedded in regions of extensive first year ice. Rather, results suggest that ridge and rubble field features in this band may be occurring intermittently. From the observed mean ridge spacing we would expect high coherence at wavenumbers near 0.006 , 0.014 and 0.008m^{-1} for Sites 7, 8 and 9, respectively. Assuming that the mean angle of attack of the data gathering is 45° to the ridge axis, and noting that the mean angle of repose for all the data analyzed thus far is 30° , we can determine the mean effective ridge width from the mean ridge depth for each site. These wavelengths correspond to 0.027 , 0.018 and 0.023m^{-1} for Sites 7, 8 and 9, respectively.

The ridge width/spacing wavenumber band, determined from two independent statistics, is particularly narrow (0.014 - 0.018m^{-1}) for Site 8 compared to results for the other sites. For Site 8, we find high coherence for closely spaced tracks, as might be expected, at 0.04km (306° azimuth), 0.06km (90°) and to a lesser extent at 0.09km (306°). There is low coherence for track separations of 0.12 and 0.19km (both at 306°), high coherence at 0.31km (306°) and 0.29km (90°), and virtually none at 0.44km . The ridge width/spacing band is broader for Site 7, (0.006 - 0.03m^{-1}) than Site 8, but in the three parallel tracks we have relatively little coherence at 0.09km separation and high coherence at 0.220 and 0.80km . For site 9 the keel width/keel spacing band (0.008 - 0.023m^{-1}) is also broader than for Site 8. For the one set of parallel tracks at Site 9, with 0.22km separation, we find no coherence in this band. The above results for the three sites are consistent with results for a non-homogeneous ice field in which ridge structures with associated ridge spacings and widths are intermittent with

other uncorrelated structures. These results are in qualitative agreement with analyses of photo mosaics of the upper ice surface¹⁰ in the Beaufort Sea near-shore zone and main ice pack where shear and pressure ridges, respectively, were the ordered 'patches' imbedded in a field of randomly oriented features. For Site 7, large multi-year ice floes could provide the 'patches', i.e., be the source of nonrandom deformation in a field of thin first year ice. For Site 8 we can only speculate on the source of the 0.2km patch of nonrandom structure, e.g. it could be a zone of several linear shear ridges in an area dominated by curvilinear pressure ridges.

In the mid-range of wavenumbers, corresponding to $0.05 < k < 0.25\text{m}^{-1}$, coherence also did not decrease monotonically with increased track separation. Some of the longer scales in this band, corresponding to ridge variability, behaved much like the ridge structures themselves. Indeed, these scales of order 10m have previously been observed to correspond to ridge variability¹¹ or variability associated with individual floes, with associated vertical scales of order 1m ¹². For the shorter scales contained in the mid-range of wavenumbers, the results indicated behavior more like long block dimensions, as described below.

In the high wavenumber band, corresponding to $k > 0.25\text{m}^{-1}$, most of the blocks and rubble occur. We would expect to see high coherence for close parallel tracks which, have sampled the same ridge for part of the track. For first year pressure ridges, high coherence might be expected to occur in a triad of coherent wavenumber bands for ridge building processes involving one ice thickness. The triad would include characteristic block length, width and thickness. A useful empirical relationship has been developed¹¹ between block length (l) and thickness (t) for first-year sea ice in ridges. Their results show that

$$l = 2.85 t^{3/4}$$

with a correlation coefficient of 0.90 , and the ratio of width to length has been found^{11,13,14} to be a constant, insensitive to block thickness, where the ratio $w/l = 0.65 \pm 0.08$. A significant number of ridges also show bimodal block thickness distribution (35 - 40%) and 10% were made up of three or more ice thickness categories¹⁴.

TABLE 1: SITE SUMMARY

SITE	PROVINCE	ICE CHARACTER	NO. PARALLEL LEGS, SEPARATION (m)
7c	Offshore	Thin first year Multi-year floes	3(60,250,1000)
8c	Central Arctic Basin	Heavily Ridged Multi-year	5(40,50,110,200,300)
8f	Central Arctic Basin	Heavily Ridged Multi-year	4(10,120,1000)
9c	Offshore	Heavily Ridged Medium first year	1(250)

FIGURE CAPTIONS

Figure 1. Three dimensional ice morphology for Site 7. The data have been mapped to a 50m grid, which is shown. The sloping boundaries of the sampled regions are an artifact of the mapping process.

Figure 2. Three dimensional ice morphology for Site 8, mapped to a 50m grid.

Figure 3. Three dimensional ice morphology for Site 9, mapped to a 50m grid.

Figure 4. Ice morphology (m) for Site 8, 306° azimuth. The lateral separation of the tracks is 0.04km. The track designator indicates the site, pattern, and leg.

Figure 5. Coherence and phase estimates for the Site 8, 306° azimuth, 0.04km separation data shown in Figure 4. Coherence values above 0.31 are significant at the 0.90 confidence level.

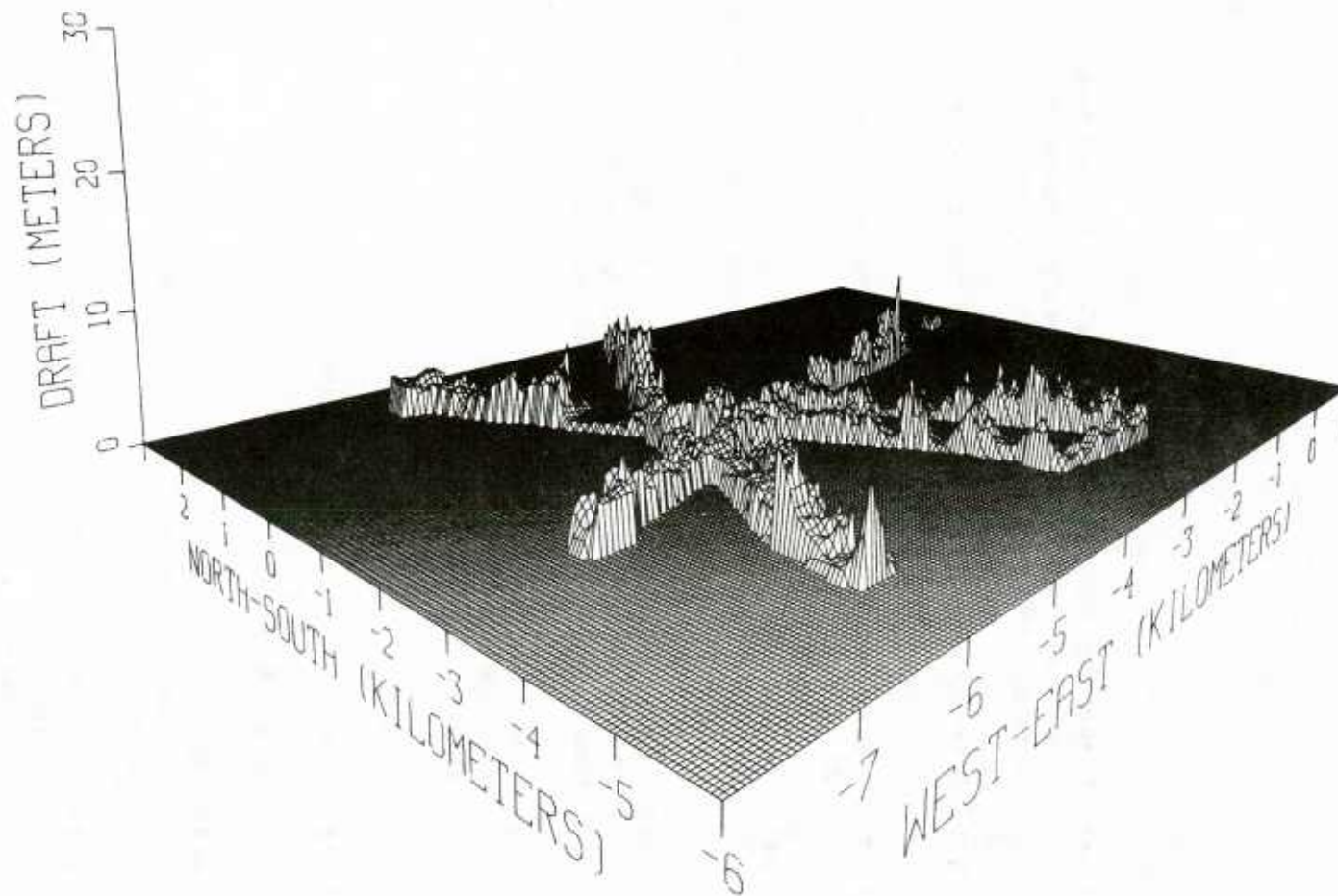
Figure 6. Coherence and phase estimates for the Site 8, 306° azimuth, 12km separation. Coherence values above 0.31 are significant at the 0.90 confidence level.

Figure 7. Coherence and phase estimates for the Site 8, 306° azimuth, 0.19km separation. Coherence values above 0.31 are significant at the 0.90 confidence level.

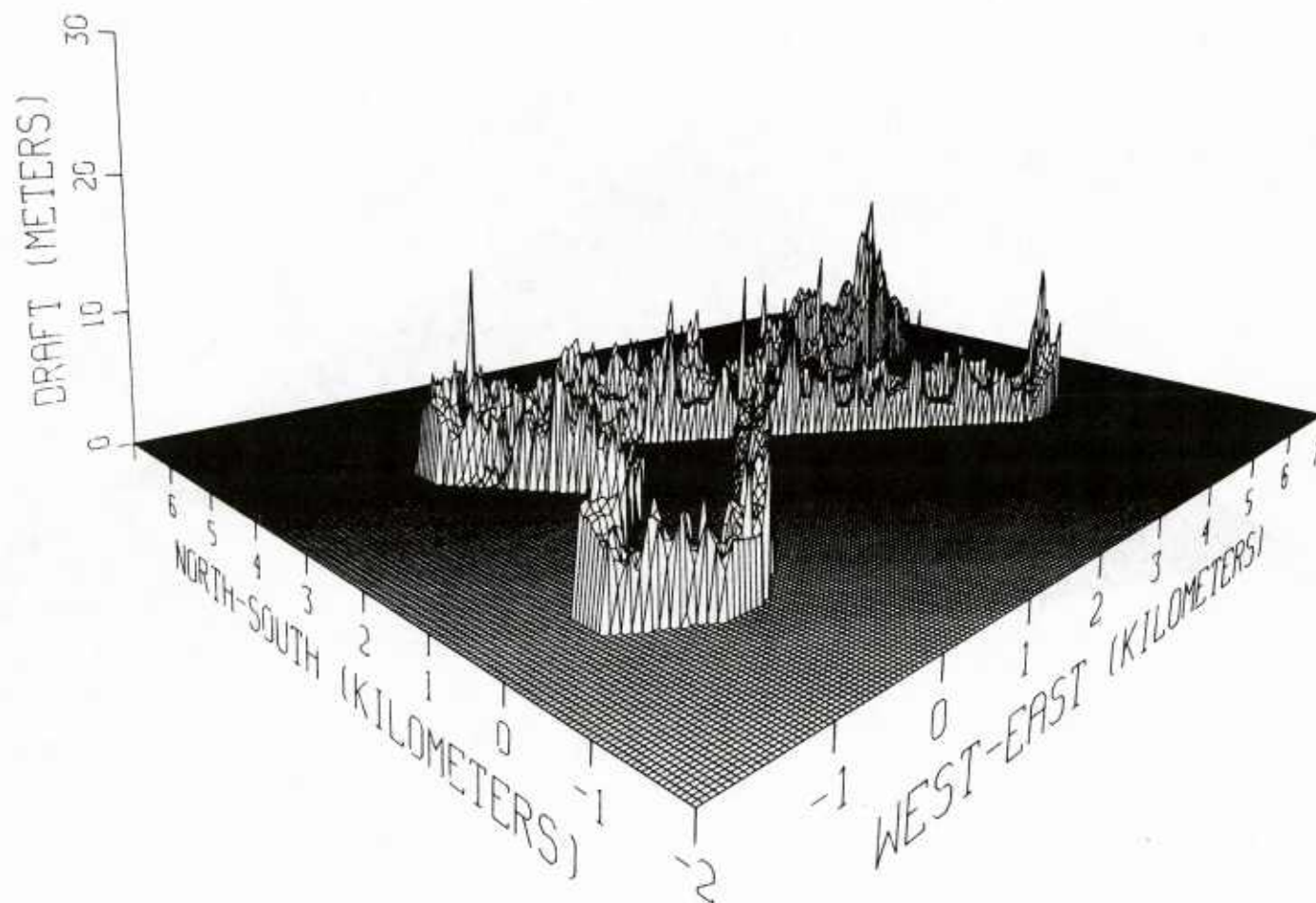
Figure 8. Coherence and phase estimates for Site 7, at 0.22km separation. Coherence values above 0.31 are significant at the 0.90 confidence level.

Figure 9. Coherence and phase estimates for Site 9, at 0.22km separation. Coherence values above 0.31 are significant at the 0.90 confidence level.

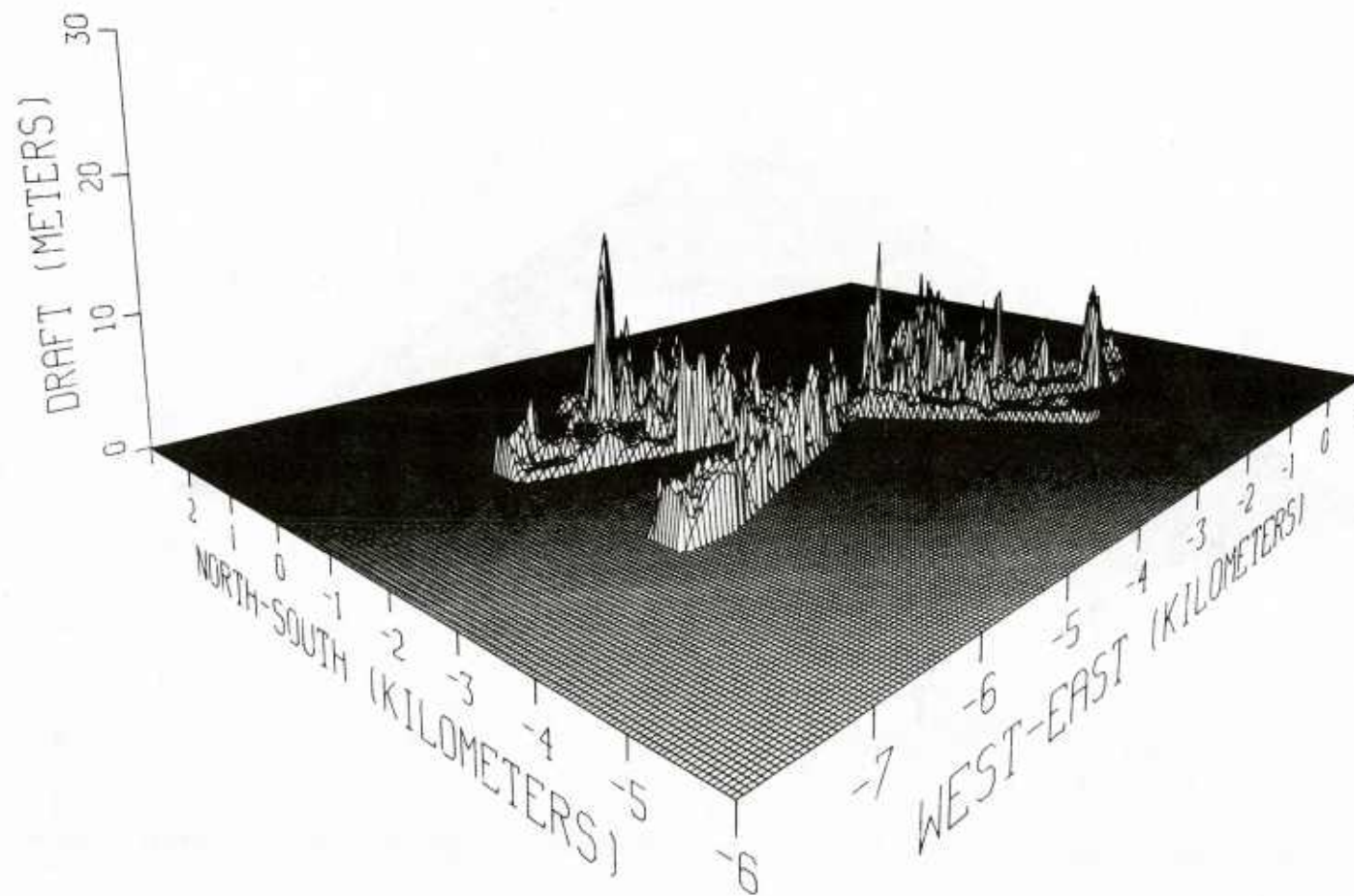
SITE 7-RUN C



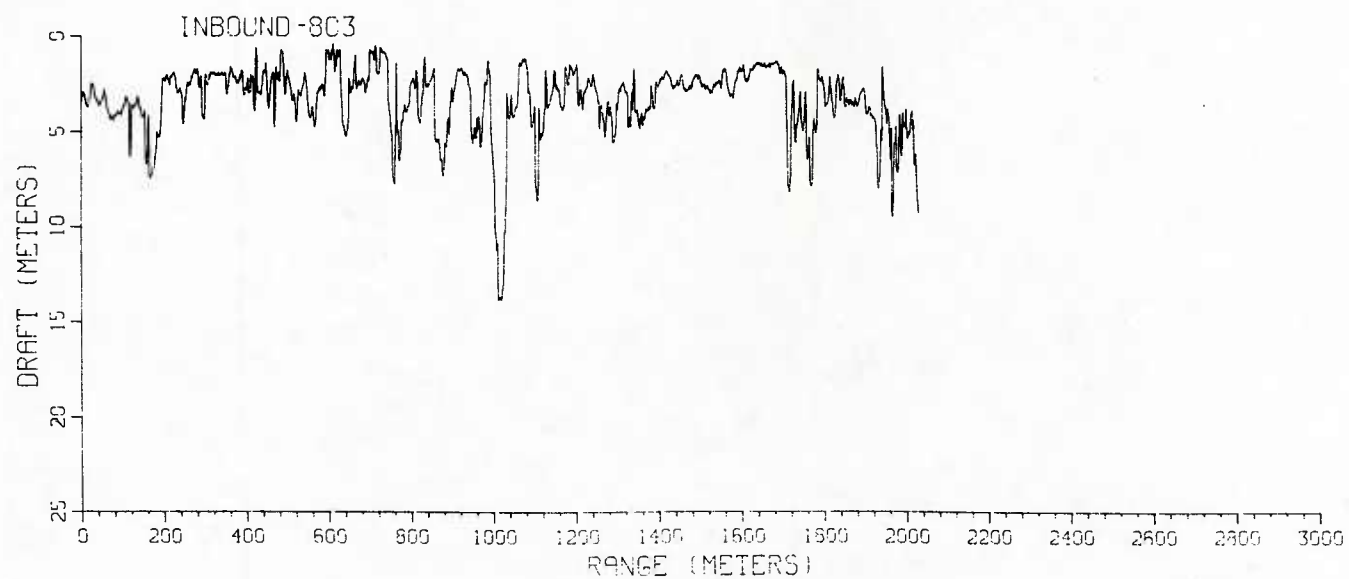
SITE 8-RUN C & F



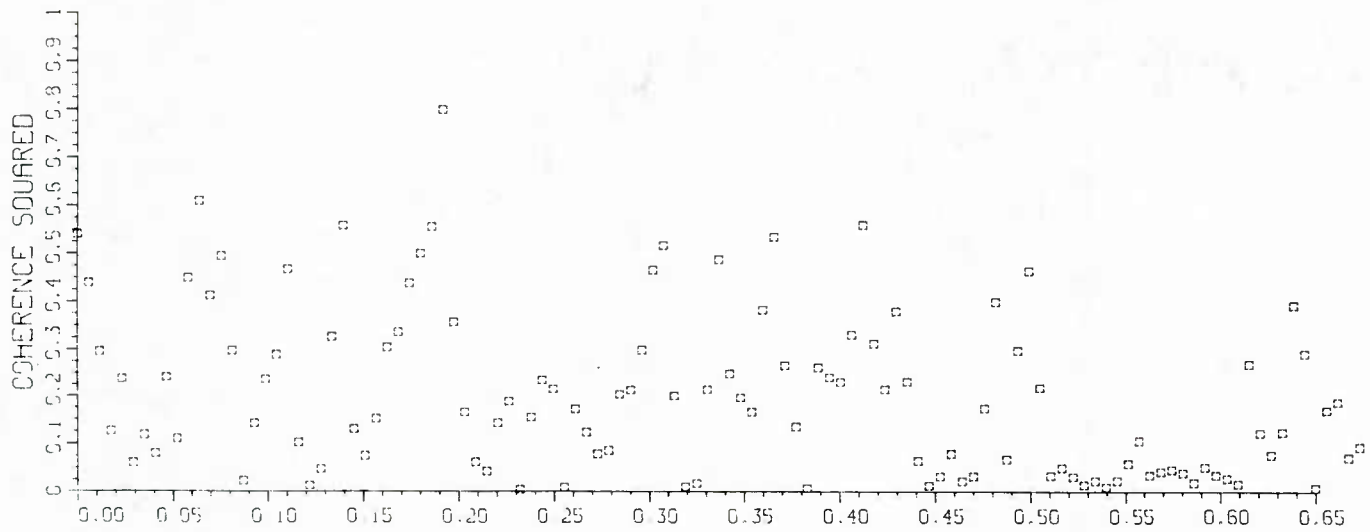
SITE 9-RUN C & F



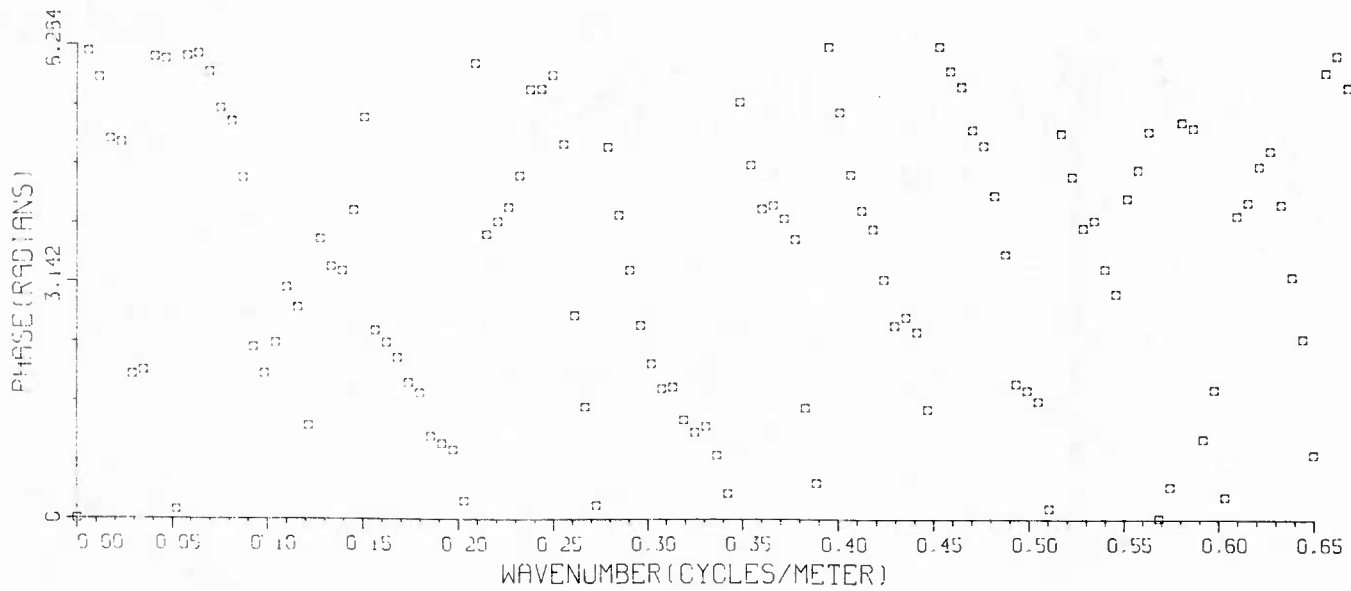
ICE MORPHOLOGY
SITES 8C3IN, 8F3IN



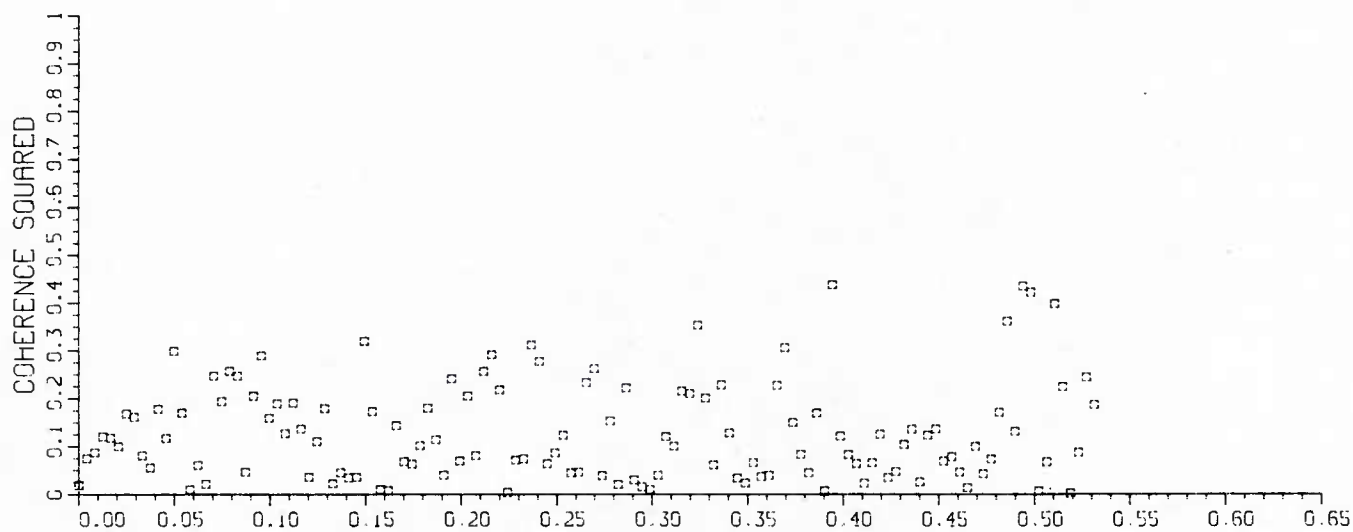
COHERENCE VS WAVENUMBER SITES 8C3IN, 8F3IN



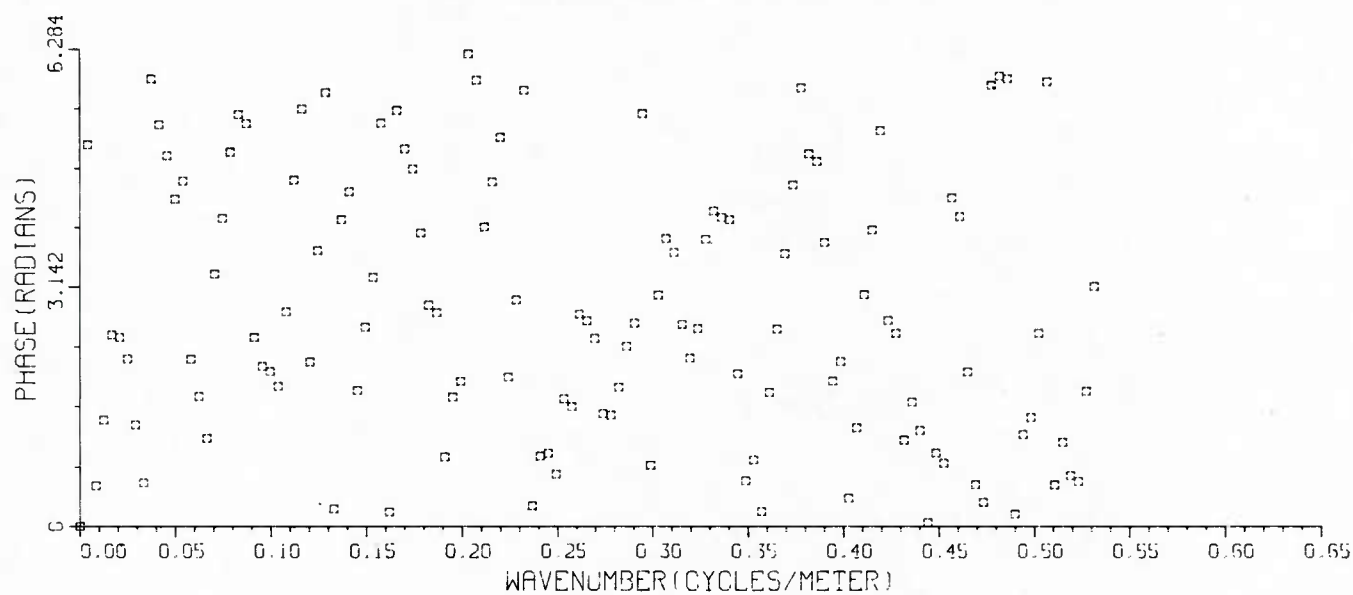
PHASE VS WAVENUMBER



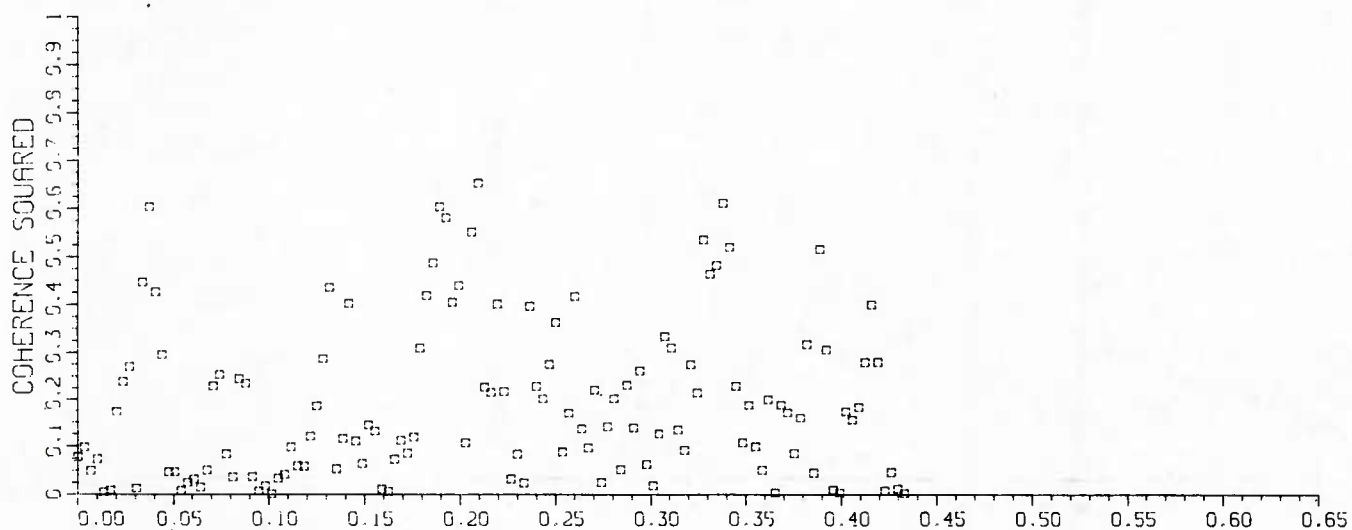
COHERENCE VS WAVENUMBER SITE 8F3



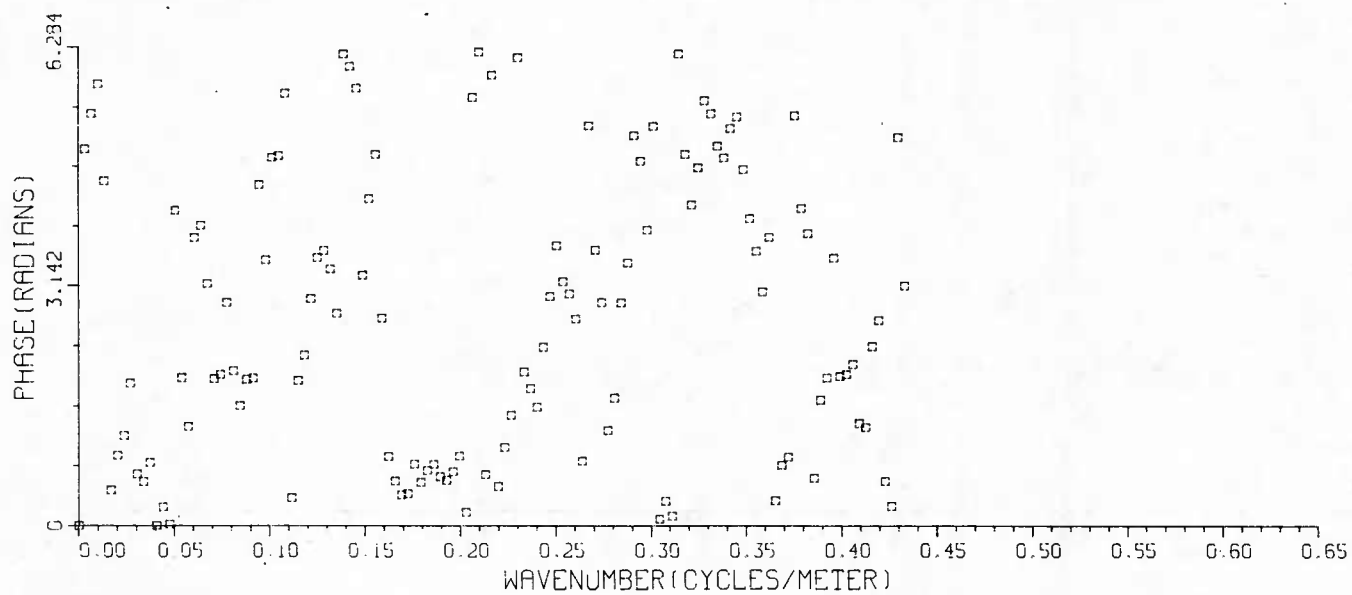
PHASE VS WAVENUMBER



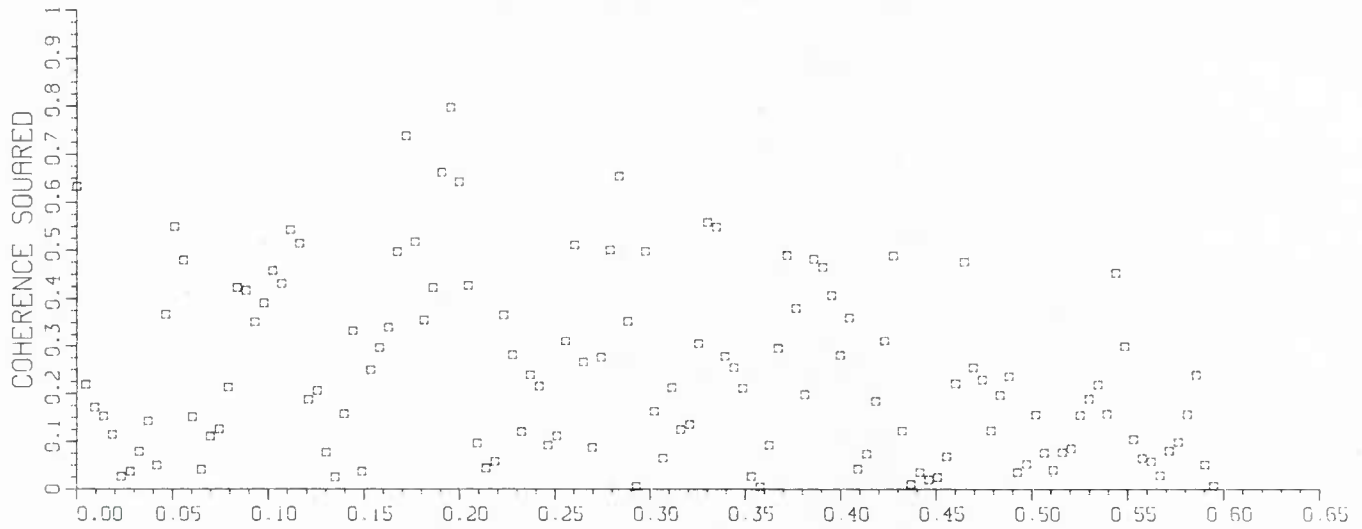
COHERENCE VS WAVENUMBER SITES 8F30T, 8C30T



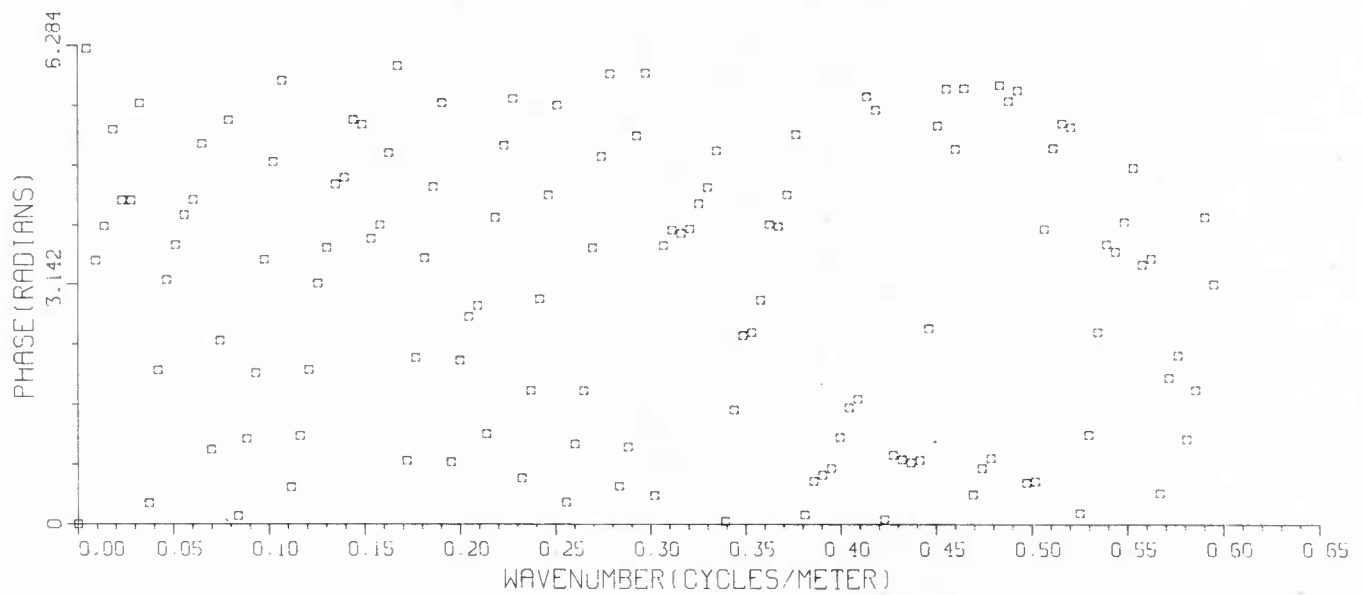
PHASE VS WAVENUMBER



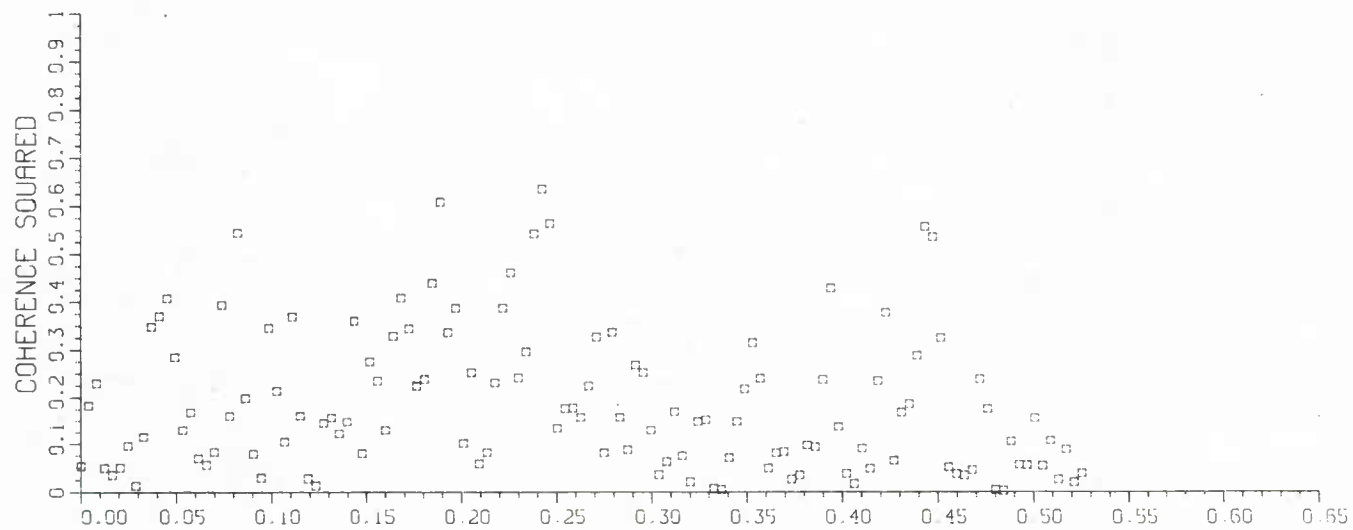
COHERENCE VS WAVENUMBER
SITE 7C4



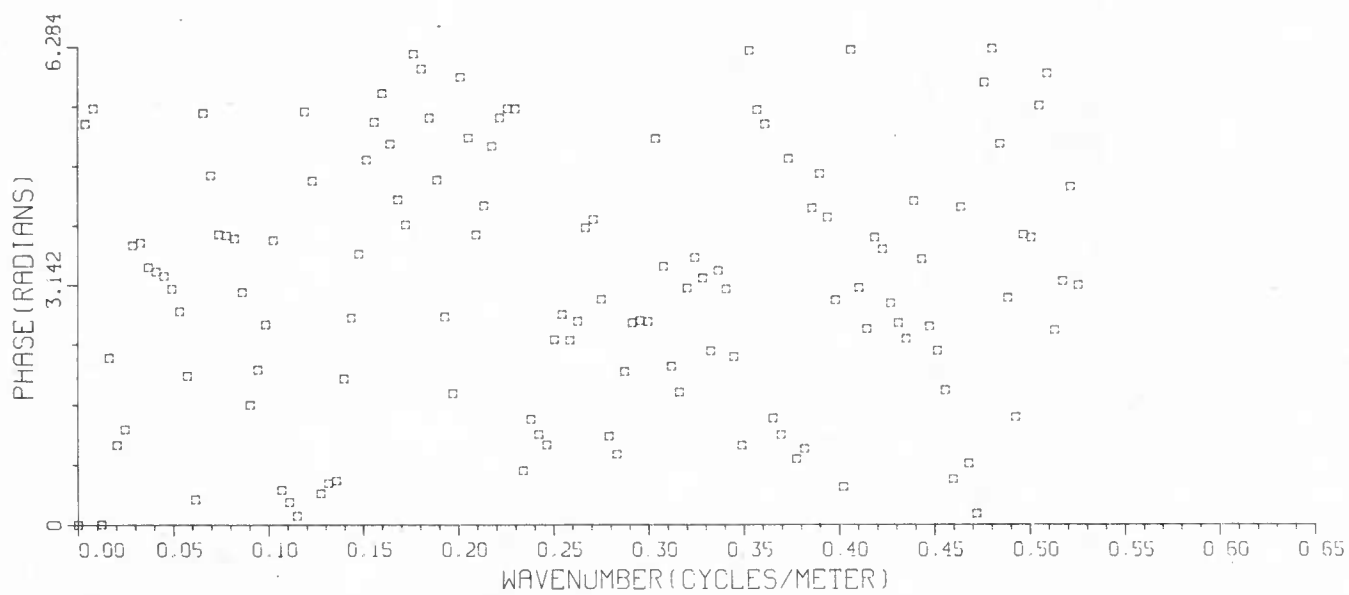
PHASE VS WAVENUMBER



COHERENCE VS WAVENUMBER
SITE 9C3



PHASE VS WAVENUMBER



For Site 7, the likely candidate for ridge building material was 0.3m thick undeformed ice. According to the above relationship, the wavenumber peaks associated with the block dimensions would be expected at 0.87, 1.29 and 3.33m^{-1} , wavenumbers exceeding the sampling used here. The high coherence found for the track separated by 0.22km may be due to features associated with the multi-year ice floes, for which there exists very little information on small scale features.

For Site 9 there were fairly long stretches of undeformed ice that ranged in thickness between 0.9-1.0m. High coherence peaks in wavenumber would be expected to occur at 1.0, 0.54 and 0.36m^{-1} . We find peaks at 0.44 and 0.39, and 1.0 is beyond our sampling capability.

For Site 8, the data set for the tracks separated by 0.60km it is possible to make an argument for a bimodal block thickness distribution with the four very high coherence peaks. The peak at 0.27m^{-1} paired with 0.435m^{-1} peak ($w/l = 0.62$), and the 0.35m^{-1} peak paired with the 0.5m^{-1} peak ($w/l = 0.70$). A second set of parallel tracks, with a 40m separation, may also have sampled the similar ridge phenomena in the block and rubble generic wavenumber band (shown in Figure 8). We can come up with three pairs of wavenumber with coherence peaks ($0.64/0.41$, $0.5/0.27$ and $0.37/0.19\text{m}^{-1}$) with reasonable w/l ratios representing ridge building blocks with mean thicknesses of 0.8, 1.4 and 2.2m respectively.

In future experiments we hope to obtain better resolution data to approximately 0.3m in order to include the building blocks for first year ice in our coherence analysis. These data are obtainable with a high resolution imaging sonar presently available which is deployed through a hole in the ice. Also to examine ice direction properties in proper detail greater azimuthal coverage is required, from a more highly sampled conventional sonar survey or the high resolution imaging sonar.

ACKNOWLEDGEMENTS

We wish to thank Richard Shell for computer programming support of this work. This research is supported by NUSC IR-IED and Arctic Program Office funds.

REFERENCES

- (1) Francois, R.E., High resolution observations of under-ice morphology, APL-UW Rep. 7712, 1977, 1-29.
- (2) Hibler, W.D., III, and L.A. LeSchack, Power spectrum analysis of undersea and surface sea-ice profiles, J. Glaciol., 11, 63, 1972, 345-356.
- (3) Hibler, W.D., III, Two dimensional statistical analysis of Arctic sea ridges, Sea Ice Conference Proceedings, Reykjavik, 1972, 261-275.
- (4) Leblanc, L.R., D.J. O'Neill, S.E. Overdeep, and J.R. Kelly, Analysis of the under Arctic ice roughness spectrum, NUSC Tech. Rep., in prep., 1985.
- (5) Mellen, R.H., and H.W. Marsh, Underwater sound reverberation in the Arctic, J. Acoustic. Soc. Am., 35, 1963, 1645-1648.
- (6) Weeks, W.F., Sea ice properties and geometry, AIDJEX Bull. No. 34, Dec. 1976, 137-205.
- (7) Overdeep, S.E., and G.C. Bishop, Sea ice pressure ridges: an algorithmic approach to their classification, morphology, and statistical aspects, in prep. for submission to J. Geophys. Res., 1985.
- (8) Cooley, J.W. and J.W. Tukey, An algorithm for the machine computation of complex Fourier series, Math. Comput., 1965, 19, 297-301.
- (9) Amos, D.E. and L.H. Koopmans, Tables of the distribution of the coefficient of coherence for stationary bivariate Gaussian processes. Nat. Tech. Info. Serv., U.S. Dept. Comm., 1963, 327 pp.
- (10) Mock, S.J., A.D. Hartwell, and W.D. Hibler III, Spatial aspects of pressure ridge statistics, J. Geophys. Res., 1972, 77, 30, 5945-5953.

- (11) Tucker, W.B. III and J.W. Govoni, Morphological investigations of first-year sea ice pressure ridge sails. *Cold Regions Science and Technology*, 1981, 5, 1-12.
- (12) Maykut, G.A., University of Washington heat and mass balance program, MIZEX Bull., Oct 84, MIZEX 84 summer experiment PI preliminary reports, CRREL Spec. Rep. 84-29, 76-77.
- (13) Tucker, W.B. III, D.S. Sodhi, and J.W. Govoni, Structure of first-year pressure ridge sails in the Prudhoe Bay region. *The Alaskan Beaufort Sea: Ecosystems and Environments*, 1985, 115-135.
- (14) NUSC/CRREL, unpublished data.

THE NUMBER OF ELASTIC CONSTANTS OF SEA ICE

Edward R. Floyd and Burton L. Markham

Arctic Submarine Laboratory
Naval Ocean Systems Center
San Diego, California 92152

ABSTRACT

In principle, broad sheets of sea ice tend to form polycrystalline aggregates with transverse isotropy. The elastic tensor of transverse isotropy is described by five independent constants [A. E. H. Love, *The Mathematical Theory of Elasticity* (University Press, Cambridge, 1927) p. 160] while only two independent constants are needed to describe the isotropic elastic tensor. Herein, we develop an effective elastic tensor for sea ice by assuming a nearly isotropic, transverse isotropy for broad sheets of sea ice. We describe the deviation from isotropy by a virtual, finite perturbing strain which maintains transverse isotropic sea ice. By a perturbation expansion, we show that the coefficients of this effective elastic tensor for sea ice may be described by only four independent constants. The relationship among the coefficients of this effective elastic tensor are developed in terms of the four independent constants.

1. INTRODUCTION

Sea ice is a polycrystalline aggregate that forms in broad, horizontally stratified sheets. This stratification manifests a transverse isotropy to first approximation (the term sea ice is reserved herein for pack ice). Polycrystalline aggregates with transverse isotropy (along the x,y-plane) have second-order strain coefficients for an elastic tensor that can be described by five independent constants such that:^{1,2}

$$c_{11} = c_{22}; \quad c_{33}; \quad c_{12} = c_{21};$$

$$c_{13} = c_{23} = c_{32} = c_{31};$$

$$c_{44} = c_{55}; \quad c_{66} = (c_{11} - c_{12})/2$$

where all other second-order coefficients are equal to zero.

Herein, we examine the elastic tensor for sea ice under the assumption that it has nearly isotropic, transverse isotropy. By this assumption, the difference between the symmetry of the polycrystalline aggregate for sea ice and

isotropic aggregates of ice is small. Our hypothesis is that elastic tensor of horizontally stratified sea ice may be described by a small, virtual perturbation of isotropic polycrystalline aggregates of ice. This virtual perturbation is time-independent and reduces the symmetry of the isotropic polycrystalline aggregate of ice to transverse isotropy. The perturbation is sufficiently small, but finite, so that a perturbation expansion of the elastic energy density function need only consider a power series in strain up to third-order terms. (While the elastic tensor is second order in strain, it is actually a fourth-order tensor as strain itself is a second-order polar tensor. Likewise, the third-order elastic coefficients³ are actually elements of a sixth-order tensor as they are third-order coefficients for second-order tensors. Herein, we shall denote the coefficients by order of strain except where explicitly noted to be the actual tensor order.) The perturbation that we apply herein is a simple virtual strain that induces a preferred vertical direction which, in turn, reduces isotropy to transverse isotropy. An effective elastic tensor (second order in strain) may then be developed for this perturbed system for subsequent strains much smaller than the perturbing virtual strain. We then proceed to develop the relationships among the second-order coefficients of this effective elastic tensor. We also show herein that the second-order coefficients for such an effective elastic tensor for transverse isotropy that is nearly isotropic may be described by only four independent constants.

2. THEORY

For isotropy, the second-order elastic coefficients are well known and may be described by two independent constants such that:

$$c_{11} = c_{22} = c_{33};$$

$$c_{12} = c_{13} = c_{23} = c_{32} = c_{31} = c_{21};$$

$$c_{44} = c_{55} = c_{66} = (c_{11} - c_{12})/2$$

where all other coefficients are zero. For isotropy, the third-order elastic coefficients are given by^{4,5}

$$C_{111} = C_{222} = C_{333};$$

$$C_{122} = C_{133} = C_{311} = C_{211} = C_{233} = C_{322}$$

and equal to the other permutations of the subscripts thereof;

$$C_{123} \text{ equal to the other permutations of the subscripts thereof;}$$

$$C_{144} = C_{255} = C_{366} = (C_{122} - C_{123})/2$$

and equal to the other permutations of the subscripts thereof;

$$C_{155} = C_{166} = C_{244} = C_{266} = C_{344}$$

$$= C_{355} = (C_{111} - C_{122})/4 \text{ and equal to the other permutations of the subscripts thereof;}$$

$$C_{456} = (C_{111} + 2C_{123} - 3C_{122})/8$$

and equal to the other permutations of the subscripts thereof.

All other third-order elastic coefficients are zero.

Let us perturb an isotropic material with a virtual, static, finite strain of only one component, ξ_{zz} . This virtual strain manifests the horizontal stratification of sea ice and reduces the symmetry from isotropy to transverse isotropy. ξ_{zz} is mathematically convenient; otherwise our results would be invariant with other strains that maintain transverse isotropy. The perturbing strain, ξ_{zz} , is sufficiently small so that the perturbed elastic energy density function, U , for additional infinitesimal, but real strains, ϵ_{ij} where $i, j = x, y, z$, may be described by a power series expansion in strain up to the third order.

$$U = (1/2)c_{ijkl}(\xi_{ij} + \epsilon_{ij})(\xi_{kl} + \epsilon_{kl})$$

$$+ (1/6)C_{ijk\ell mn}(\xi_{ij} + \epsilon_{ij})(\xi_{kl} + \epsilon_{kl})$$

$$+ \epsilon_{kl})(\xi_{mn} + \epsilon_{mn})$$

where on the right side of the above equation c and C are explicitly denoted to be fourth- and sixth-order tensors respectively and where, in only the above equation, the Einstein summation convention over the set $[x, y, z]$ on the indices appearing twice in any product. Note that by supposition for the perturbing strain $\xi_{ij} = \delta_{ij} \xi_{zz}$ where δ_{ij} is the Kronecker delta. The perturbed elastic energy density function may be expressed in terms of the independent constants for isotropy of the second- and third-order elastic coefficients by

$$U = (c_{11}/2)[\epsilon_{xx}^2 + \epsilon_{yy}^2 + (\xi_{zz} + \epsilon_{zz})^2]$$

$$+ c_{12}[\epsilon_{yy}(\xi_{zz} + \epsilon_{zz}) + (\xi_{zz} + \epsilon_{zz})\epsilon_{xx} + \epsilon_{xx}\epsilon_{yy}]$$

$$+ [(c_{11} - c_{12})/4][\epsilon_{yz}^2 + \epsilon_{zx}^2 + \epsilon_{xy}^2]$$

$$+ (c_{111}/6)[\epsilon_{xx}^3 + \epsilon_{yy}^3 + (\xi_{zz} + \epsilon_{zz})^3]$$

$$+ (c_{122}/2)[\epsilon_{xx}\epsilon_{yy}^2 + \epsilon_{xx}^2\epsilon_{yy}$$

$$+ \epsilon_{yy}(\xi_{zz} + \epsilon_{zz})^2$$

$$+ \epsilon_{yy}^2(\xi_{zz} + \epsilon_{zz})$$

$$+ (\xi_{zz} + \epsilon_{zz})\epsilon_{xx}^2$$

$$+ (\xi_{zz} + \epsilon_{zz})^2\epsilon_{xx}]$$

$$+ c_{123}[\epsilon_{xx}\epsilon_{yy}(\xi_{zz} + \epsilon_{zz})]$$

$$+ [(c_{122} - c_{123})/4][\epsilon_{xx}\epsilon_{yz}^2 + \epsilon_{yy}\epsilon_{zx}^2$$

$$+ (\xi_{zz} + \epsilon_{zz})\epsilon_{xy}^2]$$

$$+ [(c_{111} - c_{122})/8][\epsilon_{xx}(\epsilon_{xy}^2 + \epsilon_{zx}^2)$$

$$+ \epsilon_{yy}(\epsilon_{yz}^2 + \epsilon_{xy}^2)$$

$$+ (\xi_{zz} + \epsilon_{zz})(\epsilon_{zx}^2 + \epsilon_{yz}^2)]$$

$$+ [(c_{111} + 2c_{123} - 3c_{122})/8][\epsilon_{yz}\epsilon_{zx}\epsilon_{xy}].$$

The equilibrium perturbed elastic energy density function, U_0 , for sea ice is given by

$$U_0 = (c_{11}/2)\xi_{zz}^2 + (c_{111}/6)\xi_{zz}^3.$$

For the stress X_x , we have that

$$X_x = \partial U / \partial \epsilon_{xx}$$

$$= c_{11}\epsilon_{xx} + c_{12}(\epsilon_{yy} + \xi_{zz} + \epsilon_{zz})$$

$$+ c_{111}0(\epsilon^2) + c_{122}[\xi_{zz}\epsilon_{xx}$$

$$+ \xi_{zz}\epsilon_{zz} + 0(\epsilon^2)]$$

$$+ c_{123}[\xi_{zz}\epsilon_{yy} + 0(\epsilon^2)]. \quad (1)$$

We can now establish some of the second-order coefficients of an effective elastic tensor, Λ , for the perturbed system by marshalling those terms that are linear in ϵ in Eq. (1). Explicitly noting that Λ is actually a fourth-order tensor, we could also determine $\Lambda_{ijk\ell}$ by keeping only zeroth-order terms with respect to ϵ of $\partial^2 U / \partial \epsilon_{ij} \partial \epsilon_{k\ell}$. From Eq. (1), we have that

$$\Lambda_{11} = c_{11} + \xi_{zz}c_{122},$$

$$\Lambda_{12} = c_{12} + \xi_{zz}c_{123},$$

and

$$\Lambda_{13} = c_{12} + \epsilon_{zz}c_{122}.$$

By transverse symmetry, examination of the stress Y_y leads to $\Lambda_{22} = \Lambda_{11}$ and $\Lambda_{23} = \Lambda_{13}$. In the case of the stress Z_z , we have

$$\begin{aligned} Z_z &= \partial U / \partial \epsilon_{zz} \\ &= c_{11}(\epsilon_{zz} + \epsilon_{zz}) + c_{12}(\epsilon_{xx} + \epsilon_{yy}) \\ &\quad + c_{111}[(\epsilon_{zz}^2/2) + \epsilon_{zz}\epsilon_{zz} + 0(\epsilon^2)] \\ &\quad + c_{122}[\epsilon_{zz}(\epsilon_{yy} + \epsilon_{xx}) + 0(\epsilon^2)] \\ &\quad + c_{123}0(\epsilon^2). \end{aligned} \quad (2)$$

Equating linear coefficients of ϵ in Eq. (2), we can establish that

$$\Lambda_{33} = c_{11} + \epsilon_{zz}c_{111}.$$

The terms $c_{11}\epsilon_{zz}$ and $c_{111}\epsilon_{zz}^2/2$ in Eq. (2) are of order zero with respect to ϵ_{zz} and these terms contribute to the virtual perturbing stress associated with the static virtual perturbing strain ϵ_{zz} which maintains the elastic energy density function at its perturbed equilibrium, U_0 . Λ_{33} describes

the real stress beyond the perturbing stress.

For the stress, Y_z , we have that

$$\begin{aligned} Y_z &= \partial U / \partial \epsilon_{yz} \\ &= [(c_{11} - c_{12})/2]\epsilon_{yz} \\ &\quad + [(c_{111} - c_{122})/4][\epsilon_{zz}\epsilon_{yz} + 0(\epsilon^2)] \\ &\quad + c_{123}0(\epsilon^2). \end{aligned} \quad (3)$$

Equating linear coefficients of ϵ in Eq. (3), we can establish that

$$\begin{aligned} \Lambda_{44} &= (c_{11} - c_{12})/2 + \epsilon_{zz}(c_{111} - c_{122})/4 \\ &= [(c_{11} + \epsilon_{zz}c_{122}) + (c_{11} + \epsilon_{zz}c_{111}) \\ &\quad - 2(c_{12} + \epsilon_{zz}c_{122})]/4 \\ &= (\Lambda_{11} + \Lambda_{33} - 2\Lambda_{13})/4. \end{aligned}$$

By transverse symmetry, examination of the stress Z_x leads to $\Lambda_{44} = \Lambda_{55}$. In the case of the stress X_y , we have that

$$\begin{aligned} X_y &= \partial U / \partial \epsilon_{xy} \\ &= [(c_{11} - c_{12})/2]\epsilon_{xy} + c_{111}0(\epsilon^2) \\ &\quad + [(c_{122} - c_{123})/2][\epsilon_{zz}\epsilon_{xy} + 0(\epsilon^2)]. \end{aligned} \quad (4)$$

Equating linear coefficients of ϵ in Eq. (4), we can establish that

$$\begin{aligned} \Lambda_{66} &= (c_{11} - c_{12})/2 + \epsilon_{zz}(c_{122} - c_{123})/2 \\ &= (\Lambda_{11} - \Lambda_{12})/2 \end{aligned}$$

which is consistent with transverse isotropy.

All other second-order coefficients of the effective elastic tensor, Λ , for the perturbed system are zero. Thus, the tensor Λ contains only four independent constants: Λ_{11} , Λ_{12} , Λ_{13} , and Λ_{33} . The deviation of the tensor with the isotropic elastic tensor (second order in strain) is linear with respect to the perturbing strain, ϵ_{zz} .

3. SUMMARY

For sea ice that has nearly isotropic, transverse isotropy, an effective elastic tensor may be described by

$$\begin{aligned} \Lambda_{11} &= \Lambda_{22}; \quad \Lambda_{33}; \quad \Lambda_{12} = \Lambda_{21}; \\ \Lambda_{13} &= \Lambda_{23} = \Lambda_{32} = \Lambda_{31}; \\ \Lambda_{44} &= \Lambda_{55} = (\Lambda_{11} + \Lambda_{33} - 2\Lambda_{13})/4; \\ \Lambda_{66} &= (\Lambda_{11} - \Lambda_{12})/2 \end{aligned}$$

where all other second-order coefficients are zero.

REFERENCES

1. A. E. H. Love, *The Mathematical Theory of Elasticity* (University Press, Cambridge, 1927) p. 160.
2. W. P. Mason, *American Institute of Physics Handbook* 3rd ed., compiled by B. N. Taylor, W. H. Parker and D. N. Langenberg (McGraw-Hill, New York, 1972) p. 3-99.
3. R. F. S. Hearmon, *Acta Cryst.* **6**, 331-340 (1953).
4. F. D. Murnaghan, *Finite Deformations of an Elastic Solid* (Wiley, New York, 1951) p. 95.
5. R. N. Thurston and K. Brugger, *Phys. Rev.* **133**, A1604-A1610 (1964).

MECHANICAL PROPERTIES OF MULTI-YEAR
PRESSURE RIDGE ICE SAMPLES

J.A. Richter-Menge and G.F.N. Cox

U.S. Army Cold Regions Research and Engineering
Laboratory, Hanover, New Hampshire

ABSTRACT

Over 500 laboratory tests have recently been completed on ice samples collected from multi-year pressure ridges in the Alaskan Beaufort Sea. Tests were performed in uniaxial constant-strain-rate compression and tension and in confined compression. The tests were conducted at two temperatures, -5° and -20°C , and four strain rates ranging from 10^{-2} to 10^{-5} s^{-1} . This discussion summarizes the sample preparation and testing techniques used in the investigation and presents data on the compressive, tensile and confined compressive strength of multi-year ridge samples. This information is necessary for designing arctic structures and vessels that must withstand the impact of a multi-year pressure ridge.

1. INTRODUCTION

Multi-year pressure ridges are thick accumulations of broken ice blocks that have survived at least one melt season. Surface melting and subsequent freezing of the water in the ridge cavities produce a massive ice feature with few or no voids. Multi-year pressure ridges in excess of 30 meters thick have been observed off the Beaufort Sea coast (1).

Data on the mechanical properties of multi-year sea ice are necessary for developing arctic structures and vessels that must be designed to withstand the impact of a multi-year pressure ridge. Recently we completed a study that involved testing over 500 multi-year ridge ice samples. This study was designed to help us understand the structure and mechanical properties of the ice. The program consisted of two phases. The first phase included collecting samples of 10 different multi-year pressure ridges in the southern Beaufort Sea, developing a variety of test techniques, and performing 282 uniaxial compression, tension and confined compression tests on vertically cored samples (2,3). The majority of the tests were uniaxial constant-strain-rate compression tests. The results of the Phase I tests indicated that there was no significant difference in the mean compressive strength between samples taken from different pressure ridges (4). The main factor contributing to variations in the strength from test to test was associated with the extreme local variability of ice structure within a ridge (5).

The second phase of the program also included a field sampling program in the Alaskan Beaufort Sea (6). Vertically cored ice samples were collected from four different multi-year ridges. Matched horizontal and vertical pairs were also collected from one ridge to investigate the effect of sample orientation on the mean compressive strength. A total of 188 tests were completed. In Phase II the tests were equally divided among constant-strain-rate compression and tension and confined compression tests.

This paper briefly describes the sample preparation and test techniques developed in the program. Data on the compressive, tensile and confined compressive strength of the multi-year ridge ice samples will also be summarized. Additional results on the initial tangent modulus, residual strength and failure strain are given in Cox et al. (2,6).

2. ICE DESCRIPTION

Thin sections of each ice sample and two continuous vertical multi-year ridge cores revealed that the ice structure in a multi-year pressure ridge is highly variable (7). This variation is a result of the ridge building and consolidation processes that take place during the formation of a multi-year ridge. In general the ice structure in a multi-year ridge sample can be classified according to one of three major ice texture categories: granular, columnar or a mixture of columnar and granular (5). The number of samples of a given ice structure varied from one test condition to another. It is important to note this variation since work on multi-year ridge samples has shown that the mean compressive strength is significantly influenced by the percentage of columnar test specimens and the orientation of the ice crystals in these samples (6). Further analysis of the crystal orientation of columnar samples within the ridge has also shown that, in the ridges we sampled, most of the columnar blocks were lying in a nearly horizontal position or with the direction of crystal elongation nearly vertical (8).

The average salinity and density of the ice samples are presented in Table 1. In general the ice collected in the first phase of the program had a slightly higher density than the ice collected in the second phase. The average salinity of the

Table 1. Average salinity and density (-20°C) of ice samples obtained from ridges A, B and C during Phase II and all ridges from Phase I.

	Phase I	Phase II			
		Ridge A	Ridge B	Ridge C	Three ridges
Salinity ($^{\circ}/_{\infty}$)	1.26 ± 0.82	0.38 ± 0.49	1.29 ± 0.87	2.29 ± 1.19	1.34 ± 1.18
Density (Mg/m^3)	0.891 ± 0.026	0.834 ± 0.046	0.870 ± 0.035	0.888 ± 0.024	0.865 ± 0.042

samples collected during the first and second phases were similar.

3. SAMPLE PREPARATION AND TEST TECHNIQUES

Dumbbell specimens were prepared from 4-1/4-in.-diameter ice cores. Samples were first rough-cut on a bandsaw, and the ends were milled square on a milling machine to produce a 10-inch-long test specimen. Synthane end caps were then bonded to the sample using fresh water to freeze them to the milled end planes. The end-capped samples were turned on a lathe to a dumbbell shape. Compression samples had a neck diameter of 4.0 in., and the tension samples had a neck diameter of 3.5 in. The form tools used to prepare both the dumbbelled compression and tension samples had a radius of curvature equal to twice the diameter of the finished neck. This radius was chosen to minimize stress concentrations near the sample end planes. Every effort was made to produce properly sized, precision-machined test samples using recommended methods (9,10).

All of the tests — compression, tension and confined compression — were performed on a closed-loop electrohydraulic testing machine. The machine had two actuators with capacities of 1.1 and 0.11 MN and a fast-response, high-flow-rate servo-valve. The load frame of the machine had a capacity of 2.2 MN. Test temperatures were controlled within 0.5°C by placing the sample in an environmental chamber mounted between the columns of the testing machine. The lower machine platen was also refrigerated to eliminate any thermal gradient problems. Load and sample strain data were recorded on an XY plotter, a strip chart, and an FM magnetic tape recorder.

Strain rates in the unconfined uniaxial compression and tension tests were controlled by monitoring the full sample strain with an extensometer, which was attached to the synthane end caps bonded to the test specimen (Fig. 1). Strains on the necks of the specimens were also monitored with a pair of direct current displacement transducers (DCDTs) to provide accurate strain, strain rate and modulus data. The unconfined tests were programmed to continue to 5% full sample strain to examine post-yield behavior and the residual strength of the ice. Since this resulted in considerable deformation of the test specimen, strain rates could not be controlled by the transducers mounted on the ice.

Confined compression tests ($\sigma_1 > \sigma_2 = \sigma_3$) were performed using the triaxial cell shown schematically

in Figure 2. The cell was designed so that the confining radial pressure ramped in constant proportion to the applied axial stress ($\sigma_2/\sigma_1 = \text{constant}$). For a right circular cylindrical specimen, the ratio of the confining pressure to the axial stress is determined by the ratio of the diameter of the piston entering the cell (4.2 in.) to the diameter of the piston in the upper cylinder. Two ratios of confining pressure to axial stress were used, 0.25 and 0.50. The larger ratio was obtained by placing a reduction collar in the upper piston and using a correspondingly smaller diameter piston. Hydraulic fluid was used as the confining medium. A latex membrane was placed around the test specimen to prevent hydraulic fluid from permeating into the sample void spaces. The strain rate in the confined compression tests was controlled by the averaged output of two extensometers mounted on the shaft going into the triaxial cell (Fig. 3).

Details of the sample preparation and test techniques are given in Mellor et al. (3).

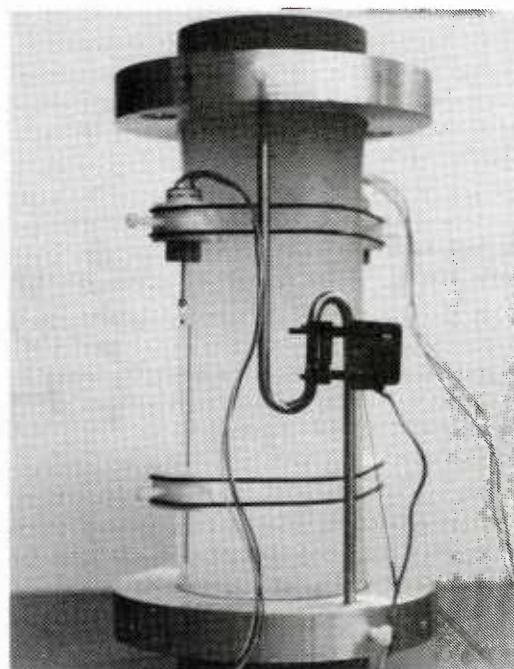


Figure 1. Instrumented unconfined uniaxial compression test. The same instrumentation was used in the uniaxial tension tests.

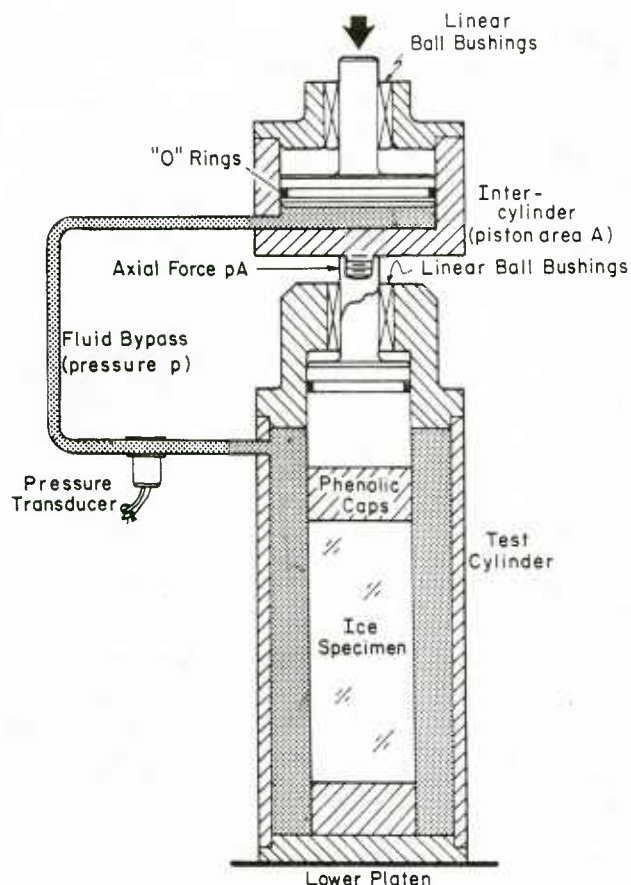


Figure 2. Schematic diagram of triaxial cell used for confined compression tests.

4. RESULTS AND DISCUSSION

Constant-Strain-Rate Uniaxial Compression Tests

Two hundred twenty-two constant-strain-rate uniaxial compression tests were performed on vertically cored multi-year ridge ice samples in the first phase of the program. The tests in Phase I were conducted at two strain rates 10^{-5} and 10^{-3} s^{-1} , and two temperatures, -20° and -5°C . In Phase II, 69 uniaxial compression tests were performed. These samples were tested at the same temperature but at different strain rates (10^{-4} and 10^{-2} s^{-1}) to supplement the tests performed in Phase I. Unlike Phase I, the Phase II unconfined compression tests were performed on both horizontal and vertical samples to assess the effect of sample orientation on ice strength. A summary of the compressive strength data for both phases of the project is given in Table 2. The mean compressive strength of the ice is plotted against strain rate in Figures 4 and 5.

At a given temperature and strain rate, the compressive strength data show considerable scatter. These large variations in strength can be explained by large variations in the ice structure and porosity (5). The strength of each specimen depends not only on the type of ice present in the specimen,

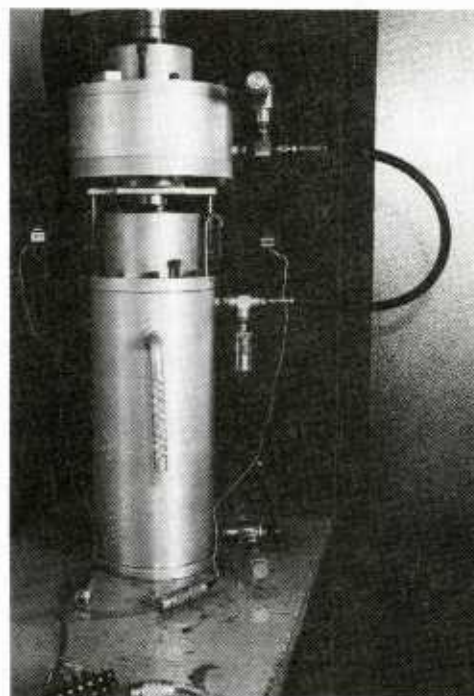


Figure 3. Triaxial cell used for confined compression tests.

which is highly variable from sample to sample, but also on the ice grain size and crystal orientation. Strength variations are further increased by variations in the ice porosity.

Based on our understanding of the variation of ice strength with strain rate, we would expect a power law relationship between ice strength and strain rate in the ductile range (11). On log-log paper, strength versus strain rate would plot as a straight line. The combined average test results of Phases I and II at -5°C do not show this tendency. The average strength of the 10^{-4} s^{-1} is lower than anticipated. However, at -20°C the 10^{-4} s^{-1} Phase II test average is in reasonable agreement with the 10^{-5} s^{-1} averages obtained in Phase I.

Since the strength of sea ice decreases with increasing porosity, it appears that the above observations can be explained in terms of the average ice porosity of the samples tested at each strain rate and temperature. In Table 2 mean porosities are given for the samples tested at each test condition. At -5°C the 10^{-4} s^{-1} tests have a much higher porosity than the tests conducted at 10^{-5} and 10^{-3} s^{-1} . At -20°C the mean porosities of the 10^{-5} , 10^{-4} and 10^{-3} s^{-1} tests are similar, and the average strength values do show a power law relationship.

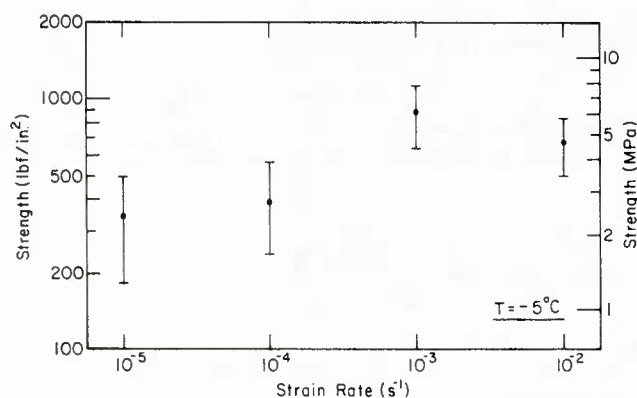


Figure 4. Mean uniaxial compressive strength versus strain rate for multi-year ridge samples tested at -5°C . The bars denote one standard deviation.

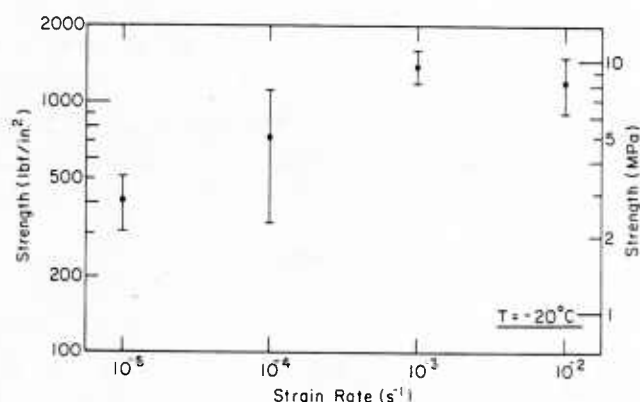


Figure 5. Mean uniaxial compressive strength versus strain rate for multi-year ridge samples tested at -20°C . The bars denote one standard deviation.

Table 2. Summary of compressive strength data for Phases I and II.

		Maximum		Minimum		Mean		Mean porosity (o/oo)	Number of samples
		(MPa)	(lbf/in. ²)	(MPa)	(lbf/in. ²)	(MPa)	(lbf/in. ²)		
-5°C (23°F)									
10 ⁻⁵	s ⁻¹ V*	7.52	1090	0.47	68	2.34±1.08	340±157	44	71
10 ⁻⁴	s ⁻¹ V	5.52	800	1.87	271	3.07±1.23	445±179	69	9
10 ⁻⁴	s ⁻¹ H	3.87	561	1.21	175	2.35±0.74	341±108	78	10
10 ⁻⁴	s ⁻¹ all	5.52	800	1.21	175	2.69±1.04	390±151	73	19
10 ⁻³	s ⁻¹ V	10.90	1580	2.39	346	6.06±1.63	879±237	46	69
10 ⁻²	s ⁻¹ V	6.42	931	2.69	390	4.67±1.17	677±169	68	9
-20°C (-4°F)									
10 ⁻⁵	s ⁻¹ V	4.26	617	1.17	170	2.79±0.69	404±100	36	41
10 ⁻⁴	s ⁻¹ V	12.73	1846	3.34	485	6.17±3.10	894±450	50	13
10 ⁻⁴	s ⁻¹ H	7.02	1018	1.68	243	3.74±1.67	543±242	33	12
10 ⁻⁴	s ⁻¹ all	12.73	1846	1.68	243	5.00±2.70	725±392	42	25
10 ⁻³	s ⁻¹ V	12.68	1838	7.03	1020	9.63±1.39	1396±202	39	41
10 ⁻²	s ⁻¹ V	10.48	1520	4.12	597	8.24±2.05	1195±297	74	9

*H - horizontal; V - vertical.

In addition to the variation in average ice porosity, we also note that at the $10^{-4} s^{-1}$ test condition, the mean compressive strength was obtained using both horizontal and vertical samples. At a given test temperature the mean compressive strength of the $10^{-4} s^{-1}$ horizontal samples alone is lower than the strength of the vertical samples (Table 2). The variation is a result of the orientation of the ice crystals in the columnar samples tested in each group, as discussed earlier (8). Results from tests on first-year sea ice samples indicate that the hard fail direction in columnar sea ice occurs when loads are applied parallel to the direction of elongation of the crystals (12, 13). Consequently the mean compressive strength of vertically cored multi-year ridge samples (loaded parallel to the direction of crystal elongation) will be higher than the mean compressive strength of horizontal ridge samples (loaded perpendicular

to the direction of elongation). The variation will depend on the number of columnar ice samples and their exact crystal orientation with respect to the loading direction. A high percentage of vertical columnar ice samples will be reflected in a relatively high mean compressive strength. This effect of sample orientation results in a lower mean compressive strength when the vertical and horizontal test data at $10^{-4} s^{-1}$ are combined.

In both the -5° and -20°C tests conducted at a strain rate of $10^{-2} s^{-1}$, there is an apparent decrease in ice strength relative to the tests conducted at $10^{-3} s^{-1}$. We attribute this decrease in strength to the much larger porosity of the $10^{-2} s^{-1}$ samples.

Table 3. Summary of uniaxial tensile strength data for Phase II.

	Maximum		Minimum		Mean		Mean porosity	Number of samples
	(MPa)	(lbf/in. ²)	(MPa)	(lbf/in. ²)	(MPa)	(lbf/in. ²)	(o/oo)	
-5°C (23°F)								
10 ⁻⁵ s ⁻¹ V*	1.03	149	0.57	82	0.82±0.17	119±24	78	9
10 ⁻³ s ⁻¹ V	0.83	120	0.41	60	0.61±0.16	89±23	108	9
-20°C (-4°F)								
10 ⁻⁵ s ⁻¹ V	0.92	134	0.49	71	0.71±0.16	103±23	82	9
10 ⁻³ s ⁻¹ V	0.92	134	0.48	69	0.75±0.16	109±23	77	9

*V - vertical.

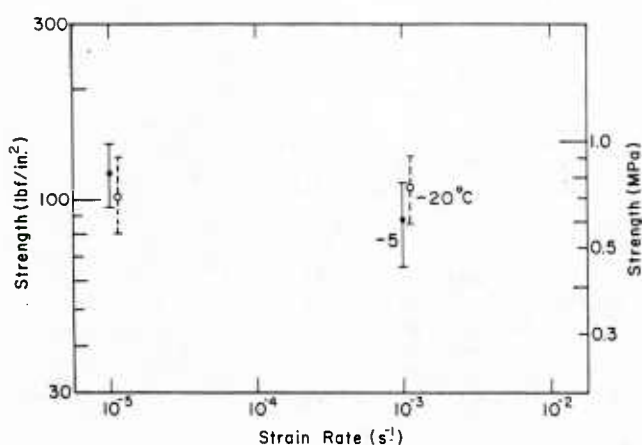


Figure 6. Mean uniaxial tensile strength versus strain rate for multi-year ridge samples tested at -20° and -5°C. The bars denote one standard deviation.

Constant-Strain-Rate Uniaxial Tension Tests

Thirty-six constant-strain-rate tension tests were performed on vertically oriented multi-year pressure ridge samples during the second phase of the program. The tests were conducted at two strain rates (10⁻⁵ and 10⁻³ s⁻¹) and two temperatures (-20° and -5°C). Nine tests were done at each test condition. A summary of the tensile strength data is given in Table 3. Strength data are plotted against strain rate in Figure 6.

In general the mean tensile strength shows no significant variation with strain rate or temperature. This behavior is consistent with data on the tensile strength of freshwater polycrystalline ice summarized by Mellor (11). At strain rates greater than 10⁻⁵ s⁻¹, the tensile strength of freshwater polycrystalline ice shows little or no variation with strain rate, and from -5° to -20°C, the strength only shows a very small increase. In contrast the results from Dykins' (14) uniaxial tensile tests on first-year sea ice show a strong temperature dependency. However, this large

strength variation is not due to changes in temperature of the pure ice matrix but rather a change in the ice brine volume or porosity. Since the salinity of the multi-year test specimens is very low, the brine porosity and strength of the ice show little variation with temperature.

The effect of ice crystal structure was also evident in the tensile tests on multi-year ridge samples. While the strength of the sample was not greatly influenced by the structural composition of the sample, the location of the failure plane was dependent on structural variability. For all test conditions, there was a definite tendency for the ice to fail in the part of the specimen containing the coarsest grains. This tendency has been observed in tensile tests on freshwater polycrystalline ice (15, 16, 17, 18). There were exceptions, however. For example, in a few tests containing brecciated ice (ice composed of columnar fragments in a granular matrix), failure occurred in the finer-grained granular ice when the columnar fragments were oriented with the direction of crystal elongation parallel to the load. In some ice samples containing both fine and coarse grains, failure was not associated with grain size. Instead, flaws in the specimen such as large voids and structure discontinuities controlled the fracture location (Fig. 7). Low strength values were usually associated with large voids and cavities in the specimen.

Confined Compression Constant-Strain-Rate Tests

A total of 55 confined compression or conventional triaxial tests ($\sigma_1 > \sigma_2 = \sigma_3$) were performed on multi-year pressure ridge samples at different test temperatures, strain rates and confining pressures during Phase II of the program. The number of tests at each test condition is summarized along with the confined compressive strength data in Table 4. The mean confined compressive strength of the ice, σ_1 , for each test condition is plotted against the confining pressure ($\sigma_2 = \sigma_3$) at failure in Figure 8. Mean uniaxial (unconfined) compressive strength data from the first phase of the test program are included for comparison. In making comparisons between the unconfined and confined compressive strength data, it should again be noted that the Phase I ridge samples generally had a lower porosity.

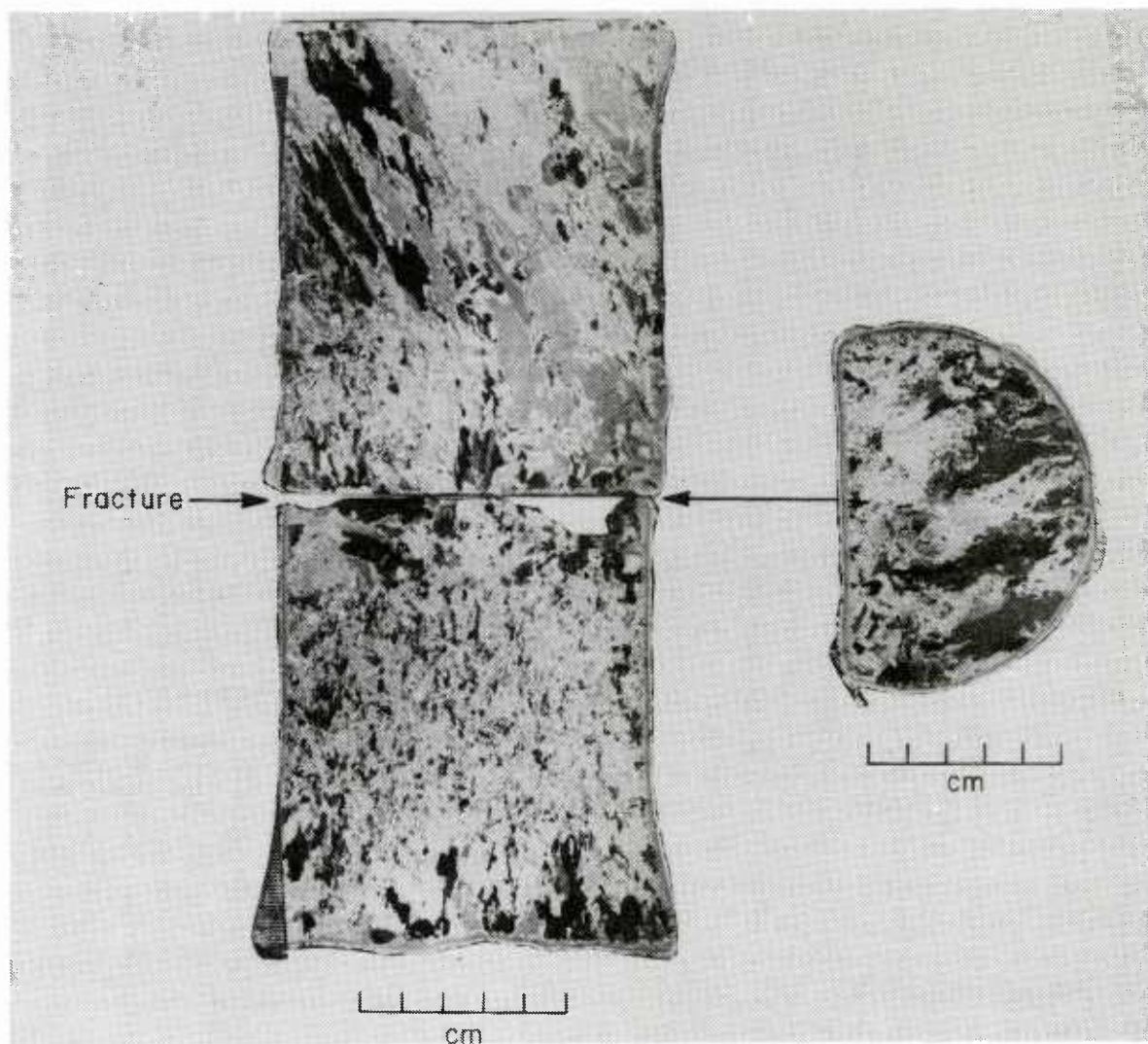


Figure 7. Photographs of ice thin sections taken in crossed polarized light to illustrate the location of fracture plane with respect to ice structure in a tension sample.

Table 4. Summary of confined strength data for different strain rates, temperatures and confining-pressure-to-axial-stress ratios (σ_2/σ_1).

σ_2/σ_1	Maximum		Minimum		Mean		Mean porosity (o/oo)	Number of samples	
	(MPa)	(lbf/in. ²)	(MPa)	(lbf/in. ²)	(MPa)	(lbf/in. ²)			
-5°C (23°F)									
10 ⁻⁵ s ⁻¹ V*	0.25	3.95	573	1.14	166	2.86±0.98	415±142	79	10
10 ⁻⁵ s ⁻¹ V	0.50	6.61	959	2.28	330	3.81±1.59	552±231	86	9
10 ⁻³ s ⁻¹ V	0.50	17.94	2602	5.43	788	11.70±3.41	1697±495	78	9
-20°C (-4°F)									
10 ⁻³ s ⁻¹ V	0.25	17.07	2475	11.58	1679	14.77±1.90	2141±275	77	9
10 ⁻⁵ s ⁻¹ V	0.50	11.03	1600	3.95	573	6.59±1.97	956±286	82	9
10 ⁻³ s ⁻¹ V	0.50	38.63	5602	8.34	1210	23.50±8.73	3408±1266	57	9

* V - Vertical.

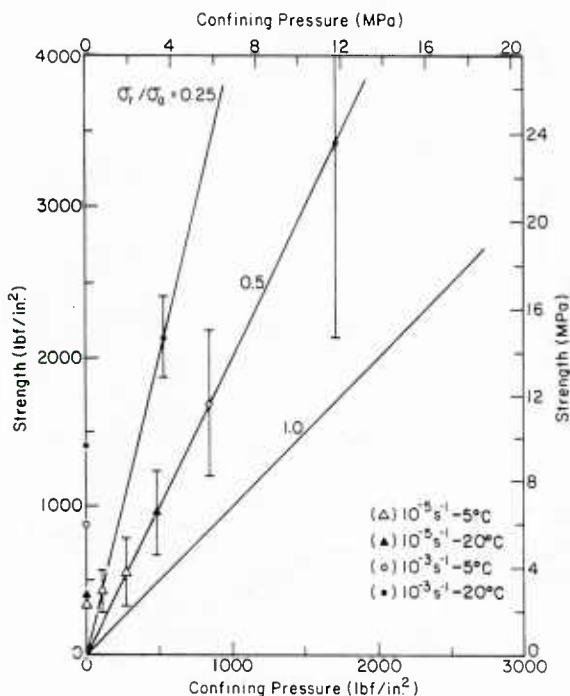


Figure 8. Mean compressive strength versus confining pressure for multi-year ridge samples at different temperatures and strain rates. The bars denote one standard deviation.

The confined compressive strength increases with increasing temperature, increasing strain rate, and increasing confining pressure. Due to variability of the ice structure between samples, the data show considerable scatter. The data at 10^{-5} s^{-1} suggest that failure of the ridge ice samples at low strain rates may be described by Tresca or von Mises yield criteria. The yield surface parallels the hydrostat ($\sigma_2/\sigma_1=1$). This supports the observations made by Jones (19), who investigated the confined compressive strength of freshwater polycrystalline ice at low strain rates.

5. CONCLUSIONS

The combined test results of this extensive test program provide a foundation for developing constitutive laws and failure criteria for multi-year pressure ridges. These results are incomplete, however, without a thorough examination of the influence of ice structure on the test results. Preliminary structure analyses have shown that the structure has a profound effect on the mechanical properties of the ice. Work is currently being done to structurally characterize each multi-year ridge ice specimen and to define the role that structure plays in determining ice strength.

It does appear that, in multi-year pressure ridges containing a large proportion of columnar sheet ice blocks, the horizontal ice strength may be significantly less than the vertical ice strength. This is because there may be preference for ice blocks to lie in a nearly horizontal position during

ridge formation. The results of this study and those of earlier investigators (12) have shown that horizontal sheet ice samples are significantly weaker than vertical sheet ice samples. More field studies of the internal structure of first-year and multi-year pressure ridges are needed to capitalize on this finding. Using ice strength data from vertically oriented ridge specimens may be conservative in horizontal ridge loading problems.

In general the compressive strength of multi-year ridge ice samples increases significantly with an increase in strain rate from 10^{-5} to 10^{-3} s^{-1} . Beyond 10^{-3} s^{-1} , where the ice is failing in a brittle manner, the compressive strength appears to level off. At a given strain rate, there is an increase in the compressive strength with a decrease in temperature and a decrease in porosity. An increase in the confining pressure surrounding the ice sample also results in an increase in strength.

The mean tensile strength of the multi-year ridge samples shows little variation with strain rate or temperature. Variations in strength are generally the result of the highly variable ice structure. There is a tendency for the tensile ice strength to decrease with increasing porosity.

Finally we note that one important addition to this series of test data still remains to be completed. This involves an investigation of the mechanical properties of multi-year ridge ice at high temperatures (-2°C). Information in this region of temperatures is needed to define the mechanical properties of pressure ridge keels.

6. ACKNOWLEDGEMENTS

This study was sponsored by Shell Development Company and the Minerals Management Service of the Department of the Interior with support from Amoco Production Company, Arco Oil and Gas Company, Chevron Oil Field Research Company, Exxon Production Research Company, Gulf Research and Development Company, Mitsui Engineering and Shipbuilding Company, the National Science Foundation, Sohio Petroleum Company, Texaco, the U.S. Department of Energy and the U.S. Coast Guard.

7. REFERENCES

1. Kovacs, A., Grounded ice in the fast ice zone along the Beaufort Sea coast of Alaska. U.S. Army Cold Regions Research and Engineering Laboratory, CRREL Report 76-32, 1976.
2. Cox, G.F.N., J.A. Richter-Menge, W.F. Weeks, M. Mellor and H.W. Bosworth, Mechanical properties of multi-year sea ice, Phase I: Test results. U.S. Army Cold Regions Research and Engineering Laboratory, CRREL Report 84-9, 1984.
3. Mellor, M., G.F.N. Cox and H.W. Bosworth, Mechanical properties of multi-year sea ice: Testing techniques. U.S. Army Cold Regions Research and Engineering Laboratory, CRREL Report 84-8, 1984.

4. Weeks, W.F., Variation of ice strength within and between multi-year pressure ridges in the Beaufort Sea. Proceedings, Third International Offshore Mechanics and Arctic Engineering Symposium, New Orleans, 1984, vol. 3, pp. 134-139.
5. Richter, J.A. and G.F.N. Cox, A preliminary examination of the effect of structure on the strength of ice samples from multi-year pressure ridges. Proceedings, Third International Offshore Mechanics and Arctic Engineering Symposium, New Orleans, 1984, pp. 140-144.
6. Cox, G.F.N., J.A. Richter-Menge, W.F. Weeks, M. Mellor, H.W. Bosworth, G. Durell and N. Perron, Mechanical properties of multi-year sea ice, Phase II: Test results. U.S. Army Cold Regions Research and Engineering Laboratory, in prep.
7. Richter-Menge, J.A. and G.F.N. Cox, Structure, salinity, and density of multi-year sea ice pressure ridges. Proceedings, Fourth International Offshore Mechanics and Arctic Engineering Symposium, Dallas, 1985.
8. Richter-Menge, J.A. and G.F.N. Cox, The effect of sample orientation on the compressive strength of multi-year pressure ridge ice samples. Proceedings, ASCE Arctic '85 Conference, San Francisco, CA., 1985.
9. Hawkes, I. and M. Mellor, Uniaxial testing in rock mechanics laboratories. Engineering Geology, 1970, vol. 4, pp. 177-285.
10. Schwarz, J., R. Frederking, V. Gavrillo, I.G. Petrov, K.I. Hirayama, M. Mellor, P. Tryde and K.D. Vaudrey, Standardized testing methods for measuring mechanical properties of ice. Cold Regions Science and Technology, 1981, vol. 4, pp. 245-253.
11. Mellor, M. Mechanical behavior of sea ice. U.S. Army Cold Regions Research and Engineering Laboratory, Monograph 83-1, 1983.
12. Peyton, H.R., Sea ice strength. Geophysical Institute, University of Alaska, Report UAG-182, 1966.
13. Wang, Y.S., Crystallographic studies and strength tests of field ice in the Alaskan Beaufort Sea. Proceedings, Fifth International Conference on Port and Ocean Engineering under Arctic Conditions, Trondheim, Norway, 1979, vol. 1, pp. 651-665.
14. Dykins, J.E., Ice engineering: Tensile properties of sea ice grown in a confined system. Naval Civil Engineering Laboratory, Technical Report R689, 1970.
15. Hawkes, I. and M. Mellor, Deformation and fracture of ice under uniaxial stress. Journal of Glaciology, 1972, vol. 11, no. 61, pp. 103-131.
16. Haynes, F.D. Effect of temperature on the strength of snow ice. U.S. Army Cold Regions Research and Engineering Laboratory, CRREL Report 78-27, 1978.
17. Currier, J.H. and E.M. Schulson, The tensile strength of ice as a function of grain size. Acta Metallurgica, 1982, vol. 30, pp. 1511-1514.
18. Schulson, E.M., P.N. Lim and R.E. Lee, A brittle to ductile transition in ice under tension. Philosophical Magazine, 1984, vol. 49, pp. 353-363.
19. Jones, S.J., The confined compressive strength of polycrystalline ice. Journal of Glaciology, 1982, vol. 28, no. 98, pp. 171-178.

EXPERIENCE WITH A BIAXIAL ICE STRESS SENSOR

Gordon F.N. Cox

U.S. Army Cold Regions Research and Engineering Laboratory
72 Lyme Road
Hanover, New Hampshire 03755-1290

ABSTRACT

A biaxial ice stress sensor has been developed to measure the magnitude and direction of the principal stresses in an ice sheet. Controlled laboratory tests indicate that the sensor has a resolution of 20 kPa and an accuracy of better than 10% under a variety of loading conditions. The sensor has been successfully used to measure thermal ice pressures in lakes and ice loads on a caisson-retained island in the Beaufort Sea.

1. INTRODUCTION

Reliable, inexpensive ice stress measurements are needed to solve a variety of ice-related problems. These include measuring and monitoring ice loads on marine and hydraulic structures; determining the magnitude of ice forces associated with ice drift, ride-up, pile-up and pressure ridge formation; measuring thermal ice pressures in reservoirs; and assessing the effects of ice convergence on the performance of large icebreakers and tankers.

During the past several years, a biaxial ice stress sensor has been under development at Oceanographic Services, Inc., CRREL, and IRAD Gage, Inc.^{2,5,6} This paper summarizes the results of controlled laboratory tests that were performed to evaluate the new biaxial gauge and presents the results from two ice stress measurement field programs.

2. BIAXIAL ICE STRESS SENSOR

The biaxial ice stress sensor consists of a stiff cylinder made of steel (Fig. 1 and 2). It is 20.3 cm long and 5.7 cm in diameter, and it has a wall thickness of 1.6 cm. The ends of the sensor are threaded such that a rounded end cap can be attached to the lower end of the sensor. Extension rods can also be screwed to the top of the sensor to position the sensing portion of the gauge at any desired depth in the ice sheet.

Principal ice stresses normal to the axis of the gauge are determined by measuring the radial deformation of the cylinder wall in three directions. This is accomplished by using the vibrating wire technology advanced by IRAD Gage.⁴ Three tensioned wires are set 120° from each other across the cylinder diameter (Fig. 2). The diametral deforma-

tion of the gauge in these three directions is determined by plucking each wire with a magnet/coil assembly and measuring the resonant frequency of the vibrating wires. A thermistor is also placed inside the cylinder to measure the gauge temperature. Both ends of the sensor are sealed to protect the wires and electronics from moisture. The sensor and data logging equipment are fabricated by IRAD Gage.

Despite the stiffness of the gauge, it is very sensitive to loading. Radial displacements as small as $5.0 \times 10^{-3} \mu\text{m}$ (2.0×10^{-7} in.) can be measured. This corresponds to a sensor resolution of about 20 kPa (3 lbf/in.²) when it is embedded in ice.

This design offers several advantages. The sensor is rugged and leakproof, and it can be easily installed in the ice using conventional ice augering equipment. As the sensor output is frequency, it is not affected by leakage to ground, poor contacts and long lead lengths. The sensor is also inexpensive (\$1900, including labor and materials).

The magnitude and direction of the principal stress (p , q and θ_1) are calculated from the radial deformation (V_{r1} , V_{r2} and V_{r3}) of the sensor wires by solving three simultaneous equations:

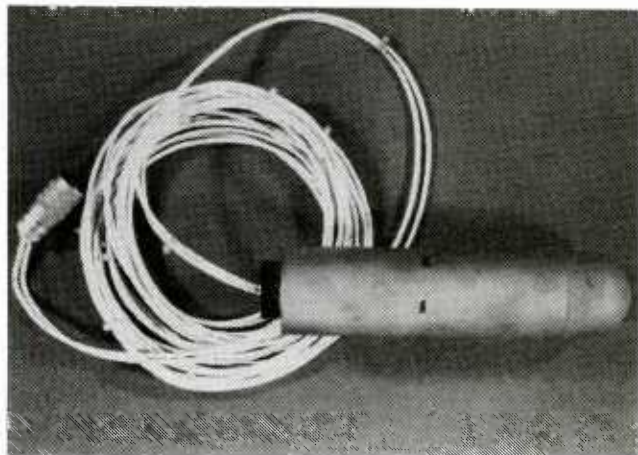


Figure 1. Biaxial ice stress sensor.

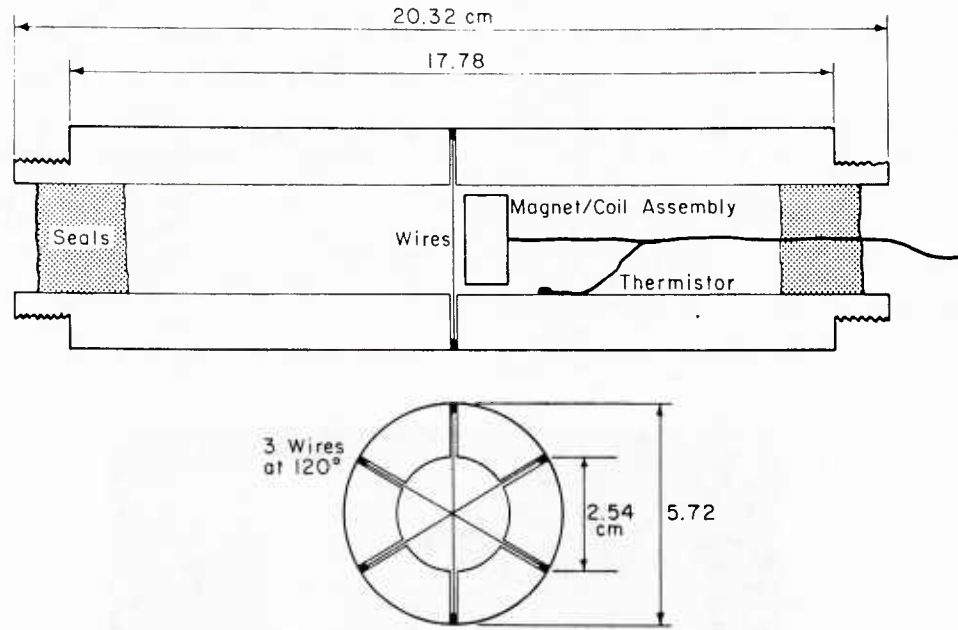


Figure 2. Schematic of biaxial ice stress sensor.

$$V_{r_1} = A(p+q) + B(p-q) \cos 2\theta_1$$

$$V_{r_2} = A(p+q) + B(p-q) \cos 2(\theta_1 + 60^\circ)$$

and

$$V_{r_3} = A(p+q) + B(p-q) \cos 2(\theta_1 + 120^\circ)$$

where A and B are constants that depend on the gauge geometry and the mechanical properties of the ice and the gauge. The sensor is designed such that A and B are relatively insensitive to variations in the ice modulus, E_i , and Poisson's ratio, ν . Equations for A and B are given in Cox and Johnson.² They are derived from analytical solutions that describe the behavior of an elastic ring welded in an elastic plate.¹⁰

The biaxial ice stress sensor is not calibrated in ice. It is calibrated in a hydraulic pressure cell to determine the initial frequency and the effective length of each vibrating wire. The gauge is radially loaded and the measured deformation of the gauge is compared to the radial deformation of a thick-wall cylinder.

3. EVALUATION TESTS

Controlled laboratory tests were performed to evaluate the biaxial ice stress sensor. Tests were first conducted to determine the temperature sensitivity of the gauge. The sensor was then frozen into large ice blocks and loaded in a biaxial loading machine to study the response of the sensor under different loading conditions. The effects of differential thermal expansion between the sensor

and surrounding ice were also examined, as was long-term sensor drift.

Temperature Sensitivity

The temperature sensitivity of the gauge was determined by placing the sensor in a glycol bath inside an environmental chamber. The temperature of the chamber and bath were varied, and sensor readings were taken at different temperatures. The sensor output was found to vary linearly with temperature, about 5 kPa/°C. Compared to the resolution of the gauge (20 kPa), the temperature sensitivity is small. In many short-term applications of the gauge, temperature corrections would not be needed. However, in situations where large variations in ice temperature did occur, the sensor output would have to be corrected to obtain the highest possible accuracy.

Biaxial Loading Tests

The response of the sensor to different loads was evaluated by freezing the sensor into large ice blocks and loading the blocks in a hydraulic, biaxial loading machine. The ice blocks used in these tests were 61 cm x 61 cm x 18 cm thick. The length and width of the ice blocks were chosen to accommodate the entire area of influence of the sensor, about ten diameters.

The blocks were grown from both fresh and saline water. The grain size of the crystals in the blocks varied between 0.5 and 2 cm. The fresh water blocks had both horizontal and vertical c-axis crystals, while the saline ice blocks had predominantly horizontal c-axis crystals. The c-axis did not show any preferred alignment in the

horizontal plane. The saline ice blocks had an average salinity of about 5 ‰.

The biaxial loading machine used in the stress sensor verification tests is shown in Figure 3. The machine consisted of two 0.4-MN-capacity hydraulic rams supported by two independent I-beam frames. The inside ram and frame rolled on casters to minimize shear stresses on the block during biaxial loading as well as to compensate for any lack of planar squareness of the ice blocks. The platens consisted of aluminum blocks covered with sheets of Teflon. They were only 58 cm wide to allow for about 3 cm of block strain during a

biaxial loading test. The platens were also free to rotate in the vertical plane to compensate for the lack of end squareness of the ice blocks.

Loads were applied to the ice blocks using the rams and a hydraulic hand pump. Control valves were used to direct the hydraulic fluid to one or both rams, and a hydraulic dial gauge was used to measure the load. The entire loading system was calibrated with a load cell prior to testing. Applied uniaxial stresses on the ice blocks had an accuracy of about 20 kPa. In a few tests, block strains were measured with direct current distance transducers attached to the platens.

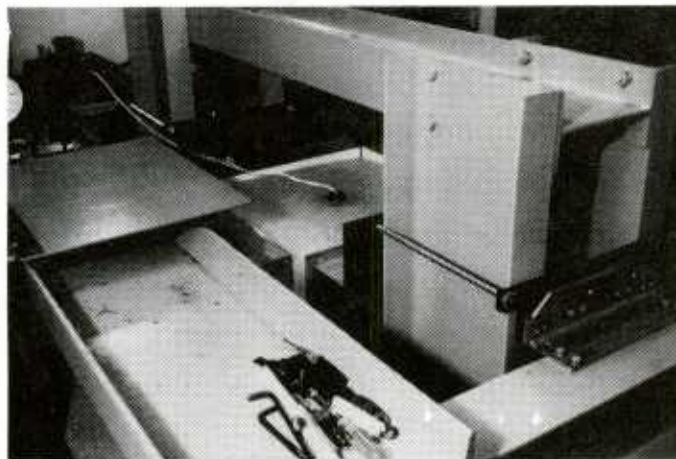


Figure 3. Ice block and sensor in biaxial loading machine.

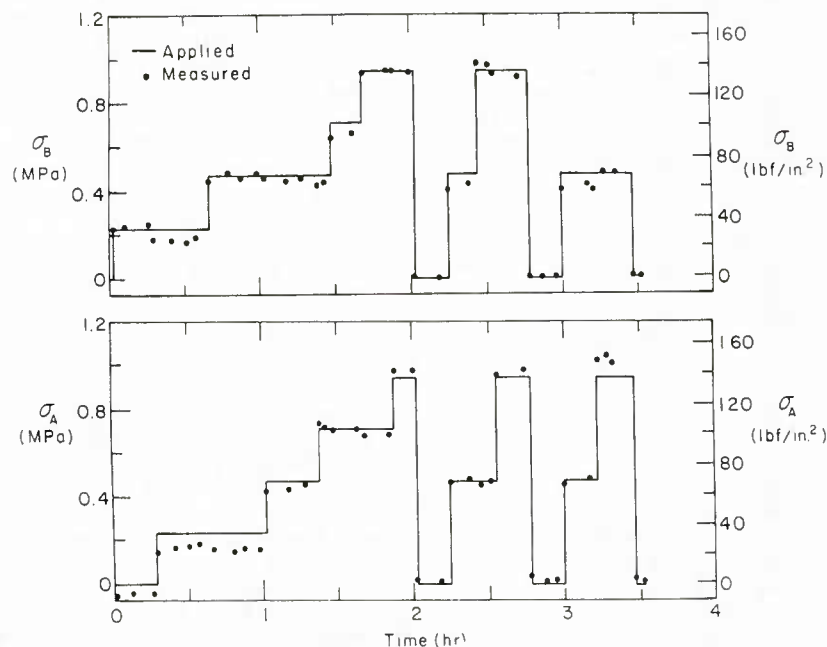


Figure 4. Measured versus applied stress for biaxial loading test where σ_A and σ_B are the loads in the two loading directions.

Four blocks were used in the loading tests to evaluate the sensor response to variations in the ice modulus, loading rate and loading direction. The results from a biaxial loading test on a saline ice block are shown in Figure 4.

The results of all the tests indicate that the sensor responds immediately to applied loads. In general, measured stresses were within 10% of the applied stress for both uniaxial and biaxial loading. The sensor response did not appear to be affected by ice creep, and when the applied stresses were removed, the measured stresses fell close to zero. Reliable stress measurements were also obtained well beyond yielding or failure of the ice. In addition the sensor usually determined the direction of the applied stresses to within 5°.

Differential Thermal Expansion

Metge et al.⁸ postulated that the response of a steel ice stress sensor would be greatly affected by differential thermal expansion between the ice and the gauge. To evaluate the effects of differential thermal expansion, a sensor was frozen into an ice block that was insulated on the top and bottom with foam. The temperature of the sensor and the block were then varied from -20°C to 0°C and back to -10°C to examine the response of the gauge. After the stress measurements were corrected for changes in temperature, the stress readings were generally within or equal to the resolution of the sensor, 20 kPa.

If ice were an elastic material, differential thermal expansion would be a problem. Because ice creeps under low stress, localized thermal stresses in the ice around the sensor rapidly relax and are unable to build up to any significant value.

Long-Term Drift

During the course of the evaluation, sensor readings were obtained to examine the stability of the unloaded gauge. Over a period of about 200 days, one of the wires in the sensor drifted, in a linear manner, 540 kPa, or about 2.7 kPa/d. According to IRAD Gage, the gauge fabricator, this behavior is caused by outward displacement of the clamps holding the wires in the sensor. It is therefore important in long-term measurement programs to obtain zero stress readings at a given temperature just before and after the measurement program.

4. THERMAL ICE PRESSURES IN LAKES

After the biaxial sensor successfully completed the rigorous laboratory tests at CRREL, several sensors were installed in the ice in a nearby lake to obtain field experience in deploying the sensor, as well as some preliminary measurements of thermal ice pressures. Field measurements are needed to verify and possibly improve existing thermal ice thrust prediction models for the design of dams, piers and other hydraulic structures subjected to ice.

The field measurement program was performed on Canaan Street Lake, Canaan, New Hampshire, during February and March, 1983³. Three sensors were installed in the ice about 25 m from shore on the northeast side of the lake. The sensors were placed about 6 m apart parallel to the shoreline. The sensing portion of the gauges was located 0.13 m below the surface of the 0.36-m-thick ice sheet. The results from two sensors are given in Figure 5; the data from the third sensor were rejected because the sensor exhibited considerable drift.

In general the stress measurements from the two sensors are in close agreement. This is particularly true for the stress components perpendicular to the shore. The difference between the stress measurements parallel to the shore is greater. Considering the proximity of the sensors to the beach, this may be due to the variation in the shear stress along the shore boundary. Spatial differences in stress may also be due to active cracks in the ice. The ice sheet was covered with snow, so the crack distribution pattern was not studied.

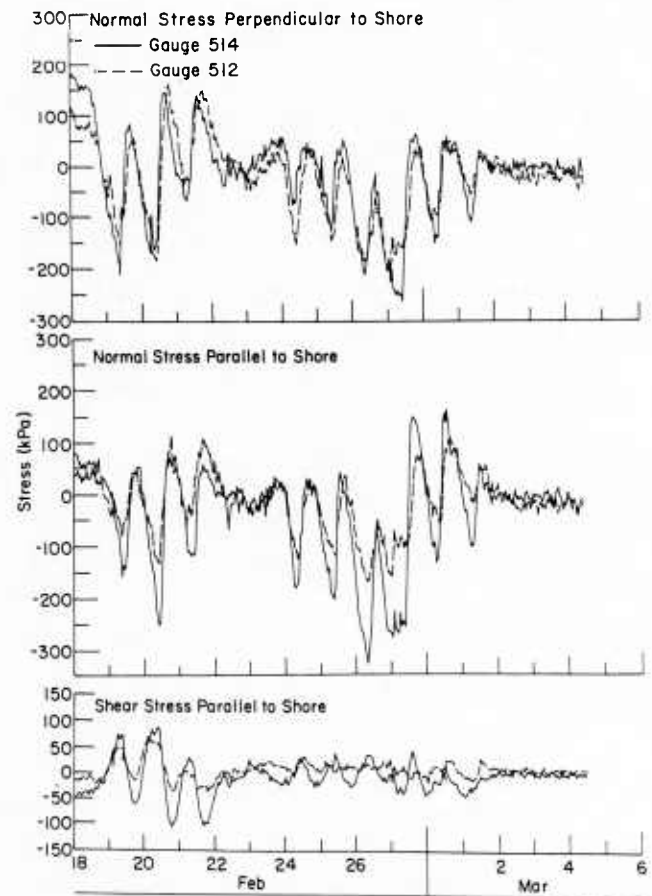


Figure 5. Measured ice stresses in the ice on Canaan Street Lake, NH.

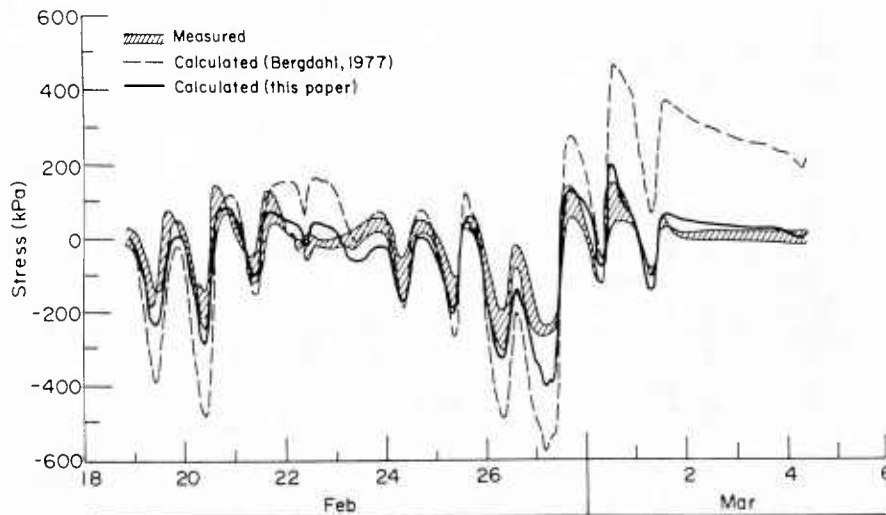


Figure 6. Measured (Gauge 514) versus calculated ice stresses.

Maximum compressive stresses perpendicular to the shoreline were about 140 kPa, while maximum tensile stresses approached 240 kPa. Peak stresses were greater parallel to the shoreline, about 210 kPa in compression and 310 kPa in tension.

Given the rate of change of temperature in the ice and the ice rheology, it is possible to calculate thermal ice pressures. Figure 6 presents calculated pressures using a model developed by Bergdahl¹ and an improved model developed by the author. In general, Bergdahl's model over-predicted stresses in the ice. By using more appropriate values for the ice modulus and a temperature-dependent creep rate factor, much better agreement was obtained between measured and calculated ice pressures.

5. ICE FORCES ON OFFSHORE ARCTIC STRUCTURES

Estimates of the magnitude of ice forces on offshore arctic structures can be obtained from analytical models, scale model tests, and field measurements. Unfortunately analytical models and model tests usually only provide upper-bound ice load estimates. In such models conservative assumptions are made to compensate for a lack of understanding of the ice failure mode and the large-scale mechanical properties of the ice cover. Field measurements of ice stress are needed to obtain actual ice loads on structures and for model tuning and verification.

During the spring of 1984, 18 biaxial ice stress sensors were deployed at six sites near ESSO's caisson-retained island (CRI).⁷ The CRI was located on a man-made berm in 14.5 m of water in Mackenzie Bay, Canada. In addition to measuring the total ice load on the island, the sensors provided information on the vertical and lateral stress distribution in the ice sheet.

The stress results from one of the six sites are shown in Figure 7. Here, P and Q are the principal stresses (positive value for compression), and θ is

the angle measured counterclockwise from the principal stress direction P to magnetic north. At this site the ice was 1.7 m thick, and sensors were placed at depths of 0.10, 0.42 and 1.09 m to provide a vertical stress profile.

It is evident from Figure 7 that the vertical stress distribution in an ice sheet can be complex. Contrary to our expectations, maximum stresses were not only observed in the top part of the ice sheet, but also in the middle and bottom of the ice sheet at different times. Secondary principal stresses were usually much smaller. During significant stress events (> 100 kPa), the principal stress directions tended to be aligned in the top, middle and bottom of the ice sheet, whereas during relatively quiet periods (< 100 kPa), the stress directions varied considerably with depth. Stresses at all depths also varied in a cyclic manner, in response to diurnal fluctuations in the air and ice temperatures.

The maximum measured compressive stress was about 500 kPa. This stress was measured in the top portion of the ice sheet at Site 1 on 27 March. The corresponding average full-thickness ice stress at this site was about 300 kPa. Tensile stresses were always lower than 140 kPa and may be a measure of the large-scale tensile strength of the ice cover.

The complexity of the vertical stress distribution suggests that the ice sheet was in a state of bending, and superimposed on the bending stresses, we also had local thermal stresses. This is probably reasonable, in that upward and downward bending of the ice sheet was observed along a rubble pile in front of the structure. Flexure failure of the ice sheet at the rubble pile would also explain the relatively low measured ice stress values.

The total load acting on the CRI and surrounding rubble during the measurement program is shown in Figure 8. Also shown are the ice temperature, wind speed and direction. The force vectors point in the direction of the applied load, and the wind

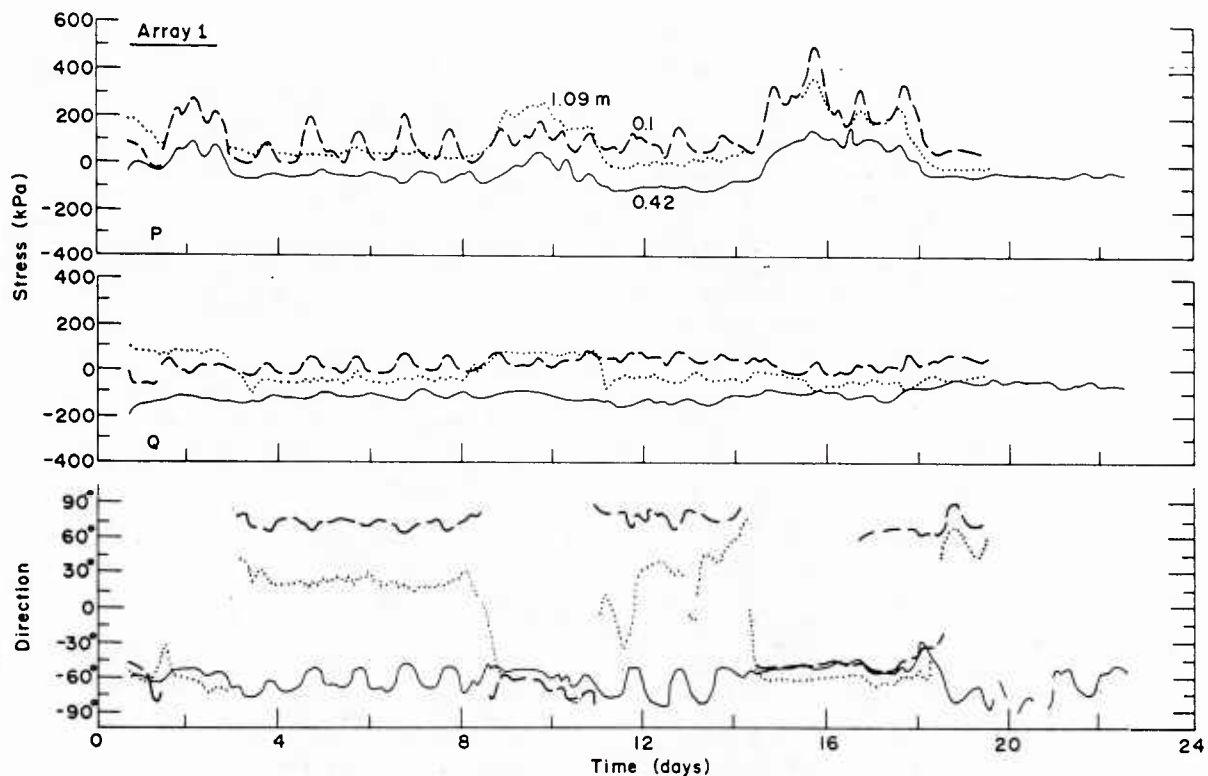


Figure 7. Vertical variation of ice stress at Site 1 during the latter part of March. Day 0 corresponds to March 12.

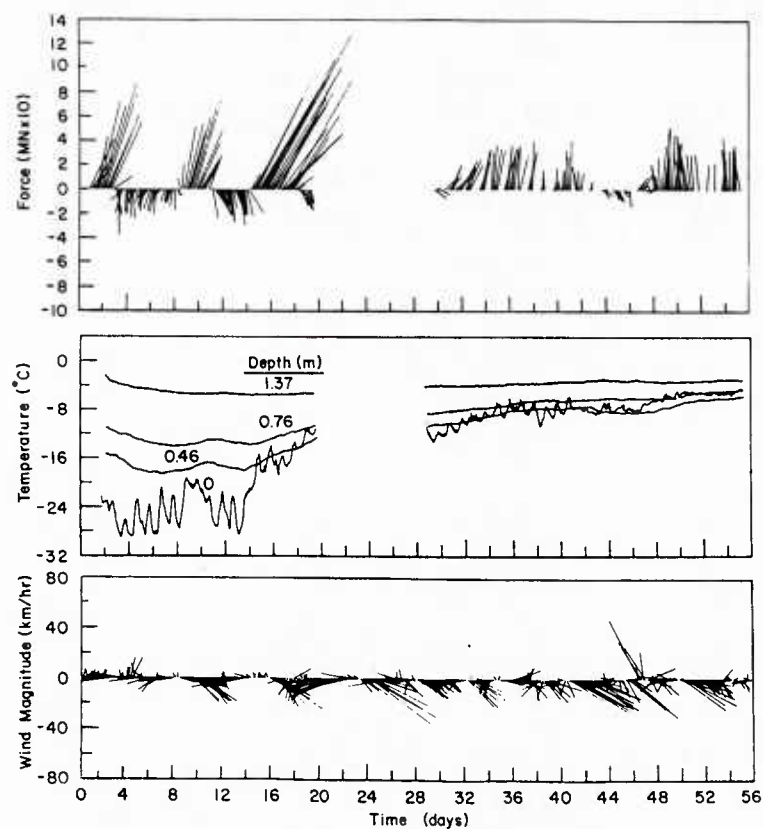


Figure 8. Ice forces acting on CRI-ice island-rubble complex, ice temperature, and wind data for measurement program.

vectors point in the direction the wind was blowing to. The maximum calculated load was 150 MN.

The ice load, ice temperature, and wind data indicate that all significant ice stress events were of thermal origin. During periods of high stress, winds were predominantly blowing to the south, while the forces were toward the north. The high-stress periods actually correspond very well to periods of ice sheet warming. The stresses are produced by the seaward motion of the ice as a result of the expansion of the ice sheet between the structure and the coastline.⁹

6. CONCLUSIONS

The biaxial ice stress sensor has proven to be a useful tool for understanding the stress distribution in ice sheets, thermal ice pressures, and ice forces on arctic structures. It is hoped that the gauge will be used in other applications, such as the measurement of ice stress in the arctic basin. Simultaneous measurements of stress and strain will enable researchers to formulate more realistic large-scale rheological models of the arctic pack for models of sea ice dynamics. The gauge may also be helpful for assessing the effects of ice convergence on the performance of icebreakers, submarine breakthrough in ice sheets, and sea ice penetration by projectiles.

7. REFERENCES

1. Bergdahl, L., Physics of ice and snow as effects thermal pressure. Chalmers University of Technology, Göteborg, Sweden, Report Series A:1, 1977.
2. Cox, G.F.N. and J.B. Johnson, Ice stress measurements. USA Cold Regions Research and Engineering Laboratory Report 83-23, 1983.
3. Cox, G.F.N., A preliminary investigation of thermal ice pressures. Cold Regions Science and Technology, 1984, vol. 9, pp. 221-229.
4. Hawkes, I. and W.V. Bailey, Design, develop, fabricate, test and demonstrate permissible low cost cylindrical stress gauges and associated components capable of measuring change of stress as a function of time in underground coal mines. U.S. Bureau of Mines Contract Report H0220050, NN, 1973.
5. Johnson, J.B. and G.F.N. Cox, The OSI ice stress sensor. Proceedings of the Workshop on Sea Ice Field Measurements, St. John's, Newfoundland. Center for Cold Oceans Resources Engineering, C-CORE Report 80-21, 1980, pp. 193-207.
6. Johnson, J.B. and G.F.N. Cox, Stress sensor particularly suited for elastic, plastic, and viscoelastic materials. United States Patent 4,346,600, 31 August, 1982.
7. Johnson, J.B., G.F.N., Cox and W.B. Tucker III, Kadluk ice stress measurement program. POAC '85, Narssarssuag, Greenland, 1985.
8. Metge, M., A. Strilchuk and P. Trofimenkoff, On recording stresses in ice. Proceedings, IAHR Third International Symposium on Ice Problems. 18-21 August, Hanover, N.H. USA Cold Regions Research and Engineering Laboratory, 1975, pp. 459-468.
9. Sanderson, T.J.O., Thermal ice forces against isolated structures. IAHR Ice Symposium, Hamburg, 1984.
10. Savin, G.N., Stress concentrations around holes. New York: Pergamon Press, 1961.

THE NUMERICAL SIMULATION OF SEA ICE INDUCED GOUGES ON THE SHELVES OF THE POLAR OCEANS

W.F. Weeks and W.B. Tucker III

USACRREL 72 Lyme Rd., Hanover, NH 03755

ABSTRACT

A simulation model for sea ice-induced gouges on the shelves of the polar seas is developed by assuming that the annual occurrence of new gouges is given by a Poisson distribution, the locations of the gouges are random, and the distribution of gouge depths is specified by an exponential distribution. Once a gouge is formed it is infilled by assuming a sediment input based on stratigraphic considerations and by calculating bed-load transport using methods from sediment transport theory. If currents are sufficient to transport sediment, rapid infilling of gouges occurs. In that these threshold currents are small for typical grain sizes, this suggests that the gouging record commonly represents only a few tens of years.

1. INTRODUCTION

That the keels of drifting pressure ridges can disturb the sea floor, resulting in entrained sediment in grounded ice masses, has been known for some time (6). Although this matter was initially largely of academic interest, it has recently become of considerable applied interest in that gouges in excess of 6 m deep are now known to have formed by this process along the coast of the Beaufort Sea in areas where oil and gas accumulations are known to occur. Such gouges clearly pose a threat to inadequately buried or insufficiently protected subsea structures such as pipelines or communication cables.

A variety of different studies have been undertaken since the early 1970's on the gouging phenomenon as observed on the Beaufort Shelf. A reasonably complete listing of the more important papers on this subject, as well as a general discussion of the physical environment of the Beaufort Shelf, can be found in Weeks et al. (16). In the present work we will be particularly concerned with papers that examine the statistical characteristics of these gouges (7,8,14,15,16) as well as with studies that help characterize the sedimentary and oceanographic environment in which the gouges occur (1,3,4,11).

A major difficulty in interpreting available data on gouging results from the fact that reliable observations on the rate of formation of new gouges and on the rate of infilling of existing gouges are, at best, limited. What is usually available are "snapshots" of the seafloor that provide us with the number of gouges and their orientations

(via side - scan sonar) and also their depths (via precision fathometry) at a given instant of time. To adequately use such "snapshots" it is necessary to know the period of time over which the observed gouge set formed. Needless to say, in assessing the hazards associated with the gouging process, it makes a great difference whether a given gouge set formed during the last 25 years or during the last 5000 years (to bracket the extreme positions on this matter). This latter figure results from the fact that observed sedimentation rates appear to be quite low on the Beaufort Shelf (0.05 to 0.2 cm yr^{-1}) based on the observation that on the average only about 3 m of recent (Holocene) sediments have accumulated since the study area was covered by the sea approximately 5000 years ago. Taking 0.06 cm yr^{-1} as a representative sedimentation rate (10) for the Alaskan Beaufort Shelf away from the major sediment source of the Mackenzie River, it can easily be calculated that it would take 1666 years to fill a 1-m-deep gouge and 5000 years to fill a 3-m-deep gouge. Clearly if no other process contributes significantly to gouge infilling, an observed gouge set could represent a long period of time.

It is also obvious that even on the relatively protected Beaufort Shelf, where the effective fetch in the summer is limited by the presence of nearby pack ice, hydrodynamic activity resulting from storms during ice-free periods is sufficient to rapidly erase gouges occurring in shallower water. For instance, field observations (4) have shown that the presumed large waves and wind-driven shelf currents associated with the extensive open water conditions observed during the summer of 1977 were sufficient to erase all gouges to a depth of 13 m and to cause pronounced infilling of gouges occurring in deeper water. Clearly in shallower waters the rates of sediment infilling associated with such episodic events are much greater than the average sediment accumulation rate. Recent work (11) has also suggested that even in the deepest water where gouges are observed (64 m or less along the Alaskan Beaufort Coast), the oceanographic conditions are sufficiently dynamic to result in the bedload transport of medium to coarse sand with the presumed result of rapid gouge infilling when viewed on a time scale of 5000 years.

Unfortunately there is, as yet, no direct method of determining the age of an existing gouge. Even if an appropriate technique can be developed, the problem of obtaining an adequate sample of the gouges that occur along the Beaufort Shelf would

appear to be daunting in that during many summers inhospitable ice conditions limit ship operations in the deeper shelf waters of most interest.

The present paper takes a rather different view of this general problem by attempting to develop a numerical model that for a given year sequentially estimates (1) the number of new gouges and (2) their initial depths. Then after combining the new gouges with gouges that are already in existence, a calculation is made of (3) the infilling of each gouge based on (4) the estimates of the appropriate environmental conditions. As will be seen estimates 1, 2 and 4 are essentially stochastic in nature while estimate 3 is deterministic. The overall model is therefore of a mixed nature. Then by sequencing the model through a variable number of years, one can begin to examine the evolution of the gouge depth distribution as a function of time as well as the effects of changes in different environmental parameters on model output. The result is a different method of examining the gouging phenomenon that provides one with new insights that can then be applied to the study of sets of field observations.

2. MODEL COMPONENTS

In the following we examine the general nature of the different components of the model as well as the observational basis for the assumptions that we will make relative to each of these components.

SEQUENCE OF EVENTS

In idealizing the gouging process we will separate the year into two seasons, winter and summer with winter representing the time period when the Beaufort Shelf is covered with essentially continuous pack ice and summer representing the time when the area is either ice-free or ice concentrations are low. The great majority of gouges undoubtedly form during the winter when the ice is thick and strong and large lateral stresses can be transmitted through the pack (ice-induced gouges obviously cannot form during ice-free summer periods). Probably gouging is most frequent during the early portion of the winter and during breakup when ice motions may be large.

Gouge infilling, on the other hand, is a process that must largely occur during the summer based on two different types of considerations. First the principal introduction of sediments into the Beaufort Sea from rivers such as the Colville and the Mackenzie occurs with the peak flows of the late spring and early summer. Second, it is only in the absence of an extensive ice cover, which both damps waves and limits the effective transfer of momentum from the atmosphere to the ocean, that currents and waves of sufficient energy to drive effective sediment transport and gouge infilling can occur. Therefore during each year the simplification of assuming gouge formation during the winter followed by gouge infilling during the summer is not only convenient but realistic.

NUMBER OF NEW GOUGES

We will use the Poisson distribution in our initial attempt at modeling the variations in the rate of new gouge formation. Our reasons are as follows: the distribution is simple in that it is completely described by one parameter (the mean annual gouge formation rate g), it is discrete in that we are representing a counting process (either a gouge has formed or it has not), it is capable of dealing with the occurrence of zero values, and it is the appropriate distribution to use when dealing with a Poisson process which describes the frequency of random events occurring at a constant rate on a continuous time scale. Also the Poisson distribution has proven to be extremely useful in treating a wide variety of arrival problems in science and engineering. The limited amount of information currently available on the number of new gouges $\text{km}^{-1} \text{yr}^{-1}$ is reviewed in Weeks et al. (16).

LOCATION OF NEW GOUGES

Studies of gouge distributions as observed along the Beaufort Coast (16) indicate that observed variations in the number of gouges per 100 m can also be well described by a Poisson distribution and that the spacings between gouges are given by an exponential distribution. Both of these results are to be expected if gouge occurrence in space is random (that gouging is a Poisson process in space as well as in time). It should, however, be remembered that in areas where there is appreciable bottom relief, gouges tend to be concentrated on the seaward-sides of shoals with low concentrations (shadow zones) occurring on the sheltered landward-sides.

GOUGE ORIENTATIONS

Data collected along the Beaufort coast indicate that there is an appreciable variation in gouge orientation with circular standard deviations of dominant orientations ranging from 7 to 17 degrees. Along the Alaskan coast, orientations showed the most variability in lagoons and shallow water (0-10 m) areas. In deeper water variations generally decreased. The average orientation in water deeper than 20 m was 98°T which is just a few degrees (ca. 10) less than parallel to the coast in this region (100°T). In most shallow water areas gouges occur at slightly higher angles to the coast (27 to 39°). Along the Canadian coast, north of the area between Mackenzie Bay and Cape Bathurst, mean orientations are similar (99 to 107°T) but their relation to the direction of the isobaths appears more variable as the topography is generally more complex.

DEPTH OF NEW GOUGES

Observations on the depth of gouge sets are invariably made from samples of indeterminate ages as they occur at a given time. The data have been found to be satisfactorily described by an exponential distribution

$$f_X(x) = \lambda e^{-\lambda x} \quad x \geq 0 \quad (1)$$

over four decades of relative frequency (7,8,16) with the free parameter λ varying systematically with water depth. For the Alaskan Beaufort, λ values vary from about 10 m^{-1} in shallow water to 2.5 m^{-1} in 30 m of water. The only published information on the relative frequency of occurrence of the depth of new gouges (16) suggests a similar type of distribution. It should also be pointed out that there are other reasons for believing that the exponential distribution is an appropriate distribution for new gouge depths. For example it is known that pressure ridge keel depths in the Beaufort Sea to the north of our present study area can be well described by an exponential distribution (13). In addition gouges are produced by the deepest of such keels (the extreme values) and the extreme value distributions that result from sampling a wide variety of initial distributions of an exponential type are also exponential in nature.

There is no information on the variation in λ with water depth for new gouges. In that the reported values were obtained in the water depth range of 4 to 20 m with a mean of roughly 15 m, the associated value of λ of 4.52 m^{-1} would appear to be somewhat lower than the value of 5.5 m^{-1} estimated from existing gouges. This is reasonable in that observations on the infilling of trenches in the sea floor indicate that deep trenches fill faster than shallow trenches.

INFILLING OF GOUGES

Regional Deposition: We will arbitrarily divide the sedimentation processes on the Beaufort shelf into two types. The first of these are the processes leading to the general deposition of sediment over the region. Observations on the thickness of the Holocene sediments indicate that sedimentation rates vary widely (thicknesses range from 0 to 10-m). A representative rate for the Alaskan Shelf is roughly 0.10 cm yr^{-1} although values as high as 0.60 cm yr^{-1} are found in the vicinity of Prudhoe Bay (2). For the Canadian Beaufort the rate gradually decreases from 0.2 cm yr^{-1} in shallow water (0 to 10 m) to 0.03 cm yr^{-1} in deeper water (50-80 m). A reasonable mean is 0.10 cm yr^{-1} , a value similar to the Alaskan mean. As might be expected, values also decrease with distance from the sediment source at the mouth of the Mackenzie (7).

As there is not enough information to attempt anything much more sophisticated, we will treat this sedimentary input as the deposition of a uniform, constant thickness annual layer over the sea floor. The sediment that falls into a gouge will be assumed to be concentrated in the bottom of the gouge as opposed to being "draped" over the sides of the gouge. This results in the most rapid infilling of the widest and presumably the deepest gouges.

Bedload Transport: A more difficult task is to calculate the infilling of each gouge that is in addition to that resulting from regional deposition. This process, which is driven by the wave

and current regime of the region, will be referred to as the local transport. It is this local transport that is believed to be the dominant factor in modifying the ice-produced bottom topography by infilling and ultimately erasing existing gouges (4,9). Fortunately recent investigations of sediment transport in the coastal environment particularly as focused on the infilling of trenches in the seafloor have made such calculations possible. In the following we will utilize the computational scheme suggested by Fredsoe (5). For details the reader should refer to the original paper. Also in the current paper we will only consider the bed-load transport produced by steady currents. As this neglects the suspended sediment component we are systematically underestimating the amount of sediment transport by a few percent. In later extensions of this work we plan to include this component as well as the effects of waves.

3. PROGRAM DESCRIPTION

A general flow diagram for the simulation program is shown in Figure 1. Inputs for a simulation run include the length of the run (number of years), the parameters α and λ which specify the Poisson distribution for the frequency of gouges and the exponential distribution for gouge depths and a set of information specifying the sedimentological and hydrodynamic environment. This environmental data set includes the water depth, current velocity, gouge slope (assumed to be constant), sediment grain size and relative density and the angle between the current and the gouges. The amount of bed-load transport by the assumed current is then

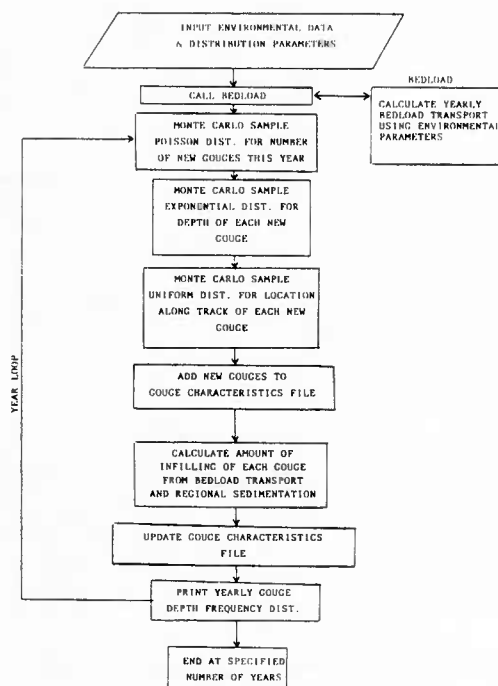


Figure 1. Flow diagram for the gouge simulation model.

calculated from the environmental parameters. Once calculated this quantity is taken as constant for every year of that particular run. This amount of transport q_b ($m s^{-1}$) is given (5) by

$$q_b = \sqrt{(\gamma-1)gd^3} 5p (\sqrt{\tau_d} - 0.7 \sqrt{\tau_{dc}}) \quad (2)$$

where

$$p = \{1 + [0.267/(\tau_d - \tau_{dc})]^4\}^{-1/4} \quad (3)$$

here γ is the relative sediment density, g is the gravitational constant, d is the mean grain diameter of the sediment, τ_d is the shear stress on the bed and τ_{dc} is the critical bed shear stress from the Shields diagram specifying the environmental conditions under which particles of that particular sediment just start to move.

The program then enters the "yearly" loop in which the number of new gouges are generated and infilling of existing gouges takes place. First the number of new gouges is obtained by Monte Carlo sampling of the Poisson distribution

$$f_X(x, \alpha) = \frac{\alpha^x e^{-\alpha}}{x!} \quad \begin{array}{l} x = 0, 1, 2, \dots; \\ \alpha > 0 \end{array} \quad (4)$$

Here α is the average rate of formation of new gouges per year per kilometer. Next the depth and along track location of each of the new gouges is established by Monte Carlo sampling of the exponential distribution and a uniform distribution respectively assuming a 1 km long track. The parameter λ which controls the shape of the exponential distribution is determined as a function of water depth (an input parameter).

The new gouge locations and depths are then merged with the gouge characteristics file which contains the depth and width of each preexisting gouge occurring along the sample path. Each new gouge is examined for overlap with preexisting gouges. Should overlap occur, the deeper of the two gouges is retained and the other gouge is deleted from the file.

Next infilling is calculated for all gouges. As discussed earlier, this is considered to occur in two steps. First the regional infilling with assumed constant thickness $h_R(1)$, where 1 is the sequential number of years, is introduced into each gouge. The general procedure and the appropriate equations are outlined in Figure 2. Then if the current is sufficiently large that bed-load transport occurs, the amount of sediment introduced per meter of gouge $A_{L(1)}$ (m^3/m) is calculated from

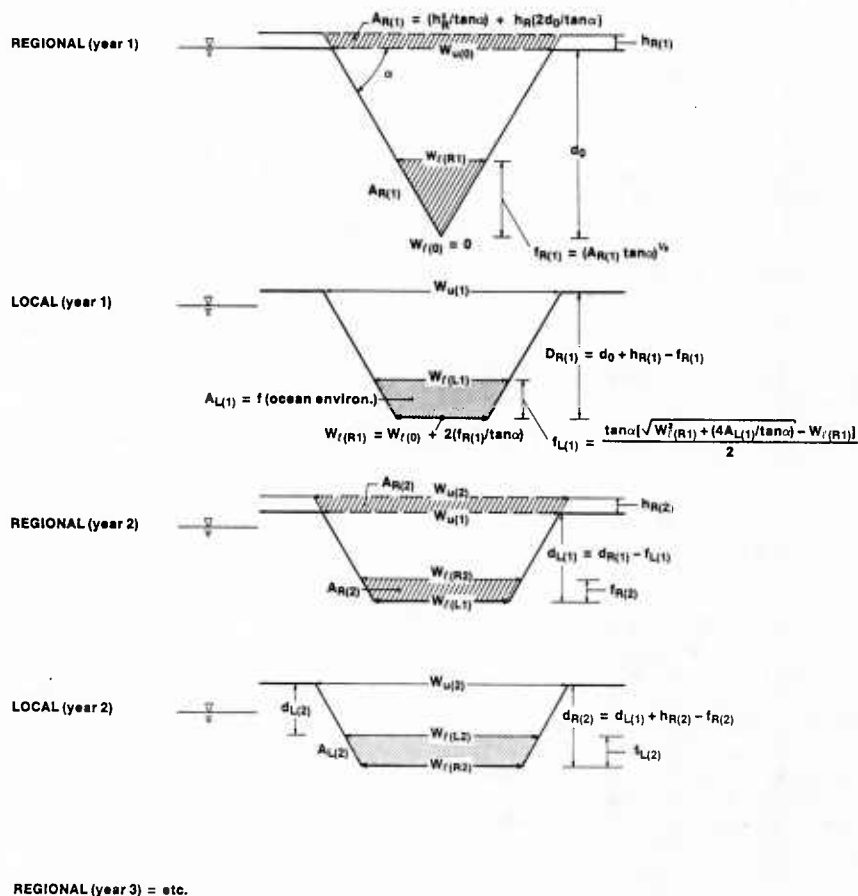


Figure 2. Diagram showing the gouge infilling strategy and the associated equations.

$$A_{L(i)} = 2D \frac{\sqrt{\delta}}{\sqrt{\pi}} (\sqrt{t + t_0} - \sqrt{t_0}) \quad (5)$$

where D is the gouge depth, δ is a parameter which is a function of q_b and also corrects the transport for the angular differences between the alignments of the current and of the gouge, t is the amount of time during which the current has been active and t_0 is a time constant. During the infilling process no modification of the gouge sides or of slope angles is assumed. The filled gouges are then deleted from the file and the bottom widths and depths of the surviving gouges are stored in the gouge characteristics file. At designated time intervals the gouges are binned according to depth and the depth frequency distribution is printed. The program then cycles back to the gouge creation routines unless the specified number of years has been completed.

4. PRELIMINARY RESULTS

As will be seen the modeling results are highly dependent on the assumed properties of the seafloor sediments. Corings of the subsea sediments along the Beaufort coast (12) have shown that, as along most coasts, sediment properties are highly variable. However, all holes showed fine-grained surface sections of marine sediments (fine sand, silt and clay) 2- to 12-m thick. As gouging is a surficial phenomenon we will only consider the properties of this layer which showed the following compositional variation: gravels, 0 to 5%; sands 5 to 75%; silts, 15 to 60%; and clays, 5 to 30%. The average values are 2% gravel, 51% sand, 31% silt and 15% clay. As sand and silt on the average comprise 82% of the surface sediment layer, in the following we will examine representative mean grain sizes for these two size classes (sand, 0.1 mm; silt, 0.01 mm). For both of these cases we will assume the following associated environmental conditions: water depth $D = 20$ m, average rate of new

gouge formation $g = 10$ gouges $\text{km}^{-1} \text{yr}^{-1}$, parameter for gouge depth distribution $\lambda = 3.5 \text{ m}^{-1}$, slope of gouge sides = 15° , relative density of the sediment $\gamma = 2.65$, rate of regional sediment deposition $h_R = 0.10 \text{ cm yr}^{-1}$, and the angle between the gouge and the current = 45° . With these conditions fixed we can then examine the effect of changes in the current velocity (v) on the resulting calculated gouge distribution. In the following, in calculating the amount of gouge infilling, we will assume that the current, taken to be constant, only operates for two months of each year (during the ice-free season).

Assuming that the sea floor is composed of unconsolidated sand, Figure 3 shows the estimated number of gouges that would be observed along a 1-km line plotted as a function of time for three different velocities $v = 0.1, 0.3$ and 0.5 m s^{-1} . Figure 4 shows the histograms of gouge depths as they are estimated to occur at the end of a 50-year period. For the sand considered, $v = 0.1 \text{ m s}^{-1}$ is just above the threshold. The results are rather surprising at first glance. At the end of 50 years, although on the average 500 gouges have occurred, only 161 gouges show in the record in the case of no sediment motion. This low value results from the low assumed angle for the slopes of the gouge sides which causes the gouges to be relatively quite wide (e.g. a 2-m deep gouge would be almost 15-m wide). Therefore many gouges occur "on-top-of" preexisting gouges. For instance, at the end of 50 years, 620-m of the 1-km track is gouged indicating a probability at that time of a new gouge occurring at an already gouged location to be 62%. Clearly in future work the general covering problem should be carefully considered. If current velocity is only slightly above the threshold velocity there is a drastic reduction in the number of gouges due to infilling (161 to 24) and at a current velocity of 0.5 m s^{-1} there are no gouges (all the gouges that formed have been infilled).

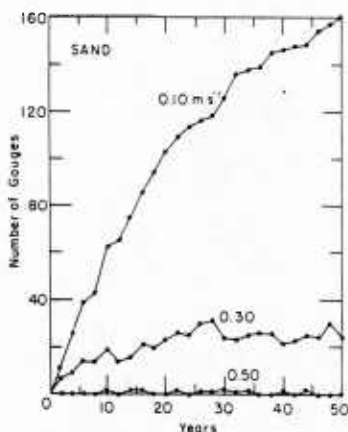


Figure 3. The number of gouges (intersecting a 1-km line) shown as a function of time and mean current velocity assuming seabed is composed of unconsolidated sand (see text for details).

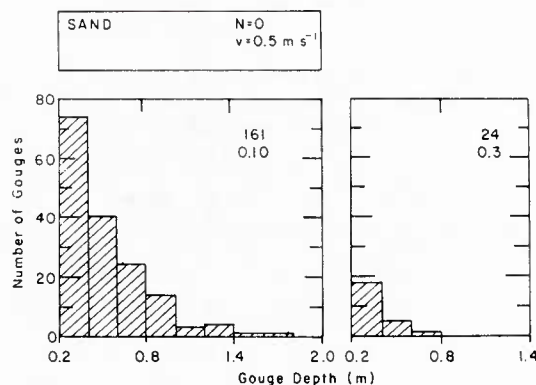


Figure 4. Histograms of the number of gouges of different depths (intersecting a 1-km line) that occur after a 50-year simulation assuming a seabed of unconsolidated sand.

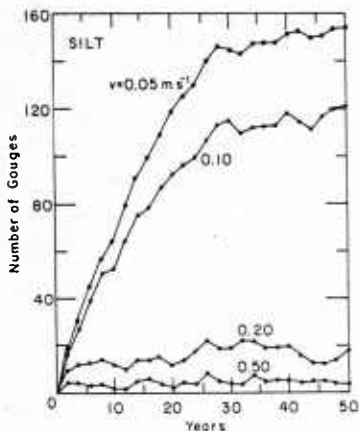


Figure 5. The number of gouges (intersecting a 1-km line) shown as a function of time and mean current velocity assuming seabed is composed of unconsolidated silt (see text for details).

MUST NOT

The results for silt (Figs. 5 and 6) are similar with $v = 0.05 \text{ m s}^{-1}$ being below and $v = 0.10 \text{ m s}^{-1}$ being just above the threshold value for sediment movement. Note that the 0.10 m s^{-1} histogram shows both fewer gouges and a systematic bias toward smaller gouges when contrasted with the 0.05 m s^{-1} histogram. At the higher current speeds there is a drastic decrease in both the number and the depth of the existing gouges.

5. CONCLUSIONS

To date work on the ice gouging phenomenon has been completely focused on the question of safe burial depths for offshore pipelines. This is a complex problem in that deep burial, that would clearly place the pipeline beneath a maximum probable gouge, invariably places the line nearer or even in subsea permafrost where the heat produced by the flowing oil could cause melting, compaction and slumping with the possibility of associated pipeline failure.

The naval problem is somewhat different in that it presumably would be primarily focused on emplacing reliable communication lines and sensing devices on the floors of the arctic shelves. Fortunately such systems do not usually generate significant amounts of heat and could reasonably safely be installed near bonded permafrost without anticipating significant problems. The difficulty is in establishing the appropriate environmental conditions that apply to a given site or region. If this type of information can be obtained prior to system installation, modeling approaches such as discussed in this paper could be very useful in optimizing emplacement procedures to provide a maximum system lifetime.

In the future we plan to utilize this simulation model to explore a number of problems relating to gouging, for instance sensitivity studies of a

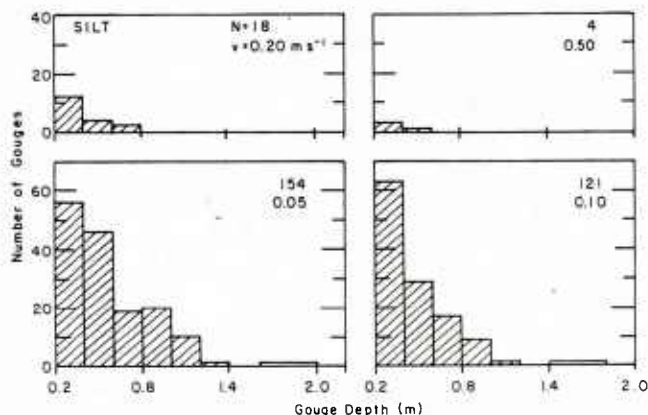


Figure 6. Histograms of the number of gouges of different depths (intersecting a 1-km line) that occur after a 50-year simulation assuming a seabed of unconsolidated silt.

variety of sediment and environmental parameters. We also intend to more fully develop the model to include suspended sediment and combined wave and current regimes. Associated with this latter effort we are attempting to develop an expanded wave and current climatology for the Beaufort coast.

6. ACKNOWLEDGEMENTS

This research program was supported by the Arctic Technology Program of the Department of Energy.

7. REFERENCES

- 1) Aagaard, K. (1984) The Beaufort undercurrent. In "The Alaskan Beaufort Sea: Ecosystems and Environments" (P.W. Barnes, D.M. Schell and E. Reimnitz, eds.) Academic Press, New York, 47-71.
- 2) APO, Akaska Project Office (1978) Environmental Assessment of the Alaskan Continental Shelf, Interim Synthesis: Beaufort/Chukchi. NOAA Environmental Research Laboratories, Boulder, Colorado.
- 3) Barnes, P.W. and Reimnitz, E. (1974) Sedimentary processes on Arctic shelves off the north coast of Alaska. In "The Coast and Shelf of the Beaufort Sea" (J.C. Reed and J.E. Sater, eds.). Arlington, Virginia: Arctic Institute of North America, p. 539-76.
- 4) Barnes, P.W. and Reimnitz, E. (1979) Ice gouge obliteration and sediment redistribution event, 1977-1978, Beaufort Sea, Alaska. U.S. Geological Survey Open File Report 79-848, 22 pp.

- 5) Fredsoe, J. (1979) Natural backfilling of pipeline trenches. *Journal of Petroleum Technology*, October, 1223-1230.
- 6) Kindle, E.M. (1924) Observations on ice-bourne sediments by the Canadian and other arctic expeditions. *American Journal of Science* 7:251-86.
- 7) Lewis, C.F.M. (1977a) Bottom scour by sea ice in the southern Beaufort Sea. Department of Fisheries and the Environment, Beaufort Sea Technical Report 23 (draft). Beaufort Sea Project, Victoria, British Columbia, 88 pp.
- 8) Lewis, C.F.M. (1977b) The frequency and magnitude of ice drift groundings from ice-scour tracks in the Canadian Beaufort Sea. In "Proceedings 4th International Conference on Port and Ocean Engineering Under Arctic Conditions," Memorial University, Newfoundland, 1:567-76.
- 9) Pilkington, G.R. and Marcellus, R.W. (1981) Methods of determining pipeline trench depths in the Canadian Beaufort Sea. POAC'84 Proceedings, the 6th International Conference, II, 674-687.
- 10) Reimnitz, E., Barnes, P.W., Toimil, L.J. and Melchoir, J. (1977) Ice gouge recurrence and rates of sediment reworking, Beaufort Sea, Alaska. *Geology* 5:405-408.
- 11) Reimnitz, E., Barnes, P.W. and Phillips, R.L. (1984) Geological evidence for 60 m deep pressure ridge keels in the Arctic Ocean. *IAHR Ice Symposium 1984, Hamburg, Proceedings Vol. II: 189-206.*
- 12) Sellmann, P.V. and Chamberlain, E.J. (1980) Permafrost beneath the Beaufort Sea: Near Prudhoe Bay, Alaska. *Journal of Energy Resources Technology* 102:35-48.
- 13) Wadhams, P. and Horne, R.J. (1980) An analysis of ice profiles obtained by submarine sonar in the Beaufort Sea. *Journal of Glaciology* 25(3):401-424.
- 14) Wahlgren, R.V. (1979a) Ice-scour tracks on the Beaufort Sea continental shelf - Their form and an interpretation of the processes creating them. M.A. Thesis, Dept. of Geography, Carleton University, Ottawa, 183 pp.
- 15) Wahlgren, R.V. (1979b) Ice-scour tracks in eastern Mackenzie Bay and north of Pullen Island, Beaufort Sea. In "Current Research," Part B. Geological Survey of Canada, Paper 79-1B:51-53.
- 16) Weeks, W.F., Barnes, P.W., Rearic, D.M. and Reimnitz, E. (1983) Statistical aspects of ice gouging on the Alaskan Shelf of the Beaufort Sea. *CRREL Report 83-21*, 34 pp.

Cryospheric Data Management System for Special Sensor Microwave Imager DMSP Data
A Status Report

Ronald Weaver, Scientific Manager

National Snow and Ice Data Center
CIRES, University of Colorado, Boulder, Colorado 80309

ABSTRACT

In 1986 the Defense Meteorological Satellite Program will launch a high resolution, microwave imager which for the first time, will provide real-time microwave data on sea ice, atmospheric moisture and precipitation, soil moisture, and ocean parameters. Both the U.S. Air Force and the Navy plan operational use of the Special Sensor Microwave Imager (SSM/I) data. However, there will also be many applications for these data after operational needs are met.

National Snow and Ice Data Center (NSIDC) has been funded by NASA Polar Oceans Program to develop a computer based Cryospheric Data Management System (CDMS). This will extract the polar SSM/I data and make them readily available to the "secondary" or non-operational user community.

1. INTRODUCTION

Satellite based data sources for study of polar oceanography will increase dramatically during the next decade due to the planned launching of several satellites. Currently planned satellites include GEOSAT, TOPEX, N-ROSS, DMSP-SSM/I, ERS-1, and RADARSAT. Each of these satellites either include partial or complete capabilities for passive and active microwave imaging, profiling, and altimetry systems. There will exist unprecedented opportunity for utilization of these data in sea ice, sea state, surface winds, and atmospheric sounding, research^{1,2}.

With respect to sea ice observations, these sensor systems for the first time will provide routine high resolution, daily, all-weather coverage. The SSM/I will be the first operational passive microwave imaging sensor. Based on current research trends (cf.³) and a survey of potential Nimbus 7 Scanning Multichannel Microwave Radiometer (SMMR) sea ice data users⁴, we conclude that the SSM/I microwave data will be of wide interest to the research community.

In order to assure effective use of the SSM/I data for polar cryospheric research, NASA Polar Oceans Program organized a Science Working Group (SWG) for the SSM/I. The SWG was tasked to decide (a) which problems of sea ice research could most appropriately be addressed using SSM/I data and (b) what are the associated SSM/I data requirements to help solve these problems. The remainder of this paper describes the implementation of the SWG recommendations³ for data requirements.

2. CDMS DESIGN RATIONALE

The need for a computer-based integrated data management and access system has been recognized by the NSIDC for several years⁵. The NSIDC/WDC experience, as reported in Glaciological Data,^{6,7,8}, has shown some problem areas associated with producing climatological archives which arise from the fact that most sea ice/snow cover analyses are performed on an operational basis. Several consequences of this approach are apparent. Because of time constraints not all of the potential data sources are necessarily included in the analysis, and there is little opportunity for quality checking of the data or products. Furthermore, the final analyses are often not in a form that can be readily used by the researcher. Snow and ice data are frequently presented in chart form, whereas most research purposes require some form of numerical gridded data. In addition, snow and ice information tends to be fragmented and scattered among multiple federal, state and foreign institutions.

The CDMS design (figure 1) responds to these problems by providing a single inventory focal point for snow and ice data, improved access to a subset of the currently produced digital data sets (e.g. SSM/I), and analytical tools to aid data use. The CDMS attempts to conform to the principles enumerated in the National Research Council Committee on Data Management and Computation report⁹ for effective data management.

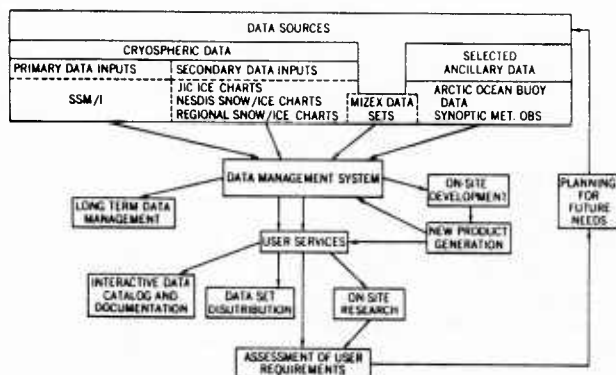


Figure 1. Conceptual schematic diagram of the Cryospheric Data Management System.

3. SENSOR DESCRIPTION AND DATA FLOW

The SSM/I is a passive microwave radiometer system which will be installed on a Block 5D-2 DMSP satellite in sun-synchronous near-polar orbit. The first launch is scheduled for early 1986 with subsequent launches between 1987 and the late 1990's. During some time periods, two SSM/I sensors may be in operation simultaneously, producing two distinct data streams.

The instrument will operate at four frequencies: 19.3, 22.2, 37.0, and 85.5 GHz. Vertical and horizontal polarizations are provided for each frequency, except the 22.2 GHz channel which has only vertical polarization. The 19.3, 22.2 and 37.0 channels will have a scene station resolution of 25 km, and the 85.5 GHz channel will have a resolution of 12.5 km¹². The satellite orbital characteristics permit daily global coverage. In the polar regions repeat coverage is possible each 12 hours due to the orbital overlap.

The data from the SSM/I package will be transmitted to earth data processing stations at Fleet Numerical Oceanography Center (FNOC) and the Air Force Global Weather Central (AFGWC). At these locations engineering values will be converted to equivalent antenna brightness temperatures (System Data Records [SDR's]) and, in some cases, into environmental parameter data (Environmental Data Records, [EDR's]).

The CDMS will receive SSM/I data from FNOC through Satellite Data Services Division (SDSD) of the National Environmental Satellite, Data and Information Service (NOAA-NESDIS) under the aegis of the DoD-NOAA Shared Processing Agreement. Initially these data will be transferred on magnetic tape from FNOC to NESDIS-SDSD, where tape copies will be made and forwarded to NSIDC. When the proposed satellite

data communications link between FNOC, AFGWC and NESDIS is operational, the FNOC to NESDIS portion of the data transfer will be over high speed satellite channels. However, NSIDC will continue to receive data from SDSD via magnetic tape (see figure 2).

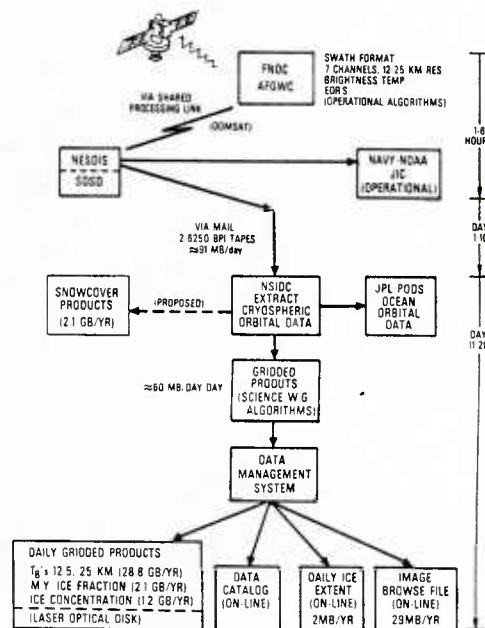


Figure 2. Schematic diagram of SSM/I data flow and proposed CDMS-SSM/I data products.

4. CDMS-SSM/I IMPLEMENTATION

The SSM/I data constitutes the first data set to be placed in the CDMS. The specific SSM/I related functions to be implemented include the following:

- Extract SSM/I cryospheric data from the orbital input data stream,
- Create mapped data sets,
- Provide an interactive data catalog,
- Distribute data to the user community,
- Implement revised microwave algorithms,
- Provide special products upon user request.

Rather than design a totally new computerized data base management system for SSM/I data, NSIDC in conjunction with its NASA sponsors, decided to utilize the existing the Pilot Ocean Data System (PODS), which meets the above stated functional needs. The PODS system is being

adapted for SSM/I data by its developers at the Jet Propulsion Laboratory (JPL). The PODS software will be transferred to NSIDC via a "technology transfer" arrangement and will be installed on NSIDC's VAX750 computer system.

Additionally, CDMS will become the first operational remote node on the proposed NASA Ocean Data System (NODS), also under development at JPL. Integration into NODS will provide CDMS users access to the federated data catalog as well as virtually any data set in NODS.

The hardware required to process and manage the SSM/I data includes a VAX 11/750 minicomputer with supporting magnetic disk and tape systems. In order to efficiently store the projected large volume of data, laser optical disks will be employed when stable, functioning devices become available. JPL is currently requesting bids for laser optical disk systems which meet PODS (and CDMS) needs. It is hoped that such a device will be available within the next 18-24 months. Should optical disk not be available, then the primary storage medium will be magnetic tape (see figure 3).

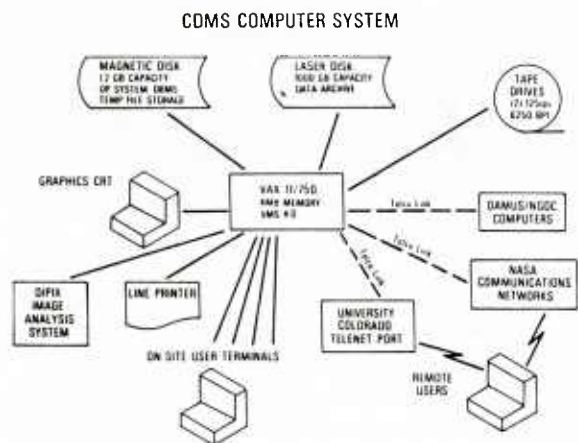


Figure 3. CDMS computer system configuration. Laser optical disk, graphics display, and high speed communications hardware have not been acquired yet.

Users will access CDMS via telephone dial-up service, either directly or through a packet switching network such as Telenet. The PODS system provides a menu-driven interface which takes the user through the data selection and tailored product generation process. Selected data may be downloaded over the telephone link if small in size, or automatically copied to magnetic tape for delivery to the user's location.

5. SSM/I PRODUCTS

The SWG recommended that the SSM/I archive contain four distinct data sets. These include: swath-oriented brightness temperatures (SDR's) for all frequencies and polarizations; gridded average brightness temperatures for polar regions; gridded average total ice concentration and multiyear ice fraction for polar regions; and daily ice boundaries. CDMS will contain each of these data types in addition to maintaining a data catalog, browse image collection, and brightness temperature monitor areas. Each of these are described below.

The swath-oriented brightness temperature archive is the basic collection of SDR data from which all the other data products are generated. The swath data will be reformatted into a rapid access archive residing on optical disk and will be accessed by either temporal and geographic indexes. Since the data set will be large, on the order of 28,000 MB per year, user access will be by staging data from optical disk to magnetic tape, or in limited cases to magnetic disk.

The SDR's will be binned into polar grids (see figure 4) and averaged on a daily basis. Separate grids for each frequency and polarization will be generated. Grid resolutions will vary depending on the channel frequency. Spatial resolution of the 85.5 GHz channel will be 12.5 km and all other channels will be 25 km. Brightness temperature data can also reside on optical disk and be staged to magnetic disk for limited analysis by the user. The grids will require about 2,150 MB of storage space per year.

The gridded brightness temperatures will be combined to produce multiyear ice fraction, concentration, and ice edge products on a daily basis. The SWG algorithms will be employed rather than using the Navy's operational set. The SWG algorithms are currently under development but will be completed by SSM/I launch. Grid resolution of the ice products is 25 km, except the daily ice edge, which is 12.5 km.

A data catalog and inventory of CDMS data will be maintained. The user will access the data catalog first, to determine the data sets available within his temporal and geographic specifications. The PODS software permits direct correlation of selected data within the catalog subsystem to extraction of the requested data from the data management system.

In order to permit rapid visual scanning of the SSM/I gridded products, a low resolution browse image collection will be assembled. The browse images will be stored in a device independent graphics metacode format permitting rapid conversion to various types of graphics display devices. The design goal is to permit the user to access one image of data in approximately 15-30 seconds of clock time over dial-up circuits.

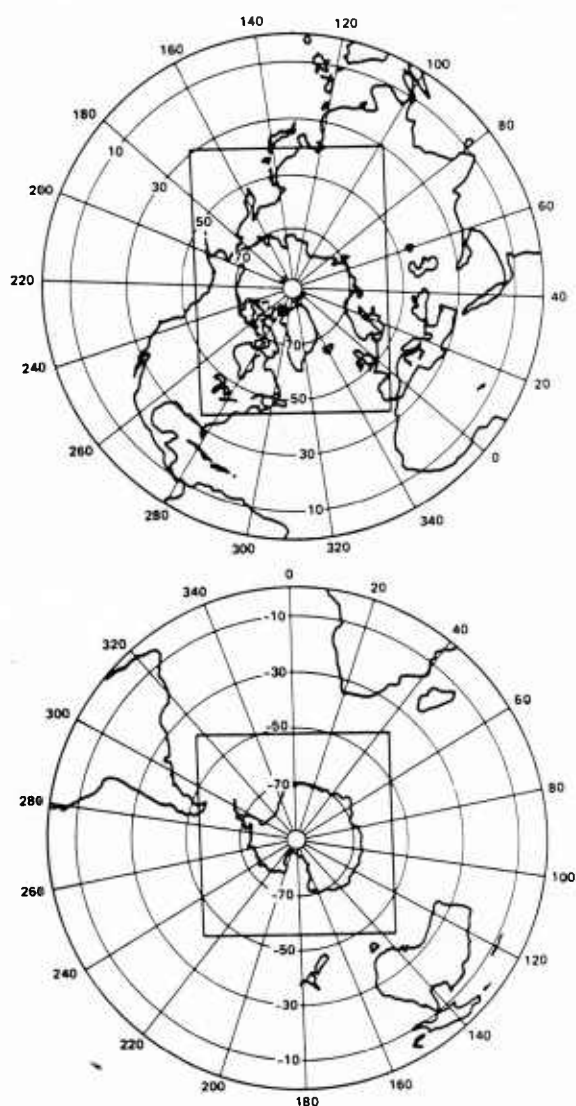


Figure 4. Geographical areas in the northern and southern hemispheres to be covered by the CDMS-SSM/I gridded SDR and ice product data sets, (after ³).

Spacecraft sensors tend to undergo long-term changes in sensitivity, usually in the form of a degradation. Consequently, the calibration of SSM/I will be routinely validated by examining at least monthly, the brightness temperatures of certain monitor areas. These monitor areas are regions of the earth a few hundred kilometers across, known to have a small variation in microwave emission over long periods. Possible regions include the Southeast Pacific, the Amazon rain forest, and the Antarctic ice sheet. By using the measured brightness temperatures of these features, and by linearly adapting SSM/I SDR radiances to keep these values constant, consistent brightness temperatures should be

provided to the algorithms used to generate geophysical parameters for research purposes. Routine checks of earth location will also be made.

6. PROPOSED SERVICES

The PODS software, which will be used in the CDMS utilizes a menu driven user interface¹¹. In order to select data for extraction, the user steps through a series of options presented one screen at a time. The menu system may be circumvented by expert users. Requests for data are automatically queued to the VMS operating system. If operator intervention is required, for example for a tape mount, the PODS system requests and monitors the request.

Users will gain access to the CDMS on-site or remotely via dial-up ports and/or through a packet switched network such as Telenet. Currently planned modems will support up to 1200 baud connections. Connection to a higher speed satellite based network is under consideration. The products described in Section 5 will be available to users. Most likely, additional data analysis on the CDMS computer will not be permitted due to its limited capacity. Therefore, analysis of the extracted data will be carried out at the user's home institution.

7. CONCLUSIONS

Implementation of the CDMS for SSM/I data will permit for the first time rapid access to a satellite microwave data set by the secondary user community. Future cryospheric information such as radar altimetry over continental ice sheets from proposed European Space Agency satellites or GEOSAT could also be distributed through this system. When CDMS is expanded to its full potential, it will provide a single integrated access point for most cryospheric satellite and ground based data sets.

7. ACKNOWLEDGEMENTS

Startup funds for the Cryospheric Data Management System have been provided by NASA Polar Oceans Program (EE) under grant NASA-NAGW-641, Dr. Roger G. Barry, Principal Investigator.

The NSIDC, originally proposed in 1978 and established by NOAA in 1982, provides a broader focus for now and ice data management than exists within the mission agencies. It accomplishes this by providing a national focal point for data-related matters, especially the development of standard procedures and formats for data bases, and by seeking to ensure that appropriate data handling procedures accompany the development of new observational systems and programs. The National Snow and Ice Data Center is operated by the Cooperative Institute for Research in Environmental Sciences, University of Colorado for NOAA-NESDIS through a contract with the National Geophysical Data Center, Boulder, Colorado.

6. REFERENCES

1. European Space Agency (1985) "A Programme for International Polar Oceans Research (PIPOR)", PIPOR Science Working Group Report, ESA SP-1074, 46p.
2. Joint Oceanic Institutions Incorporated, Satellite Planning Committee (1985) "Oceanography from Space, A Research Strategy for the Decade 1985-1995; Part 2, Proposed Measurements and Missions", 33p.
3. National Aeronautics and Space Administration, Science Working Group for Special Sensor Microwave Imager (1984) "Passive Microwave Remote Sensing for Sea Ice Research", 55p.
4. Barry, R. G. (1983), "Continuation Proposal for NASA contract number NAGW-363: Pilot Study and Evaluation of SMMR-Derived Sea Ice Data Base, 10p.
5. Barry, R. G., Crane, R. G., Weaver, R. L., and Anderson, M. L., (1984), "Sea-Ice and Snow-Cover Data Availability, Needs and Problems", Annals of Glaciology, International Glaciological Society, Vol. 5, pp 9-15.
6. Glaciological Data. Report GD-7, Inventory of Snow Cover and Sea Ice Data (1978) Boulder, CO, World Data Center-A: for Glaciology, 171p.
7. Glaciological Data. Report GD-8, Ice Cores (1980) Boulder, CO, World Data Center-A: for Glaciology, 139p.
8. Glaciological Data. Report GD-13, Workshop Proceedings: Radio Glaciology, Ice Sheet Modeling (1982) Boulder, CO, World Data Center-A: for Glaciology, 113p.
9. National Research Council. Committee on Data Management and Computation (1982) Data Management and Computation. Vol. 1: Issues and Recommendations, 167p.
10. Hollinger, J. P., and R. C. Lo (1983) SSM/I Project Summary Report. Naval Research Laboratory. NRL Memorandum Report 5055, 106p.
11. Johnson, John A. (1984) The NASA/JPL Pilot Ocean Data System Catalog. Proceedings of the Pecora Symposium, IEEE, pp 148-152.

THE JOINT ICE CENTER
CAPABILITIES AND LIMITATIONS IN SEA ICE
ANALYSIS AND FORECASTING

Hardi S. Rosner
Lieutenant Commander, USN

Navy-NOAA Joint Ice Center
4301 Suitland Road
Washington, D.C. 20390

ABSTRACT

The capabilities and limitations of the Joint Ice Center to produce operational sea ice analyses and forecasts are examined. Remotely sensed data from National Oceanic and Atmospheric Administration (NOAA), Defense Meteorological Satellite Program (DSMP), and National Aeronautics and Space Administration (NASA) satellites are combined with conventional ice observations collected from aircraft, ships and shore stations to construct operational ice analyses. Forecast guidance products from the Fleet Numerical Oceanography Center (FNOC) and the National Meteorological Center (NMC) are utilized along with analog and statistical methods to produce both short range and long range ice forecasts. Sea ice analysis and forecast products are disseminated using a variety of communications means.

INTRODUCTION

The United States Navy, originally through the U.S. Naval Oceanographic Office and now through the Naval Polar Oceanography Center, has been providing sea ice analysis and forecasting services to the Department of Defense since the 1950's. The Joint Ice Center (JIC) was established in 1976 as a result of a severe ice season on the North Slope of Alaska which brought into focus the necessity for commercial concerns to have timely and accurate ice related support.

JIC products and much of the government data utilized in their construction are or can be made available to both military and commercial users. Presented in this paper are descriptions of JIC data sources, analysis methods, products, and the available dissemination channels.

DATA SOURCES

Over the past 30 years, both data sources and analysis methods have slowly evolved. The sea ice analysis is a manual synthesis of a wide variety of data with differing scales and accuracy. Due to the remote nature of the polar regions and the difficulties and expense involved in collecting ground truth data, the use of remote sensing techniques is imperative to the timely production of an operational analysis. Despite the value of ground truth data, 80-90% of the data used in sea

ice analyses are satellite derived. Descriptions of these data and analysis methods follow. A detailed summary of JIC products and data sources is found in Godin (1981).

1. Ship Reports

Although ship reports represent point data sources they are extremely valuable because of their accuracy and are considered highly reliable ground truth data. These data come in two basic formats. The first, and by far the most common, is the ICE group appended to the ship synoptic weather observation. Although limited to 5 digits, this group contains information concerning the concentration of the ice, the form or forms of ice, the stage of ice development, the orientation of the ice edge and a subjective categorization of the overall ice situation faced by the reporting ship as well as information concerning icebergs. The second format is the ship ice observation. These observations are reported in multigroup numerical codes that provide detailed data on ice conditions. Codes used are national codes which vary significantly.

2. Shore Reports

Shore reports are also ground truth data and are received in a variety of formats ranging from plain language descriptions to multigroup numerical codes similar to the ship sea ice observation codes. These reports are available in the Baltic and Gulf of Bothnia, and for Greenland, Canada, and Alaska.

3. Aerial Sea Ice Reconnaissance

Aerial visual and radar observation of sea ice is the largest source of ground truth data. These data are received in a variety of methods ranging from national numerical codes to graphic transmissions of completed ice reconnaissance charts. These data include concentration, ages and stages of ice, topography, forms of ice and data on leads and polynyas. While aerial reconnaissance is the source of the greatest amount of first order sea ice data, it is not practical to fly sea ice reconnaissance over the entire Arctic. Aerial reconnaissance is normally limited to the major shipping routes.

4. Visible and Infrared Imagery

Visible and infrared imagery is available

operationally from the NOAA TIROS-N series satellites (currently NOAA 6 and NOAA 9) and from DMSP satellites. All of these satellites are in polar orbits. A description of each of these satellite systems follows:

a. NOAA TIROS-N Series Satellites: The sensor onboard the NOAA TIROS-N series satellites is the Advanced Very High Resolution Radiometer (AVHRR) which provides visible and infrared imagery with a 1 km resolution at the satellite's subpoint. The data is provided in two resolution levels and two transmission modes. Direct transmission and delayed transmission of the recorded data are the available modes. High resolution 1 km data is known as High Resolution Picture Transmission (HRPT) in the direct transmission mode and Local Area Coverage (LAC) in the delayed transmission mode. The spacecraft does not have sufficient recorder time available to provide daily global LAC coverage. A 4 km resolution data stream is directly transmitted as an analog signal known as the Automatic Picture Transmission (APT) mode. Four km data is also digitally recorded to provide daily global coverage known as Global Area Coverage (GAC). While the methods used to reduce the resolution of APT and GAC imagery differ, the resolution is normally 4 km for both. The JIC receives visible GAC imagery daily. Infrared GAC imagery is not currently operationally available due to limited computer processing capability. NOAA's satellite receiving ground station at Gilmore Creek, Alaska (65N, 148W) permits daily HRPT data coverage for the Beaufort, Chukchi, and Bering Seas as well as portions of the East Siberian Sea, the Canadian Archipelago, and the central Arctic Basin. The remainder of the high resolution data for the Arctic must be recorded and downlinked as LAC data. The limited recorder space available and the large number of users vying for the recorded imagery limits high resolution coverage of the entire Arctic to approximately once a week.

b. DMSP Series: Visible and infrared imagery are available to the JIC daily from DMSP satellites as a polar stereographic mosaic. Although the sensors onboard the spacecraft are of higher resolution, the resolution of the mosaic is approximately 4-6 km depending upon location. This provides the only global daily infrared coverage available to the JIC.

5. Passive Microwave Data

Passive microwave data is available from the Scanning Multichannel Microwave Radiometer (SMMR) on the NIMBUS-7 satellite. The radiometer senses the microwave radiation emitted from the surface of the earth. This radiation is measured as brightness temperature (which is different from the physical temperature). Brightness temperature data from SMMR is operationally processed at the NASA Goddard Space Flight Center into total ice concentration and multiyear fraction categories. It is then displayed as a gridded polar mosaic printer graphic with a resolution of 60 km even though the resolution of the SMMR sensor is 25 km. Until late 1982, passive microwave data was

available from the Electrically Scanning Microwave Radiometer (ESMR). The brightness temperature data from the ESMR was processed into a photographic image rather than being processed through an algorithm.

ANALYSIS METHODS

1. Analysis from Visible and Infrared Imagery

LAC and HRPT visible and infrared imagery are the highest resolution satellite data available to the JIC. The imagery is manually gridded using discernable geographic landmarks and then manually analyzed. Because the albedo of ice and snow are in the same range as the albedo of clouds, the analyst must use pattern and texture recognition techniques to distinguish between cloud cover and ice cover in the visible imagery. Similarly, the temperature ranges of the clouds and the ice in the Arctic overlap and similar techniques for the analysis of infrared imagery must be used. The ability to distinguish between cloud cover and ice cover is largely a function of the resolution of the imagery with more textural characteristics being discernable at higher resolutions. Imagery with a resolution coarser than 4 km is of marginal utility because too many of the textural characteristics are indistinguishable.

The major drawback to using visible and infrared imagery for sea ice analysis is their inability to penetrate cloud cover. Cloud cover in the Arctic varies from 30-90% with the cloud cover over the marginal ice zone (MIZ) ranging from 60-90%. It is not uncommon for a given region of the Arctic to remain cloud covered for a period of 3 weeks or more. Additionally visible imagery is useless in the darkness of the Arctic winter. Infrared imagery is of marginal utility during the summer as the surface temperature of the ice approaches the sea surface temperature. However, this imagery does have value during the summer as an aid in defining geographic landmarks which are significantly warmer than the ocean. This aid is needed due to the difficulty in identifying these landmarks on the visible imagery.

New sea ice does not have a sufficiently large difference in either albedo or temperature from the sea water to be discernable on the available visible or infrared imagery. Ice is generally not detectable with 1 km resolution imagery until it reaches the thickness of young ice (10-30 cm).

2. Analysis from Passive Microwave Data

The character of the microwave radiation emitted from sea ice varies with the age of the ice. This variation is due primarily to the change in the salinity of the ice as the age increases. With passive microwave data, it is possible to distinguish the ages of sea ice as well as determine the concentration of the ice. The greatest advantage to passive microwave is its ability to penetrate cloud cover and darkness. Despite the coarse resolution of SMMR data, its all-weather, day/night capability makes it an extremely valuable analysis tool. Passive microwave does have several severe limitations

other than its coarse resolution. Because the radiometer senses the radiation emitted by the surface of the ice, an ice floe covered with melt ponds and wet snow during the summer may be sensed as open water. Additionally, the sensor antenna has several side lobes which may cause contamination when near a strong microwave emitter such as a landmass. To complicate the summertime problems, SMMR data may be contaminated by liquid precipitation. This contamination can be identified and eliminated by the analyst by examining a time series of SMMR data and synoptic weather maps. Precipitation regions will move much faster than will the ice. On the positive side, microwave sensors are capable of sensing thin ice before it is discernable in visible or infrared imagery.

3. Methodology

The first stage of the analysis process is to plot all ground truth data. These ship and shore reports and aerial observations are then evaluated for "reasonableness". Available high resolution visible and infrared imagery is analyzed and transposed to the work chart. GAC imagery is then analyzed to fill any regions that were not covered by LAC or HRPT. SMMR data is analyzed and transposed to the work chart as the initial analysis. All the data is then evaluated by the analyst and compared against the previous week's analysis. Where questions arise on imagery interpretation, nearby weather reports are reviewed for types of cloud cover, presence of fog and air temperature. This data is very helpful in identifying subtle differences between clouds and ice. In regions where insufficient data exists to define the ice edge, an estimated edge is identified based on calculated ice drift for the preceeding week and growth/decay expectations based on air temperatures and empirical ice thickness calculations.

The analysis is reviewed by the ice forecasters for continuity and credibility based on the previous week's analysis and the meteorological conditions prevalent during the week as well as climatology. Any late data arriving after the analysis is completed will not effect the distributed charts. However, any errors noted in the analysis will be corrected on the master analysis to prevent the error propagating to the next week's analysis and to maintain the most accurate archive possible.

Ice charts are labeled in the World Meteorological Organization's (WMO) "egg" code and distributed to foreign and domestic users by mail. At the end of a calendar year, the master charts are reviewed for accuracy and are forwarded to the National Climatic Data Center (NCDC). NCDC digitizes the data in the Sea Ice Grid (SIGRID) format. The data are then archived along with the weekly analysis charts at the World Data Center-A for Glaciology in Boulder, Colorado.

PRODUCTS

The JIC constructs products on three scales: global, regional and local. Global scale products

are designed for use by strategic planners and for small scale analyses such as climate studies. Regional scale products are used to support general operations in a specified area such as Great Lakes shipping or ocean fishing fleets. Local scale products are designed to provide tactical support to units operating in and under ice covered waters.

1. Global Scale Ice Analyses

Global ice conditions are mapped weekly on a scale of 1:11.6 million for the Arctic and 1:16 million for the Antarctic. The maps are azimuthal equidistant projections centered at the pole. The smallest homogeneous area resolved by the mapping system is less than 20 km under the best conditions and over 100 km under the worst. Figure 1 is an example of the weekly Eastern Arctic Ice Analysis.

The mapped features depicted in the ice analyses include classes of ice concentration, classes of ice age, ice edge position, major leads and large polynas. In addition, Antarctic ice maps contain positions of ice bergs which are greater than 30 km in length. Arctic ice maps contain monthly updated theoretical ice thickness at selected Arctic stations during seasons of ice growth.

2. Regional Scale Ice Analyses

Regional ice analyses are routinely produced for Alaskan waters and the Great Lakes. Figure 2 is an Alaska Region Ice Analysis produced in a 1:8 million scale azimuthal equidistant projection map. Although mapped features for the regional maps are similar to those of the global scale, the larger scale permits a more detailed analysis of ice boundaries and characteristics.

3. Local Scale Ice Analyses

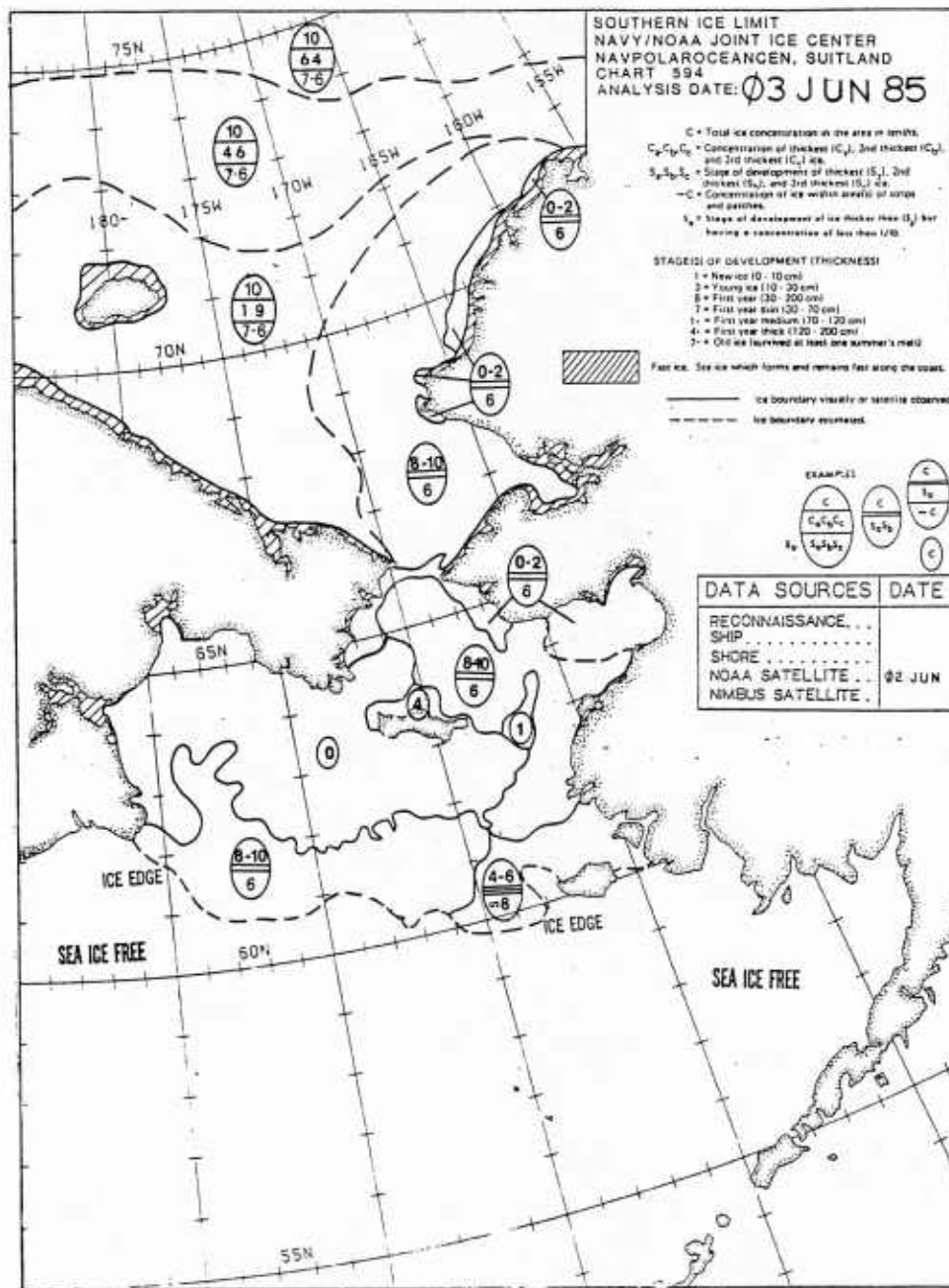
Local scale analyses are produced on an as required basis for U.S. Navy, U.S. Coast Guard, and NOAA ships operating in and near ice infested waters. These analyses are almost always disseminated as alphanumeric messages and are provided on a time scale that varies from daily to twice weekly depending upon the needs of the vessel.

4. Ice Forecasts

Sea ice forecasts differ from ice analyses in that they predict the future state of ice conditions. Ice analyses are often the starting point from which the ablation, formation, or movement of sea ice is predicted. Ice forecasts are produced for various geographical areas in a number of spatial and time scales.

The primary objective of the JIC ice forecasting program is to provide ice prediction services in response to user specified temporal and spatial requirements. Existing services include the preparation of the following information:

- (1) short-term ice forecasts for the ensuing 24-96 hour period which provide close tactical support over a specified locality for an ongoing exercise;



Sea/McMurdo Sound Forecasts.

The JIC also utilizes the Pacific Marine Environmental Lab Bering Sea ice model. It is a Lagrangian model that includes thermodynamic effects to forecast Bering Sea ice motion.

5. Dissemination

JIC analysis and forecast products are available by mail, facsimile, telecopier, and alphanumeric messages. Some JIC ice analyses and forecasts are

also available through electronic alphanumeric messages. Alphanumeric messages are available in near real time. Table 1 identifies JIC products available by mail and electronic messages. Table 2 identifies products available through NOAA facsimile circuits. Arrangements to receive these products can be made through the identified distribution centers.

FUTURE DEVELOPMENTS

The major thrust of future developments at the

JOINT ICE CENTER (JIC) PRODUCTS AND DISTRIBUTION CENTERS

Table 1

PRODUCT	FREQUENCY	PRODUCT DESCRIPTION AND FORMAT	DISTRIBUTION CENTER
Arctic Ice Atlas	Yearly	Compilation of weekly operational Eastern and Western Arctic Sea Ice Analyses. Available by mail in hardcopy and microfiche formats.	NTIS
Antarctic Ice Atlas	Bi yearly	Compilation of weekly operational Antarctic Sea Ice Analyses. Available by mail in hardcopy and microfiche formats.	NTIS
JIC Digital Data		JIC Arctic Ice and Antarctic Ice Analyses (1972-1982) in digital format. Available by mail on computer tape.	WDC-A
Eastern Arctic Southern Ice Limit	Weekly	Analysis of arctic sea ice from 95°E westward to 95°W. Hardcopy available by mail.	JIC
Western Arctic Southern Ice Limit	Weekly	Analysis of arctic sea ice from 95°W westward to 95°E. Hardcopy available by mail.	JIC
Antarctic Northern Ice Limit	Weekly	Analysis of antarctic ice conditions. Hardcopy available by mail.	JIC
Great Lakes Ice Analysis	Twice Weekly	Analysis of Great Lakes Ice conditions. Hardcopy available by mail.	SDSD
Southern Ice Limit Eastern and Western Arctic/7 Day Ice Forecast	Weekly	Plain language alphanumeric message of arctic ice conditions. Available through electronic transmissions.	NNODDS
30 Day Western Arctic Ice Forecast	Semi-Monthly	30 day arctic sea forecast from 95°W westward to 95°E. Hardcopy available by mail.	JIC
30 Day Eastern Arctic Ice Forecast	Semi-Monthly	30 day arctic sea forecast from 95°E westward to 95°W. Hardcopy available by mail.	JIC
30 Day Western Ross Sea Ice Forecast	Semi-Monthly Dec-Feb	Available only through electronic transmissions.	NNODDS
Western Arctic Seasonal Outlook	Yearly Early May	Predicted opening date of coastal route to Prudhoe Bay and other statistics. Hardcopy available by mail.	JIC
Eastern Arctic Seasonal Outlook	Yearly Early May	Predicted opening dates for Greenland coastal stations and general seasonal ice conditions. Hardcopy available by mail.	JIC
Western Ross Sea and McMurdo Sound Seasonal Outlook	Yearly Early Nov	Predicted seasonal fast ice and general ice conditions. Hardcopy available by mail.	JIC
KEY:			
NTIS	National Technical Information Service 5285 Port Royal Road Alexandria, VA 22314		NNODDS Navy NOAA Oceanographic Data Distribution System Fleet Numerical Oceanography Center Monterey, CA 93940
WDC-A	World Data Center-A for Glaciology Campus Box 449 Boulder, CO 80309		SDSD NOAA, NESDIS Satellite Data Services Division World Weather Building Room 100 Washington DC 20233
JIC	Joint Ice Center 4301 Suitland Road Washington, DC 20390		

Joint Ice Center will focus on the ability to exploit the digital satellite data that is currently available, to incorporate the new sources of satellite data that will be available in the future, and to improve the speed and scope of dissemination avenues. These efforts include the development of a digital image processing capability at the Joint Ice Center. This capability will permit the utilization of visible, infrared and passive microwave data at full resolution and the ability to accurately earth locate the data. The advent of a spaceborne synthetic aperture radar will provide the JIC with its first high resolution all weather data source. Dissemination means will have to be increased in order to service a wider variety of customers ranging from the fishing fleet operator with only a UHF or HF radio to the sophisticated user who will receive a computer

compatible digital graphic via satellite communications.

Additionally, digital ice fields will be transmitted to FNOC in order to initialize the Hibler ice model. This dynamic Arctic basin model (which also includes thermodynamics) will become operational later this year.

CONCLUSIONS

JIC ice analyses are produced on various time and spatial scales through the integration of conventional and satellite derived data from NOAA, DMSP, and NASA satellites as well as ship and aerial observations. Ice forecasts are generated for time periods ranging from 1 day to several months through the employment of

JOINT ICE CENTER FACSIMILE SCHEDULE

Table 2

FACSIMILE CIRCUIT	ALASKA REGION ICE ANALYSIS	ANTARCTIC ICE ANALYSIS	30-DAY WESTERN ARCTIC ICE FORECAST	GREAT LAKES ICE ANALYSIS
<u>National</u> ¹				
Day	Th, Su			We, Sa
Greenwich Mean Time (GMT)	11:19 GMT			11:19 GMT
Chart Number	452			452
<u>Digital</u> ¹				
Day	Th, Su			We, Sa
Greenwich Mean Time (GMT)	12:41 GMT			12:41 GMT
Chart Number	452			452
<u>Alaska</u> ¹				
Day	Mo, We, Fr		() ²	
Greenwich Mean Time (GMT)	15:20 GMT		21:50 GMT	
Chart Number	594		593	
<u>WEFAX</u> ³				
<u>GOESWEST</u>				
Day		Daily ⁴		
Greenwich Mean Time (GMT)		0302 GMT		
Chart Number		0312 GMT		
		409, 410		
<u>GOES CENTRAL</u>				
Day		Daily ⁴		
Greenwich Mean Time (GMT)		0305 GMT		
Chart Number		0335 GMT		
		409, 410		
<u>NOTES</u>				
1. For acquisition information contact: NOAA, NWS Communication Division/WOTS3 ATTN: User Agreements Contact 8060 13th Street Silver Spring, MD 20910				
2. Slots are open daily, chart is transmitted twice monthly.				
3. For acquisition information contact: NOAA, NESDIS ATTN: WEFAX Coordinator World Weather Building Washington, DC 20233				
4. Chart is updated weekly and transmitted daily in two sections.				

statistical/empirical and analogue techniques. Ice products are available to DOD and commercial users through the JIC and various U.S. Government distribution centers and communications networks.

REFERENCES

- Barnett, Don G., "A long-range ice forecasting method for the north coast of Alaska," Sea Ice Processes and Models, Robert S. Pritchard, ed., University of Washington Press, Seattle, 1980, pp 360-372.
- Gerson, D.J., "A numerical ice forecasting system," Naval Oceanographic Office, Reference Publication RP-8, 1975.
- Godin, R.H., "Sea ice charts of the Navy/NOAA Joint Ice Center," Snow Watch 1980, World Data Center-A for Glaciology (Snow and Ice) Report GD-11, 1981, pp 5845-5852.

Skiles, Frank L., "Empirical wind drift of sea ice," Arctic Drifting Stations, Arctic Institute of North America, 1968, pp 239-252.

Stringer, W.J., D.G. Barnett, R.H. Godin, "Handbook for sea ice analysis and forecasting," Naval Environmental Prediction Research Facility, Contracter Report CR 84, 1984.

Thorndike, A.S. and Colony, R., "Sea ice motion in response to geostrophic winds," Journal of Geophysical Research, 87, (C8), 1982.

APPENDIX

1. LIST OF PARTICIPANTS
2. LIST OF PARTICIPANTS BY ORGANIZATION

PARTICIPANTS LIST
ARCTIC OCEANOGRAPHY CONFERENCE
JUNE 11-14, 1985

AARON, ARNOLD
NAVAL UNDERWATER SYSTEM CENTER
NEWPORT RI 02841

ABBOTT, PHIL
ATLANTIC APPLIED RESEARCH CORP
129 MIDDLESEX TURNPIKE
BURLINGTON MA 01803

ALLEN, J
NAVOCEANO
NSTL MS 39529

ANDERSON, JOHN
POLAR RESEARCH LAB
6308 CARPINTERIA AVE
CARPINTERIA CA 93013

ANDREWS, JIM
NORDA
NSTL MS 39529

ANGELL, GORDON
APPLIED MATHEMATICS INC
1663 ROUTE 12
P O BOX 637
GALES FERRY CT 06335

ARVESON, PAUL
DAVID TAYLOR NAVAL SHIP R & D
BETHESDA MD 20084

ATKINSON, K
NAVOCEANO
NSTL MS 39529

AVERY, O
NAVOCEANO
NSTL MS 39529

BALES, SUSAN
DAVID TAYLOR NAVAL SHIP R & D
CENTER
CODE 1561
BETHESDA MD 20084

BARNES, BOB
OPNAV
OP-22 PENTAGON
WASHINGTON DC 20350

BARRETT, R L
NAVOCEANO
NSTL MS 39529

BEAL, ALLAN
ARCTIC SUBMARINE LABORATORY
NAVAL OCEAN SYSTEMS
CENTER CODE 19
SAN DIEGO CA 92152

BEATTY, FRANK
NAVOCEANO
NSTL MS 39529

BEESON, E L
NAVOCEANO
NSTL MS 39529

BETCHER, BOB
COMNAVOCEANCOM
NSTL MS 39529

BISHOP, GARNER
NAVAL UNDERWATER SYSTEMS CENTER
CODE 3631, BLDG 679/1
NEWPORT RI 02841

BLAHA, J
NAVOCEANO
NSTL MS 39529

BLIZARD, MARVIN
OFFICE OF NAVAL RESEARCH
800 N QUINCY ST
ARLINGTON VA 22217

BLUMENTHAL, RICHARD
NAVOCEANO
NSTL MS 39529

BONNETT, DAVID
TRACOR
P O BOX 1325
SILVERDALE WA 98383

BRADY, JAMES
CHIEF OF NAVAL MATERIAL
ASW SYSTEMS DIVISION
DEPT OF NAVY
WASHINGTON DC 20360

BRANCH, GEORGE
NORDA
NSTL MS 39529

BRIGHAM, LAWSON W
US COAST GUARD
ICE OPERATIONS DIVISION (G-010)
2100 2ND ST SW
WASHINGTON DC 20593

BROWN, NEIL
ATLANTIC APPLIED RESEARCH CORP
129 MIDDLESEX TURNPIKE
BURLINGTON MA 01803

BROWN, W E
NAVOCEANO
NSTL MS 39529

BROZENA, JOHN
NAVAL RESEARCH LAB
WASHINGTON DC 20375 5000

BUCCA, PAUL
NORDA
NSTL MS 39529

BURDETTE, ERNEST L
TRITON SYSTEMS INC
109 E SCENIC DR
PASS CHRISTIAN MS 39571

BURGE, RAYMOND
NORDA
NSTL MS 39529

BURKE, TRAVIS
NORDA
NSTL MS 39529

BUSH, CARROLL
SPARTON ELECTRONICS
2400 E GANSON
JACKSON MI 49202

CANADA, RAYMOND
NATIONAL DATA BUOY CNTR
NSTL MS 39529

CAR, MARTIAL
NAVOCEANO
NSTL MS 39529

CARNES, MICHAEL
NAVOCEANO
NSTL MS 39529

CARROLL, J C
NAVOCEANO
NSTL MS 39529

CARUTHERS, JERRY
NORDA CODE 220
NSTL MS 39529

CHIN BING, STAN
NORDA
NSTL MS 39529

CLARK, DICK
TETRATECH INC
1191 N FT MYER DR
ARLINGTON VA 22209

CHERKIS, NORMAN
NAVAL RESEARCH LAB
WASHINGTON DC 20375-5000

COLLIER, MARTIN
NAVOCEANO
NSTL MS 39529

COLONY, ROGER
POLAR SCIENCE CNTR
UNIV OF WASHINGTON
SEATTLE WA 98105

COSTOLO, J HOUSTON
NAVOCEANO
NSTL MS 39529

COUSINS, BERNIE
COMNAVOCEANCOM
NSTL MS 39529

COX, GORDON
USA CRREL
72 LYME ROAD
HANOVER NH 03755

CRANFORD, KENNETH
NORDA
NSTL MS 39529

CRUMPLER, A
NAVOCEANO
NSTL MS 39529

CUMMINGS, J
NAVOCEANO
NSTL MS 39529

CUMMINGS, TIM
COMNAVOCEANCOM
NSTL MS 39529

DAVIS, THOMAS
NAVOCEANO
CODE 022
NSTL MS 39529

DEBLANC, BETTY
NAVOCEANO
NSTL MS 39529

DELANEY, DENNIS
NAVOCEANCOMFAC
NSTL MS 39529

DENNER, WARREN
SCIENCE APPLICATIONS INT'L CORP
205 MONTECITO AVE
MONTEREY CA 93940

DICUS, RONALD
NAVAL RESEARCH LAB
CODE 5120
WASHINGTON DC 20375

DIPIAZZA, NICHOLAS J
NAVOCEANO
NSTL MS 39529

DOHODA, TERENA
NAVAL UNDERWATER SYSTEMS CENTER
NEW LONDON LAB
NEW LONDON CT 06320

DONALD, JAMES
NAVAL UNDERWATER SYSTEMS CENTER
NEW LONDON LAB
NEW LONDON CT 06320

DONOVAN, BARRY
NAVAL EASTERN OCEANOGRAPHY CENTER
MCADIE BLDG (U-117)
NAVAL AIR STATION
NORFOLK VA 23511

DURHAM, DON
NORDA CODE 350
NSTL MS 39529

ELCHENKO, STEPHEN
NAVAL AIR DEVELOPMENT CENTER
CODE 3041
WARMINSTER PA 18974

ENGLEBRETSON, RON
SCIENCE APPLICATIONS INTL CORP
205 MONTECITO
MONTEREY CA 93940

EPPLER, DUANE
NORDA
NSTL MS 39529

ERICHSEN, ROBERT
NATIONAL DATA BUOY CENTER
NSTL MS 39529

EVANS, DICK
COMNAVOCEANCOM
NSTL MS 39529

FAGOT, MARTIN
NORDA
NSTL MS 39529

FARMER, L. DENNIS
NORDA
NSTL MS 39529

FARQUHAR, BROOKE
NORDA
800 N QUINCY ST
ARLINGTON VA 22217 5000

FARWELL, BOB
NORDA
NSTL MS 39529

FEATHERSTONE, JOHN
GENERAL DYNAMICS
79 CHARTER OAK DR
EAST LYME CT 06333

FECHER, MICHAEL
NAVAL UNDERWATER SYSTEMS CENTER
CODE 3331
FORT TRUMBELL
NEW LONDON CT 06320

FERER, K M
NORDA
NSTL MS 39529

FISHER, ROBERT A
NORDA
NSTL MS 39529

FLOYD, NED
ARCTIC SUBMARINE LAB
NAVAL OCEAN SYSTEMS CENTER (CODE 19)
SAN DIEGO CA 92152

FLUM, ROBERT S
MAT-08-ASW SYSTEMS DIVISION
DEPARTMENT OF THE NAVY
WASHINGTON DC 20362

FRANC, L
NAVOCEANO
NSTL MS 39529

FRENCH, JON
NORDA
NSTL MS 39529

GARCIA, RON
COMNAVOCEANCOM
NSTL MS 39529

GARRISON, GERALD
APPLIED PHYSICS LAB
UNIVERSITY OF WASHINGTON
1013 NE 40TH STREET
SEATTLE WA 98105

GEBHARDT, KIM
COMNAVOCEANCOM
NSTL MS 39529

GEDDES, WILBURT
PLANNING SYSTEMS INC
SLIDELL LA 70458

GOLDSBY, RICHARD
NAVAL ELECTRONIC SYSTEMS COMMAND
WASHINGTON DC 20363-5100

GORDON, DAVID
NAVAL OCEAN SYSTEMS CNTR
CODE 711
SAN DIEGO CA 92152

GOUGH, ED
PLANNING SYSTEMS INC
SLIDELL LA 70458

GOW, ANTHONY
USA CRREL
72 LYME RD
HANOVER NH 03755

GRASSIT, KIP
NATIONAL DATA BUOY CENTER
NSTL MS 39529

GREEN, ALBERT
NORDA
NSTL MS 39529

GREENE, CHARLES
GREENERIDGE SCIENCES
5276 HOLLESTER AVE
SUITE 408
SANTA BARBERA CA 93111

GREENE, ROBERT
SCIENCE APPLICATIONS INTL CORP
1710 GOODRIDGE DRIVE
MCCLEAN VA 22102

GREEN, MIKE
GENERAL DYNAMICS
ELECTRIC BOAT DIVISION
EASTERN POINT RD
GROTON CT 06340

GREIFINGER, PHYLLIS
R AND D ASSOCIATES
4640 ADMIRALTY WAY
P O BOX 9695
MARINE DEL REY CA 90291

GROSSKOPF, BILL
ARCTEC INC
9104 RED BRANCH ROAD
COLUMBIA MD 21045

GRUSSENDORF, MARK
NORDA
NSTL MS 39529

HACHMEISTER, LON
ENVIROSPHERE CO.
400 12TH AVE NE
BELLEVUE WA 98004

HAEGER, STEVE
NAVOCEANO
NSTL MS 39529

HAMILTON, GLEEN
NATIONAL DATA BUOY CENTER
NSTL MS 39529

HANNON, JAMES
SIPPICAN
OCEAN SYSTEMS, INC.

HARLETT, JOHN
APPLIED PHYSICS LABORATORY
UNIVERSITY OF WASHINGTON
1013 NE 40TH ST
SEATTLE WA 98105

HART, W
NAVOCEANO
NSTL MS 39529

HARVEY, PHIL
PRECISION ECHO, INC
3105 PATRICK HENRY
SANTA CLARA CA 95054

HAYES, RICHARD
US COAST GUARD
COMMANDAT (G-010)
2100 2ND STREET SW
WASHINGTON DC 20593

HEIBERG, ANDY
POLAR SCIENCE CNTR
4057 ROOSEVELT WAY NE
SEATTLE WA 98105

HENDERSON, J. RUSSELL
ODSI DEFENSE SYSTEMS INC
3255 WING ST
SUITE 550
SAN DIEGO CA 92110

HIGGS, R
NAVOCEANO
NSTL MS 39529

HILL, PAUL
NAVAL UNDERWATER SYSTEMS CNTR
CODE 01Y
BLDG 101
NEWPORT RI 02841

HINMAN, KEN
COMNAVOCEANCOM
NSTL MS 39529

HOLLAND, C RANDY
NORDA
NSTL MS 39529

HOLLINGER, JIM
NAVAL RESEARCH LAB
CODE 7781
WASHINGTON DC 20375

HORBACH, ARTHUR
NAVAL AIR DEV CNTR
WARMINSTER PA 18974

HORN, DEAN A
MIZEX ONR/MIT
CODE 425 AR
800 N QUINCY ST
ARLINGTON VA 22217

HORSLEY, LAVERNE
NORDA
NSTL MS 39529

JENSEN, JOHN
NAVAL WAR COLLEGE
NEWPORT RI 02841

JEZEK, KEN
USA CRREL
72 LYME ROAD
HANOVER NH 03755

JOBST, W J
NAVOCEANO
NSTL MS 39529

JUDD, RANDALL
NAVAL OCEAN SYSTEMS CNTR
CODE 541
SAN DIEGO CA 92152

KAHN, NORMAN
CIA
OSWR/STD
WASHINGTON DC 20505

KEENAN, RUTH
SCIENCE APPLICATIONS INTL CORP
P O 721
WOODS HOLE MA 02543

KEIFFER, RICHARD
NAVOCEANO
NSTL MS 39529

KELLEY, EDWARD J
NAVAL INTELLIGENCE SUPPORT CNTR
(NISC-3622)
4301 SUITLAND RD
WASHINGTON DC 20390

KELLY, R.G.
NORDA
NSTL MS 39529

KERLING, JEFF
NAVOCEANO
NSTL MS 39529

KERR, GEORGE A
NORDA CODE 223
NSTL MS 39529

KETCHUM, ROBERT
NORDA
NSTL MS 39529

KIES, PHIL
NATIONAL DATA BUOY CNTR
NSTL MS 39529

KNOTT, MARTHA
NORDA
NSTL MS 39529

KOCH, ROBERT
APPLIED RESEARCH LAB
UNIV OF TEXAS--AUSTIN
AUSTIN, TX 78712

KOEHR, JIM
COMNAVOCEANCOM
NSTL MS 39529

KORDENBROCK, JAMES
DAVID TAYLOR NAVAL SHIP
R AND D CNTR
CODE 1231
BETHESDA MD 20084

KOVACS, AUSTIN
USA CRREL
72 LYME RD
HANOVER NH 03755

KOZAK, RON
NATIONAL DATA BUOY CENTER
NSTL MS 39529

KRAVITZ, JOSEPH
OFFICE OF NAVAL RESEARCH
ARLINGTON VA 22217

KWARK, K C
NORDA CODE 251
NSTL MS 39529

LADOUCE, JEFF
COMNAVOCEANCOM
NSTL MS 39529

LANDRUM, GERALD
NORDA
NSTL MS 39529

LASSELL, DONALD
CHIEF OF NAVAL MATERIAL
ASW SYSTEMS DIVISION
DEPT OF NAVY
WASHINGTON DC 20360

LAWRENCE, MIMI
NORDA
NSTL MS 39529

LAWRENCE, THOMAS N
NORDA CODE 223
NSTL MS 39529

LEAR, W
NAVOCEANO
NSTL MS 39529

LECOURT, E J
ARCTEC INC
9104 RED BRANCH ROAD
COLUMBIA MD 21045

LENKO, DANIEL
NAVAL SURFACE WEAPONS CNTR
WHITE OAK MD 20903

LEVINE, ED
NAVAL UNDERWATERS SYSTEMS CNTR
CODE 3632
NEWPORT RI 02841

LEWANDO, A
NAVOCEANO
NSTL MS 39529

LEWIS, JAMES K
SCIENCE APPLICATIONS INT'L CORP
1304 DEACON
COLLEGE STATION TX 77840

LI, HUON
NORDA
NSTL MS 39529

LOHANICK, ALAN
NORDA
NSTL MS 39529

LOUAPRE, MERLIN
AEROJET ELECTROSYSTEMS CO
1100 W HOLLYVALE
AZUSA CA 91702

LOVE, RICHARD H
NORDA
NSTL MS 39529

MAGID, HERBERT
CHIEF OF NAVAL MATERIAL
ASW SYSTEMS DIVISION
DEPT OF NAVY
WASHINGTON DC 20360

MANG, RICHARD
NORDA
NSTL MS 39529

MARKHAM, BURT
ARCTIC SUBMARINE LAB
NAVAL OCEAN SYSTEMS CNTR
CODE 19
SAN DIEGO CA 92152

MARKHAM, DAVID
NAVWESTOCEANCEN
BOX 113
PEARL HARBOR HI 96860

MARKL, R
NAVOCEANO
NSTL MS 39529

MARLOW, MARGIE
NAVOCEANO CODE 5100
PSTL MS 39529

MARTIN, ROBERT
NORDA CODE 113
NSTL MS 39529

MARTINO, R
NAVOCEANO
NSTL MS 39529

MAST, CLARENCE
SPARTON ELECTRONICS
2400 EAST GANSON
JACKSON MI 49202

MATT, JOSEPH J III
NAVOCEANO/OP-009G
WASHINGTON DC 20350

MAY, JENNIFER
MATRIX

MCAULIFFE, WARREN
VITRO CORP
14000 GEORGIA AVE
SILVER SPRINGS MD 20910

MCCAFFREY, JOE
NORDA CODE 320
NSTL MS 39529

MCCALL, JERRY
NATIONAL DATA BUOY CENTER
NSTL MS 39529

MCDERMID, JACK
NORDA
NSTL MS 39529

MCPHERSON, TERRY
NORDA
NSTL MS 39529

MCQUEARY, WILLIAM
NAVOCEANO
NSTL MS 39529

MELE, MICHAEL
NAVAL AIR DEVELOPMENT CNTR
CODE 3041
WARMINSTER PA 18974

MELLBURG, LEONARD
NAVAL UNDERWATER SYSTEMS CNTR
CODE 3632
NEWPORT RI 02841

MEREDITH, ROGER
NORDA CODE 245
NSTL MS 39529

MERRIFIELD, R
NAVOCEANO
NSTL MS 39529

MICHELENA, ED
NATIONAL DATA BUOY CNTR
BLDG 3205
NSTL MS 39529

MICHELENA, JANET
NAVOCEANO
NSTL MS 39529

MILBURN, DARRELL
NORDA CODE 251
NSTL MS 39529

MILES, RON
NORDA
NSTL MS 39529

MILLER, RALPH
COMPUTER SCIENCES CORP
NSTL MS 39529

MILLER, ROBERT
SPARTON ELECTRONICS
1215 JEFFERSON DAVIS HIGHWAY
ARLINGTON VA 22202

MITNICK, RONALD
NAVAL UNDERWATER SYSTEMS CNTR
NEW LONDON LAB
NEW LONDON CT 06320

MOERSDORF, PAUL
COMNAVOCEANCOM
NSTL MS 39529

MOORE, C T
NAVOCEANO
NSTL MS 39529

MORISON, JAMES
POLAR SCIENCE CNTR
4057 ROOSEVELT WAY NE
SEATTLE WA 98105

MOSELEY, WILLISM
NORDA
NSTL MS 39529

MUENCH, ROBIN
SCIENCE APPLICATIONS INTL
13400B NORTHRUP WAY #36
BELLEVUE WA 98005

MURPHY, DONALD
INTERNATIONAL ICE PATROL
AVERY POINT
GROTON CT 06340

MURPHY, DONALD
NORDA
NSTL MS 39529

MUSGROVE, J W
NAVOCEANO
NSTL MS 39529

NELSON, TOM
COMNAVOCEANCOM
NSTL MS 39529

NEWCOMB, JOEL
NORDA
NSTL MS 39529

NEWMAN, DAVE
DEFENSE SYSTEMS INC
7903 WESTPARK DRIVE
MCLEAN VA 22102

NEWMAN, J F
NAVOCEANO
NSTL MS 39529

NIELSEN, RICHARD
NAVAL UNDERWATER SYSTEMS CNTR
NEW LONDON LAB
NEW LONDON CT 06320

NORTHRIDGE, BRUCE
NORDA CODE 270
NSTL MS 39529

OBROCHTA, BOB
NAVAL RESEARCH LAB
WASHINGTON DC 20375-5000

O'CONNOR, NEIL
COMNAVOCEANCOM
NSTL MS 39529

OFFUTT, JOHN
DAVID TAYLOR NAVAL SHIP R & D CNTR
BETHESDA MD 20084

OGG, BRADLEY
NAVAL ELECTRONICS SYSTEM COMMAND
WASHINGTON DC 20363

OLSEN, WAYNE
COMNAVOCEANCOM
NSTL MS 39529

O'NEILL, CHARLES J
NAVOCEANO
NSTL MS 39529

ONORATI, ROGER
NORDA
NSTL MS 39529

ORR, C
NAVOCEANO
NSTL MS 39529

OVERDEEP, SUZANNE
NAVAL UNDERWATER SYSTEMS CENTER
CODE 3632, BLDG 679/1
NEWPORT RI 02841

OWNBEY, JIM
COMNAVOCEANCOM
NSTL MS 39529

PAIGE, M
NAVOCEANO
NSTL MS 39529

PARTRIDGE, RAY
NATIONAL DATA BUOY CENTER
NSTL MS 39529

PEARSON, ROBERT
NAVAL EASTERN OCEANOGRAPHY CNTR
MCADIE BLDG
U-117 NAVAL AIR STATION
NORFOLK VA 23511

PERKINS, HENRY
NORDA
NSTL MS 39529

PFARRER, P
NAVOCEANO
NSTL MS 39529

PFEIFFER, JOHN
NAVAL ENVIRONMENTAL PREDICTION
RESEARCH FACILITY
MONTEREY CA 93943 5006

PHILLIPS, SANDY
ORI INC
6295A EDSALL ROAD
ALEXANDRIA VA 22312

PICKETT, R L
NORDA
NSTL MS 39529

PITZ, MARCELLUS
MATRIX CORP
8150 LEESBURG PIKE
SUITE 1000
VIENNA VA 22180

PLOE, ROBERT
DAVID TAYLOR NAVAL SHIP R&D CTR
BETHESDA MD 20084

POLLAK, KEN
FLEET NUMERICAL OCEANOGRAPHY CNTR
MONTEREY CA 93943

POLLIO, J
NAVOCEANO
NSTL MS 39529

POSEY, JOE
NORDA
NSTL MS 39529

POSEY, PAM
NORDA
NSTL MS 39529

PRELLER, RUTH H
NORDA
NSTL MS 39529

PRICE, WALTER
BATH IRON WORKS CO

RADL, CHARLES NAVAL RESEARCH LAB WASHINGTON DC 20375-5000	RUDOLPH, DIETER CNO (OP-952) WASHINGTON DC 20393
RAMSDALE, DAN NORDA NSTL MS 39529	RUSHTON, R S NAVOCEANO NSTL MS 39529
RESHEW, JERRY W COMNAVOCEANCOM NSTL MS 39529	RYCHNOVSKY, R.E. SANDIA NATIONAL LAB LIVERMORE CA 94550
REYNOLDS, L M NAVOCEANO NSTL MS 39529	SACKINGER, W.M. GEOPHYSICAL INSTITUTE UNIV OF ALASKA FAIRBANKS AK 99701
RICHTER-MENGE, JACQUELINE USA CRREL 72 LYME RD HANOVER NH 03755	SANDERS, PAUL NAVAL INTELLIGENCE SUPPORT CENTER 4301 SUITLAND RD WASHINGTON DC 20390
RIEDLINGER, SHELLEY NORDA NSTL MS 39529	SCARZELLO, JOHN NAVAL SURFACE WEAPONS CNTR SILVER SPRING MD 20903
RITTER, ALBERT NAVAL SEA SYSTEMS COMMAND DEPT OF THE NAVY WASHINGTON DC 20362 5101	SCHATZLE, FRANK MAR INC 6110 EXECUTIVE BLVD SUITE 410 ROCKVILLE MD 20852
ROBERTSON, TONY LOCKHEED AIRCRAFT CO P O BOX 551 BURBANK CA 91520	SCHEMP, JAMES DAVID TAYLOR NAVAL SHIP R&D CTR BETHESDA MD 20084
ROCKER, KARL NAVAL CIVIL ENG LAB PORT HUENEME CA 93041	SCHLEMMER, ROBERT NAVOCEANO NSTL MS 39529
ROGALSKI, ROBERT DAVID TAYLOR NAVAL SHIP ANNAPOLIS MD 21402	SCHMIDT, ED NAVAIRDEV CEN WARMINSTER PA 18974
ROOT, RICHARD NORDA NSTL MS 39529	SCHULTZ, LARRY ARCTEC INC 9104 RED BRANCH RD COLUMBIA MD 21045
ROSLING, THOMAS THEATER NUCLEAR WARFARE PROGRAM	SCHUSTER, JOHN NAVAL UNDERWATER SYSTEMS CNTR NEW LONDON LAB NEW LONDON CT 06320
ROSNER, HARDI NAVAL POLAR OCEANOGRAPHY CENTER 4301 SUITLAND ROAD WASHINGTON DC 20390	

SEARCY, WILLIAM
NAVOCEANO
NSTL MS 39529

SEARS, J.
NAVOCEANO
NSTL MS 39529

SEESHOLTZ, COMMODORE R
CNO (OP-952)
WASHINGTON DC 20390

SHANK, M
NAVOCEANO
NSTL MS 39529

SHARP, JIM
NATIONAL DATA BUOY CNTR
NSTL MS 39529

SHORT, JOHN
NAVAL UNDERWATER SYSTEMS CNTR
NEWPORT RI 02841

SHUCHMAN, ROBERT
RADAR DIVISION
ENVIRONMENTAL RESEARCH INST
OF MICHIGAN
P O BOX 8618
ANN ARBOR MI 48107

SIVAK, LESLIE
COMNAVOCEANCOM
NSTL MS 39529

SMART, JEFFREY
JOHNS HOPKINS UNIV
APPLIED PHYSICS LAB
LAUREL MD 20810

SMEH, NIKOLAUS
NAVAL UNDERWATER SYSTEMS CNTR
NEW LONDON LAB
NEW LONDON CT 06320

SMITS, KUNO
NORDA
NSTL MS 39529

SOKOL, DAVID
COMNAVOCEANCOM
NSTL MS 39529

SPEER, PAUL
CENTER FOR NAVAL ANALYSES
2000 N BEAUREGARD
ALEXANDRIA VA 22311

SPAGUE, V G
NAVOCEANO
NSTL MS 39529

SPIGAI, JOE
MARTIN MARIETTA AEROSPACE
BALTIMORE DIVISION
103 CHESAPEAKE PARK PLACE
BALTIMORE MD 21220

SPYCHALSKY, STEPHEN
NORDA
NSTL MS 39529

ST AMAND, PIERRE
NAVAL WEAPONS CENTER
CODE 013
CHINA LAKE CA 93555

STAHL, PETER
NAVAL UNDERWATER SYSTEMS CNTR
NEW LONDON LAB
NEW LONDON CT 06320

STARKEY, DONALD
DEFENSE SYSTEMS INC
7903 WESTPARK DRIVE
MCLEAN VA 22101

STEPHENS, JOHNNY
TRITON SYSTEMS INC
109 E SCENIC DR
PASS CHRISTIAN MS 39571

STINUS, JOE
NAVOCEANO
NSTL MS 39529

STRATHMAN, PHYLLIS
COMNAVOCEANCOM
NSTL MS 39529

STUERMANN, WALT
NAVSEA CODE 92D
NAVAL SEA SYSTEMS COMMAND
DEPT OF THE NAVY
WASHINGTON DC 20362

TARANTO, RICHARD
ANALYSIS AND TECHNOLOGY INC
2611 JEFFERSON DAVIS HIGHWAY
ARLINGTON VA 22202

TAPPERT, FREDERICK
DAUBIN SYSTEMS CO

THEIS, GARY
NAVAL SYSTEMS WEAPONS CNTR
10901 NEW HAMPSHIRE
SILVER SPRING MD 20903

THOMAS, BOB
SANDIA NATIONAL LAB
P O BOX 5800
ALBUQUERQUE NM 87185

TIPPER, RON
NAVAL POLAR OCEANOGRAPHY
9819 SUMMERDAY DRIVE
BURKE VA 22015

TITUS, JAMES
GENERAL DYNAMICS
79 CHARTER OAK DRIVE
EAST LYME CT 06333

TOLSTOY, ALEX
NAVAL RESEARCH LAB
WASHINGTON DC 20375 5000

TOOMA, SAM
NORDA
NSTL MS 39529

TOWLES, TERRY
COMPUTER SCIENCE CORP
NSTL MS 39529

TUCKER, WALTER
USA CRREL
72 LYME ROAD
HANOVER NH 03755

TUPAZ, JESS
COMNAVOCEANCOM
NSTL MS 39529

UNTERSTEINER, NORBERT
APPLIED PHYSICS LAB
UNIV OF WASHINGTON
1013 NE 40TH ST
SEATTLE WA 98105

VALENT, PHILIP
NORDA
NSTL MS 39529

VENSKÉ, NORMAN
COMMANDANT (G-010)
US COAST GUARD HEADQUARTERS
2100 SECOND ST SW
WASHINGTON DC 20593

VINSON, P
NAVOCEANO
NSTL MS 39529

VISITAINER, R
NAVOCEANO
NSTL MS 39529

VON DER HEYDT, KEITH
WOODS HOLE OCEANOGRAPHIC INST
WATER STREET
WOODS HOLE MA 02543

VON ZWECK, ORTWIN H
NAVOCEANO
NSTL MS 39529

VOTAW, CHARLES
NAVAL RESEARCH LAB
WASHINGTON DC 20375-5000

WARGELIN, R
NAVOCEANO
NSTL MS 39529

WARN VARNAS, ALEX
NORDA
NSTL MS 39529

WEAVER, RONALD
CIRES
UNIV OF COLORADO
BOULDER CO

WELSH, PAT
NORDA
NSTL MS 39529

WEEKS, W F
USA CRREL
72 LYME RD
HANOVER NH 03755

WHEATLEY, BOB
NORDA CODE 270
NSTL MS 39529

WHICKER, FOLGER
NORDA
NSTL MS 39529

WIDHALM, KENNETH
CHIEF OF NAVAL MATERIAL
ASW SYSTEMS DIV
DEPT OF NAVY
WASHINGTON DC 20360

WIESENBURG, DENIS
NORDA
NSTL MS 39529

WILEM, FRANK
TRITON SYSTEMS INC
109 E SCENIC DRIVE
PASS CHRISTIAN MS 39571

WILKINSON, RICHARD
NORDA
NSTL MS 39529

WILLIAMS, NEIL
UNIV OF MIAMI
4600 RICKENBACKER CSWY
MIAMI FL 33149

WILSON, BRETT
NDBC
NSTL MS 39529

WILSON, JAMES
POLAR RESEARCH LAB
6308 CARPINTERIA AVE
CARPINTERIA CA 93013

WON, I J
NORDA
NSTL MS 39529

WOODFIN, RONALD L
SANDIA NATIONAL LAB
ORG 333
P O BOX 5800
ALBUQUERQUE NM 87185

WOODS, JOHN
NAVOCEANO
NSTL MS 39529

YEW, C H
DEPT AEROSPACE ENGINEER
RM 316 WRW
UNIVERSITY OF TEXAS-AUSTIN
AUSTIN TX 78712

YULE, ROBERT
LOCKHEED ADVANCED MARINE SYSTEMS
P O BOX 4000
SANTA CLARA CA 95054

ZAROFF, JOSEPH
NAVAL AIR DEVELOPMENT CNTR
WARMINSTER PA 18974

ARCTIC OCEANOGRAPHY LISTING OF ATTENDEES BY ORGANIZATION

Advanced Marine Systems

Yule, Robert B.

Aerojet Electrosystem Com.

Louapre, Merlin E.

Analysis & Technology Inc.

Taranto, Richard

Antisubmarine Warfare Systems Project

Flum, Robert S.

Lassell, Donald L.

Magid, Herbert

Widhalm, Kenneth C.

Applied Mathematics Inc.

Angell, Gordon

Applied Physics La, Johns Hopkins University

Smart, Jeffrey

Applied Physics Lab, University of Washington

Garrison, Gerald R.

Harlett, John C.

Heiberg, Andreas

Morison, James H.

Untersteiner, Norbert

Applied Research Lab, University of Texas

Koch, Robert A.

Yew, Chinghsie

Arctec Inc.

Grosskopf, William G.

Lecourt, Everett J. Jr.

Schultz, Lawrence A.

Atlantic Applied Research

Abbot, Philip Allen

Brown, Neal A.

Bath Iron Works Corp.

Price, Walter W., III

Center for Naval Analyses

Speer, Paul E.

Central Intelligence Agency

Kahn, Norman M.

Chief of Naval Materials

Brady, James H. R. CDR

Chief of Naval Operations

Barnes, Robert C.

Commander, Naval Oceanography Command

Betcher, Robert

Cousins, Bernard

Cummings, T.

Delaney, Dennis LCDR

Evans, Richard H.

Garcia, Ronald A. CDR

Gebhardt, Richard K.

Hinman, Kendall CPT

Koehr, James E. CPT

LaDouce, Jeff

Moersdorf, Paul

Nelson, Thomas S. CDR

Nielsen, Richard J.

O'Connor, Neil F.

Olsen, Wayne CDR

Ownbey, James W.

Reshew, Jerry

Rudolph, Dieter K. CDR

Seesholtz, John

Sivak, Leslie

Sokol, David C.

Strathman, Phyllis

Tupas, Jesus B. CPT

Computer Science Corp.

Miller, Ralph

Towles, Terry L.

D W Taylor Naval Ship R & D Center

Arveson, Paul T.

Bales, Susan L.

Kordenbrock, James U.

Offutt, John D.

Ploe, Robert J.

Rogalski, Robert D.

Schemp, James D.

Daubin Systems Corp.

Tappert, Frederick D.

Defense Systems Inc.

Starkey, Donald L.

Newman, David R.

Environmental Research Institute of MI

Shuchman, Robert A.

ENVIROSPHERE, INC.

Hachmeister, Lon

Fleet Numerical Oceanography Center

Pollak, Kenneth D.

General Dynamics

Featherstone, John M.

Green, John M.

Titus, James M.

Geophysical Institute, University of Alaska

Sackinger, William M.

Greeneridge Sciences

Greene, Charles

International Ice Patrol

Murphy, Donald L.

Lockheed

Robertson, Anthony W.

Mar, Inc.

Schatzle, Francis Joseph

Martin Marietta

Spigai, Joseph J.

Matrix Corp.

May, Jennifer T.

Pitz, Marcellus

National Data Buoy Center

Canada, Raymond H. J.

Erichsen, Robert L.

Grassit, Kip

Harlett, John

Kies, Phil

Kozak, Ronald P.

McCall, Jerry

Michelena, Eduardo

Partridge, Ray Mikel

Sharp, James

Wilson, Warren B.

Naval Air Development Center

Elchenko, Stephen M.

Horbach, Arthur W.

Mele, Michael V.

Schmidt, Edward T.

Zaroff, Joseph W.

Naval Civil Engineering Lab

Rocker, Karl Jr.

Naval Eastern Oceanography Center

Donovan, Barry M. LCDR

Pearson, Robert T. CDR

Naval Environmental Prediction Research Facility

Hoverdale, John B.

Pfeiffer, John F. CDR

Naval Intelligence Support Center

Kelley, Edward J.

Sanders, Paul A.

Naval Ocean Research & Development Activity

Andrews, E. Dr.

Branch, George H.

Bucca, Paul J.

Burge, Raymond

Burke, Travis A.

Caruthers, Jerald

Chin Bing, Stanley A.

Cranford, Kenneth E.

Durham, Donald

Eppler, Duane T.

Fagot, Martin G.

Farmer, L. Dennis

Farquhar, Brooke

Farwell, Robert W.

Ferer, Kenneth M.

Fisher, Robert A.

French, Jon

Green, Albert W. Jr.

Grussendorf, Mark J.

Holland, C Randy

Horsley, Laverne E.

Kelly, R. G.

Kerr, George A.

Ketchum, Robert D. J.

Knott, Martha E.

Kwark, K. C.

Landrum, Gerald W.

Lawrence, Mimi Z.

Lawrence, Thomas N.

Li, Huon

Lohanick, Alan W.

Love, Richard H.

Mang, Richard A.

Martin, Robert L.

McCaffrey, Joe

McDermid, Jack G.

McPherson, Terry LCDR

Meredith, Roger W.
Milburn, Darrell
Miles, Ron
Moseley, Willis M.
Murphy, Donald A.
Newcomb, Joel J.
Northridge, Bruce W.
Onorati, Roger CPT
Perkins, Henry T.
Pickett, Robert L.
Posey, Joe W.
Posey, Pam G.
Preller, Ruth H.
Ramsdale, Dan J.
Riedlinger, Shelley K.
Root, Richard M.
Smits, Kuno
Spychalsky, Stephen E.
Tooma, Samuel G. Jr.
Valent, Philip
WarnVarnas, Alex
Welsh, Pat
Wheatley, Bob
Whicker, Folger
Wiesenburg, Denis
Wilkinson, Richard
Won, I J

Naval Ocean Systems Center

Beal, M. A. Dr.
Floyd, Edward R.
Gordon, David F.
Judd, Randall R.
Markham, Burton L.

Naval Oceanographic Office

Allen, J.
Atkinson, K.
Avery, O.
Barrett, R.L.
Beatty, William
Beeson, E.L.
Blaha, J.
Blumenthal, Richard
Brown, W.E.
Car, Martial
Carnes, Mike
Carroll, J.C.
Collier, Martin
Costolo, J. Houston
Crumpler, A.
Cummings, B.
Davis, Thomas

Deblanc, Betty
Dipiazza, Nicholas
Evans, Richard
Frank, L.
Hart, W.
Haeger, Steve
Higgs, R.
Jobst, W.J.
Keiffer, Richard
Kerling, Jeffrey
Lear, W.
Lewando, A.
Markl, R.
Marlow, Margie
Martino, R.
Matt, Joseph J III
McQueary, W.B.
Merrifield, R.
Michelena, Janet
Moore, C. T.
Musgrove, G. W.
Newman, J. F.
O'Neill, Charles
Orr, C.
Paige, Marshall
Pfarrer, P.
Pollio, J.
Reynolds, L. M.
Rushton, R. S.
Schlemmer, Robert
Searcy, William
Sears, J. CPT.
Shank, M.
Sprague, U. G.
Stinus, Joseph W.
Vinson, P.
Visitainer, R.
Von Zweck, Ortwin
Wargelin, R
Woods, John

Naval Polar Oceanography Center

Anderson, John
Rosner, Hardi S.
Tipper, Ron

Naval Postgraduate School

Geernaert, Gerald L.

Naval Research Lab

Brozena, John M.
Cherkis, Norman Z.
Dicus, Ronald L.

Hollinger, Jim
Obrochta, Bob
Radl, Charles J.
Tolstoy, Alexandria I.
Votaw, Charles W.

Naval Sea Systems Command

Ritter, Albert D.
Stuermann, W. P. CDR

Naval Surface Weapons Center

Lenko, Daniel S.
McClure, Charles F.
Scarzello, John
Theis, Gary A. LCDR

Naval Underwater Systems Center

Arron, Arnold
Bishop, Garner
Dohoda, Terena M.
Donald, James
Fecher, Michael P.
Hill, Paul D. LT
Goldsby, Richard E.
Levine, Ed
Mellburg, Leonard
Mitnick, Ronald W.
Ogg, Bradley R. LT
Overdeep, Suzanne
Schuster, John G.
Short, John
Smeh, Nikolaus J.
Stahl, Peter B.

Naval War College

Jensen, John A.

Naval Weapons System Center

St. Amand, Pierre

Naval Western Oceanography Center

Markham, David G. LCDR

ODSI Defense Systems Center

Henderson, J. Russell

Office of Naval Research

Blizard, Marvin
Horn, Dean A
Kravitz, Joseph

ORI Inc.

Phillips, Sandy

Planning Systems Inc.

Geddes, Wilburt
Gough, Ed

Precision Echo Inc.

Harvey, Phil

R & D Associates

Greifinger, Phyllis

Sandia National Lab

Rychnovsky, R. E.
Thomas, Bob

Science Applications Int'l Corp.

Denner, Warren
Englebretson, Ron
Greene, Robert
Keenan, Ruth
Lewis, James K
Muench, Robin

Sippican

Hannon, James

Sparton Electronics

Bush, Carroll
Mast, Clarence
Miller, Robert

Tetrattech Inc.

Clark, Dick

Theater Nuclear Warfare Program

Rosling, Thomas

Tracor

Bonnett, David

Triton Systems Inc.

Burdette, Ernest L.
Stephens, Johnny
Wilem, Frank

University of Colorado

Weaver, Ronald

University of Miami

Williams, Neil

USA CRREL

Cox, Gordon
Gow, Anthony

Jezek, Ken
Kovacs, Austin
Richter-Menge, Jacqueline
Tucker, Walter
Weeks, W F

US Coast Guard
Brigham, Lawson W.
Hayes, Richard
Venske, Norman

VITRO Corp.
McAuliffe, Warren

Woods Hole Oceanographic Inst.
Von Der Heydt, Keith

U221977